AVC-VTN-15-G06

"Underground Explosions"

By
Vitaly V. Adushkin and Alexander Spivak

Translated from Russian to English
By
Anastasia Stroujkova and Paul Richards

Final Technical Report
DOS Contract No. SAQMMA13M2475

Prepared for
Air Force Technical Applications Center
Directorate of Nuclear Treaty Monitoring (HQ AFTAC/TT)
Patrick Air Force Base, FL 32925

Sponsored and Monitored by
U.S. Department of State / AVC
2201 C Street, NW
Washington, DC 20520

September 9, 2015

REPORT DOCUMENTATION PAGE

Form Approved
OMB No. 0704-0188

1. REPORT DATE *(DD-MM-YYYY)*	2. REPORT TYPE	3. DATES COVERED *(From - To)*
09/09/2015	Final Technical Report	30/09/2013 - 09/09/2015

4. TITLE AND SUBTITLE
Translation of Russian Language Book "UNDERGROUND EXPLOSIONS"
Drs. Vitaly V. Adushkin and Alexander A. Spivak

5a. CONTRACT NUMBER
SAQMMA13M2475

5b. GRANT NUMBER

5c. PROGRAM ELEMENT NUMBER

6. AUTHOR(S)
Dr. Anastasia Stroujkova and Professor Paul Richards

5d. PROJECT NUMBER

5e. TASK NUMBER

5f. WORK UNIT NUMBER

7. PERFORMING ORGANIZATION NAME(S) AND ADDRESS(ES)
Weston Geophysical Corp.
181 Bedford St., Suite 1
Lexington, MA 02420

8. PERFORMING ORGANIZATION REPORT NUMBER
WGC-2015-03

9. SPONSORING/MONITORING AGENCY NAME(S) AND ADDRESS(ES)
U.S. Department of State
2201 C Street NW
Washington, DC 20520

10. SPONSOR/MONITOR'S ACRONYM(S)
DOS/AVC/MNA

11. SPONSOR/MONITOR'S REPORT NUMBER(S)

12. DISTRIBUTION/AVAILABILITY STATEMENT
UNLIMITED

13. SUPPLEMENTARY NOTES

14. ABSTRACT
“Underground Explosions”, a Russian language book authored by Drs. Vitaly V. Adushkin and Alexander A. Spivak has been translated into the English language, with support from Bureau of Arms Control, Verification, and Compliance, U.S. Department of State, under DOS award SAQMMA13M2475.

15. SUBJECT TERMS
Underground explosions, underground nuclear explosions, nuclear test moniotring

16. SECURITY CLASSIFICATION OF:			17. LIMITATION OF ABSTRACT	18. NUMBER OF PAGES	19a. NAME OF RESPONSIBLE PERSON
a. REPORT	b. ABSTRACT	c. THIS PAGE			Rongsong JIH (COR@DOS/AVC)
					19b. TELEPHONE NUMBER *(Include area code)*
Unclassified	Unclassified	Un-Classified	UU	563	202-647-8126

(THIS PAGE INTENTIONALLY LEFT BLANK)

V. V. Adushkin and A. A. Spivak

Underground Explosions

September 30, 2015

Contents

Introduction

Interest in phenomena associated with large underground explosions increased significantly following the original development of nuclear weapons. The need to conduct nuclear tests under the ground, and the opportunities to use nuclear explosions for industrial applications (mining, using nuclear explosions as sources of seismic waves for seismic sounding of large territories, etc.) led to a critical need for comprehensive study of the various features of nuclear explosions. Noteworthy also is a political value of nuclear weapons, as a factor providing global stability in relationships between different countries.

This book describes the results of fundamental research related to nuclear explosions as a powerful source of seismic waves in the medium, whose value will only increase with time.

Looking at the history of nuclear testing we note the dates of the first nuclear explosions conducted by different countries:

1. July 16, 1945 first nuclear explosion (USA, Alamogordo, NM);
2. August 29, 1949 first nuclear test in the USSR (Semipalatinsk Test Site);
3. October 3, 1952 first nuclear test conducted by the United Kingdom (Australia Test Site); [This was on an island offshore Australia, and it's not appropriate to indicate that Australia had a test site]
4. November 1, 1952 first thermonuclear test (USA, South Pacific, Eniwetok Atoll);
5. August 12, 1953 first thermonuclear test conducted in the (former) Soviet Union
6. February 13, 1960 first nuclear test conducted by France (Reggane Test Site, Sahara);
7. October 16, 1964 first nuclear test in China (Lop Nor);
8. September 22, 1979 joint nuclear test between South Africa and Israel (in southern Atlantic Ocean).[1]

We note that the nuclear test of September 22, 1979 (the so-called event 747) was detected by an American satellite (VELA) above the southern Atlantic Ocean. Based on the intensity of the fireball and the duration of the radiated signal the yield has been estimated as approximately 2-3 kt ("Izvestiya" of April 29, 1985). According to the press ("Izvestiya" March 20, 1981) there was a second test conducted by South Africa on December 15, 1980. Official reports about these nuclear tests conducted jointly by the South Africa and Israel were released by TASS (the official Telegraph Agency of the Soviet Union) in 1979 – 1980.

The several international treaties progressively banning more and more types of nuclear explosive tests are historical milestones, on the way to an eventual comprehensive ban on nuclear weapons tests:

[1] In western forums, the very existence of this test is disputed, and if it was conducted by Israel then it is not clear there was the involvement of South Africa. Can the Russian authors supply us with Russian sources of information on this event showing that is was a nuclear test by Israel? That is, with the content of the material released by TASS, as given in the paragraph that follows the link to this footnote?

- LTBT (the Limited Nuclear Test Ban Treaty) – a treaty banning all nuclear tests in three media: atmosphere, space, and underwater, signed in Moscow August 3, 1963; entered into force October 10, 1963.
- TTBT (the Threshold Test Ban Treaty between the USSR and USA) – a treaty limiting the yield of tests on nuclear test sites at 150 kt, signed in Moscow, July 3, 1974, entered into force December 11, 1990.
- PNET (the Peaceful Nuclear Explosion Treaty between the USSR and USA), signed in Moscow May 28, 1976, entered into force December 11, 1990.
- CTBT (Comprehensive Nuclear-Test-Ban Treaty) negotiated in Geneva, opened for signature at the United Nations, New York on September 24, 1996, and now signed by over 180 countries, but not yet entered into force as of March 2014.

The LTBT of 1963 considerably reduced environmental damage from radioactive explosion products, but did not stop research and development of nuclear weapons (more than 1500 underground test explosions were conducted after 1963).

The first underground nuclear explosions conducted by different countries were:

1. November 29, 1951 — USA (Nevada Test Site);
2. October 11, 1961 —USSR (Semipalatinsk Test Site);
3. November 7, 1961 — France (Reggane, Sahara);
4. March 1, 1962 — England (Nevada Test Site, USA);
5. September 23, 1969 — China (Lop Nor);
6. May 18, 1974 — India (Thar);
7. May 28, 1998 — Pakistan (Pokhran).

The first underground nuclear test in the USA was conducted at the Nevada Test Site on November 29, 1951. This test with a code name JANGLE-UNCLE had a yield of 1.2 kt and was conducted at a depth of 5.2 m in alluvium. The explosion created a crater with a radius of 39.6 m and a depth of 16.2 m. The second underground nuclear test (TEAPOT-S, 1.2 kt) was also conducted in alluvium. It was at a depth of 20.4 m and also created a crater with radius 44.5 m and a depth of 27.2 m. In 1957 five underground nuclear tests were conducted, three of them in boreholes, and the other two in tunnels. These explosions included the first contained nuclear test, RAINIER, with a yield of 1.7 kt, that was emplaced and tamped in a tunnel in tuff. A contained explosion means one that does not produce significant deformation at the surface, and the release of radioactive products is either absent or is reduced to insignificant gas seepage. [2]

The USSR started to prepare for underground testing in 1959, when two large chemical explosions were conducted in Tyuya-Muyun Mountain (Kyrgizstan). These explosions had yields of 190 t and 600 t. They were conducted in order to determine the depth of burial needed to provide full containment. Since the first underground nuclear explosion was planned to be

[2] The adjective “camouflet” is often used in Russian where western writers would use “contained” or “fully-contained.” We shall often use the Russian word later in this book. (Note added by translators.)

conducted at the Degelen Testing Area (of the Semipalatink Test Site), another 600 t chemical explosion was carried out in a neighboring tunnel (B-2t) in order to determine the depth of burial for the nuclear explosion. The first underground nuclear explosion in the USSR was conducted on October 11, 1961, in Tunnel B-1 (1.2 kt, depth of burial – 118 m). During the same year France conducted its first underground nuclear test in the granite massif at the Reggane Test Site (Sahara desert). This explosion with a yield of approximately 20 kt had a code name AGATE.

Five more countries with nuclear weapons later started underground nuclear testing (China, India, Pakistan, South Africa and Israel).[3] Table 1 shows the number of nuclear tests conducted by all countries with nuclear weapon capabilities, based on published data (e.g. Bocharov et al, 1998; Summary…, 1993; Nuclear…, 1997).

Thus, 2152 nuclear tests were conducted by all countries (possessing nuclear weapons) between 1945 and 1998. Of those 525 nuclear explosions were conducted in atmosphere and space, 19 of those were conducted at depths between 10 and 500 km. Eight nuclear tests were conducted underwater.

The period of intensive underground testing began in the USSR in 1961-1962 and continued until 1987-1989. During this period between 40 and 70 nuclear tests were conducted each year globally. During this time USA and the USSR conducted 149 peaceful nuclear explosions intended for the deep seismic sounding, oil and gas production, creating under- ground cavities for storage of gas condensate and industrial waste, extinguishing burning oil wells, fragmentation of the deposits, and construction of of water reservoirs and channels.

The USSR conducted 748 nuclear tests, 522 of which were underground. In this book the term underground test means detonation of one or more nuclear devices in the same tunnel or borehole. If we assume that the term underground test means simultaneous or close in time explosions (but not necessarily closely spaced), then the number of Soviet nuclear tests becomes 715, with 969 detonated devices (Nuclear…, 1997).

The USA conducted 1087 nuclear tests, 870 of which were underground. We note that different publications report different numbers. For example, according to the DOE data, the total number of nuclear tests is 1051 (Summary, 1993), while the publication Nuclear (1997) has a number 1056 nuclear tests with 1151 nuclear devices. Other publications (e.g. New…, 1991; Chronology…, 1996) show that there were 1085 and even 1099 nuclear tests. This discrepancy is caused by different definitions of the term nuclear test. For example, according to the DOE detonation of several nuclear devices within 0.1 s located within 2 km from one another considered a single nuclear test.

The last nuclear test in the USSR was conducted on 10.24.1990 at Novaya Zemlya test Site. The USA conducted their last nuclear test on 09.23.1992 at the Nevada Test Site. France and China ended their nuclear testing during the year when the CTBT was signed (01.28.1996 and 07.29.1996 respectively). After a single nuclear test in 1974, India conducted three nuclear tests on 05.11.1998 and two nuclear tests on 05.13.1998. Pakistan joined the nuclear testing on

[3] This statement, including Israel as a nation that has conducted nuclear testing, was the official view of the Soviet Union, and we have simply translated the Russian text here. (Note added by translators.)

05.28.1998 detonating five nuclear devices simultaneously, and concluded testing on 05.30.1998. Pakistan joined the nuclear testing on 05.28.1998 detonating five nuclear devices simultaneously, and concluded testing on 05.30.1998 by detonating two more nuclear devices. The explosions conducted in 1998 by India and Pakistan conclude the nuclear testing (according to current policy).

Creation of nuclear weapons required research into nuclear explosion effects on military and civilian infrastructure, and consequences for the environment, which has led to several new developments in science and technology. In the end, these fundamental studies opened a new page in our understanding of high energy physical processes carried out on our planet.

For example, creating nuclear charges involved developing completely new technologies related to high energy plasma at high pressure and temperature, and interaction between the radiation (possibly electromagnetic) from the explosion and the surrounding medium. As a result, a new theory of thermonuclear reactions has been developed and confirmed by experiments during the largest hydrogen (thermonuclear) tests.

Studies conducted during the preparations for nuclear tests in different media (underground, underwater, atmospheric) were important for studies of the Earth and for development of new directions in geophysics. Nuclear tests had significant effects on the environment and were accompanied by very complex phenomena, such as large-scale irreversible changes to the materials and to the physical properties of continuous media including, thermal effects, electromagnetic and nuclear radiation, as well as the formation of different types of waves (shock, seismic, electromagnetic).

Unique experimental data were obtained as a result of these studies, which provided the basis for an important conclusion about the uncertainty of the effects of the strong energy sources on the medium, which in its background (ambient) state is in constant motion due to internal and external energy sources (the distance scale of the disturbance to the equilibrium, in this case, is close to the size of a natural evolving cell). In the beginning of the nuclear testing period, geophysical methods were not developed enough to evaluate the effects and the consequences of nuclear explosions. There was a need to reevaluate the established and simplified view of (certain) geophysical processes (in the natural medium).

Experimental instrumentation existing at the time was not adequate for measurements of the physical phenomena caused by nuclear explosions in different media (in atmosphere, space, water and underground). Therefore new equipment had to be developed in order to determine the damaging factors of the nuclear weapons, to develop protective measures against nuclear explosions, and to develop technologies for safe nuclear testing. Some examples of the new equipment include developing high-speed optical recording systems capable of recording 2-3 millions frames per second, heat, light, roentgen and radiation detectors, new seismic recorders with high sensitivity and broad frequency range.

Solution of the problems related to nuclear explosions in different media (atmosphere, space, water and underground) required separate theoretical and experimental investigations. There were no existing recipes and solutions. In some cases new and unexpected results were obtained

during the nuclear experiments. Processing and analysis of the experimental data resulted in developing of the new theories regarding the explosions and related phenomena, as well as the response of the geological medium to the strong disturbances.

For example, the theory of a strong point explosion was developed as a result of the first atmospheric explosions (e.g. Sedov, 1967).[4] Academician S. A. Christianovich developed a new theory for a "gas-dust thermic," meaning a rising vortex due to an extremely hot mass of lower density, with a formation of a toroidal ring. He included the irregular reflection of weak shock waves, taking into account nonlinear effects (Christianovich, 1998). Conducting near-surface nuclear explosions enabled the unexpected discovery of "separation of the shock front', sometimes called "hydrodynamic separation" together with reconstruction of the hydrodynamic flow due to formation of thermal boundary layer, created by faster heat and visible light radiation (Sadovskii and Adushkin, 1988). This effect allowed development of a new scaling theory of gas dynamic flows (Taganov, 1968).

A series of previously undiscovered geophysical phenomena were observed following nuclear explosions in space, including prolonged glowing in the atmosphere, formation of extremely strong auroras, and long-term changes in the structure and electrical conductivity of the ionosphere. These phenomena, caused by nuclear explosions in space, have significantly broadened our understanding of various physical and chemical processes taking place in the atmosphere/ionosphere/magnetosphere system. These observations stimulated fundamental research that continues today.

Studies of underground nuclear explosions play important role in scientific study of the structure and dynamic processes of the Earth crust. An underground nuclear explosion entails a complex process, including a sequence of related processes of different nature: formation of the plasma cloud, formation of the hydrodynamic zone within the solid matter, shock front propagation, deformation and damage of the emplacement medium including formation of the hierarchical block structure, and finally seismic wave propagation.

Studies of the effects of the underground nuclear explosions in the Earth crust include the following four aspects:

- Study of large scale explosions for military purposes (e.g. Physics, 1997; Mechanical, 2002).
- Study of the mechanical effects of nuclear explosions in order to use them for peaceful purposes (Johnson and Higgins, 1965; Kedrovskii et al, 1970).
- Study of evolutionary patterns in geological media with complex structure at different levels (scales) in order to use nuclear explosions as an instrument of intensifying energy and mass exchange, as well as for deformation and relaxation processes (Kocharyan and Spivak, 2004).

[4] The original work was done by Taylor (1941) and von Neumann (1941), and was discovered independently by Sedov in1946, who published it much later. (Note added by translators.)

- Study of the effects of nuclear explosions in order to monitor for the occurrence of nuclear testing, which is important to support non-proliferation of nuclear weapons and monitoring of the international treaties (e.g. Seismic, 1992).

We note that the theory of underground explosions was developed as a result of the experimental and theoretical studies of the processes following the nuclear explosions as well as the study of rock deformation subjected to dynamic stresses of different intensity (e.g. Rodionov et al, 1971). Based on this theory the important characteristics of underground explosions, including the cavity size, extent of the different damage zones, seismic wave parameters, can be determined from elastic and strength characteristics of the emplacement rocks.

Studies of underground explosions has led to significant progress in the development of geomechanics a science studying mechanical properties of rocks and rock massifs, ambient stresses in the rock formations, and deformation and damage processes due to natural and man-made causes.

As a result of these studies the following problems were solved: determining safety and stability of underground structures subjected to large underground explosions, possibilities of peaceful use of nuclear explosions in order to create underground cavities in salt and hard rocks, fragmentation of rock underground during mining operations, degassing of the coal seams and other industrial applications. Studies were performed to investigate dynamic structures involving faults and block motion associated with deformation of heterogeneous rock massifs, as well as the dependence of these phenomena on the scale of external forces and the speed of deformation (e.g. Rodionov, 1986).

Development of the solid state theory allowed predicting the evolution of the deformation of the rock massifs (formations) in time, as well as the models of the hierarchical block movement and their deformation taking into account their differential movement with restricted rotations. In addition new views on the seismic regime of the earth crust as deformation process due to stress and strain accumulation at heterogeneities and near tectonic faults (e.g. Adushkin and Spivak, 1993; Kocharyan and Spivak, 2002).

Study of the deformation of the block medium during underground nuclear explosions of different yields provided unique material, which can be used to develop theoretical models of the mechanics of block-hierarchical media. In this case the explosion can be viewed as an instrument (or tool) to study properties of geophysical media.

The experimental data accumulated to this day shows that continuum mechanics and linear elasticity cannot adequately describe deformations of geologic systems and in situ rock. The behavior of block media involves relative movement of different blocks along tectonic faults, which cannot be described using continuum models.

Indeed, presence of structural discontinuities (faults and fractures) significantly complicates the medium description and our ability to predict the effects of underground nuclear explosions. This often leads to unusual effects caused by local discontinuities within the medium, sometimes at distances where the strong effects should not be observed. This is important to take into account when designing important structures, as well as for providing seismic and radiation

safety measures during large scale explosions, including the problems related to escape (release) of gas products into the atmosphere.

The formation and evolution of each geological structure determines the specific hierarchy of structural discontinuities (faults), and as a result its block structure. A real geological structure such as a rock massif has preexisting structural discontinuities of different scales: from 10^{-8} m (defects of the crystalline structure) to 106 m (length of the largest tectonic faults). This difference in the scale length determines not only the broad spectrum of the structural element sizes, but also the mechanical effects of underground nuclear explosions at different distances from the source. The block structure of a real geophysical medium causes inhomogeneous deformations due to external forces. Indeed, the average deformation of the medium represents a combined deformation of blocks and the deformation of the material between the blocks. Since the material between the blocks is often softer (less strong) than the rock, the deformation of the block medium typically takes place along the boundaries between the blocks and along the zones made of weaker material (e.g. Kocharyan ad Spivak, 2003).

Seismic waves radiated by the nuclear explosions turned out to be very informative tool to study the geological structure of the crust as well as the entire Earth (Adushkin et al, 1996). Significant advantage of using nuclear explosions as seismic sources is the fact that their coordinates and origin times are known. Due to the significant energy released by nuclear explosions the waves can be detected at large distances. In addition, the explosion source mechanism is less complex than the earthquake source mechanism. Therefore, the waves produced by explosions have more impulsive first arrivals, which simplifies their analysis.

These advantages were utilized during deep earth sounding in order to determine the new prospects for oil, gas and other natural resources (e.g. Nuclear, 1997). Thirty nine underground nuclear explosions were conducted along 14 different profiles with combined length of 70,000 km. The length of separate profiles was between 1,500 and 4,000 km, while the number of the shot points for each profile varied between 3 and 5 with the distances between the shot points of 500-900 km.

The data obtained as a result of this work include the depth structure of different regions of the country (FSU, A.S.) in a form of long velocity profiles through the crust and reaching into the upper mantle. Seismic sounding results confirmed the existence of ten gas and gas-condensate deposites in the area of the Enisei-Khatanga depression, and about ten others in the areas of Vilyuy syncline and Verchoyansk depression.

New results related to the dynamics of the Earth core was obtained by the authors by analyzing the travel times of the waves from nuclear explosions at Novaya Zemlya recorded at Station Novolazarevskaya (NVL) in Antarctica between 1966 and 1990 (Adushkin et al, 1998). The results of the data analysis for the 25 year period have shown that the travel time difference for PKP phase that traveled through the liquid and the solid core changes in time. The travel time differences were explained by the differential rotation of the solid inner core with respect to the earth as a whole with a speed of $1.3 \pm 0.5°$ per year. This result is very important for

understanding of the nature of the Earth magnetic field, which is generated by the electrical currents inside the outer core.

Another original result was obtained while analyzing the data for PKiKP phases reflected from the Earth's inner core and detected at small epicentral distances from nuclear explo- sions at the Semipalatinsk Test Site along the line STS BRVK at the Borovoye Geophysical Observatory (BRVK), at a distance of approximately 6º. All earlier recorded PKiKP data were recorded in the distance range $20^\circ < \Delta < 40^\circ$. The average travel time for these phases detected at BRVK was 17 min, with periods in the range 0.42 – 0.62 s, and the peak-to-peak amplitudes were in the range 4.5 – 12.2 nm.

The observed travel times and amplitudes suggest the possibility of a high-velocity layer at the base of the liquid outer core, with thickness of approximately 3 km, density of 12,100 kg/m3, the *P*-wave velocity of 12 km/s, and the a density jump of 600 kg/m3 (Adushkin et al, 1998). One of the possible causes of existence of this layer is probably a differential rotation of the solid inner core with respect to the Earth as a whole, described earlier (the inner core rotates faster than the planet).

Robust detection of the PKiKP and PKP phases provides an independent opportunity to study the effects of the differential rotation of the Earth's inner core. The results of the seismic studies using nuclear explosions support the need to consider temporal changes in the medium, as part of the development of Earth models.

This monograph reflects major results of the authors' work related to the mechanical and seismic effects of underground explosions conducted at the Semipalatinsk and Novaya Zemlya Test Sites, as well as for peaceful nuclear explosions.

Major features and effects of large explosions are considered from the point of view of prediction of the deformation of the real geophysical media, and include

- damage and fragmentation at different distances from an explosion,
- changes to the medium porosity and permeability.

The latter is important for providing safety during nuclear explosions, as well as for justifying use of large underground explosions for non-traditional technologies (such as preparation of the large ore bodies for in situ leaching, underground gasification of coals, underground melting of sulfur, fragmentation of rocks, and intensifying the production of oil and gas.

After a brief overview of the effects of underground explosions as a whole (in Chapter 1), we describe the surface effects of underground explosions. Early chapters emphasize nuclear explosions, and the comparison with shallow chemical explosions is deferred to Chapter 10. Thus, Chapter 2 describes field observations of the ejection action of nuclear explosions. The effects of gas content (production) of the medium on the size of the craters are shown. Under-buried nuclear explosions and formation of craters and retarcs are described in Chapter 3.

A large section (Chapter 4) deals with seismic effects of underground nuclear explosions. Particular attention is given to the effects of structural and tectonic features on seismic wave propagation.

Chapter 5 provides the results of studies of the fluid-filtering properties (associated with porosity and permeability) of the broken rock mass in the vicinity of underground nuclear explosions, as well as some effects related to its granularity and structural characteristics.

A significant section of the book is devoted to physical modeling of a point charge in different types of solids to represent various rock media (Chapter 6). We describe major quantitative effects of an explosion on a solid medium, when medium properties do not significantly influence specific mechanical effects. A section describing explosions in compressible media is developed separately. The derived characteristics of a deformed medium for an explosion that takes place in homogeneous material, allow us to generalize the different stages of evolution of the phenomena in order to understand processes taking place during explosions in non-homogeneous media.

Of particular interest is the data obtained during experiments on the effects of artificial heterogeneities, such screens (elongated void spaces between the source and receiver), on the spatial distribution of damage during nuclear explosions (Chapter 7).

We paid significant attention to the complex structure of real geophysical media because the possibility of predicting and controling underground explosion effects depends greatly on knowing information about the medium structure. Structural heterogeneities are one of the most important characteristics of rock massifs, determining the major features of their deformation and breakage under external forces.

Medium heterogeneity can be expressed as discontinuities and zones of weakness (tectonic faults, fractures of different scales, layering etc). The heterogeneity defines not only the geometrical characteristics of the structure (e.g. size and shape of the structural blocks), but also the mechanical (e.g. strength) and fluid-filtering (porosity and permeability) properties of geological structures, which play important roles in the response of the medium to external forces. Results based on measurements during several nuclear explosions (Chapter 8) show the significant influence of heterogeneities on medium deformation.

Chapter 9 of this monograph describes the release of incondensable gases (produced by nuclear explosions) into atmosphere. We describe processes related to gas formation in the cavity, and to the dynamics of gas products being transported through the damaged medium. Other mechanisms of transport (flow) of the explosion products into the atmosphere, as well as the effect of the collapse of the cavity on the time of the gas appearance at the surface.

The important problem of using large chemical explosions in construction is described in Chapter 10.

The authors are grateful to their colleagues in the Institute of the Dynamics of Geospheres of the Russian Academy of Sciences, who participated in laboratory experiments and field observations of nuclear explosions. The authors thank L.D. Godunova, S.B. Kishkina, K.A. Zaitsev, G.N. Ivanov, and V.V. Ezhakova for their help in preparation of this book.

(THIS PAGE INTENTIONALLY LEFT BLANK)

Chapter 1.
Major mechanical effects of an underground explosion

1.1. Classification of underground nuclear explosions

We distinguish between explosions that are truly underground, and those that are near or above the ground surface. These two types couple energy differently into the solid ground.

For truly underground chemical explosions the depth of burial *W* of the (chemical) explosive charge exceeds the charge radius. For corresponding nuclear explosions the depth of burial therefore exceeds the radius of a TNT equivalent charge. These conditions are met when the scaled depth of burial *W* is

$$\bar{W} = \frac{W}{q^{1/3}} > 5(m/kt^{1/3})$$

where *q* is the explosive yield – an energy unit taken as the equivalent amount of TNT.

If this condition is met, the major part of the explosive energy is transferred into the ground. Depending upon the depth of burial and resulting effects visible on the free surface, truly underground explosions are further divided into cratering explosions (sometimes called ejection explosions), partially-contained explosions (sometimes called loosening explosions), and fully-contained explosions (or camouflet explosions, using the Russian term).

During *ejection* explosions the rock is intensely damaged, lifted, and thrown into the air. The explosive cavity is open and gas created by the explosion is released into the atmosphere. A visible crater is made in the ground surface. Ejection explosions are particularly effective for moving rocks. If an ejection explosion is conducted on an inclined surface, which helps in moving debris down the slope, this type of explosion is called [collapse blasting] or a directional explosion. Generally, the term *directional explosion* is related to a broader class of ejection explosions, including those conducted beneath horizontal surfaces, when conditions are created for moving rocks in a specific direction. This can be achieved by using different methods, including: a sequence of explosions (sometimes called “ripple firing”, or millisecond delay initiation); varying the shape of the charge; or pre-explosion excavation; or some other techniques.

For *loosening*, *dilatant*, or *retarc-producing* explosions, the height of the free surface uplift does not exceed the depth of burial. A surface uplift called a *retarc* – which is the word for “crater” spelled backwards – made of the broken loosened rocks is created, which allows the cavity gas to escape under pressure. Loosening explosions are effective for rock breaking. In this case rock movement can only be induced by a force of gravity if the explosion is conducted on a steep slope.

In Russian the term *camouflet* explosion refers to a contained explosion, where the influence of the free surface is not important. In practice this type of explosion can be further divided into

the class of fully contained explosions, where the damage zone does not extend to the free surface, and the class of partially contained explosions, where the entire column between the explosive cavity and the free surface is damaged, leading to fractures and residual deformation of the free surface. In both cases the main effects of the explosion (melting, vaporization, cavity formation, near-source rock damage, and fracturing) are confined to the emplacement rock; there is no opening in the uplift, and there is no direct release of the cavity gas into the atmosphere. Due to rock collapse into the cavity a subsidence crater can be formed. The intensity of gas release (post-explosion) into the atmosphere depends upon gas production of the emplacement rocks, and the depth of the explosion. The minimum depth needed to achieve a contained explosion is 70 – 120m/kt$^{1/3}$.

For a *surface explosion* (or burst) the charge is located either at the surface, or above the surface (in which case the parameter *W* plays the role of the height of burst *H*), or below the surface with the depth of burial less than the charge radius (or for the nuclear explosion less than the radius of the TNT equivalent charge). Depending upon the charge placement during the detonation there are three types of the surface explosions: *near-surface*, *contact* (the English term is "surface burst") and *shallow* (just below the surface).

An explosion is called near-surface (burst) if the sHOB is $\bar{W} \leq 2\, m/kt^{1/3}$, so that the fireball touches the earth surface no later than the end of the first phase, when the shock front still radiates light (radiation in the visible spectrum ? Not sure what's the right way to say this in English).

Near-surface explosion with sHOB $\bar{W} \leq 35\, m/kt^{1/3}$ forms a crater on the surface due to melting and vaporization, as well as compression.

For the near-surface explosions with sHOBs in the interval $2 - 5\, m/kt^{1/3}$ the melting and vaporization processes are more significant, however the rock compression is still the main mechanism of the crater formation. Moving the charge even closer to the surface below the sHOB of $\bar{W} \leq 2\, m/kt^{1/3}$ causes the ground extrusion above the surface and material ejection out of the crater forming a birm or lip around the crater perimeter.

For a *contact* explosion the energy center of the nuclear charge coincides with the earth surface. If the center of the mass of the charge is located below the surface, such explosion is called *shallow*. Charge placement with respect to the surface plays an important role in the energy partitioning between the ground and the atmosphere, and consequently in the size of the crater and the wave parameters.

Figure 1.1 shows approximate relationships between the depth or height of the explosion and the part of the energy transferred to the ground (parameter η). The ratio of the energy transferred into the ground increases with the increase of sDOB (thus this ratio increases by an order of magnitude compared to the surface explosion when the sDOB is $\bar{W} = 10\, m/kt^{1/3}$). For an above-ground explosion the energy transferred to the ground significantly decreases (for instance for the explosion with the sHOB of $\bar{H} = 1\, m/kt^{1/3}$the energy transferred to the ground decreases by 70% compared to the surface explosion).

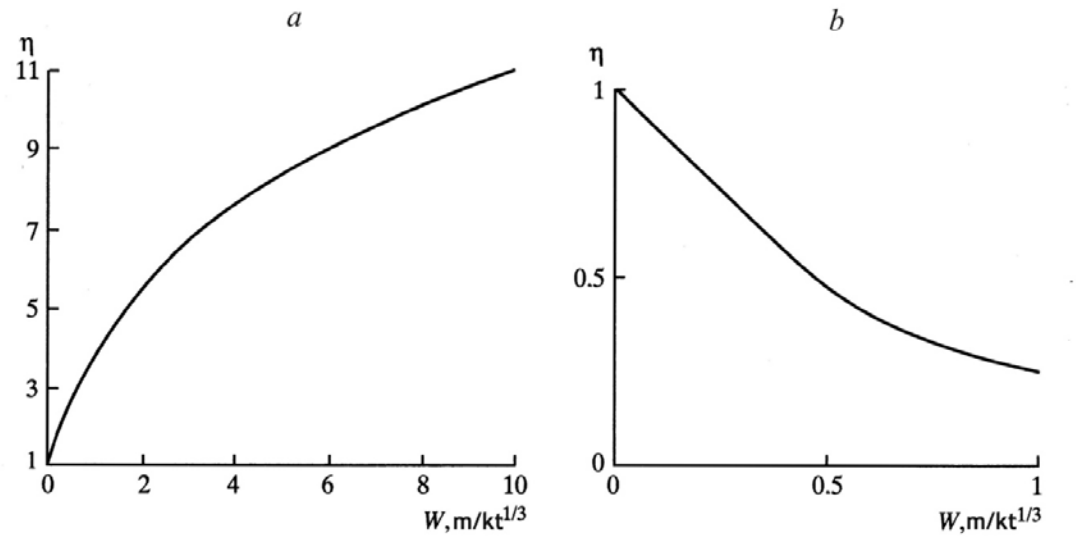

Figure 1.1: The ratio of energy transferred to the ground, to the amount of energy going into the ground for a surface explosion, is shown (a) for underground explosions at different depths, and (b) for atmospheric explosions at different heights.

1.2. Initial stage of the underground nuclear explosion

One of the features of the nuclear explosion is release of the tremendous amount of energy within a very short period of time (approximately 1 μs). High concentration of energy is created in the explosion chamber (which typically has a volume of about 100 m^3), resulting in high pressures on the order of 1-10 TPa and temperatures on the order of 10^6 – 10^7 °C (e.g. Underground Nuclear Explosions, 1962; Teller et al., 1968). At this stage of a nuclear explosion there is no gas formation and energy is released in the form of radiation energy and kinetic energy of plasma particles.

Gas products of the explosion are formed later from the vaporization of the emplacement rocks due to radiation and the strong shock wave. At first the energy transfer to the emplacement medium occurs through the radiative heat conduction, causing formation of a heat wave that exists up to distances of 0.2 – 0.4 $m/kt^{1/3}$ (Zel'dovich and Raizer, 1966). Expansion of plasma leads to compression of the medium away from the explosion center, which creates a strong shock wave. Shock wave compression causes an increase in pressure, temperature, internal energy and entropy of the material. Overheated matter becomes supercritical and moves away from the center.

At the initial stage the shock wave energy transferred to the matter is sufficient for a complete vaporization of the material during the rarefaction. The volume of the vaporized rock depends on its properties and on the energy density in the explosive chamber. For fully tamped explosions the radius of vaporization is 1.8 – 2.5 $m/kt^{1/3}$. Later this vaporized material in the

form of overheated rock vapors and the products of rock decomposition, acts as a gas propellant that exerts mechanical work on the surrounding medium.

Beyond the vaporized zone, rock melting occurs up to a radius of about 3 – 5 m/kt$^{1/3}$. This happens because the energy of the shock wave is less intense as a result of internal, and melting occurs during the subsequent rarefaction phase. For some natural materials certain parameters of the vaporized zone were calculated, including the radius of the vaporized zone R_e, mass of the vaporized material M_e per 1 kt, the pressure of the explosive products in the vaporized zone P_e, as well as the mass of the melted material M_m per 1 kt (Broud, 1975; Higgins, 1970) (Table 1.1).

The zone where the strong shock wave is observed is called the *hydrodynamic zone*. This zone extends through the zone of melting and through the part (of the damage zone) where the rock fails under compression at the shock front. Here the stress is so high that the differences in the principal stresses and the effects of subsequent volume changes can be neglected. Partial rock vaporization and partial decomposition of the rock-forming minerals take place in this zone. During the unloading phase incondensable gases (including CO_2, waver vapors etc) are produced in this zone, thus affecting the properties of the cavity gas. Hydrodynamic stage of the explosion ends when the gas pressure and the stress at the shock front falls to approximately $0.1\rho\, C_p^2$ (where ρ is the density of rock, C_p is the acoustic velocity), which corresponds to the order of magnitude of the mechanical strength of the single crystals.

Table 1.1 Explosion characteristics for different rock types

Rock type	Parameter				
	ρ, g/cm^3	R_e, m/kt$^{1/3}$	M_e, t/kt	P_e, Mbar	M_m, t/kt
Granit	2.67	1.83	68.6	1.8	200-500
Water saturated tuff	1.97	2.06	72.1	1.11	350-650
Dry tuff	1.76	2.15	73.2	0.865	500-900
Alluvium	1.6	2.20	71.4	0.703	800
Salt	2.24	2.25	106.9	0.920	-
Water	1.0	3.30	150.5	0.196	-

There are differences between the physical processes that take place during the early stages of nuclear and chemical explosions (for example, thoseusing TNT). During a TNT explosion gases are produced only as a result of decomposition of the chemical explosives. The initial pressures during a chemical explosion are on the order of 10 GPa and the temperatures are on the order of $10^2 – 10^3$ degrees. Due to lower initial parameters nuclear explosions are less efficient in producing mechanical work than the chemical explosions. For instance, the chemical explosions are twice as effective in generating seismic energy as nuclear explosions.

During nuclear explosions gases are produced in part by rock vaporization, therefore their thermodynamic properties depend on the rock properties. The details of cavity gas produced in different rock types are different, as they depend not only on the physical and mechanical properties of rocks, but also on their chemical properties. This is an important difference between the gas products created by chemical and nuclear explosion. These gases act as propellants that exert mechanical work on the surrounding rocks during expansion. Unlike the chemical explosions, the nuclear explosion can have broad variation in initial energy density (and initial pressure) in the explosion chamber. This parameter plays an important role in source processes, particularly for small values of energy density. For instance, by increasing the volume of the chamber it is possible to reduce the seismic effect of an explosion by two orders of magnitude.

Thus, differences in thermal processes, dependence of the cavity gas on rock chemistry and possible variations of energy density for the nuclear explosion make it difficult to use chemical explosions to predict mechanical effects of nuclear explosions. However, for the nuclear explosions, where the initial pressure in the cavity exceeds $1\rho\, C_p^2$, the effect of the initial energy density is not significant. In this case, the only parameter needed to characterize the explosive source is the total energy, because the volume of the evaporated zone and the final cavity size for a given rock type are proportional to the explosive energy. This is why it becomes possible to use self-similarity in order to develop empirical expressions and to predict mechanical effects for both nuclear and chemical explosions.

During the expansion of the explosive cavity, the pressure and the temperature of the explosive products decrease. The state of matter in the cavity changes due to cooling and condensation. When the pressure in the cavity drops, the mass of the vaporized, melted and chemically decomposed material will increase. Gases migrate from the rock massif into the cavity. Condensation of the vaporized rocks, consisting mostly of the oxides of silica, calcium and magnesium, occurs relatively fast. On the other hand, condensation of the low-temperature (incondensable) gases, such as water vapor and carbon dioxide, is slow and can take hours or days.

Because of this, and also because of the gas migration from rock massif into the cavity, the presence of water and other gas forming components in the rocks can significantly influence mechanical effects (cavity size, extent of the damage zone, shock wave parameters, seismic effects, ejection etc) as well as the radiation effects of the explosion.

1.3. Explosive cavity and the stress wave

[1]The final size of the cavity is one of the main parameters describing the mechanical effect of an underground explosion. Surveying of the underground nuclear cavities using different methods (tunnels into the cavities, drilling boreholes through the melt, pumping gas and fluids etc) produced a large body of experimental material regarding their sizes in different rock types. The

[1] This section concerns shock waves as opposed to P-waves. It includes comment on estimating yield (for chemical explosions as well as for UNEs).

cavity volume in hard crystalline rocks is (2–7) · 10^3 $m^3/kt^{1/3}$ (the radius is 8 – 12 $m/kt^{1/3}$), while in less hard rock (tuff, alluvium) the cavity volume is (1.4–1.8) · 10^4 $m^3/kt^{1/3}$ (the radius is 15 – 17 $m/kt^{1/3}$).

It was determined that the cavity size is self-similar as a function of yield. Based on the experimental data for the cavity radius r_c and assuming that the cavity reaches the maximum volume when the gas pressure reaches the lithostatic pressure at the explosion depth W, the following expression was proposed (Allen, Duff, 1969; Boardman et al., 1964):

$$\frac{r_c}{q^{1/3}} = \frac{B}{(\rho g W)^{1/3}\chi} \text{ (in units of } m/kt^{1/3}), \quad (1.1)$$

where q is the explosion yield in kt, B is a coefficient depending on the emplacement medium, W is the depth of burial, χ is the effective adiabatic exponent of the explosion products[2]. Using χ = 4/3 the value of B can be determined for different rock types: B = 65.9 – based on the data from 15 explosions in alluvium, B = 78.1 based on the data from 10 explosions in tuff, B = 63.6 – based on the data from two explosions in salt.

We note that radius the explosive cavity determined by both direct measurements and by indirect methods agree well for different explosions. For instance, the cavity radius produced by SALMON (USA)[3] is on average 17 m, which corresponds to a scaled radius of r_c = 9.9 $m/kt^{1/3}$. For comparison: the radius produced by an explosion in borehole A-III (Azgir, USSR, 22 December 1971) is r_c = 9.7 $m/kt^{1/3}$, the radius produced by an explosion in borehole A-II (Azgir, USSR, 1 July 1968) is r_c = 10.9 $m/kt^{1/3}$.[4]

Based on the analysis of all available data, Murphy obtained the following empirical formula for the radius of cavity in salt as a function of depth W and yield q (Murphy, 1981):

$$r_c = 24\frac{q^{0.29}}{W^{0.11}}.$$

This relationship well describes the experimental data with an average error of 1 m.

There was an attempt to take into account moisture and gas content when determining the nuclear cavity size. As a result of this analysis based on 46 contained nuclear explosions (data from Higgins, Butkovich, 1967) the following relationship was developed to determine the volume of the cavity V_c:

$$\frac{V_c}{q} = \frac{2.5\cdot 10^5}{(\gamma W)^{0.75}}\left[1 + \frac{3.9\eta}{(\gamma W)^{0.25}}\right] (m^3/t), \quad (1.2)$$

[2] This symbol is usually taken as γ

[3] Springer et al. (2002) give the yield and depth as 5.3 kt and 828 m for this PNE on 22 October 1964 in a salt dome in Mississippi.

[4] Sultanov et al. (1999) give the yield and depth as 96 kt and 986 m for the 1971 PNE, and 27 kt and 597 m for that in 1968.

where γ is the rock density in g/cm^3, η is the gas content in the rock per unit mass, in %.[5]

A defect of (1.1) and (1.2) is their independence on the rock strength. It was first shown during French nuclear explosions in the extremely strong granites of Sahara, that strength is very important in determining the size of the cavity. Delort (1971) proposed to use the following expression that uses the strength of rock:

$$\frac{r_c}{q^{1/3}} = \frac{B}{(\rho g W + \sigma_s)^{1/3} \chi} \text{ (m/kt}^{1/3}\text{)}, \tag{1.3}$$

where $\sigma_s \sim 22\ MPa$ is an effective strength of the medium.

More detailed analysis based on the results of 46 underground nuclear explosions (Clossmann, 1969) produced a better (from a statistical point of view) relationship:

$$r_c = \frac{21 q^{0.306} E^{0.514}}{\rho^{0.844} \mu^{0.576} W^{0.161}}, \tag{1.4}$$

which describes a cavity radius as a function of yield q, depth of burial W, and the medium parameters: density ρ, Young modulus E, and the shear modulus μ.

The most detailed study of the cavity formation in hard rock was conducted by Rodionov et al. (1971). This research shows that in the typical case, when the rock strength exceeds the lithostatic pressure, the cavity volume (and the radius) is determined by the rock compressional strength σ_* and the acoustic impedance $\rho\ C_p^2$:

$$\frac{V_c}{q} = \frac{38}{\rho\ C_p^2} \left(\frac{\rho\ C_p^2}{250 \sigma_*} \right)^{2/3}; \quad \frac{\rho_c}{q^{1/3}} = \frac{2.08}{(\rho\ C_p^2)^{1/3}} \left(\frac{\rho\ C_p^2}{250 \sigma_*} \right)^{2/9}. \tag{1.5}$$

For the explosion in plastic rocks, such as salt or clay, the cavity volume is given by:

$$\frac{V_c}{q} = \frac{45}{\rho\ C_p^2} \left(\frac{\rho\ C_p^2}{250 \tau} \right)^{0.86}, \tag{1.6}$$

where τ is the yield strength. Unlike Equations (1.1)-(1.4) which were derived using the assumption that the cavity expansion stops when the cavity pressure reaches the lithostatic pressure, Equations (1.5)-(1.6) are based on the assumption that the cavity size is determined by the strength and the elastic properties of rocks. Therefore, the effect of the DOB on the cavity volume when $\rho g W \le \sigma_*$ is only due to changes in the rock properties with depth.[6] Typically all rocks exhibit significant increase in their acoustic impedance with depth, as well as some increase in strength. Increase in the impedance $\rho\ C_p^2$ causes decrease in the cavity size, which increases the energy of the explosive products. Obviously, this effect should be taken into

[5] Note the use here of g for rock density, and not r. This may be either average density above the working point or the specific weight ($\rho\ g$). In Chapter 9 after Eq. 9.36 we find the definition $\gamma = \rho\ g$ (specific weight). However after that equation the Russian text gives units of g/cm^3.

[6] The impaction here is that effects due to overburden pressure can be neglected (note added by translators).

account when comparing explosions of different sizes, particularly ejection (cratering) explosions, which can use this energy to increase the acceleration of the ejected rocks.

The time T of the cavity expansion to its maximum is determined by the radius of the crush zone R_* (or the radius of plastic deformations):

$$T = \frac{2R_*}{C_p}\left(\frac{\rho\, C_p^2}{250\sigma_*}\right)^{1/6}, \tag{1.7}$$

The time of the cavity expansion in hard rock (e.g. basalt, granite, sandstone) is 30-50 ms/kt$^{1/3}$, the pressure of the explosion products at the end of the expansion is 30-50 MPa. In softer rocks (e.g. tuff, alluvium) the cavity expansion time is 70-90 ms/kt$^{1/3}$, and the pressure is 5-20 MPa.

The explosive cavity usually collapses and may partially fill with rubble. The collapse forms the chimney with the radius of approximately 1.2 r_c and the height of (4-6) r_c in hard rocks and (8-10) r_c in softer rocks. In most cases the collapse reaches the surface and forms subsidence crater.

Sometimes cavities in hard rocks may remain stable if their sizes are below some critical value. For example the cavity in granite formed by a 1.2 kt explosion (Semipalatinsk Test Site, 29 October 1968) remained stable.

Cavities in salt may remain stable even if they have large volume on the order of 10^5 m^3. Stability of the roof and the time before the cavity collapse depend on various factors, mainly the cavity size and the strength (cohesion) of the damaged medium, for example salt. Other factors preventing collapse include slow pressure decay, presence of melt, and low medium porosity.On the other hand, presence of moisture may promote collapse due to water vaporization in the pores during the final stages of cavity growth. The observations show that the cavity collapse in alluvium may take place within seconds to tens of minutes, while in granite it may take hours.

As the shock wave caused by sudden pressure rise in the chamber propagates through the medium, its amplitude and the propagation velocity decreases. When the amplitude drops to $0.1\rho\, C^2$ (which corresponds to scaled distances of 3-4 m/kt$^{1/3}$) and below, shock wave transforms into a stress wave (an elastic precursor arriving before the shock wave, is related to a maximum amplitude slow rise of particle velocity). The velocity profile in the stress wave is close to triangular, and can be characterized by three parameters: the peak particle velocity v_0, the rise time θ for the velocity to reach the peak value, and the duration of the positive phase of motion τ. The most important parameter is the peak velocity.

Numerous peak velocity measurements were conducted for the nuclear explosions in different rock types. For example, based on the peak velocity measurements in Nevada Test Site (USA) and in granites of the French Reggane Nuclear Test Site (in the Sahara), experimental relationships were obtained between the peak velocity v_0 and the peak radial stress σ_0 (Table 1.2) as a function of the scaled distance

$$\bar{r} = r/q^{1/3}, \tag{1.8}$$

where r is the distance from the explosion. Table 1.2 also shows the range for $\bar{r}$ where the measurements were conducted.

The velocity measurements were conducted in the rock massif away from the earth (free) surface. Table 1.2 shows that the measurement distance range is between 20 m/kt$^{1/3}$ and (1-2) $\cdot 10^3$ m/kt$^{1/3}$, and the peak velocity ranges between $0.1 \leq v_0 \leq 10^2\ m/s$ at these distances.

Figures 1.2-1.4 show the peak velocity v_0, peak acceleration a_0 and absolute amplitude of the radial displacement u_0 plotted against scaled distances for the rocks shown in Table 1.2. The parameters of the stress wave and their attenuation are clearly dependent on the rock type. For instance, Figure 1.2 shows that the highest velocity amplitudes are observed in hard crystalline rocks, such as quartz porphyrites and granites.

Table 1.2 Formulas for determining peak velocity in the stress wave for underground nuclear explosions

Rock type	Parameter		
	$\bar{r}$, m/kt$^{1/3}$	v_0, m/s	σ_0, kg/cm^2
Quartz porphyrite, granite	20-150	$6.6(100/\bar{r})^{1.66}$	$1000(100/\bar{r})^{1.66}$
Nevada granite -	30-160 160-1000	$4.3(100/\bar{r})^{2.4}$ $3.2(100/\bar{r})^{1.25}$	$700(100/\bar{r})^{1.85}$
Nevada tuff -	30-80 80-1000	$2.75(100/\bar{r})^{2.15}$ $1.65(100/\bar{r})^{1}$	$120(100/\bar{r})^{2.2}$
Sahara granite	50-2000	$5.36(100/\bar{r})^{1.73}$	$850(100/\bar{r})^{1.73}$

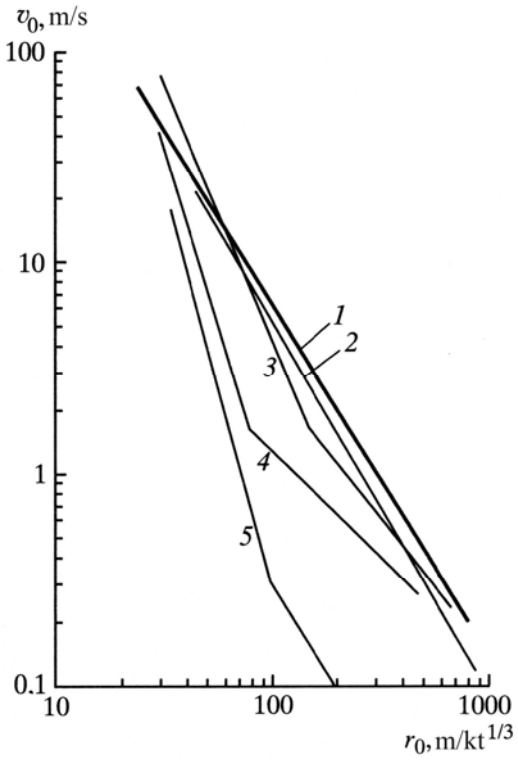

Figure 1.2 Peak velocity as a function of the scaled distance. Nevada Test Site rocks (1,3-5): 1 – quartz porphyrites, 3 – granite, 4 – tuff, 5 alluvium; 2 – Sahara granite

.

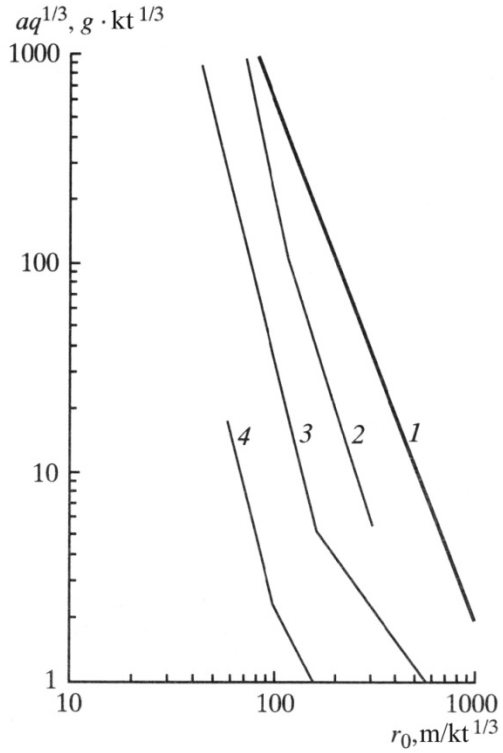

Figure 1.3 Peak radial acceleration in the stress wave as a function of the scaled distance. *1* – Sahara granite; *2 – 4* Nevada test site rocks: *2* – granite, *3* – tuff, *4* – alluvium.

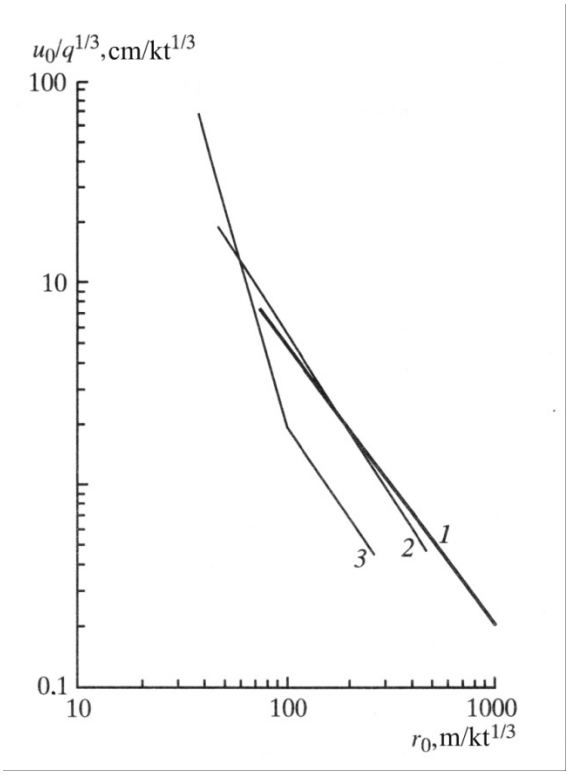

Figure 1.4 Maximum displacement in the stress wave as a function of the scaled distance. *1* – Sahara granite; *2 – 3* Nevada test site rocks: *2* – granite, *3*– alluvium.

For softer rocks the velocity amplitude at the same scaled distances is lower by approximately an order of magnitude. The attenuation in softer rocks is significantly higher compared to the hard rocks at distances less than 100 – 200 m/kt$^{1/3}$.

Figure 1.3 also shows that the peak acceleration in the stress wave significantly attenuates with distance from 10^3 – 10^4 g/kt$^{1/3}$ at distances 40 – 80 m/kt$^{1/3}$ to 1 g/kt$^{1/3}$ at distances 200 – 1000 m/kt$^{1/3}$. The acceleration amplitudes also depend on the rock type: they are higher in hard rock by 2-3 orders of magnitude compared to the amplitudes in tuff or alluvium.

The stress wave displacement amplitude in granite (Figure 1.4) decreases from 10 cm/kt$^{1/3}$ to 0.1 cm/kt$^{1/3}$ in the distance rage from 50 m/kt$^{1/3}$ to 1000 m/kt$^{1/3}$, which corresponds to the decay rate of $r^{-1.5}$. In alluvium the amplitudes decay at the same rate starting from distances $r \geq 100$ m/kt$^{1/3}$. The absolute value of the displacement for alluvium is lower by a factor of 3 compared to granite.

As we get closer to the charge (in the scaled distance rage of 30 – 60 m/kt$^{1/3}$), the amplitude of the stress wave in the alluvium becomes higher than in granite. The rate of the amplitude decay in alluvium is high (approximately $\propto r^{-3}$) in this distance range up to 100 m/kt$^{1/3}$.

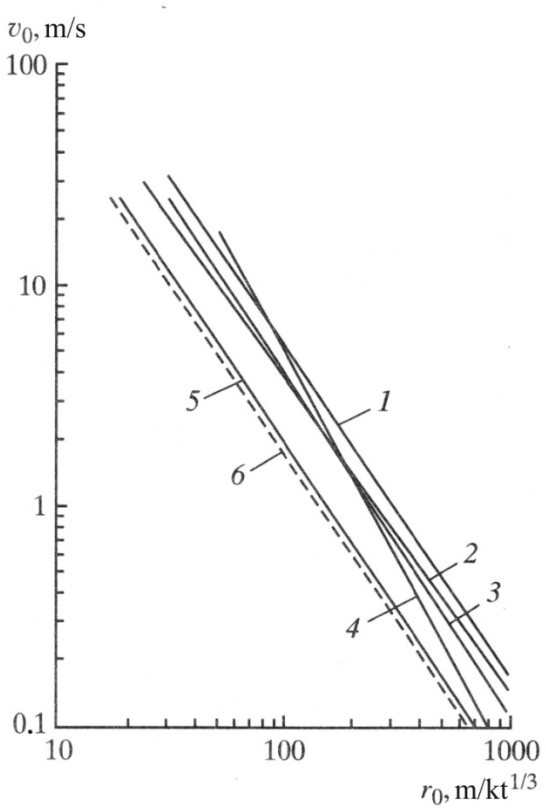

Figure 1.5 Peak velocity as a function of the scaled distance for the rocks of the Semipalatinsk Test Site (*1*, *6*) and Novaya Zemlya Test Site (*2* – *5*): *1* – Degelen granite, *2* – sandstone, *3* – hard shale, *4* – fractured shale, *5* – layered shale along bedding; *6* – TNT explosion at Murzhik testing Area (dashed line).

Numerous velocity measurements were conducted for the nuclear explosions at the Soviet test sites, both Semipalatinsk and Novaya Zemlya. Figure 1.5 shows the plot of the peak velocity as a function of scaled distance for both nuclear and chemical (TNT) explosions conducted in the hard rock of the Degelen Testing Area (Semipalatinsk Test Site). Also shown the results for the Novaya Zemlya rocks (including hard sandstones, shales, fractured shales, quartzites).

The results of these measurements can be expressed as the generalized expression in the form:

$$v_0 = A\left(\frac{r}{q^{1/3}}\right)^{-n}, \tag{1.9}$$

where the exponent *n* and the coefficient *A* depend on the parameters of the explosion and the physical properties of the rocks.

Table 1.3 shows the values of the empirical coefficients *A* and *n* for different rock types (for the following values of parameters from Equation 1.9, where *q* is in kt, and *r* is in m).

It follows from Equation 1.9 that explosions with different yields obey self-similarity relationships, while the peak velocities and their decay rate with distance for the hard rock is only slightly dependent on the rock type. This conclusion is confirmed by the experiments at both Soviet test sites (Figure 1.5, lines 1-3), as well as the experiments at the Nevada test Site (Figure 1.2, lines 1,2).

Table 1.3 Parameters of the pressure wave created by underground explosion in crystalline rocks

Test site	Rock type	Parameter	
		A	n
Semipalatinsk	Degelen granite	$1.44 \cdot 10^4$	1.65
Novaya Zemlya	Hard shale, sandstone	$1.19 \cdot 10^4$	1.6
	Layered shale, cross-bedding	$1.74 \cdot 10^4$	1.67
	Layered shale, along bedding	$9.6 \cdot 10^3$	1.67
	Fractured shale	$1.6 \cdot 10^5$	2.1

Thus, for the explosions in hard unfractured rocks the peak velocity is robust characteristics of the explosive source.

For softer rocks, such as fractured and layered slates (Figure 1.5, lines 4,5) and Nevada tuff (Figure 1.2, line 4), the peak velocity amplitude decreases, and the rate of decay increases with increasing distance.

Measurements of the stress wave at Novaya Zemlya have shown that distance dependence of the rise time θ and the duration of the positive phase τ in the stress wave are given by:

$$\theta = (0.0287r + 0.45q^{1/3}) \cdot 10^{-3} \text{ (s)}, \qquad (1.10)$$

$$\frac{\tau}{q^{1/3}} = 3.7\left(\frac{r}{q^{1/3}}\right) \cdot 10^{-3} \text{ (s)},$$

where q is the yield in tons, r is distance in m.

To compare the mechanical efficiency of the underground chemical and nuclear explosions, the experiments were conducted in granites of the Semipalatinsk Test Site using chemical (TNT) charges with yields between 0.1 and 10 t. The relationship between the peak velocities and distances is shown in Figure 1.5 with the dashed line (6).The relationship is given by

$$v_0 = 230\left(\frac{r}{q^{1/3}}\right)^{-1.75} \text{ (m/s)}, \qquad (1.11)$$

where q is the yield in tons, r is distance in m.

For tamped nuclear explosions conducted in Degelen granite (a relatively unfractured rock massif with the elastic velocity of C_p = 5 – 5.5 km/s) the expression from Equation 1.8 becomes:

$$v_0 = 320\left(\frac{r}{q^{1/3}}\right)^{-1.65} \text{ (m/s)}, \qquad (1.12)$$

where q is the yield in tons, r is distance in m.

A comparison between expressions (1.11) and (1.12) shows that the peak velocity for the TNT equivalent for the nuclear explosion is approximately 0.5 (the yield of a TNT charge should exceed the yield of a nuclear charge by a factor of two to produce the same peak velocity).[7]

We note that the expression 1.12 is universal for hard relatively unfractured rocks regardless of their composition, and therefore determines the maximum possible peak velocity achievable for an underground explosion.

For nuclear explosions in Degelen granite the peak acceleration a and the maximum displacement u_0 as a function of distance are given by:

$$aq^{1/3} = 2.5 \cdot 10^6 \left(\frac{r}{q^{1/3}}\right)^{-2.4}, \qquad (1.13)^8$$

$$\frac{u_0}{q^{1/3}} = 0.36 \left(\frac{r}{q^{1/3}}\right)^{-1.65}, \qquad (1.14)$$

where q is the yield in tons, r is distance in m, u_0 is in m, and a is the acceleration in units of g.

Analysis of the wave records from the underground explosions shows residual deformations in the medium. The magnitude of the residual deformations shows good correlation with the final cavity radius, which suggests that cavities form predominately due to medium displacement away from the source. It turns out that in the zone of strong deformations the residual deformations are close to the maximum of the observed displacements. However with distance increase the values of the residual displacements decrease much faster than the maximum amplitude of motion in the stress wave. It is likely that at larger distances there is a return motion, while at close distances where the rock is broken, there is no return motion. Existence of the residual deformations in the elastic zone suggests irreversible elastic compression after the explosion. The boundary where the values of the residual displacements coincide with the maximum displacements defines the zone of irreversible deformations (e.g. Rodionov et al, 1971).

Based on the measurements of the rise time θ and the duration of the positive phase τ in the Degelen granite their relationship with the explosive yield and distance (to the source) is expressed as follows:

$$\theta = (2.5 - 4.5) \cdot 10^5 q^{1/3} \left(\frac{r}{q^{1/3}}\right)^{0.75} \text{(s)}, \qquad (1.15)^9$$

$$\tau = (3 - 4) \cdot 10^{-3}\, q^{1/3} \text{ (s)},$$

where q is the yield in tons, r is distance in m.

Empirical formulas in equations (1.12) – (1.15) were obtained using data from nuclear explosions with high energy density in the explosive chamber. In such cases the parameter $\zeta = q/V_c$ exceeds 100 t/m^3 (V_c is the volume of the chamber).

[7] Isn't this exactly the opposite to what was found as a result of NPE?

[8] Note from translators: it is not clear to us why the a on the left-hand side of (1.13) is multiplied by $q^{1/3}$

[9] It is possible that one of the multiples should be 10^{-5} instead of 10^5.

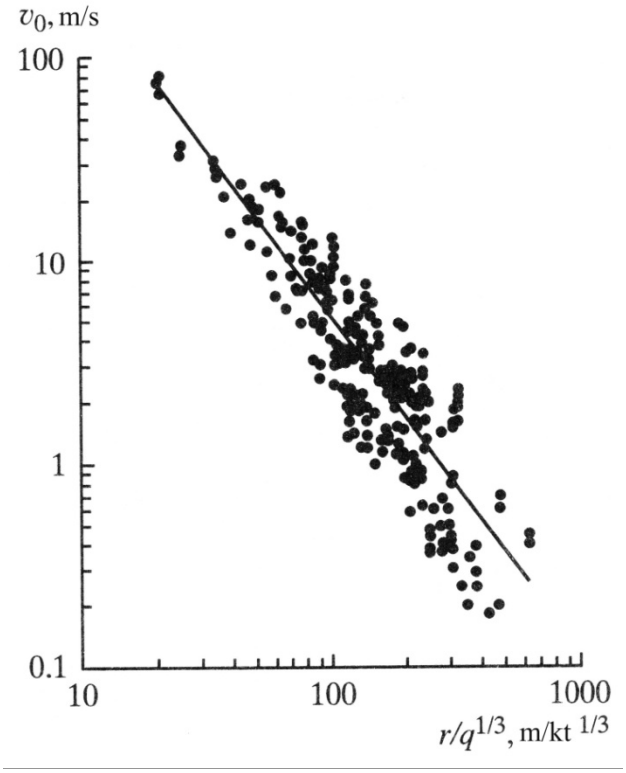

Figure 1.6. Peak velocity as a function of the scaled distance for 19 explosions conducted at the Degelen Mountain

The analysis of the experimental data shows that the energy density affects the stress waves starting from $\zeta \leq 10$ t/m^3. Thus, if the initial energy density is reduced to 1 t/m^3 and everything else stays the same, the peak velocity is reduced by a factor of two. If ζ is reduced to 0.01 t/m^3 the value of v_0 is reduced by an order of magnitude.

Reducing the initial energy density also affects the temporal characteristics of the stress wave. For instance, analysis of the waveforms shows that for the energy density in the range $5 \leq \zeta \leq 100$ t/m^3 the rise time is given by the formula:

$$\theta = 5.5 \cdot 10^{-5} q^{1/3} (1 + 1.35\zeta^{-0.43}) \left(\frac{r}{q^{1/3}}\right)^{0.75} \text{(s)},$$

where q is the yield in t, r is distance in m.

Going back to the peak velocity, we note that the properties of rocks and rock massifs significantly affect the parameters of the stress wave. Figure 1.6 shows the results of the peak velocity measurements for 19 explosions with different yields conducted at the Degelen massif at different times. The analysis shows that a significant scatter in the experimental data can be explained by the differences in the conditions in which these explosions took place.

Thus, during the first years of the Semipalatinsk Test Site operation the explosions were conducted in relatively unfractured rock massifs built by rocks with high strength. This group of the experiments includes explosions in Tunnels 21, 106, 127, 141, A-4, E-1 etc. For these experiments the absolute depth exceeded 200 m. Pre-existing deformations in these rocks were

healed and had high strength. The plot of $v_0(r)$ for this group of the experiments is shown in Figure 1.7 (Adushkin et al, 1995). Analytically this relationship is well described by Equation 1.11.

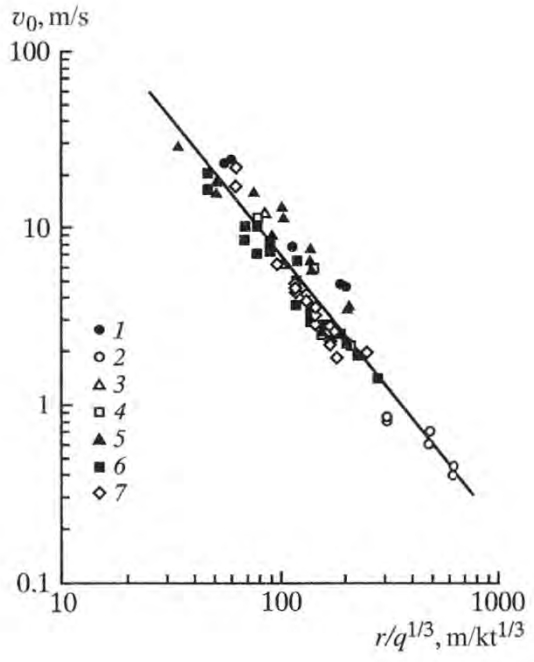

Figure 1.7 Peak velocity for explosions conducted in low-fracture hard rocks. 1 – 7 tunnels: 1 – 106, 2 – 127, 3 – 141, 4 – 172, 5 – A-4; 6 – E-1, 7 – 21.

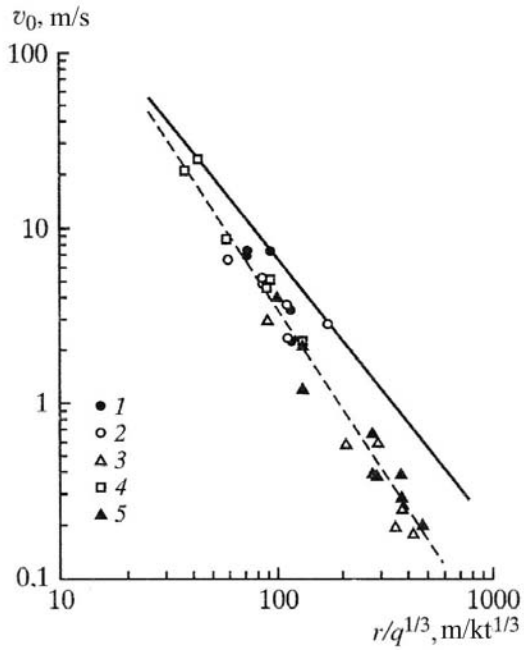

Figure 1.8 Peak velocity for explosions conducted in fractured rocks. 1 – 5 tunnels: 1 – K, 2 – K-2, 3 – 215, 4 – 200M, 5 – 103.

In the later years the tests at the Semipalatinsk were conducted in weathered rock massifs at shallow depths (e.g. Tunnels K, K-2, 103, 215, 200M etc). The strength of rocks in these massifs is significantly lower than the rocks where the experiments of the previous group were conducted. The structure of the testing area is represented by well-developed tectonic faults with reduced mechanical strength. The presence of faults explains the reduction in *P*-wave velocities, which is close to $4 \leq C_p \leq 4.3$ km/s for these rocks. The peak velocities for this group of explosions are shown in Figure 1.8 (Adushkin et al, 1995). It is clear from Figure 1.8 that the amplitude decay with distance is significantly higher than for the explosions of the first group. The relationship can be analytically described using a formula:

$$v_0 = 340\left(\frac{r}{q^{1/3}}\right)^{-1.95} \text{ (m/s)}, \tag{1.16}$$

where q is the yield in t, r is distance in m.

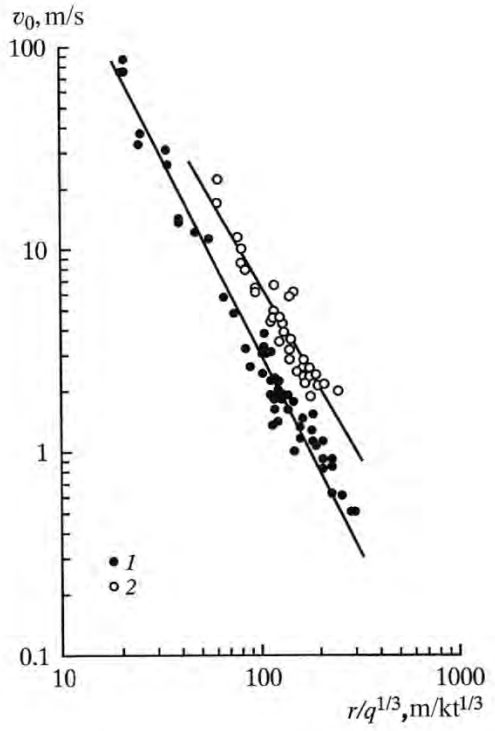

Figure 1.9 Peak velocity for the first explosions (1) and repeat explosions (2) conducted at the Semipalatinsk Test Site. Tunnels: 1 – 21, 608, 172, 2 – 90, 168.

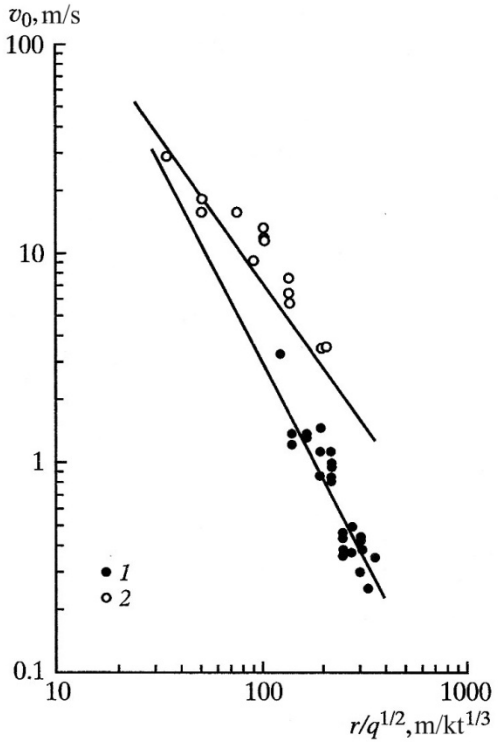

Figure 1.10 Peak velocity for the explosions in Tunnels A-4 (1) and Z-3 (2).

During the last years of the nuclear testing at the Semipalatinsk Test Site at the Degelen massif repeat explosions were conducted (either in the preserved parts of previously used tunnels, or in the new tunnels in the rock massifs affected by previous explosions). For example, the nuclear tests conducted in Tunnel 21 (February 26, 1967), Tunnel 608 (July 12, 1968), and Tunnel 190 (April 15, 1984) were conducted in the same rock massif. Explosion in Tunnel Z-3 (December 24, 1965) was conducted in the same massif as the experiment A-4 (May 16, 1964), while the explosion in Tunnel E-2 (September 29, 1968) was conducted in the same massif as the experiment E-1 (February 13, 1966) (Semipalatinsk…, 2003). The measurements show (Figure 1.9) that the amplitude attenuation with distance for the repeat explosions conducted in the areas affected by previous explosions, is significantly higher (Adushkin et al, 1995). According to the experimental data, the relationship $v_0(r)$ for the earlier explosions can be approximated by Equation 1.12, while for the repeat shots this relationship is close to Equation 1.16.

The effect of the rock fractures on the stress wave is even more significant for the highly fractured areas of the Degelen massif ($C_p \leq 4$ km/s). In these areas the relationship $v_0(r)$ is given by the formula:

$$v_0 = 400\left(\frac{r}{q^{1/3}}\right)^{-2} \text{ (m/s)}, \tag{1.17}$$

where q is the yield in tons, r is distance in m.

In addition, the duration of the positive phase for these rocks increase to (10-15) $\cdot 10^{-3}$ s/kt$^{1/3}$, while the returning motion in the stress wave is practically non-existent.

Let us look at the experimental data obtained during the experiments in salt, which were the most thoroughly characterized.

There were two American experiments in salt described in literature: SALMON (October 22, 1964, yield 5.3 kt, depth 828 m) and GNOME (December 10, 1961, yield 3.1 kt, depth 365 m) (e.g. Rodgers, 1966; Randolph, 1966), as well as one peaceful nuclear explosion in the salt dome Azgir (USSR; April 22, 1966, Hole A-1, yield 1.1 kt, depth 160 m) (Rodionov and Tzvetkov, 1971). In addition there is a description of the parameters of the stress wave in the near field of the underground explosions in salt in the works by Adushkin et al (1993) and Kitov (1995).

Figure 1.11 shows the plot of the peak velocity as a function of scaled distance. The data for Salmon, Gnome and A-1 are described by the relationship (for $50 \le r_0 \le 1000$ m/kt$^{1/3}$):

$$v_0 = 10\left(\frac{r}{q^{1/3}}\right)^{-1.6};\ v_0 = 8\left(\frac{r}{q^{1/3}}\right)^{-1.6};\ v_0 = 9.4\left(\frac{r}{q^{1/3}}\right)^{-1.63} \qquad (1.18)$$

where q is the yield in t, r is distance in m.

The stress wave amplitude for GNOME is slightly lower than the amplitudes for SALMON and A-1. The data for explosion A-1 obtained from the explosion in the salt dome in the USSR territory plot between the data points for Salmon and Gnome, even though some of the experimental points agree with velocities recorded from Salmon.

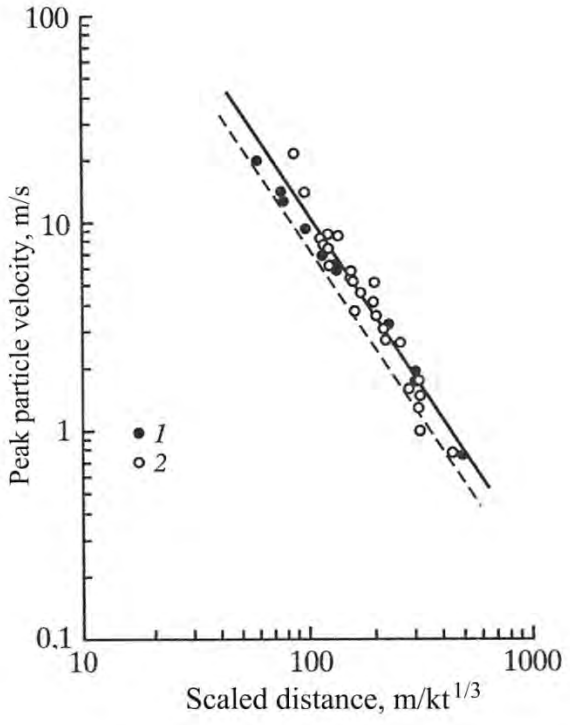

Figure 1.11 Shock wave displacement amplitude for the underground explosions in salt. Experiments: *1* – A-1, *2* – SALMON, the dashed line shows the linear regression for GNOME, the solid line shows the linear regression for SALMON

1.4. Characteristics of the damage zones created by underground explosions at the Semipalatinsk Test Site

Post-explosion studies show that the degree of damage of rock massifs depends on the distance r from the explosive source. In the vicinity of the explosive cavity, whose radius for non-porous(?) media is $(7.5 – 9) \cdot q^{1/3}$ m, where q is the explosion yield, the rock is deformed and crushed. In the distance range $10q^{1/3} \leq r \leq 30q^{1/3}$ m the initially weakly fractured medium becomes intensely and chaotically fractured. At greater distances from the cavity ($r \geq 30q^{1/3}$ m) a network of radial fractures is observed, which extends up to $(100 – 130) \cdot q^{1/3}$ m.

The zone of irreversible deformations is characterized by an increase in porosity, decrease in core production, and significant changes in permeability of the rocks as well as the rock massif as a whole.

The radius of the crushed zone R_d is proportional to the cavity radius, and the proportionality coefficient depends on rock strength and compressibility (Rodionov et al, 1971):

$$\frac{R_d}{r_c} = \left(\frac{\rho\, C_p^2}{4\sigma_*}\right)^{1/3}. \tag{1.19}$$

For crystalline rocks the radius of the crushed zone is approximately $(2.5 - 5) \cdot r_c$, depending on the medium properties. Zone of radial fractures is located outside of the crushed zone. The radius of the zone of radial fractures depends on the radius of the crushed zone:

$$\frac{R_f}{R_d} = \left(\frac{\sigma_*}{2(\sigma_t + \rho q W)}\right)^{1/2}, \tag{1.20}$$

where σ_t is the tensile strength of the material. Depending on the rock properties the radius of the radial fractures may exceed the radius of the crushed zone by a factor of 2-3. Since the expression in (1.20) depends on the lithostatic pressure, the relationship between R_d and R_f depends on the explosion yield[10]. For example, for the 1 kt explosion in granite the radius of the radial fracture zone exceeds the radius of the crushed zone by a factor of 3.2, while for a 1 Mt explosion the factor is 1.9, other things being equal.

Expressions in (1.19) and (1.20) are supported by the observations from field experiments. In reality the boundary between crushed and fractured rocks is not clearly defined. Together these zones form the zone of inelastic deformation around the cavity. Study of the rock properties after the explosions is very difficult and involves digging exploratory tunnels and drilling boreholes into the damage zone.

Stresses from explosions create discontinuities (fractures) in the rock medium resulting in loss of cohesion between its structural elements, leading to a block-like hierarchical structure (Adushkin, Spivak, 1993a). It is worth noting that break-up of the rock mass into mostly discontinuous (“weakly connected”) structural elements does not always causes their complete separation along the newly formed discontinuity surfaces. Fully contained explosions are

[10] Because depth depends on the yield.

detonated far away from the free surface, therefore large deformations and stresses from explosions, as well as the residual deformations, often result in dense packing of the individual fragments in the damaged rock massif. This is confirmed by experiments with ejection of rocks damaged by an explosion (Guschin, 1975). In addition to creating discontinuities between different blocks (by breaking them apart), explosions cause changes in rock properties (within the individual blocks) and to the rock massif as a whole.

Analysis of the mechanical conditions of the rock massif after the explosion is performed by using an approach based on dividing the medium into parts (zones) with similar structural and mechanical characteristics. It is important to separate zones with significant damage and zones with block structure.

Understanding the interaction between separate blocks is particularly important when studying explosion zones that consist of blocks with different sizes. These zones include: a zone of intense fracturing where each block is divided into smaller blocks, whose sizes are determined by the fractures; a zone of block fractures, where the explosion changes the boundary conditions between the blocks rather than the sizes of the blocks; and a quasi-elastic zone with pronounced local changes from explosions, significantly different from the average characteristics.

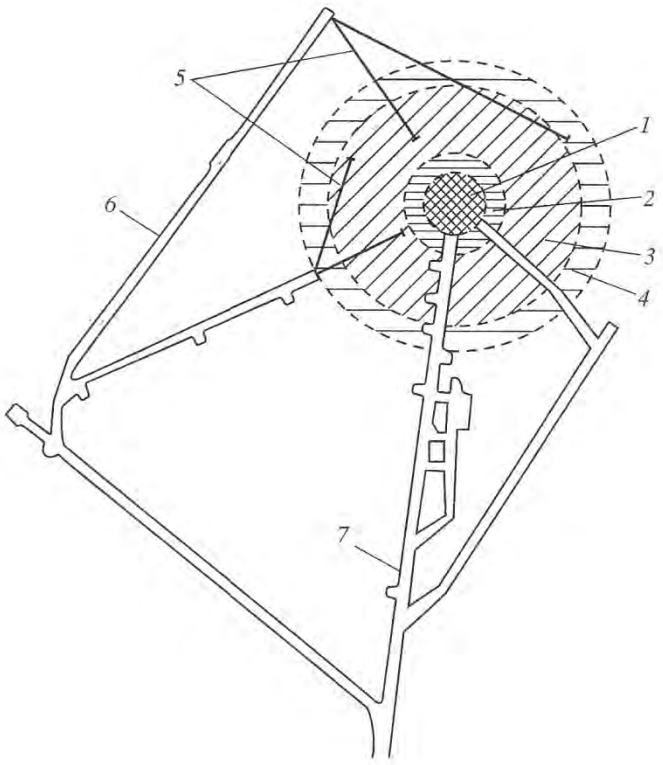

Figure 1.12 Schematics for the experiment in Tunnel B-1 (09.12.1973). 1 – cavity, 2 – crushed zone, 3 – damage zone, 4 – zone of block fractures, 5 – experimental boreholes, 6 – exploratory tunnels dug after the explosions, 7 – Tunnel B-1.

Different techniques were employed to study the effect of an underground explosion on the rock massif in which the explosion occurred. After the explosions at the Degelen Testing Area clearing of the rock mounds and opening of the test tunnels, additional tunnels and drifts were dug both from underground chambers and from the free surface (Figure 1.12). In addition, boreholes were drilled in the direction of the explosion center. This allowed study of the rock properties at very close distances up to and including the explosive cavities. The studies included visual observation, photographs of the tunnel walls and the collapsed rocks, taking rock samples for laboratory analyses. Post-explosion fractures were compared with pre-explosion conditions, and granulometric analysis of rock fragments was conducted. In some cases geophysical studies as well as permeability studies were conducted. Almost all experiments included rock sample analysis. All rock samples were analyzed using hydraulic machines.

Measurements of the uniaxial compressional strength were conducted using cylindrical rock samples with height and diameter of 45 mm. Tensional strength was determined by breaking 30 mm thick samples with a steel wedge. Shear strength was determined by using cylindrical samples with diameter and height of 45 mm by placing them in a steel cell with the angle of 45° or 60°.

The degree of fracturing of the rock massif before and after the explosion was determined by either photographing of the tunnel walls, or by counting individual fractures. Characteristics of the largest fractures and tectonic faults were measured. In some cases the character of the fractures was determined using cores from the boreholes.

Studies of the distribution of fragment size of the damaged rocks at different distances from explosions were conducted by determining the volume or weight fraction of each particle size either by sieving or by performing measurements from photographs.

Geophysical studies were conducted in most cases using seismic methods. Three different methods were used to determine *P*-wave velocities:

1. *Seismic profiling of the tunnel walls*. Seismic profiles are located along the tunnel wall. Waves were generated by using small explosions in small holes drilled in the tunnel walls. The profile lengths were from several meters to several tens of meters.
2. *Method of combined reflected and refracted waves*. Seismometers were located inside the tunnel as well as on the surface. Seismic waves were generated using explosions at the free surface.
3. *Seismic imaging*. Seismometers were located in the tunnel, while the waves were generated in other tunnels.

Rock permeability studies were conducted using a specially developed method, in which air was pumped into the boreholes drilled through different areas of the rock massif (Rodionov et al, 1976a; Spivak and Svintsov, 1982).

Seismic methods were used to study mechanical properties of the rock massif. In addition exploratory boreholes were drilled to various depths at different epicentral distances from the explosions (Figure 1.13). Rock properties at different depths and changes in these properties

were subjectively evaluated by determining the amount of core recovery, energy needed to drill, loss of the drill bits/tools, and loss of drilling fluids.

The reliability of the information obtained by using the borehole methods is lower than by tunnel surveys. Therefore, the majority of data about the rock properties in the zones of irreversible deformations were obtained for the explosions conducted in the tunnels. However these data can be used to extend (extrapolate?) to the explosions in deep boreholes, because the parameters determined from both tunnel and borehole explosions are comparable.

1.4.1. Explosions in the tunnels of Degelen Mountain.

The effect of an explosion on the rock massif of this site can be illustrated using the results of seismic imaging conducted after a fully contained explosion with yield of 12.5 kt (Kocharyan, 1996) (Figure 1.14). The cavity (scaled radius $r_c/q^{1/3}$ is approximately 7-9 m/kt$^{1/3}$) with the collapse chimney are located near the epicenter of the explosion. A region with a radius of approximately 35 m/kt$^{1/3}$ in the cross-section represents a zone of intense damage (a crush zone). The *P*-wave velocity in this zone is approximately C_p = 1.1 – 1.4 km/s.

Other zones with different degrees of damage follow as we move away from the epicenter (Figure 1.14, items marked 3 and 4). At scaled distances of 120 m/kt$^{1/3}$ the velocities obtained using seismic imaging become close to the average velocities for the unbroken massif. In some experiments changes in C_p can be traced to larger distances, up to 300 m/kt$^{1/3}$. We emphasize that at larger distances changes in seismic velocities are observed mainly within the zones of pre-existing tectonic deformations.

Based on the results of geological and geophysical surveys studying the effects of the tunnel explosion on rock massifs the following zones are observed (Adushkin, Spivak, 2004):

A cavity, which often has asymmetrical ellipsoidal shape with average dimensions of 7-10 m/kt$^{1/3}$ depending on the rock strength. The major axis of the ellipsoid extends either along the bedding plane or along the direction of the major tectonic deformations.

A crush zone which surrounds the cavity and reaches to distances of 12-14 m/kt$^{1/3}$ from the center of the explosion. The rocks in this zone turn into powder even with slight mechanical action. Granite looks lighter in color with mineral grains microfractured and sometimes deformed. Strength and elastic moduli of these rocks are significantly reduced, and they become more permeable (Spivak, 1980b).

Zone of intense deformation can be identified up to 35-40 m/kt$^{1/3}$. In addition to displaced rock blocks, crushing of the rock is observed in this zone (new fractures are formed). Two subzones are observed within this zone: sub-zone of crushing (up to 20-25 m/kt$^{1/3}$) and sub-zone of new fractures.

In the *sub-zone* of *crushing* the massif is broken by new and old (renewed) fractures. Granite is lightly colored, but it turns into its natural pink color away from the center. Massif looks like a brick wall with distorted joints. In the inner part of the zone granite is broken into gravel-size particles, while toward the end of the zone the size of the rock fragments is on the order of tens of centimeters. The number of fractures increases by a factor of 4 to 40 in comparison with the

pre-existing fracturing. Overall the massif is bonded and not falling apart, so that tunnel digging requires drilling and blasting. The rock porosity reaches 10.5 %.

In the *new fractures sub-zone* (distances up to 35-40 m/kt$^{1/3}$) the rock has its natural color. The number of fractures increases by a factor of 2-4. The massif has clear block structure. The size of the fragments is mainly determined by the natural fractures. The block sizes decrease toward the center from 1.0 – 3.0 m to 0.2 – 0.8 m. Shallow fractures have larger openings. Displacement is observed along steeper fractures. Rock strength gradually increases from the center toward the periphery. Seismic velocities in the zone of intense deformations range from 1.6 – 2.4 to 3.5 – 4.0 km/s.

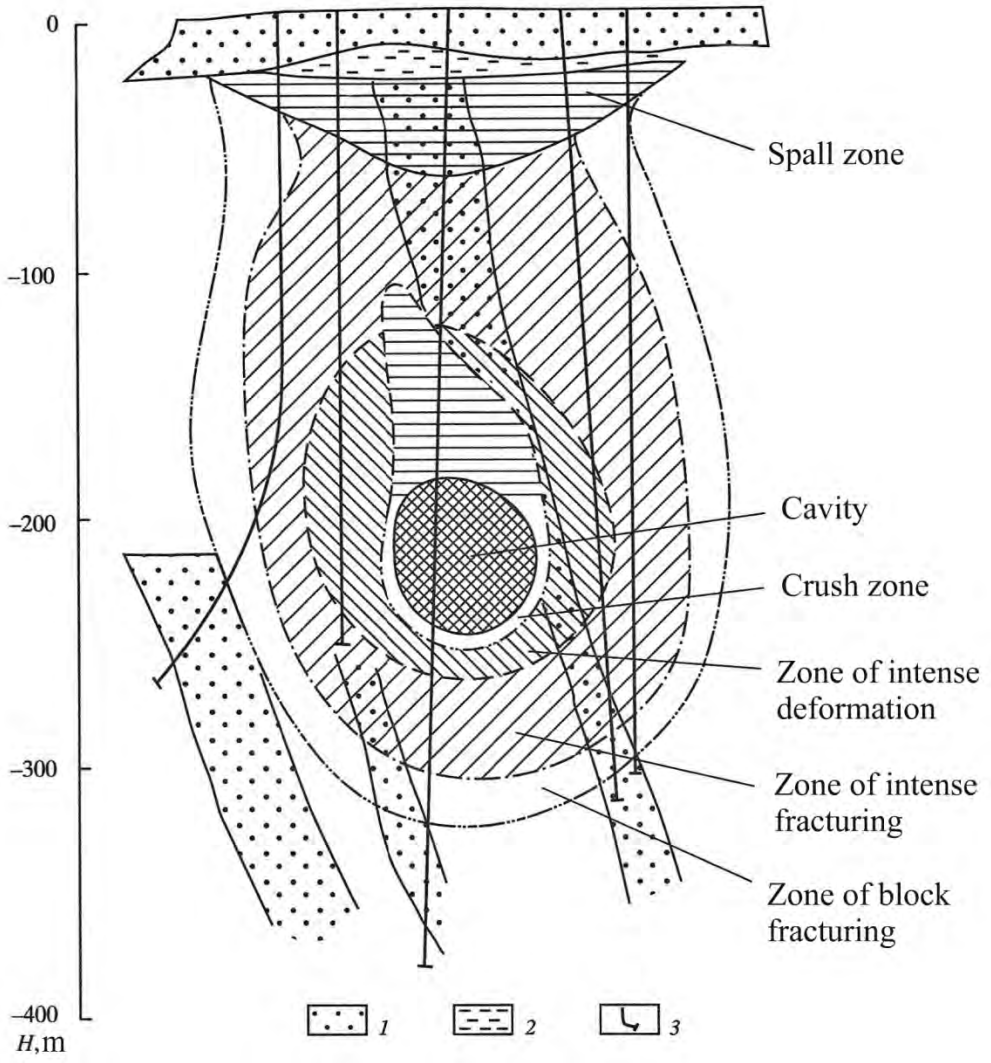

Figure 1.13 Schematics for the experiment “Borehole 102”. *1* – gravel deposites, *2* – gray clays, *3* – exploratory boreholes.

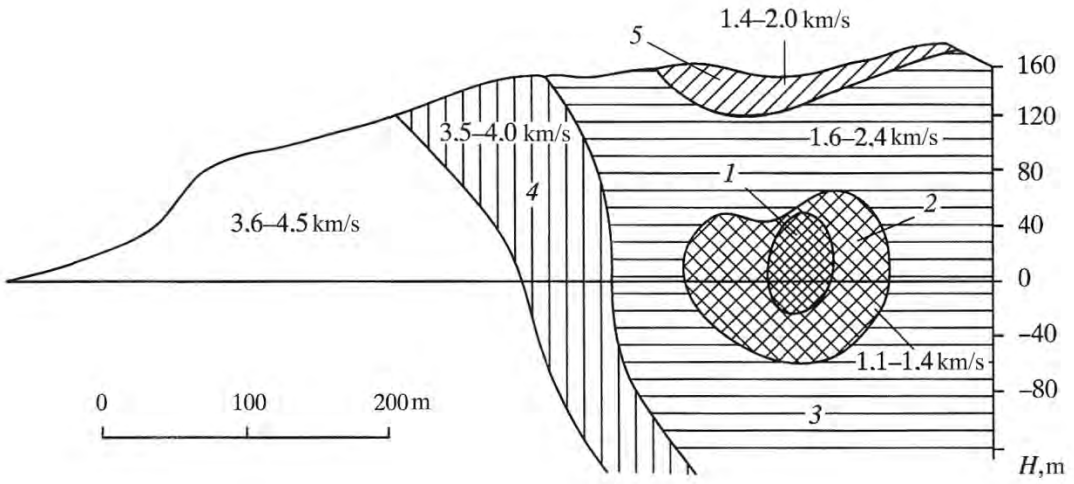

Figure 1.14 Results of the seismic imaging of the rock massif conducted after 12.5 kt explosion: *1* – cavity and chimney, *2* – crush zone, *3* – zone of inelastic deformations, *4* – zone of localized inelastic deformations. Seismic velocities are also shown in the cross-section.

A zone of inelastic deformations extends up to 120–130 m/kt$^{1/3}$; however it can reach 150 m/kt$^{1/3}$ in some directions. In this distance range new fractures are rarely created, but are sometimes observed. The fracture openings are 2–10 mm on average, while in weaker areas they can reach 10-50 mm. The rock fragments have natural color and physical properties similar to the intact rocks. *P*-velocities are reduced by 5 – 10 %. Permeability is close to that of the intact rocks. Drilling in this zone is similar to the drilling into the intact massif. Significant block movement and opening of the existing fractures is observed, as well as the signs of the "hidden fractures" and changes in elastic properties of the massif due to joint and fracture opening. A *sub-zone of renewed fractures* is observed within the zone of inelastic deformations up to distances of 50-60 m/kt$^{1/3}$.

A zone of local inelastic deformations is observed up to distances 200 – 220 m/kt$^{1/3}$. Within this zone inelastic deformations along structural discontinuities can be detected instrumentally. These post-explosion changes can be manifested as rocks fallen from the tunnel ceilings, typically in the areas of tectonic deformations. In some cases pre-existing tectonic deformations may become "renewed" allowing gas formed by the explosion to seep from the cavity.

Results of field studies suggest that the mechanical effects of an explosion on rock massif are determined by its pre-existing structure. For example, presence of a tectonic discontinuity (of IV – V order)[11] near the working point determines the asymmetry of the explosion cavity. Moving away from the epicenter, structural discontinuities play even more important role in the changes to the mechanical properties of rocks. In addition, the nature of damage strongly depends on the local pre-existing geological conditions.

[11] There are different orders of tectonic faults/deformations in Russian literature

These zones observed during studies of the nuclear explosion effect at Degelen Mountain are asymmetric, with maximal changes extended along the direction of the tunnel and toward the ground surface. The configuration of the damage zones, the degree of fracturing and the parameters of gas migration are affected not only by the ambient rock heterogeneities, anisotropy and presence of tectonic deformations, but also by the presence of the man-made zones of weaknesses (such as pre-existing tunnels).

1.4.2. Explosions in the deep holes of the Balapan massif.

The following zones were determined as a result of geological and geophysical surveys conducted at the Balapan Testing Area (Figure 1.13).

A *cavity* forms at the working point with the scaled radius of 10-13.6 m/kt$^{1/3}$.The cavities are partially or completely filled with debris with sizes ranging from dust-size particles (powder? A.S) to 3-5 cm. Solidified melt is found below the explosion center forming a "lake". The average porosity of the debris reaches 20-25% and the permeability coefficient reaches 25-30 m/day.

Futher away from the center the *crush zone* is observed with a thickness of 3 – 4 m/kt$^{1/3}$. The rocks at these distances are pulverized with some inclusions of rock fragments no bigger than 3 – 4 cm. When saturated with water these rocks look like clay. Their hydraulic conductivity is between 0.4–1 and 3 Darcy. The porosity exceeds the initial values by a factor of 2-6.

A zone of intense deformation extending to 35-40 m/kt$^{1/3}$ is represented by broken mass with the debris sizes ranging between 2–3 cm and 5–7 cm. This zone typically has asymmetrical shape determined by the geological and tectonic structure (the zone is elongated in the direction of fracturing). The original texture is not preserved. Porosity increases to 2–3 times the initial value. Based on the pumping experiments the value of the filtration coefficient is on average 0.25 – 0.2 m/day[12].

A zone of intense fracturing extends to scaled distances of 50–55 m/kt$^{1/3}$. This zone is characterized by new fracture forming along the pre-existing fractures, structural elements and weakness zones. This fracturing is particularly intense along the planar tectonic discontinuities, which coincide with radial and tangential directions with respect to the explosion center. Shearing motions occur along the radial fractures, while openings form along the concentric fractures. Rock strength is reduced by 20–30%, while the reduction of the acoustic speed is 10–25%. The hydraulic conductivity increases especially along the rock layering by a factor of up to 1000.

Formation of the new fractures along the pre-existing zones of weaknesses is observed in this zone. It is caused by opening of the primary micro- and macro-fractures, as well as by forming the new fractures along the structural boundaries within the rock. The most intense damage occurs along the natural layering. The degree of damage decreases with increase in distance from the center of the explosion. Areas with more intense damage often surrounded by less damaged

[12] Not sure about the second value, perhaps a typo

mass. Based on the analysis of the cores the number of fractures is from 4-6 per meter of core to numbers too high to count. These deformations can be explained by heterogeneities in physical properties and by predominant fracturing along the pre-existing detachment surfaces. Hydraulic conductivity varies between 0.001-10 m/day. The hydraulic conductivity along layering is 1-10 m/day, across layering it is 0.01 – 1 m/day, and below the cavity it is 0.01 – 0.03 m/day. The porosity of the massif is 10-25%.

A zone of block fracturing (zone of renewed fractures) has approximately symmetrical shape mostly similar to the zone of intense fracturing. In the map view the radius of this zone reaches 65-70 m/kt$^{1/3}$. It has greater thickness along strike; the smallest thickness is below the cavity and across layering. The zone size increases when it crosses areas of tectonic deformations. There are no newly formed fractures in this zone; most of the deformations are due to opening of the pre-existing fractures. Some areas show more significant fracturing caused by spalling when the wave passes through areas with sharp changes in rock strength, zones of foliation or boundaries between different rocks. The thickness of damage zones in these areas reaches 1.5 – 2 m.

Rock strength in the zone of block fracturing is reduced by 10-15%, acoustic velocity is reduced by 5-15%. Permeability coefficient ranges between 0.05 and 10 Darcy, with the highest values observed closer to the center of explosion.

Collapse chimney forms as a result of collapsing of the damaged rock above the cavity. The chimney is characterized by loose mass of rock debris with fragment sizes close to the sizes observed in the major zones of irreversible deformations.

In the case of the dipping layers the upper part of the chimney is asymmetric and inclined up dip. The height of the chimney is 40-110 m. The fragment sizes vary from clay-size particles at the bottom to 10-15 cm and larger on the outer part. The hydraulic conductivity reaches 200 Darcy. Porosity may reach 25%, and the seismic velocity is 2270 m/s.

An apical void forms above the chimney, characterized by the intact rocks above the void. The arch can be found by the drop of the drill bit down by 2.8 – 8.5 m.

A zone of shear (or tensile) fractures forms as a result of explosions conducted near boundaries between media with different acoustical properties. At the free surface shear (tensile) fractures are observed in the wide area up to distances of 100-200 m/kt$^{1/3}$ (in some cases up to 1000 m/kt$^{1/3}$). The depth of these fractures is determined by the specific structure of the rock massif where the explosion is conducted, and typically it is 10-30 m/kt$^{1/3}$.

A zone of free surface deformations typically expressed as residual fractures in the rock massif. In some cases it is characterized by an uplift, often with a collapse crater in the middle. The radius of the uplift zone is 60-140 m/kt$^{1/3}$, and the height of the uplift is 0.7-2 m/kt$^{1/3}$.

1.5. The frequency–size distribution of damaged rock fragments

The intensity of the rock damage caused by an explosion can be characterized by the size of the rock fragments. The study of the frequency – size distribution is conducted by measuring either volumetric or mass fraction of the fragments of different size. Table 1.4 shows an example of

frequency-size distribution for the fragments created as a result of a fully-contained explosion PILE DRIVER with yield 60 kt, as well as for the rock pile created by DANNY BOY (0.42kt) (Rabb, 1970).[13]

Table 1.4 Information on the distribution of fragment size for Nevada Test Site explosions

Fragment size *x*, m	Weight fraction of the fragments with sizes greater than *x*, %	
	PILEDRIVER	DANNY BOY
0.012	89	92
0.025	85	89
0.05	80	85
0.1	70	76
0.15	55	70
0.3	40	57
0.6	15	37
0.9	5	25
1.2	2	17

The analytical function to determine the distribution of the fragments requires some probabilistic considerations regarding the rock damage mechanism. One of the commonly used models in mining is Rosin-Rammler distribution

$$\frac{m_t(x)}{m_0} = exp\left[-\left(\frac{x}{x_0}\right)^{\alpha}\right], \tag{1.21}$$

where $m_t(x)$ is the weight of the fragments with size larger than x, m_0 is the total weight of rocks, x_0 and α are the distribution parameters, such that x_0 characterizes the degree of fragmentation, and α determines its homogeneity.

Figure 1.15 shows an illustration of application of Rosin-Rammler analysis to the data from Table 1.4. It is clear in this case that the experimental curves describing the frequency - size distribution in Rosin-Rammler coordinates are practically linear (in a log – log log plot). Thus this distribution in terms of just two parameters is adequate for the description of the fragmentation caused by large explosions. Here we shall use Rosin-Rammler model to describe the frequency-size distribution of fragments without discussion of its merits or deficiencies. It is

[13] PILE DRIVER (2 June 1966), 62 kt at a depth of 463 m in granite, and DANNY BOY (5 March 1962), 0.43 kt at 34 m in basalt, were both UNEs at the Nevada Test Site (Springer et al., 2002).

important to note that the results of the characterization of fragmentation caused by an explosion are independent of the choice of the distribution.

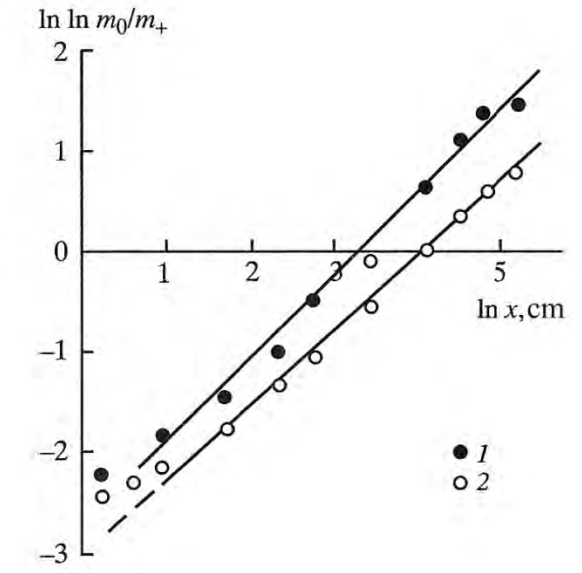

Figure 1.Fragment size distribution in log-log coordinates for Rosin-Rammler distribution for two US nuclear explosions: *1* – PILE DRIVER, *2* – DANNY BOY.

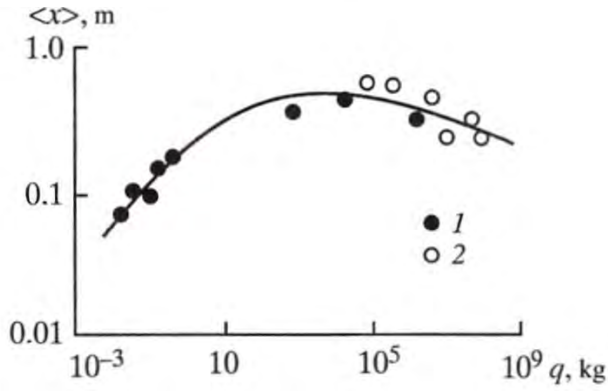

Figure 1.16 Average fragment size produced by underground explosions as a function of yield: *1* – chemical explosions, *2* – underground nuclear explosions.

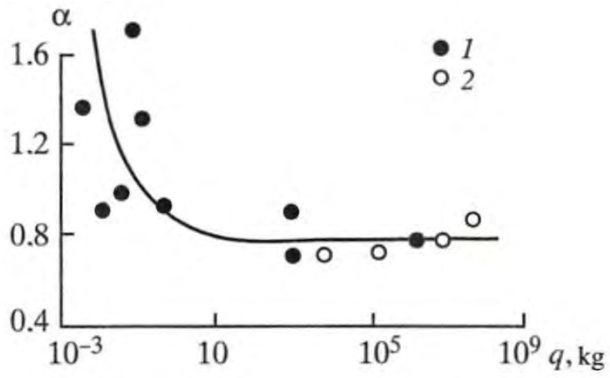

Figure 1.17 Parameter α for Rosin-Rammler distribution as a function of yield: *1* – chemical explosions, *2* – underground nuclear explosions.

Figures 1.16 and 1.17 show a compilation of the existing data for the frequency-size distribution of rock fragments for nuclear and chemical explosions describing the average fragment size $\langle x \rangle$ and α as a function of the explosion yield (Bronnikov and Spivak, 1981b).

Figure 1.16 shows that the average size of the fragments does not change monotonously as a function of yield. For chemical explosions of smaller yields ($10^{-2} \leq q \leq 10^2$ kg) the average fragment size increases with the yield increase:

$$\langle x \rangle = 0.23 q^{0.35} \text{ (m)}, \tag{1.22}$$

where q is yield in kg. For larger yields ($q \geq 10^3$ kg) the average fragment size weakly depends on the yield as:

$$\langle x \rangle = 0.42 q^{-0.12} \text{ (m)}, \tag{1.23}$$

where q is yield in kt.

We interpret the experimental curve of $\langle x \rangle(q)$ against scaled distance in Figure 1.18 as follows. The largest deformations of the medium at close distances are reached after the shock front passes. Rock damage takes place in the narrow shock front (multiple fracture formation). Applying geometrical similarity of the underlying parameters we conclude that for the rock crushed as a result of deformation behind the shock front, average fragment size should increase as $q^{1/3}$. We propose that this mechanism woks for explosions with smaller yields, which is supported by Equation 1.21.

In case of large explosions, the rock damage occurs due to shock loading, and the degree of damage is determined not only by the amplitude of the wave, but also by the duration of the compression phase τ_p during which the stress amplitude exceeds the rock strength. The duration of the positive phase should only be taken into account if it is close to $\langle x \rangle / c$. The same is true for τ_p.

For large explosions, the rock damage occurs as a result of the stress wave, and the only parameter determining the fragment size is the wave amplitude. If the medium is homogeneous, the average fragment size is determined by the stress magnitude created by the wave. Therefore, inside the volume proportional to the yield, the frequency–size distribution should be scale - independent.[14] Considering that at fixed distances from the explosion the wave amplitude is proportional to $q^{n/3}$, where n is the measure of attenuation (n ~1.6) and the peak displacements are proportional to $q^{2/3}$, we conclude that in reality the growth of the fragment size should decrease as q increases due to additional crushing of rock inside the volume (the result of piston action of the explosive products). The magnitude of this effect increases with yield as $q^{(2-n)/3}$. This reasoning agrees with Equation 1.23.

A change in mechanism of fragmentation with the yield increase affects the uniformity of fragmentation. For smaller explosions, when damage takes place in a volume, material is subjected to multiple crushing. Thus smaller explosions cause more uniform fragmentation of rock in comparison with larger explosions, where the rock damage takes place within the shock front causing a single event of crushing. A good illustration to this is the plot of parameter α (Figure 1.17). Indeed, with the yield increase the value of α decreases (suggesting decrease in uniformity of fragmentation). We note that the degree of uniformity is practically independent of yield in the broad range of q, starting from q ~ 100 kg. This significantly simplifies the

[14] The Russian authors may have meant that the frequency-size distribution may be independent of the magnitude of the stress loading, or the yield of the event. A direct translation would be that the “integral granulometric content of the fragmented mass should not be dependent on the scale of loading (action)”. Check later.

estimates of the fragment size distribution, because the value of α can be taken approximately constant ($\alpha = const \approx 0.8$).

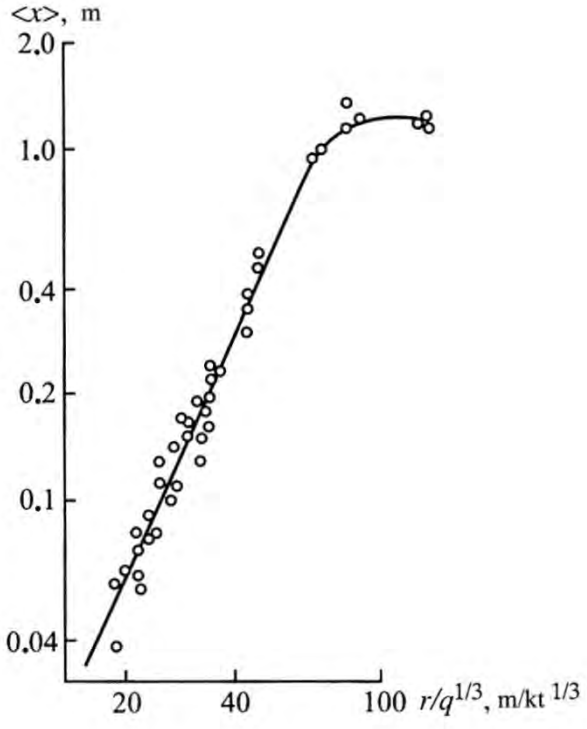

Figure 1.18 Average fragment sizes for a 2 kt underground explosion as a function of scaled distance.

Reduction of the intensity of the explosion effects on the medium with distance caused by the geometrical spreading and losses due to dissipation leads to changes in frequency-size distribution of the blasted rock. Large deformations near the cavity create high degree of fragmentation with average fragment size close to 0.02 m. Close to the boundary of the damage zone the fragment size is determined by the fracture spacing before the explosion. As an illustration, Figure 1.18 shows the average fragment size as a function of distance for an explosion with the yield of approximately 2 kt (Spivak, 1980a).

As a result of cavity collapse and subsequent subsidence and dilatation of the material above the cavity, a chimney forms filled with broken loose material. The shape of the chimney is close to cylindrical. The radius of the chimney is close to the cavity radius r_c, and the height is approximately (4 – 8) r_c. The rock in the chimney is loose, with the volume of void approximately equal to the volume of the cavity. As the charge depth increases, the size of the cavity as well as the size of the chimney decrease.

1.6. Scaling relationships and use of laboratory modeling of explosions

Study of natural and man-made phenomena involves establishing quantitative relationships describing the main properties of the system. For instance, the main purpose of study of mechanical phenomena following underground explosions is determining functional

relationships between the quantities which characterize the phenomena. Study of the functional relationships is based on the general laws of motion and equilibrium of mechanical systems, represented by differential equations. Because of the complexity of mathematical problems describing underground explosions, some of which are unsolvable, the main source of information is an experiment (both full-scale and laboratory, which models the large experiments at a smaller scale).

Qualitative and theoretical analysis is necessary in order to correctly conduct an experiment, to be able to generalize the results for different sets of parameters, as well as to obtain general relationships describing the system evolution. Such theoretical analysis is needed in order to: 1) select controlling parameters of the experiment, and 2) to determine governing scaling relationships based on these parameters (e.g. Sedov, 1967). Selection of the controlling parameters is based on adequate mathematical formulation of the phenomenon, or, in the case where mathematical modeling is not possible, on qualitative estimate of the system evolution and understanding its physics.

The quantitative description of the processes accompanying the underground explosion is based on preliminary accumulation of large volume of data, which in most cases requires conducting complex and lengthy experiments. The situation is simplified if physical mechanisms of each process is known and can be reproduced (either experimentally or numerically). Reproducing (or simulating in case of mathematical description) the main characteristics of the process in order to study the process is known as modeling. Analog experiments, also called experimental (or physical) modeling is the most effective method of study of the physical phenomena. This type of modeling involves reproducing the phenomenon in controlled conditions and at a convenient scale,

No model of a real process can fully reproduce the phenomenon, because the choice of a model is based on certain assumptions about the physical nature of the process and depends on the specific problem and on completeness of the object description. However the schematic representation of reality should be able to provide a full and accurate description of the mechanism. The quality of the model is determined by the amount of available underlying information about the object of study, as well as the possibility of the description of different aspects of the specific process in terms of a single model.

Modeling is widely used to study various physical and mechanical processes in the continuous medium. It is one of the most important methods to obtain complete and systematic information about the phenomenon, needed for solving practical problems. It is important to note that modeling is in fact the only way to study processes in complex systems that are very complicated or impossible to do using full-scale experiments.

In most cases modeling involves similarity transformations (or scaling) of the process, which means replacing the process in real life with a similar process using a model, often on a smaller scale. Thus the purpose of modeling is to determine the most important effects and relationships using a model, and later transferring the results into the real conditions. The advantages of this approach include the exact knowledge of the experimental parameters, reproducibility etc,

allowing to determine the relationships between the parameters and between different aspects of the process in a short time. In addition, modeling experiment provides limitless opportunities for varying the conditions (parameters) of the experiment.

In addition to obtaining primary data reflecting the parameter changes in space and time, small-scale analog experimentations can be used to analyze existing experimental and theoretical results and apply those to different conditions. This eliminates the need to repeat large and expensive full-scale experiments.

Small-scale analog experimentation is based on study of similar phenomena and processes, which determines the capability of the model to reflect the important features of the system under investigation. Similar physical processes are such that 1) belong to the same type, 2) can be described using the same equations, 3) have similar geometry, and 4) allow comparison using similar physical parameters. These properties of similarity also define the modeling rules.

Real-life processes and phenomena are characterized by significant diversity in their manifestation. Some subjects appear to be simple with a clear structure of the internal and external connections. Other phenomena are complex; and their schematic representation and parameterization can be a subject of study on its own. Therefore it is important to separate modeling based on complete similarity between the model and the object of study and partial similarity, when the model cannot reproduce the entire complexity of the effects accompanying the process. The latter is typically used to study complex processes, whose physical mechanism is not fully understood or it cannot explain some features of the object of study.

Sometimes modeling based on partial similarity is used in cases where accounting for all features of the real process is very complicated, or where it prevents comprehensive study of the most significant features of the process. For example it is used to determine the effect of a group of parameters on the results.

One example is the laboratory experiments studying explosive process in block made of canifole (Chapter 7)[15]. The process of damage of rosin with a micro-explosion is not fully similar to the process of rock damage during the underground explosion. First of all, there is a significant difference in physical properties between rock and rosin; second, the scale is very different causing differences in the physical processes during such explosions. Nevertheless, this type of experiment allows determining qualitative effects of the parameters (e.g. cavity size, screening) on the degree and homogeneity of fragmentation, which is important to know when planning the large scale underground explosion.

Complete similarity is achieved when all of the parameters are identical between the model and the real experiment. In practice it means equality of the dimensionless parameters (criteria complexes and simplexes) in the similarity equations describing the class of the processes. Defining a complete set of parameters is easy if there is a mathematical framework describing the process with a good degree of approximation. If such a framework does not exist or it is not well developed, it is difficult not only to determine the complete set of parameters, but also to determine some (scaling) parameters. It happens because in many cases it is difficult to

[15] Rosin is a pitch-like substance used to prepare violin bows

determine whether a specific parameter affects the process individually or in combination with other parameters.

Selection of scale-invariant physical relationships from a number of different physical parameters gives an opportunity to expand the capabilities of modeling. Thus, modeling of complex (multi-component or multi-stage) processes that occur continuously can be simplified by modeling each individual sub-process separately, since the individual processes are characterized by different parameters and have to be modeled separately.

In this case the output (the results of the previous process) can be used as the input for the next one. For example, modeling of the process of fragmentation of the rock mass (in mining) using different methods of explosive technology should be performed in two stages.

The first stage models the explosive disintegration of the rock medium accounting for all features of the explosive method; the second process is the ejection of the crushed rock mass. The second process is modeled separately, because the parameters for each of them (when converted to real-life scale) are different. In this approach using a small-scale experiment, an inherent characteristic of the explosion should be chosen as the scaling criterion for multi-scale application. For example scaling could be based on a measure of dilatancy or bulking of the broken (exploded) rock mass, which characterizes the specific scheme of fragmentation for self-similar grain-size distributions, between the model and the real system.

The choice of the model parameterization is determined by a specific problem. To avoid subjectivity in parameter evaluation it is necessary to constantly improve modeling methods. Determining general similarity (scaling) relationships is very important for development of the framework for experimental study of physical processes. Special attention should be paid to development of the methods of functional modeling and modeling based on partial similarity, which provides the most practical description of real processes.

Let us look at the qualitative analysis of an underground explosion. The evolution and the results of the underground explosion are determined by the following system of parameters.

1. Parameters characterizing the explosive source: total energy released by the explosive charge E, the pressure in the cavity P, effective (characteristic) size of the explosive source $R = \sqrt[3]{3q/4\pi\varepsilon} \sim q^{1/3}$, where ε is the specific energy content of the TNT, q is the TNT equivalent of a nuclear explosion.
2. Parameters characterizing the conditions of the explosion: depth of burial W, the coupling parameter – the radius of the charge cavity R_c.
3. Medium parameters: rock density - ρ, P-wave velocity – C_p, Young modulus – Y, Poisson coefficient – ν, rock strength - σ_*, internal friction coefficient - k_f.
4. Space x_i (i = 1,2,3) and time t coordinates.

According to this parameter set the explosion evolution and its effects could be described in terms of the following dimensionless parameters:

$$\frac{tC_p}{R};\ \frac{x_i}{R};\ \frac{E}{\rho W C_p^2};\ \frac{P}{\rho C_p^2};\ \frac{\sigma_*}{\rho C_p^2};\ \frac{Y}{\rho C_p^2};\ \frac{W}{R};\ \frac{R_c}{R};\ \nu;\ k_f.$$

Using this framework any explosion characteristic $F(x, t)$ can be expressed as a function of these dimensionless parameters. For example the *P*-wave amplitude is given by

$$\frac{v_0}{C_p} = f\left(\frac{tC_p}{R}; \frac{x_i}{R}; \frac{\sigma_*}{\rho C_p^2}, \dots \nu; \ k_f\right).$$

The last relationship suggests self-similarity of underground explosions if the size of the source is defined as *R* (which is the same as using the parameter $q^{1/3}$).

Small scale analog experimentation is a very effective method of study of complex natural and man-made processes. The experiments allow us to study the effect of different parameters on the explosion evolution and the results. In this monograph physical modeling is used to study ejection explosions, as well as fully-contained explosions conducted under different conditions (shallow explosions, explosions in larger cavities, explosions with a screen made of a hollow space). We note that transfer of the results from modeling to the full scale explosions (including their analysis and generalization) demonstrated usefulness of the information and validity of the models.

We now look at the characteristics of the underground explosions from the physical and theoretical point of view (Gubkin, 1978). Analysis of waves generated by the explosions in solid medium is typically based on empirical data, since theoretical description of the properties of damaged medium in the non-linear zone is complicated. A matematical formulation of the problem using general principles of continuum mechanics leaves undetermined such parameters as internal energy, entropy, elastic stresses that created in the medium during its motion. Determining the mechanism of dissipation of the wave energy during fragmentation is an important problem of the continuum mechanics.

Currently the motion generated by an explosion is seen as follows. At high pressures (exceeding 10^5 kg/cm^2) medium behaves as a fluid. The properties of this fluid are described by using empirical equations of state obtained from the data on shock compressibility of solid materials. At lower stresses it is assumed that the medium behavior is elasto-plastic. The principal components of the stress tensor σ_R, $\sigma_\theta = \sigma_\varphi$, determined by plastic flow, are related through the universal relationship (using spherical symmetry: σ_R, σ_θ and σ_φ are the radial and two tangential components of the stress tensor respectively). For example, a relationship in the following form can be used:

$$\sigma_R - \sigma_\theta = const \cdot (\sigma_R + 2\sigma_\theta)\sigma_R,$$[16]

assuming that the maximum shear stress is proportional to the pressure. Also the conditions $\sigma_R - \sigma_\theta = const$ or $\sigma_\theta = 0$ can be used. One of such conditions is sufficient to describe motion with central symmetry without using the energy equation, if we make certain assumptions about the elastic properties of the fractured medium.

[16] Not sure about the dimensions…

The radius of the damage zone plays a major role in generating elastic waves by underground explosions. Displacement u, velocity v and the radial component of the stress tensor σ_r in a spherical elastic wave at a distance r from the center are given by the following expressions:

$$u = \frac{\ddot{\Psi}(\tau)}{C_p r} + \frac{\dot{\Psi}(\tau)}{r^2}; \tag{1.24}$$

$$v = \frac{\dddot{\Psi}(\tau)}{C_p r} + \frac{\ddot{\Psi}(\tau)}{r^2}; \tag{1.25}$$

$$-\sigma_r = \rho \frac{\dddot{\Psi}(\tau)}{r} + 4\mu \frac{\ddot{\Psi}(\tau)}{C_p r^2} + 4\mu \frac{\dot{\Psi}(\tau)}{r^3}; \tag{1.26}$$

where the function $\Psi(\tau)$ determining the wave profile depends on the time τ measured from the arrival of the wave into the point r, C_p is the P-wave velocity, ρ is the density, μ is the shear modulus. Before the wave arrives into the point r the value of the function $\Psi = 0$, after the wave passes ($\tau \to \infty$) it attains the limiting value Ψ_1. At the same time its derivatives $\dot{\Psi}$ and $\ddot{\Psi}$ become zero. The value Ψ_1 has a very simple interpretation as a quantity proportional to the volume displaced by the explosion:

$$\Psi_1 = u_1 \cdot r^2 = \frac{\Delta V}{4\pi},$$

where u_1 is the final displacement in the elastic region at a distance r. At larger distances only the first terms in (1.24)-(1.26) are important. For instance, the equation determining the velocity at large distances r is given by:

$$v = \frac{\ddot{\Psi}(\tau)}{C_p r}.$$

Because of the strong high-frequency attenuation the elastic waves at large distances have predominant period exceeding the characteristic impulse time τ_0 observed near the center of the explosion. Therefore the amplitude at large distances is determined by the low-frequency source radiation. The Fourier transform of the velocity $v(r,t)$ is given by:

$$v(r,t) = \frac{1}{2\pi}\int_{-\infty}^{\infty} \bar{v}(r,\omega) e^{i\omega t} d\omega.$$

The spectrum is given by:

$$\bar{v}(r,\omega) = \frac{1}{C_p r}\int_0^{\infty} \dddot{\Psi}(\tau) e^{-i\omega\tau} d\tau = \frac{i\omega}{C_p r}\int_0^{\infty} \ddot{\Psi} e^{-i\omega\tau} d\tau.$$

For low frequencies ($\omega < 2\pi/\tau_0$) this expression becomes:

$$\bar{v}(r,\omega) = \frac{i\omega}{C_p r}\int_0^{\tau_0} \ddot{\Psi} d\tau = \frac{i\omega}{C_p r}\dot{\Psi}_1 = \frac{i\omega}{C_p r}\frac{\Delta V}{4\pi}.$$

Thus the low-frequency amplitude is proportional to ΔV. Figure 1.19 shows the displacement record as a function of time at a distance r = 229 m for a nuclear explosion SALMON with the yield of 5.3 kt ($2.22 \cdot 10^{13}$ J) (Rodgers, 1966; Werth and Randolph, 1966). The explosion was

conducted in salt (with density ρ = 2.24 g/cm^3, shear modulus $\mu = 1.04 \cdot 10^5$ kg/cm^2, and a bulk modulus $K = 2.9 \cdot 10^5$ kg/cm^2) at a depth of 828 m. From Figure 1.19 the final displacement of the medium u1 is approximately 12 cm, which can be used to calculate the volume change:

$$\Delta V = 4\pi r^2 \cdot u_1 \approx 80{,}000\, m^3.$$

Now we compute ΔV assuming that the medium does not break during the explosion, but instead deforms according to the laws of linear elasticity. Gas pressure created by the explosion in the cavity with radius r_c is given by:

$$P = 3(\gamma - 1)E_0/4\pi r_c^3.$$

This pressure applied to the cavity wall creates an elastic wave leading to the volume increase according to the condition on the boundary $r = r_c$. Simple calculation yields the displaced volume

$$\Delta V = \frac{3(\gamma-1)E_0}{4\mu},$$

which does not depend on the cavity radius.

Using the values $E_0 = 2.22 \cdot 10^{13}$ J, $\mu = 1.04 \cdot 10^5$ kg/cm^2, and γ=1.25 we can estimate the volume $\Delta V = 400\, m^3$, or approximately 200 times smaller than determined during Salmon experiment. This comparison shows that damaged medium cannot support extremely large shear stresses and hold high gas pressure in the cavity. The force exerted by an explosion with high energy density on the rock mass surrounding the damage zone is more significant than for explosions with smaller energy density. Therefore we conclude that if an explosion is conducted in a large enough cavity, the low-frequency amplitude will be significantly reduced.

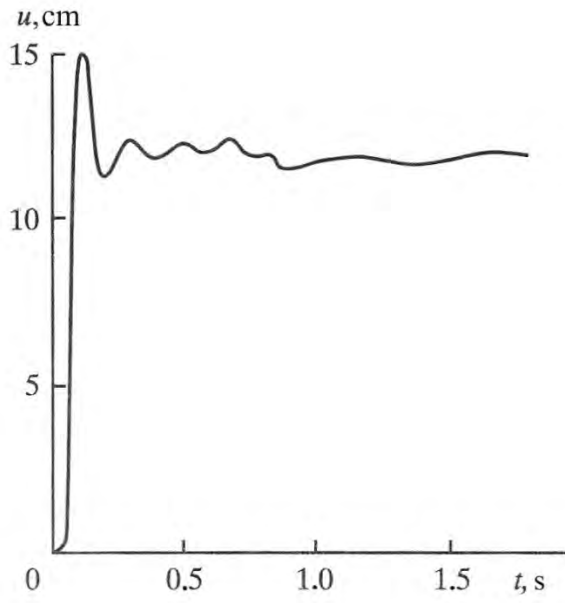

Figure 1.19 Particle displacements as a function of time for a nuclear explosion.

The analysis above shows an important role of the yield strength, both shear and tensile, below which the medium maintains its elastic properties and does not fracture. The lower the strength, the higher the fraction of energy transferred to the surrounding medium due to an increase of the size of non-linear plastic zone. Since natural media contains large number of fractures, its damage will be limited by the value of the lithostatic pressure.

In the non-linear zone the shock front soon broadens, so that the velocity in the wave front increases gradually to its maximum value (as opposed to shock waves in liquids and gases, for which the thickness of the shock front is infinitely small and the maximum value is reached as a step). Experimental measurements of the peak velocity values are typically interpolated to produce a power law as a function of distance *r* to the center (similar to Equation 1.8):

$$v_m = v_0 \left(\frac{r_c}{r}\right)^{-n}$$

The exponent n in this formula is close to 1.5. The shock compressibility data for solid materials show that v_0 may be related to the pressure acting on the medium at the initial moment via the following expression:

$$P = \rho v_0(\alpha + \beta v_0),$$

where α and β are the constants (α is close to $\sqrt{K/\rho}$, where K is the bulk modulus, ρ is the density, and β is a dimensionless constant varying for different media between 1.2 and 1.7). For the explosions with very high energy density, when the initial pressure significantly exceeds medium elastic moduli, the velocity v_0 is proportional to $\sqrt{\rho}$. Assuming that n = 1.5 and given that ρ is proportional to $E_0 r_c^{-3}$, we conclude that the peak velocity v_0 is independent on the initial cavity radius r_c:

$$v_0 = const \left(\frac{E_0^{1/3}}{r}\right)^n.$$

(THIS PAGE INTENTIONALLY LEFT BLANK)

Chapter 2.

Excavation by Underground Nuclear Explosions

Major characteristics of excavation explosions are related to the large scale of these explosions, to the high energy density at the source, and to the specifics of formation of gas by-products of the explosion. Experiments with these explosions have shown that their excavation effect significantly depends on emplacement-rock properties, including their moisture content as well as the presence of other gas-forming components. These properties of nuclear explosions do not allow usage of existing methods that have been developed for estimating the main parameters for chemical explosions. In addition, the generally higher yields for the nuclear explosions compared to chemical explosions require correction of the scaling relationships.

In this chapter we present a full account of the experimental data for all nuclear explosions of excavation type. We describe a method of laboratory modeling of excavation explosions. Using this method we obtain physics-based scaling relationships suitable for calculation of parameters for nuclear explosions of excavation type. We also show how the scaling relationships change with explosion yield variations.

2.1. Excavation explosions

The total number of nuclear explosions that have been used for excavation is limited. They include nine American and seven Soviet explosions, conducted in order to explore possibilities of using the excavation action of nuclear explosions for civil engineering purposes. The main parameters related to the placement of the nuclear charges, and sizes of the formed craters with respect to the original surface, are shown in Table 2.1 (where q is explosive yield; W is depth of burial; R, H, and V are respectively the radius, depth, and volume of the crater; $n = R/W$ is the excavation parameter, sometimes called the ejection coefficient; and $k = q/V$ is the specific energy consumption) (Nuclear , 1970; Toman, 1970; Nuclear…, 2000). Table 2.1 also shows data related to excavation (cratering) explosions that were initially designed to be partially confined (SULKY, 18 December 1964, USA; BH. 125, 4 November 1970, USSR).

Table 2.1 shows that the excavation work produced by nuclear explosions is relatively efficient. However, the value of the specific energy consumption is somewhat higher for nuclear than for chemical explosions (Rodionov, 1970). This can be explained by the greater size of nuclear explosions as well as by characteristics of the formation of gas by-products due to melting, vaporization, and chemical decomposition of the emplacement rocks. Thus for nuclear explosions with "normal excavation" ($n \approx 1$) the value of specific energy consumption is approximately 10 kg/m^3 for nuclear explosions on the order of 1 kt, and increases by a factor of 2 with a yield increase to 100 kt. In the same conditions the specific energy consumption for chemical explosions decreases from 4–6 kg/m^3 for a 1 kt explosion to 1.5–3 kg/m^3 for a 1 ton explosion (Dokuchaev et al., 1963; Murphy and Vortman, 1961).

Table 2.1. Parameters of the excavation nuclear explosions

Explosion #	Explosion	Rock type	Parameter							
			q, kt	W, m	$W/q^{1/3}$	R, m	H, m	V, m^3	n	k, kg/m^3
N/A	JANGLE-S	Alluvium	1.2	-1.06	-	13.7	6.4	$1.26 \cdot 10^3$	-	-
1	JANGLE-U	"	1.2	5.2	4.9	39.6	16.2	$2.8 \cdot 10^4$	7.65	42.9
2	TEAPOT-S	"	1.2	20.4	19.2	44.5	27.5	$7.4 \cdot 10^4$	2.2	16.2
3	NEPTUNE	Tuff	0.115	30.5	62.7	33	10.5	$1.7 \cdot 10^4$	1.0	6.8
4	DANNY BOY	Basalt	0.42	33.5	44.7	32.6	19.0	$2.75 \cdot 10^4$	0.97	15.3
5	SEDAN	Alluvium	100	193	41.6	185	97	$5.1 \cdot 10^6$	0.95	19.6
6	CABRIOLET	Rhyolite	2.3	52	39.4	55	36	$1.38 \cdot 10^5$	1.06	16.7
7	SCHOONER	Tuff	31	108	34.4	130	63.4	$1.74 \cdot 10^6$	1.2	17.8
8	BUGGY	Basalt	1.1 x 5	41.1	39.8	38.7	19.8	$2 \cdot 10^5$	0.95	27.5
9	PALANQUIN	Rhyolite	4.3	85	52.3	36.3	21	$3.58 \cdot 10^4$	0.43	120.1
10	SULKY	Basalt	0.09	27.4	61.1	9.8	-3.0	$-9 \cdot 10^3$	0.36	-
11	BH 1003	Aleurolite	1.1	48	46.5	60	20	$1.1 \cdot 10^5$	1.25	9.9
12	BH 1004	Sandstonne	140	175	33.7	207	100	$6.4 \cdot 10^6$	1.18	21.9
13	BH T-1	Argillite [shale]	0.24	31.4	50.6	37	21	$3.7 \cdot 10^4$	1.19	6.5
14	BH T-3	Aleurolite	0.21 [1] x 3	31.4	52.8	35	16	$7.7 \cdot 10^4$	1.12	8.2
15	TAIGA	Sandy clay	15 x 3	127	51.5	170	8 – 15	$5 \cdot 10^6$	1.34	9.0
16	BH 101	Sandstone	80	227	52.7	145	15	$5 \cdot 10^5$	0.64	160
17	BH 125	Porphyrite	19	151.3	56.7	97	17.5	$5 \cdot 10^5$	0.65	63.3

[1] In the text the yield is 3 x 0.24 kt

Table 2.2. Physical properties of rocks for excavation nuclear tests

Explosion #	Explosion	Rock type	Parameter							
			ρ, g/cm^3	C_p, m/s	Strength, kg/cm^2		υ	η	η_w / η_{CO2}	η_e
					σ_*	σ_t				
1	JANGLE-U	Alluvium	1.6	920	-	-	0.25	0.1	0.1/0	0.1
2	TEAPOT-S	“	1.7	1220	-	-	0.25	0.1	0.1/0	0.1
3	NEPTUNE	Tuff	2.0	2200	360	12	0.12	0.153	0.153/0	0.153
4	DANNY BOY	Basalt	2.62	4250	1900	140	0.22	0	0/0	0
5	SEDAN	Alluvium	1.8	1530	60	2	0.3	0.12	0.12/0	0.12
6	CABRIOLET	Rhyolite	2.5	4000	910	280	0.26	0.1	0.1/0	0.1
7	SCHOONER	Tuff	2.35	2030	700	-	0.25	0.07	0.07/0	0.07
8	BUGGY	Basalt	2.6	3100	1400	140	0.23	0.1	0.1/0	0.1
9	PALANQUIN	Rhyolite	2.5	4000	940 – 980	240	0.26	0.1	0.1/0	0.1
10	SULKY	Basalt	2.6	4000	1170	140	0.2	0	0/0	0
11	BH 1003	Aleurolite	2.69	3650	320 – 770	80	0.33	0.054	0.036/0.018	0.05
12	BH 1004	Sandstonne	2.56	4800	430 – 600	70	0.34	0.21	0.19/0.02	0.194
13	BH T-1	Argillite [shale]	2.54	4670	500 – 700	140	0.31	0.128	0.05/0.078	0.07
14	BH T-3	Aleurolite	2.61	4360	850 – 890	70	0.3	0.04	0.02/0.02	0.024
15	TAIGA	Sandy clay	2 – 2.3	1800	20 – 50	-	-	0.3	0.3/0	0.3
16	BH 101	Sandstone	2.61	4000	650	50	-	0.129	0.068/0.06	0.081
17	BH 125	Porphyrite	2.75	4930	1124	110	0.25	0.12	0.05/0.07	0.065

Figure 2.1. Crater created by an underground nuclear explosion SEDAN (USA)

The largest examples of nuclear excavation explosions, SEDAN (6 July1962, USA) and BH 1004 (15 January 1965, USSR), with yields on the order of 100 kt and crater volumes over 106 m3, have demonstrated the possibilities of practical use of nuclear explosions for movement of large volumes of rocks. Three experiments with charges located in a row, demonstrated possibilities of using nuclear explosions for excavating substantial channels and large pits in the ground.

Table 2.1 indicates that a small number of nuclear excavation explosions were conducted in substantially different rock types, ranging from porous and wet alluvium and tuff, to hard crystalline rocks (basalt, sandstone, etc). Table 2.2 shows the major physical properties and gas content of rocks used for excavation (where ρ is the density; σ∗ is compressive strength; σt is tensile strength; *C* is the *P*-wave velocity; ν is the Poisson coefficient; and η is the total gas content characterized by the weight fraction of gas-forming components). Gas content is determined by measuring the weight loss of a rock sample, after heating it to temperatures of 1000º–1100º, i.e. close to melting.

The main components of gas content are water vapor (η_{ω}) and carbon dioxide (η_{CO2}). American explosions were conducted in rocks with simple gas-content properties. Both porous rocks (tuff and alluvium) and hard rocks (basalt and rhyolite) are silicates containing only free

water. Alluvium is represented by lightly cemented clastic material with the addition of clay particles. These sediments are often poorly sorted and may contain fragments of different sizes from fine-grained sand to pebbles and boulders. The density of alluvium in the near-surface layers is 1.4 – 1.6 g/cm^3; porosity is 30 – 40 %, and seismic velocity is500 – 900 m/s. At depth of tens or hundreds of meters the density reaches 1.8 – 2.2 g/cm^3; porosity is 20 – 30 %; moisture content is 7 – 18%; cohesion is 3 kg/cm2, and seismic velocity is 1000 – 2000 m/s (Boardman et al., 1964).

One of the notable American excavation explosions in alluvium was SEDAN (Nordyke, 1962), a nuclear charge with yield of 100 kt detonated at a depth of 193 m in a 914 mm diameter borehole. The explosion created a symmetrical crater with diameter of 3780 m, a depth of 97 m, and a volume of $5.1 \cdot 10^6$ m^3. The deviation from circular shape for the crater was at most several percent (Figure 2.1). The ejected material was lifted (thrown) to a height of 600 m. The major part of the ejected material was deposited within a radius of 2 km. The maximum height of the ejecta blanket reached 30 m.

A series of three nuclear explosions with the same yield (1.2 kt) was conducted in alluvium in the USA. The series included two excavation explosions and an above ground explosion (JANGLE-S), for which the charge was placed at a height of 1.06 m. These explosions demonstrated the significant effect of depth-of-burial on crater size. For instance, an increase of the depth-of-burial for the 1.2 kt charge from 5.2 m to 20.4 m resulted in an increase of the radius, and of the depth of the crater, by a factor of 3 – 4; while the volume increased by a factor of over 50.

Volcanic tuffs used as emplacement medium for many American excavation explosions show strong gradient (with depth) in physical and mechanical properties. As a rule the density of tuff near the surface is 1.5 – 1.6 g/cm^3, porosity is 25 – 40 %, moisture content is 15 – 20 %, and compressive strength is 200 – 300 kg/cm2. With depth increase the density of tuff becomes 1.7 – 2.2 g/cm^3, seismic velocity is 1800 – 4200 m/s, and compressive strength is 200 – 300 kg/cm2. The tuff massif used for the SCHOONER nuclear test was even more complex (Tewes, 1970). It can be divided into three layers: a strong tuff with density of 2.4 g/cm^3 that extends down to 38 m, then down to 103 m there is a porous tuff with density of1.2 – 1.5 g/cm^3 and moisture content of 10 – 40 %, with an underlying strong tuff below 103 m. The nuclear charge placed at 108 m was near the boundary between two layers. As a result the crater had an unusual shape: the slopes in the upper (strong) part were 75, while in the lower part (within the porous layer) the slopes were 35 – 40◦.

The US underground nuclear test called NEPTUNE was also conducted in tuff, although unlike other excavation explosions the charge, with low initial energy density ($2 \cdot 10^{-3}$ kt/m^3), was placed at the base of the mountain with a slope close to 30º. Due to collapse of the upper part of the crater the bottom and the lower part of the crater were filled. As a result the upper radius (along the ridge) of the crater was approximately 25% larger than the lower crater with respect to the point of the line of the least resistance (LLR) projection to the surface of the slope.

Basaltic rocks, in which some of the US nuclear explosions were conducted, are characterized by density of 2.4 – 2.7 g/cm^3, porosity m = 5 to 15%, seismic velocity of 2.2 – 5.0 km/s, compressive strength of 1.2 – 2.5 g/cm^2, and tensile strength of 100 – 200 kg/cm^2. Table 2.3 shows drilling data for the analysis borehole located 8 m from the epicenter of the nuclear explosion DANNY BOY conducted in the US on 5 March 1962 (Nordyke and Wray, 1964). The test produced a relatively symmetrical crater (Figure 2.2), however the ejecta height was non-uniform and varied between 4.5 and 7.5 m. The underground nuclear test SULKY was conducted in the same rock massif, but produced a mound with a crater in the middle (Figure 2.2), instead of a crater in the ground. The US test BUGGY (12 March 1968) was also conducted in basalt. It involved detonation of 5 nuclear charges, 1.1 kt each, placed in a row, 45.7 m apart from each other and all at the same depth of 41.1 m. This explosion was intended to study the possibility of using nuclear explosions for constructing canals. It produced a pit with a width of 77.4 m and a length of 260.6 m with respect to the ground surface.

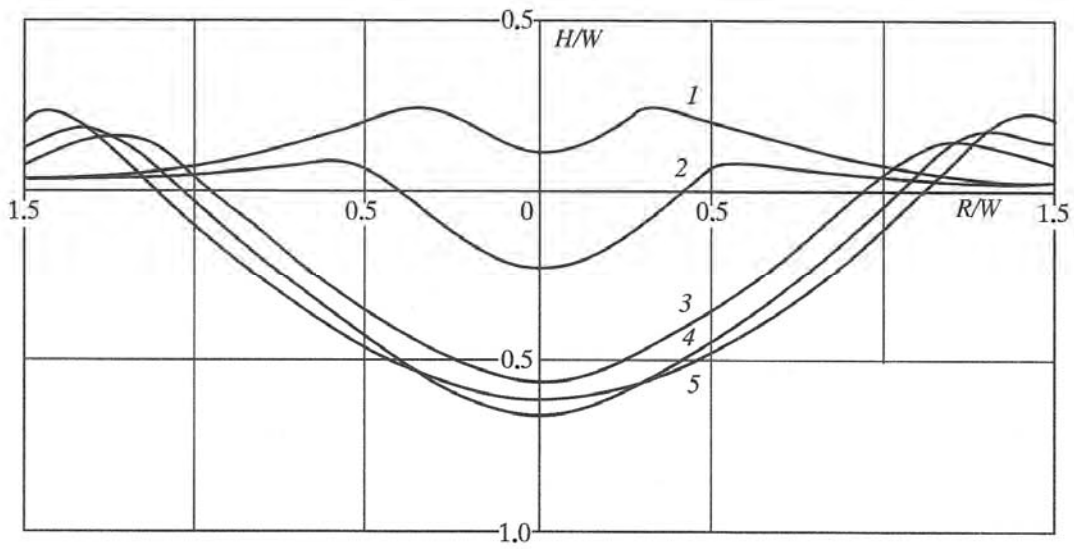

Figure 2.2. Topographical profiles through craters created by in hard rock by the following nuclear tests: 1 – SULKY; 2 – PALANQUIN; 3 – DANNY BOY; 4 – CABRIOLET; and 5 – BH 1003 (USSR)

Table 2.3. Rock parameters from drilling data for DANNY BOY

Depth, m	Paramater						
	ρ, g/cm^3	ρ_s, g/cm^3	m, %	σ_*	υ	C_p, m/s	C_s, m/s
4.9	2.41	2.87	16	1180	0.25	4240	2680
7.3	2.59	2.84	8.9	2410	0.18	5020	2990
23	2.66	2.84	6.3	2450	0.18	4490	2640
39	2.58	2.82	8.5	1620	0.25	4120	2650

Rhyolite (porphyrite trachite) is similar to basalt in physical properties, with lower density (ρ = 2300 ÷ 2500 kg/cm^3) and lower compressive strength (σ_* = 900 ÷ 1000 kg/cm^2) (Terhune et al, 1970). Possibly due to these differences in physical properties, or perhaps due to higher moisture content, excavation efficiency of UNTs CABRIOLET (January 26, 1968, USA) and PALANQUIN (April 14, 1965, USA) was higher than for explosions in basalts (e.g. Table 2.1). No exact data about moisture content for basalt and rhyolite is available, except for the notion that they are dry rocks with insignificant (<1%) water content. The observations have shown that during the explosion in rhyolite and during BUGGY the phase of gas acceleration was noted, which suggests the presence of gas components. During DANNY BOY and SULKY (December 18, 1964) no gas acceleration and no gas venting was observed. Therefore in the future analysis we assume that the emplacement basalt for DANNY BOY and SULKY was dry (η = 0), while the emplacement rocks for other rhyolite and basalt explosions has moisture content of 1% (η_w = 0).

Soviet excavation nuclear explosions were conducted mainly at the STS with flat topography (Peaceful…, 1970). Nuclear charges were placed into the competent rocks with complex geological structure, represented by tilted layers of sandstones, shales, aleurolites, gravelites, porphyrites etc. The emplacement rocks have high gas content due to high water content, presence of carbonate rocks and minerals containing crystallization and hydroxyl water molecules. All testing areas were broken with dense fracture networks, therefore rocks were heterogeneous with different rock types juxtaposed next to each other.

The first excavation explosions in BH 1004 (January 15, 1965) was conducted in one of these sites near the riverbed of Shagan River. The charge with yield of 140 kt was detonated in a borehole with diameter of 900 mm at a depth of 175 m. The emplacement rocks were represented by water-saturated sandstones with layers of aleurolites and coal seams. The density at the working point was 2430 – 2660 kg/m^3, porosity – 14 - 20%, moisture content – 19%, compressive strength – 13 – 39 MPa, and total gas content – 0.21.

Figure 2.3 shows the snapshots of the throwout development for the explosion in BH 1004. The initial ground surface velocity in the epicenter was 100 m/s. After 2.5 s the velocity of the uplift reached 140 m/s and the hot gas venting occurred.

Maximum uplift reached height of 960 m, the ejecta cloud reached the height of 4.8 km. The explosion created a crater with the following dimensions relative to the ground surface: diameter 400 – 430 m, depth 100 m, volume $6.4 \cdot 10^6$ m^3, the ejected mound height of 20 – 35 m.

In addition several more cratering explosions were conducted at the STS: 1) 1.1 kt explosion (October 14, 1965) in BH 1003 at depth of 48 m in shale; 2) 80 kt explosion in BH 101 (December 18, 1966) at depth of 227 m in sandstones and porphyrites; 3) 19 kt explosion in BH 125 (November 4, 1970) at the depth of 151.3 m in layered porphyrites shale. The crater sizes and the rock properties around the nuclear chamber are presented in Tables 2.1 and 2.2 respectively.

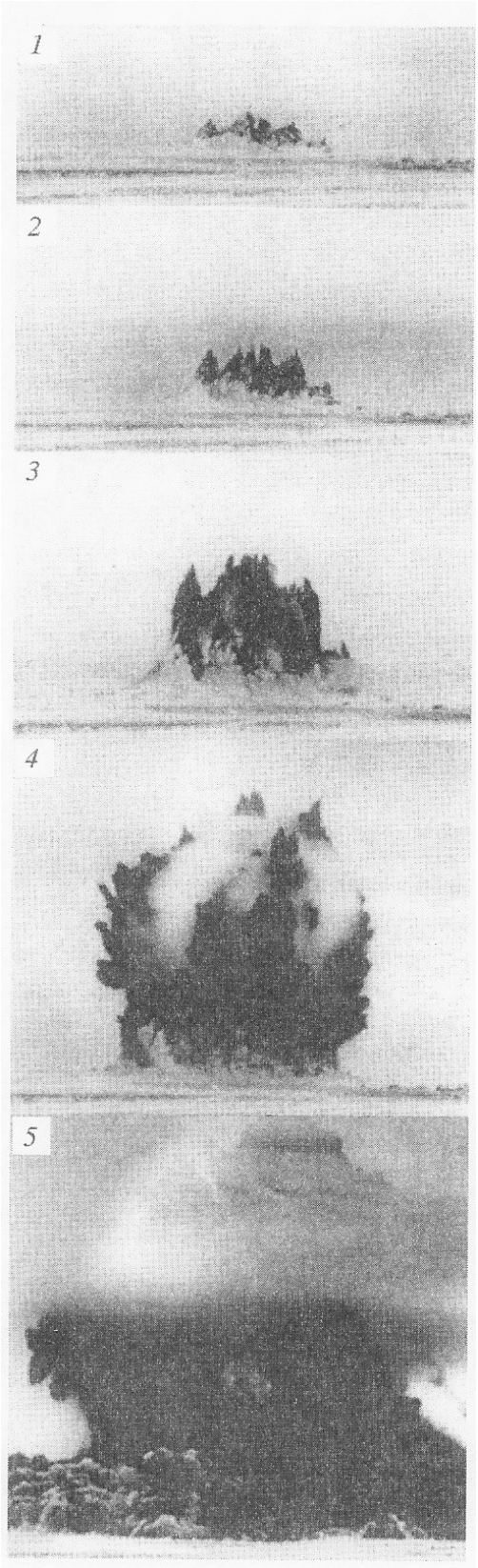

Figure 2.3. Snapshots showing development of explosion conducted in BH 1004. The snapshots are shown for the following times from detonation: *1* – 0.5 s; *2* – 0.65 s; *3* – 1.5 s; *4* – 3.6 s; and *5* – 5.5 s.

In addition excavation explosions were conducted at the STS as a part of peaceful nuclear explosion (PNE) program[2]: 1) 0.24 kt explosion (October 21, 1968) in BH T-1 at depth of 31.4 m in argillites with some sandstones; 2) three 0.24 kt charges placed in a row at depth of 31.4 m with 40 m spacing between the boreholes with a code-name T-3 (November 12, 1968) in aleurolites/argillites with layers of sandstone. As a result of this nuclear test a pit was formed with a length of 142 m, width of 60 – 70 m, depth of 16 m, and height of ejected mound of 7 – 16 m.

The basement rock at the sites of these explosions was covered with a layer of loose sediments of different thickness. Alternatively the surface rocks were represented by highly fractured basement rocks with layers of clay with a layer of alluvium deposits at the surface (clay, sand) with a thickness of 2 – 5 m. Thus the total thickness of loose sediments was: for explosion in BH 1003 – approximately 5 m, in BH 1003 – 21 m, in BH 101 – 40 m, in BH 125 – 25 m. For T-1 and T-3 explosions the sediment thickness was 24 and 18 m respectively.

Increase in gas content in the presence of clay material promoted the excavation efficiency of Soviet excavation explosions in comparison with the American explosions. Comparison between the values of specific energy consumption *k* (Table 2.1) for explosions with similar values of scaled depth of burial illustrates this point.

Another soviet excavation explosion with charges placed in a row (other than T-3) was test Taiga conducted on March 23, 1971 as a part of the PNE program in the area of planned Pechoro-Kolvinskii Canal in Perm Region (Nuclear …, 1970)[3]. The explosion was conducted in a forested swampy area. Three nuclear charges 15 kt each were placed at the same depth (127.4 m) with a spacing of 163 m between the charges. The charges were placed close to the boundary between two different rock types. Underlying basement rocks included alevrite, argillite and marl with a density of 2300 – 2600 kg/m^3, porosity of 8 – 16%, moisture content of 9%, seismic velocity of 3500 – 4500 m/s, and compressive strength of 50 – 130 MPa. A layer of sandy clay situated above the basement had a density of 2000 – 2300 kg/m^3, and a moisture content of 30%. Sandy clay layer was covered with a layer of water-saturated sand with thickness of 10 – 30 m, density of 1800 – 1900 kg/m^3, and a volume moisture content of 30 – 50%.

Figure 2.4 shows the snapshots of the throwout cupola development for explosion Taiga. Initial velocity of uplift in the epicenter of the central explosion was 70.6 m/s, while the velocity in the epicenters of the side explosions were 61.6 and 80.8 m/s. Maximum height of the cupola uplift in the epicenter was 220 – 260 m. Ground velocity between the charges was almost twice as high as the epicentral velocity due to compression wave interference at the free surface. The height of the cupola uplift reached 300 – 500 m.

[2] When the bilateral Peaceful Nuclear Explosions Treaty was negotiated in the 1970s between the US and the USSR, it was formally agreed to define a "Peaceful Nuclear Explosion" as any nuclear test explosion conducted outside recognized nuclear weapon test sites such as that at Semipalatinsk. Nevertheless the technical community has often regarded some of the nuclear tests at this weapons test site as being PNEs—namely those that were conducted to explore civil engineering applications. (Note added by translators.)

[3] It is not clear how an explosion conducted in 1971 could be described in a publication from 1970 (Note from the translators)

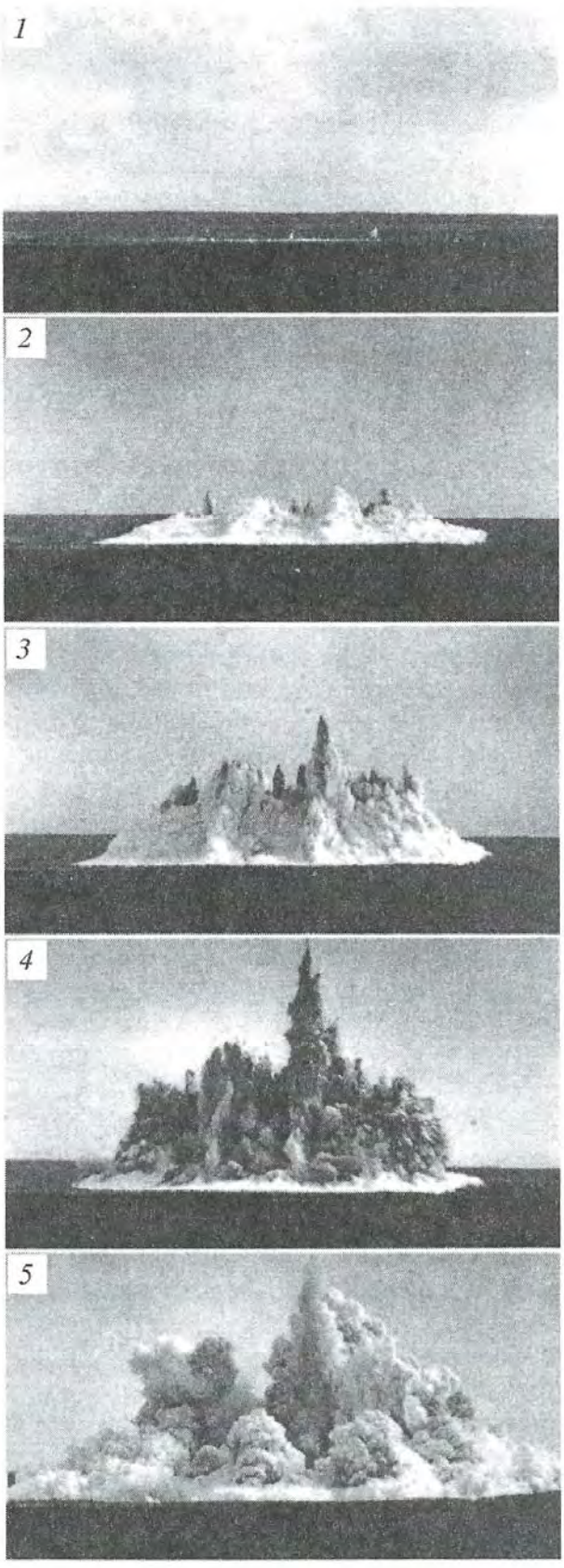

Figure 2.4. Snapshots for explosion “Taiga” shown for the following times from detonation: *1* – 0.2 s; *2* – 1 s; *3* – 2 s; *4* – 4 s; and *5* – 6 s

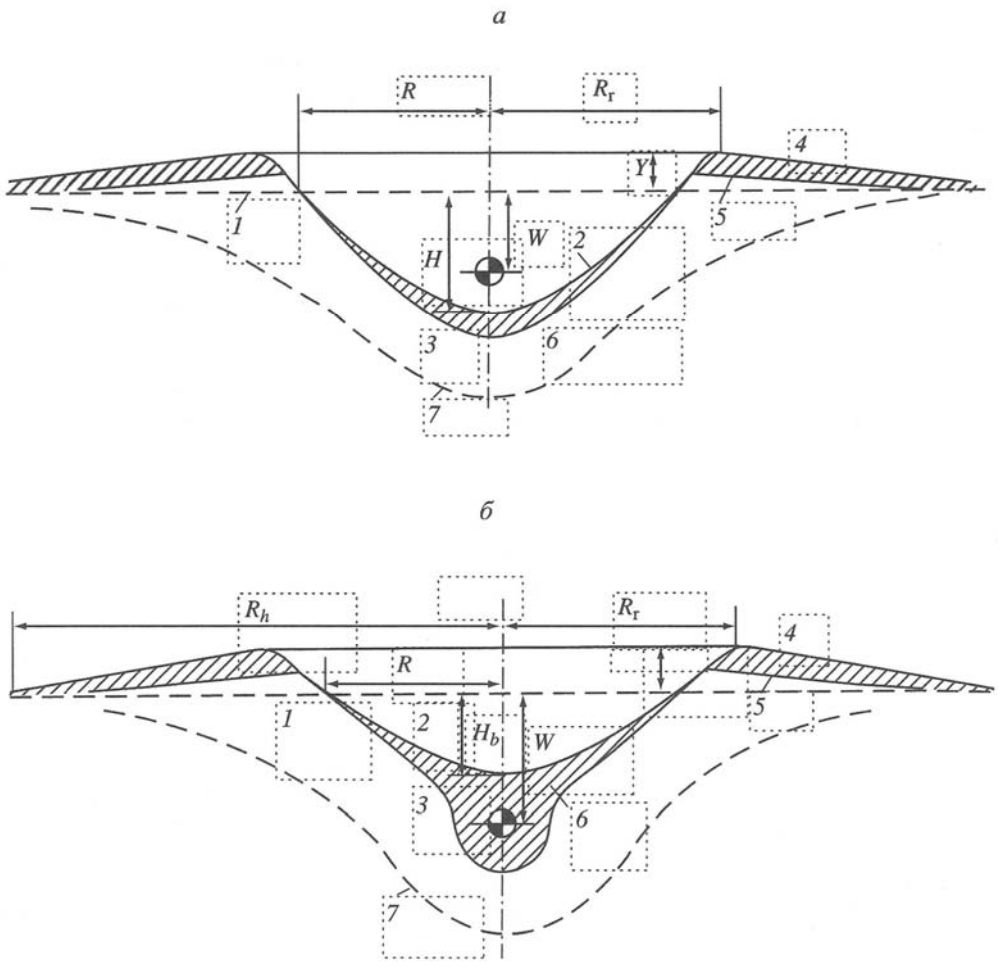

Figure 2.5. Schematic cross-sections through ejection craters: a) crater with "enhanced excavation" ($W < W_{opt}$), b) crater with "normal excavation" ($W < W_{opt}$). The numbers show: *1* – initial position of the ground surface; *2* – contour of the visible crater; *3* – contour of the "true" crater; *4* – outer mound (ejecta blanket); *5* – zone of residual deformations; *6* – inner ejecta blanket; *7* – boundary of the damaged rocks.

High values of the initial velocities and significant height of uplift set this test apart from T-3 explosion conducted in hard rock (gravelite and aleurolite). Test Taiga had approximately the same scaled depth of burial (Table 2.1), but lower initial velocity (28 – 39 m/s) and lower cupola uplift (80 – 110 m). Evidently this can be explained by the fact that explosion Taiga was conducted in water-saturated loose sediments (this is why the uplift shape resembles the shape observed during underwater explosions). In addition, despite high velocities of the uplift the opening of the cupola occurred late (5 – 7 s after beginning of the uplift venting of hot gases was observed at the surface above two charge boreholes). There was no increase in the amplitude of the horizontal component of the ground motion during the end stage of the explosion. During T-3 explosion amplitudes of the horizontal component of ground motion reached 10 – 12 m/s and only 1 – 5 m/s during Taiga.

Explosion Taiga produced a pit with the length of 700 m, width of 340 m, depth between 8 and 15 m with slopes of 8 – 10° and height of the mound of 6 – 11 m.

According to the observations excavation efficiency of nuclear explosions varies significantly depending on the scaled depth of burial, physical properties of the emplacement rocks and their gas content. The highest excavation efficiency is reached for explosions with an optimal depth of burial. In this case two different types of ejection craters can be formed depending on the scaled depth of burial (Figure 2.5). Explosions with sDOB less than optimal produce craters with depths greater than explosion DOB. These craters with enhanced excavation have excavation index $n \geq 1.5$. Formation of these craters is accompanied by significant release of radioactive material into atmosphere. Explosions with depth greater than optimal produce craters with depth less than the explosion DOB. These explosions release smaller amounts of radioactive gas from the cavity, nevertheless a significant amount of radionuclides (produced as a result of nuclear reactions from their radioactive precursors) is released into the atmosphere.

There are "visible" and "true" explosive craters as well as the ejecta blanket. The term "visible crater" is applied to the part of the crater located below the original ground surface. The dimensions and the volume of this part characterize the excavation efficiency of the explosion. The "true" crater includes rocks which do not rise into air during the explosion. It is always greater than visible crater. For explosions with "enhanced excavation" the size of the visible crater approaches the true crater size and become equal when ejecta escapes and does not fall back into the crater. In all rock types, visible craters have hyperbolic shapes with the slopes representing asymptotes. In alluvium and shale the slopes are approximately 29 – 33° from the horizontal, while in hard rock the slopes are 35 – 40°. Ejecta blankets are formed by broken rocks lifted in the air by the explosion and falling back either outside of the crater or inside of the crater (and becoming crater fill).

Table 2.4 shows the experimental data related to the dimensions of the ejecta mound: volume V, maximum radius y, radius along the ridge R_r, radius of the ejecta mound R_m, maximum ejection distance R_e. In addition a value of the dilation coefficient N is also provided for the outer mounds. According to the measurements the volume of the outer mound in hard rock is 1.1 – 1.6 times greater than the crater volume. This is due to rock dilation within the mound (N = 1.1 ÷ 1.4) and due to a residual uplift of the ground surface. The height of the mound changes between 0.2 and 0.6 of the crater depth, while the radius of the mound is greater than the crater radius by a factor of 3 – 6. However for explosions in alluvium the volumes of the outer mounds were smaller than the volume of the crater due to compaction of alluvium during explosions. Thus the density of the ejected material for explosion SEDAN was 2.2 g/cm^3, while the initial density was 1.8 g/cm^3.

Sizes of the deformation zones depend mainly on the scaled depth of burial. Thus for an explosion conducted at the optimal depth vertical extent of the zone of intense deformations is 2 – 3 times the radius of the cavity, horizontal size at the working point is 3 – 5 times the cavity radius, at the ground level – 3 – 6 times the crater radius. Thus there is significant increase in size of the zone of intense deformations toward the free surface compared to the size below the

charge placement. Geological structure, layering orientation and tectonic deformations significantly affect the explosion damage zone.

Table 2.4. Experimental data for characteristic sizes of the ejecta mounds

Explosion	Rock type	Parameter					
		V_h/V	y/H	R_r/R	R_m/R	R_e/R	N
DANNY BOY	Basalt	1.92	0.24 – 0.4	1.25 – 1.3	2.5 – 2.8	–	1.1 – 1.4
SEDAN	Alluvium	0.64	0.06 – 0.3	1.1 – 1.3	3 – 5	11.5	1.0
CABRIOLET	Rhyolite	1.34	0.26	1.22 – 1.25	3.5 – 4	–	1.1 – 1.15
SCHOONER	Tuff	1.21	0.2 – 0.3	1.13 – 1.17	4 – 6.3	16 – 23	–
BUGGY	Basalt	1.61	0.62	1.2 – 1.5	4 – 5	–	1.2 – 1.35
PALANQUIN	Rhyolite	2.76	0.27	1.25 – 1.3	2 – 2.5	13 – 14	–
BH 1003	Aleurolite	1.09	0.22 – 0.45	1.2 – 1.3	2.3 – 3	6.0	1.09
BH 1004	Sandstonne	1.04	0.27 – 0.43	1.3 – 1.4	2.9 – 3.2	5.0	1.08
BH T-1	Shale	1.38	0.38 – 0.4 7	1.4 – 1.5	3.0 – 3.8	5.6	1.15
BH T-3	Aleurolite	1.52	0.5 – 0.8	1.4 – 1.7	3.7 – 4.1	5.6	1.3
BH 101	Sandstone	0.24	0.47 – 1.1	1.35 – 1.4	1.5 – 2.3	4.5	1.0
BH 125	Porphyrite	0.53	0.4 – 1.3	1.35 – 1.47	1.8 – 1.9	5.7	1.0

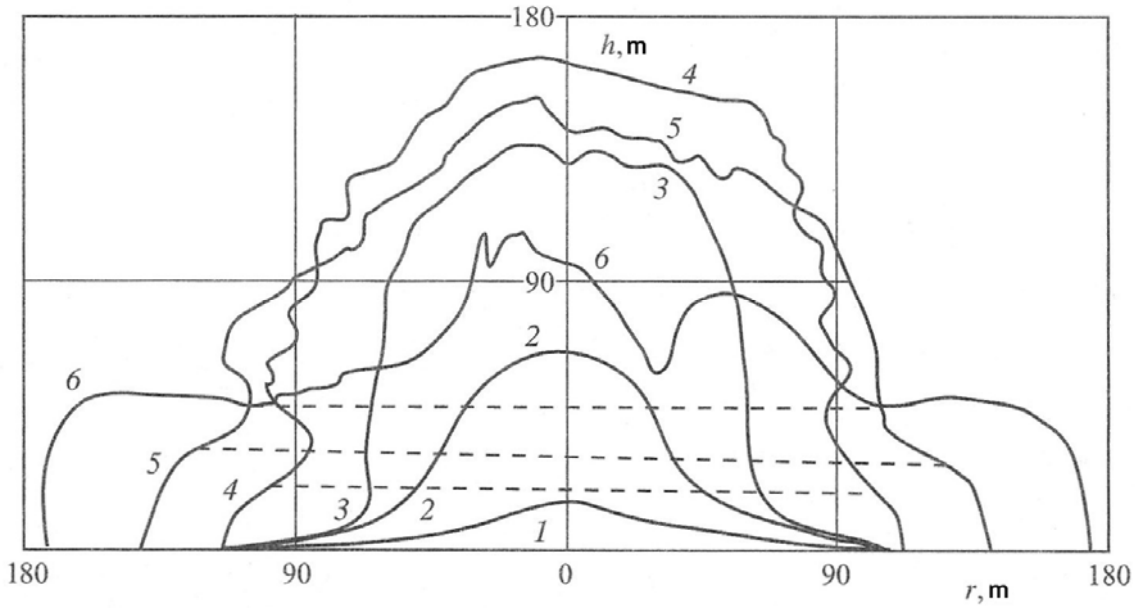

Figure 2.6. Contours of rising cupola and base surge produced by explosion detonated in BH T-1. The contours are shown at the following times from detonation: *1* – 0.5 s; *2* – 1.4 s; *3* – 3.4 s; *4* – 6.5 s; *5* – 8.5 s; and *6* – 11.5 s.

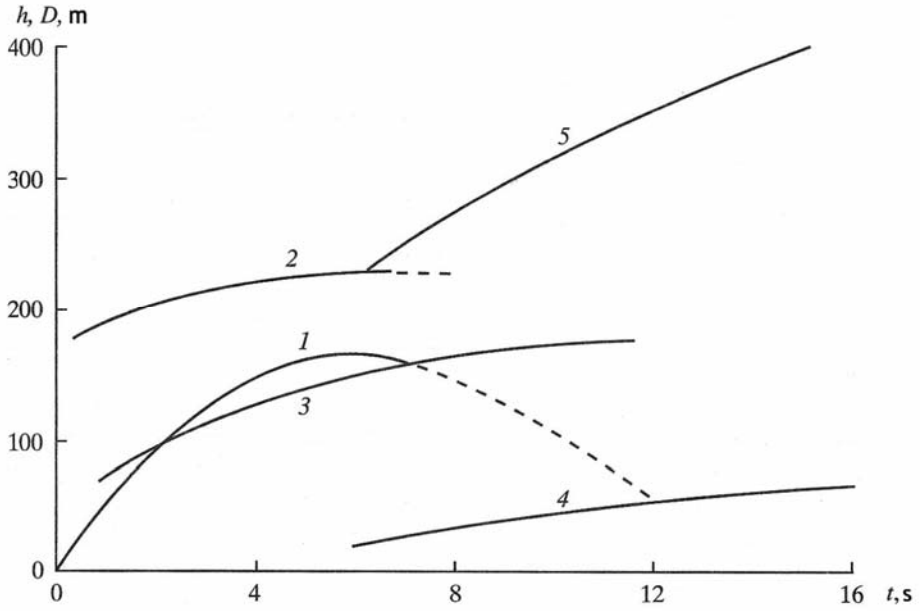

Figure 2.7. Cupola dimensions as a function of time for explosion in BH T-1: *1* – cupola height; *2* – diameter at the base, *3* – diameter of the cylindrical part of the cupola; *4* – base surge; *5* – height of the dust cloud.

Kinematic parameters of the motion of the free surface during excavation explosions contain great deal of information regarding the role of different factors for crater formation. As an example, Figure 2.6 shows the development of a cupola and a "base surge" for explosion in BH T-1, while Figure 2.7 shows their change in time. Characteristic dimensions of the cupola are: diameter of the cylindrical part 100 – 120 m (3.5*W*), diameter at the base approximately 200 m (6*W*), maximum height 170 m (5.4*W*). Collapse of the cupola created a "base surge" with height increasing from 20 to 50 m during propagation. Propagation of the base surge ceased after 25 – 30 s. A gas-dust cloud forms, which moves with the wind.

Development of the cupola is characterized by the initial uplift velocity and maximum ejection velocity. Figure 2.8 shows the change of the velocity of motion of the epicentral part of the cupola with time for several nuclear explosions as well as a chemical explosion SCHOOTER (q = 0.454 kt, W = 38 m) in alluvium (Teller et al, 1968). Initial uplift velocity is determined by the reflection of the compression wave from a free surface, which in hard rock is equal to twice the velocity of the compression wave.

Maximum ejection velocity is determined by gas acceleration, which forms as a result of expansion of the explosive cavity towards the free surface. The stage of gas acceleration is especially pronounced during nuclear explosions in rocks with high gas content, as well as for chemical explosions in soft sediments. Gas acceleration is hardly ever observed for explosions in hard dry rock, where spall motion becomes effective. Factual data related to the change of uplift velocity from initial v_i to maximum v_m, as well as the time of the beginning of the stage of gas

acceleration t_2, its duration t_m and the time of the venting t_0 are presented in Table 2.5. The explosion culminates cupola breakdown, when the hemispherical uplift turns into flying debris.

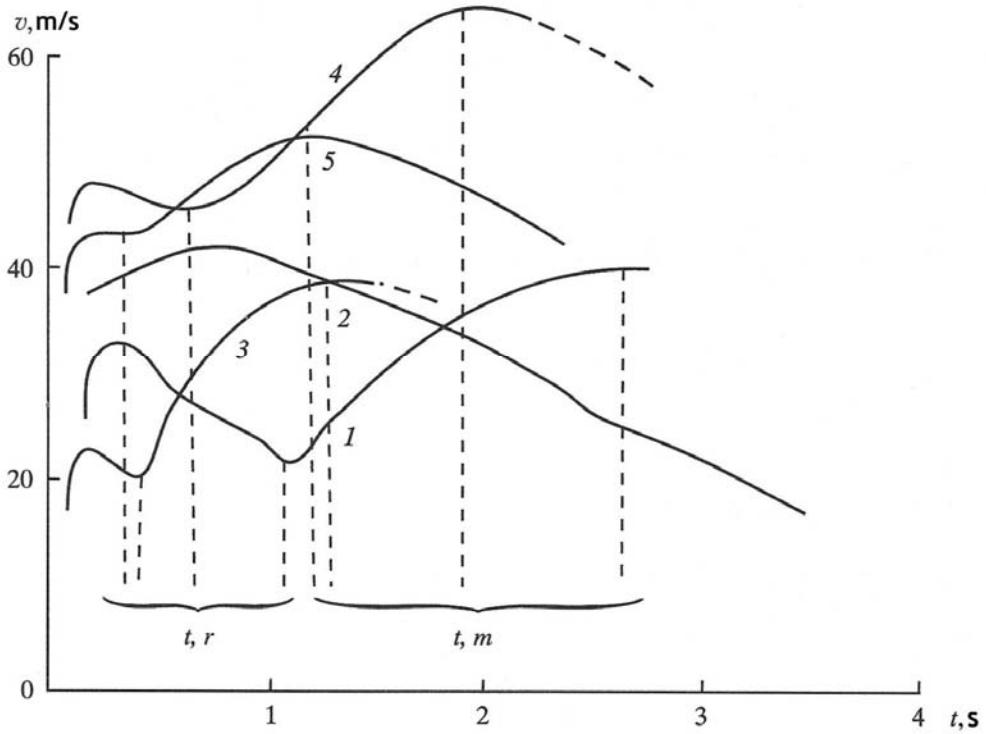

Figure 2.8. Changes in the cupola rise velocity with time for the following explosions: *1* – SEDAN; *2* – DANNY BOY; *3* – SCOOTER; *4* – SCHOONER; *5* – BH T-1.

According to the table maximum velocity exceeds the initial velocity by a factor of 1.2 – 1.8. Duration of the gas acceleration stage is characterized by the time when the maximum velocity is reached t_m and varies from 1 – 1.5 s for explosions on the order of 1 kt to 2.5 – 3 s for explosions with yields on the order of 100 kt. The data show that the duration of the gas acceleration stage is not self-similar.

Maximum ejection velocity and the duration of the gas acceleration stage determine the maximum height of the cupola uplift h_m, which is also provided in Table 2.5. As it turns out the actual height of the uplift exceeds the height estimated using the initial uplift velocity by a factor of 2 – 5. It also suggests that the distances traveled by rock ejecta are also not self-similar with respect to the explosion yield, and that the effect of gas acceleration, which propels the rock above the charge, is greater than the effect of the shock wave which affects only the spall layer.

Gas acceleration stage culminates in venting of the cavity gas into atmosphere. The venting time t_0 determined by either time when hot gas appears at the top of the cupola, or by detection of radioactivity in atmosphere are given in Table 2.5. The fact of gas venting through the cupola and its intensity is related to the rock gas content. For explosions in dry rock with low gas content venting was not detected (e.g. DANNY BOY, BUDDY, SULKY). For explosions in

rocks with high gas content (SEDAN, BH 1004 and 1003) venting occurred in the moment when the uplift velocity reached its highest point.

Table 2.5. Characteristics of excavation explosions

Explosion	Parameter						
	v_i, m/s	t_2, *s*	v_i, m/s	t_m, *s*	t_0, *s*	h_m, *s*	h_m/W
DANNY BOY	38	-	42	0.8	-	135	4.0
SEDAN	33	1.05	40	2.8	2.5	200	1.04
CABRIOLET	30	-	45	0.8 – 1	1.0	460	8.8
SCHOONER	48	0.6 – 0.7	65	1.8 – 2	1.75	100	1
BUGGY	24 – 35	0.2 – 0.3	45	1.2 – 1.3	-	100 – 135	2.4 – 3.3
PALANQUIN	-	-	12.2	0.45	0.45	20	0.24
SULKY	26	-	-	-	-	35	1.28
BH 1003	35	0.4	58	1.4 – 1.6	1.0	190	4.0
BH 1004	100	2.3 – 2.4	140	2.8	2.5	960	5.5
BH T-1	43	0.2 – 0.3	53	1.2 – 1.3	1.5	170	5.4
BH T-3	28 – 33	0.5	41	1.0 – 1.2	1.5	85 – 120	2.5 – 3.8
Taiga	62 – 81	-	-	-	5 – 7	220 – 255	1.7 – 2.1
SCHOOTER	21.3	0.4	39	1.2	-	150	3.9

The analysis presented above shows that although the number of excavation explosions was small, they were conducted in a broad variety of rock types with different physical properties and a large range of yields (according to Table 2.1 the yields varied over three orders of magnitude). The experimental data has provided a good overall picture of the excavation capabilities of nuclear explosions.

However the limited number of nuclear excavation explosions, and significant differences in their yields and emplacement rock properties, make it difficult to determine the specific effect of individual factors on the excavation efficiency. This makes it difficult to determine robust relationships between the explosion yield, DOB, rock properties, and the results of excavation. This can be illustrated by applying scaling laws to estimate parameters of excavation explosions. As it turns out, including gravity as one of the determining parameters leads to breaking of self-similarity, which significantly complicates the development of empirical formulas for excavation explosions.

Here we can recall the results of parameter estimation for chemical excavation explosion (Adushkin et al., 1973). It was determined for explosions with small yield that the volume of the crater is proportional to the weight of the explosives. This means that self-similarity applies and the relationships for the excavation explosions can be written in a form:

$$q = kW^3 f(n), \tag{2.1}$$

where q is weight of explosions, W is the depth of burial, k is a coefficient depending on rock properties and type of explosives, and $f(n)$ is a function determining the excavation/ejection parameter n. Formula 2.1 is valid for depths of burial less than 10 – 20 m and if $f(n)$ can be given in a form:

$$f(n) = 0.4 + 0.6n^3.$$

This relationship is known as M.M. Boreskov's formula. The form of the function $f(n)$ evolved with development of explosive technology [something like this] (Adushkin et al, 1973). Study of scale-dependence began in 1957, when the USSR conducted a large series of experimental chemical explosions in loess and clay with charges ranging between 0.1 and 1000 t (Dokuchaev et al., 1963). For the first time the effect of gravity on the crater size was established. The experiments have shown that, with the increase of explosive yield, self-similarity breaks down and the weight of explosives increases faster with the increase of sDOB than the volume of ejected rock.

Based on the results of these experiments a formula for large charges was proposed in a form:

$$q = kW^3 (1+nW) f(n). \tag{2.2}$$

Later after analyzing data from mining explosions with charges over 10^3 t the following formulas were proposed:

$$q = kW^{7/2} f(n),\ q = kW^3 (W/25)^{1/2} f(n) \tag{2.3}$$

with different forms for the excavation parameter $f(n)$. However applying formulas 2.2 and 2.3 to nuclear charges was unsuccessful. Efforts to develop parameters for excavation explosions with yield ranging between 1 and 10 kt and DOB of 40 – 400 m (when the effect of gravity becomes determining) were directed on generalization of the experimental data using scaled parameters for the crater radius R, depth H, and volume V:

$$\frac{R}{q^{1/3}} = f_1\left(\frac{W}{q^{1/p}}\right);\ \frac{H}{q^{1/3}} = f_2\left(\frac{W}{q^{1/p}}\right);\ \frac{V}{q^{1/3}} = f_1\left(\frac{W}{q^{1/p}}\right). \tag{2.4}$$

The linear scale in these equations were adjusted by using the yield exponent p >3. The parameter p in Equation 2.4 is often called scale coefficient or similarity parameter. Violet (1961) noted that the yield exponents are not strictly speaking similarity coefficient, therefore he calls those "yield exponent". Due to lack of data related to nuclear explosions the USA conducted a series of chemical excavation explosions during 1951 – 1968. The explosions were conducted in alluvium ($q \approx 0.01 \div 454\ t$), clay ($q \approx 0.1 \div 100\ t$), basalt ($q \approx 0.5 \div 20\ t$), granite and sandstone ($q \approx 0.1 \div 100\ t$), shale/slate ($q \approx 20\ t$), and tuff ($q \approx 0.1\ t$) (Vortman, 1969).

Analysis of these data shows that p = 3.33 provides the best fit to the experimental data (Murphey and Vortman, 1961). Statistical analysis of only TNT data in alluvium shows that the smallest scatter of the data is achieved for p = 3.4 (Nordyke, 1962). After joint analysis of chemical and nuclear explosions in alluvium and basalt the empirical formulas 2.4 with p = 3.4 become widely used. These expressions are used to estimate the relative efficiency of nuclear and chemical explosions, to predict the craters sizes and to determine the optimal depth of burial for different yield and different emplacement conditions.

Detailed analysis by Violet (1961) shows that different values of parameter p in relationships 3.4 should be used to estimate crater radius ($p \approx 3.9$), crater depth ($p \cong 3.4$), and depth of burial ($p \approx 3.6$). Absence of a single scaling parameter for description of the emplacement parameters and the crater sized makes analysis complicated. This situation is due not only to a wide range of yields of chemical and nuclear explosions, but also to the differences in the amount of gas available to perform excavation work and in thermodynamic properties of rocks, depending on mineral composition and gas content of rocks. This is why crater sizes produced by nuclear explosions are more sensitive to changes in rock properties than the craters produced by chemical explosions.[4]

A combination of these factors makes it impossible to create a single scaling relationship in a form 2.4, where the only parameters are the explosion yield and depth of burial. White (1971) came to a similar conclusion, also noting that crater formation does not satisfy similarity relationships, therefore the results obtained by analysis of the results of small explosions cannot be applied to large explosions.

Therefore methods are needed that correctly account for the explosion yield, high energy density at the source, rock properties and their changes with depth, as well as the effects of geological and tectonic structure. In the next section we present one such method developed as a result of laboratory experiments.

A new framework was developed using physical modeling and comparison between the laboratory and full-scale field data. These methods account for the effects of not only depth of burial but also gas content of rocks on the crater dimensions. Effect of the size of explosion on self-similarity was also analyzed.

2.2. Methods of physical modeling of excavation explosions

Analog modeling is widely used in different scientific fields and is an efficient way to study explosion processes. However, underground explosions (particularly shallow cratering explosions) are extremely complex processes, which cannot be recreated in terms of a single model due to variety of physical processes and qualitative differences between various phases of

[4] In Chapter 10, the authors note that nuclear explosions vaporize rocks and high explosive does not. Therefore, nuclear explosions release more gas from the emplacement rocks, due to higher temperatures and stronger shocks. High explosive shots produce gases mostly derived directly from the explosive materials. (Note added by translators.)

development. Therefore in order to study underground explosions different mathematical models can be used to study different aspects of the process, including the issues related to dynamic loading and accounting for the material properties. Building models for complex processes always involve simplifications. Building models for complex processes always involves simplifications. We use simplifications and assumptions for experimental schemes to explain observational results. The fewer details the scheme contains, the simpler the analysis will be and the better it will represent the physical meaning of the process. Therefore creating schemes (schematization) is the first and the most important stage of the model development.

2.2.1. Schematization of the excavation explosions

Schematization (or separation of the explosion process into a series of simpler stages) was conducted using chemical explosion data related to mechanism of energy transfer from explosives to ejected rocks. This process can be divided into three stages (Dokuchaev et al, 1963).

The first stage includes the time interval from the moment of detonation to the moment when the compression wave reaches the free surface. At this stage ground motion is spherically symmetric, similar to the motion caused by fully contained explosions. Rocks are deformed due to passage of the shock wave. Even though the time interval during which the symmetry is preserved is short, the effect of the initial shock wave stage is significant. Estimates show that for explosions with excavation parameter $n \leq 3$ cavities are expanded to sizes close to sizes for fully contained explosions. A significant part of the energy derived from the explosion is not used for excavation, instead it is ”wasted” on rock damage, plastic deformation, and heating. Some part of the kinetic energy transferred into rock by a shock wave is spent on rock movement. In fact, duration of the first stage is longer, because a significant break of the symmetry occurs somewhat after the shock wave reaches the free surface. The time scale of the first stage is 0.05 – 0.1 $s/kt^{1/3}$. During this time the formation of the uplift [cupola] just begins, and its height is 2 – 5 $m/ kt^{1/3}$, which is an order of magnitude less than the depth of burial.

During the second stage the energy of the explosion products is spent predominately on upward acceleration of the damaged rock mass. Because of this acceleration initially spherically-symmetric velocity field becomes distorted; the velocity of motion increases and reaches a maximum value which significantly exceeds the initial velocity. A characteristic cupola of rising rocks forms as a result. During this stage a supply of kinetic energy that is needed for excavation is created. The major force opposing the work of explosion products is gravity, acting upon the rock mass. Part of the energy is spent of overcoming friction and cohesion forces. The thickness of the rising rock mass decreases as it rises. A further rise of the cupola leads to its fragmentation. By the end of the second stage the kinetic energy of the gas products of an explosion is almost entirely depleted.

The third and final stage of ejection involves inertial movement of ejected rock in the gravity field. The distance that fragments travel depends on their kinetic energy, initial angle of motion, and the air resistance.

The first (initial) stage entails breaking of rocks due to the cavity expansion and propagation of compression and rarefaction waves. Kinetic and elastic energy stored by the rock during stage one is small compared with the energy of gas in the cavity. Crater size is determined by the development during the second stage, where the propellant effect of cavity gases generates the kinetic energy needed for rock ejection and excavation.

Observations and calculations show that the role of gas acceleration in crater formation increases with the increase in explosion yield. The motion of fragments during stage three has almost no effect on the ejection crater size, in the range from several depths of burial to the optimal depth. Experimental explosions have shown that in these cases all the rock originally contained within the crater volume is thrown outside of the crater.

Dividing the explosion process into two main stages (the shock wave, and gas acceleration), the following schematization of the process is developed: let us assume that the first (shock wave) stage of the explosion process is finished. The size of the explosion cavity is known. Rocks surrounding the cavity are damaged all the way up to the free surface. The size of the damage zone is known and it exceeds the depth of burial by a factor of 2 or 3. The initial strength of rock does not matter since the damaged rocks are fragmented. Cohesion between rock fragments is low and the medium obeys the laws of dry friction. Kinetic energy of rocks during the shock wave stage is not taken into account. The determining process is then the motion of broken/fragmented rock due to gas pressure in the gravity field. The effects of work exerted on the rock mass by cavity gas depend on gas thermodynamic parameters and the depth of burial.

In this way the crater formation process is viewed as a result of the propulsion of broken rock mass by explosion gas by-products. The physical model used to recreate the second and the third stages of the explosion, involving crater formation and rock movement, is based on this description. The initial stage, involving cavity formation and rock damage around the cavity, is accounted for by choosing the initial state of the model. The initial state is the end of the first stage. Therefore the initial parameters in this model (of crater formation) are the cavity (with its size calculated as for contained explosions), and the gas parameters in the cavity. The broken/fragmented rock is represented by material with weak cohesion, such as quartz sand.

2.2.2. Self-similarity conditions

First we define a system of governing parameters for the proposed model. The parameters to be determined are the crater radius R, depth H, and volume V. The governing parameters are characteristics of the explosion, rock properties and the external forces. In model scheme the initial conditions are given by the cavity radius r_c, energy of gas in the cavity E (or pressure P), adiabatic exponent χ, and the depth of burial W. Since the ejection process is slow, we neglect rock compressibility and characterize broken rock by its density ρ, internal friction coefficient k_f, and cohesion c, which reflects the “degree of attachment” between the ejected rock and the earth. Other governing parameters also include gravitational acceleration g and atmospheric pressure above the free surface P_a. As a result the set of variables needed to describe the process of excavation include seven dimensional and two dimensionless variables, namely:

$$E,\ W,\ rc,\ \rho,\ g,\ P_a,\ c,\ k_f, \text{ and } \chi. \tag{2.5}$$

Using these governing parameters the following independent dimensionless combinations can be constructed:

$$\frac{E}{\rho g W^4},\ \frac{E}{P_a W^3},\ \frac{E}{cW^3},\ \frac{W}{r_c},\ k_f, \text{ and } \chi. \tag{2.6}$$

In order for two processes to be similar it is necessary and sufficient for the dimensionless combinations created from the complete list of the governing parameters to be equal:

$$\frac{E}{\rho g W^4} = const,\ \frac{E}{P_a W^3} = const,\ \frac{E}{cW^3} = const,\ \frac{W}{r_c} = const,$$

$$k_f = const, \text{ and } \chi = const. \tag{2.7}$$

The relationship between the initial conditions, rock properties and the crater dimensions (e.g. radius) can be generalized in a form:

$$\frac{R}{W} = F\left(\frac{E}{\rho g W^4}, \frac{E}{P_a W^3}, \frac{E}{cW^3}, \frac{W}{r_c}, k_f\ , \chi\ \right). \tag{2.8}$$

Two limiting cases can be selected from 2.8. First, in cases when the parameter $E/\rho g W^4$ can be neglected, the energy of cavity gas $E \sim W^3$ and the self-similarity principle applies. Evidently the necessary and sufficient condition for this is that $\rho g W$ term is small compared to P_a and c. This condition holds for small scale explosions. The other limiting case is when the explosion scale is large, and the only defining parameter is $E/\rho g W^4$. In this case geometrically similar craters will be created by explosions with $E/\rho g W^4$ = const, provided R/W = const. This implies that the energy of gas in the cavity is proportional to W^4, and not W^3 as it would follow from self-similarity principle. If the medium parameters stay the same, the role of the parameter $E/\rho g W^4$ will be increasing with increasing yield.

In order to reproduce large-scale explosions using the model we need to maintain the determining role of the parameter $E/\rho g W^4$, keeping it the same for both laboratory model and field experiment. In order for parameter $E/\rho g W^4$ to remain constant and keep the condition $E \sim W^4$ while reducing the linear scale of the experiment we need to increase the value of ρg. The possibilities for increasing material density are limited. Therefore during laboratory experiments an artificial increase in gravitational force is often used by using centrifugal and linear accelerators. If the linear size of the model is n times smaller than the real system, the value of the required acceleration is $a = ng$. If a linear accelerator is used, the necessary acceleration is achieved as a result of rapid slowing down after gradual acceleration, for instance by dropping the model from various heights. With centrifugal modeling, the object is placed on a rotating apparatus of large diameter, and the value of acceleration is varied by changing the centrifugal force via a change in the angular velocity of rotation.

In both configurations craters are produced by small explosions in material placed in a small container. The presence of compressional wave as well as reflected waves requires adding the dynamic properties of the medium (e.g. compressibility, elastic properties) to the list of the

governing parameters. Thus these methods cannot be described using relationships in a form 2.8. We also note that the capabilities of these modeling methods are limited due to short term nature of the acceleration on the falling platform, presence of viscous and capillary forces, Coriolis forces, etc. Additionally there have been American experiments where measurements were conducted in a flying laboratory, when accelerations ranging between 0.17 and 2.5g were created by a plane moving along a circular arc.

Here we present a different method of conducting excavation explosions in laboratory setting (Adushkin and Rodionov, 1968). A volume of compressed gas imitating explosion cavity filled with explosion gas by-products was used as an "explosion source". The size of the cavity was calculated for the fully contained explosions. According to relationships 2.8 in order to maintain self-similarity the values of parameters P_a, c, E, W, r_c need to be reduced to keep the dimensionless parameters given in 2.6 the same as in the field experiment. To achieve similarity the value of P_a was reduced by creating a vacuum above the free surface.

In order to reduce parameter c in the laboratory setting, loose materials with weak cohesion and particle sizes much smaller than the depth of burial W were used. This choice of the model also agreed with the condition that the material should be broken/fragmented. The energy E of the cavity gas in the model was set according to conditions (2.7) for a given depth of burial. Cavity radius r_c was chosen to preserve the ratio W/r_c between the large and small scale experiments. Dimensionless parameters k_t and χ are close between the large and small scale experiments.

Thus the proposed experimental scheme is based on transformation of the force fields, which allow maintaining the same proportions between the forces that exist during nuclear explosions. Different scales (yields) of explosions are achieved by changing pressure above the free surface and material cohesion while maintaining the similarity conditions (2.7).

For instance, in order to recreate conditions for large yield excavation explosion the effect of parameters E/P_aW^3 and E/cW^3 was minimized by creating a strong vacuum above the surface and using dry quartz sand. In these circumstances the term $E/\rho gW^4$ become dominant. In order to create these conditions dry quartz sand was placed into vacuum chamber. A spherical volume of pressurized gas encapsulated in plastic shell was placed into the sand mass at a specified depth. Destruction of the shell by a sudden gas expansion produced ejection of sand above the cavity creating a crater. The dimensionless combinations of the defining parameters (2.2) corresponded to the conditions observed during large explosions.

This proposed experimental method based on similarity relationships provides opportunities to study relationships between parameters of nuclear and chemical explosions in the laboratory using special devices with a vacuum chamber.

2.2.3. Experimental devices

Several experimental devices were built during development of the method. The first device had small dimensions. The experimental schematic is shown in Figure 2.9.

A vacuum chamber was built using 8 mm thick steel sheet with reinforced edges. The size of the chamber was $80 \times 80 \times 100$ cm^3. The transparent front side of the chamber was made of clear PMMA with thickness of 5 cm. The top part of the bottom wall can be opened in order to prepare the experiment and to measure the crater. Chamber was half-filled with loose material. The pressure inside the chamber could vary from atmospheric to $10^{-5} – 10^{-6}$ kg/cm^2 and could be measured using vacuum gage.

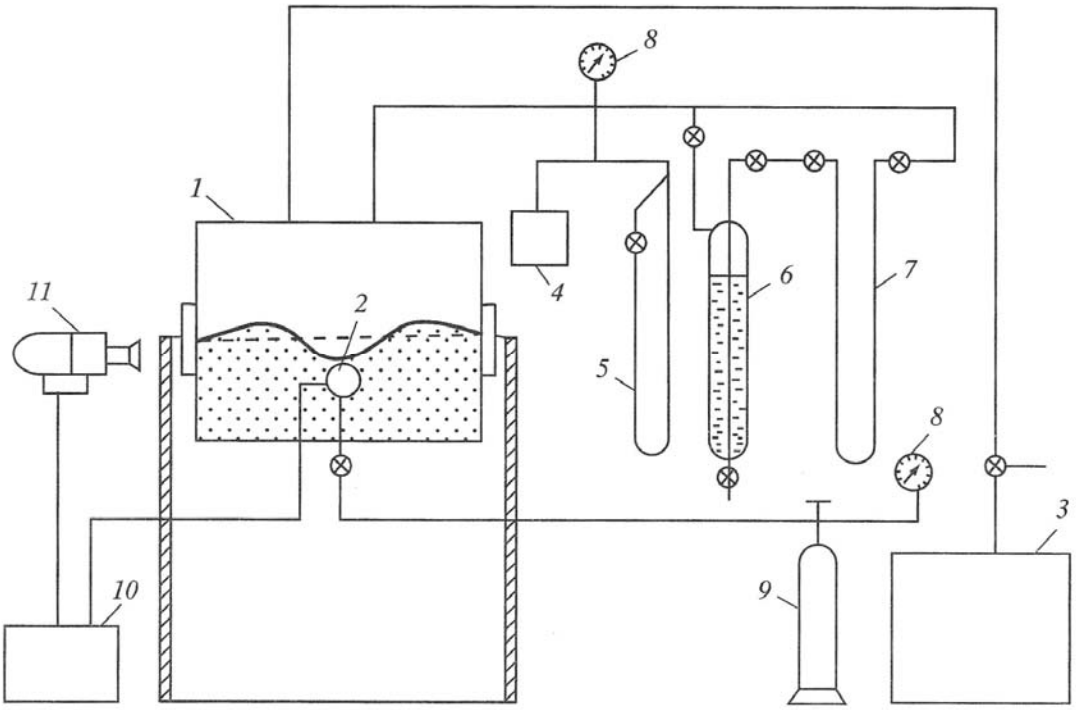

Figure 2.9. Schematic of the experimental apparatus: *1* – vacuum chamber; *2* – working volume; *3* – vacuum pump; *4* – vacuum gage; *5* – oil manometer; *6* – differential manometer; *7* – mercury manometer; *8* – manometer – vacuum meter; *9* – tank with pressurized air; *10* – detonation control block; *11* – camera.

A volume filled with air encapsulated in a thin rubber shell was placed in the sand at a specified depth. The rubber shell was held inside a net in order to maintain a certain volume. The area of the “holes” of the net casing was 80 – 90%, so it did not affect the outcome of the experiment. During pumping of air out of the chamber excess pressure inside the volume was maintained at a certain level using a differential manometer. The differential manometer is built as an air-tight cylinder with a diameter of 5 cm and height of 60 cm partially filled with mercury. An 8-mm thick tube with an open tip is placed inside the mercury volume almost down to the bottom. The upper part of the tube is connected with the working volume, while the space above the mercury surface is connected with the vacuum chamber. The desired value of the excess

pressure in the air volume can be adjusted by regulating the mercury level above the open end of the tube.

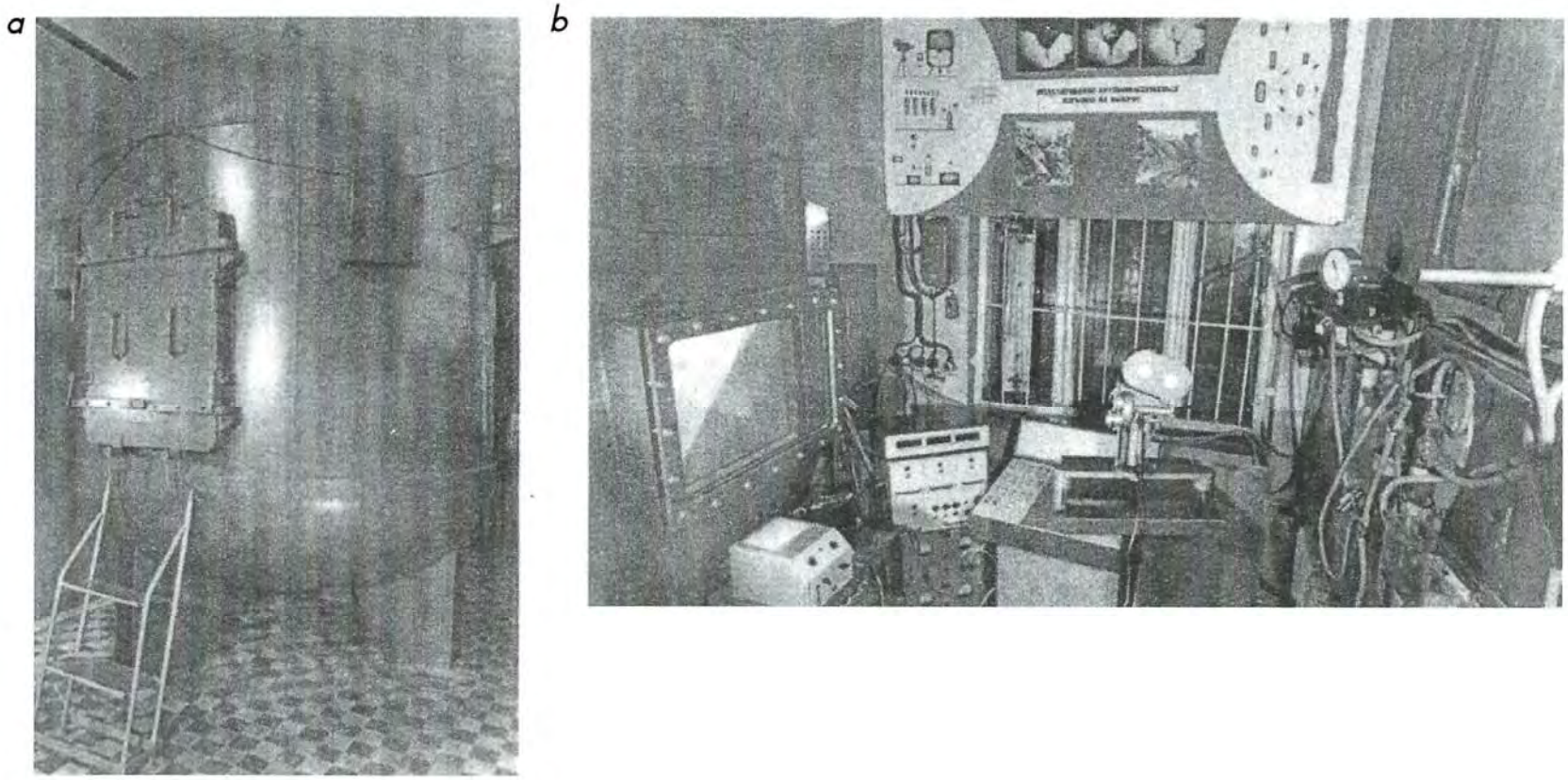

Figure 2.10. a) Experimental apparatus with the large size vacuum chamber; b) control block.

When air is pumped out of the vacuum chamber, excess air from the circular volume goes into the mercury volume while the pressure difference is preserved. The pressure in the air volume with respect to the pressure above the "ground" surface is regulated using a mercury manometer. If necessary the pressure can be reset to atmospheric after turning off the differential manometer. Once the desired degree of low air pressure is reached the rubber shell is broken by contact with a nichrome wire heated with an electric current. The released volume of gas pushes the "ground" material, making a crater. The timing of the shell breakage was synchronized with a high-speed recording camera using an electronic block.

Several nuclear explosions and some well-known chemical explosions with complicated surface topography were modeled using this apparatus. The results of these experiments demonstrated good agreement with the full-scale explosions in both crater sizes and kinematic parameters. Later an apparatus with a larger vacuum chamber (volume – 12 m^3, diameter – 2.3 m, height – 3 m) was built in order to study and predict excavation effects of large scale explosions used in mining and construction (Adushkin et al, 1982). This apparatus allowed placement of multiple (between 1 and 10) sources and initiate simultaneously or with delay. Figure 2.10 shows the photographs of the chamber (a) and the control system responsible for creating vacuum and "explosion" initiation (b).

Starting in 1972 this system was used for preliminary study of large industrial explosions intended for building of dams, mining, creating pits and channels or rock piles with predefined configuration.

2.2.4. Ground material/soil parameters in the laboratory model.

The described schematization allowed reducing the number of the main ground parameters to their density and parameters related to its shear strength. In real conditions rocks fragmented by explosions are represented by relatively uniform fragments of different sizes. Table 2.6 shows the major characteristics of these explosions and measurements of the average fragment sizes (Adushkin et al, 1073; Brooks and Anderson, 1970; Rabb, 1970). The first two explosions from Table 2.6 are fully contained, the remaining are excavation explosions. Study of the fragment size distribution shows that characteristic fragment sizes range from 0.5 – 1 cm to 1 – 2 m. The average fragment size (for η = 50%) varies in a broad range d_c = 6 ÷ 50 cm. For depth of burial between 20 and 200 m common for nuclear explosions the ratio ([between the fragment size and the DOB) is $d_c/W \approx 10^{-2} \div 10^{-3}$. During crater formation in this medium the fragments shift with respect to each other, because the friction (degree of cohesion) between the fragments is significantly smaller than the strength of the material itself. Therefore behavior of such a system is described by a mechanics of granular media, and the work by external forces is directed into moving the fragments with respect to one another. Strength of such medium is described by Coulomb's law for dry friction

$$\tau = c + k_f \sigma,\ k_f = \tan \varphi, \qquad (2.9)$$

where τ is shear stress, σ is normal stress, c is cohesion, k_f is an internal friction coefficient, and φ is an angle of an internal friction. It follows from Equation 2.9 that a resistance to shear stress is a combination of the friction forces and cohesion. The input of the frictional forces is characterized by the coefficient of the internal friction k_f, while cohesion c is related to structural connections between attached blocks and by meshing between different fragments. Parameters k_f and c are independent characteristics of shear strength of the fragmented medium. They are often used to solve static and dynamic problems related to granular materials (Taylor, 1960; Chadwick et al, 1966).

Table 2.6. Explosion characteristics

Explosion	Explosion type	Rock type	Parameter			
			q, kt	W, m	d_c, cm	d_c/W
PILEDRIVER	Nuclear	Granodiorite	66	457	18	$4 \cdot 10^{-4}$
HARDHAT	“	Granite	5.4	285	38	$1.3 \cdot 10^{-4}$
DANNY BOY	“	Basalt	0.42	33.5	34	10^{-2}
CABRIOLET	“	Rhyolite	2.5	52	6	$1.1 \cdot 10^{-3}$
SULKY	“	Basalt	0.087	27.4	25	$9 \cdot 10^{-3}$
DAGOUT	Chemical	“	0.02	18	50	$2.8 \cdot 10^{-2}$
PRESCHOONER	“	“	0.022	12.8	45	$3.5 \cdot 10^{-2}$
Burlykia	“	Granite	0.7	20 – 55	8	$2.5 \cdot 10^{-3}$

Thus the ground parameters in the model should agree with the specified parameters of the fragmented rocks, while its strength characteristics should satisfy similarity criteria (2.7). This can be achieved by changing the value of cohesion for the experimental material according to Newton’s law of dynamic similarity [?] while keeping the friction coefficient unchanged. Evidently the relationships between the fragment size and the depth of burial should be preserved (kept constant). The similarity conditions for the experimental material parameters are given as follows:

$$\frac{c_m}{\rho_m W_m} = \frac{c_f}{\rho_f W_f};\ k_{fm}/k_{ff};\ \left(\frac{d_c}{W}\right)_m = \left(\frac{d_c}{W}\right)_f . \qquad (2.10)$$

In these expressions indices “*f*” are related to parameters observed in the field experiments, while indices “*m*” stand for the model parameters. It follows from (2.10) that if the densities for the field and model materials are similar, ground cohesion should be reduced by a factor equal to a ratio between the field and model sizes.

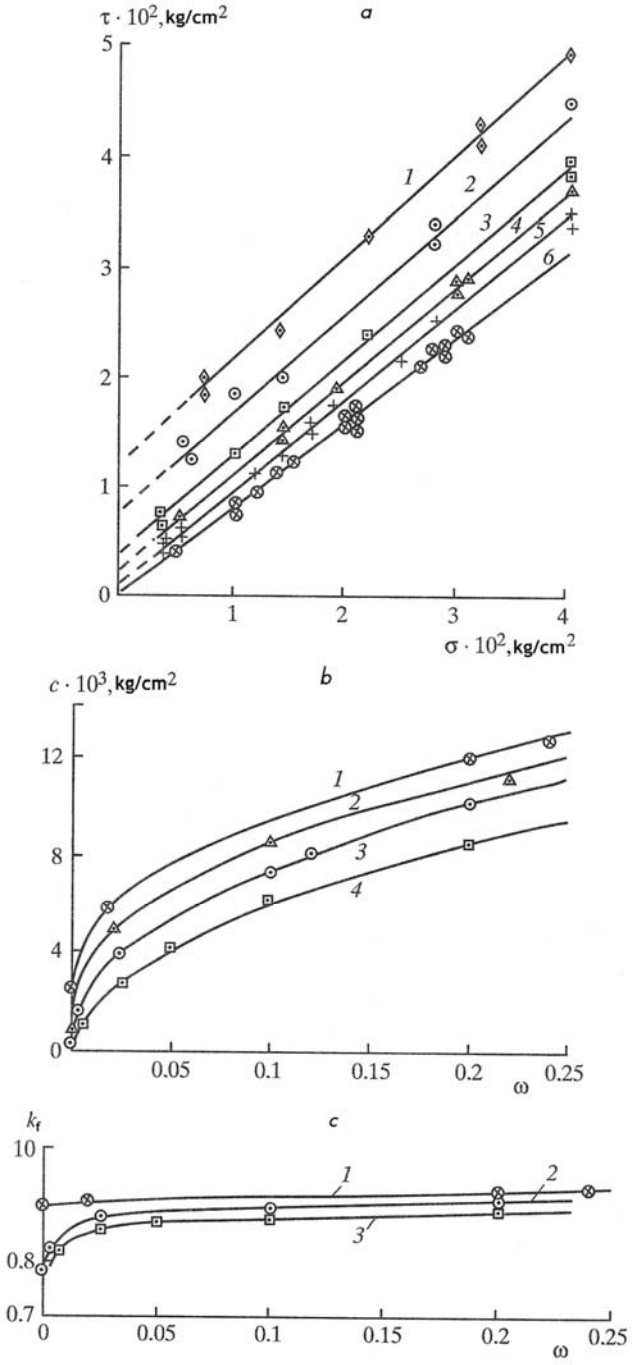

Figure 2.11. a) Relationships between the shear resistance τ and normal stress σ. Lines correspond to the following values of glycerin concentration: *1* – 0.24; 2 – 0.12; *3* – 0.05; *4* – 0.025; *5* – 0.0025, and *6* – 0. b) Relationships between internal friction coefficient and moisture [glycerin] content for the following values of density: *1* – 1.7 g/cm^3; *2* – 1.6 g/cm^3; *3* – 1.5 g/cm^3; *4* – 1.3 g/cm^3. c) Relationships between cohesion and moisture (glycerin) content for the following values of density: *1* – 1.7 g/cm^3; *2* – 1.5 g/cm^3; *3* – 1.3 g/cm^3.

Table 2.7. Parameters of experimental materials [soils?]

Material type	Parameter							
	d_c, cm	ω	γ, g/cm^3	m	C, kg/cm^3	k_f	φ^o	α^o
Dry sand	0.32	0	1.48	0.44	$1.26 \cdot 10^3$	0.78	38	36
	"	"	1.65	0.38	$2.0 \cdot 10^{-3}$	0.84	40	-
	0.06	"	1.60	0.40	$6.0 \cdot 10^{-4}$	0.85	40.5	36
	"	"	1.80	0.32	$4.0 \cdot 10^{-3}$	1.21	50	-
Wet sand	0.32	0.0025	1.25	0.54	$1.2 \cdot 10^{-3}$	0.84	40	36 – 38
	"	0.025	1.30	0.52	$2.6 \cdot 10^{-3}$	0.86	41	40 – 45
	"	0.5[0.05?]	1.35	0.51	$4.2 \cdot 10^{-3}$	0.87	41	40 – 45
	"	0.12	1.50	0.49	$8 \cdot 10^{-3}$	0.90	42	-
	"	0.24	1.70	0.50	$12.5 \cdot 10^{-3}$	0.93	43	-
Barite	0.43	0	2.9	0.29	$5.9 \cdot 10^{-3}$	0.81	39	38 – 42

Using the similarity criteria (2.10) the loose materials with weak cohesion were used, such as sand, dry cement, alabaster, crushed marble, barite, and their mixtures. Using dry quartz sand and barite proved particularly successful. Most commonly used material was quartz sand with the average particle size d_c = 0.32 mm and density γ = 1.48 g/cm^3. Sometimes quartz sand with d_c = 0.06 mm and density γ = 1.6 g/cm^3 and crushed barite with d_c = 0.43 mm and density γ = 2.9 g/cm^3 were used. In order to recreate complex topography with steep slopes small amounts of glycerin were added to sand. Glycerin was used due to its low vapor pressure (10^{-5} mm of mercury at room temperature) and due to its capability for preserving the properties of the model, with specified physical properties, for a long time.

Shear strength measurements as a function of particle size, density and moisture content were performed for the model materials using an apparatus with high sensitivity to small values of strength. Figure 2.11a shows the relationships between the limiting shear stress τ and normal stress σ for dry sand and for sand with added glycerin. The maximum shear stresses increase with the increase of normal stress and agree with Coulomb equation 2.9 with constant values of parameters c and k_f. The values of the coefficient of internal friction $k_f = \tau/\sigma$, the internal friction angle $\varphi = \tan^{-1} k_f$, and cohesion $c = \tau$ for $\sigma = 0$ were determined using least square inversion. The results are presented in Table 2.7 for different values of moisture content ω (glycerin), density γ and porosity m for quartz sand and crushed barite. The uncertainty of c and k_f does not exceed 3 – 5%.

It is worthwhile to note that dry quartz sand has cohesion on the order of $c = 10^{-3} \div 10^{-4}$ kg/cm^2 depending on the grain size and density. The internal friction coefficient is almost independent of these characteristics. Adding glycerin causes increase in resistance to shear. Even small amount of glycerin (ω = 0.0025) causes increase in cohesion by more than an order of magnitude, while the internal friction coefficient changed only slightly. Further increase in the amount of glycerin leads to slower growth of cohesion. Figure 2.11b,c shows the values of cohesion and internal friction coefficient as a function of glycerin content for different values of density ranging between 1.3 and 1.7 g/cm^3. The plot shows that the increase in shear resistance

with adding glycerin occurs mostly due to increase in cohesion with a small increase in the internal friction coefficient.

Table 2.7 shows angles of repose α, which represent the steepest slopes for a given granular material, measured in separate experiments. The values of the angles α and φ are close, however the changes in α due to changes in the material properties are less pronounced than in φ. We note that the range of change in α for the model granular materials is 36 – 45°, which correspond to the angle of repose for broken/fragmented rock.

2.2.5. The effect of gravity

One of the main problems to be solved using laboratory experiments was determining the relationships in a form (2.8) represented by a function with multiple variables. Therefore experiment setup involved significant simplifications. First, the experiments were conducted under defining effect of gravity. This condition was satisfied by creating high vacuum up to P_a = 1.0 ÷100 Pa and using dry sand with ρ = 1500 kg/m^3 and c = 10 Pa. The following experimental parameters were used: depth of burial W = 4 ÷ 20 cm, cavity radius 1.5 ÷ 5 cm, cavity pressure P = 10 ÷ 100 kPa, and energy $E = PV/(\chi\text{-}1)$, where $V = 4\pi r_c/3$ and χ = 1.4, E = 1 ÷ 10^2 J. The experiments were conducted in series so that in each series the parameter W/r_c was kept constant. In this case the dimensionless parameters containing energy can be significantly simplified:

$$\frac{E}{\rho g W^4} \to \frac{P}{\rho g W}, \quad \frac{E}{P_a W^3} \to \frac{P}{P_a}, \quad \frac{E}{cW^3} \to \frac{P}{c}. \tag{2.11}$$

These parameters characterize the ratio between the forces acting in the model:

$$\frac{P}{\rho g W} \sim 10 \div 100, \quad \frac{P}{P_a} \sim 100 \div 1000 \quad \frac{P}{c} \sim 10^3 \div 10^4. \tag{2.12}$$

It follows from relationships (2.12) that forces opposing the ejection resulting from atmospheric pressure and cohesion are one or two orders of magnitude smaller than the gravitational force. In these circumstances the dimensionless parameters E/P_aW^3 and E/cW^3 can be neglected and the only important parameter containing energy is $E/\rho gW^4$. We note that lack of cohesion for dry sand does not mean that the energy spent on overcoming shear resistance also equals zero. Friction forces produced during moving of the sand volume by pressurized gas lead to energy dissipation. However these losses are accounted for by including dimensionless parameter k_f. For a given type of material and a given configuration of the gas cavity the dimensionless parameters k_f and χ were also constant, therefore they could also be eliminated from analysis.

The ratio of forces recreated in (2.12) applied to actual field experimental conditions with P_a = 100 kPa correspond to an explosion with ρgW = 1 ÷ 10 MPa, or the depth of burial of W = 20 ÷ 400 m.[5] To create a crater for these depths of burial the yield of explosion needs to be q = 1 ÷ 10^3 kt. Thus the situation recreated in the laboratory experiment represents the large scale excavation explosions.

[5] W=20 m corresponds to 0.5 MPa, not 1 MPa

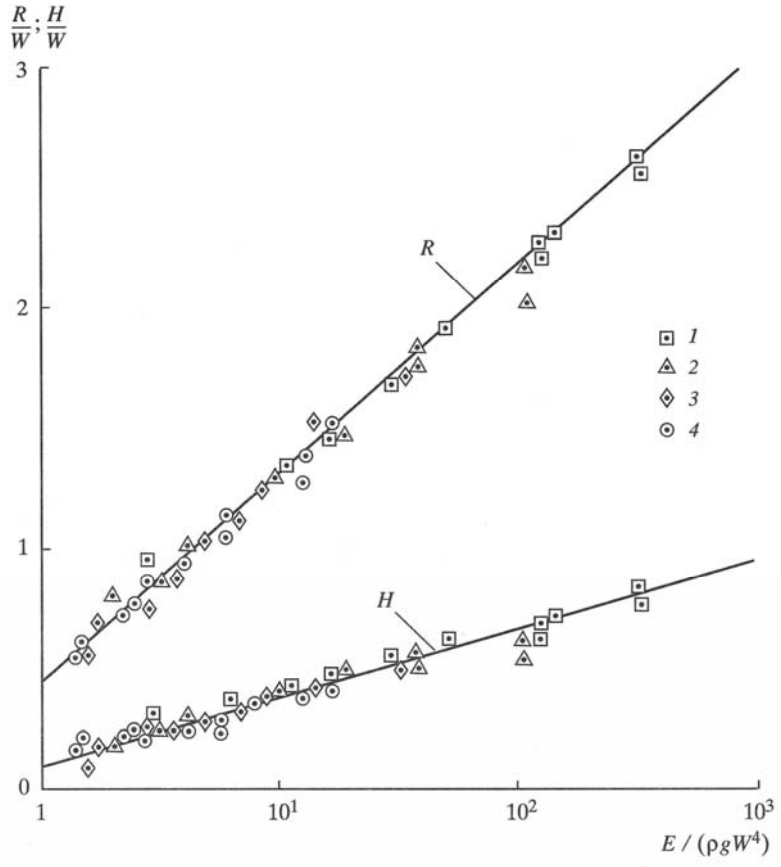

Figure 2.12. Crater radius and depth as a function of energy of cavity gas for the following values of relative depth of burial W/r_c: 1 – 1.6; 2 – 2.4; 3 – 3.2; 4 – 4.8.

Under these conditions the relationships in 2.8 are reduced to a function of two variables:

$$R/W = \mathrm{F}\{\, E/\rho g W^4,\ W/r_c \,\}. \qquad (2.13)$$

To study the function in (2.13), a series of four experiments were conducted. In each series the value of W/r_c was fixed at values 4.8, 3.2, 2.4, and 1.6. Each experiment in the series was conducted with variable values of energy of cavity gas E, depth of burial W and cavity radius r_c. Measurements were made of the final crater dimensions and development of the cupola with time. Figure 2.12 shows the results of measurements for crater radii and depths plotted in coordinates given in (2.13). Different symbols show the series with fixed values of W/r_c. As it turns out crater dimensions are largely independent on this parameter at least in the range $1.6 \leq W/r_c \leq 4.8$, corresponding to the change in cavity radius almost by an order of magnitude. Therefore the crater size is determined only by the energy of gas in the cavity and independent of the size of the cavity. Using these experimental results the following empirical relationships were obtained:

$$R/W = 0.45 + 0.85 \lg (E/\rho g W^4),\ H/W = 0.07 + 0.28 \lg (E/\rho g W^4), \qquad (2.14)$$

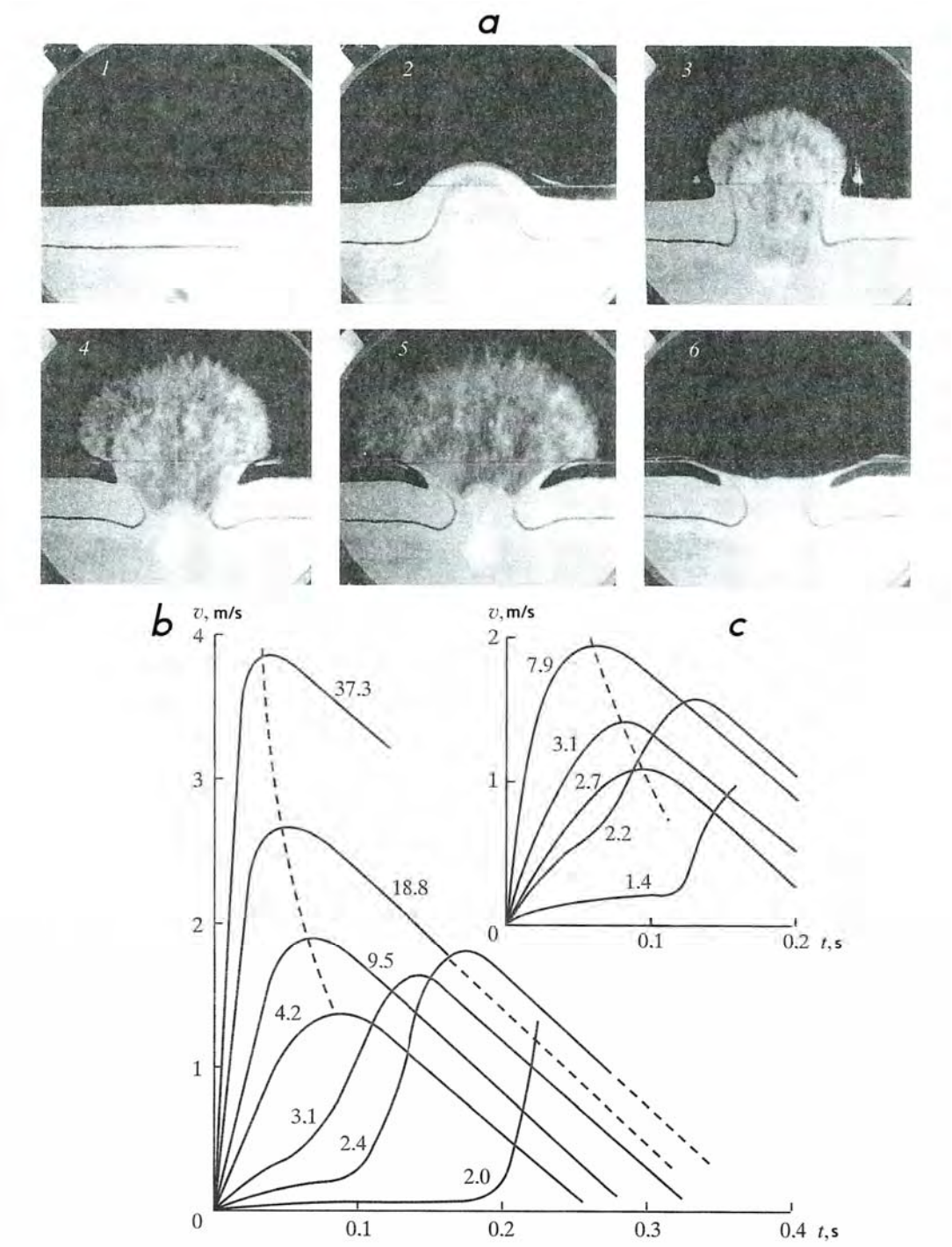

Figure 2.13. a) Snapshots showing ejection evolution during a laboratory experiment for the following times from detonation: *1* – 0 s; *2* – 0.08 s; *3* – 0.15 s; *4* – 0.22 s; *5* – 0.29 s; and *6* – 0.6 s. b) Velocity of cupola rising as a function of time for the following values of W/r_c: *1* – 2.4; *2* – 4.8. c) Velocity of cupola rising as a function of time for different values of energy parameter $E/\rho g W^4$ (shown with the numbers next to the curves).

which show that for small values of cohesion ($c/\rho gW \sim 10^{-2}$) and low pressure above the free surface ($P_a/\rho gW \sim 10^{-2}$) the model satisfy the conditions of "gravitational similarity", in which case cavity gas energy is $E \sim W^4$.

Kinematic parameters of excavations were determining by analyzing motion of the cupola. Figure 2.13a shows snapshots made during one of the experiment (r = 2.3 cm, W = 7.7 cm, P = 30.2 kPa, P_a = 0.27 kPa, n = 1.12). Figure 2.13b shows uplift (ejection) velocity as a function of time for different values of cavity gas energy for two series of experiments with W/r_c equal to 2.4 and 4.8.

Two types of the cupola development (velocity curves) are observed: monotonic increase to a maximum with subsequent downward movement due to gravity and increase of velocity with an inflection. The first type is realized for large values of parameter $E/\rho gW^4$ because cavity gas has sufficient energy to push upward the entire mass of material above it. This type of motion is characterized by maximum velocity v_m and time of gas acceleration t_m. Higher value of parameter $E/\rho gW^4$ results in higher values of maximum velocity and shorter time of gas acceleration. Upon reaching maximum velocity the cupola loses its initial shape and becomes irregular due to gas venting into atmosphere. Measurements of v_m and t_m satisfy conditions of dynamic similarity in a form of Freund criterion (v^2/gW = const) and can be described using empirical formulas:

$$\frac{v_m}{(gW)^2} = 0.74\left[\frac{W}{(E/\rho g)^{1/4}}\right]^{-2};\ \frac{t_m}{(gW)^2} = 1.15\left[\frac{W}{(E/\rho g)^{1/4}}\right]^{1.4}. \qquad (2.15)$$

Absence of the factor W/r_c suggests the defining effect of energy of cavity gas on crater development.

For small values of the parameter $E/\rho gW^4$ the character of cupola uplift qualitatively changes – the velocity increases with an inflection (Figure 2.13). This character of velocity change suggests that the energy of gas in the cavity is insufficient to push the entire mass of material. Gas escape (venting) occurs only after some material falls down into the cavity and the gas volume approaches the free surface. The region of parameter $E/\rho gW^4$ values producing inflection in the cupola movement represents *partially contained explosions* (also called "loosening explosions" in Russian literature) and will be discussed in later chapters.

2.2.6. The effect of atmospheric pressure

In order to determine the effect of atmospheric pressure on the evolution of excavation explosions, a series of experiments were conducted with fixed value of P_a/P equal to 1/500; 1/100; 1/20 and 1/5. The experiments were conducted in series with fixed parameters $E/\rho gW^4$ = const and W/r_c = const. As before dry sand was used, so that cohesion is low and $c/P_a < 10^{-1}$.

Snapshots of the ejection process for changing pressure above the surface and other parameters fixed ($E/\rho gW^4$ = 9.9 and W/r_c = 2.4) are shown in Figure 2.14. The results show that the size of the cupola decreases with the increase of pressure above the surface. Relationships between the crater radius and the energy parameter $E/\rho gW^4$ are shown in Figure 2.15 a,b for

different values of P_a/P. The dashed line shows the relationship given in 2.14 determined earlier during the experiments on the effects of gravity. Increase in the value of ratio P_a/P leads to greater deviation of the curves from 2.14. The effect of the ratio between the atmospheric and lithostatic pressure on crater radius is shown in Figure 2.15c. If $P \sim \rho g W^4$ the crater radius is strongly dependent on the ratio $P_a/\rho g W$. For $P_a \leq 0.1\ \rho g W$ radius reaches its maximum value and depends only on the parameter $E/\rho g W^4$ according to Equation 2.14.

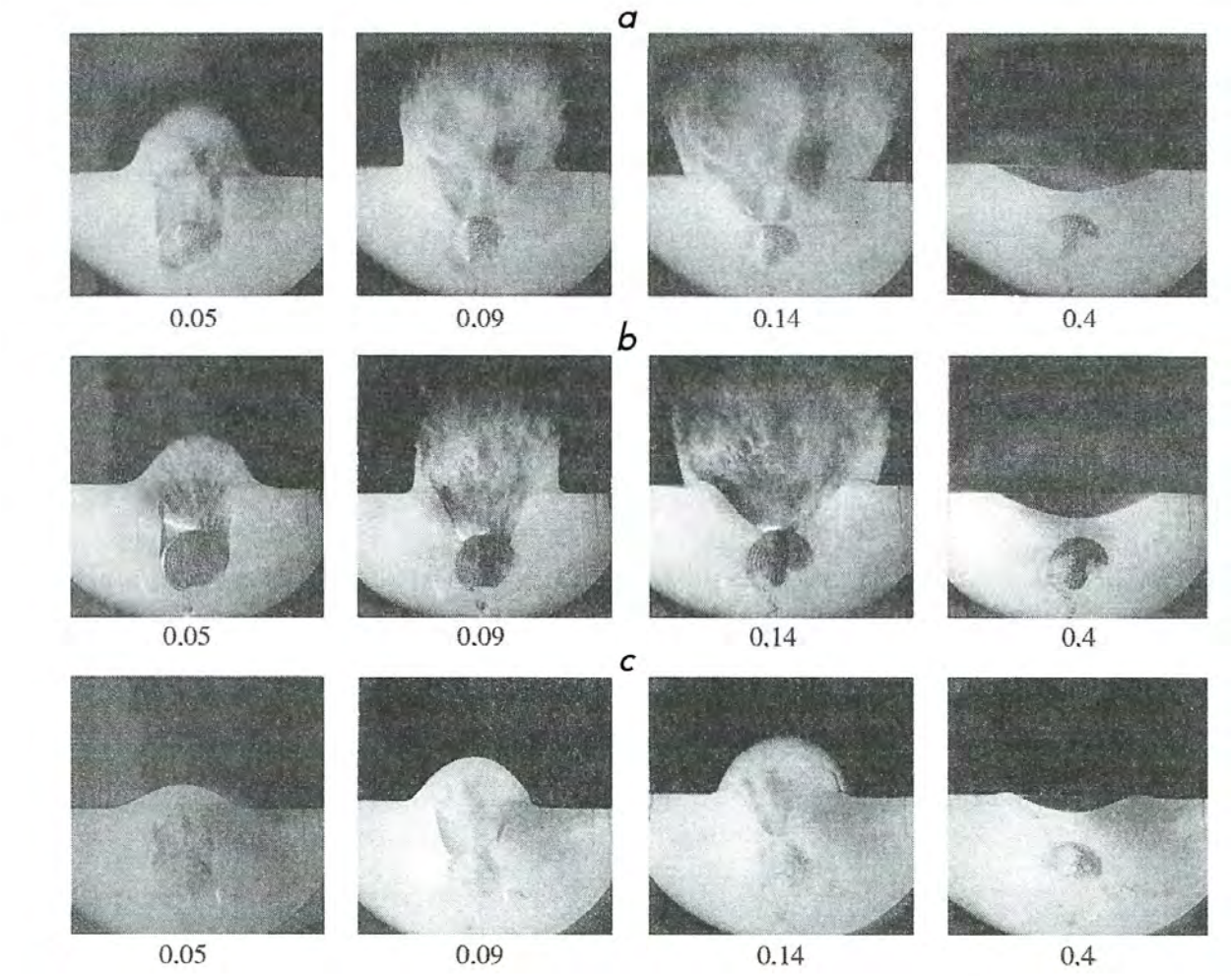

Figure 2.14. a) Snapshots showing ejection evolution [during a laboratory experiment] for different values of pressure above the free surface: a) P_a/P = 0.01, a) P_a/P = 0.05, a) P_a/P = 0.2. Time (in seconds) from the moment of cavity development is shown below each snapshot

In the opposite case when $P_a \geq 10\rho g W$, crater radius reaches its minimal value. In this limit it no longer depends on $P_a/\rho g W$ and is determined by the parameter W/r_c. Transferring this result into the full scale experiments, when P = 100 kPa, condition $P \sim \rho g W^4$ is reached for the depth of burial W = 4 ÷ 6 m for charges with yields of $q \sim 1$ t. The condition $P_a \leq 0.1\ \rho g W$ is realized when $W \geq 40 \div 60$ m and $q \geq 1 \div 10$ kt, while the condition $P_a \geq 10\rho g W$ occurs when $W \leq 0.4 \div 0.6$ m and $q \leq 10$ t. The results related to the effect of the atmospheric pressure lead to an

assumption that the forces opposing the ejection forces can be represented as a sum $\rho gW + P_a$. Then for the conditions described in the experiments Equation 2.8 can be rewritten as:

$$R/W = \mathrm{F}\{\ \bar{E},\ W/r_c\ \},\ \text{where}\ \bar{E} = E/[(\rho gW + P_0)W^3]. \tag{2.16}$$

The results of the experiments conducted according to 2.16 for different values of P_a/P are shown in Figure 2.16. Experiments with different values of W/r_c were not separated because earlier experiments have shown that this parameter does not affect crater sizes. The results of all experiments are described by a single relationship according to the empirical formula:

$$R/W = 0.\ 5 + 0.9 \lg(\bar{E}), \tag{2.17}$$

$$H/W = 0.08 + 0.31 \lg(\bar{E}).$$

Existence of a single relationship describing changes in P_a/P in the range between 0.002 and 0.2 confirms the assumption that the resisting force can be described as a sum $\rho gW + P_a$.

Using this result and considering that the kinetic energy of the ejected rocks is proportional to $\rho W^3 v^2$, where v is the velocity of uplift, we can select the following dimensionless parameters to describe excavation process:

$$\bar{v}_m = \frac{v_m}{(gW + P_a/\rho)^{1/2}};\ \bar{t}_m = \frac{t_m(gW + P_a/\rho)^{1/2}}{W};\ \bar{W} = \frac{W(\rho gW + P_a)^{1/3}}{E^{1/3}}. \tag{2.18}$$

The relationships between the maximum velocity v_m and the time it reached t_m and the depth of burial and gas energy are shown in Figure 2.17 for different values of the ratio P_a/P. These relationships can be described using empirical formulas:

$$\bar{v}_m = 0.6/\bar{W}^{1.9};\ \bar{t}_m = 1.37\bar{W}^{1.2}. \tag{2.19}$$

Relationships between the crater sizes given by (2.17) and kinematic characteristics given by (2.19) are valid only if the value of parameter E is greater than a certain limiting value E_*. The limiting value E_* was determined by examining the character of the cupola rise with time: for $E > E_*$ the velocity was increasing monotonically until it reached the maximum, while for $E > E_*$ the velocity had an inflection and the ground ejection ceased. The value of E_* was determined for each series with varying W/r_c. The relationship between the limiting value E_* and the ratio is given by an empirical formula:

$$\bar{E}_* = \frac{5.4}{(W\ /\ r_c)^{0.6}}. \tag{2.20}$$

As expected, the limiting value of $\bar{E}_*$ is close to one in order of magnitude.

The relationships between the limiting value $\bar{E}_*$ and the ratio W/r_c complicates the problem of determining the maximum possible depth for excavation explosions, because this problem depends not only on the explosion yield, but also on the cavity size, which in turn depends on the rock type and the type of the explosion.

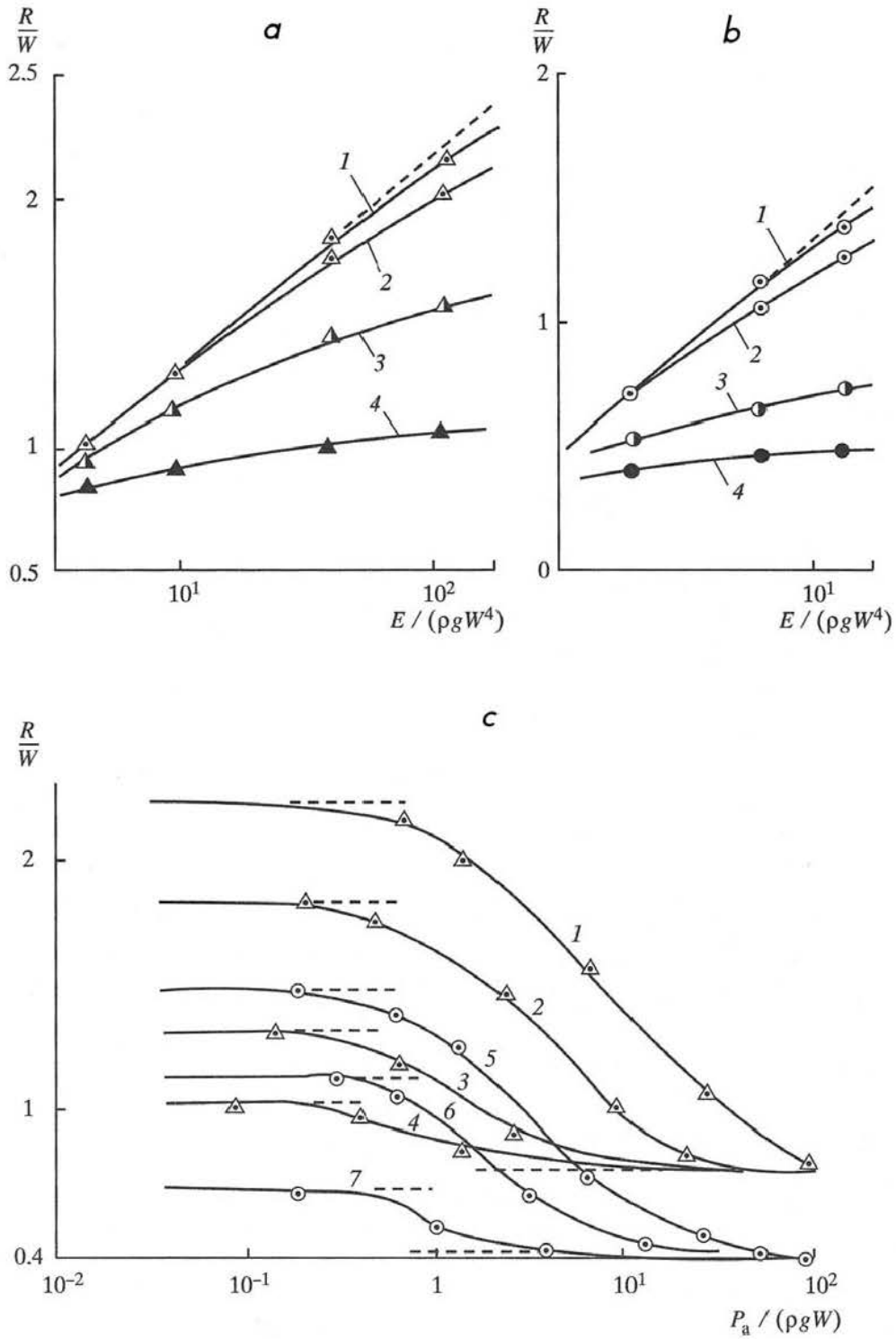

Figure 2.15. Effect of pressure above the surface on the crater size: a) W/r_c = 2.47, curve numbers correspond to different values of P_a/P: *1* – 0.005, *2* – 0.01, *3* – 0.05, and *4* – 0.2; b) curve numbers

correspond to different values of P_a/P: 1 – 0.005, *2* – 0.01, *3* – 0.05, and *4* – 0.2; c) $E/\rho g W^4$: *1* – 37.3, *2* – 18.8, *3* – 9.5, *4* – 4.8, *5* – 3.1, *6* – 2.4, *7* – 2.0.

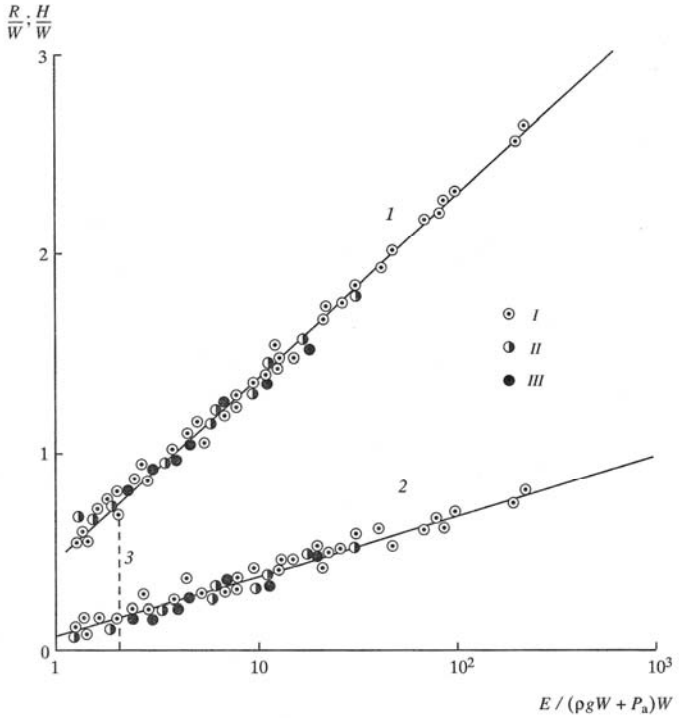

Figure 2.16. Relative crater radius *R/W* (1) and depth *H/W* (2) as a function of gas energy and depth of burial; dashed line *3* corresponds to $\bar{E}_*$; symbols *I – III* correspond to different values of P_a/P: *I* – <0.001, *II* – 0.05, and *III* – 0.2.

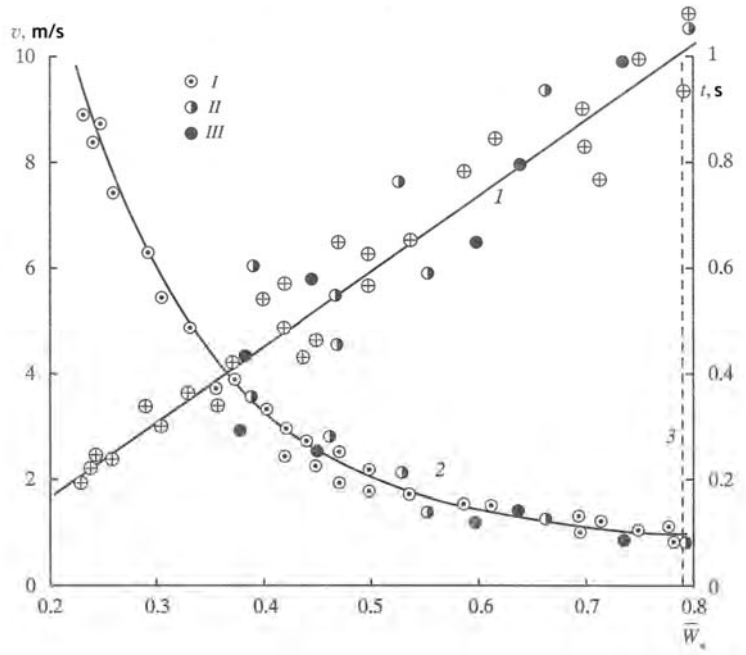

Figure 2.17. Maximum velocity of ejection the time the maximum is reached as a function of gas energy and depth of burial. Numbered lines correspond to *1* – t_m, *2* – v_m, *3* – $\bar{W}_*$; symbols *I* – *III* correspond to different values of P_a/P (same as in Figure 2.16): I – <0.001, *II* – 0.05, and *III* – 0.2.

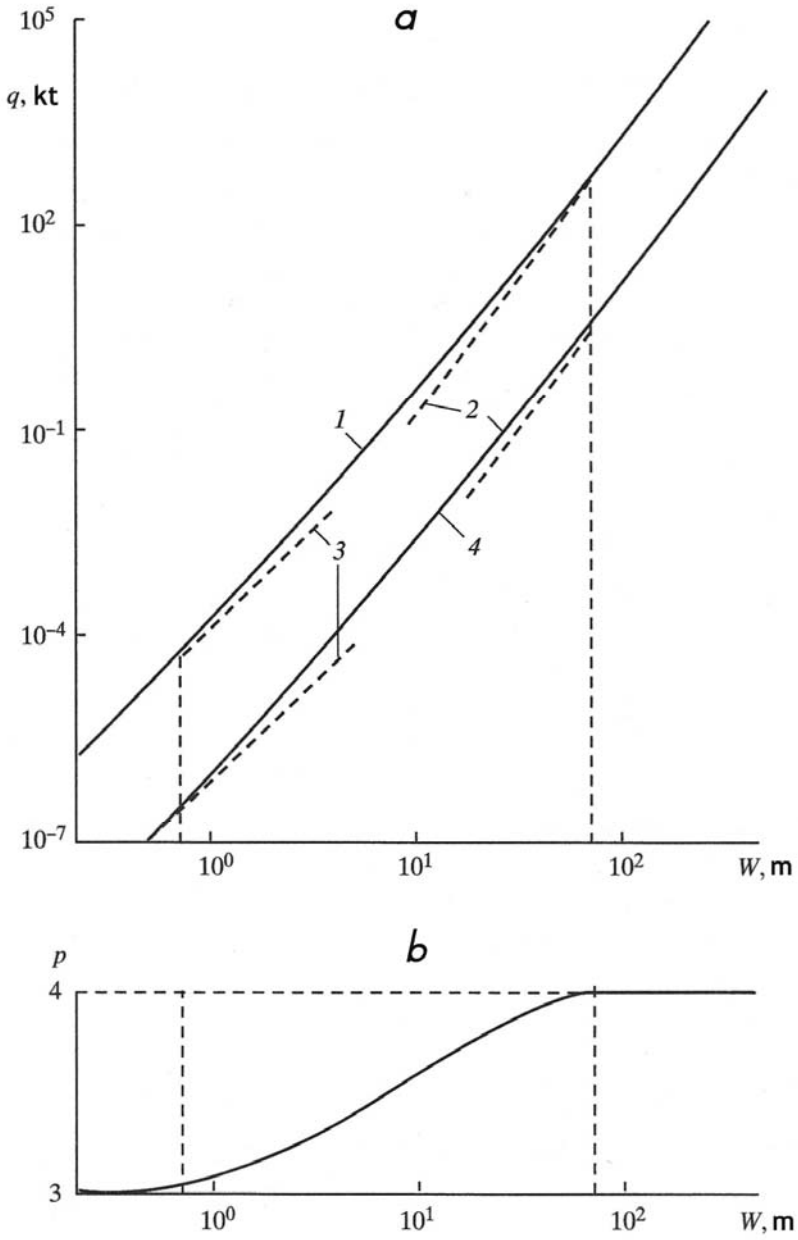

Figure 2.18. Effect of explosion yield on a) formation of geometrically similar craters, and b) scaling factor. Numbered lines correspond to different values of ejection parameter: n = 1 (line 4), n = 3 (line *1*), and to the following similarity parameter values: p = 4 (line *2*), p = 3 (line *3*)

Scaling analysis was conducted using the experimental results for excavation explosions for varying ratios between the two forces opposing the ejection: atmospheric pressure and gravity.

The conditions of formation of geometrically similar craters with n = const are satisfied if $\bar{E} = const$. Energy of gas in the cavity is related to yield as $E = \xi q$. For fixed rock properties and source type $\xi = const$, therefore the similarity condition takes the form $q/(\rho g W + P_a)$ = const. Now we consider full scale field conditions (P_a = 100 kPa) for excavation explosions in alluvium (ρ = 1800kg/m^3, ξ = 0.17), which is easy to break apart so that cohesion is small compared to P_a = 100 kPa. Figure 2.18 shows the relationship between the yield and depth of burial for two values of excavation parameter n = 1 and n = 3. The range of depths is sufficiently large $0.2 \le W \le 400$ m, so that the ratio between the atmospheric and litostatic pressures and ranges $0.015 \le P_a/\rho g W \le 30$ ($P_a \approx \rho g W$ for $W \approx 6$m). For a quantitative estimate of the scaling factor we express the relationship between the explosion yield and depth of burial in a form:

$$q \sim W^p \cdot f(n),$$

for n = const, $f(n)$ = const, and $q \sim W^p$. Figure 2.18 shows changes in the scaling factor with the depth increase. For explosions with depth $W \le 0.7$m the factor p = 3 which correspond to "geometrical similarity". For $W \ge 70$m the factor p = 4 and the "gravitational similarity" applies. In the depth range between 0.7 and 70 m the scaling factor gradually increases from 3 to 4 according to [an empirical formula]:

$$p = 3.14\, W^{0.06},\ 0.7 \le W \le 70 \text{ m}.$$

For instance p = 3.5 for W = 10 m.

2.2.7. Effect of strength properties of soil

The experiments with sand with added small amounts of glycerin were conducted in order to study the effect of strength on crater parameters. The properties of granular material were preserved with some added cohesion between the grains. The main properties of the model materials are shown in Table 2.8. According to this table, the main differences between materials involved variations in cohesion, while the internal friction coefficient varied by less than 10%. The experimental parameters condition $\rho g W \sim 1.0$ kPa and $P_a \sim 0.1$ kPa, therefore the relationship between cohesion and the pressure above the free surface is $c \sim 0.1\, P_a$ for dry sand and $c \sim P_a$ for sand with glycerin. The relationships between other forces in the model were:

$$\frac{P}{\rho g W} \sim 10 \div 100,\ \frac{P}{P_a} \sim 100 \div 1000\ \frac{c}{\rho g W} \sim 10^{-1}.$$

Figure 2.19 shows snapshots of crater/ejection development for sand with glycerin.

The measurement results for crater radii and depths are shown in Figure 2.20 using universal coordinates according to 2.16. Increase in cohesion caused crater radius decrease and depth increase. Crater dimensions did not depend on the experiment geometry and were determined by energy of the cavity gas. Using least square inversion the following empirical relationships were obtained:

$$R/W = 0.9 \lg E + 0.05,\ H/W = 0.42 \lg E + 0.05 \text{ for } c = 1.5 \cdot 10^2 \text{ Pa} \quad (2.21)$$

$$R/W = 0.9 \lg E - 0.5,\ H/W = 0.38 \lg E - 0.1 \text{ for } c = 3.5 \cdot 10^2 \text{ Pa}$$

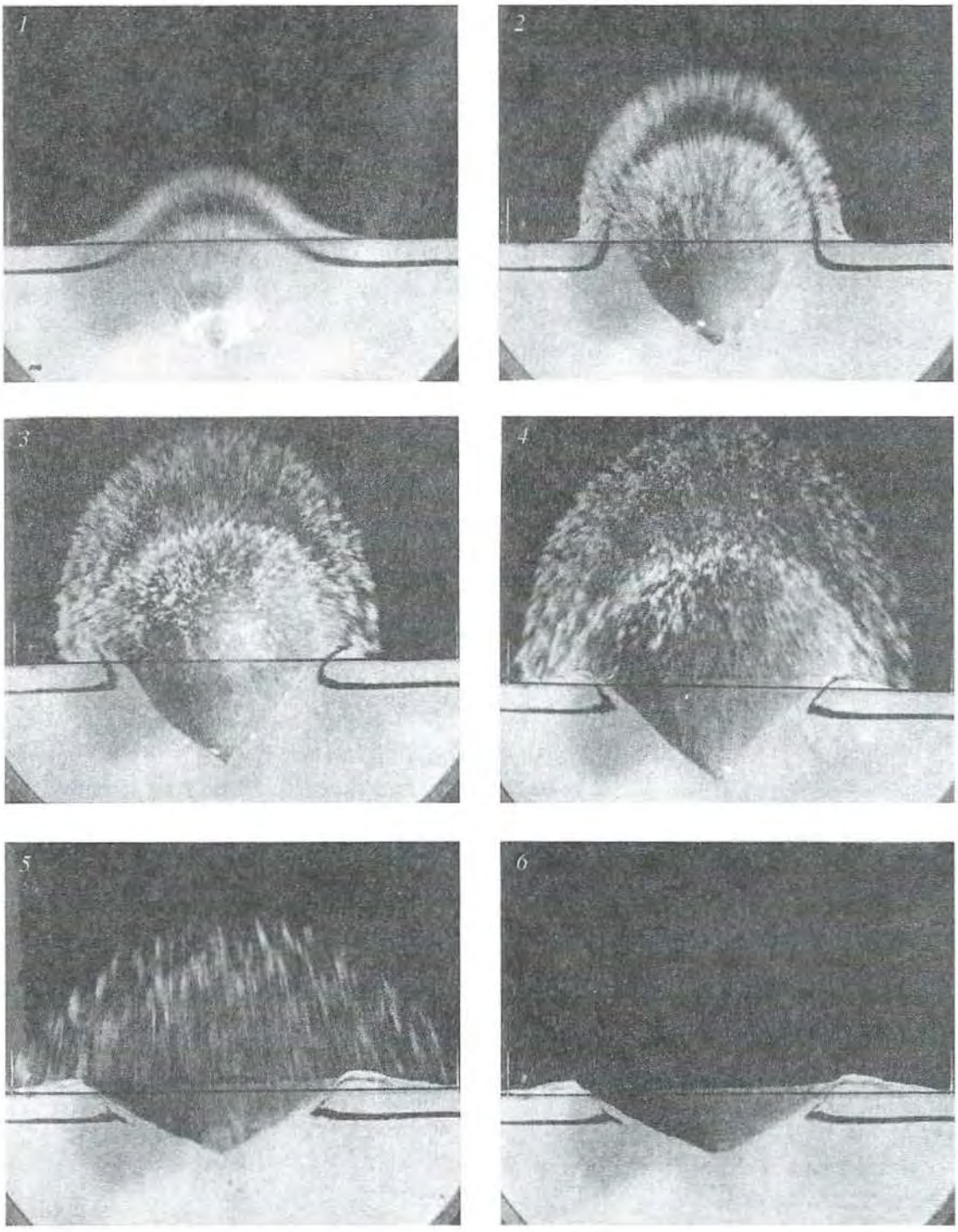

Figure 2.19. a) Snapshots showing ejection evolution during a laboratory experiment with sand with added glycerin (ω = 0.0025) for $\bar{E} = 17.3$, W/r_c = 3.2, $P_a/P = 5 \cdot 10^{-3}$. The snapshots are shown for the following times from detonation: *1* – 0.04 s; *2* – 0.13 s; *3* – 0.16 s; *4* – 0.23 s; *5* – 0.37 s; and *6* – 0.55 s

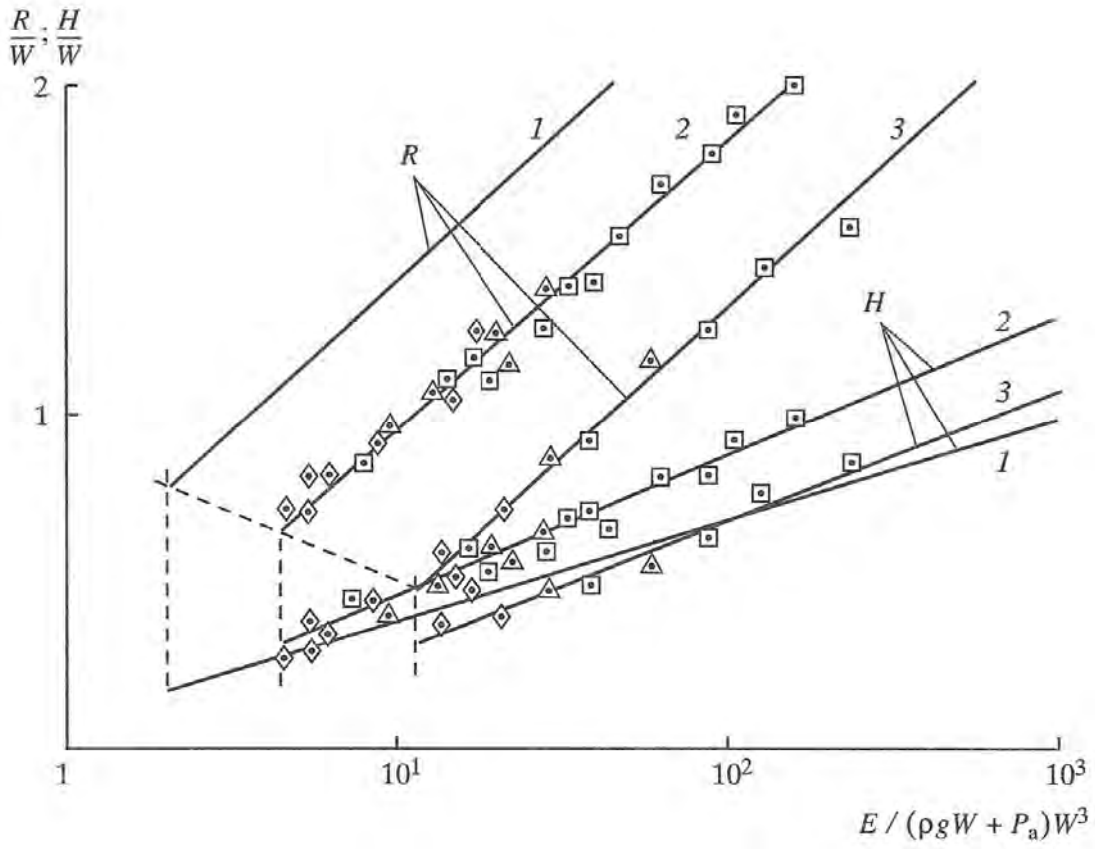

Figure 2.20. Effect of material cohesion (c) on the crater radius and depth. Numbered lines correspond to the following values of cohesion c: *1* – 10 Pa, *2* – 150 Pa, *3* – 350 Pa

Table 2.8. Main properties of the experimental materials

Parameter	Parameter value		
ω	0	0.0025	0.02
γ, kg/m^3	1500	1500	1200
$c \cdot 10^5$, Pa	10^{-4}	$1.5 \cdot 10^{-3}$	$3.5 \cdot 10^{-3}$
k_f	0.78	0.82	0.82

For each material type the value of minimum energy below which excavation ceased was determined. The higher the cohesion was, the higher the value of the limiting value of the

parameter $\bar{E}_*$. Similar to the experiments with dry sand the value of $\bar{E}_*$ depended on the ratio W/r_c. Thus, for sand with moisture (i.e. glycerin) content of 0.25% and the ratio W/r_c = 3.2 the limiting value was $\bar{E}_* = 4.2$, while for moisture (glycerin) content of 2% and W/r_c = 3.2 it was $\bar{E}_* = 11.4$ (shown with vertical dashed lines in Figure 2.20).

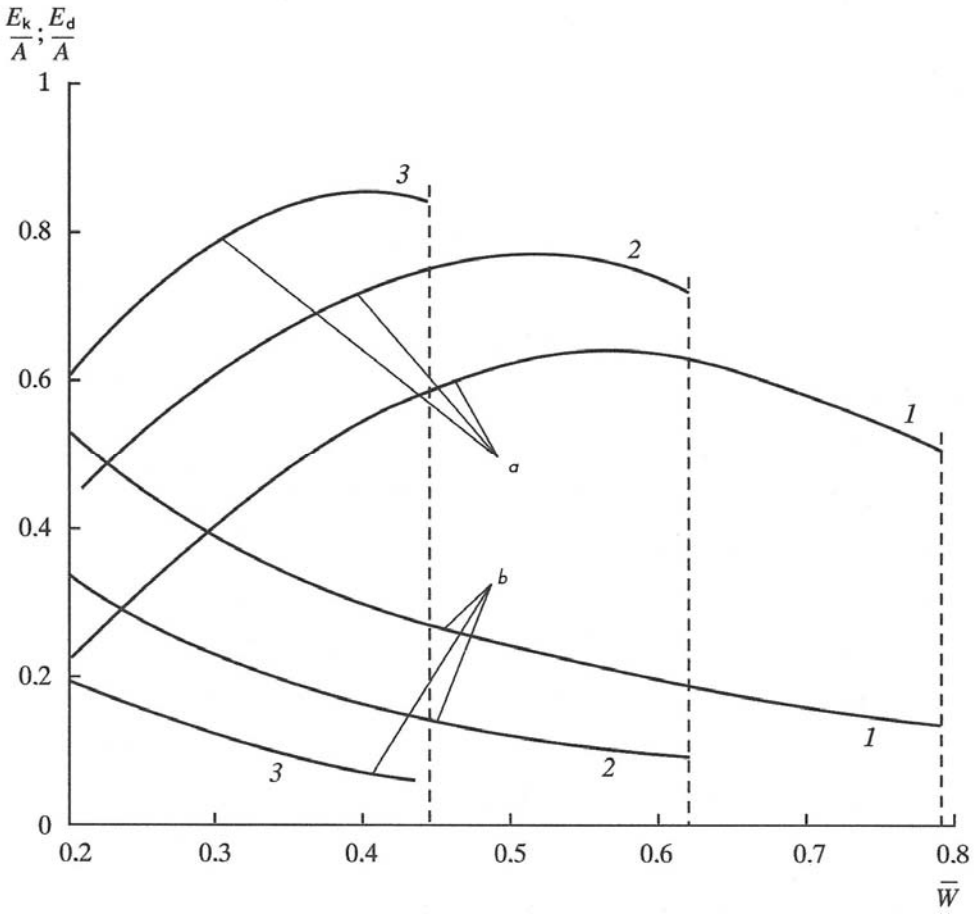

Figure 2.21. Kinetic energy E_k (shown with lines *b*) and dissipated energy E_d (lines *a*) as a function of depth of burial and total energy of cavity gas. Numbered lines correspond to the following values of cohesion *c*: *1* – 10 Pa, *2* – 150 Pa, *3* – 350 Pa. [Same as in Figure 2.20]

Observations of the kinematic parameters of excavation for materials with cohesion show that the character of velocity change with time is independent of the type of material. However the increase in cohesion with other parameters being unchanged reduces the value of the maximum velocity and the time when the maximum is reached. Study of energy consumption during excavation in laboratory experiments was performed using velocity measurements data for cupola rise. The energy of gas is spent on the work against gravity and atmospheric pressure, as well as on material acceleration and work against friction. Using film recordings it was determined that during gas acceleration phase the velocities of different layers were similar and

the motion was radial. Kinetic energy was determined using the average rise velocities of different cupola elements as a sum:

$$E_{c?} = \sum_{i=1}^{n} \frac{m_i v_{mi}^2}{2}, \tag{2.22}$$

where i is a number of elements, m_i is the mass of each element, v_{mi} is the maximum velocity of each element accounted for the direction of motion. [not sure what this means] Figure 2.12 shows changes in kinetic energy determined at the moment when the cupola reaches its maximum velocity as a function of the depth of burial of the source. Kinetic energy is related to work produced during isentropic expansion:

$$A = \frac{pV_c}{\chi - 1}\left[1 - \left(\frac{P_a}{P}\right)^{\frac{\chi-1}{\chi}}\right]. \tag{2.23}$$

The fraction of kinetic energy relative to the total energy of explosion decreased with the increase of the depth of burial for all material types. For dry sand the portion of kinetic energy varied between 50 and 12% of the total explosion energy. After increase in cohesion the portion of kinetic energy was in the range between 35 and 5%.

The potential energy E_p required for lifting rock within a conical volume with the base area $S = \pi n^2 W^2$ and the height equal to the depth of burial W in gravitational field to a height of $h = v_m \cdot t_m$ is equal to:

$$E_p = \frac{\pi}{3} \rho g n^2 W^3 v_m t_m. \tag{2.24}$$

In this case, dissipated energy lost on work against the friction and cohesion forces during the ejection is:

$$E_d = A - (E_k + E_p). \tag{2.25}$$

Changes in dissipated energy as a function of depth of burial are shown in Figure 2.21. For dry sand dissipated energy is between 20 and 65% of the total work performed by gas during its expansion. Increase in cohesion results in the increase in dissipated energy to 45 – 85%. Depending on the depth of burial, the value of dissipated energy has a maximum, which is called *optimal depth of burial*.

In conclusion we comment on the measurement uncertainties for the initial parameters, their dimensionless combinations, and the final results for the laboratory experiments. The radius of the cavity encapsulated in the metal lattice was measured using the volume of displaced fluid with 0.1 mm uncertainty. Depth of burial was measured using a metal ruler with an uncertainty of 1 mm. Excess pressure was measured using mercury manometer with uncertainty of 1.5 mm of mercury. The pressure above the free surface was measured using an oil manometer with an error of 1.5 mm of oil. The error in measurement of the initial density was 0.05 g/cm^3. As a result, the uncertainty in determining the dimensionless parameters $\bar{E}$ and W/r_c varied in the

range 2 – 6% and 1 – 2% respectively. Accuracy of the measurements of the crater linear dimensions, which measured in the range 10 – 30 cm for the radius and 2 – 10 cm for the depth, was 2 – 5%.

2.2.8. Comparison between the results of laboratory and field experiments

In order to compare crater sizes and kinematic parameters of the ejection obtained in laboratory experiments with similar field data it is necessary to have information about sizes of the cavity and energy of gas by-products at the end of the "camouflet" phase of nuclear explosions for different rock types. Numerous measurements of cavity sizes are available for fully contained explosions conducted at the Semipalatinsk Test Site (e.g. Chapter 1) and at American and French test sites in hard rock (Table 2.9), alluvium (Table 2.10) and tuff (Table 2.11).

Table 2.9. Explosive cavity sizes in hard rocks

Explosion	Rock type	Parameter		
		q, kt	W, m	r_c, m
HARDHAT	Granite	5.4	286.4	19.2 – 20.1
SCHOAL	"	12.5	367.4	25.6 – 26.8
PILEDRIVER	"	61[6]	463.5	39.1 – 44.5
HANDCAR	Dolomite	12	402.5	21.2
GASBUGGY	Sandstone	26	1292	25.7
MONICA	Granite	120	785	36
HALFBEAN	Rhyolite	313	820	76.2
BOXCAR	"	1300[7]	1161	94.5

Table 2.10. Explosive cavity sizes in alluvium

Explosion	Parameter		
	q, kt	W, m	r_c, m
MAD	0.43	181.1	11.3
STILLWATER	2.7	181.5	24.7
BRAZOS	8.4	256.3	27.7
PARROT	1.2	180	14.6
ARMADILLO	6.5	240	23.8

[6] Table 2.7 lists the yield for PILEDRIVER as 66 kt. Check

[7] BOXCAR listed (by Sandia) yield is 1.3 kt. Something is wrong here. Wonder how they even got that cavity size…

FISCHER	12.4	364	37.5
PAR	38	406	48.8
CHINCHILLA 1	1.8	150	17.1
STOAT	4.7	302.6	24.6
AGOUTI	5.8	261.1	36.0
DORMOUSE 1	11	261.1	34.7
HAYMAKER	46	408.7	49.7 – 56.1
PETREL	1.2	180.9	18
CYCLAMEN	13	305	28
CIMARRON	11.2	304.8	32.6

Table 2.11. Explosive cavity sizes in tuff

Explosion	Parameter		
	q, kt	W, m	r_c, m
RAINIER	1.7	274	18.9
LOGAN	5.0	283	28
BLANCA	19.2	255	39.6 – 44.3
ANTLER	2.6	402	19.8
PLATTE	1.7	191	21.6
HOOSIC	3.4	187.3	25.9
AARDVARK	38	434.3	47.8
MUDPACK	2.7	152	23.2
DISCUS	21	337	32.6
BENHAM	1100	1402	103
GREELEY	825	1215	76.5
KNICKERBOCKER	71	635	46
REX	16	671	30.2
SCOTCH	150	977	60
TAMALPAIS	0.07	125	9.14

The results of cavity radius measurements for various types of rocks as a function of the explosion yield are shown in Figure 2.22. According to this plot the relationship between the radius and the yield satisfies the condition of geometrical similarity:

$$r_c = \bar{r}_c q^{1/3}, \tag{2.26}$$

where the values of $\bar{r}_c$ are: 16.2 m/kt$^{1/3}$ for tuff, 15 m/kt$^{1/3}$ for alluvium, 9.2 m/kt$^{1/3}$ for dolomite, 11.1 m/kt$^{1/3}$ for Nevada granite, and 7.3 m/kt$^{1/3}$ for Sahara granite. However for explosions with yields over 100 kt in tuff and alluvium the experimental points [measurements] plot below the line given by Equation 2.6 and are better approximated using formula:

$$r_c = \frac{70q^{1/3}}{(\rho g W)^{1/4}}, \tag{2.27}$$

shown in Figure 2.22 with a dashed line.

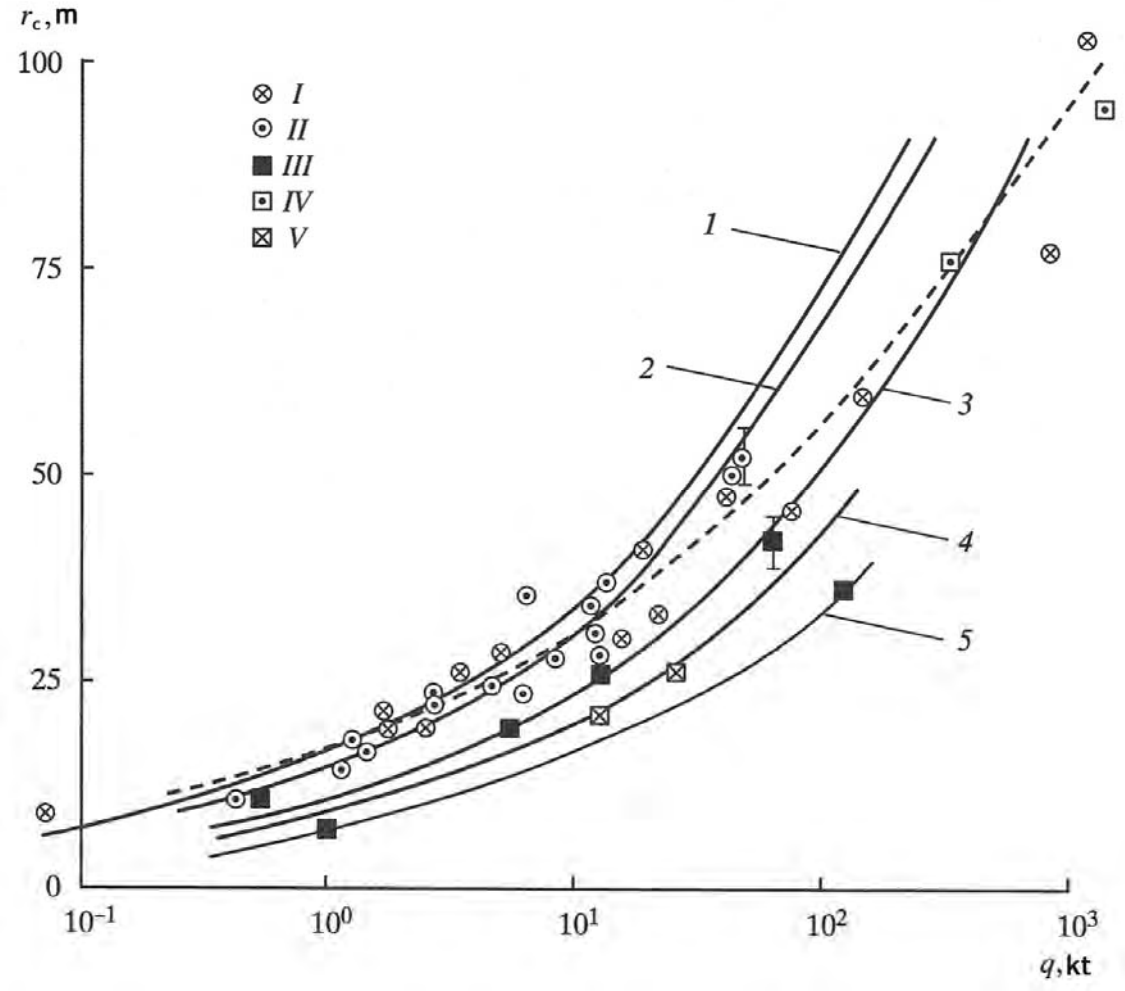

Figure 2.22. Relationships between the radius of the cavity and the energy [yield] of nuclear explosions (dashed line shows the result of calculations using Equation 2.27). The numbered lines correspond to the following values of the scaled cavity radius $r_c/q^{1/3}$: *1* – 16.2 m/kt$^{1/3}$, *2* – 15 m/kt$^{1/3}$, *3* – 11.1 m/kt$^{1/3}$, *4* – 9.2 m/kt$^{1/3}$, *5* – 7.3 m/kt$^{1/3}$. The symbols correspond to the following rock types: *I* – tuff, *II* – alluvium, *III* – granite, *IV* – rhyolite, *V* – dolomite

Cavity sizes for explosions conducted at the Semipalatinsk Test Site also agree with Equation 2.26. For tunnel explosions conducted in porphyrites and granites at Degelen the average value is

$\bar{r}_c = 7.3\, m/kt^{1/3}$, for borehole explosions conducted at Balapan the radius is $\bar{r}_c = 11 \div 13.6\, m/kt^{1/3}$, and for Murzhik it is $\bar{r}_c = 14.6 \div 15\, m/kt^{1/3}$. For comparison between the field data with the laboratory experiments we will use simple empirical relationships 2.26 – 2.27 as well as a well-known Equation 1.5 for nuclear explosions conducted in hard rock, for which the cavity radii were not measured.

To calculate cavity radius Equation 1.5 can be rewritten as:

$$r_c = \frac{0.61 q^{1/3}}{\left(\rho\, C_p^2 \sigma_*^2\right)^{1/9}}.$$

It can be also rewritten using different units:

$$r_c = \frac{354.6 q^{1/3}}{\left(\rho\, C_p^2 \sigma_*^2\right)^{1/9}}. \tag{2.28}$$

where q is in kt, r_c is in meters, C_p is in m/s, σ_* is in kg/cm^2.

Equations 2.28 provide physically based relationships between the cavity sizes and physical properties of rocks. For hard rock the typical parameter values are ρ = 2.5 ÷ 2.7 g/cm^3, C_p = 3500 ÷ 6000 m/s, $\sigma_* = 50 \div 200\, MPa$ corresponding to the cavity radii in the range $\bar{r}_c = 8 \div 13\, m/kt^{1/3}$, which agrees with the measurements.

Equations 2.26 – 2.28 provides ways to control cavity radius calculations for different types of rocks. Comparison between these formulas shows that the parameter $\bar{r}_c$ has a clear physical meaning as a function of physical properties of rocks $\bar{r}_c = f(\rho, C_p, \sigma_*)$. Thus in order to determine a physical model of an excavation nuclear explosion it is possible to use cavity radius as a known (empirical) parameter, which takes into account a combination of individual physical properties of the emplacement medium.

The second parameter needed for comparison between the laboratory and the field experiments is the energy of gas in the cavity at the end stage of the cavity expansion. Energy of cavity gas is determined using the equation of state (EOS) for gas, which defines the relationships between gas pressure, density, temperature, and specific internal energy. These equations of state, which account for rock vaporization, melting and thermal decomposition, as well as dissociation and ionization at high temperatures, have been determined for silicate and carbonate rocks (Bobrovskii et al, 1976; Broud, 1975).

In order to calculate the EOS the following assumptions and approximations were used:

- Gas products of explosions contain silicon oxide and water vapor for silicate rocks, and calcium oxide (with added magnesium oxide in dolomite) and carbon dioxide for carbonate rocks.
- Energy concentration for nuclear explosions is high and the radius of the zone affected by a heat wave is 0.3 m/kt$^{1/3}$.
- Heat exchange between the cavity and the surrounding rock is neglected.
- The pressure is the same in the entire zone of gas production.

These relationships are usually called “effective adiabatic”. Figure 2.23a shows the pressure of cavity gas products as a function of cavity volume. Line 1 correspond to gas-free (dry, zero gas content) silicate rock (η = 0), including granite, alluvium and tuff. Lines 1a and 1b correspond to isothermal and isentropic approximation of the EOS for gas-free silicate rocks. The plot shows that at high pressure line 1 lies between lines 1a and 1b, while at lower pressure line 1 coincides with the isentropic approximation. Line 2 corresponds to silicate rocks containing 1% of water (by weight) with the initial density of 2.67 g/cm^3. Lines 3 – 6 correspond to adiabatic expansion for gas products of explosions for mixtures of quartz and water with weight moisture content of 2, 5, 10 and 20% respectively.

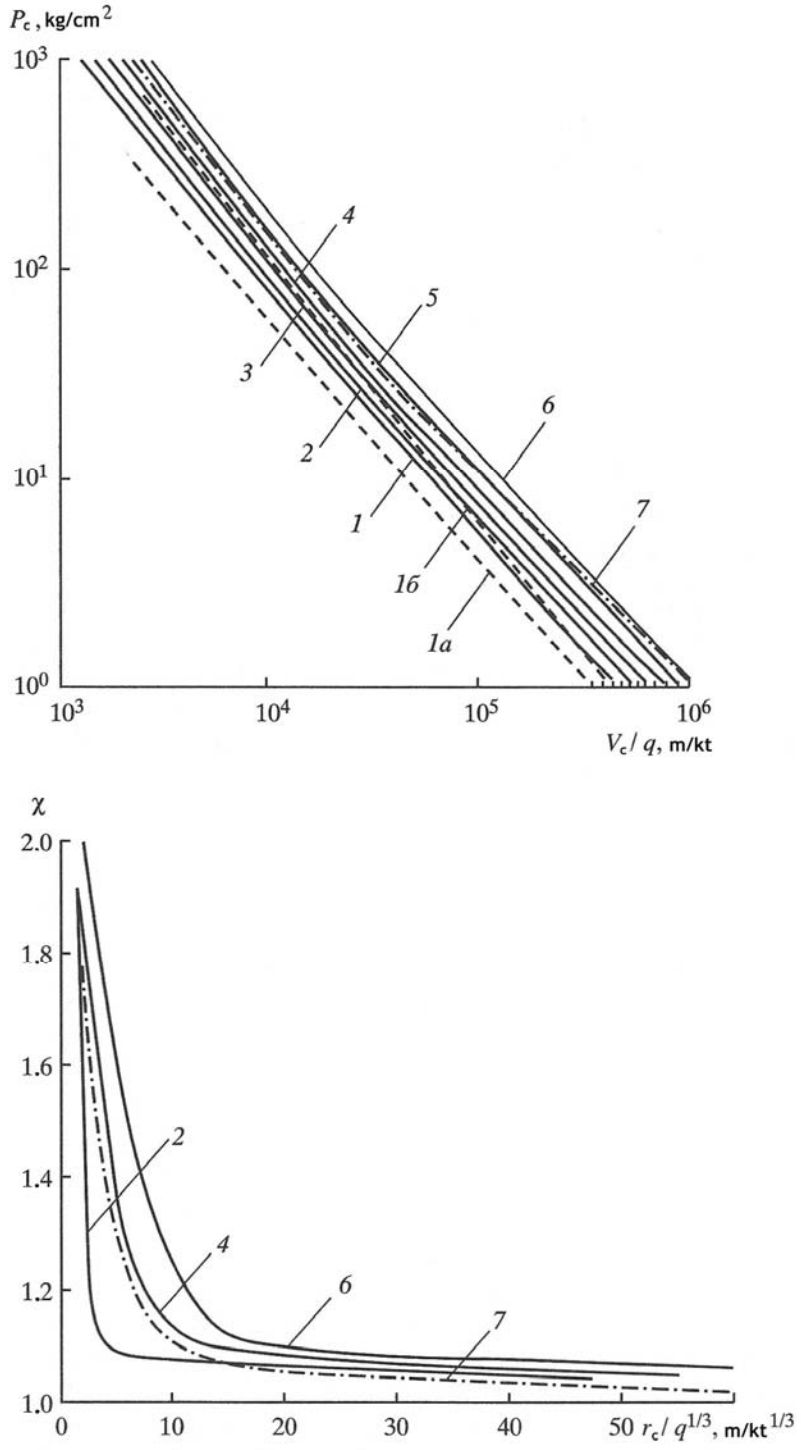

Figure 2.23. Changes in a) pressure and b) adiabatic exponent during cavity expansion caused by nuclear explosions in the following rock types (lines marked with numbers): *1* – gas-free rock, *1a* – isothermal approximation, *1b* – isentropic approximation, *3* – SiO_2 + 2% water, *4* – SiO_2 + 5% water, *3* – SiO_2 + 10% water, *3* – SiO_2 + 20% water, *7* – dolomite

Table 2.12. Pressure of explosion by-products in the cavity produced by nuclear explosions in silicate rocks for different values of strength σ_*, and moisture content ω

Rock type	σ_*, MPa	$r_c/q^{1/3}$, m/kt$^{1/3}$	Parameter					
			ω = 0	ω = 1%	ω = 2%	ω = 5%	ω = 10%	ω = 20%
Granite	200	8.8	36	42	52	60	70	82
“	140	9.5	26	31	37	42.5	47.5	55
“	70	11.1	14.5	17	20	22.5	24	29
Alluvium, tuff	-	15.0	5.2	5.8	6.6	7.2	8	11

Table 2.13. Pressure and temperature of explosion by-products in the cavity produced by nuclear explosions in dolomite of different strength

Rock type	Parameter			
	σ_*, MPa	$r_c/q^{1/3}$, m/kt$^{1/3}$	P_c, MPa	T_c, K
Dolomite	140	9.3	53	5200
“	70	11	27	4700

Table 2.14. Adiabatic exponent for gas by-products of nuclear explosions

Rock	Parameter	
	$B \cdot 10^{-6}$	χ
Gas-free	4.32	1.18
Granite	1.91	1.14
Shale	2.29	1.14
Calcite	5.73	1.22
Dolomite	1.48	1.03
In BH 101	1.19	1.02
In BH 1003	0.98	1.03

Carbonate rocks are represented in Figure 2.23a with the curve for the adiabatic expansion for dry dolomite ($CaMg(CO_3)_2$). Dry dolomite has gas content of 47% by weight due to release of carbon dioxide. To calculate energy of the cavity gas in addition to the provided adiabatic expression we used the equations of state for clay shale and calcite. In addition we considered two types of rocks with both water and carbon dioxide, in which the explosions were conducted in boreholes 1003 and 101 (Table 2.2). Effective adiabatic curves plotted in Figure 2.23a show

that gas content of rocks has significant effect on the pressure in the cavity. Table 2.12 shows the final pressures in the cavities for some silicate and carbonate rocks. Pressure and temperature of the gaseous products in the nuclear cavity in dolomite are shown in Table 2.13.

As shown in Table 2.12, increase in water content leads to increase in cavity pressure. Considering that the water content in hard (unfractured) granite is not very high (ω = 0÷5%), while the water content of tuff and alluvium can reach 10-20%, the range of the final pressure in the explosive cavity can be 10 – 40 MPa (highlighted with dashed lines in Table 2.12).The gas temperature in the cavity may vary between 3500 – 4700 K. Table 2.13 shows that a nuclear explosion in hard dolomite (σ^* = 140 MPa) may result in a pressure of 53 MPa and a temperature of 5200 K, while in less strong dolomite (σ^* = 70 MPa) the pressure and temperature would be 27 MPa and a temperature of 4700 K respectively. Tables 2.12 and 2.13 also show that the underground nuclear explosions are characterized by high pressures in the cavities at the end of the expansion, reaching several hundred atmospheres in hard crystalline rocks. Note that the final cavity size has a significant effect on cavity pressure: increase of the radius by 20-30% results in pressure decrease by a factor of 2-3.

At relatively low cavity pressures (less than 10 MPa) the adiabatic equations for the products of the nuclear explosions can be expressed as:

$$P = Bq^{\chi}/V_c \text{ (kg/cm}^2\text{)} \tag{2.29}$$

(where V_c is the cavity volume in m^3, q is yield in kt) with different values for the coefficient B and for different rock types (Table 2.14).

In reality the coefficients B and χ in (2.29) are not constants and they decrease with decreasing cavity pressure. For instance, the value of the exponent changes from χ = 1.3÷1.6 for pressures around 10^2 MPa, to χ = 1.02÷1.08 for pressures on the order of 1 – 10 MPa. The energy of the gas explosion products in the cavity is determined using the EOS given by:

$$E = \frac{PV_c}{\chi - 1};\ \chi = -\frac{d\ln P}{d\ln V};\ \text{S=const,} \tag{2.30}$$

by calculating the adiabatic exponent from the slope of the curves. Figure 2.23b shows the calculated values for the adiabatic exponents depending on the cavity radii for several rock types. There is a significant effect of the degree of expansion and the amount of the un-condensable gases in the rock on the adiabatic exponent. Thus, at early stages of expansion in rocks of all types the adiabatic exponent decreases from 1.8-2 to 1.1-1.2.

Further expansion of the cavity gas leads to the decrease of the adiabatic exponent to low values of 1.02 – 1.06 in rocks with low gas content (silicates and dry carbonates). In rocks with high water content the adiabatic exponent stays at higher values around 1.05 – 1.15. Using these values of adiabatic exponent in Equation 2.30 can lead to extremely high values of pressure. Therefore, for comparison between the laboratory and field experimental data, instead of Equation 2.30, we can use an expression for potential work of cavity gas. This expression describes gas expansion from pressure reached during the explosion to atmospheric pressure:

$$A = \int_P^{Pa} P(V)dV. \tag{2.29}$$

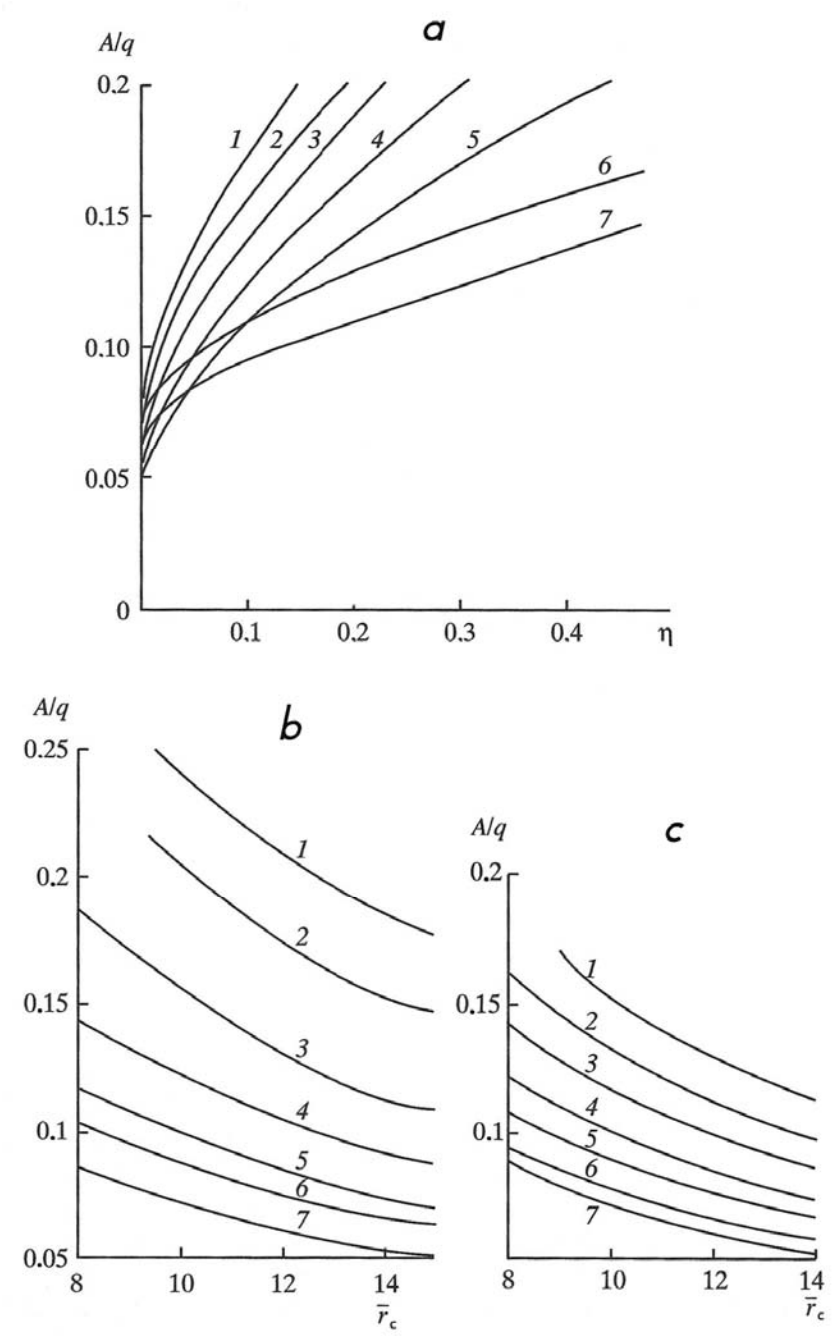

Figure 2.24. a) Potential work performed by gas by-products of underground nuclear explosions as a function of cavity size and gas content for silicate rocks. Lines *1 – 4* are for granite with the following values of $r_c/q^{1/3}$: *1* – 8.8 m/kt$^{1/3}$, *2* – 9.5 m/kt$^{1/3}$, *3* – 11.1 m/kt$^{1/3}$, *4* – 12.5 m/kt$^{1/3}$; lines: *5* – alluvium with $r_c/q^{1/3}$ = 15.0 m/kt$^{1/3}$, *6* – dolomite with $r_c/q^{1/3}$ = 9.3 m/kt$^{1/3}$ and *7* – dolomite with $r_c/q^{1/3}$ = 11 m/kt$^{1/3}$. b) Potential work performed by gas by-products of underground nuclear explosions as a function of cavity size and gas content for carbonate rocks for the following values of water-related gas content η_ω: *1* – 0.3, *2* – 0.2, *3* – 0.1, *4* – 0.05, *5* – 0.03, *6* – 0.01, *7* – 0. c) Potential work performed by gas by-products of underground nuclear explosions as a function of cavity size and gas content for carbonate rocks for the following values of CO_2 content η_{CO2}: *1* – 0.47, *2* – 0.3, *3* – 0.2, *4* – 0.1, *5* – 0.05, *6* – 0.01, *7* – 0.

Relationships between the work performed by cavity gas and the rock properties (e.g. elastic moduli, strength, gas content) were obtained using the results of integration for different adiabatic curves for the wide range of rock types. For example Figure 2.24a shows this relationship for the silicate rocks described in Table 2.12, for which gas content is represented only by free water (in which case $\eta = \eta_\omega$).

Figure 2.24b shows similar relationships for dry carbonate rocks, which produce carbon dioxide during explosions, for which $\eta = \eta_{CO2}$. As follows from Figure 2.24, work performed by gas depends not only on rock gas content, but also on strength and elastic moduli of rocks. In harder rocks the cavity sizes are smaller, resulting in higher pressure, greater work performed by gas, and higher increase in work due to increase in rock gas content. Using the results of these calculations it was found that potential work performed by cavity gas at the moment when the final [camouflet] cavity size is reached for gas-free rock ($\eta_\omega = \eta_{CO2} = 0$) is given by the formula:

$$\frac{A}{q} = \frac{0.49}{(\bar{r}_c)^{0.84}}, \tag{2.32}$$

where $\bar{r}_c$ is in m/kt$^{1/3}$.

For silicate rocks containing only free water the potential work as a function of cavity size and water content (by weight) is given by the expression:

$$\frac{A}{q} = \frac{0.49}{(\bar{r}_c)^{0.84}}(1 + 5.8\eta_\omega^{0.7}), \tag{2.33}$$

where $\bar{r}_c$ is in m/kt$^{1/3}$.

Equation 2.33 can be used for calculation of work performed by cavity gas during explosions in granite, quartzite, basalt, rhyolite, tuff, alluvium etc. For these rocks gas content is determined only by the presence of free water.

In order to determine the effect of gas content on the effective adiabatic expansion curve for carbonate rocks, we use the observation that the adiabatic curves for explosion gas products in dolomite with high gas content $\eta_{CO2} = 0.47$ are almost the same as the ones for silicate rocks with water content $\eta_\omega = 0.1$ (Figure 2.23a). This fact is explained by a high molecular weight of carbon dioxide ($\mu = 44$ g/mol), compared to the molecular weight of water vapor ($\mu = 18$ g/mol). In addition the temperature of carbon dioxide formation (due to rock chemical decomposition) is significantly higher than the temperature of water vaporization. According to this result, carbon dioxide is approximately 4.7 times less effective for performing the excavation work than the same amount (by weight) of water vapor. Replacing the gas content in Equation 2.33 according to $\eta_\omega = \eta_{CO2} / 4.7$ we obtain the relationship between the potential work and gas content for carbonate rocks:

$$\frac{A}{q} = \frac{0.49}{(\bar{r}_c)^{0.84}}(1 + 1.96\eta_{CO2}^{0.7}), \tag{2.34}$$

where $\bar{r}_c$ is in m/kt$^{1/3}$.

Equation 2.34 should be used for calculation of work produced by cavity gas for explosions conducted in dry dolomite, limestone, carbonate shale etc, where gas is only represented by carbon dioxide.

In some rocks gas produced during nuclear explosions includes both water vapor and carbon dioxide. In this case adiabatic expansion curves can be recalculated by introducing an effective gas content appropriately calibrated to water content:

$$\eta_e = \eta_\omega + \eta_{CO2} / 4.7 \tag{2.35}$$

The validity of this approach was confirmed, for instance, during calculations of the EOS for gas by-products generated by the nuclear explosions in BH 1001 and 1003. Introducing of the effective gas content (as in 2.35) and using Equation 2.33 we obtain the value of potential work of cavity gas for rocks with mixed gas content:

$$\frac{A}{q} = \frac{0.49}{(\bar{r}_c)^{0.84}}(1 + 5.8\eta_e^{0.7}), \tag{2.36}$$

where $\bar{r}_c$ is in m/kt$^{1/3}$.

Using the relationship $r_c = 0.62V_c^{1/3}$ we obtain a similar function of the cavity volume:

$$\frac{A}{q} = \frac{0.73}{(\bar{V}_c)^{0.28}}(1 + 5.8\eta_e^{0.7}), \tag{2.37}$$

where $\bar{r}_c$ is in m/kt$^{1/3}$.

Mixed gas content is common for various rocks at the Semipalatinsk Test Site and Novalya Zemlya, including argillites, aleurolites (both are commonly referred as shales in western publications), sandstones, porphyrites, conglomerates, slates etc.

Results of calculations of the equations of state for explosion gas products have demonstrated a significant effect of rock gas content on gas parameters. The higher the gas content is, the higher the pressure and the energy of the gas in the cavity for a given cavity size. The increase in cavity gas energy at the moment when it reaches its “camouflet” value, due to the increase in gas content, causes the increase in mechanical work produced by a nuclear explosion. The increase in mechanical work done by an explosion is related to an increase of non-condensable gas in the zones of vaporization, melting and thermal decomposition, and their release at the later stages of cavity development (from these zones).

Formation of non-condensable gas compensates in part for dissipated energy, and significantly increases the excavation efficiency of underground nuclear explosions.[8] In gas-free rocks the final cavity is filled only by products of rock evaporation. For these explosions the relationships between the volume, pressure and temperature are not very strong, therefore mechanical work performed by these gases during their expansion is small and energy dissipated in the surrounding rocks is not used to increase the mechanical work of excavation.

[8] Part of the energy converted into heat, and thus dissipated, comes back as additional pressure of heated gas.

Table 2.15. Parameters of the excavation nuclear explosions

Explosion #	Explosion	Rock type	Parameter						
			ρ_a, g/cm^3	q, kt	W, m	r_c, m/kt$^{1/3}$	W/r_c	A/q	$\bar{A}$
1	JANGLE-U	Alluvium	1.6	1.2	5.2	15	0.3	0.109	2145
2	TEAPOT-S	“	1.6	1.2	20.4	15	1.3	0.109	153.3
3	NEPTUNE	Tuff	2.0	0.115	30.5	15	4.2	0.129	3.20
4	DANNY BOY	Basalt	2.47	0.42	33.5	9.3	4.8	0.075	3.85
5	SEDAN	Alluvium	1.7	100	193	15	2.8	0.116	2.05
6	CABRIOLET	Rhyolite	2.5	2.3	52	11	3.5	0.081	4.03
7	SCHOONER	Tuff	1.74	31	108	15	2.3	0.096	4.28
8	BUGGY	Basalt	25	1.1 x 5	41.1	10.7	3.5	0.068	4.1
9	PALANQUIN	Rhyolite	2.5	4.3	85	11	4.7	0.081	1.1
10	SULKY	Basalt	2.5	0.09	27.4	10.5	5.8	0.068	1.61
11	BH 1003	Aleurolite	2.3	1.1	48	12.9	3.9	0.098	3.46
12	BH 1004	Sandstonne	2.56	140	175	12.1	2.7	0.171	4.37
13	BH T-1	Shale	2.4	0.24	31.4	11.8	4.1	0.117	4.52
14	BH T-3	Aleurolite	2.4	0.21 x 3	31.4	11.0	4.7	0.093	3.14
15	TAIGA	Sandy clay	2.1	15 x 3	127	17	3.1	0.159	1.7
16	BH 101	Sandstone	2.6	80	227	12	4.3	0.121	0.7
17	BH 125	Porphyrite	2.7	19	151.3	10	5.6	0.131	0.74

An increase in rock gas content causes an additional amount of gas released from heated rocks surrounding the cavity, which increases rock damage, excavation efficiency and seismic wave amplitudes. In order to improve excavation efficiency, utilization of the dissipated energy of an explosion is particularly important during the final stages of cavity expansion. The added energy due to formation of non-condensable gas can play a defining role in the development of the gas acceleration stage, and affects the values of optimal and maximal depth of burial.[9] The formation of non-condensable gas is also significant for the problems of gas migration through broken rock, and their escape into the atmosphere for fully-contained explosions.

Relationships 2.32 – 2.37 allow us to calculate the potential work of the cavity gas using known physical properties of rocks (their elastic parameters, strength and gas content), after the cavity reaches its "camouflet" value. These relationships together with formulas 2.26 –2.28 for the cavity radius are used in this work as initial parameter values for comparison between the full scale explosions and laboratory experiments. These parameters are also used for modeling, and thus for prediction, of the excavation efficiency of underground nuclear explosions.

Let us now compare crater sizes, ejection velocity and duration of the gas acceleration stage recorded for nuclear explosions with the corresponding laboratory measurements. In order to do this we need to replace the total energy released in the cavity (E) with the value of work (A):

$$\frac{A}{E} = 1 - \left(\frac{P_a}{P_c}\right)^{\frac{\chi-1}{\chi}};\ E = \frac{P_c V_c}{\chi-1};\ \ \chi = 1.4. \tag{2.38}$$

Now we can compare the crater sizes between the laboratory and full size scales using the coordinates

$$R/W = F\{\ \bar{A},\ W/r_c\ \},\ \bar{A} = A/[(\rho g W + P_a)W^3], \tag{2.39}$$

which is similar to Equation 2.16. The pressure of gas products during the final stages of cavity expansion for nuclear explosions in rocks of any types is two or three orders of magnitude higher than the atmospheric pressure. Therefore full-scale explosions have to be compared with the laboratory experiments with P_a/P = 0.005÷0.01 (in this case A/E = 0.73÷0.83). These results expressed in terms of the variable used in 2.39 are given by:

$$R/W = 0.\ 56 + 0.9 \lg(\bar{A}), \qquad H/W = 0.12 + 0.3 \lg(\bar{A}). \tag{2.40}$$

The dimensionless parameters of excavation explosions needed for comparison with the laboratory experiments are shown in Table 2.15. The parameters were determined using the physical properties of rocks and their gas content from Table 2.2.

The dimensionless parameter $\bar{A}$ depending on the lithostatic pressure was calculated using the average density of rock ρ_a between the charge and the surface (also shown in Table 2.15). Figure 2.25 shows the results of comparison between the crater dimensions for laboratory (shown with the solid lines) and full scale experiments. For most explosions crater radii agree

[9] Maximal depth is such that explosions below this depth will be contained rather than leading to material ejection/excavation.

with the relationship determined using laboratory results. Crater radii for explosions in basalt and for explosion TEAPOT-S are somewhat smaller than predicted (by 10 – 15%). Data points for PALANQUIN, BH 101 and 125 plot within the zone of partially contained explosions, which is marked with a vertical dashed line in Figure 2.25.

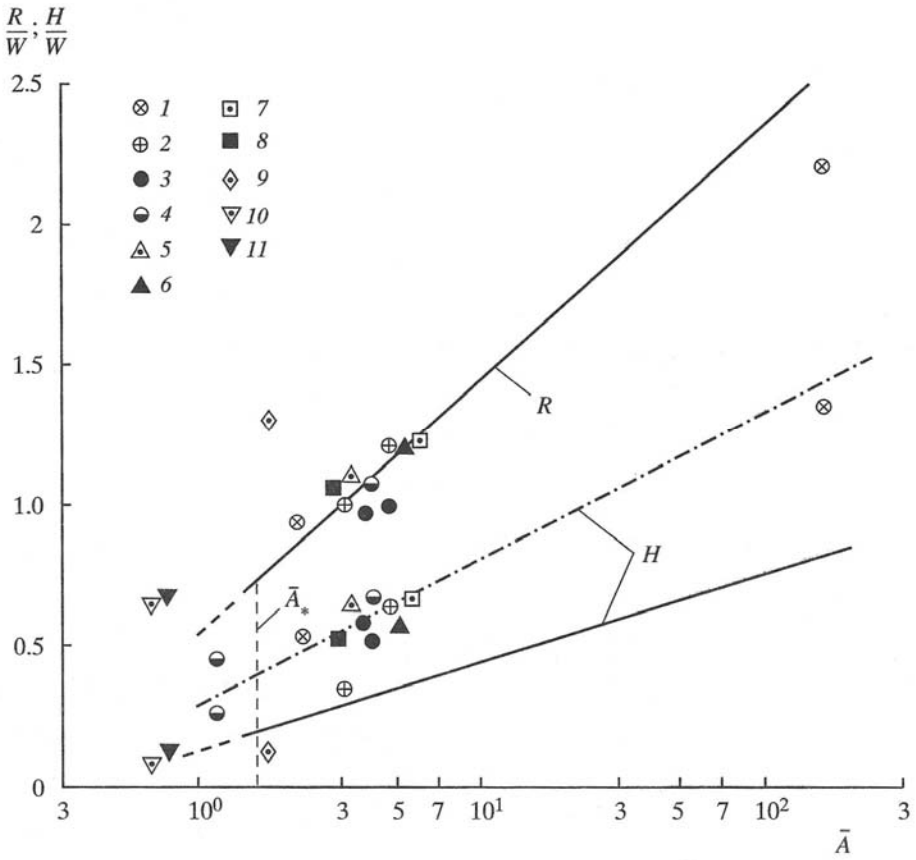

Figure 2.25. Comparison between the measured nuclear crater sizes and the model (shown with solid lines) for the following tests: *1* – SEDAN, TEAPOT-S, *2* – NEPTUNE, SCHOONER, *3* – DANNY BOY, BAGGY, *4* – CABRIOLET, PALANQUIN, *5* – BH 1003, *6* – BH 1004, *7* – BH T-1, *8* – BH T-2, *9* – Taiga, *10* – BH 101, *11* – BH 125

Crater radius produced by explosion Taiga is 70% larger than predicted by the model due to sliding of the slopes caused by soil liquefaction. Crater depths for the majority of nuclear explosions exceed the model predictions, possibly due to greater stability of the crater walls in the full scale experiments. The relationship between the crater depth, excavation parameter and the explosion depth for the laboratory experiments is given by $H = 0.3nW$, while for the full scale experiments this relationship is $H = 0.52nW$ (shown with dash-dot line in Figure 2.25).

To compare kinematic parameters between the full scale and laboratory experiments we use dimensionless parameters determined in 2.18, where E is replaced with A:

$$\bar{W}_A = \frac{W(\rho g W + P_a)^{1/3}}{A^{1/3}};\ \bar{v}_m = \frac{v_m}{(gW + P_a/\rho)^{1/2}};\ \bar{t}_m = \frac{t_m(gW + P_a/\rho)^{1/2}}{W}. \quad (2.41)$$

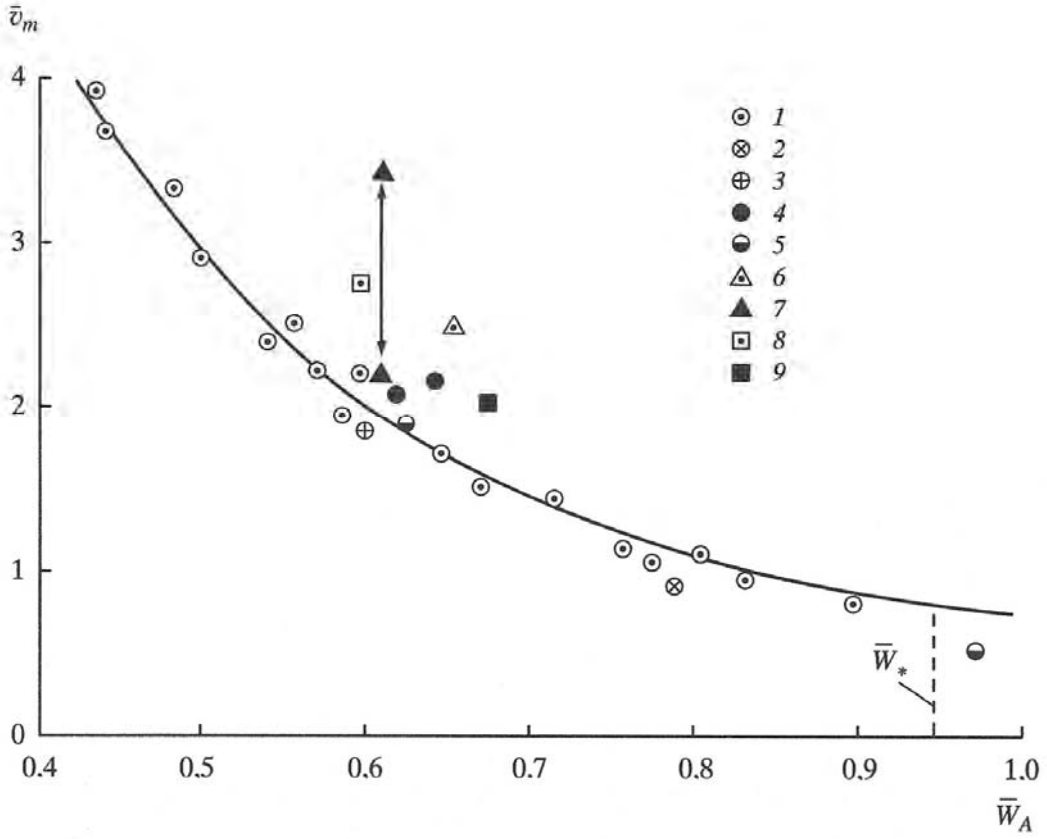

Figure 2.26. Comparison between the maximum ejection velocity for nuclear explosions with the model obtained using the laboratory experiments (shown with the solid line) [for the following tests]: 1 – laboratory experiments, *2* – SEDAN, *3* – SCHOONER, *4* – DANNY BOY, BAGGY, *5* – CABRIOLET, PALANQUIN, *6* – BH 1003, *7* – BH 1004, *8* – BH T-1, *9* – BH T-3

Figure 2.26 shows comparison for the maximum ejection velocity v_m. The solid line corresponds to the laboratory experiments relationships and given by:

$$\bar{v}_m = 0.75/\bar{W}^{1.9}. \quad (2.42)$$

Individual data points correspond to the maximum ejection velocity v_m for nuclear explosions from Table 2.5. Ejection velocities for alluvium, tuff and rhyolite agree with Equation 2.42. Ejection velocities for basalt and for Semipalatinsk rocks exceed the values predicted by 2.42 by 20 – 40%. The data point corresponding to the explosion in BH 1004 exceeds the model prediction by 60%. It is possible that high velocities can be explained by spallation in basalts and by a presence of thick clay near-surface layer near observed at the Semipalatinsk Test Site (at Balapan). With regard to the explosion in BH 1004 we note that if instead of the maximum

velocity of 140 m/s we use the cupola velocity before gas venting equal to 100 m/s, the value will agree with Equation 2.42 (the new point is shown with an arrow in Figure 2.26).

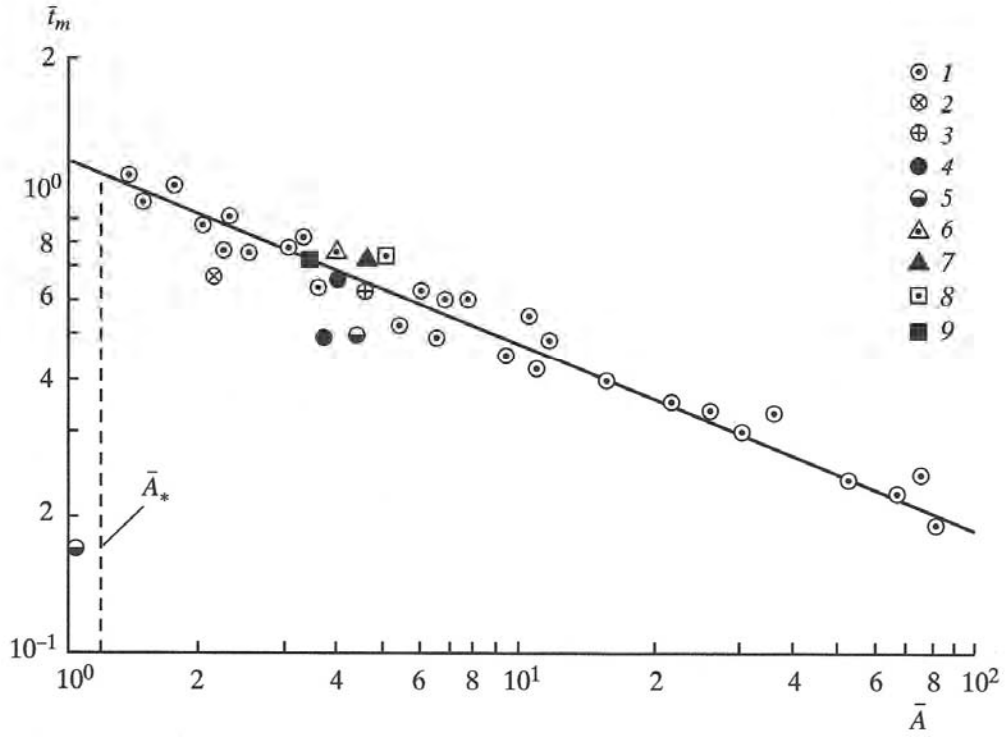

Figure 2.27. Comparison between the duration of the gas acceleration stage for excavation nuclear explosions with the laboratory experiments (model shown with the solid line) [for the following tests]: *1* – laboratory experiments, *2* – SEDAN, *3* – SCHOONER, *4* – DANNY BOY, BAGGY, *5* – CABRIOLET, PALANQUIN, *6* – BH 1003, *7* – BH 1004, *8* – BH T-1, *9* – BH T-3. [same as Figure 2.26]

Duration of the gas acceleration stage t_m corresponds to the time interval before the velocity reaches its maximum value. It nearly coincides with the time when the gas venting into atmosphere occurs (Table 2.5). Comparison of t_m between the model and the nuclear explosions is shown in Figure 2.27. Using the laboratory experiments the following empirical relationship was developed:

$$\bar{t}_m = 1.3/\bar{A}^{0.4}. \tag{2.43}$$

Data points for seven nuclear explosions agree with Equation 2.43 within the model measurement uncertainty (10 – 15%). Data points (time measurements) for DANNY BOY and CABRIOLET are 25 – 25% lower. The data for PALANQUIN is an order of magnitude lower than predicted. It is possible that the earlier gas venting for this experiment was caused by poor containment of the charge borehole.

In addition to comparison between the data and the modeling results using the general relationships, each explosion was modeled in the laboratory under similarity conditions for the following dimensionless parameters:

$$\bar{A} = const, \frac{W}{r_c} = const, \frac{P_c}{P_a} = const. \quad (2.44)$$

Dry sand was used as the experimental material, so we neglect its cohesion. Experimental measurements included final crater dimensions and kinematic parameters of the cupola development. The results of measurements for ejection parameter as well as the parameters of the models for some nuclear explosions are summarized in Table 2.16.

The scaling factor of the model varies in the range M = 1/300÷1/2200. Comparison between the ejection coefficient obtained during laboratory experiments n_m and the coefficient for the full scale explosions n_f shows that individual modeling (in which scaling was done for each explosion) improved the similarity between the laboratory and full scale experiments (the differences do not exceed 5 – 10% around the optimal depth).

Thus the laboratory experiments conducted with weak material cohesion and lowered atmospheric pressure provide adequate agreement with the measurements for nuclear explosions with yields ranging between 0.1 and 100 kt. These results demonstrate that gravity plays significant role in this yield range.

Table 2.16. Results of the analog experiments modeling the excavation nuclear explosions

Explosion	Parameter					
	W_m, cm	W_m / r_c	$\bar{A}$	P_c / P_a	n_m	n_f
TEAPOT-S	4.2	1.3	153.3	80	2.46	2.2
NEPTUNE	8.4	4.2	3.2	100	1.05	1.0
DANNY BOY	9.6	4.8	3.85	280	1.14	0.97
SEDAN	9.0	2.8	2.05	100	0.9	0.95
CABRIOLET	11.3	3.5	4.03	180	1.03	1.06
SCHOONER	10.5	2.3	4.28	90	1.27	1.2
PALANQUIN	15.0	4.7	1.1	180	0.56	0.43
BH 1003	7.8	3.9	3.46	150	1.12	1.1
BH 1004	8.1	2.7	4.37	160	1.2	1.18
BH T-1	10.5	4.1	4.52	190	1.15	1.19

2.3. The effect of explosion yield on the crater sizes of excavation explosions

Comparison between the laboratory experiments with full scale nuclear explosion have shown that the relationship (Equation 2.40) between the crater radius and the work performed by cavity gas given by $R = W$ (0. 56 + 0.9 log ($\bar{A}$)) can be used for practical calculations. In order to do that we express work performed by an explosion using the total energy (yield) $A = \xi q$ and transform Equation 2.40 by dividing both sides by $q^{1/3}$:

$$\frac{R}{q^{1/3}} = 0.9\frac{W}{q^{1/3}}\lg\frac{4.2\xi q}{(\rho g W + P_a)W^3}. \tag{2.45}$$

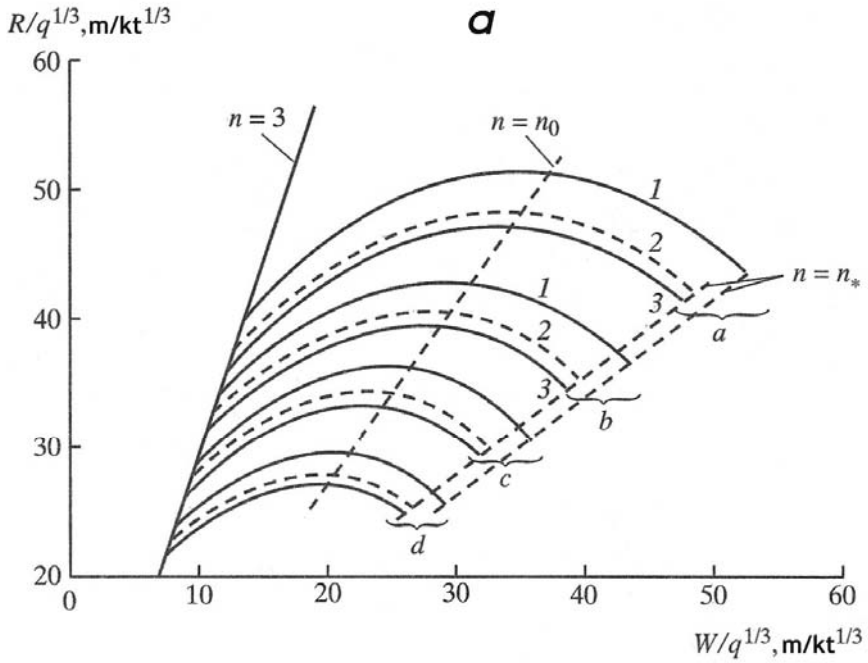

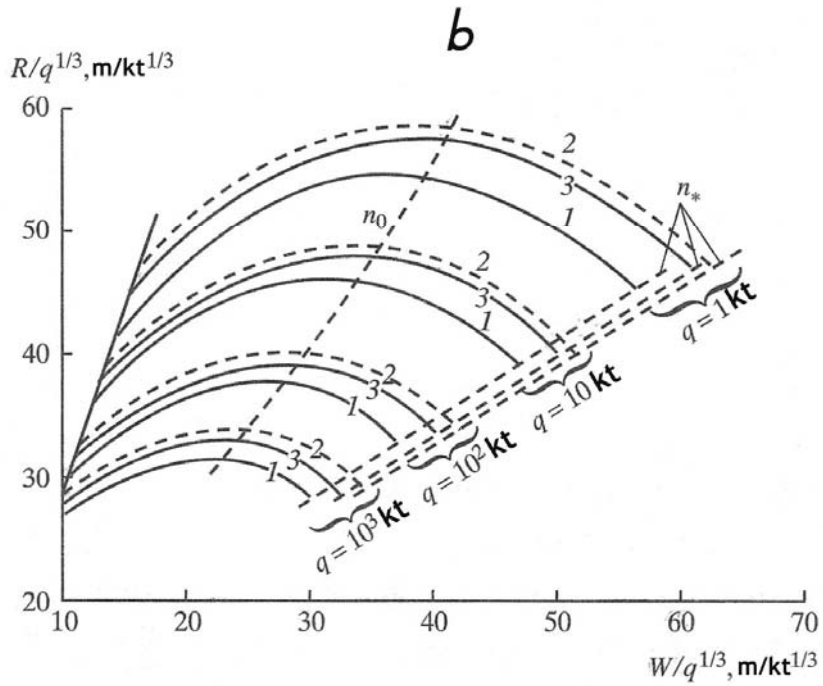

Figure 2.28. a) Crater radius as a function of depth of burial and energy (yield) of explosion for silicate rocks. The numbered lines correspond to rocks with following properties: *1* – $r_c/q^{1/3}$ = 8.8 m/kt$^{1/3}$, η = 0.01; *2* – $r_c/q^{1/3}$ = 8.8 m/kt$^{1/3}$, η = 0; *3* – $r_c/q^{1/3}$ = 12.5 m/kt$^{1/3}$, η = 0.01. b) Crater radius as a function of depth of burial and energy (yield) of explosion for carbonate rocks. The numbered lines correspond to rocks with following properties: *1* – $r_c/q^{1/3}$ = 11.1 m/kt$^{1/3}$, η = 0.12; *2* – $r_c/q^{1/3}$ = 11.1 m/kt$^{1/3}$, η = 0.24; *3* – limestone, η = 0.44

The efficiency coefficient ξ depends on the specific conditions for each explosion, in particular on the cavity size and rock gas content according to Equations 2.32 – 2.36. In physical terms the parameter ξ determines the part of the total energy of explosion contained in the explosive cavity during the final stages of its expansion, which is used to perform mechanical work of excavation. The cavity size depends on rock elastic moduli and strength according to 2.28. Therefore the efficiency coefficient is a function of the following parameters $\xi = \xi(\rho, C_p, \sigma_*, \eta)$. After substituting the expression for the efficiency coefficient $\xi = A/q$ from Equation 2.36 into Equation 2.45 and using the expression of the volume weight of rock $\gamma = \rho g$ we obtain an expression that can be used for calculation of the crater radius as a function of depth and the major rock properties:

$$\frac{R}{q^{1/3}} = 0.9\frac{W}{q^{1/3}}\lg\frac{8.8\cdot10^8(1+5.8\eta_e^{0.7})}{(\bar{r}_c)^{0.84}(\gamma W+10)(W/q^{1/3})^3}, \tag{2.46}$$

where q is in kt, W is in meters, $\bar{r}_c$ is in m/kt$^{1/3}$, γ[10] is in g/cm^3, η_e is the weight fraction of the effective gas content according to 2.35. The value of γ in 2.46 represents the average volume weight for the entire rock column above the charge:

$$\gamma = \sum_i \gamma_i W_i \,/\, \sum_i W_i \,, \tag{2.47}$$

where γ_i and W_i are the volume weight and thickness of individual layers of rock with distinct properties. As follows from the experimental data (Table 2.1) crater depth and the volume are related with its radius via the relationships:

$$H = (0.52 \pm 0.06)R;\ V = (1.45 \pm 0.15)R^2H. \tag{2.48}$$

Equations 2.46 and 2.48 determine the major parameters for craters formed by nuclear explosions in the wide range of hard and less hard rocks, with the exception of water-saturated clay-rich sands and high-plasticity rocks such as clays. Thus Equations 2.46 and 2.48 are valid in the limited range of the excavation parameter $0.7 \le n \le 3$.

The effect of the explosion yield, rock properties and gas content on the crater dimensions was investigated using Equation 2.46 for granite, alluvium, and hard rock with mixed gas content (including water and carbon dioxide).

[10] If $\gamma = \rho g$, then why is it in g/cm^3? (Note from the translators)

Figure 2.28a shows a plot of crater radii as a function of the depth of burial (using scaled variables) for nuclear charges in granite (ρ = 2.67 g/cm^3, C_p = 5200 m/s, η_ω = 0.01) for two values of strength σ_*=2000 kg/cm^2 (r_c = 8.8 m/kt$^{1/3}$) and σ_*=700 kg/cm^2 (r_c = 12.5 m/kt$^{1/3}$). Crater sizes for dry granite with r_c = 8.8 m/kt$^{1/3}$ are shown with a dashed line. Addition of 1% of water to hard granite increases the maximum crater size by 8 – 12% if other parameters stay the same. Reduction in strength causes the decrease of the crater radius due to an increase in the cavity size and corresponding reduction in the cavity pressure and gas energy.

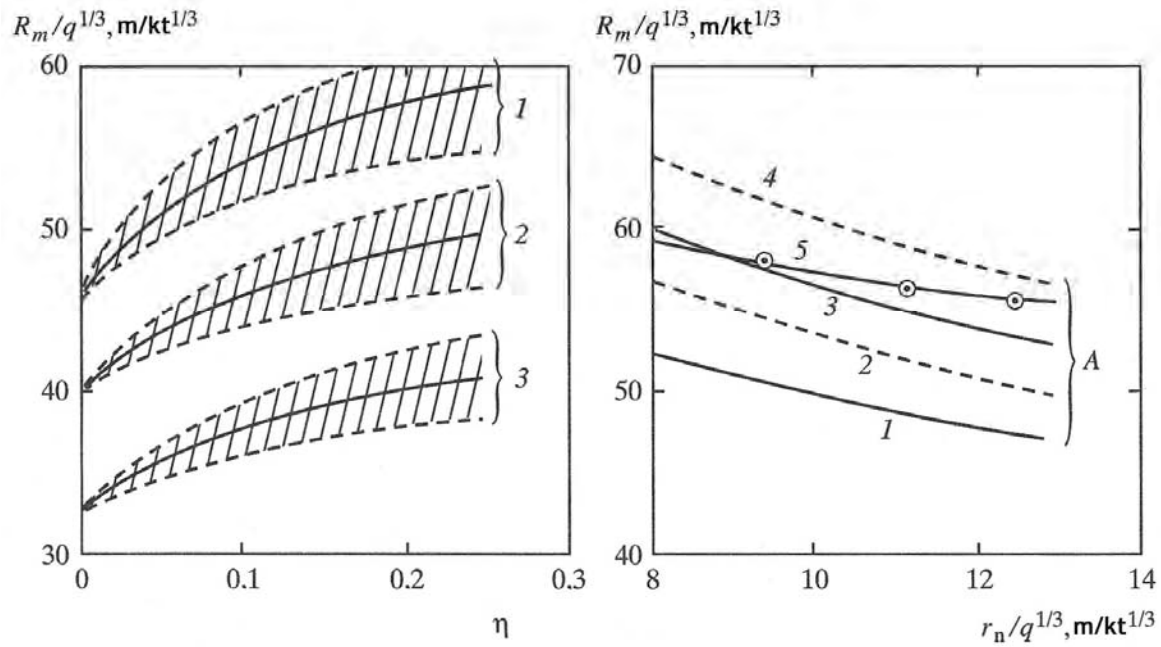

Figure 2.29. Effect of a) rock gas content and b) cavity radius on crater size produced by an explosion at an optimal depth for the following rock types: *1* – granite, η = 0.01; *2–4* – Semipalatinsk Test Site rocks: *2* – η = 0.06; *3* – η = 0.12; *4* – η = 0.24; *5* – limestone, η = 0.44

Figure 2.28b shows crater radius as a function of the depth of burial and yield of nuclear charges conducted in rocks with mixed gas content, which is common, for example, for the Semipalatinsk Test Site. The rock at the working point has the following properties: ρ = 2.5 g/cm^3, C_p = 5200 m/s, σ_*=700 kg/cm^2 (r_c = 11.1 m/kt$^{1/3}$). Gas content is represented by two values η = 0.12 and 0.24 (in this case $\eta_\omega = \eta_{CO2}$). The crater sizes for dry limestone (ρ = 2.75 g/cm^3, C_p = 5700 m/s, σ_*=1400 kg/cm^2, r_c = 9.3 m/kt$^{1/3}$), η_{CO2} = 0.44) are also shown. As it turns out, the crater radius for limestone is somewhat lower than for the rock with mixed gas content with η = 0.24, despite higher gas content and reduced cavity radius for limestone. This result shows that not only the value of gas content, but also its nature affects crater sizes. It also confirms lower excavation efficiency of carbon dioxide in comparison with water vapor.

The effect of the ratio between the main gas components for mixed gas content on the maximum crater size formed by explosions at the optimal depth of burial is shown in Figure

2.29a. The range of change for the crater radius with changing gas components (between water vapor and carbon dioxide) is shown as shaded region[s]. The effect of the ratio becomes more significant with the increase of the total gas content. Thus for the total gas content η = 0.24 transition from carbon dioxide to water vapor results in an increase in the cavity radius by 20%.

The effect of rock properties (elastic moduli and strength) on the crater size can be conveniently demonstrated as a function of the cavity radius. This relationship for the maximum crater radius created by 1 kt charge at the optimal depth of burial is shown in Figure 2.29b.Cavity radius changes only due to variation of rock strength. In this case the crater radius depends on the cavity radius as $R_m \sim \bar{r}_c^{0.23}$. In real conditions [for real rocks] strength reduction is accompanied by reduction in density and seismic velocity. In these circumstances the effect of cavity radius on the crater size is less pronounced. This situation is illustrated in Figure 2.29 b using an example of limestone (line *5*). The three dots shown in the figure indicate the crater radii for the following properties:

1. ρ = 2.75 g/cm^3, C_p = 5700 m/s, σ_*=1400 kg/cm^2, $\bar{r}_c$ = 9.3 m/kt$^{1/3}$;
2. ρ = 2.5 g/cm^3, C_p = 5200 m/s, σ_*=700 kg/cm^2, $\bar{r}_c$ = 11.1 m/kt$^{1/3}$;
3. ρ = 2.2 g/cm^3, C_p = 3500 m/s, σ_*=700 kg/cm^2, $\bar{r}_c$ = 12.4 m/kt$^{1/3}$.

Thus the cavity size, as an integral characteristic accounting for elastic properties and strength of rocks, affects the crater size.

The relationships between the crater radius and the depth of burial are shown in Figures 2.28 and 2.29 using similarity coordinates. The relationships show that the increase in the explosion yield narrows the range of scaled depths for which the ejection/excavation occurs. It also causes the decrease in the scaled crater radius and the optimal depth of burial. Optimal explosion conditions are marked with dashed lines $n = n_0$, which corresponds to the value of the excavation coefficient n_0 = 1.3÷1.4. In addition there is a tendency in reduction of the parameter n_0 with the increase of the explosion yield. For explosions conducted at the maximally possible for excavation depth the crater radius decreases. For these explosions the excavation parameter is denoted as $n = n_*$, which depends on the rock type and the explosion yield and ranges $n_* = 0.7 \div 0.9$.

2.4. Effect of rock gas content on the excavation efficiency of explosions

In order to determine the explosion yield as a function of depth and excavation parameter we rewrite Equation 2.45 in the form:

$$q = 0.238 \frac{(\rho g W + P_a) W^3}{\xi} \cdot 10^{n/0.9}. \qquad (2.49)$$

For practical calculations we transform Equation 2.49 by replacing the expression for excavation parameter $\xi = A/q$ from Equation 2.36 and using the expression of the volume weight of rock $\gamma = \rho g$ defined in Equation 2.47:

$$q = 1.14 \cdot 10^{-9} \frac{(\gamma W + P_a)W^3}{1+5.8\eta_e^{0.7}} \cdot 10^{n/0.9}. \quad (2.49)$$

where q is in kt, W is in meters, $\bar{r}_c$ is in m/kt$^{1/3}$, γ is in g/cm^3, η_e is the effective gas content.

Equations 2.49 – 2.50 determine the nuclear yield as a function of depth of burial, excavation parameter, rock gas content and the cavity radius, which in turn is a function of elastic properties and strength of rocks. The structure of Equations 2.49 – 2.50 reflects the fact known from the theory of geometrical similarity. According to that theory the energy of the excavation charge is proportional to the cube of the depth of burial for small scale explosions, for which the effect of gravity can be neglected, and proportional to the forth power of the depth of burial for the large scale explosions. The effect of the explosion yield on the relationship between the crater size and the depth of burial can be analyzed using the coordinates of "gravitational similarity" by dividing both sides of Equation 2.45 by $q^{1/4}$:

$$\frac{R}{q^{1/4}} = 0.9 \frac{W}{q^{1/4}} \lg \frac{4.2\xi q}{(\rho g + P_a/W)(W/q^{1/4})^4}. \quad (2.51)$$

If $\rho g W \gg P_a$ we obtain an asymptotic formula:

$$\frac{R}{q^{1/4}} = 0.9 \frac{W}{q^{1/4}} \lg \frac{4.2\xi q}{\rho g (W/q^{1/4})^4}. \quad (2.52)$$

Numerical calculations show that the differences between the crater radius estimates from Equation 2.51 and 2.52 are approximately 20% for $q = 10^{-1}$ kt, approximately 10% for $q = 1$ kt, less than 5% for $q = 10$ kt, and become virtually identical for $q \geq 10^2$ kt. If we limit the accuracy to 5%, than the asymptotic formula 2.52 can be used starting from $q \geq 10$ kt. This would simplify yield estimate using Equation 2.50:

$$q = \frac{1.14 \cdot 10^{-9} \gamma W^4}{1+5.8\eta_e^{0.7}} \cdot 10^{n/0.9}. \quad (2.53)$$

Table 2.17. The value of equivalent yield for full scale explosions

Explosion #	Explosion	Rock type	Parameter			
			q, kt	η	η_e	q_e, kt
1	JANGLE-U	Alluvium	1.2	0.1	0.1	2.6
2	TEAPOT-S	"	1.2	0.1	0.1	2.6
3	NEPTUNE	Tuff	0.115	0.153	0.153	0.29
4	DANNY BOY	Basalt	0.42	0	0	0.42
5	SEDAN	Alluvium	100	0.12	0.12	231
6	CABRIOLET	Rhyolite	2.3	0.01	0.01	2.8
7	SCHOONER	Tuff	31	0.07	0.07	58.9
8	BUGGY	Basalt	1.1 x 5	0	0	1.1 x 5
9	PALANQUIN	Rhyolite	4.3	0.01	0.01	5.3

10	SULKY	Basalt	0.08	0	0	0.08
11	BH 1003	Aleurolite	1.1	0.054	0.05	1.9
12	BH 1004	Sandstonne	140	0.21	0.194	398
13	BH T-1	Shale	0.24	0.128	0.07	0.46
14	BH T-3	Aleurolite	0.21 x 3	0.04	0.024	0.3 x 3
15	Taiga	Sandy clay	15 x 3	0.3	0.3	52.5 x 3
16	BH 101	Sandstone	80	0.128	0.081	160
17	BH 125	Porphyrite	19	0.12	0.065	35.3

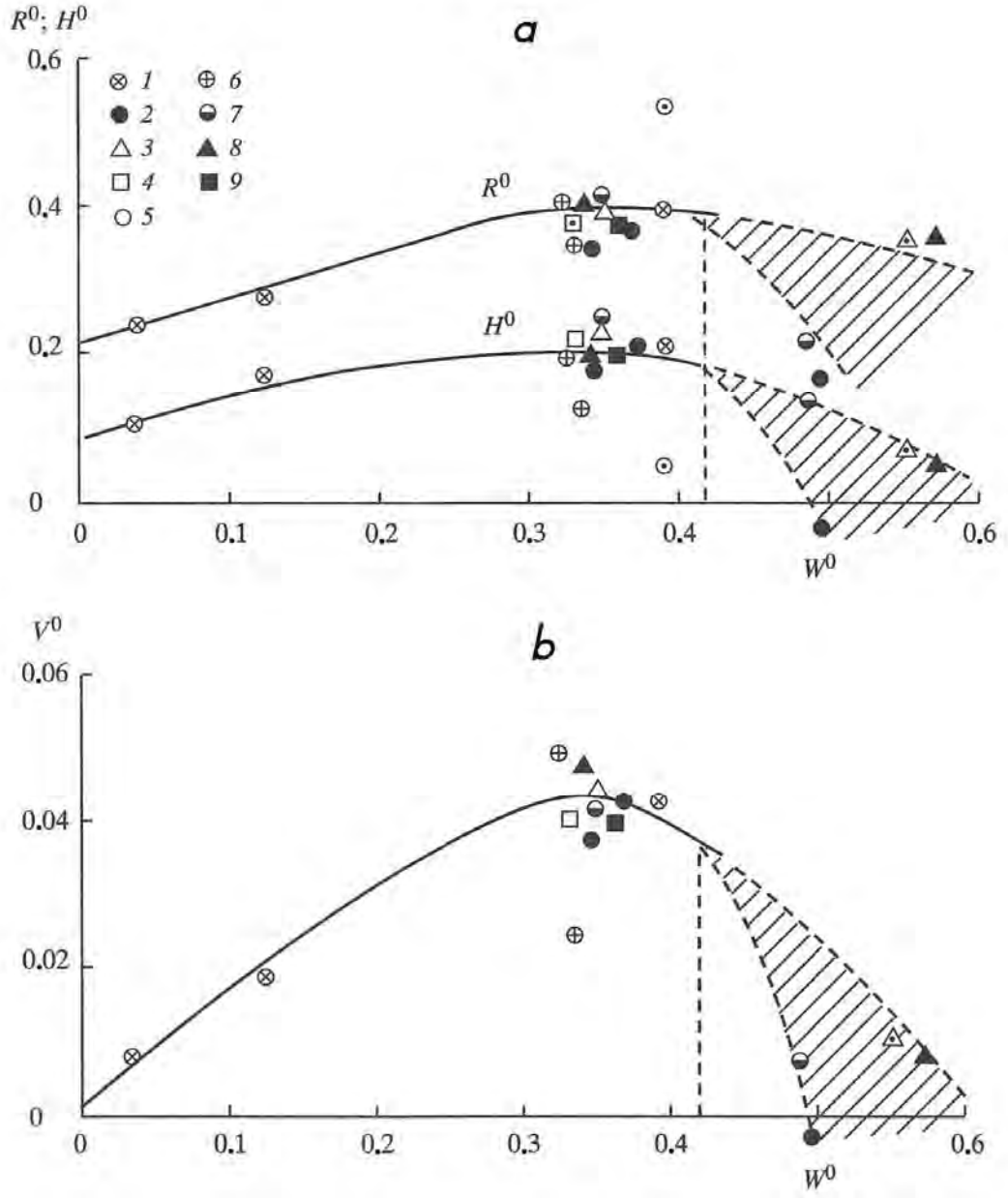

Figure 2.30. a) Crater radius and depth and b) crater volume as a function of depth of burial and yield of explosion plotted in scaled coordinates. The symbols correspond to: *1* – alluvium, *2* – basalt, *3* –

conditions in BH 1003 and 125, *4* – BH T-1, *5* – Taiga, *6* – tuff, *7* – rhyolite, *8* – BH 1004 and 101, *9* – BH T-1

Using the above analysis of the effect of the explosion yield and rock gas content on excavation efficiency we can summarize the experimental data for excavation explosions. The crater dimensions can be expressed in terms of the emplacement geometry and rock properties in the form:

$$R^0 = f_1(W^0),\ H^0 = f_2(W^0),\ V^0 = f_3(W^0), \tag{2.54}$$

where

$$W^0 = \frac{W}{(q_e/rg)^{1/4}};\ R^0 = \frac{R}{(q_e/rg)^{1/4}};\ H^0 = \frac{H}{(q_e/rg)^{1/4}};\ V^0 = \frac{V}{(q_e/rg)^{3/4}}.$$

The parameter q_e is an equivalent explosion energy, which depends on rock gas content:

$$q_e = q(1 + 5.8\eta_e^{0.7}). \tag{2.54}$$

The values of the equivalent charges (yields) are provided in Table 2.17. The crater sizes using the scaled variables from 2.54 are shown in Figure 2.30.

The majority of the data points are concentrated along the curves, including those with significantly different densities (e.g. alluvium and basalt) and gas content (e.g. sandstone and rhyolite). The point corresponding to explosion Taiga represents an outlier due to sliding of the water saturated crater slope. Crater dimensions for explosion NEPTUNE are lower than expected, in particular the depth and the volume, which can be explained by a collapse of the upper rim of the crater formed on the side of the mountain sloping at 30°. Explosions PALANQUIN, SULKY, BH 101 and 125 also show significant scatter. However based on their emplacement conditions these explosions belong to partially confined explosion type (shaded area in Figure 2.30) rather than the excavation type. Analysis of the data (for the crater parameters in variables 2.54) the optimal W_{opt}, maximal W_* depth of burial as well as the maximum crater dimensions can be described using the relationships:

$$W_{opt}^0 = 0.33;\ W_*^0 = 0.42;\ R_m^0 = 0.39;\ H_m^0 = 0.195;\ V_m^0 = 4.3 \cdot 10^{-2},$$

leading to the formulas:

$$W_{opt} = 47\gamma^{-1/4}[q(1 + 5.8\eta_e^{0.7})]^{1/4}\ ;\ W_* = 60\gamma^{-1/4}[q(1 + 5.8\eta_e^{0.7})]^{1/4}\ ; \tag{2.56}$$

$$R_m = 56\gamma^{-1/4}[q(1 + 5.8\eta_e^{0.7})]^{1/4}\ ;\ H_m = 28\gamma^{-1/4}[q(1 + 5.8\eta_e^{0.7})]^{1/4}\ ;$$

$$W_m = 12.7 \cdot 10^4\gamma^{-3/4}[q(1 + 5.8\eta_e^{0.7})]^{3/4}\ ,$$

where q is in kt, γ is in g/cm^3, W, R_m, H_m are in m[eters], η_e is the effective gas content. However Equations 2.54 – 2.56 do not take into account strength and elastic properties of the emplacement media. Therefore for explosions conducted in arbitrary media it is advisable to calculate crater parameters using Equations 2.45 – 2.50.

2.5. Optimal and the maximum depth for excavation explosions

Optimal and maximal depth of excavation explosions is of particular interest for the purposes of peaceful use of nuclear explosions. Explosions conducted at the optimal depth create craters with the largest possible volumes, while explosions with the maximal possible depth of burial for excavation explosions still create sufficiently large craters and minimize the radioactive pollution. In order to determine relationships between the optimal depth of explosion and the explosion yield, rock elastic moduli, strength and gas content we use the observation that craters with the largest volume correspond to explosions with the excavation parameter n_0 = 1.3÷1.35 (Figure 2.28). Then it follows from Equation 2.40 that the conditions for the optimal excavation correspond to the value of energy parameter $\bar{A}_{opt} = 7.2$. We express the work of the cavity gas using the explosion energy $A = \xi q$ to obtain the relationship between the optimal depth and the explosion yield:

$$(\rho g W_{opt} + P_a) W_{opt}^3 = 0.139 \xi q \, . \tag{2.57}$$

Substituting the expression for the excavation efficiency parameter $\xi = A/q$ from Equation 2.36 and using the expression for the average weight of rock above the charge $\gamma = \rho g$ we obtain the expression for the optimal depth as a function of the charge yield, gas content and the cavity size in a form convenient for calculations:

$$(\gamma W_{opt} + 10) W_{opt}^3 = 2.9 \cdot 10^7 \frac{q(1+5.8\eta_e^{0.7})}{(\bar{r}_c)^{0.84}}. \tag{2.58}$$

where q is in kt, W_{opt} is in meters, $\bar{r}_c$ is in m/kt$^{1/3}$, γ is in g/cm3, η_e is the effective gas content].

The optimal depth of burial of nuclear explosion is defined here using the criterion of the maximum radius of the resulting crater, although strictly speaking the largest volume in full scale experiments id observed at somewhat smaller depth of burial (by approximately 10%) due to an increase in the crater depth. Gas content of the emplacement rock has the strongest effect on the value of the optimal depth in the range of lower values of gas content up to 5 – 10%. For rocks with mixed gas content the optimal depth of burial also depends on the ratio between gas components (water vapor and carbon dioxide) increasing with the increase of water content.

In case $\rho g W_{opt} \gg P_a$, Equation 2.57 can be simplified:

$$W_{opt} = 73.4 \frac{[q(1+5.8\eta_e^{0.7})]^{0.25}}{\gamma^{0.25}(\bar{r}_c)^{0.21}} \, , \tag{2.59}$$

which corresponds to Equation 2.56 for the optimal depth of burial with $\bar{r}_c = 8.8$ m/kt$^{1/3}$,

To determine the maximum depth of burial resulting in an ejection crater we use Equation 2.20 and replace gas energy with the value of work performed by gas (Equation 2.38) to obtain an expression:

$$\bar{A}_* = 4.34 \left(\frac{r_c}{W_*}\right)^{0.6}, \tag{2.60}$$

where W_* is the maximum depth of burial that can still produce an ejection crater. Substituting the expressions $A = \xi q$ and $r_c = \bar{r}_c q^{1/3}$ into (2.60) we obtain the relationship between the maximum depth and the energy (yield) for an excavation nuclear explosion:

$$(\rho g W_* + P_a) W_*^{2.4} = 0.23 \frac{\xi q^{0.8}}{(\bar{r}_c)^{0.6}}. \quad (2.61)$$

Using Equation 2.36 and including the average weight above the charge given by 2.47 we obtain the final expression for maximum depth of burial for the excavation nuclear explosion as a function of yield, gas content and the (camouflet) cavity size:

$$(\gamma W_* + 10) W_*^{2.4} = 4.9 \cdot 10^7 \frac{(1+5.8\eta_e^{0.7}) q^{0.8}}{(\bar{r}_c)^{1.44}}. \quad (2.62)$$

where q is in kt, W_{opt} is in m[eters], $\bar{r}_c$ is in m/kt$^{1/3}$, γ is in g/cm^3, η_e is the effective gas content.

The effect of yield of explosion and rock gas content on the maximum depth of burial (resulting in excavation explosion) is similar to the effect of these factors on the optimal depth of the excavationexplosion. For $\rho g W_* \gg P_a$ Equation 2.62 can be simplified:

$$\frac{W_*}{q^{1/3}} = \frac{182}{q^{0.1}} \left[\frac{(1+5.8\eta_e^{0.7})}{\gamma (\bar{r}_c)^{1.44}} \right]^{0.294}. \quad (2.63)$$

In this case it follows from Equation 2.60 that to satisfy excavation conditions the amount of energy released by a nuclear explosion divided by the work against gravity has to satisfy the relationship $\xi q / \rho g W_*^4 \gg 1.6$ (for a typical value of $\frac{W_*}{r_c} = 5$). Using these relationships it is also possible to determine the maximal depth of burial for excavation explosions conducted in rocks with known properties.

Using the results of this section we note another issue of interest due to a treaty limiting the yield of the nuclear tests at $q \leq 150$ kt. Limiting the depth of burial $W/q^{1/3} \geq a$ simultaneously implies yield limitation. Thus, for explosion with yield of 100 kt the limiting depth of burial (if excavation is the intended use, off course) is $W/q^{1/3} \geq 35 \div 40$ m/kt$^{1/3}$. Therefore limiting depth of burial by a value of $W/q^{1/3} \geq 40$ m/kt$^{1/3}$ allows detonation of charges no larger than 100 kt and still producing ejection craters.

2.6. Velocity of the ejected material and gas venting times

Crater formation due to underground explosion is characterized by the initial and maximal velocities of ejecta. Initial velocity is determined by the elastic properties and strength of rocks at the reflecting surface. For explosions in hard rock the particle velocity at the surface is described by the relationship $v_i = 2v_0$, while for loose sediments such as sand the relationship becomes $v_i = v_0$. Wave reflection results in spallation; therefore the initial velocity is sometimes called spallation velocity. Empirical formula 1.8 shows that the initial velocity does not depend on the explosion yield and satisfy conditions of geometrical similarity.

Subsequent change of the ejection velocity is determined by the stage of gas acceleration. At the end of this stage the ejection velocity can exceed the initial velocity, and is therefore called the maximum velocity. To calculate the maximum velocity of material ejection during nuclear explosions we use equation 2.42 which was determined using laboratory experiments. After substitution of the expressions for the dimensionless parameters (Equation 2.41) and the relationship between the work done by gas and the explosion yield $A = \xi q$ we obtain:

$$\frac{v_m}{(gW + P_a/\rho)^{1/2}} = 0.75 \left[\frac{(\rho g W + P_a)^{1/3} W}{(\xi q)^{1/3}}\right]^{-1.9}. \quad (2.64)$$

After replacing the efficiency coefficient $A = \xi q$ from Equation 2.36 substituting $\gamma = \rho g$ from Equation 2.47 we obtain:

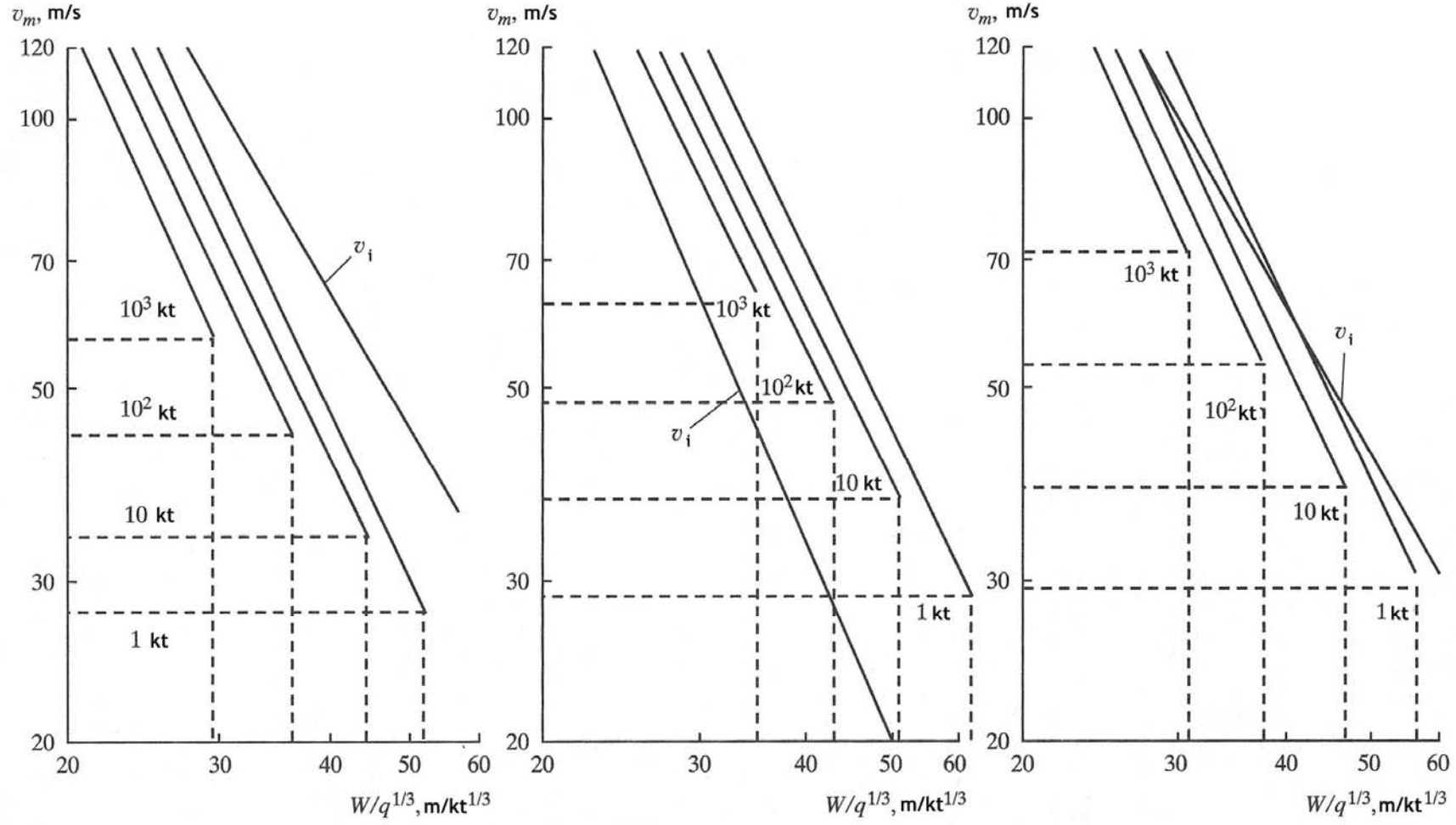

Figure 2.31. Effect of yield on the maximal v_m and initial v_i ejection velocities for nuclear explosions conducted in a) granite, b) alluvium, and c) carbonate rock.

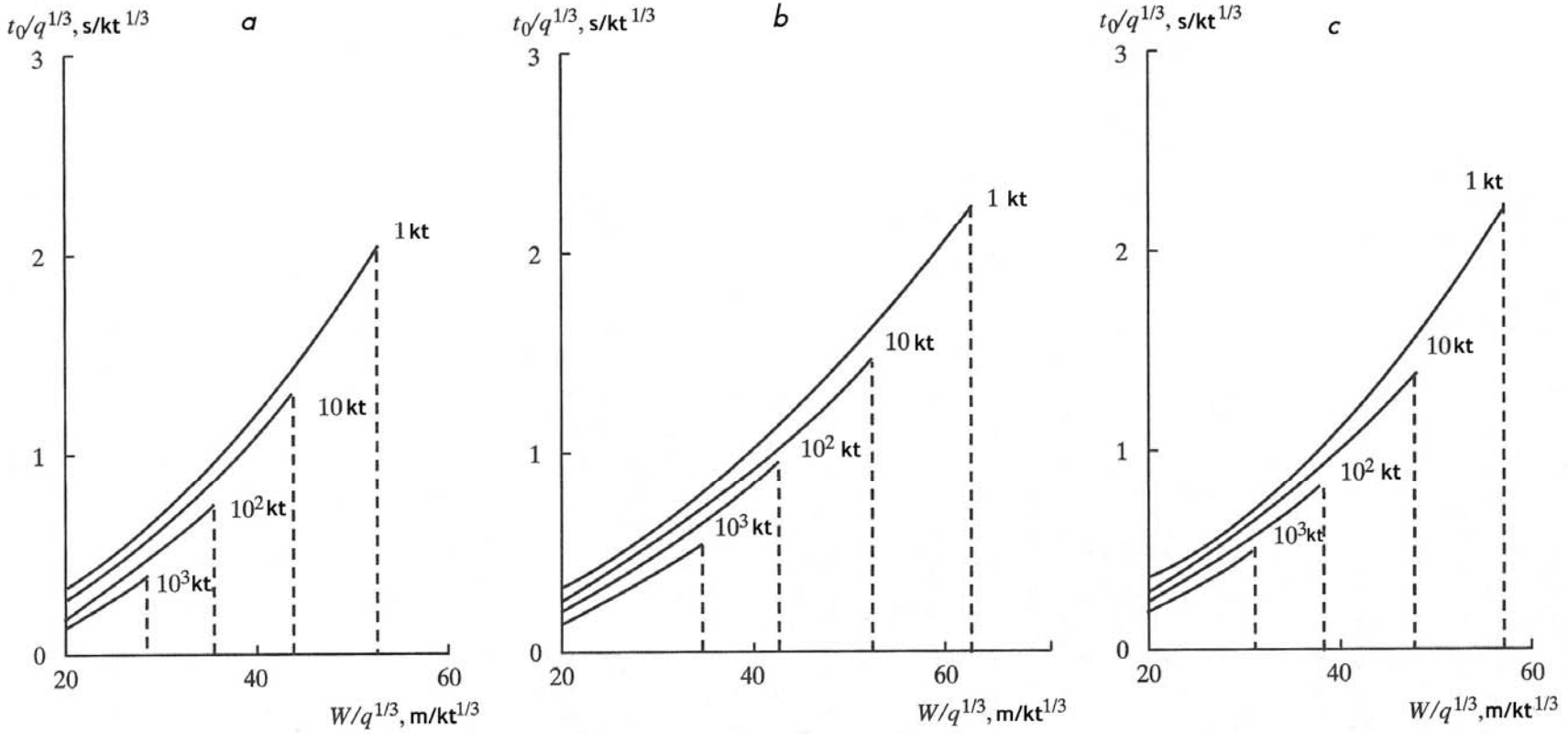

Figure 2.32. Effect of the nuclear yield on gas venting times for nuclear excavation explosions conducted in a) granite, b) alluvium, and c) carbonate rock

$$v_m = \frac{4.4 \cdot 10^5 (1+5.8\eta_e^{0.7})^{0.63}}{\gamma^{0.5}(\gamma W + 10)(\bar{r}_c)^{0.53}} \left(\frac{W}{q^{1/3}}\right)^{1.9}, \quad (2.65)$$

where q is in kt, W is in meters, $\bar{r}_c$ is in m/kt$^{1/3}$, γ is in g/cm^3, η_e is the effective gas content.

It follows from the structure of Equations 2.64 – 2.65 that the ejection velocity at the end stage of gas acceleration depends not only on scaled depth of burial, but also on the explosion yield, average density of rocks in the ejection column (above the charge), rock gas content and the cavity size. Effect of the explosion yield is illustrated in Figure 2.31 using examples of granite (ρ = 2.67 g/cm^3, $\bar{r}_c = 8.8\ m/kt^{1/3}$, η_e = 0.01), alluvium (ρ = 1.6 g/cm^3, $\bar{r}_c = 15\ m/kt^{1/3}$, η_ω = 0.12), and rock with mixed gas content (ρ = 2.5 g/cm^3, $\bar{r}_c = 11.1\ m/kt^{1/3}$, η_ω = 0.12, $\eta_\omega = \eta_{CO2}$).

For all rock types the increase in the explosion scale resulted in decrease of ejection velocity expressed in scaled coordinates (decrease by 20 – 30% corresponds to the increase in yield from 1 to 100 kt). Also due to a decrease in maximum depth of burial (vertical dashed lines in Figure 2.31) the minimum ejection velocity grows (for instance the velocity grows from 25 – 30 m/s for 1 kt to 45 – 50 m/s for 10^2 kt).

Figure 2.31 also shows the relationships for the initial velocities. As it turns out, the relationships between the initial velocity and the ejection velocity at the end of the gas acceleration stage depends only on the rock type. Thus for explosions in granite and basalt the initial velocity is always higher than the ejection velocity at the end stage of gas acceleration. Therefore it is expected that during explosions in hard rock with low gas content the maximum acceleration is reached during the spall motion, which masks the gas acceleration stage.

The gas acceleration stage becomes more pronounced with the increase of the explosion yield. For explosions in alluvium of any yield the velocity of the cupola at the end stage of gas acceleration is always higher than the initial velocity. Laboratory data agree with this conclusion. For explosions in hard rock with high gas content (e.g. emplacement rock for borehole explosions at the Semipalatinsk Test Site) the initial velocity was approximately equal to the velocity at the end of gas acceleration stage. Similar observations were made during excavation explosions in BH 1003 and T-1.

It also follows from Equation 2.65 that an increase in moisture content without changing the mechanical properties of rocks results in an intense increase in ejection velocity (in these circumstances when the water content in granite is about 10% the velocity of ejection at the end stage of gas acceleration may exceed the initial velocity). Increase in moisture content accompanied by a decrease in rock strength and elastic moduli results in less intense increase in ejection velocity. Increase in the cavity radius with fixed moisture content causes decrease in ejection velocity. For excavation explosions detonated in rocks with mixed moisture content the ratio between the main gas components plays an important role, with an increase in ejection velocity when the portion of water vapors increases for the same value of the gas content.

The time at which venting of cavity gas into atmosphere occurs is an important characteristic determining the radiation situation after the explosion. Based on the experimental results for the

excavation explosions we assume that the venting time t_0 coincides with the time of the gas acceleration action t_m (Table 2.5). Therefore to analyze the effect of different parameters of explosions and the rock properties on the gas venting time we use Equation 2.43 with substitution of the dimensionless parameters 2.41 and the relationship between the work performed by cavity gas $A = \xi q$:

$$\frac{t_o(gW + P_a/\rho)^{1/2}}{W} = 1.2\left[\frac{(\rho gW + P_a)W}{\xi q}\right]^{0.4}. \quad (2.66)$$

After replacing the efficiency coefficient $A = \xi q$ from Equation 2.36 substituting $\gamma = \rho g$ from Equation 2.47 we obtain:

$$\frac{t_0}{q^{1/3}} = \frac{1.8\cdot 10^{-4}\gamma^{0.5}(\bar{r}_c)^{0.34}}{(1+5.8\eta_e^{0.7})^{0.4}(\gamma W + 10)^{0.1}}\left(\frac{W}{q^{1/3}}\right)^{2.2}, \quad (2.65)$$

where q is in kt, W is in meters, $\bar{r}_c$ is in m/kt$^{1/3}$, γ is in g/cm^3, η_e is the effective gas content.

It follows from Equation 2.67 that venting time does not satisfy the geometrical similarity criteria and depends on the explosions yield, gas content of the emplacement rocks, average density above the charge and the cavity size. The effect of yield on venting time is shown in figure 2.32 for the same rock types for which the velocity if ejection were calculated. Vertical dashed lines show the maximum possible depth of burial.

An increase in yield results in decrease in the venting time in coordinates of geometrical similarity (15 – 20% decrease for the yield increase from 1 to 10^2 kt). Increase in rock moisture content also results in the decrease in venting times. However the effect of moisture content is weak: increase in water content by an order of magnitude results in the decrease in venting time by 25 – 30%. The effects of the cavity radius and the ratio between different gas components are also weak. The major role for the venting time is played by the scaled depth of burial and the explosion yield. Placing the charge in the interval between the optimal and the maximal depths of burial the venting of gas into atmosphere will occur in 1 – 2 s for 1 kt explosion, 1.5 – 2.5 s for 10 kt explosion, and 2.5 – 3.5 s for 100 kt explosion.

Chapter 3.

Formation of explosive (subsidence) craters and mounds/retarcs

An increase in the scaled DOB of the explosive charge leads to reducing the cratering action of the explosion. Instead of cratering explosions they become partially contained explosions. Further increase in scaled depth of burial (sDOB) results in fully contained (camouflet) explosions.

Partially contained explosions create mounds (sometimes called retarcs) at the surface due to increase in volume of rock due to damage and moving it toward the free surface[1]. Gas venting occurs in the middle of the mound, and a crater forms either due to rock ejection or due to subsidence. Retarc formation is particularly pronounced for small scale explosions in hard rocks.

Fully contained (camouflet) explosions may produce subsidence craters mostly due to collapse of broken rocks into the cavity. In hard rock dilating during explosions subsidence crater is formed in the epicentral part of the uplift. This scenario is characteristic for the UNTs conducted in boreholes at Balapan Testing Area at Semipalatinsk Test Site. In porous rocks, such as alluvium at Nevada Test Site, the uplift was almost absent, while the subsidence craters were forming (Figure 3.1; e.g. Houser, 1969).

Explosion yield and scaled depth of burial, as well as physical properties of rocks, significantly affect the final results of the partially contained and fully contained explosion. Thus, change in yield from 0.1 t to 1-10 kt for an explosion in alluvium increased range of sDOB from 100 m/kt$^{1/3}$ to 200 m/kt$^{1/3}$ for which the subsidence craters were still forming (Nordyke, 1962). Therefore increase in yield by four-five orders of magnitude the height of the chimney in alluvium increases from 3 – 4 to 12 – 14 cavity radii.

For explosions in tuff a quantitative increase in yield resulted in qualitative differences at the free surface. For 0.1 t explosions between 65 and 160 m/kt$^{1/3}$ only retarcs were formed. Increase in yield to 10 – 100 kt resulted in formation of subsidence craters (Johnson and Higgins, 1965). For example, nuclear tests BLANCA, HOOSIC, DISCUS, and BILBY detonated with sDOB between 90 – 130 m/kt$^{1/3}$ (or approximately 6 – 10 cavity radii) resulted in formation of subsidence crater (e.g. Johnson and Higgins, 1965). Tests SULKY and PALANQUIN provide characteristic examples of the effect of the explosion scale and gas-forming properties of the emplacement medium. Both explosions were expected to create mounds (retarcs) on the free surface. However the results were significantly different: SULKY formed a retarc, while PALANQUIN formed a crater (Toman, 1970).

An increase in sDOB reduces the uplift, and subsidence (collapse into the cavity) becomes the major effect on the surface. Height of the chimney and formation of a subsidence crater

[1] The word “retarc is “crater spelled backwards.

significantly depend on the yield of the explosion. For small yields a dome or a cupola[2] of considerable size can form above the cavity. The cavity collapse can be delayed indefinitely.

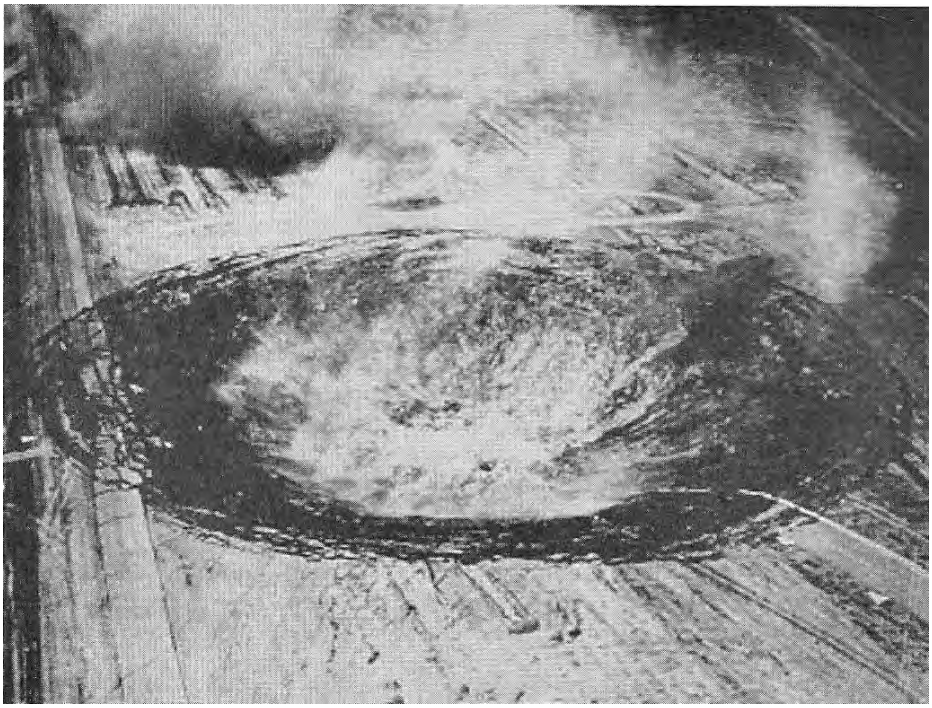

Figure 3.1. A photograph of a subsidence crater left by one of the nuclear explosions at the Nevada Test Site (USA)

For instance, explosions with yields on the order of 1 kt in hard (crystalline) rocks chimney height can reach 3 – 5 times the cavity radius, therefore the subsidence craters are not formed. Under these circumstances formation of the subsidence crater is a random process depending on the rock strength and geological structure (degree and direction of fracturing, tectonic structure, block size etc). However, with an increase in yield subsidence craters begin to form even in crystalline rocks. This happened for megaton class events in horizontal adits at Novaya Zemlya, as well as in crystalline rocks at Amchitka Test Site (Data …, 1972).

Thus the final stages of partially and fully contained nuclear explosions are affected by two opposing processes: uplift of the rock in the epicentral area and collapse of the broken rocks into the cavity, which often ends in formation of a crater. Developed analog laboratory model does not reproduce retarc formation due to the absence of a pressure wave. Therefore the retarc and crater formation were studied separately. First the models were used to study craters, later the method to calculate retarc formation was developed taking into account shear deformation and dilation of rock.

As a result of this approach the following was found:

[2] As noted in Chapter 2, "cupola" is the Russian word referring to a dome of uplifted material that grows and sometimes blows up and disperses, as in ejection explosions.

- Conditions leading to retarc formation and relationships between their sizes and their depth and yield, scale of the explosion and rock properties;
- Physically justified boundary between partially contained and fully contained explosions;
- Characteristics of gas venting into atmosphere.

3.1.Results from observations of partially contained nuclear explosions

Experiments with partially contained explosions are very limited compared to the number of fully contained explosions. One of the best-studied partially contained explosions is experimental-industrial explosion “Krystall” conducted on October 2, 1974 at the “Udachnyi” diamond mine. This experiment was conducted in order to build a dam to store rock left after diamond mining. A nuclear charge with yield of 1.7 kt was placed at a depth of 98 m in limestone frozen due to permafrost. Based on drilling data the density of the limestone increased with depth as indicated in Table 3.1.

Table 3.1. Rock properties based on drilling data for experiment “Krystall”

Paramater	Parameter value						
Depth, m	0 – 5	5 – 10	10 – 20	20 – 40	40 – 60	60 – 80	80 – 100
Density, g/cm^3	1.46	1.72	1.94	2.25	2.23	2.33	2.52

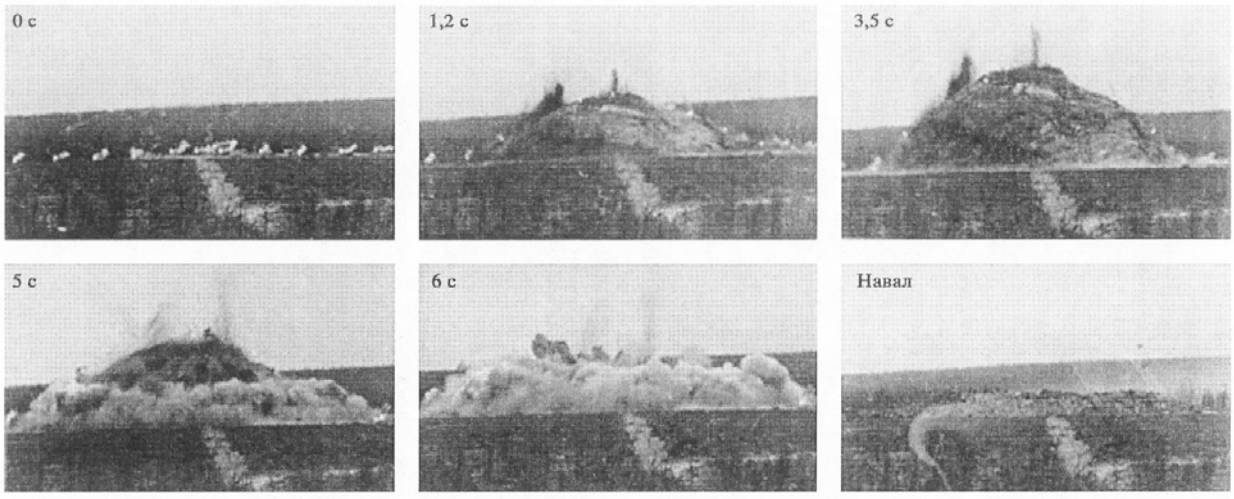

Figure 3.2: Time frames showing development of a cupola for explosion “Krystall”. Also shown time from detonation in seconds.

The properties of limestone at the shot depth were: density – 2.48 · 10^3 kg/m^3, porosity – 7.8%, P-wave velocity – 3500 m/s, gas content – 43% (with water content of 0.8 – 1%). The

average density between the surface and the working point was $2.22 \cdot 10^3$ kg/m^3. A series of movie snapshots depicting explosion evolution is shown in Figure 3.2. Initial surface velocity at the epicenter V_h was 34 m/s. Later the velocity was following the ballistic law of motion $V(t) = V_h - gt$, which suggests that there was no (upward) acceleration of the dome due to gas escape. After 3.5 s the dome reached its maximum height of 57 – 60 m (approximately $0.6W$). After 6 s after the explosion when the top of the dome was at 30 m, the gas venting occurred. Gas velocity was 50 m/s, and the cloud rose to 70-80 m. Lowering of the dome occurred without lateral movement of debris. Figure 3.3 shows the vertical slice through the retarc (mound). The slope of a free surface in the epicentral area was 6. After the explosion the volume of the retarc was $1.6 \cdot 10^5$ m^3 with the average height of 10 m and diameter at the base of 200 m.

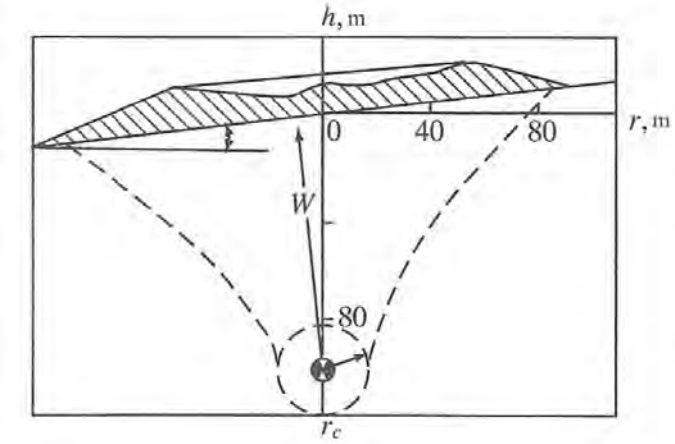

Figure 3.3: Crossection through the mound/retarc for explosion “Krystall”

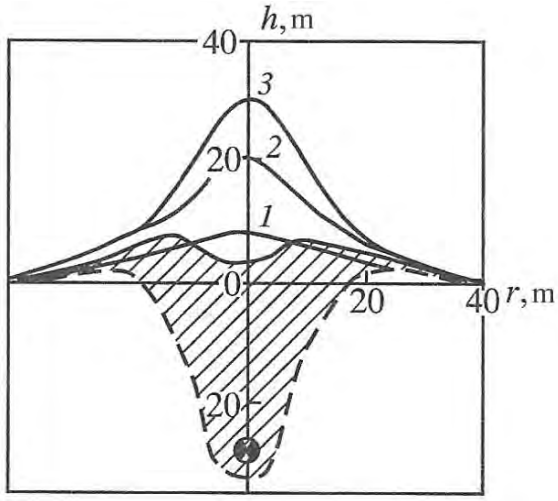

Figure 3.4: Time evolution (lines 1 – 3) and the vertical crossection of the mound/retarc created by explosion SULKY. The time from the detonation: *1* – 0.4 s, *2* – 1 s, and *3* – 2 s.

Table 3.2. Initial ground velocities within the uplift for explosion SULKY for Stations 1 – 11

Parameter	Parameter value										
	1	2	3	4	5	6	7	8	9	10	11
R_e, m	22.8	8.3	13.7	9.15	4.6	0	4.6	9.35	13.7	18.3	22.8
v_i, m/s	5.7	8.5	14.6	19.9	20.6	26.1	23.8	14.4	10.1	7.3	5.7

A subsidence crater was formed at the top of the mound with diameter of 100 m, depth of 5 m, and volume of 10^4 m^3. In the middle of the crater a pile of debris with the height of 3 m was formed due to gas venting.

A similar scenario of retarc formation was registered during SULKY (yield 0.9 kt, *DOB* 27.4 m) conducted on December 18, 1964 (Toman, 1970). The test was conducted in basalts of the Buckboard Mesa at Nevada Test Site. A vertical crossection with dome evolution is shown in Figure 3.4. Initial ground velocity was determined at time 0.18 s after the explosion using laser distance meter located on both sides of the epicenter (Table 3.2).

The ground velocity didn′t increase after that, and 2.7 s later the dome reached its highest point of 35 m, about 1.3 times the depth of burial (W). Therefore there was no gas pressure effect on the dome uplift[3] evolution. A mound/retarc was formed after the dome collapsed (from falling rocks). The maximum height of the mound was 7 m, with average height 6.3 m. The diameter of the uplifted area was 90 m, while the diameter of the rock pile was 70 m. The total volume of the mound was $8.8 \cdot 10^3$ m^3. A collapse (subsidence) crater was formed at the top of the mound with diameter 19.6 m and depth 3.5 m. After the explosion the basalt remained dry, indicating that there was no gas venting. Radioactivity was detected in the atmosphere after 100 s.

The experimental nuclear explosion “Lazurit” was conducted on December 7 of 1974 in order to create a dam in a valley at the Semipalatinsk Test Site. The explosion was detonated at the base of a mountain sloping at 20°. Nuclear charge with yield of 1.7 kt was placed in fractured quartzite at a depth of 75 m (the minimum distance to the surface was W = 70 m). Quartzite rock at the shot depth had the following physical properties: density – $2.63 \cdot 10^3$ kg/m^3, porosity – 2.7%, P-wave velocity – 4650 m/s, S-wave velocity – 2300 m/s (Poisson coefficient 0.23), compressive strength – 199 MPa, tensile strength – 50 MPa, gas content – 2.61% with water content of 0.06%. The contours showing the uplift evolution are shown in Figure 3.5. The initial velocity of the uplift in the epicenter was 21 m/s. After 1.5 s dome reached its maximum height of 26 m ($\approx 0.4W$) with linear extent along the mountain slope of about 190 m. The height of the uplift exceeded the height predicted using ballistic equation by 15%.

This means that gas pressure affected the dome formation, which can be determined from the material acceleration. Gas venting occurred at the spall surface of the exploded mass from the base of the massif two seconds after the explosion. Venting was accompanied by a bright explosion with diameter of approximately 7 m. A gas cloud formed by this explosion was moving with a wind velocity of 3 – 5 m and after 30 – 40 s reached its maximum height of 300 m. This explosion crated a rock pile with a volume of $1.3 \cdot 10^5$ m^3 and the dominant fragment sizes on the order of 10-20 cm. The largest distance the pile spread toward water flow was 50 m, while the average distance of the rock pile (from the epicenter) was 30 – 35 m. The height of the rock pile at the base of the slope of the mountain was 15 m, the length along the slope was 175 m, and the width was 200 m (shown with a line with dashes in Figure 3.5).

Another experimental nuclear explosion was detonated at Semipalatinsk test site in borehole 125 on November 4, 1970. The test was conducted for the purposes of study of the nuclear explosion excavation efficiency for depths larger than optimal. The explosion with the yield of 19 kt was conducted at depth of 151.3 m in porphyrite massif. The rock at the charge depth had

[3] The underlying concept here, appears to be that excess cavity pressure propels the rock, so there is not a simple ballistic motion of the fragments. Additional gas pressure pushes the fragments faster than the initial particle velocity motion in the gravity field.

the following properties: density – 2.75 · 10^3 kg/m^3, porosity – 2.7%, P-wave velocity – 4930 m/s, S-wave velocity – 2640 m/s, compressive strength – 112.4 MPa, tensile strength – 10.5 MPa, gas content – 11 – 14 % with water content of 0.8%. Porphyrite massive was covered with gravel and clay sediments with thickness of 10 – 27 m and the average density of 2.0 · 10^3 kg/m^3. Contours showing the uplift evolution and the vertical slice through the crater are shown in Figure 3.6. Using the laser distance meter the initial vertical velocity was determined for different distances from the epicenter (Table 3.3).

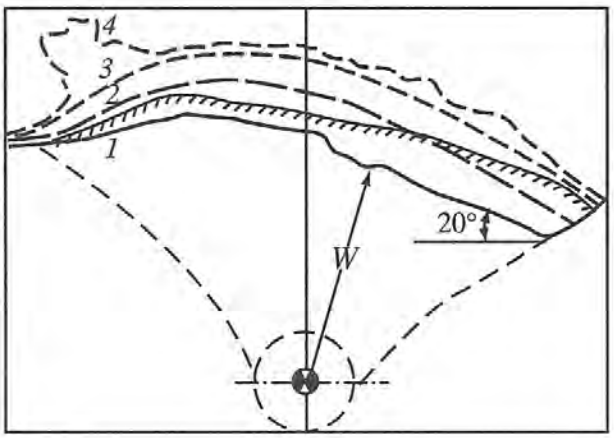

Figure 3.5: Time evolution (contours) and the resulting mound (rock pile) created by explosion "Lazurit". The time from the detonation: *1* – 0 s, *2* – 0.5 s, *3* – 1.5 s, and *4* – 3 s.

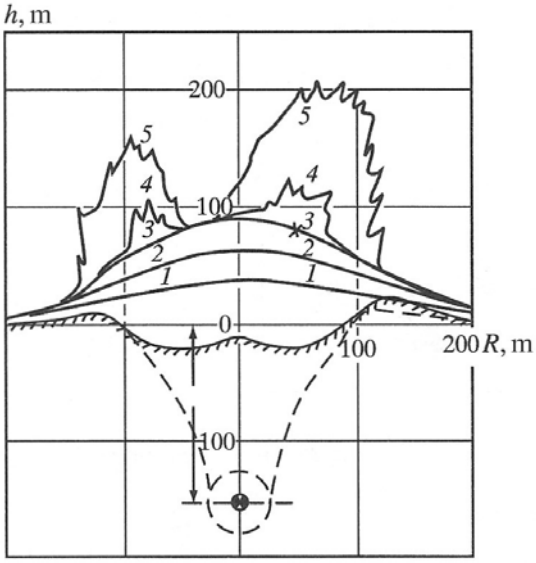

Figure 3.6: Evolution contours of the dome, gas venting and the resulting crater for explosion in BH 125. The time from the detonation: *1* – 0.9 s, *2* – 2.3 s, *3* – 3.6 s, *4* – 4.3 s, and *5* – 7.2 s.

Table 3.3. Initial ground velocities within the uplift for explosion BH 125 for Stations 1 – 11

Parameter	Parameter value					
	1	2	3	4	5	6
R_e, m	0	50	100	150	200	250
v_i, m/s	36.5	33.1	29.3	21.3	20.3	14.2

The diameter of the uplift at the base is approximately 600 m. Gas-propelled acceleration significantly affected the evolution of the uplift. Maximum height of the dome was 100m (≈0.7*W*) instead of 67 m that were predicted without the gas pressure. After 3.5 and 4 s dome (cupola) reached its maximum height of 50 and 80 m on each side of the epicenter. At that moment intense gas venting occurred in two areas with velocities of 85 m/s and 45 m/s respectively. Venting was accompanied by a bright flash (the areas of the flashes are shown in

Figure 3.6 with crosses). Two venting areas formed an asymmetric mound (with a rock pile). The rock pile had a maximum height of 23 m and was shifted toward the first more intense venting area. On the other side of the crater the rock pile was practically absent, while the free surface was uplifted by about 7 m.

The crater diameter was approximately 190-210 m at the pre-existing earth surface and approximately 270 – 294 m along the ridge of the mound, with the maximum depth of 17.5 m. The bottom of the crater was flat and it didn′t look like a typical ejection crater. First of all, a mound was formed at the bottom of the crater, possibly due to additional gas venting, which occurred 10 s after the explosion with velocity of about 100 m/s. Second, the ratio between the crater radius to the depth of burial *R/W* = 0.65 was significantly smaller than for ejection craters even for the maximum possible depth of burial ($R/W = 0.9 - 1.0$). This scenario and the final picture for the explosion in borehole 125 (BH 125) is similar to PALANQUIN: a compact mound was formed close to the crater in the middle of a larger mound.

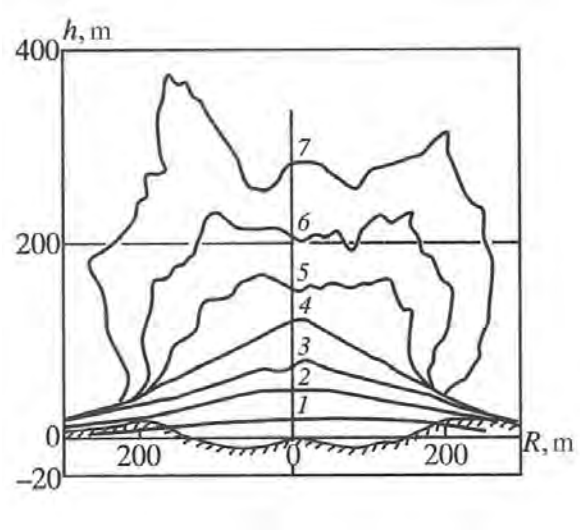

Figure 3.7: Time evolution contours of the cupola and the resulting crater for explosion in BH 101. The time from the detonation: *1* – 0.5 s, *2* – 1.0 s, *3* – 1.7 s, *4* – 4.0 s, *5* – 4.9 s, *6* – 5.6 s, and *7* – 6.6 s.

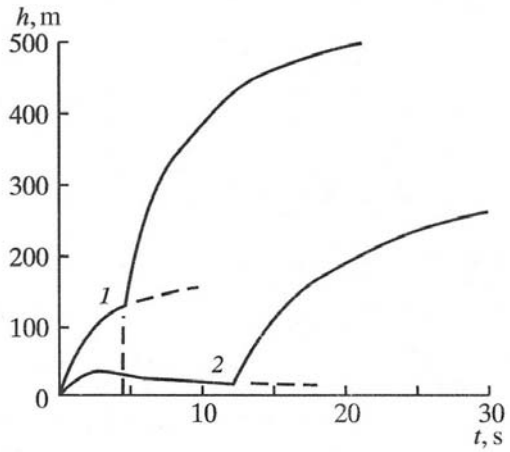

Figure 3.8: Dynamics of the cupola development and gas venting into atmosphere for explosion in BH 101 (line *1*) and BH 1204 (line *2*).

An explosion conducted in borehole 101 followed a similar scenario and produced a similar configuration of the mound and the crater. In this case a nuclear explosion with the yield of 80 kt was conducted at depth of 228 m in sandstone with density of 2610 kg/m^3, porosity of 1.53%, compressive strength of 65 MPa, *P*-wave velocity of 4000 m/s, and gas content of 13 – 16 % with water content of 0.4 – 1.6 %. The sandstone was covered with a 40-m thick clay layer, covered by clay-rich sand with a thickness up to 7m. The density of the sediments was 1830 kg/m^3, porosity – 30-45%, water saturation – 10 – 30 %, and P-wave velocity – 1600 – 2300 m/s. The average density was 2500 kg/m^3.

The evolution and the final shape of the dome are shown in Figure 3.7. The uplift velocity reached its maximum value of 48.6 m/s 1 s after the explosion. The diameter of the base of the dome was 730 m. 4.5 s after the explosion when the uplift height reached 125 m and started slowing down, gas venting occurred in several different directions (and places). Gas venting was accompanied by an increase of the velocity in the epicenter to 90 m/s, and the lateral velocity to 100 – 150 m/s. After 9 seconds the maximum height reached 400 m. After that the rising rock column started falling apart, while a gas-dust cloud continued rising up to 600 – 800 m. The dynamics of the rising dome until its breakup, movement of the upper contour of rocks after the breakup and the rise (growth) of the gas-dust cloud are shown in Figure 3.8. As a result of this explosion a crater with a volume of $5 \cdot 10^5$ m^3, radius of 145 m, and a depth of 15 m formed in the middle of a mound with a volume of $1.2 \cdot 10^7$ m^3. The crater had a flat bottom, mound at the epicenter, and looked like the crater produced by the explosion in BH 125.

Table 3.4. Dome parameters for explosion in BH 1204

Parameter	Parameter value								
R_e, m	0	100	230	400	500	600	930	1800	2075
v_i, m/s	25.8	22.0	15.6	8.7	7.0	5.2	3.9	2.4	2.2
h_m,m	32.0	24.7	12.4	3.9	2.5	1.4	0.8	0.3	0.25

Characteristics similar to the described partially confined explosions were observed for the test conducted in Borehole 1204, where a charge with the yield of 150 kt was detonated at depth of 378 m. The rock at the charge depth was represented by tuff with the following properties: density – $2.68 \cdot 10^3$ kg/m^3, porosity – 2.4%, P-wave velocity – 4630 m/s, S-wave velocity – 2640 m/s, compressive strength – 135 MPa, tensile strength – 12.8 MPa, gas content – 10.8 % with water content of 0.8%. The thickness of the sediments in the epicenter was 40 m, of which the bottom 20 m were represented by clay, and the top 20 – clay rich sand with gravel. Using the laser distance meter the initial vertical velocity and the maximum height of the uplift were determined for different distances from the epicenter (Table 3.4).

The evolution of the uplift and the gas venting are shown in Figure 3.8. The uplift reached its maximum height of 32 m ($\approx 0.09\ W$) after 2.8 s after the explosion. After the uplift collapse 12 s after the explosion an intense gas venting occurred approximately 40 m from the epicenter with a velocity of 70 m/s. During the following 40 – 50 s the gas column rose to a height of over 300 m. Another weak venting occurred 18.4 seconds later. The explosion produced a surface uplift with a radius of 500 m. The volume of the uplift was $13.4 \cdot 10^5$ m^3. A crater formed in the center of the uplift with radius of 72 m on average along the earth surface, a maximum depth of 26.1 m, and a volume of $14.8 \cdot 10^4$ m^3, or two orders of magnitude smaller than the volume of the uplift.

The maximum height of the ridge was 9.8 m. The average radius of the crater along the ridge was 11 m with a volume of $41.6 \cdot 10^5$ m^3. The maximum depth of the crater was reached at a distance of 40 m from the epicenter at the location of gas venting (Figure 3.9 a). The crater had an asymmetrical shape: the radius along one of the directions exceeded the average radius by 30% (Figure 3.9b).

An example of a fully contained explosion that created a subsidence crater without venting is a 150 kt explosion conducted in borehole 1066 at a depth of 465 m. Granite massif at the shot depth had a density of $2.63 \cdot 10^3$ kg/m^3, porosity of 2.3%, P-wave velocity of 5140 m/s, compressive strength of 130 MPa, and a gas content of 3.66 %. The thickness of clay and sand sediments in the epicenter was 13 m. During the explosion the maximum height of the uplift reached 19 m ($\approx 0.04\ W$). The volume of air displaced by the uplift created a dust cloud up to 48 m in height.

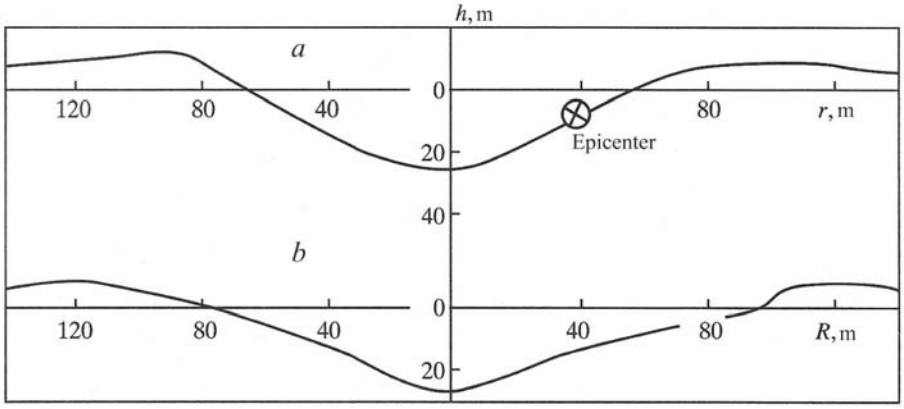

Figure 3.9: Crossection of the crater left by explosion in BH 1204: a) east – west, and b) north – south.

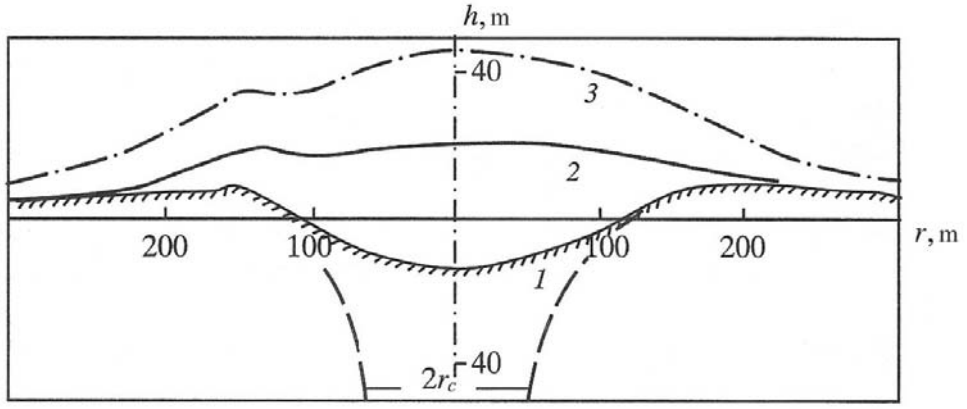

Figure 3.10: Cross-section of the crater (line *1*), maximum rise of the dome (line *2*) and dust cloud (line *3*) for explosion in BH 1066.

The initial ground velocity measured at the ground zero was 21.2 m/s. The ballistic trajectory calculated for the ground motion was identical to the observed trajectory. Therefore there was no effect from gas pressure on the ground motion. Breakthrough of the radioactive material to the

atmosphere was detected 25 hours after the explosion. The explosion created a subsidence crated with diameter of 110 m and maximum depth of 14 m with respect to the pre-explosion ground surface (Figure 3.10). An uplift formed around the subsidence area within a radius of 500 – 600 m. Maximum height of the uplift was 9 m, while the radius of the subsidence area along the ridge of the uplift was 148 m.

The presented materials show that formation of mounds/retarcs with gas venting is a common characteristic of partially confined explosions. The uplift (dome) height reached 0.6 – 1.3*W*, the initial ground velocity was 20 – 40 m/s, the time before venting varied between 2 and 12 s. Gas-driven acceleration affected the ground motion in the area of the uplift. Gas content of the emplacement rocks affected the intensity of venting and the final result of the explosion. For all explosions the ground uplift followed by the collapse and crater formation.

The explosion scenarios depended on the scaled DOB (sDOB) and the yield of the explosion, as well as the degree of rock damage. Thus, for some smaller explosions the bottom of the crater was above the ground level. Increase in sDOB causes reduction of the height of uplift and in the degree of damage (dilatation) to the rocks. The main effects of explosions with larger sDOBs were subsidence craters. Calculation of the collapse of rocks into the cavity is complicated even in the simplest case when the rock is completely broken apart and represented by sand. Therefore the mechanism of formation of subsidence craters was examined during analog laboratory experiments (Adushkin and Pernik, 1972, 1978) as we next describe.

3.2. Formation of subsidence craters

Laboratory experiments to study the mechanisms of crater the collapse crater formation were conducted using the approach described in Equations (2.5) – (2.7). Using dry sand for the model and a vacuum instead of air, conditions were achieved to make gravity the dominant force needed for satisfying scaling relationships in the following ranges:

$$\frac{P}{\rho g W} \sim 1 - 10^2, \frac{\rho g W}{P_a} \sim 10, \frac{P}{P_a} \sim 10 - 10^3, \frac{c}{P_a} \sim 10^{-1}. \quad (3.1)$$

During the experiments the ratio W/r_c was fixed and the parameter $\bar{A} = \frac{A}{(\rho g W + P_a) W^3}$ was varied by changing pressure and the cavity radius. The range of change given by $10^{-2} \leq \bar{A} \leq 10$ and $1.6 \leq \frac{W}{r_c} \leq 10$ agrees with the conditions of the emplacement of nuclear charges corresponding to partially and fully contained explosions.

3.2.1. Ground movement and cavity gas venting

Laboratory experiments have shown (Section 2.2) that an ejection crater does not form for $\bar{A} < \bar{A}_*$. Instead gas would escape into the atmosphere some time following the surface uplift. Further reduction in parameter $\bar{A}$ leads to shortening of this time interval and reduces the area of the gas venting. Snapshots of one such laboratory experiment are shown in Figure 3.11a.

A series of experiments were conducted with a vertical slice along the symmetry axis in order to document relative motion of the ground and the gas. Cavity gas moved upward along the

axial part of the massif. Layers of dyed sand and a half-sphere (cavity) with pressurized gas can be clearly seen in the snapshots. Cavity gas moved upward (due to buoyancy), while the ceiling of the semi-sphere was collapsing. As a result a collapse chimney with a sharp boundary was formed. Maximum displacement of the material was observed approximately in the middle between the boundaries of the chimney and its axes. Chimney formation was accompanied by ground subsidence over a large region around the epicenter. Gas rise and chimney formation culminated in formation of an ejection crater at the bottom of the subsidence crater and gas venting into the atmosphere.

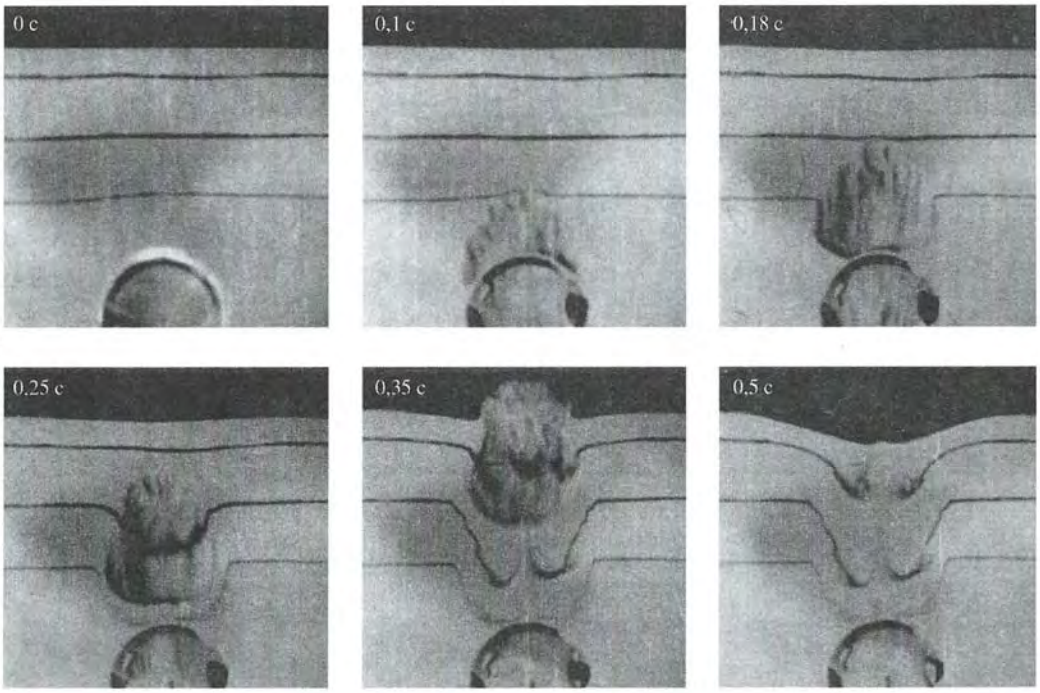

a

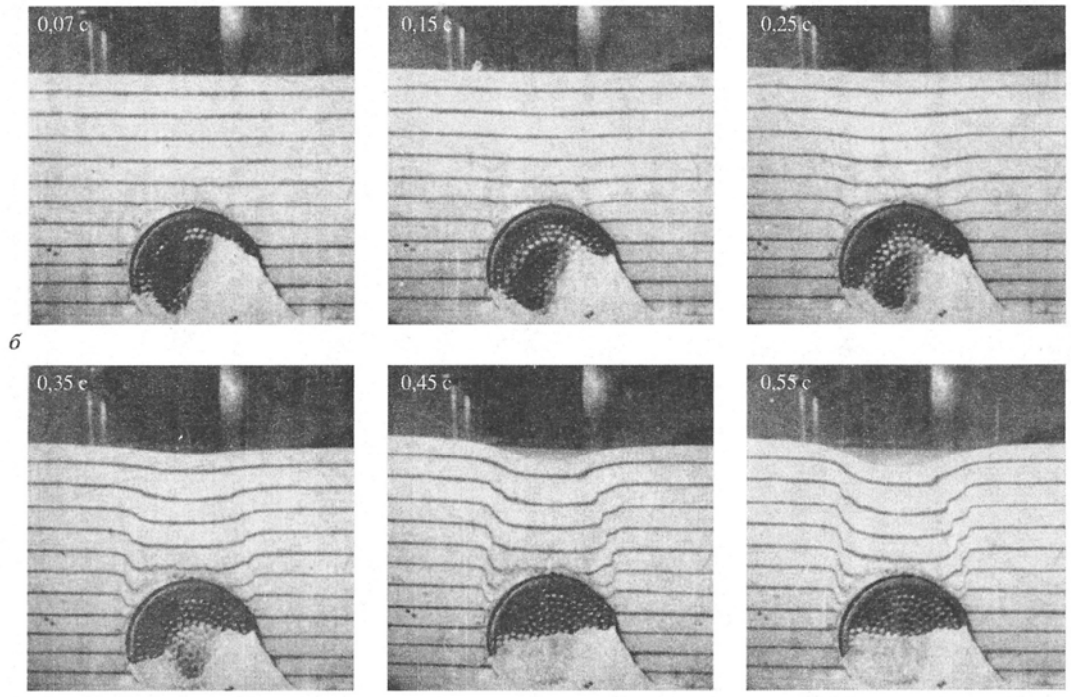

Figure 3.11: a) Chimney development and gas venting in the laboratory experiment (A=0.23, W/r_0=4.8). b) Material collapse into the cavity without rise of gas in the cavity (A=0.06, W/r_0=3.2). The numbers in each frame represent time.

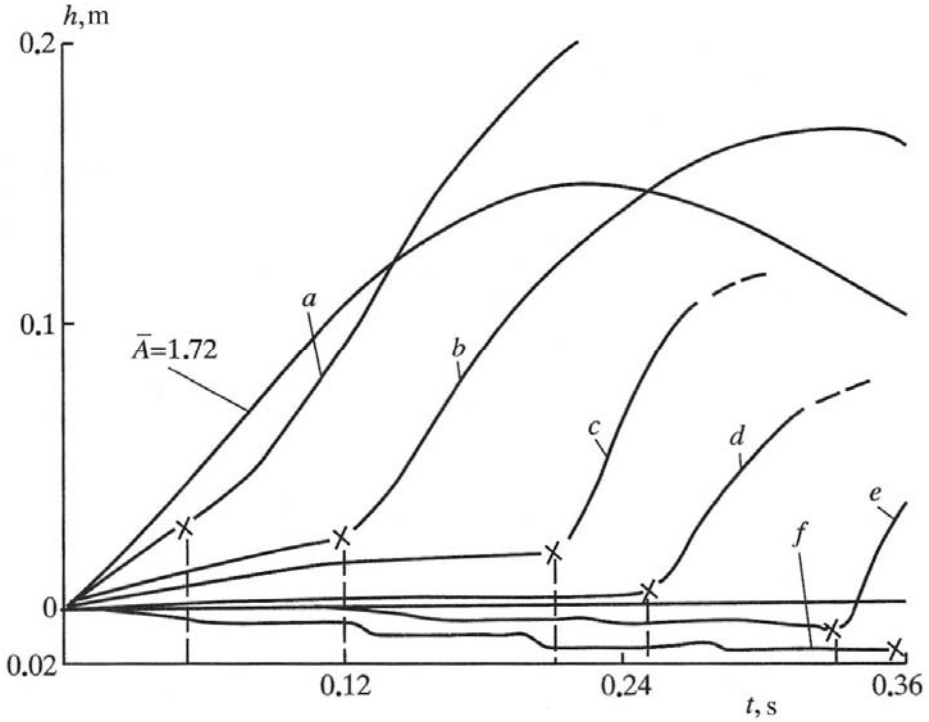

Figure 3.12: Material movement in the epicenter depending on gas energy in the cavity for W/r_0=4.8. The values of parameter $\bar{A}$ (for different curves): *a* – 1.51; *b* – 0.83; *c* – 0.57; *d* – 0.48; *e* – 0.23; *f* – 0.19.

Further reduction in the value of $\bar{A}$ causes the gas volume to move closer to the surface, and an increase in the ejection time, with a decrease in the mass of the ejected material. The surface subsidence took place much earlier than gas ejection. When the parameter reached a certain limit $\bar{A} = \overline{A_c}$, gas ejection was no longer observed. Reduction of the parameter $\bar{A}$ in the range $\bar{A} < \overline{A_c}$ causes a reduction in the area associated with rising gas. At a certain value $\bar{A} < \overline{A_{c0}}$ the rising of the gas cloud was no longer observed. In this case only ground subsidence was detected (see Figure 3.11 b). In the absence of a rising gas volume, the zone of maximum ground deformations was confined to the boundary of the collapse chimney. The layered structure inside the chimney was preserved, although significant dilatation of the material was observed. A narrowing of the chimney together with a widening of the zone of deformation toward the surface near the collapse crater was also noted.

A series of experiments was conducted and recorded on film in order to determine the height of the mound with time, for fixed values of W/r_c. Figure 3.12 shows the results for a series with fixed value W=4.8 r_c. For this series the above-mentioned changes in mound development, cavity rise, and gas venting, occurred for $\bar{A}_* = 1.66$, $\bar{A}_c = 1.21$, and $\bar{A}_{k0} = 0.083$.[4]

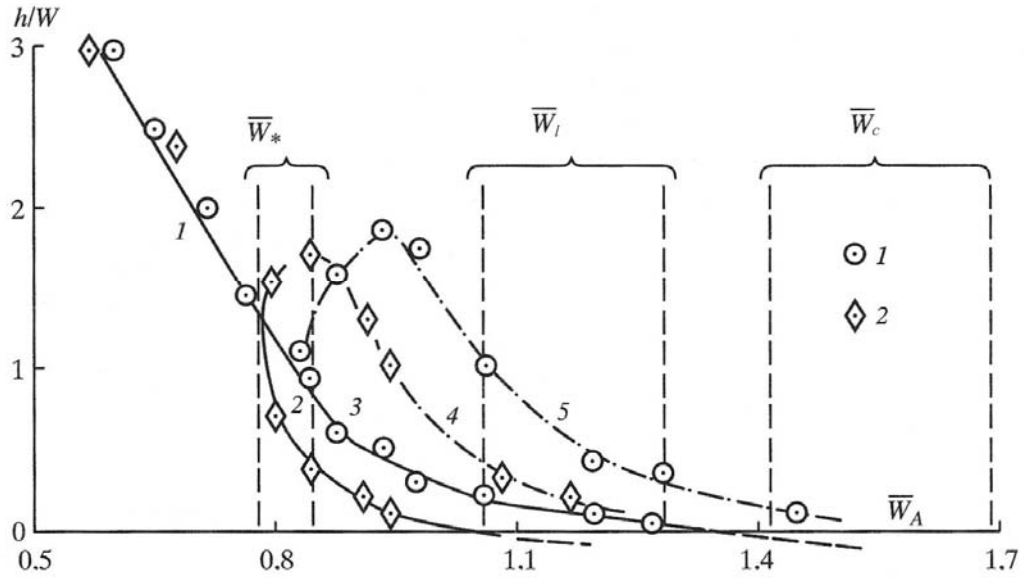

Figure 3.13: Height of the cupola uplift as a function of cavity depth. Lines 1 – 5 correspond to different experimental series. The symbols show different values of W/r_c: 1 – 4.8; 2 – 2.4.

At the moment of gas venting (marked with crosses in Figure 3.12) the velocity of material ejection reached 10 – 30 m/s, growing with increasing ejection time, because the mass of ejected material decreased. Material collapse into the cavity and ground subsidence occurs in series of steps due to localization of shear deformation associated with the formation of a system of slip zones inside the massif.

[4] For the parameter A_c the index c stands for "camouflet" or fully –contained explosion

Figure 3.13 shows the height of the uplift as a function of the dimensionless parameter $\bar{W}_A$ (equation 2.41) for two series with W=4.8 r_c and W=2.4 r_c. In the range of ejection (cratering) explosions $\overline{W_A} < \bar{W}_*$ the height of the uplift was independent of W/r_c and was determined only by the energy of cavity gas (line 1). In the range $\overline{W_*} < \bar{W}_A < \bar{W}_c$ there are two characteristic heights: the height of the uplift of the main mound (lines 2 and 3) and the height of the material ejection during the gas venting (lines *4* and *5*). In this range the height of the uplift depends not only on the energy of gas in the cavity, but also on the value of the parameter W/r_c. In the range $\bar{W}_A > \bar{W}_c$ ground uplift was absent, and ground subsidence was observed instead.

3.2.2. Major types of explosions

Based on the main characteristics of ground uplift evolution, formation of collapse chimney and gas venting, explosions can be classified into different types for different ranges of the parameter $\bar{A}$. The range $\bar{A} > \bar{A}_*$ corresponds to cratering explosions, the range $\overline{A_*} > \bar{A} > \bar{A}_c$ corresponds to partially contained explosions, and the range $\bar{A} < \bar{A}_c$ corresponds to fully contained explosions. Transformations of the major zones and the direction of the material movement in these zones are shown in Figure 3.14a. Cratering explosions are characterized by upward movement of the entire rock volume above the cavity with simultaneous venting of cavity gas. This material is then flying away from the crater, and later slides down the crater (fallback). Fully contained explosions are characterized by upward movement of the explosive cavity as a result of collapse of the cavity ceiling, formation of a collapse chimney, and an ejection zone with simultaneous gas venting (Figure 3.14b). During fully contained explosions there is no gas venting into atmosphere, the material above the cavity moves downward only with formation of a subsidence crater (Figure 3.14c).

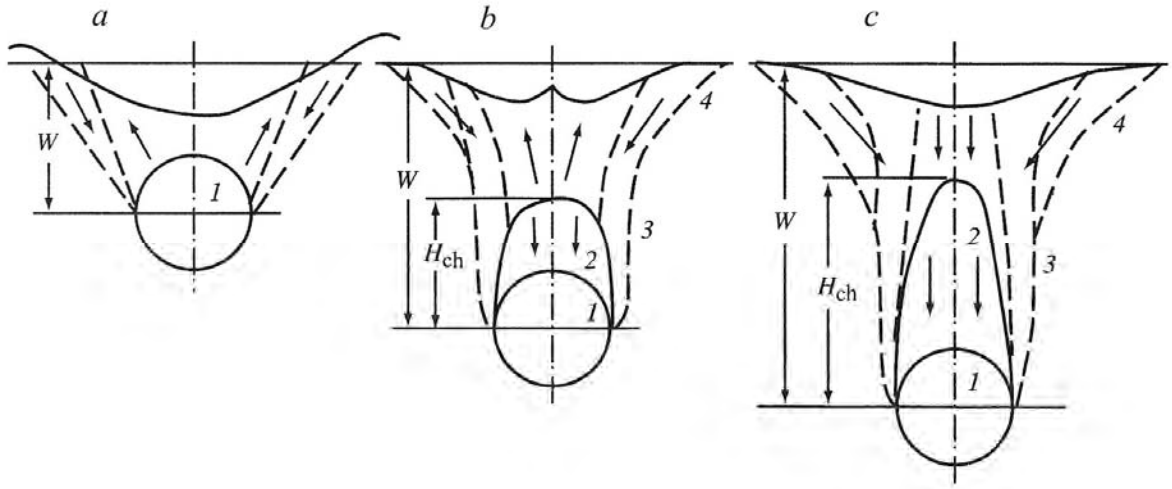

Figure 3.14: Main characteristics of material motion during a) excavation (cratering) explosions, b) partially contained explosions, and c) fully contained explosions. *1* – cavity; *2* – zone of the cavity upward motion (due to buoyancy) ; *3* – chimney; *4* – subsidence zone.

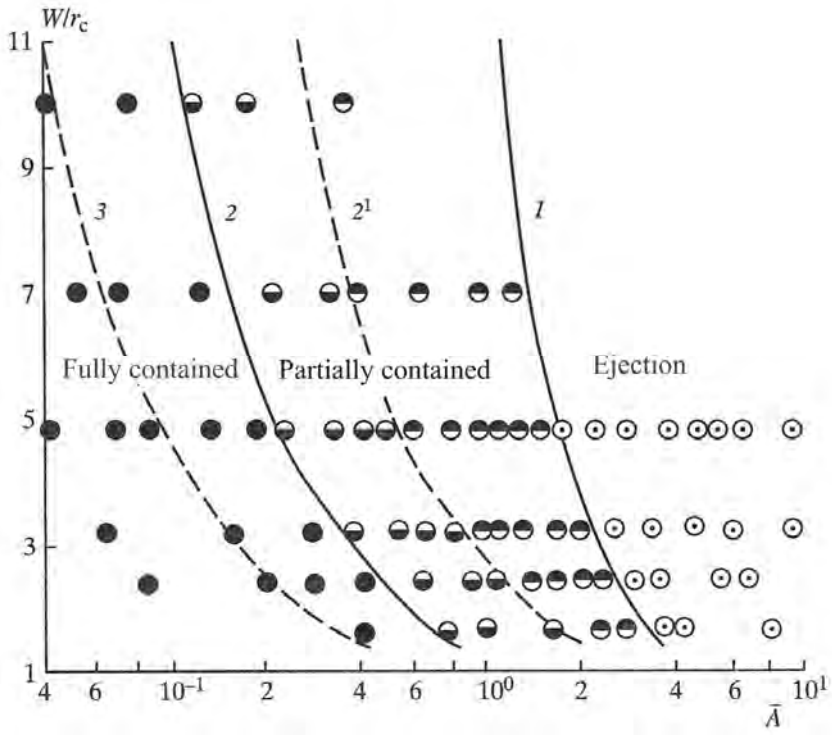

Figure 3.15: Different regimes for underground explosion in the parameter plane W/r_c and $\bar{A}$. Lines *1 – 3* show the boundaries between the regimes (zones) are given by Equations 3.2 – 3.5.

The regions corresponding to different explosion types in parameter space for parameters $\bar{A}$ and W/r_c are shown in Figure 3.15. The boundary between the cratering and partially contained explosions (shown with line *1*) corresponds to an empirical formula:

$$\bar{A}_* = 4.34\left(\frac{r_c}{W}\right)^{0.6} . \tag{3.2}$$

Experiments with a dyed sand layer around the cavity (layer thickness of about 0.1 r_c) have shown that for $\bar{A} > \bar{A}_*$ the dyed particles were found all over the crater at the surface. For $\bar{A} < \bar{A}_*$ there were no dyed particles raised to the surface. This means that the material ejection took place after some amount of material collapsed into the cavity. The boundary between partially contained and fully contained explosions (line *2*) corresponds to an empirical formula:

$$\bar{A}_c = 1.16\left(\frac{r_c}{W}\right) . \tag{3.3}$$

Another sub-division can be made inside the zone corresponding to the partially contained explosions (line 2′):

$$\bar{A}_p = 2.6\left(\frac{r_c}{W}\right), \tag{3.4}$$

which corresponds to a condition of equilibrium between the weight of the material above the cavity and gas pressure inside the cavity. For $\bar{A} > \bar{A}_p$ the initial motion of the free surface was directed upwards, while for $\bar{A} < \bar{A}_p$ it was directed downward. Line *3* separate the zone of fully contained explosions below which there was no upward motion of the cavity:

$$\bar{A}_{c0} = 0.56 \left(\frac{r_c}{W}\right)^{1.1}. \tag{3.5}$$

3.2.3. Chimney collapse and upward motion of the cavity

Experiments with film recording identified empirical relationships between the height of the cavity, the chimney sizes, and the depth of burial of the initial cavity. For $\bar{A} > \bar{A}_*$ radius of the chimney was estimated as

$$R_c = 1.2 r_c. \tag{3.6}$$

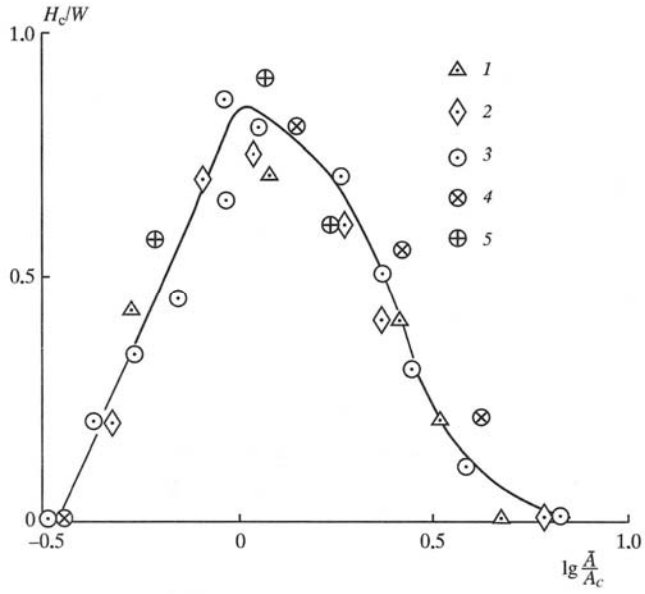

Figure 3.16: Final height of the cavity as a function of cavity gas energy and the depth for different values of W/r_c shown with the symbols: *1* – 2.4; *2* – 3.2; *3* – 4.8; *4* – 7; *5* – 10.

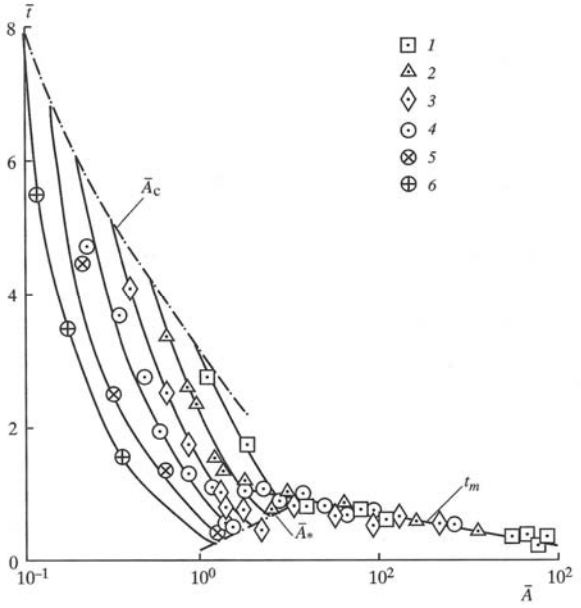

Figure 3.17: Time of the gas venting as a function of gas energy and cavity depth for different values of W/r_c shown with the symbols: *1* – 1.6; *2* – 2.4; *3* – 3.2; *4* – 4.8; *5* – 7; *6* – 10.

Changes in the relative height of the cavity rise[5] H_c/W as a function of parameter $\bar{A}$ are shown in Figure 3.16. In the range of partially contained explosions $\overline{A_*} > \bar{A} > \bar{A}_c$ the height of the cavity rise corresponds to the chimney height and is determined using the empirical formula:

[5] In this book "cavity rise" involves the process of the cavity filling by the debris, thus the void propagates upward, forming the chimney.

$$\frac{H_c}{W} = \frac{0.85}{1+10^4\left(log_{10}\frac{\bar{A}}{\bar{A}_c}-0.4\right)} \quad \text{for } \overline{A_*} > \bar{A} > \bar{A}_c \tag{3.7}$$

In this range the motion of the material and gas culminates in an "explosion" in the upper part of the mound or at the bottom of the crater with ejection of some debris. For $\bar{A} = \bar{A}_c$ the volume of gas floated to the surface without explosion (or ejection).

For fully contained explosions ($\bar{A} < \bar{A}_c$) the chimney height rapidly decreases with reduction in the parameter $\bar{A}$ according to the empirical formula:

$$\frac{H_c}{W} = 1.9\left(log_{10}\frac{\bar{A}}{\bar{A}_c} + 0.45\right) \quad \text{for } \bar{A}_c > \bar{A} > \bar{A}_{c0} \tag{3.8}$$

and becomes smaller than the chimney height. For $\bar{A} < \bar{A}_{c0}$ the cavity stops moving upward and gas release into atmosphere occurs through a filtration mechanism.

3.2.4. Gas venting into the atmosphere

Experimental measurements of the venting times for cavity gas as a function of non-dimensional emplacement parameters (according to Equation 2.41) are shown in Figure 3.17. Limiting values for parameters $\bar{A}_*$ and $\bar{A}_c$ are shown with dash-dotted lines. The relationship for the time when the maximum velocity is reached (for cratering explosions) given by Equation 2.19 is also plotted. The gas venting time for partially contained explosions depends not only on the energy parameter $\bar{A}$, but also on W/r_c.

If the relative depth W/r_c increases while $\bar{A}$ remains fixed, the dimensionless venting time decreases. This happens because the energy of the cavity gas increases with increase in W/r_c. Therefore, while the cavity moves upward, the pressure exceeds the overburden pressure and the conditions are created for ejection of material. Analysis of experimental data has shown that, for partially contained explosions, venting times due to an upward cavity movement satisfies an empirical formula:

$$t_0 = 2.5\left(\frac{W}{r_c}\right)^{0.5}\left(\frac{\bar{A}_c}{\bar{A}}\right)^{1.2} \text{ for } \overline{A_*} > \bar{A} > \bar{A}_c \tag{3.9}$$

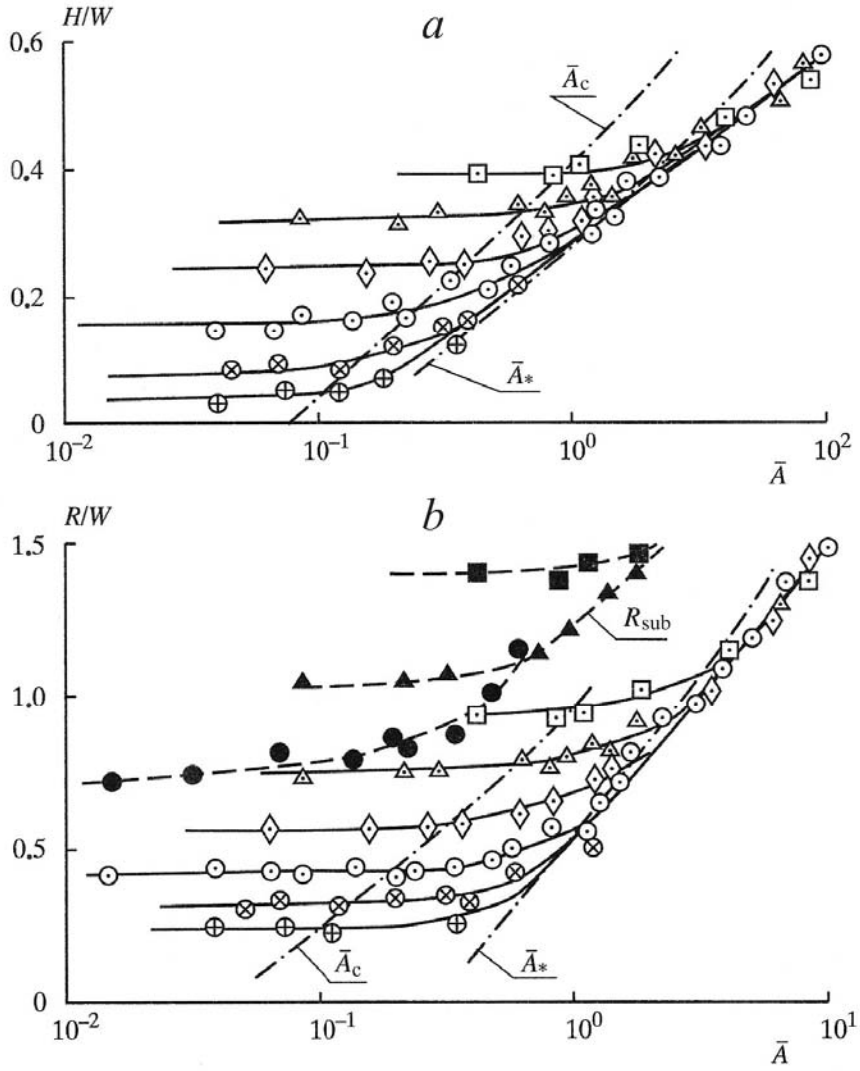

Figure 3.18: Effect of gas energy and cavity depth on a) scaled radius and b) crater size for excavation (cratering) and partially confined explosions. Different values of W/r_c are shown with the symbols (as in Figure 3.17): 1 – 1.6; 2 – 2.4; 3 – 3.2; 4 – 4.8; 5 – 7; 6 – 10.

3.2.5. Crater size

Experimental measurements of the crater size as a function of $\bar{A}$ for fixed values of W/r_c are shown in Figure 3.18. The limiting values for $\bar{A}_*$ and $\bar{A}_c$ are shown with dash-dotted lines. The region between these lines corresponds to partially contained explosions. For cratering explosions ($\bar{A} > \bar{A}_*$) crater size depends only on the energy of gas in the cavity and follows Equation 2.40. In the area of partially contained explosions ($\overline{A_*} > \bar{A} > \bar{A}_c$) crater sizes depend on both gas energy and W/r_c. The dependence on W/r_c is stronger for smaller values of $\bar{A}$. For fully contained explosions ($\bar{A} < \bar{A}_c$) a collapse crater is located inside a large area of subsidence.

The sizes of the subsidence zones are also shown in Figure 3.18b. The crater sizes for $\bar{A} < \bar{A}_c$ depend only on the value of W/r_c. In this case the radius of the subsidence zone R_{sub} is given by:

$$\frac{R_{sub}}{W} = \frac{5.9}{\frac{W}{r_c}+3.48}; \tag{3.10}$$

while the radius of the collapse crater R is:

$$\frac{R}{W} = \frac{0.58}{\sqrt{\frac{W}{r_c}-0.77}}; \tag{3.11}$$

and the depth H of the collapse crater is:

$$\frac{H}{W} = \frac{1.1 r_c}{W} - 0.069\ . \tag{3.12}$$

From the entire dataset and using Equations 3.11 and 2.40, a universal expression relating the crater radius for the entire range of the non-dimensional parameters $\bar{A}$ and W/r_c was obtained as:

$$\frac{R}{W} = 0.58 + 0.45\ log_{10}\left(\bar{A}^2 + 0.05 \cdot 10^{\frac{1.29}{(W/r_c)^{0.5}-0.77}}\right). \tag{3.13}$$

3.3. Comparison between the laboratory experiments and field data

The results of the laboratory experiments were compared with the observations for all nuclear explosions including excavation (cratering explosions), partially contained explosion and some of the fully contained explosions with the smallest sDOB ($W/q^{1/3}$). The values of dimensionless parameters $\bar{A}$ and W/r_c needed for comparison with the model were shown earlier in Table 2.15. Additional data is shown in Table 3.5 with continuing explosion numbering. Data from explosions that produced subsidence craters including an American test BLANCA as well as from some other explosions conducted at the STS and NZTS were used for analysis. The parameters $\bar{A}$ and W/r_c were calculated using the relationships 1.5, 2.28, 2.32 – 2.37 taking into account known physical properties of emplacement rocks and their gas content, as well as the lithostatic pressure determined using the average density above the charge.

3.3.1. Explosion types

Figure 3.19 shows data points for nuclear explosions from Tables 2.15 and 3.5 with the numbers corresponding to the explosion numbers in the tables. Also shown are the boundary values of parameters $\bar{A}_*$ and $\bar{A}_c$ determined from laboratory experiments, which separate the zones between ejection (cratering), partially and fully contained explosions. Cratering explosions fully agree with the experimental data. The point corresponding to UNT SEDAN is plotted near the boundary between cratering and partially contained explosions (line) toward cratering explosions, while the explosions SULKY, PALANQUIN, “Taiga” and “Lazurit” correspond to

partially contained explosions. Explosions “Krystall”, BH 101, BH 125, as well as tunnel explosions conducted at the STS belong to partially contained zone. These explosions produced subsidence (collapse) craters and significant damage to mountain slopes. Explosions BLANCA and BH 1204, which produced gas venting into atmosphere, are plotted near the boundary between partially and fully contained explosions within the zone of partially contained explosions. The remaining explosions are plotted within the zone of fully contained explosions. Therefore we conclude that there is a good agreement between the laboratory experiments and the field data.

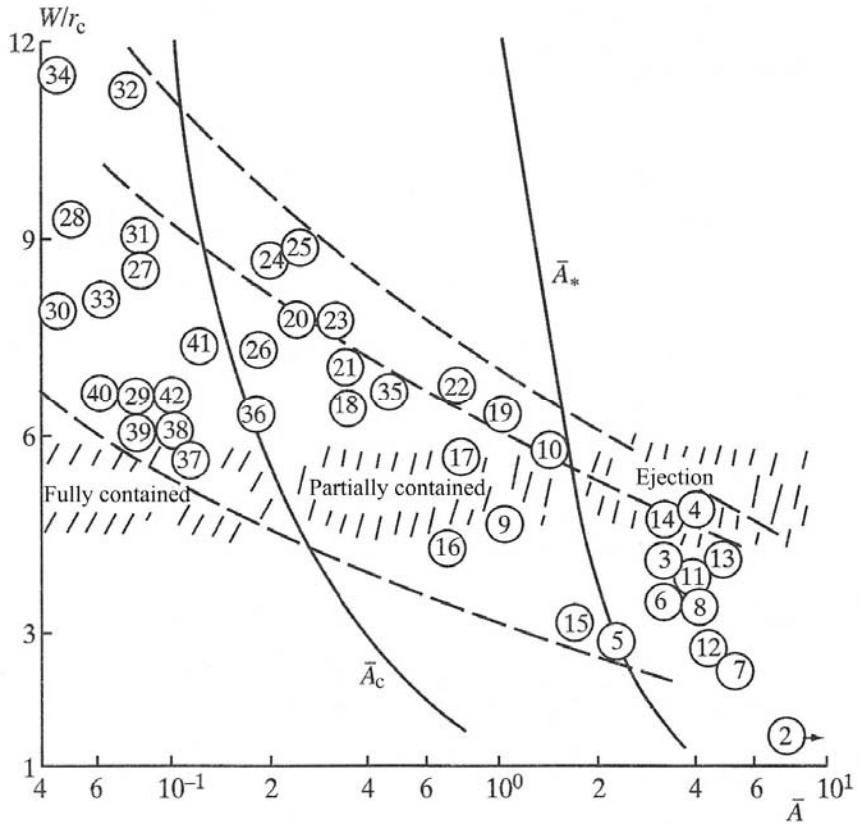

Figure 3.19: Comparison between the field data (circles) and the model in the parameter plane W/r_c and $\bar{A}$. Numbers in the circles correspond to the numbers of different nuclear explosions in Tables 2.15 and 3.5.

Figure 3.19 also shows that some of the filed experimental points formed a band (marked with dashed lines) crossing $\bar{A}_*$ and $\bar{A}_c$ boundaries. As it turns out, explosions conducted in dry and competent (hard) rocks are plotted in the upper part of the band. These explosions produce very small amount of non-condensable gas, therefore gas escape into atmosphere occurs as a result of convective transport through broken rocks. Therefore for these explosions gas breakthrough times are on the order of minutes (e.g. 1.7 min for SULKY, 9 min for explosion B-2), even if they plot close to the boundary between cratering and partially contained explosions. For explosions plotted close to the boundary between partially and fully contained explosions

gas breakthrough times are on the order of hours (e.g. 5 – 10 hours for explosions 21 [not sure whether this is entry #21 in Table 3.55 or explosion in BH21], E-1, -5).

The lower wider part of this band contains explosions conducted in wet and gas-producing rocks (Balapan Testing Area of the STS, NZTS, explosions in wet alluvium and tuff). In these conditions partially contained explosion produce intense venting of gas into atmosphere several seconds after the explosion. This particular mechanism was studied in detail using laboratory experiments. By using parameters $\bar{A}$ and W/r_c and knowing the physical rock properties and their gas content one can predict the effect of explosions on the emplacement medium, evaluate the time of gas release and plan the radiation consequences of the nuclear tests.

3.3.2. Gas venting into atmosphere

Laboratory experiments were conducted to model several cratering explosions, including "Lazirit", BH 125, "Krystall", BH 1066. The experiments were conducted satisfying non-dimensional scaling parameters (2.44). The results of these experiments including the dynamics of the dome rise and venting times are shown in Figure 3.20. Due to an absence of a pressure wave in the model the heights of the dome were smaller. This difference grew with the increase in scaled DOB. However the laboratory venting times agreed with the data from the nuclear explosions (Figure 3.20, the difference did not exceed 50%).

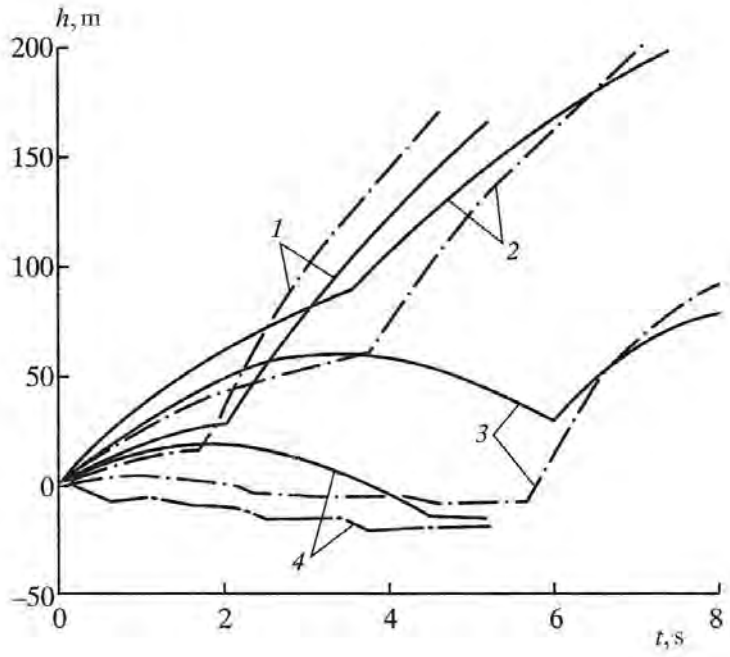

Figure 3.20: Dynamics of the cupola development and gas venting into atmosphere for field experiments (solid lines) and the model (dash-dot lines) for explosions: 1 – "Lazurit"; 2 – BH 125; 3 – "Krystall"; 4 – BH 1066.

Table 3.5 Explosion characteristics

Expl. #	Explosion	Rock type	Parameter						
			$W/q^{1/3}$, m/kt$^{1/3}$	ρ, g/cm^3	C_p, m/s	σ_*, 10^5 Pa	W/r_c	η_{H2O}/η_{CO2}	$\bar{A}$
16	BH 101	Sandstone	52.7	2.61	4000	650	4.3	0.068/0.06	0.7
17	BH 125	Porphyrites	56.7	2.75	4930	1124	5.6	0.05/0.07	0.74
18	BH 21	Granite	56.9	2.64	5460	1600	6.5	0.008/0	0.34
19	“Lazurit”	Quartzite	58.5	2.63	4650	1790	6.3	0.006/0.025	1.02
20	Tun. E-1	Porphyrites	59.2	2.64	5650	2900	7.7	0/0	0.24
21	Tun. 13	Granite	60.6	2.64	5460	1600	6.9	0.006/0	0.35
22	Tun B-2	“	65.6	2.71	5400	1800	6.7	0.011/0	0.71
23	Tun. A-5	“	67.5	2.63	5400	2180	7.6	0.014/0	0.31
24	Tun. Z-5	Porphyrites	69.4	2.63	5460	2960	8.7	0.014/0	0.22
25	Tun. A-p	Granite	83.8	2.64	5200	1600	8.9	0.017/0	0.26
26	BH 1204	Tuff-sandstone	72	2.68	4630	1350	7.3	0.05/0.058	0.19
27	BH 1066	Granite	83.9	2.63	5140	1300	8.7	0.035/0.001	0.08
28	BH 1061	Shale	89	2.73	5090	1030	9.3	0.056/0.04	0.05
29	BH 1207	Slate (or shale)	92.4	2.5	3600	350	6.5	0.058/0.05	0.08
30	BH 1054	Conglomerate	95	2.6	4700	400	7.9	0.032/0.03	0.04
31	BH 104	Sandstone	98.8	2.63	4730	765	8.8	0.04/0.04	0.08
32	BH 105	Shale	106	2.70	4600	1500	11.3	0.035/0.03	0.07
33	BH 111	“	108	2.66	4600	494	8.0	0.055/0.05	0.06
34	BH 102	Sandstone	111.2	2.65	4800	893	11.5	0.032/0.03	0.04
35	“Krystall”	Limestone	82.1	2.48	3500	700	6.7	0.01/0.42	0.47
36	BLANCA	Tuff	95	1.9	2200	360	6.4	0.175/0	0.17
37	Tun. A-6	Shale (slate)	62.7	2.67	5500	650	5.7	0.039/0.016	0.12
38	Tun. A-1	“	65.2	2.77	5250	750	5.9	0.04/0.05	0.1
39	Tun. A-8	“	67.7	2.75	5000	810	6.2	0.031/0.076	0.08
40	Tun. B-1	Carbonate shale	69.1	2.82	6000	790	6.6	0.012/0.22	0.06
41	Tun. A-9	Dolomite	71.5	2.77	5700	1460	7.4	0.004/0.423	0.15
42	Tun. A-10	Sandstone	73.3	2.7	5300	730	6.5	0.035/0.01	0.08

Figure 3.21 compares historical gas venting data for cratering explosions with the laboratory model. The solid line shows the model prediction (Equation 3.9), the circles show the data points from Table 3.6.

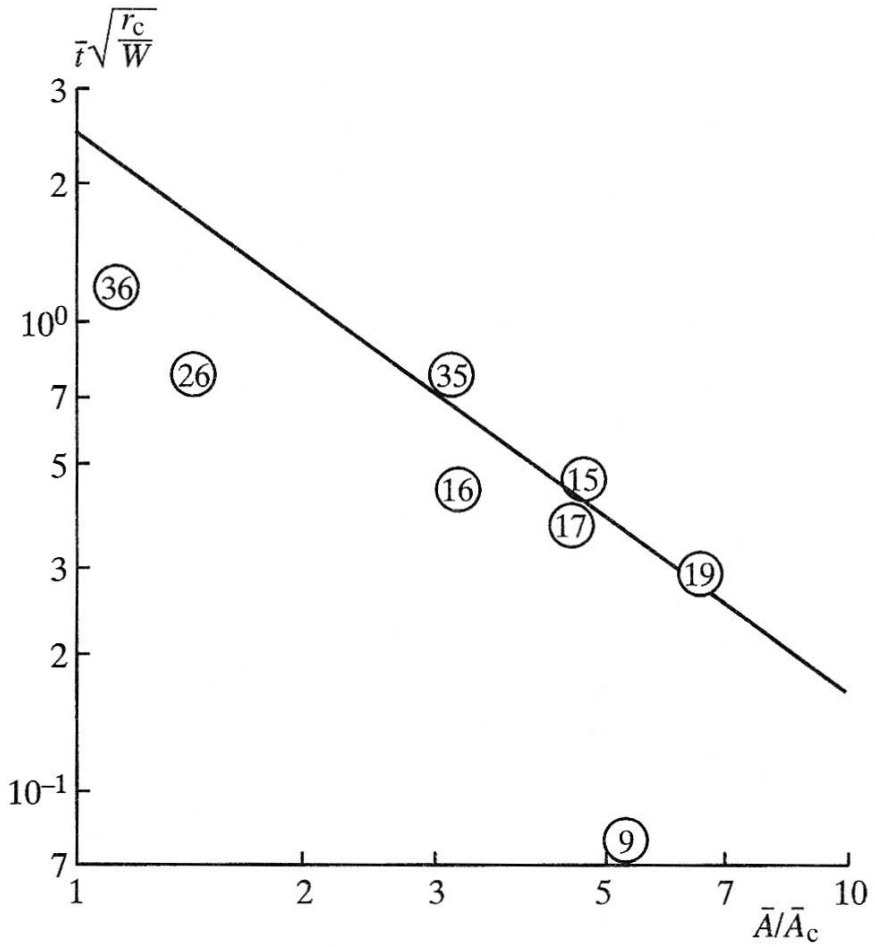

Figure 3.21: Comparison of the gas venting time between the field data (circles) and the model (solid line) for excavation (cratering) explosions. Numbers in the circles correspond to the numbers of different nuclear explosions in Table 3.6.

Most of the data points agree with Equation 3.9, while some of the data plot below the line. Thus the venting time for BLANCA (data point 36) and BH 1204 (data point 26) are approximately half that of the model prediction, while the time for PALANQUIN (data point 9) is a quarter of the prediction. It is possible that in the field experiments gas venting occurs either through medium discontinuities (faults and fractures) or through the parts of the stemming complex. A similar situation was noted when we compared the gas venting times for cratering explosions (Figure 2.27). We conclude that the laboratory results should be treated as an upper bound (of the time release) for purposes of predicting behavior in an actual nuclear explosion.

Table 3.6. (comparison results of) Gas venting times into atmosphere

Expl. #	Explosion						
		t, s	W, m	$\bar{t}$	$\bar{t}\sqrt{\frac{r_c}{W}}$	$\bar{A}$	$\bar{A}/\overline{A_c}$
9	PALANQUIN	0.45	85	0.16	0.07	1.1	5.25
15	Kanal	3.0	127	0.85	0.49	1.7	4.71
16	BH 101	4.5	228	0.95	0.45	0.7	3.2
17	BH 125	3.5	151.3	0.90	0.38	0.74	4.42
19	“Lazurit”	2.0	70	0.78	0.29	1.02	6.67
26	BH 1204	12.0	378	1.94	0.72	0.19	1.46
35	“Krystall”	6.0	95.5	1.97	0.76	0.47	3.14
36	BLANCA	15.0	255	2.96	1.18	0.1	1.13

Table 3.7. Averaged crater parameters

Expl. #	Explosion	At the rim level				At the ground level			
		R_r, m	n_r	H_r, m	V_r, m^3	R, m	n	H, m	V, m^3
9	PALANQUIN	46	0.54	28	$6.2 \cdot 10^4$	36.3	0.43	21	$6.2 \cdot 10^4$
10	SULKY	9.8	0.36	3.5	$3.5 \cdot 10^2$	–	–	–	–
16	BH 101	190	0.84	37	$3 \cdot 10^7$	145	0.63	15	$5 \cdot 10^5$
17	BH 125	140	0.93	32	$8.6 \cdot 10^5$	97	0.65	17.5	$3 \cdot 10^5$
26	BH 1204	111	0.29	35.8	$4 \cdot 10^5$	72.5	0.19	26	$1.4 \cdot 10^5$
27	BH 1066	148	0.32	23	$4.5 \cdot 10^5$	110	0.24	14	$1.5 \cdot 10^5$
29	BH 1207	180	0.57	13	$3 \cdot 10^5$	98	0.31	4.5	$2.7 \cdot 10^4$
31	BH 104	69	0.31	8.2	$6.2 \cdot 10^4$	34.5	0.15	6.1	$8.6 \cdot 10^3$
32	BH 105	47	0.21	2.8	$6.5 \cdot 10^3$	19	0.08	1.3	$5 \cdot 10^2$
35	“Krystall”	50	0.53	5	10^4	–	–	–	–
36	BLANCA	150	0.59	18	–	–	–	–	–

3.3.3. Crater sizes

Field scale partially-contained explosions produce craters at the top of the mound or on top of the broad uplift zone. Only for explosions in alluvium there was no ground uplift, and the craters were located practically at the original level. Therefore a comparison with the model was performed not only for the crater sizes measured at the original ground level (similar to cratering explosions), but also for the craters located on top of the mounds along the rim, in which case the crater sizes were measured at the rim level.

The averaged crater sizes for partially contained and even for some fully contained explosions are shown in Table 3.7. Figure 3.22 compares the radii of the nuclear craters and the laboratory experiments. A group of data points with $R \geq 0.95W$ corresponds to cratering explosions. Double points correspond to the craters located on tops of the mounds. The lower

points correspond to the radius at the ground level, while the upper points show the radii at the rim. For explosions 101 and 126 only the lower points agree with the model. Evidently for these explosions the ejection of material was dominant mechanism in crater formation. For the remaining explosions the crater sizes measured at the rim level were in agreement with the model. Therefore for these explosions material collapse into the cavity represented a main mechanism of crater formation, therefore the collapse craters were formed on top of the uplifts. For explosions in alluvium the radii of the subsidence craters were also in a good agreement with 3.11.

The overall comparison between the laboratory results and the data from the field experiments shows good agreement with respect to dome uplift dynamics and the crater sizes. Therefore the laboratory model can be used to predict different mechanical and radiation-related effects of partially and fully contained nuclear explosions.

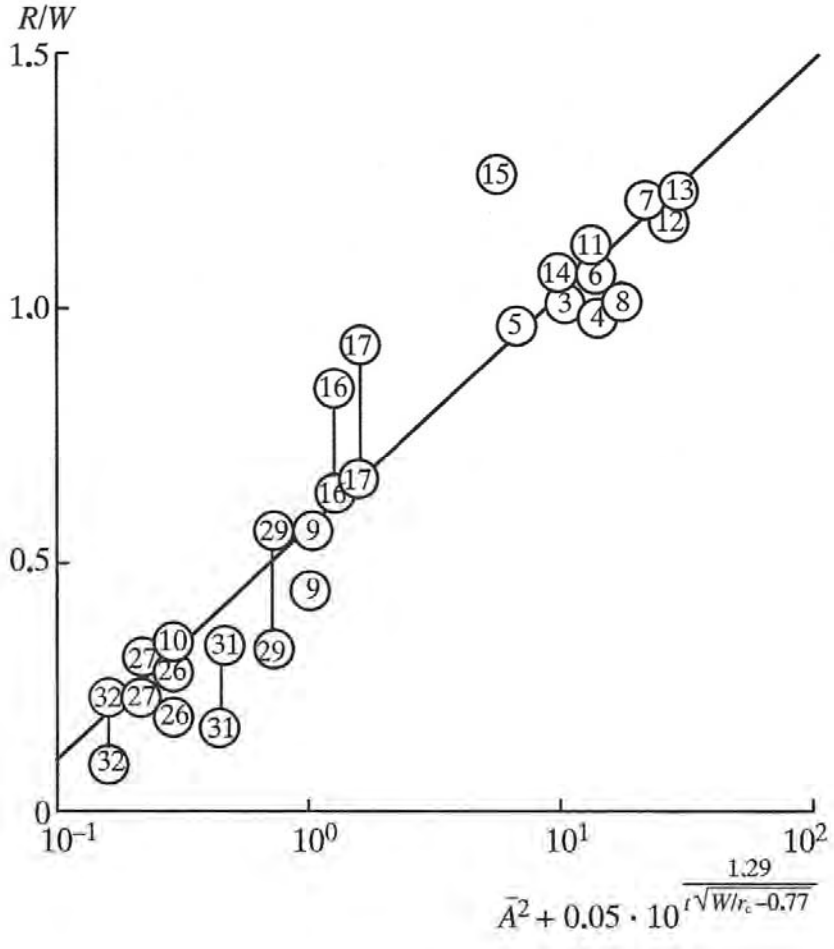

Figure 3.22: Comparison of the crater size between the field data (circles) and the model (solid line) for excavation (cratering) explosions. Numbers in the circles correspond to the numbers of different nuclear explosions in Tables 3.7 and 3.8.

3.4. Subsidence crater sizes

Subsidence craters at the ground surface typically form after explosions conducted in loose rocks. According to the Bulletin of the Seismological Society of America for 1972[6], 85% of 225 nuclear tests conducted at the NTS produced subsidence craters. Underground nuclear explosions conducted in alluvium at the NTS are the ones most similar to the laboratory experiments. Indeed, the main properties of alluvium, such as density, porosity, internal friction coefficient, are similar to the properties of the experimental material. In addition, after passing of the compression and rarefaction waves the medium components lose their cohesion and become fragmented. The thickness of alluvial deposits in Nevada varies between 100 and 700 m. Tuff is situated below the alluvium.

Table 3.8. Sizes of subsidence craters left by nuclear explosions in alluvium

Expl. #	Explosion	Parameter							
		q, kt	W, m	$W/q^{1/3}$, m/kt$^{1/3}$	R, m	H, m	V, m^3	r_c, m	W/r_c
1	FISHER	12.4	364	157.3	78.6	15.2	$1.6 \cdot 10^5$	37.5	9.7
2	STOAT	4.7	302.6	180.6	58	2.1	$6.9 \cdot 10^3$	24.4	12.4
3	AGONTI	5.8	261.1	145.3	69	12.8	$7.6 \cdot 10^4$	36.0	7.2
4	STILLWATER	3.1	181.5	124.5	61.9	12.2	$5.6 \cdot 10^4$	24.7	7.3
5	ARMADILLO	6.5	240	128.6	68	11.3	$6.1 \cdot 10^4$	23.8	10.1
6	CHINCHILLA I	1.8	150	123.3	47.9	12.8	$2.3 \cdot 10^4$	17.1	8.8
7	CIMARRON	11.2	30.8	136.3	70.8	11	$5.6 \cdot 10^4$	32.6	9.3
8	BRAZOS	8.4	256.3	126.2	53.4	9.5	$3.3 \cdot 10^4$	27.7	9.2
9	DORMOUSE I	11	261.1	117.4	97.3	29.6	$2.3 \cdot 10^5$	34.7	7.5
10	HAYMAKER	46	408.7	114.1	136.7	31.4	$6 \cdot 10^5$	49.7-56.1	7.8
11	PAR	38	406	120.8	72.4	22	$3 \cdot 10^4$	48.8	8.3
12	PARROT	1.2	180	169.4	39.7	5.5	$1.1 \cdot 10^4$	14.6	12.3
13	MERLIN	10	296	137.4	77.8	16.8	$1.3 \cdot 10^5$	32.4*	9.1
14	PETREL	1.2	180.3	170.2	44.2	5.2	$7.3 \cdot 10^3$	18	10.1
15	CYCLAMEN	13	305	127.7	83.6	16.8	$1.2 \cdot 10^5$	2.8	10.9
16	VULCAN	25	322.4	110.3	80	23.5	$1.8 \cdot 10^5$	43.8*	7.4
17	POMMARD	1.4	209	186.8	44.2	2.1	$3.7 \cdot 10^3$	16.8*	12.4

Analysis of historical data shows that the subsidence craters stop forming when explosion sDOB exceeds 200 ± 15 m/kt$^{1/3}$ for alluvium, and 150 ± 15 m/kt$^{1/3}$ for tuff. Both of these values significantly exceed the minimally allowed depth needed to provide safe radiation conditions during nuclear tests. Table 3.8 shows the subsidence crater sizes as well as the parameters of the explosions with reported yields conducted in alluvium. Stars show the cavity

[6] It is not yet clear whether this is with reference to the BSSA, or to an event bulletin. We need to figure out this reference. Maybe, use Springer *et al.?*

radii calculated using Equation 2.28. The yields of these explosions do not exceed 50 kt due to insufficient thickness of alluvium layer, so explosions with higher yields were conducted in tuff. Comparison between the data from Table 3.8 and the empirical relationships 3.10 – 3.12 are shown in Figure 3.23. The lower curves in Figure 3.23 correspond to the crater radii given by (3.11), while the upper curves show the radii of broader subsidence areas as in (3.10). All data points corresponding to nuclear explosions are grouped around the curve given in (3.11). We substitute 2.28 into (3.11) and obtain a relationship for the radius of a subsidence crater as a function of yield and depth for an explosion in alluvium:

$$\frac{R}{W} = \frac{2.25W}{\sqrt{\frac{W}{q^{1/3}} - 3}}; \tag{3.14}$$

where R and W are in meters, and q is in kt.

The average deviation of the actual radius from the radius predicted using Equation 3.14 did not exceed 20%. Regarding the (broader) subsidence zone, there are data (Johnson and Higgins, 1965) based on high-precision topographic surveys, suggesting that nuclear explosions conducted in alluvium at Yucca Plain (NTS) produced subsidence of wide areas around subsidence craters.

Comparison of the depths of the subsidence craters between nuclear explosions in alluvium and data from laboratory experiments show that the data for nuclear explosions also agree with the relationship 3.12 predicted using experimental data, however the average deviation is approximately 50% (Figure 3.23 b). Substitution of (2.26) into (3.12) yields the relationship between the crater depth and the explosion yield and depth:

$$\frac{H}{W} = \frac{16.5q^{1/3}}{W} - 0.069\ . \tag{3.15}$$

where H and W are in meters, and q is in kt.

The volumes of the craters show even greater deviation from the laboratory experiments (Figure 3.23c). The results of laboratory experiments are shown as a solid line for the value of the dilation coefficient N = 1.03. Significant scatter for the field data is caused by variation in dilation in alluvium during formation of the subsidence craters. Numerous measurements have shown that for 90% of the nuclear explosions in alluvium the dilation coefficient varied in the range $0.96 \leq N \leq 1.1$ (Khakala, 1971). Dilation ($N > 1$) occurs in most cases (70%), while the remaining explosions result in rock compression.

It is easy to show that even small changes in density during rock collapse (or filling) into the cavity results in significant changes in the volume of the crater. Indeed, if we express the volume of the subsidence crater in terms of the cavity volume V_c and the volume of the chimney V_{ch}, we obtain:

$$V = V_c - \Delta V_{ch}, \text{ where } \Delta V_{ch} = V_{ch}(N-1),\ V_{ch} = \pi H_{ch} R_{ch}^2\ .$$

If we assume that $R_{ch} = 1.2\ r_c$ and $H_{ch} = W - r_c$, we obtain:

$$\frac{V}{V_c} = 1 - 1.08(N-1)\left(\frac{W}{r_c} - 1\right). \tag{3.16}$$

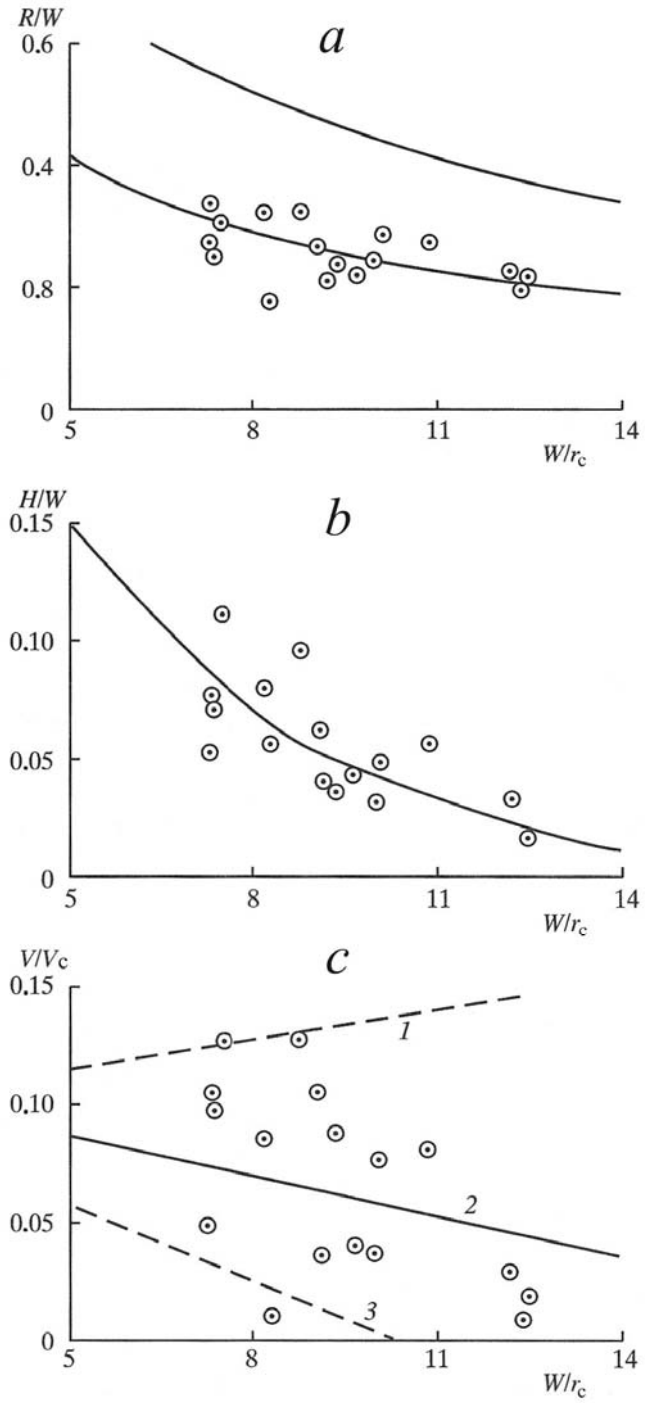

Figure 3.23: Comparison between the crater dimensions for explosions in alluvium (circles) and the model (solid line) for a) crater radius, b) depth, and c) volume. Lines correspond to different values of parameter *N*: *1* – 0.96; *2* – 1.03; *3* – 1.1.

Table 3.9. Craters sizes left by nuclear explosions in hard rocks at the NTS

Expl. #	Explosion	Rock type	Parameter						
			q, kt	W, m	$W/q^{1/3}$, m/kt$^{1/3}$	R, m	H, m	V, m^3	r_c, m
1	SULKY	Basalt	0.09	27.4	61.1	9.8	3.5	$3.5 \cdot 10^2$	4.7*
2	BLANCA	Tuff	19.2	255	95	150	18	–	40*
3	HOOSIC	“	3.4	187.3	124.6	44.8	6.1	$2 \cdot 10^4$	25.9
4	AARDVARK	“	38	434.3	131.5	125	22.9	$3 \cdot 10^5$	47.8
5	BILBI	“	235	715	115.9	224	26.5	$1.7 \cdot 10^7$	92.6*
6	MUDPAK	“	2.7	152	109.2	38.8	6.4	$1.4 \cdot 10^4$	23.2
7	DISCUS	“	21	337	122.2	145	20.4	$3 \cdot 10^5$	32.6
8	HALFBEAK	Rhyolite	313	820	120.8	198	10.7	–	76.2
9	BOXCAR	“	1300	1161	108.2	305	67.4	–	94.5
10	MILROW	Lava	1237	1200	118.8	305	4.6	$8.5 \cdot 10^5$	128*
11	CANNIKIN	“	3700	1800	116.4	800	18	–	182*

Table 3.10. Craters sizes left by nuclear explosions conducted in the USSR

Explosion	Rock type	Parameter				
		$W/q^{1/3}$, m/kt$^{1/3}$	R, m	H, m	V, m^3	r_c, m
“Krystall”	Limestone	82.1	50	5	10^4	14.6*
BH 1204	Tuff-sandstone	72	111	35.8	$4.2 \cdot 10^5$	51*
BH 1066	Granite	83.9	148	23	$4.5 \cdot 10^5$	54*
BH 1207	Shale (slate)	92.4	190	13	$3 \cdot 10^5$	48*
BH 104	Sandstone	98.8	69	8.2	$3.5 \cdot 10^4$	25.6*
BH 105	Aleurolite (shale)	106	47	2.8	$6.5 \cdot 10^4$	20*
BH 102	Sandstone	11.2	35	0.7	$9 \cdot 10^2$	19.6*
Tun. A-1	Shale (slate)	68.7	130-194	72.5	$1.5 \cdot 10^6$	105.6*
Tun. B-1	“	68.7	180-220	70	–	135*
Tun. A-2	“	72.5	112-120	25.9	$8.8 \cdot 10^5$	82*
Tun. A-4	“	75.3	120-129	37	$5.5 \cdot 10^5$	58*
6T	Chalk	112.1	240-260	12.5	$7 \cdot 10^5$	66*
2T	“	128.7	140-150	15	$2.5 \cdot 10^5$	46*

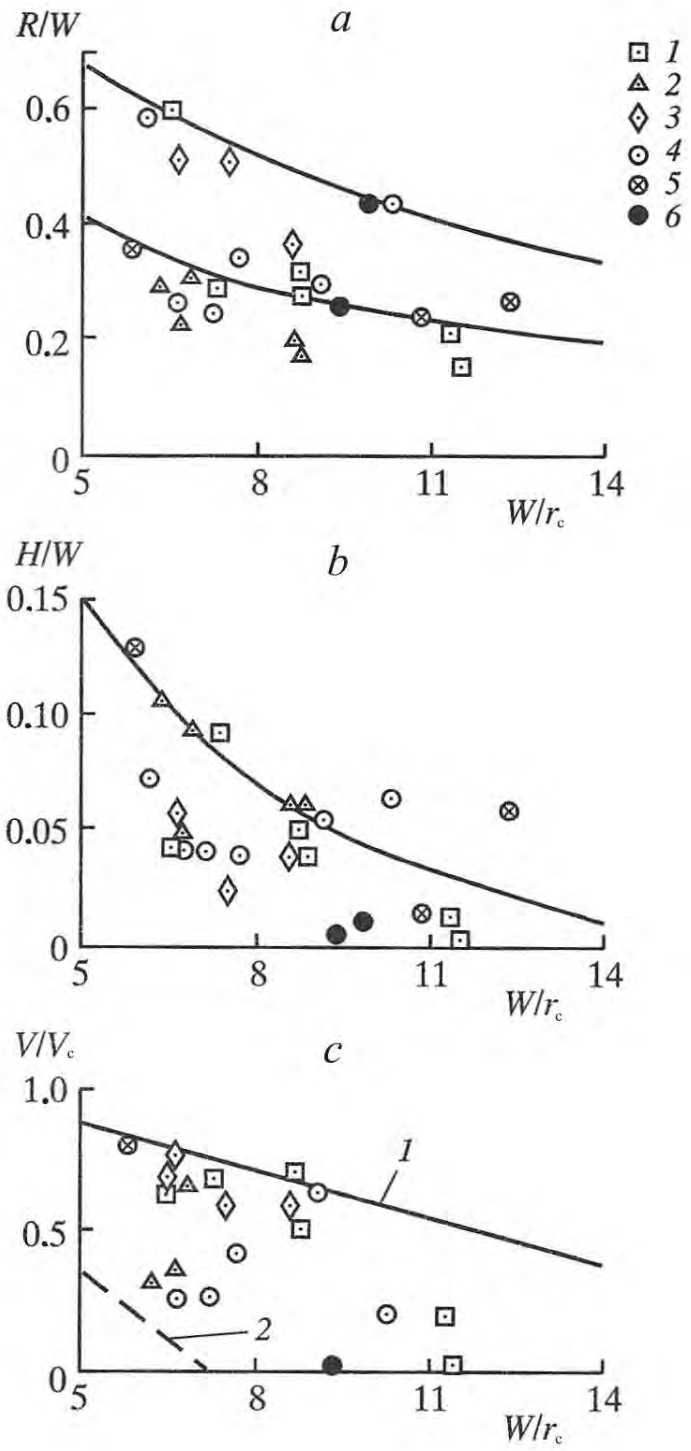

Figure 3.24: Comparison between the crater dimensions for explosions in hard rock (circles) and the model (solid line) for a) crater radius, b) depth, and c) volume, shown for experiments using symbols: *1* – borehole tests at the STS; *2* – shale; *3* – chalk, limestone; *4* – tuff; *5* – rhyolite; *6* – lava. Lines *1* and *2* are same as in Figure 3.23.

The results of calculations using Equation 3.16 are shown in Figure 3.23c as dashed lines for the values of N equal to 1.1 and 0.96. Most of the data points plot between these lines. Subsidence craters form sometimes during explosions in hard rocks, particularly for explosions with large yields. We analyze the data for the sizes of the subsidence craters formed by nuclear explosions in hard rock conducted at the NTS and Amchitka (Table 3.9), as well as the STS and NZTS (Table 3.10). In cases where the subsidence craters formed on top of the uplift (e.g. NTS basalts, Balapan) the crater sizes are measured at the crater rim. For explosions at the NZTS, where the craters are located on mountain slopes, the explosion depth in Table 3.10 is shown along the vertical line (with respect to the ground zero).

The calculated cavity radii are marked with stars. Compared to explosions in alluvium, formation of craters in hard occurs for smaller values of sDOB, namely $60 \le W/q^{1/3} \le 120$ $m/kt^{1/3}$. The sizes of the subsidence craters from Tables 3.9 and 3.10 are compared in Figure 3.24 with the empirical (model) relationships 3.10 – 3.12. The lower curve in Figure 3.24a corresponds to a radius of a subsidence crater according to (3.11), the upper curve – to a radius of the subsidence zone according to (3.10). Most of the nuclear explosion data points (19 out of 25) are grouped around the line corresponding to Equation 3.11. Therefore the radius of the subsidence crater can be represented as a function of the explosion yield and depth as:

$$R = \frac{0.58W}{\sqrt{\frac{W}{r_c q^{1/3}}} - 0.77}; \tag{3.17}$$

where r_c and W are in meters, q is in kt, the cavity radius r_c is determined using the rock properties around the charge according to Equations 2.26 and 2.28. The average deviation between the measured and the estimated radii is 30%. For the remaining 6 explosions, including the explosions with the highest yield, the crater radii corresponded to the larger subsidence zone. Therefore in some cases even explosions in hard rock create broad subsidence zones, whose radius can be estimated as a function of the event yield and depth as:

$$R = \frac{5.9W}{\frac{W}{r_c q^{1/3}} + 3.48}; \tag{3.18}$$

where r_c and W are in meters, q is in kt.

The characteristics of the subsidence zone were confirmed by the following observations from the NTS nuclear tests (Houser, 1969):

- Subsidence zones are formed around collapse craters with the radii reaching two radii of the subsidence craters.
- The subsidence zones are formed before the crater collapse.
- For nuclear explosions with intermediate yields (20 – 200 kt) in tuff the volume of the subsidence zones are 50% of the volume of the craters.

Comparison between the depths of the subsidence craters (Table 3.9 and 3.10) with the empirical formula 3.12 (shown in Figure 3.24 b as a solid line) shows that approximately half of

the data points agrees with 3.12, while the other half plot systematically below the curve. Taking this into account we rewrite the relationship for the depth of the subsidence crater (3.12) in a form: (notice that the coefficient is 11 here and 1.1 in 3.12)

$$H = 11\bar{r}_c - 0.069W\ . \tag{3.19}$$

The average deviation between the field observations and Equation 3.19 is 100%.

The observed volumes of the subsidence craters also show significant scatter as shown in Figure 3.24c. However unlike explosions in alluvium all data points for hard rock plot below the curve with $N = 1.03$. This observation shows that only dilation (volume increase) is observed during crater formation in hard rock. The scatter in the data is caused by different degree of material dilation as it collapses into a cavity. Thus an estimate using 3.16 shows that the scatter of the volumes of the craters can be explained by the coefficient of dilation in the range $1.03 \leq N \leq 1.15$.

Thus the data analysis shows that of all measurements of the subsidence craters only their radius has a robust relationship with the yield and depth of explosion. The depth and the volume of the subsidence craters are significantly affected by the dilation processes during rock damage/fragmentation.

3.5. Using the size of collapse craters to estimate yields of nuclear explosions

Using the size of a collapse crater to determine the yield of an underground explosion is of practical interest. This interest is related to periodic satellite imagery of the nuclear test areas. For instance, photos of the Nevada Test Site acquired from satellites show that the number of the collapse craters in the Yucca Flat area significantly exceed the number of reported underground nuclear explosions[7]. Satellite imagery can also detect preparations for nuclear experiments, formation of new subsidence craters and changes of topography caused by nuclear explosions in horizontal tunnels (adits).

Thus satellite imagery can provide an effective method of monitoring the underground testing, which can significantly add to the seismological methods. The combined use of the seismological and satellite methods of detection allows a more precise determination of the main parameters of nuclear explosions, including the detonation time, coordinates, and the explosive yield.

Based on Equations 3.14 – 3.19 and analysis of the conduct of nuclear explosions a method to determine the yield of the explosions was developed for three different scenarios:

- both the radius of the collapse crater and the depth of burial are known;
- only the crater radius is known;

[7] Some UNEs at the Nevada Test Site were not reported at the time of the test. A complete reporting was eventually made in the early 1990s. (Note added by translators.)

- only the depth of burial is known (based on the length of the cable that can be seen on the photograph from space).

In the first case it follows from Equation 3.17 that the explosive yield is:

$$q = \left[\frac{W}{\bar{r}_c\left(\frac{0.58W}{R}+0.77\right)^2}\right]^3 \text{(kt)}\,, \tag{3.20}$$

where W and R are the charge depth and radius of the collapse crater in meters, the cavity radius is r_c = 15 m/kt$^{1/3}$ for alluvium and tuff, r_c = 7-9 m/kt$^{1/3}$ for dry hard rock, and r_c = 10-12 m/kt$^{1/3}$ for softer rock or rocks with high gas content. Equation 3.20 should be used only when the actual radius of the collapse crater is known, in which case $R \leq 0.4W$ (Figure 3.23 and 3.24). If $R > 0.4W$ then instead of the collapse crater the measured parameter is the radius of the subsidence zone R_{sub}. In this case according to Equation 3.18:

$$q = \left[\frac{W}{\bar{r}_c\left(\frac{5.9W}{R_{sub}}-3.48\right)^2}\right]^3 \text{(kt)}\,, \tag{3.21}$$

where W and R are in meters.

In some cases the radius of the collapse crater is $R < 0.15W$. In this case using Equation 3.20 would lead to significant underestimation of the yield, which would contradict the condition that the collapse crater forms in alluvium if $W/q^{1/3} < 200$ m/kt$^{1/3}$. Therefore in cases when $R < 0.15W$ only one of the parameters (either radius of the crater or the depth of burial) with better *a priori* knowledge should be used.

In the second scenario when the radius of the crater is known, the depth of burial can be estimated. Based on the evidence of 20 explosions in alluvium and tuff with known yield and depth of burial (Tables 3.8 and 3.9) [at least one of these yields seems to be wrong] the average scaled depth of burial was calculated as $W/q^{1/3}$ = 126.7 m/kt$^{1/3}$. Substitution of this relationship into (3.20) and using r_c = 15 m/kt$^{1/3}$ we obtain:

$$q = 24.56 \cdot 10^{-6} R^3 \text{ (kt)}\,, \tag{3.22}$$

where R is in meters.

In the third scenario when the depth of burial is known but a collapse crater is not formed, the expression for the yield based on the average depth of burial is given by:

$$q = 49.1 \cdot 10^{-8} W^3 \text{ (kt)}\,, \tag{3.23}$$

where W is in meters.

However the absence of a collapse crater in alluvium or tuff is very improbable. If it occurs, it may be related to some anomalous features of the geological structure of the test site. Another reason for the absence of a crater is significant reduction of the design yield of the explosion (a

fizzle). In this case one can use a condition that collapse craters do not form if $W/q^{1/3} \geq 200$ m/kt$^{1/3}$ in alluvium, and if $W/q^{1/3} \geq 150$ m/kt$^{1/3}$ in tuff. Using this constraint we estimate that for given depth of burial the yield cannot exceed:

$$\text{in alluvium } q \leq 12.5 \cdot 10^{-8} W^3 \text{ (kt)}, \quad \text{in tuff } \quad q \leq 29.6 \cdot 10^{-8} W^3 \text{ (kt)}, \qquad (3.24)$$

where W is in meters.

Using explosions with known parameters for alluvium and tuff (Table 3.8 and 3.9) we estimate yield using equations 3.20 – 3.24. The error estimate shows that the standard deviation of the error is $\sigma = 1.5 - 2.4$. Table 3.11 shows examples of yield estimates using satellite imagery data for one of the areas of the Yucca Flat at the Nevada Test Site.

We determined yields for nine of the explosions using equation (3.20), because both the radius of the crater and the depth of burial were known. For one explosion $R > 0.4W$, therefore equation (3.21) was used. For another explosion the radius was $R < 0.15W$, therefore we used equation (3.23). Equation (3.23) was also used to estimate yields for tests #5 and #13, because there was significant deformation in the epicentral areas without well-defined craters. For tests #4 and #6 the yields were determined using equation (3.22). Tests #9, #14, and #15 did not produce any changes to the earth surface, therefore equations (3.24) – (3.24) were used. To summarize, analysis of the satellite survey data shows that equations (3.20) – (3.24) allow us to make yield estimates for nuclear tests conducted at the Nevada Test Site in alluvium and tuff.

Table 3.11. Explosion yields calculated using subsidence crater sizes and cable lengths

Expl. #	Parameter			
	R, m	*W*, m	*R/W*	*q*, kt
1	63 x 32	130	0.48 – 0.25	0.8 –2.5
2	72	225	0.32	8.2
3	60	200	0.3	4.8
4	32	–	–	0.8
5	–	120	–	0.85
6	23	–	–	0.3
7	22	120	0.18	0.25
8	46	290	0.16	11.3
9	–	520	–	42 – 69
10	35	320	0.11	16.1
11	51	250	0.2	3
12	189	530	0.36	151
13	–	150	–	1.7
14	–	200	–	1 – 3.9
15	–	250	–	2 – 7.7
16	60	220	0.27	4.8

3.6. Retarc/mound sizes

Partially contained explosions in hard rock create uplifts (mounds/retarcs) on the earth surface due dome collapse. The mounds are formed due to dilation of broken/damaged rocks in the spall area, chimney and the damage cone. Size of each zone, their role in the uplifted volume, and the degree of dilation (volume change or bulking) (in each zone) depend on the scaled DOB.

The effect of the sDOB on development (transformation) of each zone and rock dilation during partially confined explosions is shown in Figure 3.25. For shallow explosions in this range (Figure 3.25) the rock damage and bulking occurs in the spall zone and in the damage (ejection) cone. Increase in DOB causes the increase in the chimney height, the geometry of the ejection cone changes and the size of the spall zone increases (Figure 3.25b). For deeper explosions within this range (close to fully contained) rock dilation occurs mainly within the chimney and the spall zone, while the ejection cone is practically absent. A subsidence crater forms in the epicentral zone of the uplift (Figure 3.25c).

In general the initial volume V_i involved in dilation during partially contained explosions can be expressed as a sum of the volume in the spall zone V_{sp}, the chimney zone V_{ch} and the ejection cone V_{cone}:

$$V_i = V_{sp} + V_{ch} + V_{cone} . \tag{3.25}$$

A spall zone formed due to reflection of pressure wave from the flat free surface has a shape of a segment of a sphere. The curvature radius R_{sp} for the reflected wave and the depth of the spall surface H_{sp} are (given by):

$$R_{sp} = \mathrm{W} + H_{sp} , H_{sp} = C_p\tau_+ /2, \tag{3.26}$$

where C_p is the wave velocity and τ_+ is the duration of compression phase. Then the volume of the spall damage zone is:

$$V_{sp} = \pi H_{sp}^2 (R_{sp} - 0.33H_{sp}) = \pi H_{sp}^2 (W + 0.66H_{sp}) \tag{3.27}$$

We express the volume of the chimney using its radius R_{ch}, height H_{ch} and the cavity volume V_c:

$$V_{ch} = \pi R_{ch}^2 H_{ch} - V_c/2 . \tag{3.28}$$

The ejected volume in the upper part of the chimney is shaped as a funnel (cone) with a height $H_{cone} = W - H_{ch}$. The radius of the lower base of the cone is equal to the chimney radius. The radius of the upper base is equal to the radius of the crater, which changes from the radius of the ejection crater to the radius of the subsidence crater according to Equation 3.13. The initial volume of the ejection cone in the upper part of the chimney is:

$$V_{cone} = \frac{\pi(W-H_{ch})}{3} (R_{cone}^2 + R_{cone} \cdot R_{ch} + R_{ch}^2) . \tag{3.29}$$

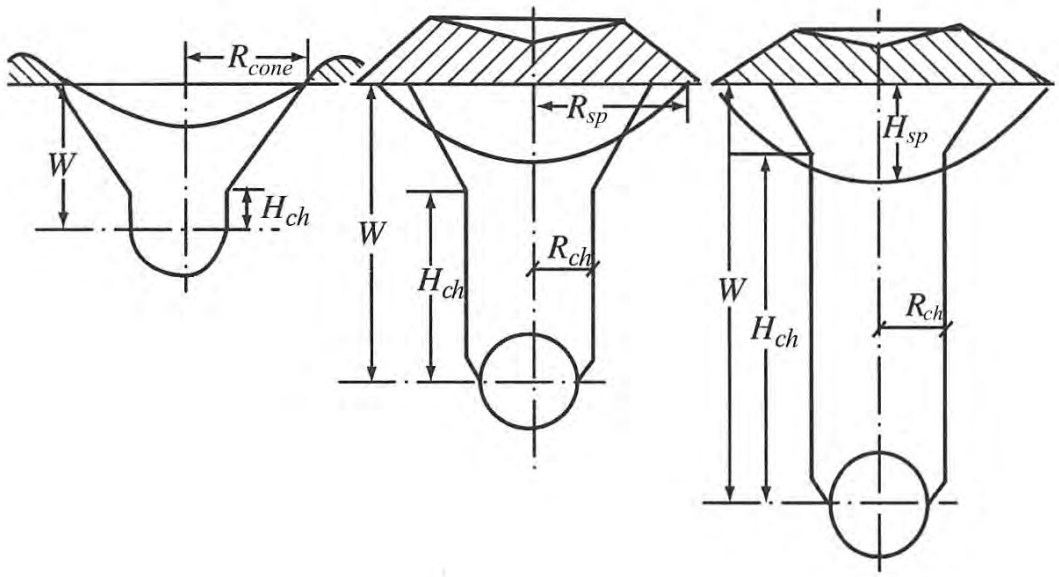

Figure 3.25: Transformation of major zones of material movement with the increase in doepth of burial for partially contained explosions.

The material in each zone is subjected to dilation (bulking) during the explosive motion. After the explosion the volume of each zone increases and becomes equal to the initial volume multiplied by the corresponding dilation (bulking) coefficient defined as the ratio between the initial and final densities. Therefore the volume of the mound/retarc is defined as a difference between the final and the initial volumes of rock in each zone:

$$V_x = V_{sp}\,(N_{sp}\,\text{-}1) + V_{ch}\,(N_{ch}\,\text{-}1) + V_{cone}\,(N_{cone}\,\text{-}1) - V_c\,, \tag{3.30}$$

where N_{sp}, N_{ch}, N_{cone} - are the bulking coefficients for each zone, and V_c is the cavity volume. The input from each zone into the final size of the retarc depends on the sDOB of explosion. Two limiting cases can be selected. For shallow explosion close to the ejection explosion limit (Figure 3.25a) in case the spall zone is inside of the ejection crater () the final volume of the mound is:

$$V_x = \frac{\pi(W-H_{ch})}{3}\,(R_{cone}^2 + R_{cone}R_{ch} + R_{ch}^2)(N_{cone}-1) + \left(\pi R_{ch}^2 H_{ch} - \frac{V_c}{2}\right)(N_{ch}-1) - V_c. \tag{3.31}$$

In this case the height of the chimney is small, and only the cavity volume should be taken into account. In the other case close to fully contained explosion limit (Figure 3.25c) the ejection cone is absent and assuming $H_{sp} \geq W - H_{cone}$ the uplift volume is:

$$V_x = (N_{sp}-1)\frac{\pi H_{sp}^2(3W+2H_{sp})}{3} + (N_{ch}-1)\left(\pi R_{ch}^2 H_{ch} - \frac{V_c}{2}\right) - V_c. \tag{3.32}$$

Table 3.12. Explosion characteristics

Explosion	Rock type	Parameter					
		q, kt	W, m	ρ_i, g/cm^3	ρ_i, g/cm^3	N	h_f, m
DANNY BOY	Basalt	0.42	33.5	2.47	1.8	1.37	33.5
SULKY	Basalt	0.09	27.4	2.5	1.8	1.38	17.5
CABIOLET	Rhyolite	2.3	52	2.5	2.0	1.25	52
PILEDRIVER	Granite	61	463.5	2.5	2.15	1.16	80
HARDHAT	“	5.4	268.4	2.4	1.97	1.22	40
HANDCAR	Dolomite	12	402.5	2.2	2.0	1.10	42
BH 1004	Sandstone	140	175	2.56	2.3	1.11	175
BH T-1	Argillite (shale)	0.24	31.4	2.4	1.8	1.33	31.4
“Baipaza”	Ryolite	1.86	30-60	2.56	2.19	1.17	100
“Medeo”	Granite	5.3	50-80	2.65	2.13	1.25	80
“Burlykiya”	“	0.7	15-45	2.6	1.87	1.39	40
Pre-Schooner I	Basalt	0.02	15	2.38	1.6	1.49	15
Pre-Schooner I	Ryolite	0.05	17	2.23	1.59	1.4	17
“Pre-Gondola”	Shale	0.02	15	1.93	1.05	1.17	15

In general case when $R_{sp} > R_{cone}$ and $H_{sp} < W - H_{cone}$ the volume of the uplift should be calculated using Equation 3.30. Linear dimensions of the retarc can be determined using geometrical relationships. The radius of the upper part of the mound is equal to the radius of the subsidence crater or the radius of the ejection cone and can be calculated using 3.11 – 3.13. Radius of the base of the mound R_x is determined by the size of the spall zone, however it is at least twice as big as the crater radius because of the rocks falling down during subsidence. As a result, the radius of the base of the mound (the outer radius) and the height of the mound are determined using the relationships:

$$R_x = R_{sp}, \quad H_x = \frac{3V_x}{\pi\left(R_{sp}^2 + R_{sp}R_{cone} + R_{cone}^2\right)} \text{ for } R_{sp} \geq 2R_{cone}, \tag{3.33}$$

$$R_x = 2R_{cone}, \quad H_x = \frac{3V_x}{7\pi R_{cone}^2} \text{ for } R_{sp} < 2R_{cone}\,.$$

To determine bulking coefficients for rocks in these zones we used data related to the properties of rock piles (mounds) formed by nuclear and large chemical explosions (Adushkin et al, 1977; Brooks and Anderson, 1970).

Table 3.12 shows the initial ρ_i and final ρ_f density of the exploded rock, height of the free fall h_f, bulking coefficient N. Also shown are rock types and the explosion yield. First eight explosions had nuclear sources, the remaining had chemical sources. In addition to the properties of the rock mounds formed by cratering explosions (#1, 3, 7, and 8) and by the explosions conducted for moving the fragments down the hill (#9 – 11), Table 3.12 also shows the properties for the material in the chimneys for the fully contained explosions (#4 – 6). Analysis

of the measurement on bulking data shows that the height of free fall is the major factor in determining its final density. The final density as a function of the free fall height is shown in Figure 3.26.

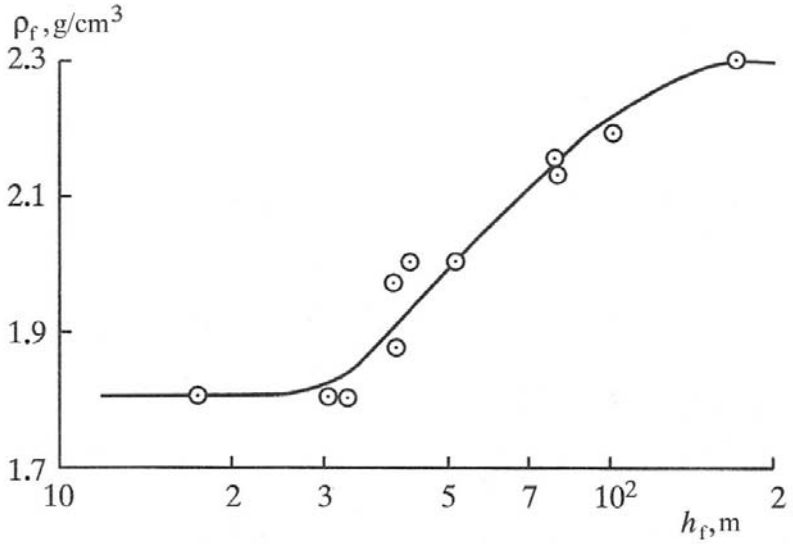

Figure 3.26: Final density of the fragmented rock mass as a function of height of the free fall.

For cratering explosions the height of the flying debris is approximately equal to the depth of burial (so that the ejection index *n*, as defined in Section 2.1, is about 1). For partially contained explosions it is approximately half of the maximum height of the dome. During chimney formation for the fully contained explosions the free fall is equal to the explosive cavity diameter. According to Figure 3.26 for height of the fall less than 30 m the density is minimal – 1.8 g/cm^3, if the height is greater than 150 m, the density reaches its maximum – 2.3 g/cm^3, in the range between 30 and 150 m the final density is determined using the relationship:

$$\rho_f = 0.62 + 0.8 \lg h_f \ (\text{g/cm}^3) \quad \text{for } 30 \text{ m} \le h_f \le 150 \text{ m}. \tag{3.34}$$

Existence of the limiting density of the rock mounds corresponds to a well-known terminal velocity due to resistance from air (up to 60 – 70 m/s after 150 – 200 m of acceleration). Therefore the main factor determining the final density of the mound is the dynamic compression of the rock mass and additional fragmentation due to fragment (particle) collisions. In this case the initial density of the material becomes unimportant and the final density depends only on the height of the fall. It follows from Equation 3.34 that with increase in the explosion yield the density of the mound also increases. Therefore the main geotechnical properties of the mounds (porosity, fragment sizes, permeability) will also improve. The fragmentation results become stable for cratering explosions with yield greater than 100 kt, and for the explosions detonated on inclined surfaces this achieved if the height of the fall is greater than 150 – 200 m.

Using these results the value of the bulking coefficient can be expressed as a function of the initial density of rock and the height of the fall as:

$$N = \begin{cases} \frac{\rho_i}{2.3} & \text{for } h_f \geq 150 \text{ m} \\ \rho_i(0.62 + 0.8 \lg h_f)^{-1} & \text{for } 30 \text{ m} \leq h_f \leq 150 \text{ m} \\ \frac{\rho_i}{1.8} & \text{for } h_f \leq 30 \text{ m} \end{cases} \quad (3.35)$$

For each zone defined above, the height of the fall is different, therefore the value of the bulking coefficient will vary between the zones according to the height of the free fall. Thus in the spall zone the velocity of the rocks changes from the maximum at the surface to zero at the spall depth. Therefore the rise of the spall zone corresponds to the increase in thickness. During this process multiple spall fractures open, rock fragments turn and therefore the entire layer dilates (becomes less dense).

After slap-down of the spall layer the bulking coefficient in the layer will depend only on the height of uplift of each individual (internal) layer. Starting from a certain height each part of the spall layer get an opportunity to turn, and it reaches maximum dilation. In order for each piece to be able to turn by 45° the thickness of the spall layer should increase by a factor of $\sqrt{2}$ and the maximum height of the dome rise should be $h_m \geq (\sqrt{2} - 1)H_{sp} \approx 0.4H_{sp}$.

For partially contained explosion the gas support (that is, the added gas-driven acceleration discussed earlier) is weak and the height to which spall rises is $h_f = v_i^2/2g$, where v_i is the initial velocity of the uplift of the free surface. Depending on the rock type this velocity varies in the range $v_0 \leq v_i \leq 2v_0$, where v_0 is the maximum velocity in the compression wave (1.8). Assuming the bulking coefficient for spall zone $N_{sp} = 1$ if no uplift takes place and $N_{sp} = N$ for $h_f = 0.4\ N_{sp}$ and that it changes quadratically in the intermediate zone, we obtain the expression for the bulking coefficient in the spall zone:

$$N = \begin{cases} N, & \text{for } h_f \geq 0.4\ N_{sp} \\ 1 + (N-1)\frac{h}{h_f}, & \text{for } h_f < 0.4\ N_{sp} \end{cases}, \quad (3.36)$$

where N depends on the initial density and rock fall height according to (3.35), and $h_f = h_m/2$.

The bulking coefficient in the chimney depends on the size of the explosive cavity (r_c) according to:

$$N_{ch} = \begin{cases} \frac{\rho_i}{2.3} & \text{for } r_c \geq 75 \text{ m} \\ \rho_i(0.62 + 0.8 \lg h_f)^{-1} & \text{for } 15 \text{ m} \leq r_c \leq 75 \text{ m} \\ \frac{\rho_i}{1.8} & \text{for } r_c \leq 15 \text{ m} \end{cases} \quad (3.37)$$

The bulking coefficient in the ejection cone depends on the size of the height of free fall, which we assume equal to the depth of the cone:

$$N_{cone} = \begin{cases} \frac{\rho_i}{2.3} & \text{for } W - h_{ch} \geq 150 \text{ m} \\ \rho_i(0.62 + 0.8 \lg(W - H_{ch}))^{-1} & \text{for } 30 \text{ m} \leq W - h_{ch} \leq 150 \text{ m} \\ \frac{\rho_i}{1.8} & \text{for } W - h_{ch} \leq 30 \text{ m} \end{cases} \quad (3.38)$$

If we know the bulking coefficients and determine the volumes of the main zones via (3.27) – (3.29), the volume of the retarc/uplift/mound can be determined using relationships (3.30) – (3.32), and its linear dimensions using (3.33). Thus in order to estimate the dimensions of the retarc we need to know the yield q and the depth W of the explosion q determining its scale, as well as the initial density of rock, P-wave velocity C_p, strength σ_* and gas content η of rock around the charge. These parameters determine the cavity size r_c and work of the cavity gas A. In addition we need to know the parameters of the pressure wave: particle v_0 or initial v_i velocities and the duration of the positive (compression) phase τ_+.

Using this approach the volumes of the retarcs/mounds formed by nuclear tests “Krystall” and SULKY were calculated. The parameters used in these calculations are shown in Table 3.13.

Table 3.13. Explosion parameters and rock properties

Explosion	Parameter							
	q, kt	W, m	ρ_i, g/cm^3	C_p, m/s	$\bar{r}_c$, m/kt$^{1/3}$	v_i, m/s	τ_+, ms	η
“Krystall”	1.7	98	2.22	3500	12.2	5.2	23	0.43
SULKY	0.09	27.4	2.6	4000	10.5	1.4	10	0

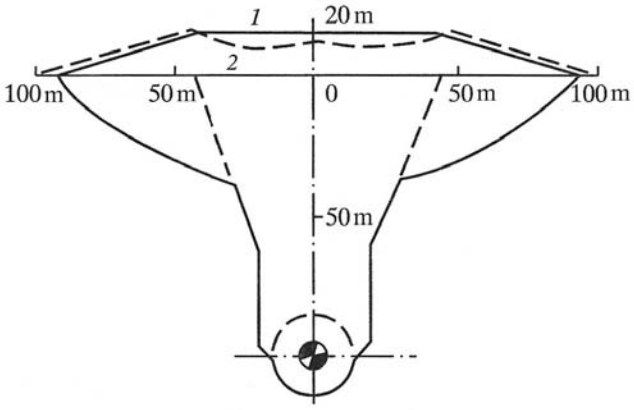

Figure 3.27: Comparison between the calculated (line *1*) and observed (line *2*) dimensions of the retarc/mound created by “Krystall”.

The geometry of the uplift and the sizes of the major zones for “Krystall” are shown in Figure 3.27. As it turns out, a wide spall zone was formed during the explosion with a radius R_{sp} = 96m and a depth H_{sp} = 40 m. The height and the radius of the formed chimney were H_{ch} = 32m and R_{ch} = 17.7 m respectively. The depth and radius of the ejection crater were $H_{cone} = W - H_{ch}$ = 66m and R_{cone} = 47m.Therefore the uplift formed by “Krystall” was formed as a result of dilation

in all main zones: in the spall zone with N_{sp} = 1.34, in the chimney with N_{ch}=1.36, and in the ejection crater with N_{cone}=1.18. Therefore the volume of the crater was calculated using Equation 3.30.

According to calculations for SULKY, the chimney is practically absent, and the uplift was formed mainly by rock dilation in the spall zone with thickness of approximately 20 m and radius of approximately 47m. The value of the bulking coefficient in the spall zone is N_{sp} = 1.54. Inside of the spall zone there is an ejection crater with a radius of 15m, with the height of the dome uplift of 35 m, and the bulking coefficient in the ejection cone is N_{cone} is 1.47. Comparison of the calculation results with the measure data are shown in Table 3.14.

Table 3.14. Explosion parameters and comparison between the observations and calculations

Explosion	V_x, m (m^3 ?)	H_x, m	R_x, m
"Krystall"			
Observations	$1.6 \cdot 10^5$	11	100
Calculations	$1.9 \cdot 10^5$	12.1	96
SULKY			
Observations	$8.8 \cdot 10^3$	6.3	45
Calculations	$17 \cdot 10^3$	8.0	47

The deviation of the calculated retarc dimensions from measured for "Krystall" are 10 – 20 %. For SULKY the estimated values are higher than the observed (5 – 30 % for linear dimensions and 90% for the volume).

Using this approach, the heights and volumes of the retarcs were estimated as a function of the explosion yield and depth in competent granite (ρ=2.67 g/cm^3, C_p = 5200 m/s, $\sigma_* = 2000\ kgf/cm^2$, $\bar{r}_c = 8.8$ m/kt$^{1/3}$, η_ω=0.01) and in hard rock similar to shale (ρ=2.5 g/cm^3, C_p = 4000 m/s, $\sigma_* = 700\ kgf/cm^2$, $\bar{r}_c = 12$ m/kt$^{1/3}$, η_ω = 0.12, $\eta_\omega = \eta_{CO2}$). The computed results are shown in Figure 3.28. Explosion yields varied from 1 to 1000 kt. The results show that for each yield there is a characteristic depth which maximizes the retarc size. The scaled value of depth corresponding to this depth decreases with with yield increase. For example the change in yield from 1 to 10^2 kt the normalized height and volume of the retarc in hard rock decreases from $H_x = (0.2 – 0.3)W$ and $V_x/q = (2 – 4) \cdot 10^5$ m^3/kt to $H_x = (0.1 – 0.15)W$ and $V_x/q = (3 – 6) \cdot 10^5$ m^3/kt, while the scaled depth of burial decreases from 65 – 75 to 45 – 50 m/kt$^{1/3}$.

This decrease in relative sizes of the retarcs and the scaled DOB which maximize the retarc size is related to the effects of gravity. The scaled sizes of the major zones participating in dilation decrease due to gravity. Therefore, with an increase in the explosion yield for partially confined explosions the range in which the scaled depth changes becomes narrower and the scaled depth maximizing the retarc size becomes smaller.

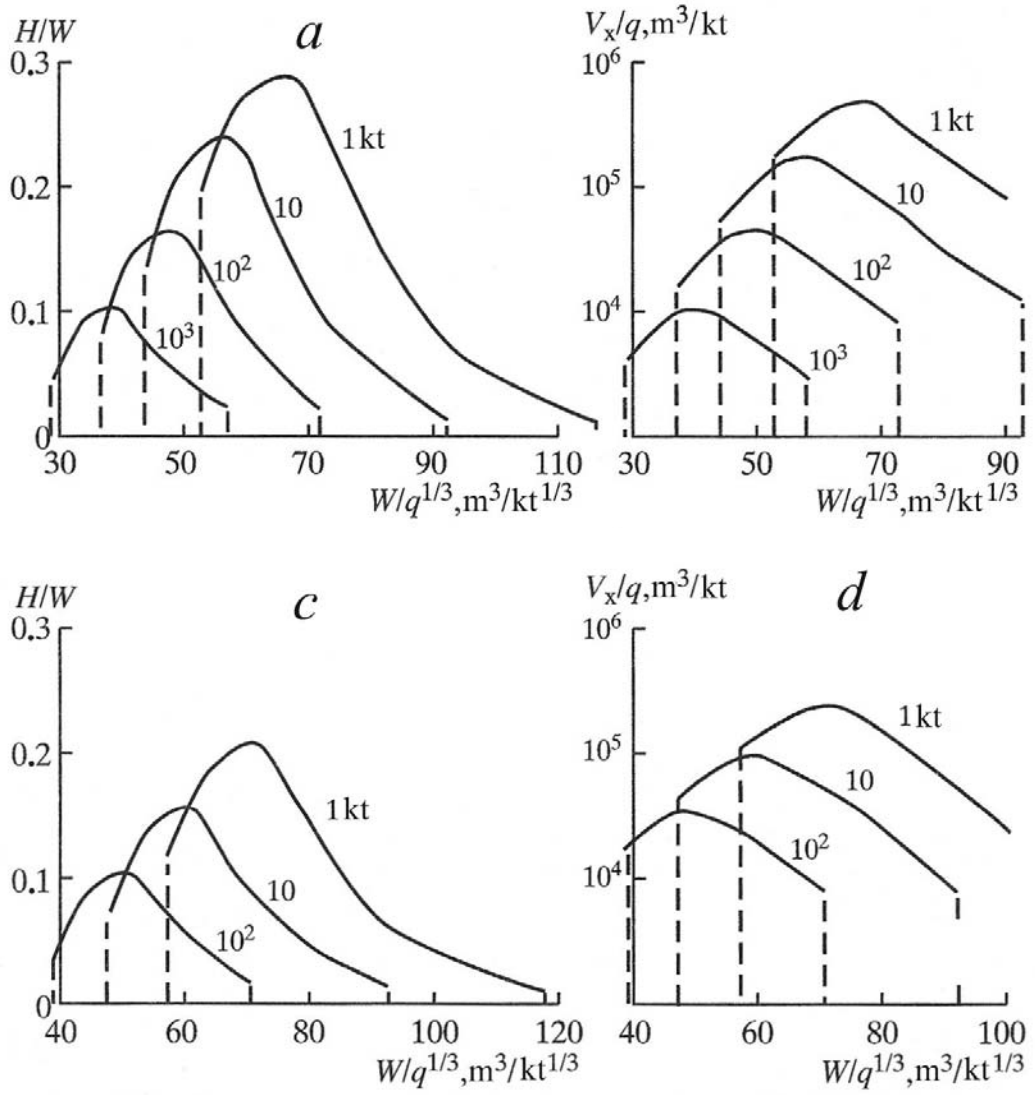

Figure 3.28: Effect of the explosion yield on the mound/retarc size for partially contained explosions in hard granite (*a, b*) and aleurolite (shale) (*c,d*). Explosion yields (in kt) are shown next to the lines.

The reduction in the bulking coefficient due to increase in height of the chimney and the dome uplift also leads to a reduction in the relative (scaled) retarc sizes. Thus an increase in yield from 1 to 10 kt causes the increase in the maximum retarc height from 20 to 35 m in very dense rock (e.g. granite) and from 10 to 20 m in less dense rocks (e.g. shale). However further increase in yield does not produce any further increase the increase in retarc height, and it is very difficult to create a retarc higher than 40m.

In addition to effects of yield and depth of explosion on retarc dimensions, we also studied the effect of the explosive cavity, gas content and elastic properties of rocks. For the sake of illustration the calculations were conducted for a nuclear explosion in granite, and each parameter varied in the allowed range while other properties were fixed. It turns out that the

effect of cavity size is insignificant: the change from 7 to 14 m/kt$^{1/3}$ leads to only 10% decrease in height. Rock gas content also has no significant effect on the retarc sizes.

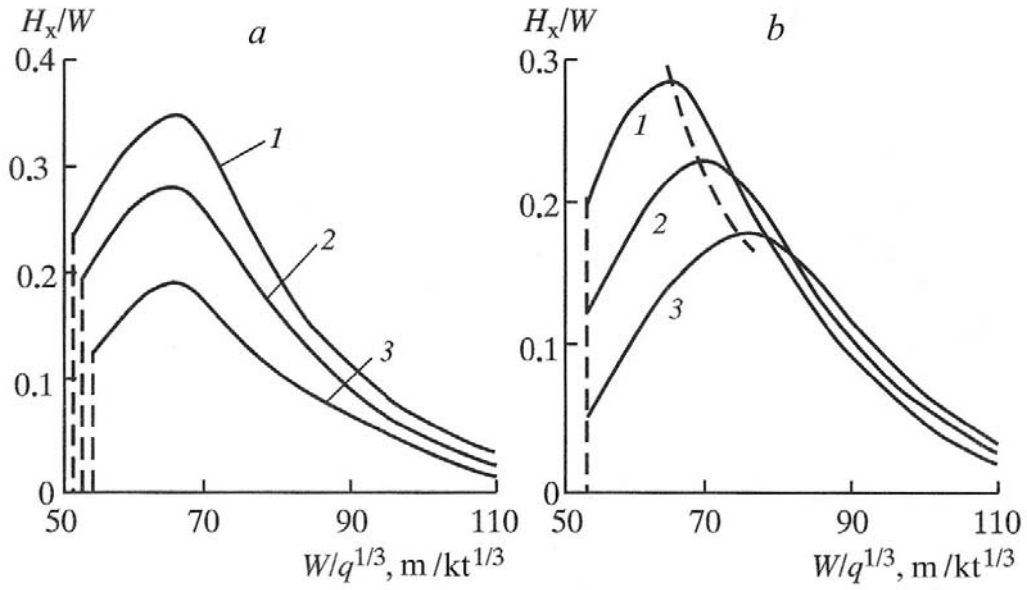

Figure 3.29: a) Effect of rock density on mound/retarc height for 1 kt explosion in hard granite for the following values of density in kg/m^3: 1 – 2800; 2 – 2670; 3 – 2400. a) Effect of rock P-wave velocity on mound/retarc height for 1 kt explosion in hard granite for the following values of velocity in km/s: 1 – 5.2; 2 – 4.2; 3 – 3.2.

The initial density of rocks (Figure 3.29 a) and *P*-wave velocity (Figure 3.29 b) have the most significant effect on the retarc sizes. For example, change in granite density from 2.4 g/cm3 to 2.8 g/cm3 caused an increase in the hill height by a factor of 1.5 – 2. The scaled DOB maximizing the height did not change. Seismic velocities also significantly affect retarc sizes. For instance decrease in velocity causes a decrease in the retarc height, while the scaled DOB maximizing the retarc size increased. It follows from these calculations that the reduction in the retarc size in shale compared to granite resulted not only from reduction in the initial density, but also from reduction in seismic velocity and increase in the cavity size.

3.7.Venting times for cavity gas

It was shown in Section 3.3 that the empirical relationship (3.9) provides adequate estimates of the venting times for nuclear explosions based on field measurements. Substituting equation (3.3) for A and W/r_c as well as other dimensionless parameters into equation (3.9) we obtain an expression for the venting time of cavity gas for fully contained explosions:

$$\frac{t_0}{q^{1/3}} = 9.3 \cdot 10^{-3} \frac{\gamma^{0.5}(\bar{r_c})^{1.7}(\gamma W+10)^{0.7}}{\left(1+5.8\eta_g^{0.7}\right)^{1.2}} \left(\frac{W}{q^{1/3}}\right)^{3.9}, \qquad (3.39)$$

where t_0 is in seconds, q is yield in kt, γ is rock density in g/cm^3, $\overline{r_c}$ is scaled cavity radius in m/kt$^{1/3}$, η_g is the mass fraction of each gas component.

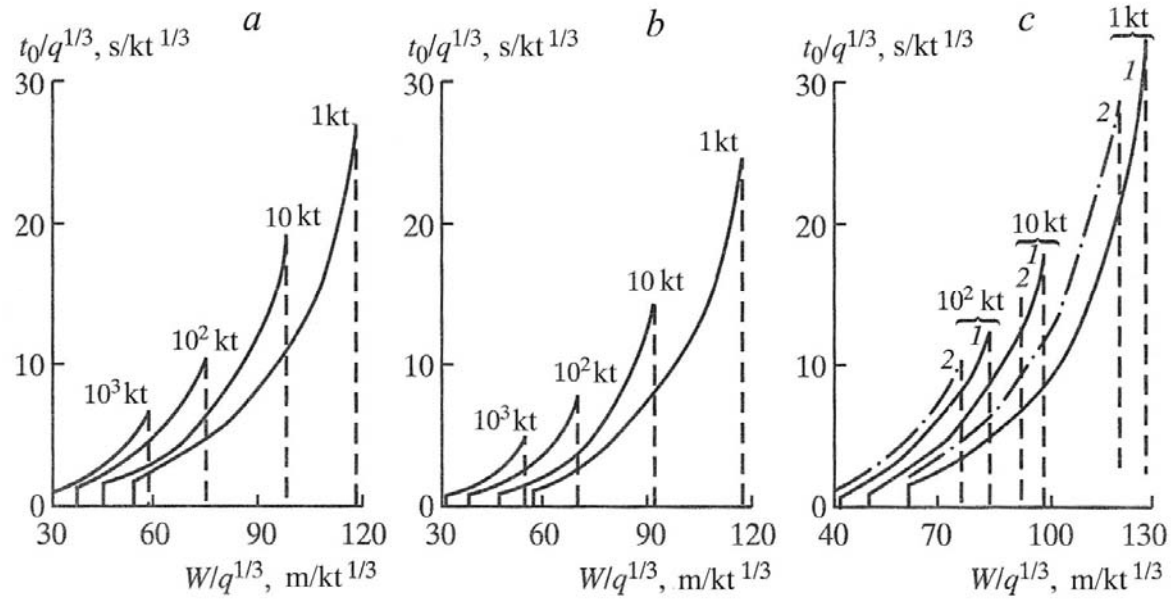

Figure 3.30: Effect of the explosion yield on gas venting time for partially contained explosions in a) aleurolite (shale) and b) limestone. Explosion yields (in kt) are shown next to the lines.

According to equation (3.9) the venting time for gas depends not only on the yield and the depth of burial, but also on the size of the cavity, the rock density, and the gas-forming properties of the rock at the shot depth. Figure 3.30 shows the venting times as a function of the scaled depth of burial for wet granite ($\eta_{H_2O} = 0.03$), shale ($\eta = 0.12$ for $\eta_{H_2O} = \eta_{CO_2}$), and limestone ($\eta_{CO_2} = 0.44$). Physical properties of these rocks have been provided in Section 2.1. Vertical dashed lines show the range for fully contained explosions. The venting times show significant scale dependency: it increases by a factor of 2 – 3 when the yield changes from 1 to 100 kt if other conditions stay the same. Increase in gas content by a factor of two causes shortening of the venting times by 20 – 30%. Replacing water vapor with CO_2 leads to an increase in venting times by a factor of 2. The main parameter determining the venting time is the scaled depth of burial. For example, if we change the depth of burial from a mound/retarc forming explosion to a fully contained explosion, the venting times would increase from about 2–10 s to about 20–50 s.

Chapter 4.

Seismic waves from large underground explosions

Seismic waves generated by nuclear and chemical explosions are comparable with natural earthquakes in their intensity and (for industrial chemical explosions) in the number of events per year. Between 1960 and 1991 the states with nuclear weapons conducted between 30 and 70 nuclear explosions per year with yields between a kiloton and a megaton. Before 1975 the yields for some explosions reached several megatons. The total energy released by underground nuclear explosions annually was on the order of 10 Mt. Systematic nuclear testing conducted by countries having nuclear weapons ended on January 28, 1996 with an explosion conducted by France at the island test site Fangataufa[1]. The total number of underground nuclear tests conducted over the years was 1613 including peaceful nuclear explosions.

Seismic signals produced by nuclear tests are equivalent to those from earthquake oscillations in the magnitude range m_b = 4 to 6. Earthquake magnitude (Richter scale) is a quantitative characteristic of the energy proportional to a (base 10) logarithm of the largest amplitudes of ground motions for waves of different types. For example the value of m_b magnitude is determined using body wave amplitudes at regional and teleseismic distances. The largest seismic magnitude generated by underground nuclear explosions was close to $m_b = 7$[2].

Chemical explosions conducted in mining or construction are also a common source of seismic waves. At the present time (early 21st century) over 6.5 millions of tons of explosives are used for industrial purposes in the world annually. This amount of explosives has the same order of magnitude as the total energy released by nuclear explosions annually during the years of nuclear testing. The majority of industrial explosions are conducted in order to break hard rocks during mining operations. These explosions are conducted using borehole charges often detonated in large groups with a total amount of explosives on the order of tens or hundreds

[1] The book was written before the DPRK tests

[2] This paragraph describes magnitudes as viewed by many Russian seismologists. A western perspective on magnitudes places greater emphasis on the empirical definition of, for example, the Richter body-wave magnitude m_b using teleseismic P-waves, which is assigned on the basis of measurements of maximum ground displacement divided by the period of the motion; applying a correction for the distance at which the measurement was made; taking the logarithm of the ratio of displacement to period; and averaging over the network of stations that contribute individual magnitude measurements for a particular event. The relationship to energy is made after further study, rather than being a part of the definition of the magnitude scale. Other magnitude scales of importance for seismic monitoring, are those based upon the amplitude of surface waves with period around 20 s (the surface-wave magnitude Ms; a scale based on the amplitude of Lg-waves (often written as m_b (Lg); and a so-called local magnitude, m_L, based on the largest amplitude of any recorded seismic motion as measured at distances of not more than a few hundred km. For purposes of rough comparison of the size of different seismic events, it may not matter which magnitude scale is being used. But for purposes of careful evaluation of methods of seismic detection and discrimination, it may be essential to have clarity on which magnitude scale is being used.

(sometimes even thousands) of tons. Up to a hundred thousand seismic events with magnitude range m_b between 2 and 5 are generated by the mining industry annually.

Earthquakes are the main source of seismic oscillations, being ground shaking due to rapid tectonic shift or deformation of a volume of rocks, accompanied by a release of stress accumulated in that area due to geodynamic loading. At each moment of time there is an earthquake taking place somewhere in the world. Large earthquakes with magnitudes m_b = 8 to 9 occur approximately once a year, while several hundreds of small earthquakes with magnitudes m_b around 2 occur each day. Table 4.1 shows the number of events N with different magnitudes taking place over the world annually. Also shown are their TNT equivalent q_{equiv} in units of mass of explosive (based on USGS data).

Table 4.1. Annual number of earthquakes of different magnitude on Earth.

Magnitude m_b	Number of events per 1 year	q_{eq}
2	10^6	50 kg
3	10^5	2 t
4	$1.2 \cdot 10^4$	50 t
5	$2 \cdot 10^3$	$2 \cdot 10^3$ t
6	$2 \cdot 10^2$	50 kt
7	20	2 Mt
8	1 – 3	50 Mt
9	≤ 1	$2 \cdot 10^3$ Mt
10	-	$5 \cdot 10^4$ Mt

The largest earthquakes have magnitudes $m_b \geq 8$. The Great San Francisco earthquake of 1906 had a magnitude of m_b = 8.3. Only five earthquakes with $m_b \geq 9$ were recorded in the world in the 20th century since the beginning of seismic observations: Aleutian (1946, m_b = 9.3), Kamchatka (1952, m_b = 9.0), Aleutian (1957, m_b = 9.1), Chile (1960, m_b = 9.4), and Anchorage (1964, m_b = 9.1). In the 21st century Sumatra-Andaman earthquake (m_b = 9.3) occurred on December 26, 2004 caused a devastating tsunami. This earthquake is the second largest recorded earthquakes (see, e.g., Khan and Gudmundson, 2005)[3].

[3] The Russian text uses the m_b symbol in reporting the size of these events, but in practice for large earthquakes it is important to move away from a scale based on teleseismic P-waves, and instead to use signals recorded from the longest available periods in order to measure the overall size of the earthquake and not be influenced by interference between signals coming from different sub-regions of such large seismic sources. The most commonly-used scale to characterize large seismic sources is the moment magnitude scale, which is not empirical, but rather is based on a source-mechanical framework that estimates the overall area of faulting times fault slip times rigidity in the source region.

Several studies (e.g. Sadovskii et al, 1985a) have estimated that the seismic energy released by all earthquakes around the world annually is approximately 10^{25} erg, which is equivalent to explosive energy of 10^3 Mt. This value is approximately 4 orders of magnitude greater than the total seismic energy released by nuclear and chemical explosions, because only about 1% of explosive energy is converted into seismic oscillations, the remaining portion is spent on irreversible deformations around the charge (including vaporization, melting, displacement, compaction and rocks damage)[4].

Studies of seismic waves radiated by nuclear and chemical explosions represent a significant component of seismology. Seismic effects of explosions have to be taken into account during conduction of industrial explosions. For instance seismic vibrations are often a factor limiting yield for industrial explosions, leading to the use of delay-fire techniques. Explosions as sources of seismic waves are often used for imaging of the crust, prospecting for natural resources, and developing earthquake engineering methods that achieve resistance to damage caused by ground shaking.

In addition to other applications, nuclear explosions also have significant value for seismic imaging of the Earth's mantle and the core. These explosions have known coordinates, origin times and energy, unlike earthquakes for which these parameters are determined using indirect measurements with significant uncertainty. Seismic waves provide an effective way of monitoring nuclear explosive testing.

4.1. The major milestones in seismic monitoring of explosions

The use of seismological methods of explosion monitoring has evolved through several stages of development. The first stage took place in the 1930s, when the destructive power of explosives became apparent in a quantitative way due to development of explosive technologies in mining and industry. In the USSR this subject was addressed in studies by Academician M. A. Sadovskii. He analyzed experimental data on damage to structures and buildings due to industrial explosions and determined that the intensity of damage is determined by the ground velocity of the seismic waves.

Experimental data were used to develop relationships between explosion yield, epicentral distance, and ground velocities. In particular a critical value of ground velocity equal to 10 – 15 cm/s was determined. Velocities exceeding this value result in damage to buildings, including damage to the plaster, wall fractures, and even more serious damage. These results were used to develop computational methods to determine safe distances during explosive work.

The next stage/period spans the 1950s and 1960s [what about the 1940s–-wartime and the first experiences with nuclear explosions?], when active nuclear testing started. During this period different countries started developing methods for monitoring of nuclear testing in order

[4] Not sure this is a fair comparison because as I understand the seismic efficiency of earthquakes is close to several %, just like explosions. Need to compare either seismic energy or released/stored energy for both

to obtain data about the nuclear potential of other countries. Methods of remote registration of the processes occurring during nuclear explosions became necessary in order to determine specifically the explosion location, the yield, and the design features of nuclear devices. In practice nuclear monitoring is performed using radionuclide, acoustic, seismic, and electromagnetic methods.

Development of seismic methods for nuclear monitoring began in the early 1950s in the Institute of Physics of the Earth, of the USSR Academy of Sciences, and involved Academicians G. A. Gamburtsev, M.A. Sadovskii, and Professor I.P. Pasechnik. Three experimental seismic stations were installed for seismic monitoring: "Mikhnevo" (1954, Moscow Region), "Kul'dur" (1955, Khabarovsk Region) and "Borovoe" (1956, Northern Kazakhstan). The latter was installed on a granite outcrop and was characterized by very low microseismic noise.

These stations were equipped with specially developed highly sensitive seismographs SKM, and USF, and with microbarographs. In addition near-source recordings were conducted during nuclear explosions at the STS and NZTS. Temporary seismic stations were also installed [for experimental seismic studies] in different regions of the former Soviet Union and around Semipalatinsk Test Site: Karasu, Bayanaul, Karkaralinsk, Ust'-Kamenogorsk, Kentau etc.

Seismic recorded from stations "Mikhnevo" (MHV), "Kul'dur" (KLD) and "Borovoe" (BRVK), as well as recordings using temporary stations located around the STS together with the seismograms recorded by the permanent network called Unified System of Seismic Observations (USSO)[5] created an experimental basis for developments of the techniques of remote nuclear monitoring. In the beginning of this period (1954 – 1962), seismic data was coming mostly from above-ground and surface nuclear explosions. The first underground nuclear explosions were recorded toward the end of this period: UNEs BLANCA (19 kt) and LOGAN (5 kt) were detonated by the USA at the Nevada Test Site in 1958, UNE in Tunnel B-1 was detonated by the USSR at the Semipalatinsk Test Site in 1961. The results of these experiments showed the ability of seismic equipment to detect and record nuclear tests at large distances.

The next stage of the development of seismic monitoring began after the Limited Test Ban Treaty was signed in Moscow in 1963, banning atmospheric, space and underwater nuclear tests. The number of underground nuclear tests conducted by the USA and the USSR significantly increased to 60 – 70 per year. Seismic monitoring became the major and practically the only method to monitor nuclear explosions. There was a need to improve technical capabilities of seismic methods by increasing their sensitivity and the amount of information they can provide. Monitoring required solving problems of explosion detection and location, identification from the background natural and man-made events, and estimation of explosion yield.

To solve these problems numerous seismic stations were installed in the USSR and abroad. These stations were equipped with short- and long-period seismographs. Seismologists of the

[5] Edinaya Sistema Seismicheskih Nablyudenii—translated as Unified System of Seismic Observations—was established in 1965 by the Presidium of the Academy of Sciences of the USSR. In 1976 this network included 60 base stations and 155 regional stations conducting continuous recording (see Sadovskii, M.A. and N.V. Kondorskaya, 1976, Perspectives on the development of the Unified System of Seismic Observations in the USSR, in Organization and Efficiency of Scientific Research, pp 30-36, Nauka, in Russian). Note added by translators.

USA turned to creating large seismic arrays in order to increase signal-to-noise ratio and to improve seismic location estimates. In 1963 the USA created the Worldwide Standardized Seismic Network (WWSSN), which included over 110 seismic stations located in 55 countries. In 1965 the Large Aperture Seismic Array (LASA) was build in the USA. The super-array was built over a 200 km x 200 km area in Montana and included 25 seismic sub-arrays with 25 short period seismometers each. LASA did not prove to be very effective and it was closed in 1976.

During the 1970s the USA added 20 small aperture arrays containing 25 – 30 sensors each, located in different countries. In addition seismic arrays ARCESS and NORESS were installed in Norway, and the long period large aperture array ALPA in Alaska. In addition American seismologists installed borehole digital seismic stations in 17 countries, as well as autonomous stations SRO and ASRO, which transmitted recorded information using satellite telemetry.

The Soviet seismologists chose a different path. They installed separate stations [as opposed to arrays] and small aperture arrays in places with high sensitivity to remote explosions and earthquakes. Thus recording of American nuclear explosions have shown that a site located within Kokchetav Anticlinorium has very favorable conditions for seismic recording from the Nevada Test Site. The three-component digital station “Borovoye” as well as small aperture seismic arrays “Krest” and “Treugol’nik” (meaning “Cross” and “Triangle”), each with a digital three component station (in addition to the array sensors) were installed in that area (e.g. Adushkin and An, 1993).

Seismic monitoring of underground nuclear explosions conducted by the USA, and later by other countries was performed using: 1) these three special stations [described earlier], 2) small-base seismic arrays, 3) data from USSO which by 1991 consisted of approximately 500 stations, of which 68 were “base” stations that recorded continuously.

Retrospective analysis of the monitoring efficiency using this national system has shown that out of 891 underground nuclear explosions conducted by the USA 500 were recorded and detected (Adushkin et al, 1996). The efficiency of this system improved with time: during the first stage (1955 – 1965) approximately 60 – 80% of explosions went undetected, during the period of 1965 – 1975 the percentage of undetected explosions was reduced to 30 – 50%. After 1975 the percentage of undetected explosions was 10 – 15 %, while after 1985 the system missed 1 – 2 explosions per year.

The most sensitive stations for detection of nuclear explosions include “Borovoye” (BRVK), “Iul’tin” (ILT), “Tiksi” (TIK), “Seimchan” (SEY), “El’tsovka” (ELT), and “Yakutsk“ (YAK).

In addition to seismic monitoring during the period of nuclear testing another important problem was seismic safety of structures within nuclear test sites and in the nearby towns. The importance of safety issues became particularly important during the program of using of nuclear explosions for peaceful purposes (between 1965 and 1988). Extensive observations were conducted during this time, especially in the near-source zone, where seismic oscillations are particularly damaging. As a result the main characteristics of seismic wave propagation were determined depending on the epicentral distance and yield, as well as the type of the emplacement rocks (salt, apatite, carbonates including limestone, clay, sandstone or shale).

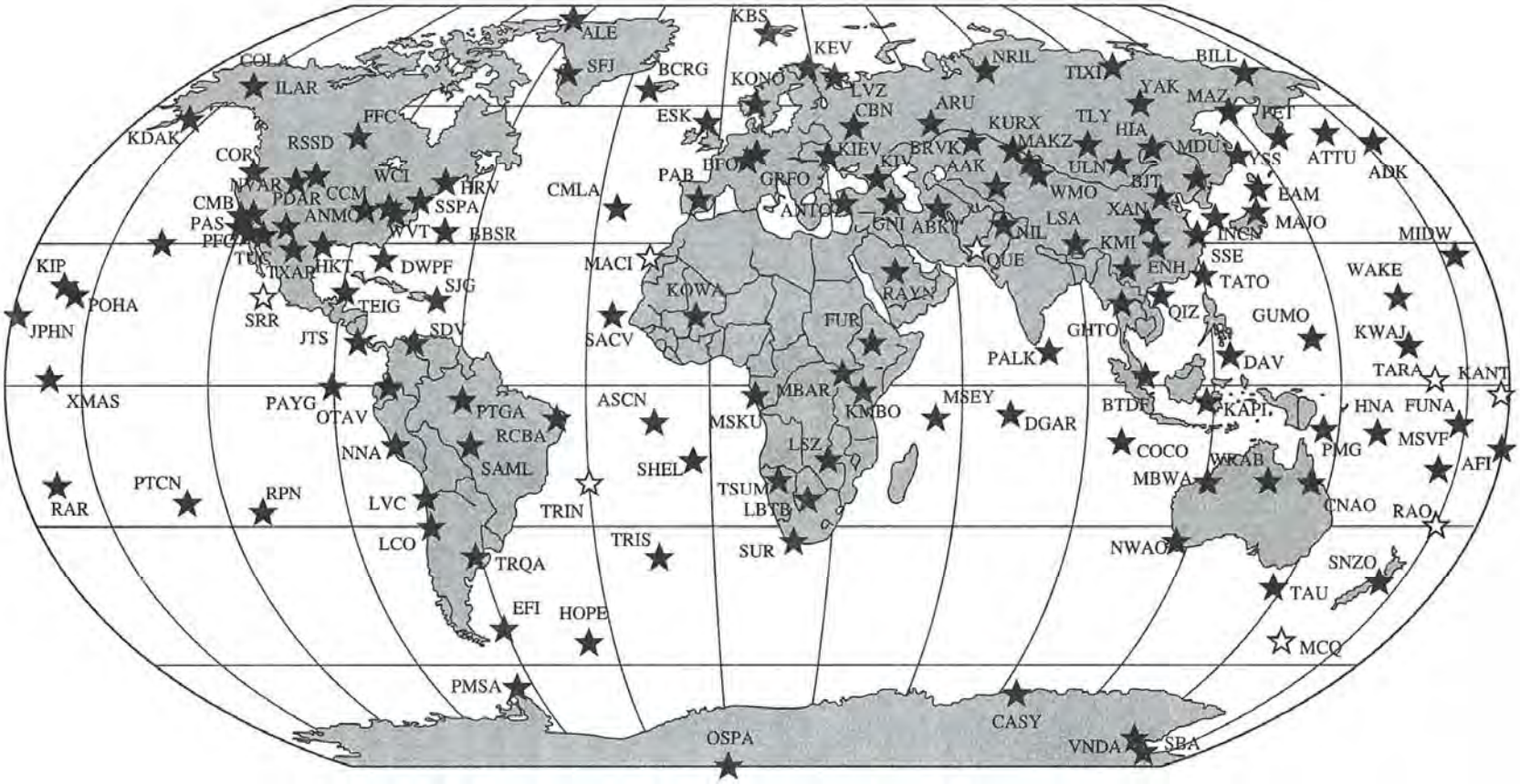

Figure 4.1. Map showing locations of Global Seismic Network (GSN) stations.

Significant achievements of this stage were summarized in a book [manual perhaps] "Methods of providing of seismic safety during conduction of underground nuclear explosions", which included a statistical approach to evaluation of the degree of damage of different types of structures (Sadovskii and Kostyuchenko, 1974). During this period (1975 – 1980) the program of Deep Seismic Sounding was performed. The program involved 15 geophysical profiles with a total length of 70,000 km, which covered the major part of Siberia, Kazakhstan and parts of the Eastern European Platform. Seismic sounding resulted in a huge volume of information used to generate geological cross-sections and to determine new prospects for oil, gas and other natural resources (Nuclear, 1997 – 2000)[6].

After the end of nuclear testing, starting in the 90s, the final stage of seismology began. During this time seismology became a science studying seismic waves from natural and man-made sources, with the key difference in this period, that in addition to teleseismic work it became possible to conduct regional monitoring. Achievements of seismology for explosion monitoring have demonstrated its efficiency for registering of signals produced in the Earth by explosions and earthquakes. These achievements were related to development of high sensitivity broadband seismic sensors, development of digital recorders and computer use.

The Incorporated Research Institutions for Seismology (IRIS) was created in the USA, as a consortium between scientific institutions in the USA and abroad. Due to the efforts by IRIS and the United States Geological Survey (USGS) the international seismic network began developing not only for the nuclear monitoring purposes, but also for the fundamental studies of the earth internal structure. The important problems also involve the earthquake mechanism and generation, their relation to tectonics, and prediction of catastrophic earthquakes.

In the present time the global seismic network (GSN) consists of 138 stations equipped with digital broadband sensors and other geophysical equipment. The stations are spread over the globe from the South Pole to Siberia and from North and South America to the islands in the Indian and Pacific Oceans (Figure 4.1). The network operates in cooperation with 100 different organizations and national seismic networks in 59 countries. To improve the sensitivity and accuracy of seismic locations some of the GSN stations are represented by seismic arrays. In some cases GSN stations are part of geophysical observatories including GPS systems, gravity meters, magnetometers, microbarographs, and meteorological instruments. Information from these stations is transmitted to national center and to the International Data Center (IDC?) using satellite telemetry.

In addition to GSN in order to insure CTBT compliance the International Monitoring System (IMS) is being developed. The IMS includes four monitoring techniques: seismic, radionuclide, infrasound and hydroacoustic. Stations of this system are spread over the globe with concentration around the regions with higher probability of unsanctioned nuclear testing (for instance Central Europe or Eastern USA have lower probability of nuclear testing etc). In the end

[6] Nuclear Tests in the USSR, Vol. 1: Objectives, General Characteristics, and Organization of Nuclear Tests [in Russian], Inst. Exp. Phys., Sarov (1997). Volumes 1-4

the IMS should consist of 50 main and 120 auxiliary seismic stations, 80 radionuclide monitoring stations, 60 infrasound and 11 hydroacoustic arrays.

The seismic network consists of digital three component stations capable of registering signals in the broad band of frequencies from 0.001 to 50 Hz. In some cases small aperture arrays are added to the stations, which allow detection and locations of weak seismic signals with magnitudes $m_b \geq 2$ to 2.5 at regional distances (up to 2000 km). Medium aperture arrays are designed to detect weak signals at the telesesmic distances (from 2000 to 10000 km). At present most of the IMS is functional and transmits signals to the international data center located in Vienna (Austria) in real time.

Once finished the IMS should provide detection of explosions for any part of the globe with yields greater than 1 kt with a probability of 0.9 (Seismic…, 1992). The IMS also includes satellites to monitor surface explosions and above-ground explosions, as well as explosions conducted in space using the American satellite system Navstar (Krukovskii and Romanov, 1990)[7]. Currently the GSN and the IMS are being equipped with modern equipment, telemetry systems and satellite channels in order to provide scientific community and monitoring centers with real time data.

4.2. Generation and propagation of seismic wave from underground explosions

Major characteristics of seismic wave generation by underground explosions have been described previously (e.g. Rodionov et al, 1971; Muller and Murphy, 1971; Adushkin et al, 1973). The major part of energy is radiated by explosions during the expansion of the cavity. At this stage the explosion causes vaporization and melting of the surrounding medium, plastic deformation and fragmentation, produces a spreading pressure wave, and forming the explosive cavity and a zone of irreversible deformations. The cavity and the damage zones eventually determine the main parameters of the radiated seismic waves.

The amplitude of the residual displacement recorded outside the zone of irreversible deformations correlates well with the final cavity size, suggesting that the cavity is mainly formed by displacing the medium into the elastic zone. This means that the seismic wave amplitude is proportional to the displaced volume. The period of seismic waves in the elastic zone is proportional to the radius of the zone of inelastic deformations $T = 2R_*/C_p$. Therefore the zone of inelastic deformations is considered a part of the explosive source. The time-dependent displacement at the spherical boundary separating this zone from the elastic zone determines the so-called displacement potential, which determines the main parameters of P-waves.

Thus an underground explosion is characterized by a simple source of oscillations, and in the first approximation can be described as a ‘‘center of expansion". Ideally such a source would produce particle displacement only in the radial direction. This is why compression waves are called longitudinal *P*-waves. However due to the heterogeneous structure of real media the

[7] This statement would appear to be incorrect—the IMS uses satellites only for sending data, not for monitoring directly. (Note added by translators.)

symmetry of the wave is perturbed, leading to shear or transverse waves *S*-waves. The oscillations of *S*-waves are not related to volume change. As a result the source of a ‘‘center of expansion" type creates both longitudinal and transverse waves. However the major portion of seismic energy in the near-source zone belongs to the *P*-wave, which plays the main role in explosion seismology.

Both calculations and experiments have shown that most of the explosion energy (90 – 95%) dissipates in the zone of inelastic deformations, with only 5 – 10% of energy reaching the elastic zone. Some part of this energy dissipates due to inelastic losses, and the remaining part travels as seismic waves, which gradually decay due to geometrical spreading, scattering and attenuation. The seismic energy radiated from explosions is determined mostly by the rock surrounding the source.

Data from Table 4.2 correlate with the measurements of the peak velocity (Chapter 1) in the sense that the greater the dissipation in the source zone, the lower the portion of energy radiated as seismic waves.

Table 4.2. Portion of explosive energy radiated as seismic waves for explosions in different rock types.

Rock type	Salt	Granite	Tuff	Alluvium	Dry alluvium
E_0/q	0.8 – 3%	1 – 2%	0.3 – 1%	0.15 – 0.2%	0.05 – 0.09%

In addition to a stress wave created by the explosion, energy is stored as tectonic (or other elastic) stresses in the surrounding medium. Energy associated with slap-down of the spall zone, and collapse of the chimney, can also be released during explosions. The direct effect of tectonic stresses on radiated seismic waves has been noted by many authors (e.g. Helle and Rygg, 1984; Kulikov, 1987).

Relaxation of tectonic stresses around an explosion source continues after the explosion. Hundreds or even thousands of aftershocks have been registered after some nuclear tests. In some cases their seismic signal strength has been close to that of the nuclear test. It is worthwhile to note that the radius of aftershock zones can significantly exceed the radius of the zone of inelastic deformations and reach 0.5 to 2 km/kt$^{1/3}$. In addition to residual deformations and aftershock generation outside of this zone, changes in rock properties are also observed, including increases in porosity and permeability, and decreases in rigidity and quality factor (Q). These changes are expressed as seismic velocity reduction and in attenuation increase, for repeated explosions. Such effects are related to heterogeneities of the real geological medium, and to the presence of faults, fractures and layers of rocks of different types, responsible for a hierarchical structure composed of blocks of different sizes. Therefore it is natural to assume that, outside of the crush/damage zone, deformations take place along zones of weakness. This means that energy dissipation mainly occurs within the material filling gaps between solid blocks, where the strength is significantly lower than strength of the intact rock itself.

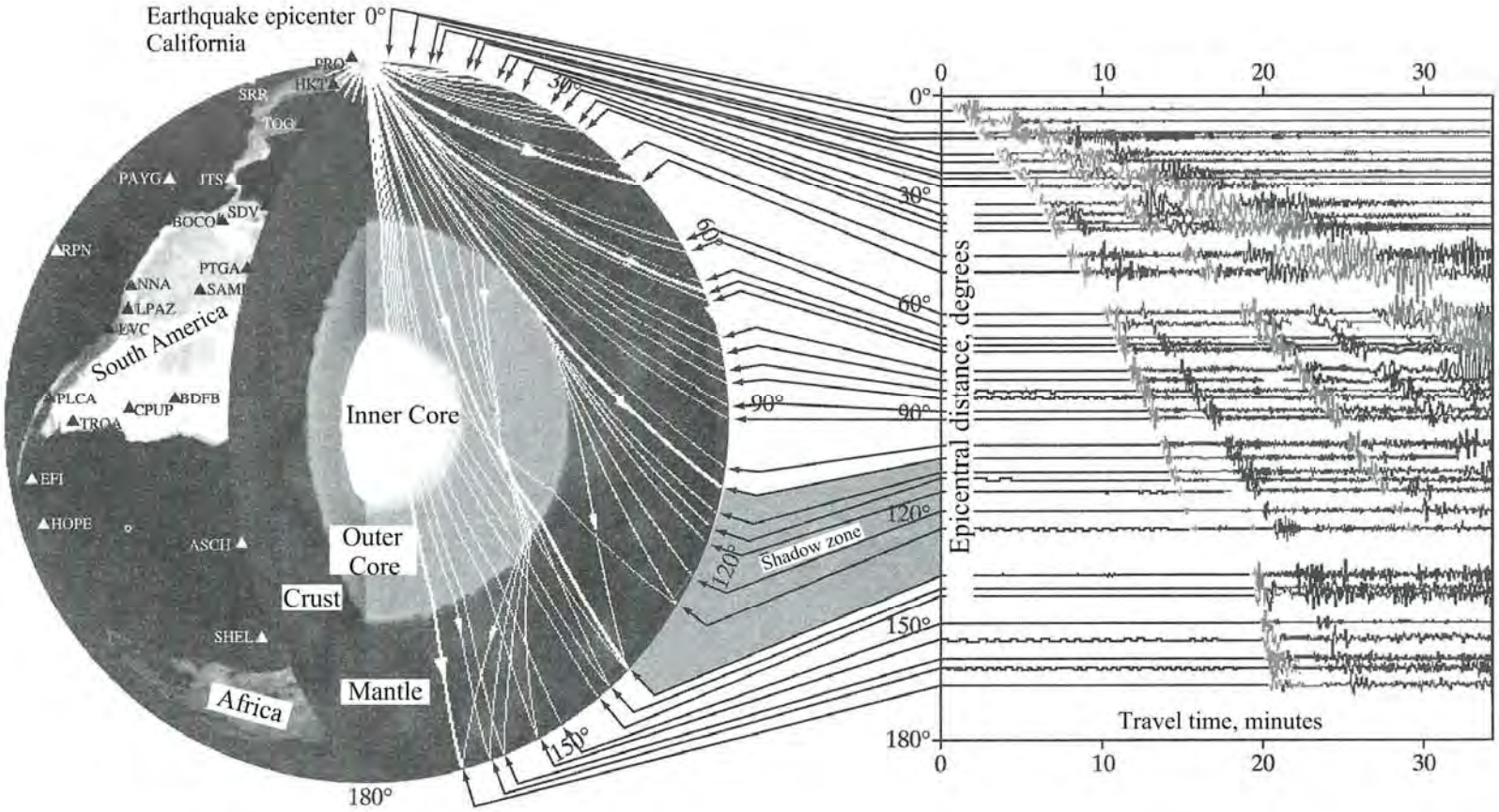

Figure 4.2. Ray paths through the Earth interior for main body wave phases.

However since these gaps occupy only a small part of the total rock volume, their properties do not significantly affect the "elastic" description of explosion processes. However the presence of these gaps significantly affects wave attenuation: the attenuation of ground velocity is higher, by a factor 1.5 to 3, than the value obtained using the elastic solution. The distance range where this discrepancy exists is almost unlimited and irreversible changes are present in the entire range of the zone of explosion influence.

Despite differences in source mechanism for earthquakes and explosions the wavefield is represented by four major types of waves: body waves including *P*- and *S*-waves, and long-period surface waves including Rayleigh and Love waves. Body waves propagate through the inner layers of the Earth, while surface waves propagate only within the outer layers. The Rayleigh wave is the most pronounced on radial and vertical components of seismic records, while the Love wave is on the transverse. The seismic wavefield becomes more complex as the distance from the source increases. This is caused by Earth's layered heterogeneous structure, which generates multiple reflections and refractions, and conversion to different seismic phases.

Figure 4.2 shows ray paths for the major phases through the Earth for *P*- and *S*-waves. The right plot shows seismograms recorded at different epicentral distances along the globe. Using the same time scale helps to illustrate arrival of different phases and their travel times. Even though all these waves were generated by a single source at the same time their propagation velocities are different.

P-waves are the first to arrive at a station, followed by *S*-waves whose velocities inside the Earth are approximately one half the velocities of *P*-waves. Surface waves arrive after *P*- and *S*-waves. At stations located close to the source the wave amplitudes are high, and the travel time differences between body and surface waves are relatively short. At larger distances, where P-wave arrival times reach 10 minutes, the travel time differences become longer.

Different *P* and *S* ray trajectories are related to the Earth's layered structure, which includes crust, mantle, liquid outer core and solid inner core as shown in Figure 4.2. Changes in seismic velocity with depth and the presence of reflecting and refracting boundaries create characteristic focusing zones as well as defocusing or shadow zones. Based on these features the Earth surface can be divided into following zones:

1. A regional zone spans the distance range from the event epicenter to a distance of approximately 10°. This zone is characterized by high amplitudes of motion for the waves that have passed through the crust and upper mantle. The following regional phases are registered in this zone: *Pg*, *Sg*, *Pn*, *Sn*, and *Lg*. The *Rg* phase is registered up to distances of several hundreds of kilometers.
2. The first shadow zone is observed outside of the regional zone in a distance range between 10° and 20°. The shadow zone is caused by wave refraction into deeper layers with higher velocities. Within the shadow, signals have low amplitudes and observations become uncertain.

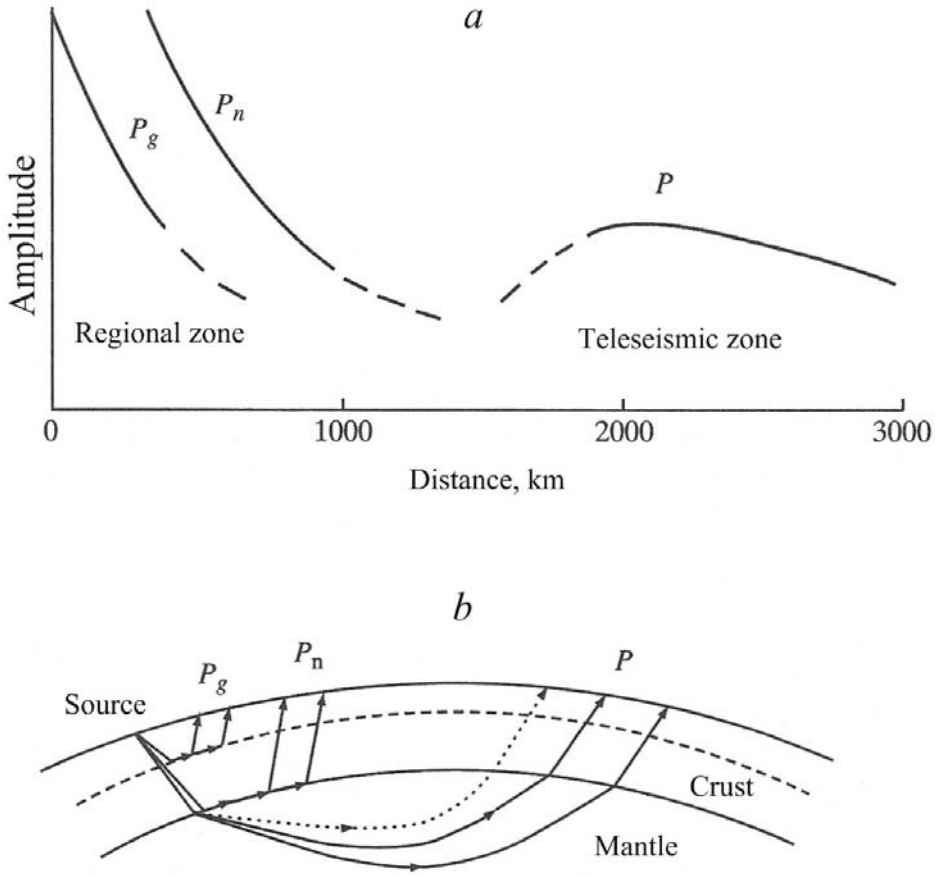

Figure 4.3. a) Schematic amplitude–distance plot for regional (Pg and Pn) and teleseismic P phases. b) Schematic ray paths for regional and teleseismic phases

3. The teleseismic zone spans between 20° and 100° (approximately 2000 – 10,000 km] and is characterized by focusing of seismic waves that pass through the middle and lower parts of the mantle. In this zone signal detection is more reliable, the amplitudes are higher than in the previous zone, and their decay with distance is slower. Teleseismic waves are also less sensitive to the presence of low-velocity layers. The following phases are registered in this zone: *P*, *pP*, *pS*, *S*, *sS*, and *sP*, as well as Rayleigh and Love waves. Figure 4.3 shows a qualitative illustration of the main differences between regional and teleseismic waves. Amplitudes of the regional phases are strong for both Pg propagating within granite and basalt layer, and Pn propagating along the crust-mantle boundary. As distance increases the amplitudes of these waves decrease until they vanish at a distance of approximately 1000 km. At distances of approximately 1700 to 2000 km the amplitudes of the first arrivals increase. It doesn't significantly change up to distances close to 9000 km. This is explained by teleseismic wave propagation through the lower mantle, which is characterized by low attenuation.

This behavior of P waves is explained by abrupt changes in seismic velocities. The velocity changes from 5.8 km/s in the upper crust to 6.5 km/s in the lower crust. Transition to the upper mantle causes velocity increase to 8 km/s or higher. In these circumstances wave trajectories are deflected into deeper layers, creating the above-mentioned shadow zone. The waves reappear at the surface at distances greater than 2000 km (Figure 4.3) [It's a Figure done by Carl Romney in 1960!].

4. The zone with distances between 100° and 140° located beyond the teleseismic zone corresponds to another shadow zone. Seismic amplitudes in this zone are low and often blend with the noise. According to Figure 4.2 the shadow zone is due to the liquid outer core. At the core-mantle boundary, seismic velocities change from 13.5 to 8.3 km/s, deflecting the ray trajectories into deeper layers and they reappear at the surface at greater distances.
5. The distance range between 140 – 180° is characterized by a presence of so-called caustic zone formed by focused ray trajectories passing through outer and inner core. In this zone signal detection improves. This zone is interesting because not only the PKP phases are focused, but also surface waves

This division of the Earth's surface into distance zones with different features is important for managing various problems, including monitoring of underground explosions, identification of the signals produced by earthquakes and explosions, as well as for optimal selection of station sites to improve sensitivity of seismic monitoring.

4.3. Regional seismic waves from underground nuclear explosions at the Semipalatinsk Test Site

Nuclear tests at the Semipalatinsk Test Site (STS) were recorded by an extensive seismic network of stations. Near-source seismic measurements were performed near the test area itself, next to the borehole or near the tunnel entrance, for almost all explosions. Near-source data were also recorded by stations located along several azimuthal directions at the Test Site and in nearby populated areas. Seismic oscillations created by underground explosions in this area represented a real hazard to recording complexes and structures located near ground zero, as well as for buildings and other construction. Damage to some buildings located even outside the Test Site was recorded at distances of hundreds of kilometers.

Seismic measurements were conducted in order to understand and analyze the causes of structural damage at these distances. A significant amount of data related to seismic waves from underground nuclear explosions was accumulated in the regional area of STS.

This regional area can be divided into several zones based on the character (and the amplitudes) of ground motions, and on the major types of seismic phases and their effect on man-made structures:

1. *Epicentral zone* with a radius of approximately 1000 m/kt is characterized by spall fractures and predominately vertical movement of material within distances of 3 to 5 times the depth of burial.
2. *Near-source zone* with distances ranging between 1 km and 10 – 15 km is characterized by dominant action of direct body waves propagating from the source in the sediment layer above the hard crystalline rocks.
3. *Intermediate zone* spans distance interval between 10 – 15 km and 80 – 100 km. The dominant phases in this distance range are body waves traveling in the crystalline basement above the Conrad waveguide.
4. *Far-field zone* is extended from 80 to 100 km, out to 1000 km. This zone is characterized by body waves critically reflected from the Moho discontinuity.

Extensive observational data were collected for each of these zones. Based on the data analysis the main seismic phases were identified and related to the geological structure. Empirical wave characteristics were tabulated as a function of distance and explosion yield.

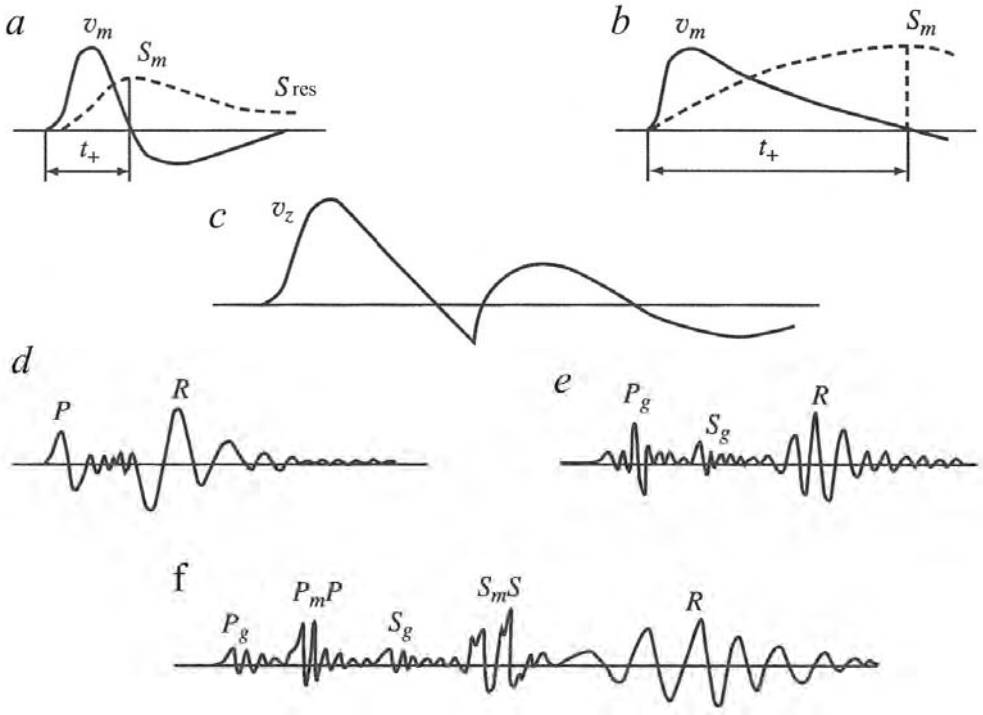

Figure 4.4. Characteristic waveforms of the ground motion produced by underground explosions: a) and b) stress wave; c) – f) seismic waves for different zones: c) epicentral zone, d) near-source zone, e) intermediate zone, and f) far-field zone

Figure 4.4 shows ground oscillation characteristics in these zones. Ground motion in the epicentral zone is determined by the pressure wave interaction with the free surface, which creates shock waves, body waves, and surface waves. Particle motions for explosions in hard rock (Figure 4.4 a) show a negative velocity phase, which suggests a returning motion following

the stress wave. For explosions in fractured or porous rocks the negative velocity phase is absent (Figure 4.4 b). Particle displacements are shown with dashed lines. The displacements in the epicentral zone show signs of spall, since, after a rapid velocity rise to the peak velocity, there is a free-fall interval where material is moving under the effects of Earth gravity. The impact of the spall zone on the underlying rock is also seen (Figure 4.4 c). If the distance or the depth of burial increases, spall is no longer observed, and the particle motions look like either free field records at depth, or contain several oscillations due to effects of a low-velocity layer at the surface. In the near-source zone the wavefield consists of the direct P-wave and the surface Rayleigh wave (Figure 4.4d). The *P*-wave propagates with velocity of 3 – 5 km /s in the sediment layer with a thickness of 2 – 7 km.

A surface wave is observed starting from distances over 0.5 – 1 km/kt^1/3 and propagates with velocity of 2.9 – 3.1 km/s. A long-period longitudinal wave called the N - phase, arriving approximately 0.15s after the P-wave, is observed for shallow ($W/q^{1/3} \leq 100 \div 150$ m/kt$^{1/3}$) and cratering (ejection) explosions. Longitudinal wave *Pg* (Figure 4.4d) is observed in the intermediate seismic zone. This phase represents a head wave or refracted wave traveling along the granite-basalt midcrustal discontinuity between depths of 5 and 20 km. Seismograms are complicated by the presence of multiple *P* phases with changing polarities traveling in the (upper) sedimentary layer. In addition, corresponding shear waves (travelling along the same paths as the *P*-waves just described) are observed in this zone. Long-period surface waves become more complex.

As a result the total duration of seismic oscillations increases with distance. A far-field zone begins with the appearance of reflections from the crust-mantle (Moho) discontinuity at a depth ranging between 30 and 50 km. The waves reflected from this boundary are denoted using subscripts P_mP and S_mS (Figure 4.4e). Amplitudes of ground velocity and displacement for these waves significantly exceed the amplitudes at closer distances (i.e., before the appearance of Moho reflections).

Analysis of the seismic wavefield shows how a simple signal generated by the source becomes complex after interaction with the free surface and traveling through a heterogeneous geological medium. In the epicentral- and near-source zones the amplitude and duration of the oscillations are mainly determined by the direct compression wave, which contains some information about the seismic source (such as rock properties, depth of burial, and number of charges).

In the intermediate- and far-field zones the amount of information about the source decreases and the wave contains more information about the geological structure of the region along the ray path. Thus by analyzing arrivals of different phases one can determine the depth of the geological boundaries, whereas the amplitude decay provides information about seismic attenuation at different depths. We shall describe the main parameters of ground motion in each seismic zone in more detail.

Epicentral zone. In this zone the ground motion is determined by the free surface reflection. The size of the epicentral zone is related to the size of the spall deformations. For depths of

burial $W/q^{1/3} \leq 150$ to 200 m/kt$^{1/3}$ (typical for Balapan), a rapid uplift occurs, separating a layer with a thickness on the order of tens of meters that subsequently undergoes free fall. The thickness of the spall zone is determined by the length of the compression wave, and the maximum thickness does not exceed half of the wavelength, so $h \leq 0.5\ C_p t_+$, where C_p is the *P*-wave velocity and t_+ is the duration of the positive phase in the stress wave.

For explosions in the given range of DOB the thickness of the spall zone overlaps with the zone of fracturing around the cavity. As a result the entire rock mass between the cavity and the surface becomes broken, which causes the development of the collapse chimney and an increase in permeability, promoting gas escape to the surface.

A sub-zone of intense spalling is defined in the epicentral zone with a scaled radius of 300 – 400 m/kt$^{1/3}$. Within this zone a complete detachment of the spall layer occurs. A zone of deformations caused by spallation is observed up to distances of 800 – 900 m/kt$^{1/3}$, where the spall deformations occur along natural discontinuities and layers.

The amplitude of the vertical component of ground velocity due to the stress wave has a defining effect on material movement deformations in the epicentral zone. The initial velocity of uplift (also called the spall velocity) depends on the scaled DOB and the geological structure of the site. Thus for explosions in hard rock with outcrops at the free surface (a situation similar to that for explosions conducted in tunnels at Degelen Mountain), the velocity v_z is equal to twice the maximum particle velocity determined in Chapter1:

$$v_z = 2v_0.$$

In particular, for explosions in hard rocks (e.g. granite, quartzite, sandstone) the amplitude of the spall velocity in the epicentral zone with a radius of 300 – 400 m/kt$^{1/3}$ is given by:

$$v_z = \frac{2.4 \cdot 10^4}{\left(\frac{W}{q^{1/3}}\right)^{1.6}} \text{ (m/s)}, \tag{4.1}$$

where W is the DOB in m, and q is the yield in kt.

For explosions in soft sediments (e.g. alluvium) the doubling of the velocity amplitude at the surface is not observed, and the velocity as a function of yield and DOB is given instead by:

$$v_z = \frac{1.6 \cdot 10^6}{\left(\frac{W}{q^{1/3}}\right)^{2.3}} \text{ (m/s)}. \tag{4.2}$$

A thick layer of soft sediments with thickness ranging from several meters to 50 – 80 m is present in Balapan Testing Area at STS. The velocity amplitude in the zone of intense spalling is determined using the empirical formula

$$v_z = \frac{3.5 \cdot 10^6}{\left(\frac{W}{q^{1/3}}\right)^{1.72}} \text{ (m/s)}, \tag{4.3}$$

where W is the DOB in m, q is yield in kt.

For explosions in hard rocks with a layer of soft sediments with thickness of 200 m the amplitude of the spall velocity in the zone of intense spalling is estimated using the formula:

$$v_z = \frac{4 \cdot 10^5}{\left(\frac{W}{q^{1/3}}\right)^{2.2}} \text{ (m/s)}, \tag{4.4}$$

where W is the DOB in m, q is yield in kt. The horizontal component velocity amplitudes observed in the epicentral zones of contained explosions are significantly smaller than the amplitudes of vertical components. In the zone with radius $r \leq 300 \div 400$ m/kt$^{1/3}$ the horizontal amplitudes may be smaller than vertical amplitudes by a factor of 10 – 100.

As we move away from the epicenter the differences between the horizontal v_x and vertical v_z components decrease, and at scaled distances in the range $r/q^{1/3} \leq 300$ to 400 m/kt$^{1/3}$ the amplitude of the horizontal component becomes v_z = (1 to 1.5) v_z. For explosions in hard rocks conducted at a scaled DOB of $W/q^{1/3} \leq 70 \div 150$ m/kt$^{1/3}$ (common for Degelen at distances in the range $0.35q^{1/3} \leq r \leq 1.5q^{1/3}$) the velocity amplitudes are given by

$$v_z = v_x{}^{8} \frac{10}{\left(\frac{r}{q^{1/3}}\right)^{1.85}} \text{ (cm/s)}, \tag{4.5}$$

$$S_z = 0.77 S_x = 1.1\, q^{1.1} r^{-2.25} \text{ (mm)},$$

$$j_z = j_x = 2.2\, q^{0.5} r^{-2.4} \text{ (g)},$$

$$T_z = 0.77 T_x = 0.07\, q^{0.46} r^{0.4} \text{ (s)},$$

where r is the distance in km, q is yield in kt, S_z and S_x are vertical and horizontal displacements, j_z and j_x are vertical and horizontal acceleration, and T_z and T_x - are the durations of the positive phase of motion.

For explosions in tunnels and boreholes conducted in soft sediments the amplitudes of v, S and j and the positive phase duration increase by a factor of 2.

Using formulas (4.1) – (4.5) it is easy to estimate the time and the height of the free surface uplift from

$$t = \frac{2v_z}{g}, \; h = \frac{(v_z)^2}{2g}. \tag{4.4}$$

Due to the relatively small size of the spall zone and the fact that it is off-limits for buildings and other structures, this zone is of no practical value, with the exception of explosions conducted at large sDOB, in which case some structures can be located within this zone.

Near-source zone extends from scaled distance of 1 m/kt$^{1/3}$ to 10 – 15 km. The peak velocities of seismic waves within this zone are from the *P*-wave, represented in this zone as the direct wave of compression. The dependence of peak ground velocities on distance from ground

[8] Not sure whether v_x Is needed in that formula and whether there should be an "=" sign after v_x.

zero is shown in Figure 4.5 for explosions in different rock types. Table 4.3 shows the empirical formulas relating the peak velocities to scaled epicentral distances.

Table 4.3. Maximum particle velocity as a function of scaled distance to the free surface.

Line number	Rock (Test site)	v_0, cm/s*
1	Salt (Azgir)	$22(r/q^{1/3})^{-1.63}$
2	Quartzite (Novaya Zemlya)	$18.9(r/q^{1/3})^{-1.6}$
3	Granite (Semipalatinsk)	$10.2(r/q^{1/3})^{-1.75}$
4	Shale (Novaya Zemlya)	$6.2(r/q^{1/3})^{-1.75}$
5	Rocks (Balapan)	$5(r/q^{1/3})^{-2}$
6	Alluvium (Nevada)	$0.8(r/q^{1/3})^{-2}$

* r is distance in meters, q is yield in kt

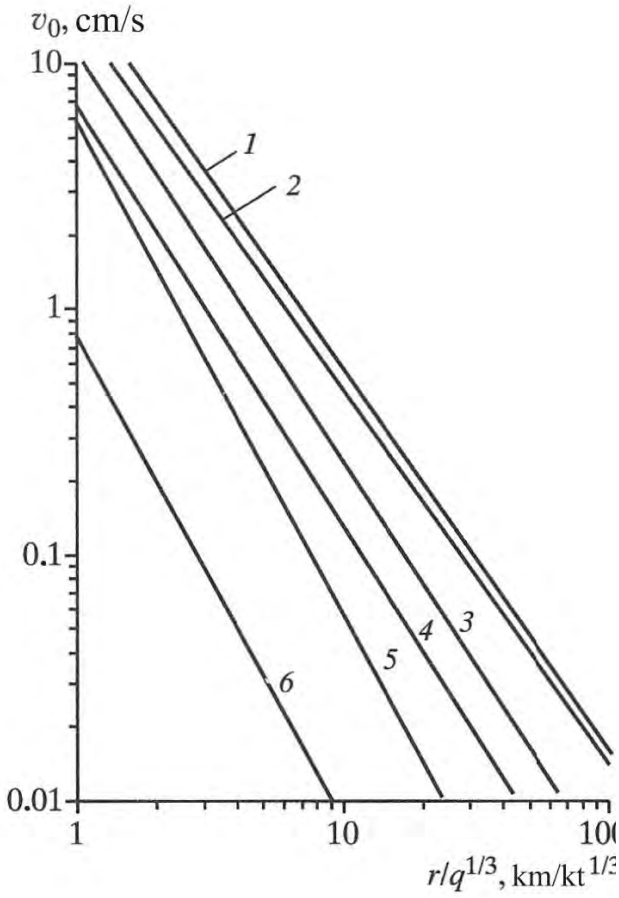

Figure 4.5. Maximum ground velocity at the free surface as a function of distance and explosion yield [numbered lines show]: 1 – salt (Azgir); 2 – quartzite (Novaya Zemlya); 3 – granite (Degelen); 4 shale [or slate] (Novaya Zemlya); 5 rocks (Balapan); 6 alluvium (Nevada).

As shown in Table 4.3, physical properties of the emplacement rocks have a significant effect on ground velocities. The highest ground velocity is observed for hard rocks regardless of their type (e.g. salt, crystalline rock). Velocity decay with distance is lower for these rocks. The lowest ground velocities are observed for explosions in soft rocks such as alluvium.

Interaction of the pressure wave with the free surface creates a reflected wave denoted *P* and a converted wave *S*, as well as surface waves of Rayleigh (*R*) and Love (*L*) types. Based on the results of numerous measurements in the near-source zone ($r \leq 10$ to 15 km) for tunnel explosions (at Degelen, rock types include granites and quartzites) and for borehole explosions at Balapan (rock types include shales and conglomerates) at the STS for common sDOB range $W/q^{1/3} \leq 70 \div 150$ m/kt$^{1/3}$ the following relationships between the horizontal v_x and vertical v_z components of *P*-wave velocity and other parameters as a function of yield and epicentral distance (Kostyuchenko et al, 1974):

$$v_{Px} = \frac{12}{\left(\frac{r}{q^{1/3}}\right)^{1.75}} \text{ (cm/s)}, \qquad v_{Px} = \frac{11.5}{\left(\frac{r}{q^{1/3}}\right)^{1.5}} \text{ (cm/s)}, \tag{4.6}$$

$$S_{Px} = 1.3\, S_{Pz} = 1.6\, q^{0.8} r^{-1.45} \text{ (mm)},$$

$$j_z = j_x = 2.2\, q^{0.5} r^{-2.4} \text{ (g)},$$

where r is the distance in m[9], q is yield in kt, S_z and S_x are vertical and horizontal displacements, and j_z and j_x are vertical and horizontal acceleration for the *P* phase.

The arrival time and the dominant period of the *P* phase for different components are given by

$$t_{\text{arr}} = 0.19\text{r (s)},\ T_{Px} = 1.3\, T_{Pz} = 0.07\, q^{0.2} r^{0.4} \text{ (s)}.$$

For explosions conducted [in different geological conditions] in tunnels in shale/shists and quartz sandstones the peak values of the horizontal *P* velocity are given by the relationship:

$$v_{Px} = \frac{5.7}{\left(\frac{r}{q^{1/3}}\right)^{1.9}} \text{ (cm/s)}, \tag{4.7}$$

where r is in m, and q is yield in kt.

Analysis of the horizontal component of the *P* phase v_{Px} deserves particular attention because it significantly affects buildings and other structures. Relationships 4.6 and 4.7 for v_{Px} as a function of scaled distance in the range between 0.3 and 10 km/kt$^{1/3}$ are plotted in Figure 4.6 with lines 1 and 2 respectively, for seismic stations located on hard rock outcrops. The motions measured on top of a soft layer with thickness more than several meters have amplitudes of velocity, displacement and acceleration that are twice as high as measurements for hard rock. The duration of the oscillations are also increased by a factor of 2 (the dashed line in Figure 4.6 corresponds to measurements in soft sediments).

[9] The Russian text indicates meters, but in other places it is in kilometers. Check.

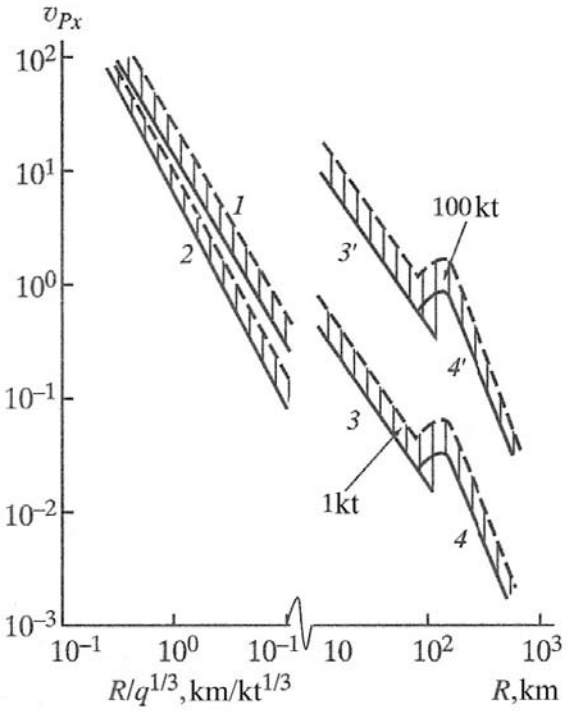

Figure 4.6. Maximum horizontal component of ground velocity in the epicentral zone as a function of distance for r < 10 km (lines 1 and 2), and in the range 10 < r < 1000 km (lines 3 and for – for 1 kt, 3' and 4' – for 100 kt).

Shallow explosions ($W/q^{1/3} \leq 150$ m/kt$^{1/3}$) also produce long-period N-wave following the P phase, which is due to an uplift of the conical zone between the cavity and the free surface. The uplift unloads the half-space by removing the weight of the conical zone, and creates a rarefaction phase. The subsequent downward motion of the mass creates a compression phase (sometimes called slapdown) (e.g., Rodionov, 1981).

The following empirical relationships were found for the N wave:

$$v_{Nx} = v_{Nz} = 9\, q^{0.67} r^{-2} \text{ (cm/s)}, \tag{4.8}$$

$$S_{Nx} = 1.3\, S_{Nz} = 2.1\, q^{0.86} r^{-1.6} \text{ (mm)},$$

$$j_{Nz} = j_{Nx} = 10^{-4} \left(\frac{2\pi}{T_{Nx}}\right)^2 S_{Nx} \text{ (g)},$$

where r is the distance in m, q is yield in kt, S_z and S_x are vertical and horizontal displacements, j_z and j_x are vertical and horizontal acceleration for the P phase.

The arrival time of the *N* phase is given by $t_{arr} = (0.19\, r + 0.14)$ (s) and the dominant period is $T_N \approx 3T_P$.

Rayleigh wave (*R*-wave) becomes visible at distances over 0.5 – 1 km/kt$^{1/3}$. Formation of the surface wave for shallow explosions is often attributed to spall effects (e.g. Viecelli, 1973). As the distance increases the amplitude of Rayleigh wave approaches the P wave amplitude, and exceeds it by the end of the near-source zone.

The amplitudes for *P*- and *R*- waves observed on vertical and radial components are larger than tangential amplitudes, particularly near the source. As the distance increases the tangential

amplitudes become larger due to heterogeneities of the medium, and surface waves of Love type (*L*-wave) can be observed. Analysis of seismic data from the STS yielded empirical relationships for parameters of *R*- and *L*- waves as a function of yield and distance for the near-source zone. For the *R*-wave with the arrival time is t_{arr} = (0.34 *r* +0.2) (s) and the amplitudes and dominant periods are given by:

$$v_{Rx} = v_{Rz} = 9\,(r/q^{1/3})^{-1.5} \text{ (cm/s)}, \quad (4.9)$$

$$S_{Rx} = S_{Rz} = 3.0\,q^{0.75}r^{-1.25} \text{ (mm)},$$

$$j_{Rz} = j_{Rx} = 10^{-4}\left(\frac{2\pi}{T_{Rx}}\right)^2 S_{Rx} \text{ (g)},$$

$$T_{Rx} = T_{Rz} = 0.4\,q^{0.2}r^{-0.4} \text{ (s)},$$

where *r* is the distance in km, *q* is yield in kt.

Amplitudes and periods for the L- wave with arrival time coinciding with the arrival time for the R- wave are given by:

$$v_L = 7.5\,(r/q^{1/3})^{-1.5} \text{ (cm/s)}, \quad (4.10)$$

$$S_L = 1.6\,q^{0.75}r^{-1.25} \text{ (mm)},$$

$$j_L = 10^{-4}\left(\frac{2\pi}{T_L}\right)^2 S_L \text{ (g)},$$

$$T_L = T_R,$$

where *r* is the distance in km, *q* is yield in kt.

Observations show that the major parameters for both body and surface waves in the near-source zone scale as $q^{1/3}$. The velocity amplitudes and their decay with distance depend on the rock type and sensor location. The amplitudes measured on vertical and horizontal components are approximately equal in this zone for both body and surface waves.

The dominant periods of oscillation for P- and R- waves have weak dependence on yield ($T_P \sim q^{0.2}$ and $T_R \sim q^{0.2}$). The period of oscillation for the P- wave changes from about 0.05 – 0.1 s at a distance of 1 km/kt$^{1/3}$ to about 0.2 – 0.4 s at distances of 10 – 15 km/kt$^{1/3}$. For the R- wave the period increases in the same distance range from about 0.3 – 0.6 s to about 1 – 2 s (in the near-source zone the period of oscillation for the surface waves is higher than the period for the body waves, by a factor of about 3 – 5), The total duration of seismic oscillations increases from 1 – 2 s at a distance of 1 km/kt$^{1/3}$ to 4 – 5 s at distances of 10 – 15 km/kt$^{1/3}$ and can be calculated using the relationship

$$t_{tot} = (0.34\,r + 0.6) \text{ (s)}.$$

An increase in sDOB greater than 150 – 200 m/kt$^{1/3}$ results in an overall decrease in surface oscillations in the near-source zone. The longitudinal P-wave produces oscillations mainly in the

vertical direction, so the vertical component of velocity becomes greater than the horizontal component:

$$v_{Pz} = (\ 1.5 \text{ to } \ 2)\ v_{Px}.$$

Surface waves can barely be identified for these explosions. The effects of yield and distance on the velocity amplitudes are given by:

$$v_{Pz} = \frac{35}{\left(\frac{r}{q^{1/3}}\right)^2} \text{ (cm/s)}, \tag{4.11}$$

where r is in m, and q is yield in kt.

The maximum velocity on the horizontal component is typically observed at later stages of the oscillations because these waves are produced by refraction of shear waves with slower propagation velocities. The relationship between v_{Px}, explosion yield, and epicentral distance, is given by

$$v_{Px} = \frac{17}{\left(\frac{r}{q^{1/3}}\right)^2} \text{ (cm/s), for } 1.5 < r < 30 \text{ km} \tag{4.11}$$

where r is in m, and q is yield in kt.

Analysis of seismic oscillations in the near-source zone have shown that a presence of the free surface makes an explosion a more complicated source of seismic waves than a simple source composed only of a center of expansion. Evidently in order to interpret the shear and surface waves it is necessary to choose separate sources of different types, one of which produces shear waves, and the other responsible for the surface waves.[10]

Studies of seismic efficiency of nuclear explosions were conducted using seismic measurements in the near-source zone, where cube root scaling applies. The studies were conducted using explosions with different sDOB, including ejection explosions with $W/q^{1/3} \leq 0.04 \div 0.06$ km/kt$^{1/3}$ ($W/q^{1/3} \leq 40 \div 60$ m/kt$^{1/3}$). Figure~4.7 shows the ratios of the displacement P-wave amplitudes to the displacement produced by a fully confined explosion, at the same epicentral distances, as a function of the sDOB. The results were obtained using seismic measurements in a large range of distances and similar geological conditions. The plot shows that the amplitudes due to surface explosions are reduced by a factor of 10 compared to those from fully contained explosions. The amplitude reduction for the ejection explosions is approximately by a factor of 2 – 3. The amplitude grows up to depths of $W/q^{1/3} > 70 \div 100$ m/kt$^{1/3}$ and then the growth levels off and the amplitudes stay mostly the same as the depth increases further.[11]

[10] This could be a way of saying that different facets of the source are responsible for the different features associated with different wave types. Note added by translators

[11] Several western studies have given evidence that, instead of leveling off, the excitation of P-waves decreases as depth increases, due to the smaller cavity generated for explosions at greater depth. (Note added by translators.)

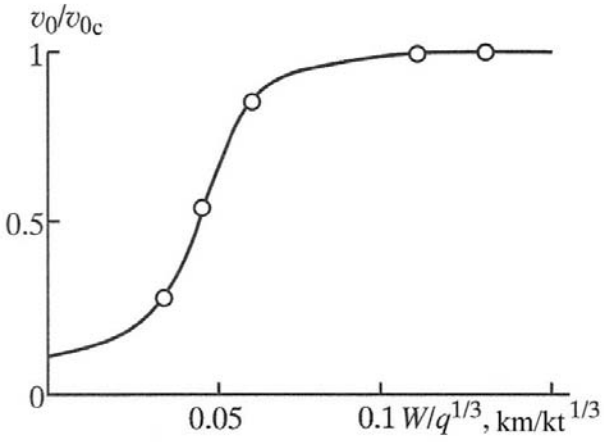

Figure 4.7. Ratio between the ground velocity v_0 and the ground velocity produced by a fully contained explosions v_{0c} as a function of the explosion depth.

Intermediate zone ranges from distances of 10 – 15 km to 80 – 100 km. In this zone the wavefield is dominated by head waves refracted at a mid-crustal granite-basalt interface. Low frequency surface wave amplitudes can still be identified (Figure~4.4). The most dangerous phase from the point of view of its seismic action is the head wave of P type with maximum velocities in the short period range from T_p = 0.1 to 0.5 s. Observations show that the amplitude of the oscillations depends not only on the explosion yield, but also on the details of the geological structure and location of the reflectors within the crust. Therefore cube root scaling is not appropriate to describe seismic wave amplitudes in this zone. To describe seismic waves,[empirical relationships can be used which relate seismic amplitudes to explosion yield and epicentral distance in the form

$$v = B\, q^{n} r^{k}. \tag{4.13}$$

Using data from international and Russian sources for maximum horizontal and vertical velocities of P waves in the intermediate zone [] the following relationships are recommended:

$$v_{Px} = 15\, q^{0.7} r^{-1.5} \ \text{(cm/s)}, \tag{4.14}$$
$$v_{Pz} = 35\, q^{0.7} r^{-1.85} \ \text{(cm/s)},$$

where r is in km, and q is yield in kt.

The dependence of v_{Px} on epicental distance for two values of yield (1 kt and 100 kt) is shown in Figure 4.6 with lines 3 and 3\prime respectively. Depending on geological structure along the ray path the ground velocity amplitudes may vary from the values predicted by (4.14) by as much as a factor of 2. For instance if the station is located on top of a soft layer the velocities are usually exceed the values predicted by (4.10) by a factor of 2. This range is shown in Figure~4.6 as shaded areas.

P-wave amplitude and period are practically independent of explosion depth as long as the conditions for a fully contained explosion are satisfied ($W/q^{1/3}$ > 70 to 120 m/kt$^{1/3}$). Displacement amplitudes can be estimated using the relationships

$$S_{Px} = 0.5\, v_{Px}\, T_P \quad \text{and} \quad S_{Pz} = 0.5\, v_{Pz}\, T_P,$$

where T_P is the dominant period of *P*-waves which is close to the period they would have for an explosion in an infinite space. It follows from equations (4.6), (4.7) and (4.9) that high frequency body wave oscillations decay faster than the low frequency surface waves. Therefore as we move away from the source there will be a distance where the surface wave amplitude becomes dominant. Surface wave amplitudes are determined by the signal at the boundary of the elastic zone [elastic radius] and the depth of burial. For example for deeper explosions ($W/q^{1/3}$ > 200 m/kt$^{1/3}$) surface waves are first observed at larger distances (over 10 – 20 km) [than for shallow explosions]. Surface wave velocities for these explosions increase up to 3.1 – 3.2 km/s. The relationship between the dominant periods for surface and P waves is given by $T_R \approx (2\ to\ 4)T_P$ and the most common period is $T_R \approx 1\ to\ 2\ s$. Maximum amplitude of the surface waves for the horizontal and vertical components in the distance range 30 – 300 km is expressed as:

$$S_{x,z} = B_{x,z}\, q^{0.9} r^{-1.4}\,, \tag{4.15}$$

where $B_{x,z}$ is a site-dependent coefficient. The amplitude and duration of oscillations in this distance range significantly depends on regional geological structure along the ray path and site conditions. Thus site and propagation effects can cause amplitude variations along different profiles up to 50 – 100 %. However this variability of local geology causes the averaging of the seismic wavefield and its relative independence on the rock properties, unlike in the near-source zone, where the seismic waves are mostly determined by the rock properties at the source. Therefore (4.15) can be successfully applied to determine yield of underground explosions along calibrated ray paths. Such method of nuclear yield estimation is given in Section 4.4.

The far-field zone extends beyond 80 km. In this zone the dominant arrivals are body waves critically reflected from Moho discontinuity (including *PmP* and *SmS* phases). Distances where these waves appear, and their amplitudes, are related to the crustal velocity structure and the character of the Moho (i.e. its continuity, depth, velocity contrast, existence of a transition zone etc). Seismic observations from nuclear explosions show that in some cases the displacement amplitude variations for *PmP* and *SmS* can reach an order of magnitude, with corresponding peak velocity changes by a factor of 2 – 3. Therefore our ability to predict the peak velocity (shear and longitudinal) for these waves reach maximum in the distance range of 80 – 150 km (e.g. Figure 4.6, line 4 for 1 kt, line 4′ for 100 kt).

Seismic amplitudes may double if thick sediment layer is present, or if the ground water table is close to the surface, a situation which is shaded in Figure~4.6. At distances of 150 – 300 km multiple reflections of body waves begin to appear, some of which may have large amplitudes. The period of oscillations increases to approximately 1 s. This increase leads to the amplitude decay with distance becoming similar to the decay in the near-source zone, so

$$v_{Px} \sim q^{0.8} r^{-(1.4 \div 1.8)}\,.$$

For example data from the Nevada Test Site show that maximum peak velocities decrease with distance as $v_P \sim (1/r)^{(1.5 \div 1.6)}$ and the peak of the spectrum is reached at 0.8 Hz. Since the dominant seismic amplitude is determined by crustal geology and velocity structure, seismic amplitudes are not described by cube root scaling and can be determined using expression in the

form (4.13) commonly used in explosion seismology. For instance it has been shown from multiple observations that a relationship $v_P \sim q^{0.8}$ can be used to predict peak velocities in the far-field zone (beyond about 80 km distance), which was used to determine the horizontal velocity amplitudes plotted in Figure~4.6.

Another important characteristic of seismic waves is the total duration of oscillations created by an event. As distance increases the total duration of oscillation increases due to differences between seismic velocities of P, S, and surface waves. The duration of oscillations within each group also increases due to multiple reflections and reverberations.

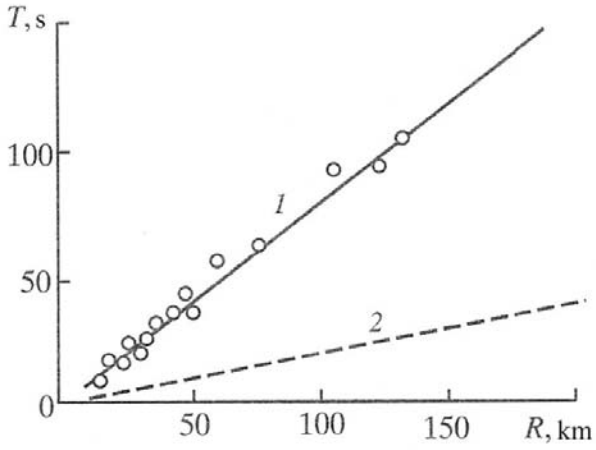

Figure 4.8. Total duration of the oscillations produced by underground explosions T (line 1) and duration of the body waves (T_b) (line 2) as a function of distance.

Figure~4.8 shows the total duration of oscillations plotted against epicentral distance for NTS and Amchitka explosions with yields ranging between 100 and 1000 kt. Also shown is the body wave duration. Seismic waves were recorded using accelerometers with a 0.01 g low amplitude cut-off [In this case the total duration of oscillations T and the duration of body waves T_b are almost directly proportional to the epicentral distance, and for distances $r \leq 10$ km they are described by

$$T = 0.8\, r \text{ (s)}, \quad T_b = 0.8\, r \text{ (s)}. \tag{4.15}$$

In determining the duration of the oscillations, the effects of yield, velocity structure along the ray path, site effects (including the effects of recording equipment), and even the type of physical variable being recorded (such as acceleration, velocity or displacement) should be taken into account. For example the presence of a soft surface layer at the recording site can increase the oscillation duration by nearly a factor of 2 compared to a station installed on a hard rock outcrop. On the other hand, using accelerometers can reduce the apparent duration by a factor of 1.5 – 2 due to their low sensitivity to surface waves.

4.4. Yield estimation for underground nuclear explosions using Rayleigh waves

Based on regional observations of seismic waves a method was developed that enabled yield estimation using seismic waves observed between 10 and 300 km.

In this distance range different seismic phases are sufficiently separated in time to allow clear identification of these waves and measurement of their main features. Rayleigh (*R*) waves have the largest displacement amplitudes produced by ~100 kt nuclear explosions at a distance of 10 km (the displacement is on the order of 10 mm); at distances of 300 km the displacement is on the order of 0.1 mm. P-waves have the largest amplitudes of ground velocity, measuring between 10 cm/s and 0.01 mm/s for the same distance range for $1 \leq q \leq 100$ kt, with frequency content ranging between 0.1 and 10 Hz. The duration of the oscillations increases with distance from 2 – 5 s to 200 – 300 s.

These observations show that in this distance range the wave amplitudes significantly exceed the microseism level (in continental shields these are on the order of 10^{-8} – 10^{-9} mm).

High signal-to-noise ratio lowers the requirements for recording equipment and seismic processing. For instance there is no need to filter the signals. More importantly due to the high signal-to-noise ratio there is no need to built structures for the seismometers, which can be installed directly at the surface, preferably on bedrock outcrops.

Thus seismic waves in the distance range between 10 and 300 km have minimum distortion due to propagation, compared to waves recorded in regional (beyond 300 km) and teleseismic zones. The shorter distance range provides higher accuracy of yield determination using seismic waves. For instance, explosions with yields less than 0.1 kt can be accurately detected and identified. In addition the separation between P-, S-, and R-waves at distances 10 – 300 km allows determination of yield using both body waves and surface waves. Lg waves can also be used. We note that, based on the results of Section 4.2, Rayleigh wave amplitude depends on the explosion depth and not on properties of the emplacement medium. On the other hand P-wave amplitudes are almost independent of depth and depend strongly on the physical properties of the emplacement rocks. Therefore using a combination of body and surface waves, as well as Lg waves, reduces the uncertainty of the yield and depth estimates.

Below we show the method of determining yield of nuclear explosions using minimum amplitudes of the surface waves observed at regional distances 10 km < r < 300 km (e.g. Adushkin et al, 1990; Adushkin, 2001). Rayleigh waves were chosen because their amplitudes are larger than those of body waves, and their dominant periods are several times higher than the periods of the body waves, thus reducing the influence of local heterogeneities. In addition Rayleigh wave amplitudes are less dependent on the emplacement rock properties. Therefore we expect good correlation between Rayleigh wave amplitude and yield.[12]

[12] Parts of the following material are also to be found in Adushkin, 2001, Yield estimation for Semipalatinsk underground nuclear explosions using seismic surface-waves observations at near-regional distances, Pure & Appl. Geoph., 158, 2217–2226. Note added by translators.

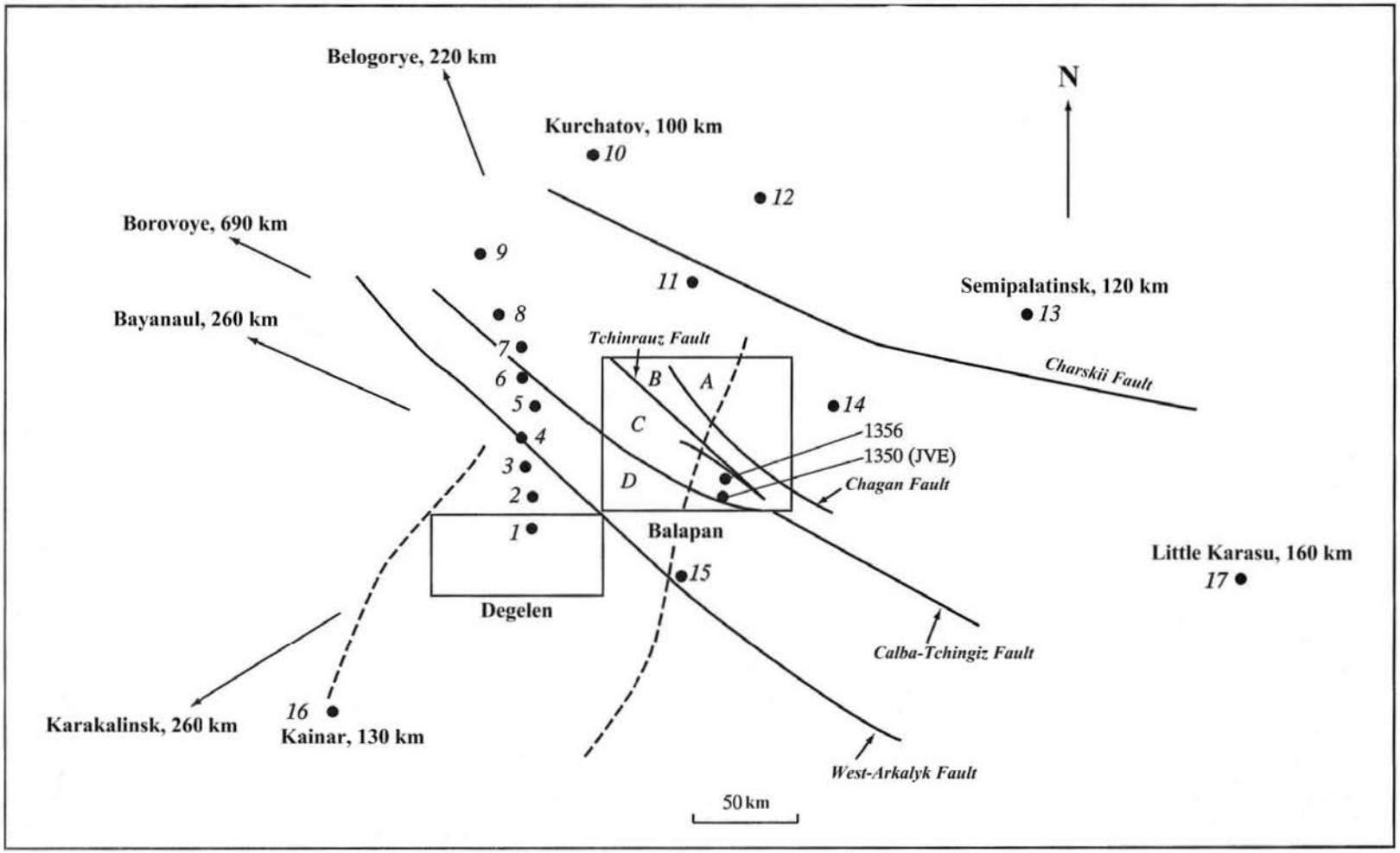

Figure 4.9. Map showing locations of the seismic stations of the near-regional Semipalatinsk network. Also shown are deep regional faults located around the test site. The letters A, B, C, show the regions separated by regional faults.

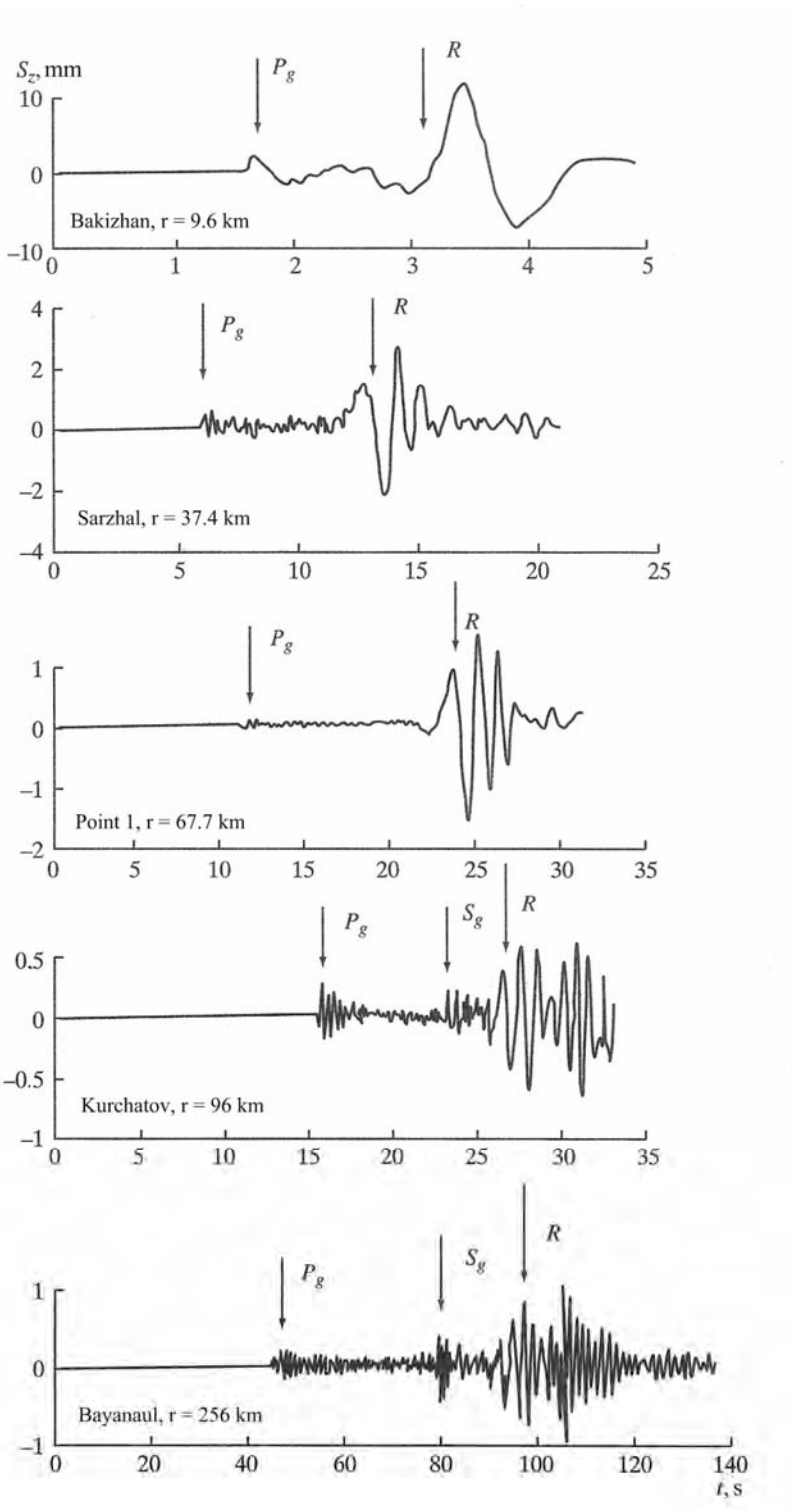

Figure 4.10. Vertical displacement waveforms recorded by a network of stations located at different distances from the 85 kt nuclear test conducted at Balapan on October 10, 1989.

During the period of nuclear testing a seismic network was installed at the STS to record the explosions. The stations of the network recorded three components of motion: radial, vertical and transverse.

Figure 4.9 shows the locations of these stations. The network consists of a north-south profile of nine permanent stations (stations 1 – 9). In addition seven temporary stations were located in small towns (populated areas) around the test site (Stations 10 – 16). The seismometers were installed either on specially prepared concrete pads, or on hard rock outcrops. The frequency responses of these instruments were essentially flat from 0.2 – 0.5 to 20 Hz, with a dynamic range of 40 – 50 dB. The data were recorded using analog magnetic tape using standard compact cassettes. Some stations were recording in analog format using photographic paper.

Figure 4.9 also shows significant tectonic faults of the region, including Kolba – Tchingiz, West Arkalyk and Charskii faults, which represent zones of inhomogeneous broken rocks with widths of tens or hundreds of meters. Observations suggest that these deep zones significantly affect seismic wave propagation, in some instances attenuating seismic waves, and forming waveguides in others.

A typical profile of vertical displacement waveforms from the 85-kt nuclear explosion conducted at Balapan on October 19, 1989 at a depth of 629 m recorded by a network of seismic stations (Figure 4.9) is shown in Figure~4.10. At distances greater than 10 km the longitudinal (*P*), shear (*S*) and surface (*R*) waves are well-separated in time, which allows their identification and determining their characteristic features. Surface waves (*R*) have the highest displacement amplitudes and their periods exceed those of body waves by a factor of 4 – 10.

On the other hand body waves (*P* and *S*) have higher velocity amplitudes (than surface waves). In general the observed seismic signals are very complex and contain large number of separate phases related to complex geological structure along the propagation paths.

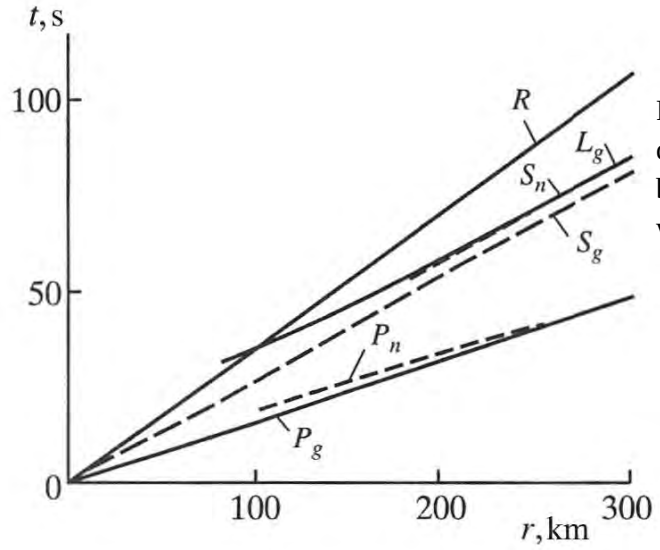

Figure 4.11. Travel time curves at regional distances from Semipalatinsk Test Site showing body wave phases *Pg*, *Pn*, *Sg* and *Sn* and surface wave (*R*).

Observed travel time curves for different phases, which can be identified and tied to known boundaries within the crust and upper mantle, are shown in Figure 4.11. According to the travel time curves, the first arrivals at distances less than 200 km are represented by the Pg phase, refracted in the upper layers of the crust with apparent velocities between 5.3 and 6.6 km/s. The Pn phase, which represents critical angle refraction along the Moho boundary, arrives first at distances greater than 200 km and has apparent velocity between 7.7 and 9.1 km/s. *Pn* amplitude becomes the largest among the P-wave group at distances close to 100 – 150 km.

Shear waves *Sn* and *Sg*, similar to longitudinal waves *Pn* and *Pg*, propagate with apparent velocities of 3.1 km/s for *Sg* and 3.9 – 5.5 km/s for *Sn*. The amplitude of *Sn* becomes the largest among the body wave amplitudes beyond 100 km[13]. The Rayleigh wave arrives the last with a dominant group velocity close to 2.75 km/s and polarization in the vertical plane. We note that the travel time curves are practically the same in all directions from the epicenter.

The first step in developing a method of determining yield of explosions using surface wave (*R*) parameters involved study of wave periods and displacement amplitudes as a function of the explosion yield and distance. Analysis of the recorded waveforms (experimental data) shows that with an increase in epicentral distance the number of phases within R wave increases and consequently increases their duration. As it turns out, the duration of oscillations and the shape of the group are practically independent of the explosion yield, physical properties of rocks, or propagation conditions along the specific ray path.

The duration of oscillations in the surface wave *R* depends only on the epicentral distance according to $\vartheta \propto r^{0.5}$. Oscillations in the *R*-wave are close to sinusoidal, however the period decreases with time. Therefore we will consider the period *T* of the phase with the maximum displacement amplitude. We note that these periods for the radial and vertical components are almost the same.

The dominant periods of R-wave are almost the same for explosions of different yields (in the range between 0.02 and 126 kt and can be expressed as a power law $T \sim q^{0.23}$. As an example Figure 4.12 shows the dependency of *T* on *r* for two explosions with yields of 28 and 3.4 kt. Similar data for different yields were used to analyze the dependence of the dominant period *T* on the explosion yield *q*. Figure 4.13 shows an example of the period of the R wave as a function of yield *q* at a distance of 10 km. Using these and similar data for different distances it was found that in the range of yields from 1 kt to 100 kt despite the different emplacement conditions the dependence of the period of *R*-wave at a fixed distance is very weak, namely $T \sim q^{0.05}$.

The dependence of R-wave amplitudes on the explosion yield and epicentral distance was also studied in detail. Figure 4.14 shows peak vertical (Sz) and radial (Sx) displacements for the *R*-wave as a function of distance for a 32 kt explosion. To reduce the effects of propagation path and radiation pattern, the amplitudes were obtained from seismograms recorded along nearly the same azimuth (the difference in azimuths was less than 10º). Similar relationships were obtained

[13] Possibly a typo. Extensive experience in western studies has shown that Lg-waves (the more common name for Sg) are the largest. (Note added by translators.)

for 15 explosions with yields between 1 and 100 kt. The results of this study show that amplitude decay with distance for this region is proportional to $r^{-1.4}$.

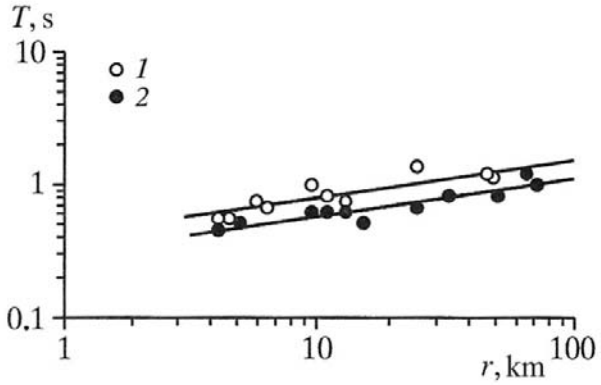

Figure 4.12. Dominant period of surface waves as a function of epicentral distance for explosions with different yields: 1 – 28 kt, 2 – 3.4 kt.

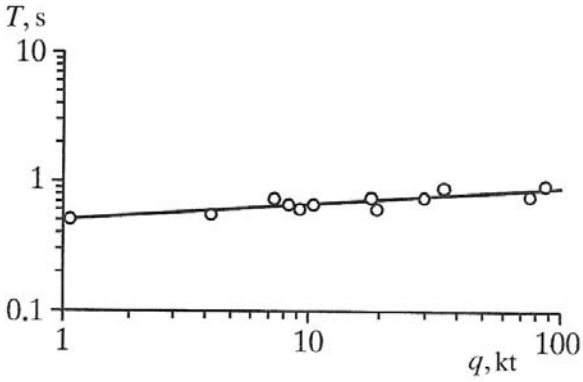

Figure 4.13. Dominant period of surface waves as a function of yield at the epicentral distance of 10 km.

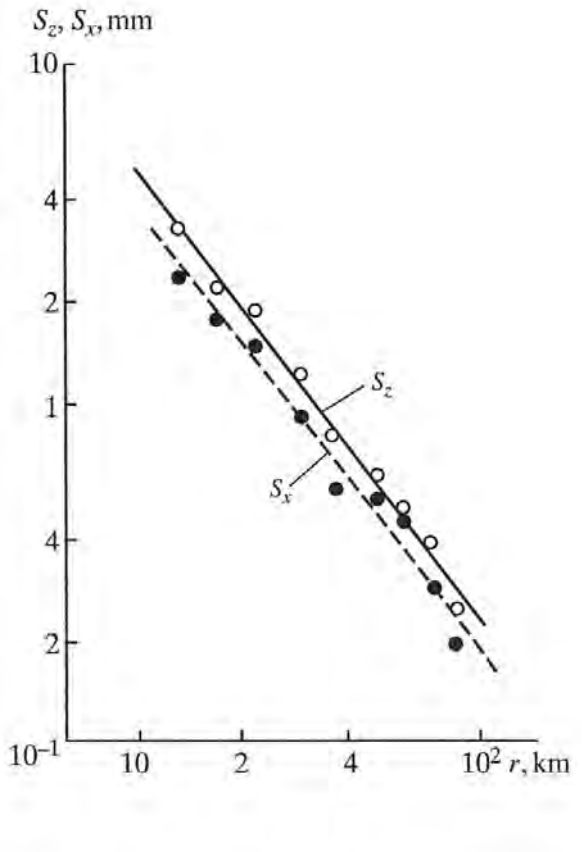

Figure 4.14. Peak displacements for radial (S_x) and vertical (S_z) components of surface waves (R) as a function of distance.

The relationship between the *R*-wave amplitude and the explosion yield was estimated using the observed amplitudes normalized by distance $S \cdot r^{-1.4}$. One of the relationships for a station located at distances between 80 and 100 km from the explosions is shown in Figure 4.15. To obtain this relationship we used explosions with epicenters located within an approximately 10 x 20 km area bounded by the regional faults. For these explosions the azimuth to the station does not vary significantly, therefore the ray paths are almost identical, and physical properties of the emplacement media were all similar.

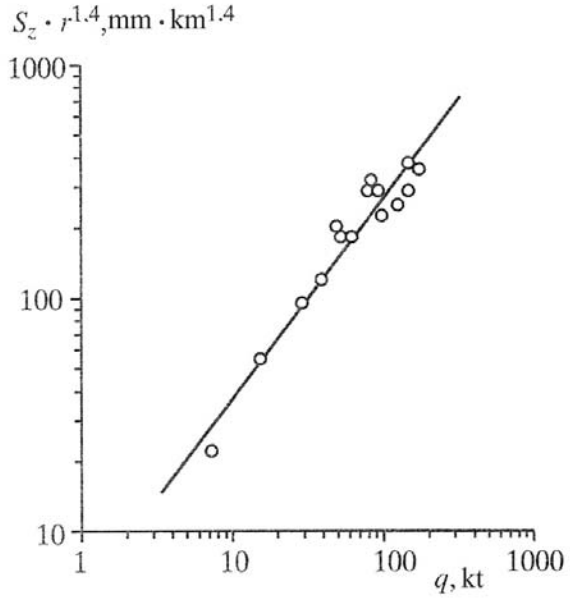

Figure 4.15. Maximum displacement S_z for surface waves (*R*) as a function of yield for a seismic station located 80 – 100 km from the explosions.

It follows from the plot in Figure 4.15 that the relationship between surface wave amplitude and yield is described by a simple formula $S \cdot r^{-1.4} \sim q^m$, where m = 0.88 for this particular seismic station. Similar results were obtained for other seismic stations with the parameter *m* varying between 0.85 and 0.92. The average value rounded to the first decimal number is 0.9. Thus the relationships between the surface wave (R) amplitude, explosion yield and epicentral distance is expressed as:

$$S = Aq^{0.9}r^{-1.4}, \tag{4.17}$$

where *A* is a station-dependent amplitude constant.

Using Equation 4.17 the coefficients A_i (i is a station number) were determined for each seismic station using the known parameters *S*, *r* and *q*. For this analysis seismograms from approximately 100 underground explosions conducted at Balapan were used. The average values of $\bar{A}_i$ for individual stations varied by a factor of 4, therefore they cannot be averaged to obtain a single scaling relationship. The individual station coefficients $\bar{A}_i$ can be used to account for the surface wave amplitude variations due to propagation.

Further reduction in variance was obtained when each station coefficient $\bar{A}_i$ was estimated separately for four different zones (zones A, B, C, and D) separated by regional tectonic faults. Using this approach the coefficients depend not only on the station location (i – station number) but also the condition at the source (index j determines one of the zones A, B, C, or D). Therefore the coefficients are denoted as A_{ij}. Subdivision of the source regions into separate zones reduced the observed standard deviation of log A_{ij} by 25% compared to the standard deviation of log A_i. Several thousands of seismograms were analyzed using this approach and the average value of $\overline{\log A_{ij}}$ was found for stations 1 – 16 shown in Figure 4.9 and four zones (A –D) for Balapan Testing Area.

Table 4.4. Average values of the station coefficients $\bar{A}_{ij}$.

Seismic Station	Station coefficient $\bar{A}_{ij}$	Seismic Station	Station coefficient $\bar{A}_{ij}$
1	8.3	9	3.0
2	8.6	10	6.3
3	5.1	11	4.6
4	4.3	12	4.0
5	3.4	13	4.3
6	8.3	14	8.3
7	7.4	15	12.6
8	7.1	16	10.0

According to Table 4.4 the average values of the station coefficients $\bar{A}_{ij}$ range between 3 and 12.6. The variations for the source regions reach as much as a factor of 3.5 across all stations. The variations for a fixed station across all source regions reach a factor of 2. The values of the station coefficients for different stations located within a single block (separated by faults) are close to each other. However the coefficients for stations located in different blocks may vary by a factor of 1.5 – 2. The differences in station coefficient values are related to regional tectonics and crustal block structure within the test site.

Thus introduction of station coefficients accounts for propagation differences, geological structure at the station site, and the emplacement medium at the source.

Using relationship (4.17) and estimated average values of the station coefficients $\bar{A}_{ij}$, the following procedure was formulated to determine the yield of nuclear explosions using of Rayleigh wave characteristics. For each seismic station the standard deviation σ_{ij} was determined between $\overline{\log A_{ij}}$ and $\log \bar{A}_{ij}$. The average value $\log \bar{A}_{ij}$ was determined using 10 – 15 seismograms, which resulted in an error of 3 to 4 %.Explosion yield was determined using (4.17) for each station via

$$\log q_i^{x,z} = \frac{(\log \bar{S}_i^{x,z} - \log \bar{A}_i^{x,z} - 1.41 gr_i)}{0.9}, \tag{4.18}$$

where $q_i^{x,z}$ is the explosive yield determined using either the *x*- or *z*-component of the maximum displacement at station *i*, r_i is the distance between the source and i^{th} station, $\log \bar{A}_i^{x,z}$ is the average value of the station coefficient for i^{th} station for x- and z-components. The accuracy of the individual yield estimates ($\log q_i^{x,z}$) depends on the uncertainty σ_{ij} in the individual station coefficients. These uncertainties are different for different stations, so the final yield estimate is determined as the average of individual estimates calculated using (4.18).

Using weighting coefficients $\alpha_{ij} = 1/\sigma_{ij}$ the final yield estimate can be written as a weighted average of the individual yield estimates:

$$\log \bar{q} = \frac{\sum_i \alpha_{ij}^x \log q_{ij}^x + \sum_i \alpha_{ij}^z \log q_{ij}^z}{\sum_i \left(\alpha_{ij}^x + \alpha_{ij}^z\right)}, \qquad \bar{q} = 10^{\overline{\log q}}. \tag{4.19}$$

The inverse variance weighting is applied under the assumption that individual yield estimates are independent. The corresponding standard deviation of the average yield estimate is given by:

$$\log \bar{q} = \sqrt{\frac{\sum_i \alpha_{ij}^x (\log q_{ij}^x - \overline{\log q})^2 + \sum_i \alpha_{ij}^z (\log q_{ij}^z - \overline{\log q})^2}{(N-1)\sum_i \left(\alpha_{ij}^x + \alpha_{ij}^z\right)}}, \tag{4.20}$$

where *N* is the number of seismograms recorded for the explosion.

Evidently the deviation of the average yield estimated using equation~(4.19) from an actual yield q_0 is determined by the deviation of the average value of the station coefficient $\lg \bar{A}_{ij}$ from the average value of $\overline{\log A_{ij}}$ determined using seismic traces from previous explosions. Thus it is determined by the standard deviation for an individual station σ_{ij}. Calculations of σ_{ij} for all seismic stations show that their values are close with the average value close to 13%. This corresponds to uncertainty in determining the yield of the explosion using one component at a single station compared to the average value of yield estimated using (4.19). In the absence of systematic error (bias) and assuming log-normal distribution of q_i, the relative error in determining the explosion yield is approximately 10%. Thus yield estimate using Rayleigh waves provides good accuracy for explosions conducted at the STS.

The accuracy of seismic yield estimates based on *R*-wave amplitudes for explosions was assessed by comparison with known or independently determined (using non-seismic methods) yields. The sample of events included 34 explosions conducted in boreholes at Balapan with yields between 1.4 and 175 kt, as well as 13 explosions conducted in tunnels at Degelen with yields ranging between 1.1 and 79 kt. The ratios between the seismic yield estimates $\bar{q}$ and the known yield q_0 for 34 Balapan explosions are shown in Figure4.16 as a function of q_0. The deviation of the estimated yield values $\bar{q}$ from the actual value q_0 does not depend on yield and appears to be random. The accuracy of the yield estimation is quite good with the standard deviation of approximately 15%. The observed deviation somewhat exceeds the estimated method error of 10%. This discrepancy could be cause by several factors, for instance some of

the estimates were based on data from fewer than 10 stations. In addition, determination of explosion yield using non-seismic methods is also subject to uncertainty due to charge designs, explosion depth in the borehole, effect of the fracture zones left by previous explosions, etc. Calculations for the Degelen explosions using the average station coefficients shown in Table 4.4 show smaller scatter and the standard deviation for these explosions was 9%. This value is consistent with the predicted accuracy of the methodology.

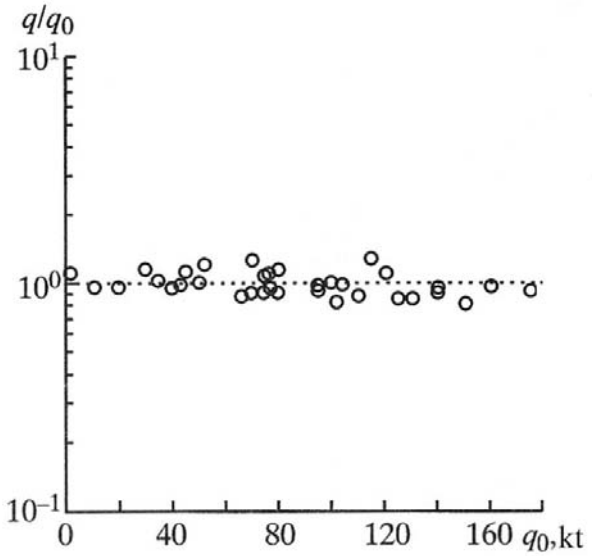

Figure 4.16. Ratios of the estimated yields using R wave parameters (q) to the actual (q_0) as a function of q_0 for a sample of 34 Balapan explosions conducted in boreholes.

Table 4.5. Maximum displacement for body S_P and surface S_R waves from the explosion in BH 1350 (JVE) for seismic stations 1 – 16.

Parameter	Parameter [for different stations]										
	1	2	3	4	5	6	7	8	9	10	16
r, km	60.8	60.4	61.5	62.8	63.1	69.8	74.8	84.7	96.9	105	31.2
S_{PX}, mm	0.18	0.20	0.11	0.19	0.16	0.12	0.10	0.19	0.11	0.18	0.93
S_{PZ}, mm	0.13	0.21	0.31	0.08	0.07	0.08	0.09	0.02	0.08	0.20	0.47
S_{RX}, mm	1.36	1.83	1.41	1.80	1.71	1.82	1.48	1.03	0.51	0.74	6.71
S_{RZ}, mm	1.86	2.91	2.11	2.53	2.08	1.94	1.68	1.53	0.47	1.08	3.93
T_R, c	1.67	1.57	1.49	1.35	1.43	1.49	1.55	1.52	1.53	1.50	1.30

The developed methodology was applied to the data from the Soviet-American Joint Verification Experiments (JVE). Two underground nuclear explosions were conducted as a part of JVE in 1988 with yields between 100 and 150 kt, one of them was conducted at the NTS, and the other at the STS.

The explosion at the STS was conducted on September 14, 1988 in the borehole 1350 (lat = 49° 52’ 41.56”, lon – 78° 49’ 24.73”, origin time 03:59:59.5 UTC) in the southern part of the Balapan Testing Area (Figure 4.9). The nuclear explosion was placed in a borehole with

diameter of approximately 1m at a depth of 642.3 m in granodiorites (density 2.59 g/cm^3, porosity 1.14%, moisture content 0.16%, total gas content 1.56 determined only by water vapor).

Examples of the seismic records showing different components of ground displacement are shown in Figure 4.18. Table 4.5 shows the measured peak displacement amplitudes for body (S_p) and surface (S_R) waves, as well as the period of oscillations in the surface waves T_R recorded at some seismic stations.

Analysis of the R-wave amplitudes for the explosion in borehole 1350 using the described methodology and taking into account the individual station coefficients produced the yield estimate of $q = 122.6 \pm 7.1\, kt$. This value is in a good agreement with the independent hydrodynamic measurements and CORRTEX measurements based on study by American scientists (as described e.g. by Sykes and Ekstrom, 1989) who obtained the value of $q = 110\, to\, 120\, kt$, as well as a Soviet study (e.g. MINATOM, 1996) that obtained the estimate $q = 122\, kt$.

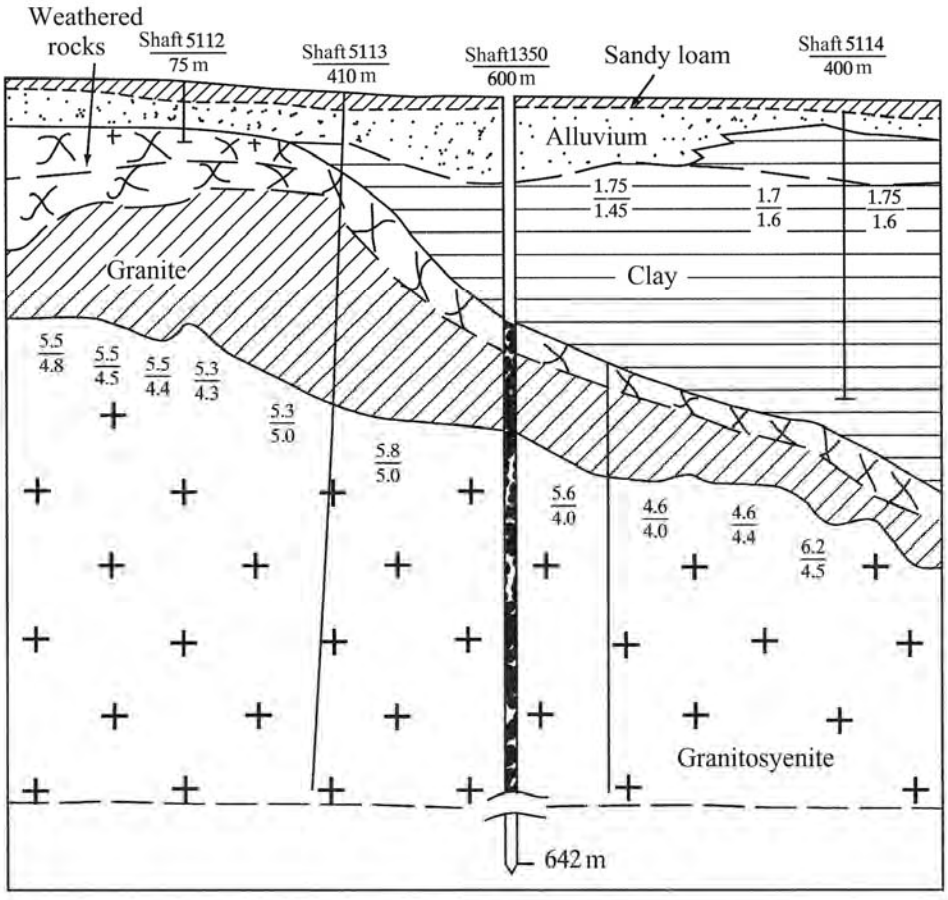

Figure 4.17. Schematic geological structure of the massif in the area of explosion in BH 1350 (JVE – Joint Verification Experiment). Numbers in the figure show seismic velocities along the boundaries. See additional explanations in the text.

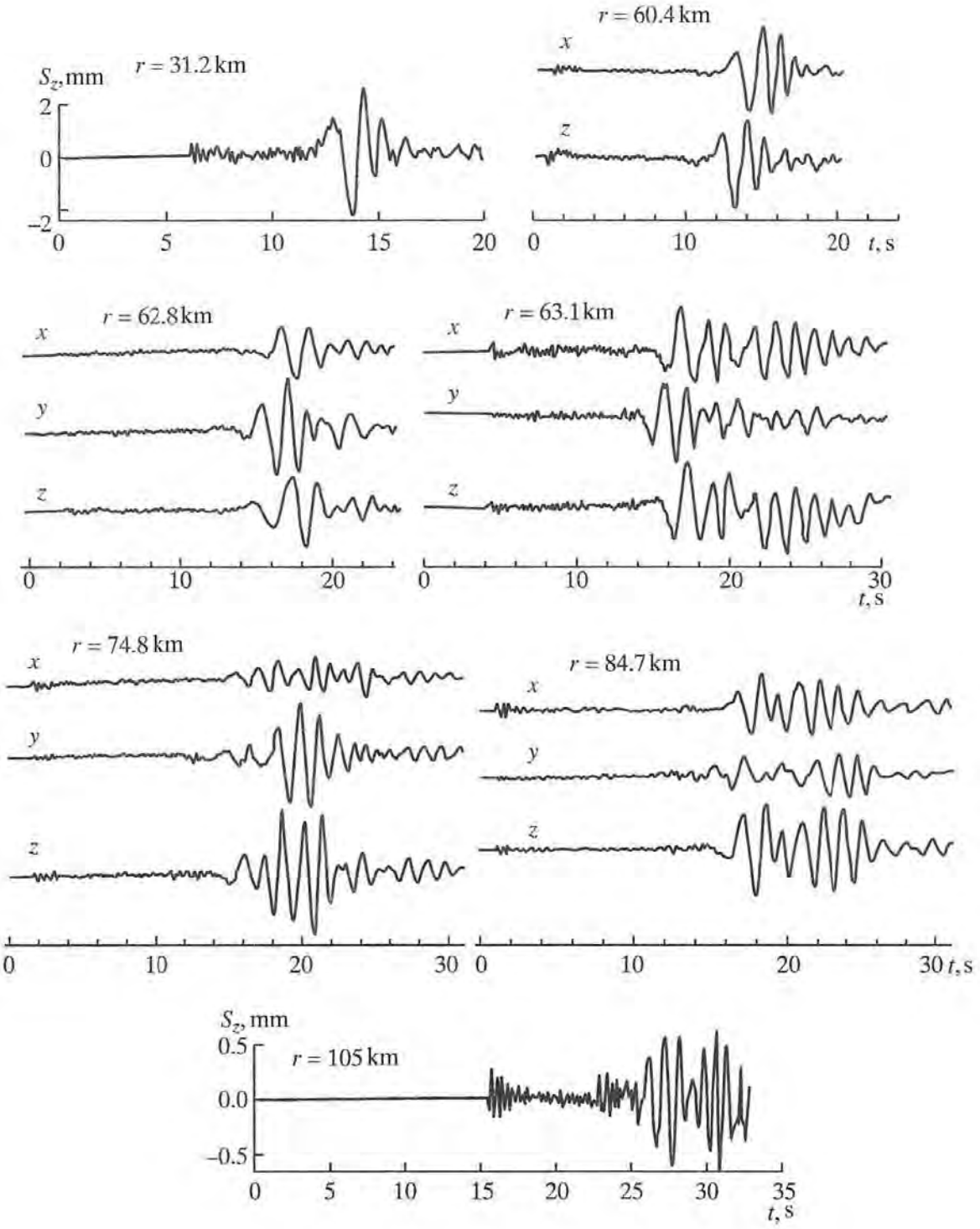

Figure 4.18. Examples of seismic displacement waveforms (x, y – horizontal components, z – vertical component) generated by an underground nuclear explosion in BH 1350 (JVE).

4.5. Seismological effects from underground nuclear explosions at Novaya Zemlya Test Site

Nuclear testing started at the Novaya Zemlya Test Site in 1955 by conducting explosions in the atmosphere (Chronology…1996). Three underwater and 87 atmospheric tests were detonated before 1962, 83 of those were high-altitude, 3 explosions were conducted above water, and 1 at the ground surface[14]. During the period between 1964 and 1990, 42 underground nuclear explosions were conducted at the Novaya Zemlya Test Site, including 36 explosions at the Northern testing area in the adits of the mountain massif located along the south bank of Matochkin Shar strait[15]. The remaining 6 explosions were conducted at the southern testing area near Chernaya Guba (Nuclear, 1997-2000). Overall, 132 nuclear tests were conducted at the Novaya Zemlya Test Site.

The region of the nuclear test site at Novaya Zemlya includes the northeastern boundary of the Fenno-Scandian (Baltic) Shield, the northern edge of the Russian Platform, and the Barentz Sea Platform. The crustal thickness in the area is 35 – 45 km. Local travel time curves indicate seismic velocities higher than those of other platform regions and higher than those associated with the Jeffreys-Bullen and Herrin travel time curves. Regional geodynamics is characterized by weak compressional stresses in the crust, expressed as local displacements of crustal blocks.

The map of regional seismicity shown in Figure 4.19 includes Novaya Zemlya earthquake epicenters of earthquakes that occurred between 1970 and 1992. Six earthquakes were detected in the region in these two decades. Their dates and magnitudes are given in Table 4.6, where parameters m_b and M_r represent body and surface wave magnitudes respectively.

A significant earthquake at Novaya Zemlya was recorded on August 1, 1986. The coordinates of this earthquake are: latitude 73.06°N, longitude 55.63°E, depth 3 km, origin time 13:56:35.2 UTC.

Table 4.6. Earthquakes in the Novaya Zemlya region during 1970s and 1980s.

Parameter	07.07.1971	12.02.1974	07.22.1974	07.07.1974	11.15.1978	08.01.1986
m_b	<3	<3	4.5	4.2	<3	4.4
M_R	<3	<3	3.5 – 4	3 – 3.7	<3	3.7

[14] Different sources provide slightly different numbers and dates of the various nuclear tests at NZTS. Working from official reports, Khalturin et al. (2005) list 85 high-altitude atmospheric tests, of which two were regarded as failures (compare with the number 83 given above). Khalturin et al. describe the first test at NZTS, in 1955, as having been underwater; the second test, in 1957, as having been at the ground surface, and the first atmospheric test at NZTS as having taken place on September 24, 1957.

[15] Concerning underground explosions at NZTS, which began in 1964, official sources list 39 separate tests, consisting of 133 separate explosive devices. Most of these underground tests involved multiple explosions fired almost simultaneously and so close to each other that their signals were effectively the same as from a single explosion. Different counting rules lead to the number 42 given above.

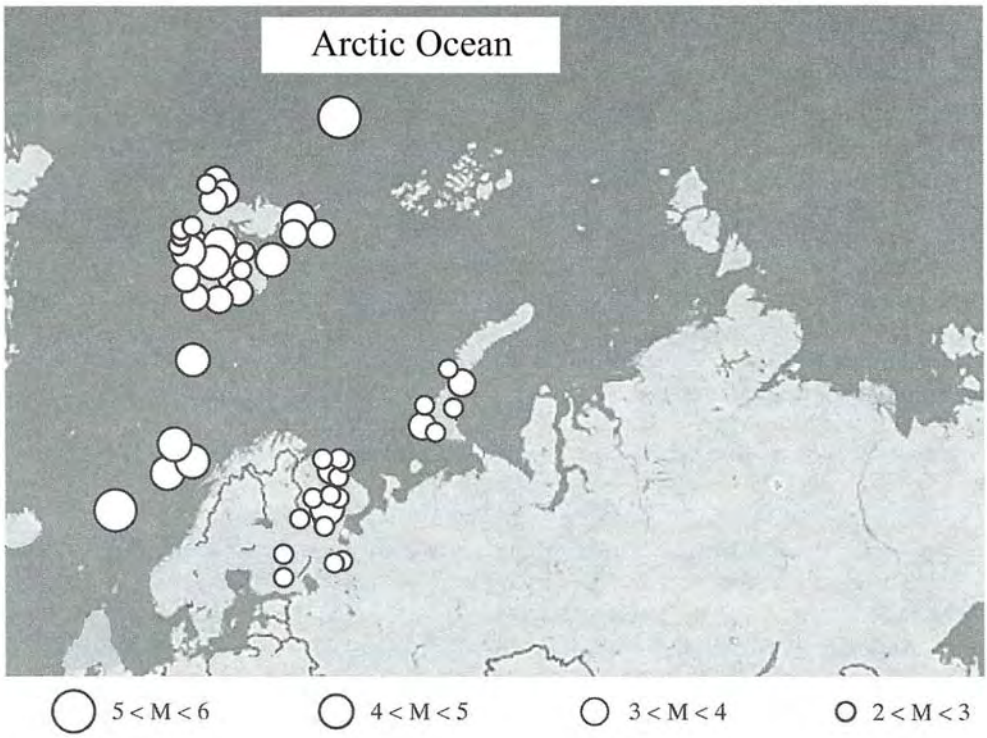

Figure 4.19. Epicenters of earthquakes which occurred in Fennoscandia in 1988 and in Novaya Zemlya during 1970 – 1992.

No more earthquakes with magnitude greater than 3 were recorded after 1986. The last earthquake that occurred in the area of Matochkin Shar with magnitude of 2.5 was recorded on December 31, 1992. This event received wide publicity among both American and Russian seismologists due to similarities in the waveforms with nuclear explosions. This event was a subject of detailed analysis in order to determine whether it was a nuclear or a chemical explosion. However the analysis has shown that it was an earthquake. Thus earthquakes with magnitudes 2.5 – 4.5 occasionally take place in the Novaya Zemlya archipelago. There is no evidence of any historical earthquakes in the area[16].

The Kola Peninsula area is more seismically active than the Novaya Zemlya archipelago. Approximately ten earthquakes with magnitudes between 2.5 and 4.4 were recorded at Kola Peninsula during 1986 – 1987. Therefore the Kola Peninsula region is considered capable of producing M6 events with maximum magnitude for natural events of 4.5 and depths up to 10-15 km. This assessment and forecast are determined using earthquakes in the area of Kandalakshskaya Guba and Kildinsko-Kovdorskii seismic region in Khibiny Massif [17].

[16] The Russian text was written prior to another earthquake in the Kara Sea, on August 16, 1997, that also attracted attention, as described by Richards and Kim, Nature, v389, 781–782, 1997

[17] The sentence appears to have inconsistencies, saying the region can have events up to M 6 and then that the maximum magnitude is 4.5. Are they saying that man-made events can be up to M6? (Unlikely).

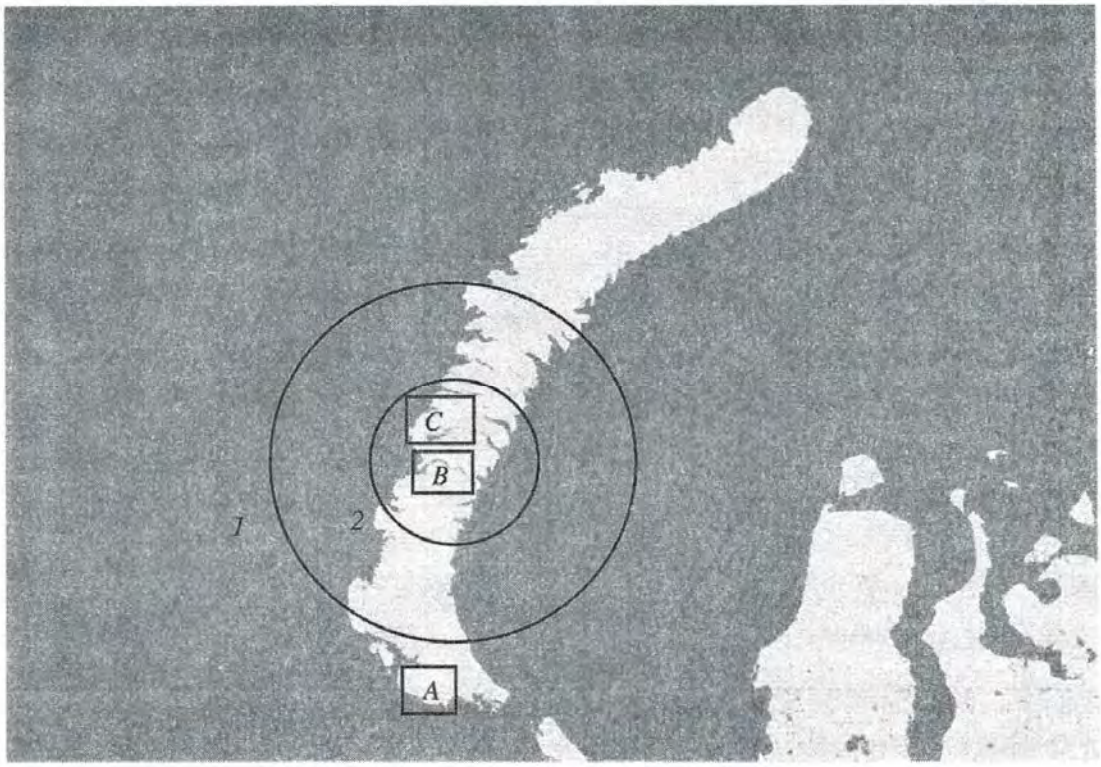

Figure 4.20. Map of Novaya Zemlya testing areas (A, B, and C) and intensity contours [check] for a 150 kt explosion. The intensity zones shown as circles: 1 – intensity 2; 2 – intensity 3.

It is well known (Nuclear, 1997 – 2000) that the nuclear tests at Novaya Zemlya were conducted in three testing areas (Figure 4.20):

- In the southern part of Archipelago in the Chernaya Guba ("Black Bay") area, where atmospheric and underground tests and one surface test were conducted from 1955 to 1962. During 1972 – 1975 underground tests were conducted in shaft in this region (Area A).
- Northern Island in the area of Sukhoy Nos ("Dry Nose") Peninsula and Mityushikha Guba, where atmospheric tests including the 50 Mt super-bomb were conducted from 1957 to 1962 (Area C).
- Northern part of the South ["Yuzhnyi"] Island in the area of Matochkin Shar Straight, where underground tests were conducted in horizontal adits from 1964 to 1990 (Area B).

Seismic recording was conducted for all tests conducted at the Novaya Zemlya Test Site. The measurements were conducted: inside the massif along the adit and at the entrance; in the near-field at distances up to 10–15 km; along a 300 km profile along the west coast; and on the mainland using temporary and permanent stations.

Particle velocity measurements inside the rock massif along the adit (tunnel) from the charge to the adit entrance were measured using strong motion recorders (types ZhIS and OSP) specifically designed for this purpose. The measurements of the particle velocity in Novaya Zemlya adits are shown in Chapter 1. In addition the wave parameters were recorded at the area

near the entrance, where vans with recording equipment, energy sources, helicopters and other equipment were located. Results of these measurements were needed to assess effects of seismic waves on these objects (equipment) and the degree of danger to these objects.

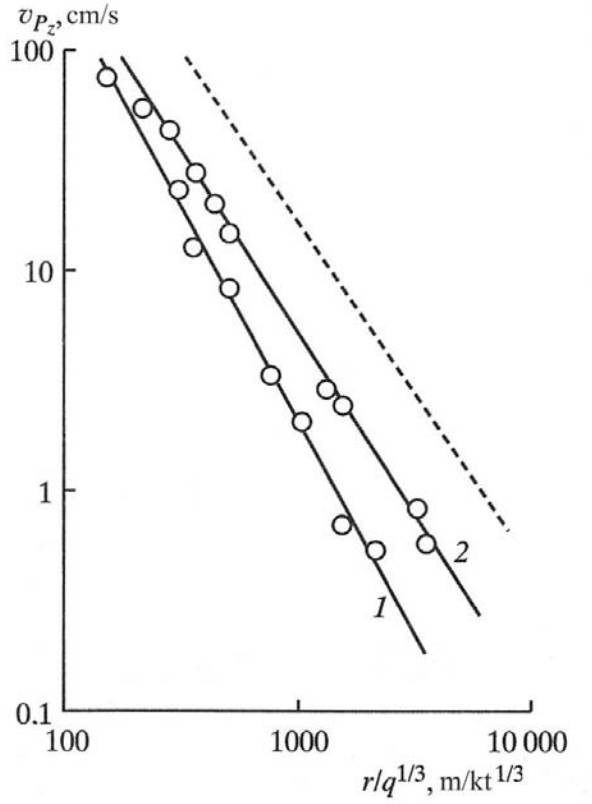

Figure 4.21. Vertical component of *P*-wave velocity amplitude as a function of scaled distance for the experiment conducted in Tunnel A-32 (measurements are made near the tunnel entrance and in the near-field). Lines show: 1 – along layering, 2 – across layering.

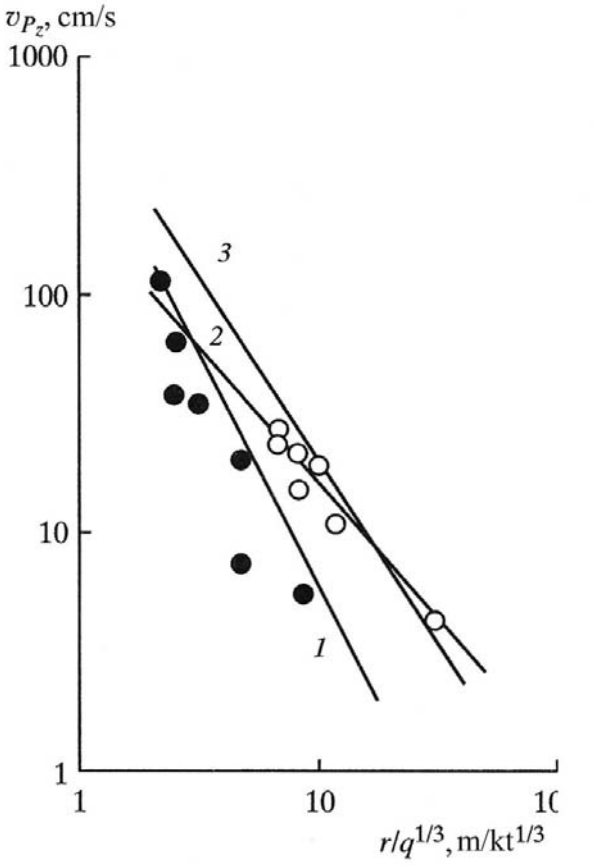

Figure 4.22. Maximum ground velocity as a function of distance produced by 1 Mt explosions at different test sites shown with lines: 1 – Novaya Zemlya, 2 – Amchitka, and 3 – Nevada Test Site.

Figure 4.21 shows an example of the vertical component of velocity as a function of distance for tests in adit A-32 along two mutually perpendicular directions. It turns out that seismic amplitudes depend not only on explosion yield and distance from the station, but also on the geological structure, including the layer orientation inside the massif.

Thus, if the velocity amplitude is expressed as a function of yield q and distance r in a form:

$$v_{Pz} = A_i \left(\frac{r}{q^{1/3}}\right)^{ni} \text{ in (cm/s)}, \qquad (4.21)$$

where q is yield in kt, and r is distance in m, then for the wave direction across layering the parameters are: A = $5.5 \cdot 10^5$, n_i=1.7 (line 2), while for the wave direction parallel to the layering direction the parameters are: A = $11.3 \cdot 10^5$, n_i=1.9 (line 1). For comparison, line 3 shows the relationship in the form 4.21 with A = $1.19 \cdot 10^4$, n_i = 1.6 used to predict ground velocities in the epicentral zone at Novaya Zemlya. The amplitudes predicted using line 3 are approximately 2-3 times larger than the observed amplitudes.

Seismic wave recording was carried out in the near-field zone up to distances of 10–15 km in order to evaluate effects of underground explosions on tunnel/adits, equipment structures and in buildings located in the town called Severnyi located 5–10 km from the explosions. The locations of the recording devices were not fixed, but were changed depending on the test location. In the epicentral zone P-wave arrives with an apparent velocity of 5.3 – 5.8 km/s. The amplitude in the period band 0.2 – 0.4 s is the main criterion determining the effect of the wave on the equipment buildings, various structures and tunnels/adits.

Based on numerous measurements for the megaton level events maximum velocity amplitude[18] as a function of yield q and distance r to the epicenter is given by the experimental relationship (Sultanov, 1996):

$$v_{Pm} = 5.2 \left(\frac{r}{q^{1/3}} \right)^{-2} \text{ in (cm/s)}, \tag{4.22}$$

where q is yield in kt, and r is distance in km. The line corresponding to Equation 4.22 is plotted in Figure 4.22 in comparison with other relationships determined for Amchitka events MILROY (q = 1.2 Mt) and KANNIKIN (q = 5 kt) and Nevada Test Site events BOXCAR (q = 1.3 Mt) and BENHAM (q = 1.15 kt) scaled to 1 Mt.

Temporary seismic networks were deployed to record seismic waves at regional distances up to 300 km from the source, including a profile along the west coast between northern and southern testing areas. The networks consisted of four to six transportable stations. Seismic observations were conducted in order to characterize different regional phases and determining parameters of the waves after their reflection and refraction from Conrad and Moho discontinuities.

Regional travel time curves for major phases for Novaya Zemlya Test Site are shown in Figure 4.23. The waves were recorded on the island as well as along the coast on the mainland by temporary stations. The following relationships were determined for identified arrivals (Sultanov, 1996):

$t(Pg) = r/6.2 + 0.25$ in s for r = 10 to 450 km;

$t(Pn) = r/8.2 + 8.9$ in s for r = 220 to 1000 km;

$t(Sn) = r/4.4 + 17.5$ in s for r = 250 to 700 km;

[18] This parameter is called PPV in western literature.

$t(Lg) = r/3.5 + 1.0$ in s for r = 120 to 450 km;

$t(R) = r/3.0 - 3.0$ in s for r = 50 to 500 km.

Thus, the first arrival at distances less than 250 km is the crustal *Pg* wave, refracted with an apparent velocity of 6.2 km/s. Further away the phase *Pn* arrives first with an apparent velocity of 8.2 km/s, refracted below the crust. The shear wave *Sn* arriving with an apparent velocity of 4.4 km/s has small amplitude and cannot always be identified with certainty. The guided wave *Lg*, with an apparent velocity of 3.5 km/s, is identified among the secondary arrivals beyond 100 km. Surface (Rayleigh) waves *R* with an apparent velocity of 3 km/s dominate the displacement seismograms, where their amplitudes are 5 – 10 time higher than the body wave amplitudes.

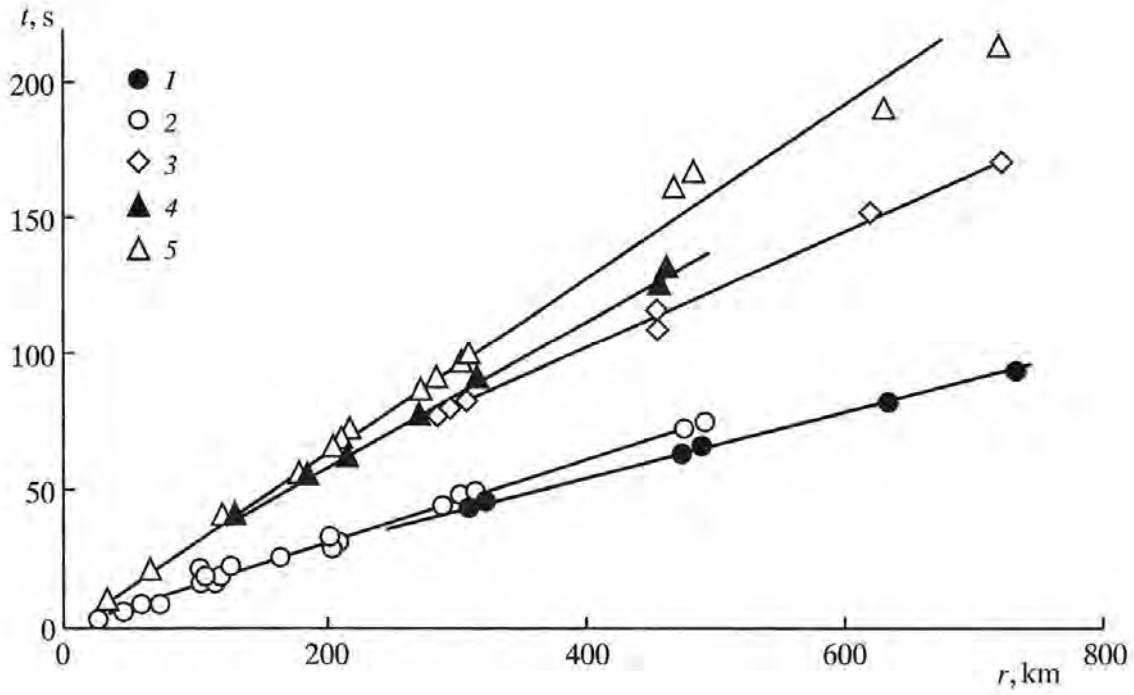

Figure 4.23. Observed travel time curves for Novaya Zemlya Test Site for different phases (velocities in km/s are shown in brackets): *1 – Pn* (8.2); *2 – Pg* (6.2); *3 – Sn* 4.8); *4 – Lg* (3.5); and *5 – R* (3.0).

Figure 4.24 shows the measurements of maximum displacement amplitudes for P and surface waves at distances ranging between 1 and 300 km. The amplitudes are for a 1.1 kt nuclear explosion conducted at Novaya Zemlya in adit "G" at a depth of 125 m. Solid dots represent the maximum *P*-wave radial displacement for periods of 0.2 – 0.4 s (line 1). Open circles show maximum vertical displacements for surface waves for periods increasing with distance from 0.3 s to 1.1 s (circles around line 2). Maximum displacement amplitudes shown in Figure 4.24 can be approximated by the relationship

$$S_{Px} = 2.53q^{0.7}r^{-1.8} \text{ in (mm)}, \qquad (4.23)$$

where q is yield in kt, and r is distance in km. Surface wave displacement amplitudes decay with distance as $S_r \sim r^{-1.4}$. A similar relationship for Nevada Test Site based on seismic records for nuclear explosions is presented in Murphy and Lahoud (1969). This relationship is shown as line 2 in Figure 4.24 after multiplying of the total vector by 0.7 to get a value for the radial component. Line 2 practically overlaps the results for surface wave amplitudes obtained at Novaya Zemlya. We note that Equation 4.23 for S_{Px} and S_r are obtained for smaller-yield explosions at Novaya Zemlya Test Site.

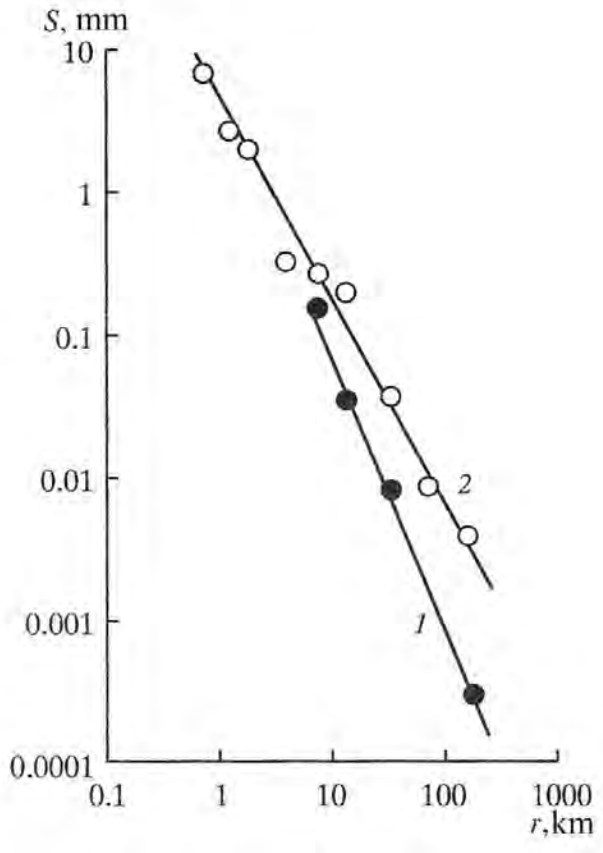

Figure 4.24. Maximum displacement amplitudes for *P*-wave (1) and surface wave (2) as a function of distance produced by 1.1 kt explosions conducted in Tunnel "G" of Novaya Zemlya Test Site.

Another characteristic feature observed on regional and teleseismic seismograms for underground nuclear tests at Novaya Zemlya is evidence of tectonic release including large amplitude Love waves, and azimuthally-dependent phase and amplitude for Rayleigh waves. Release of tectonic energy is also confirmed by prolonged continuous aftershock activity within zones up to several km from the explosion sources.

Data analysis has shown that tectonic energy release was due to both relaxation of tectonic stresses in the damage zone around the source and tectonic movement along faults. Comparing the aftershocks and the extent of the zone of inelastic deformations shows that the affected zone can reach approximately 1 km/kt$^{1/3}$. This size determines the volume of rocks potentially involved in energy release and the magnitude of this energy.

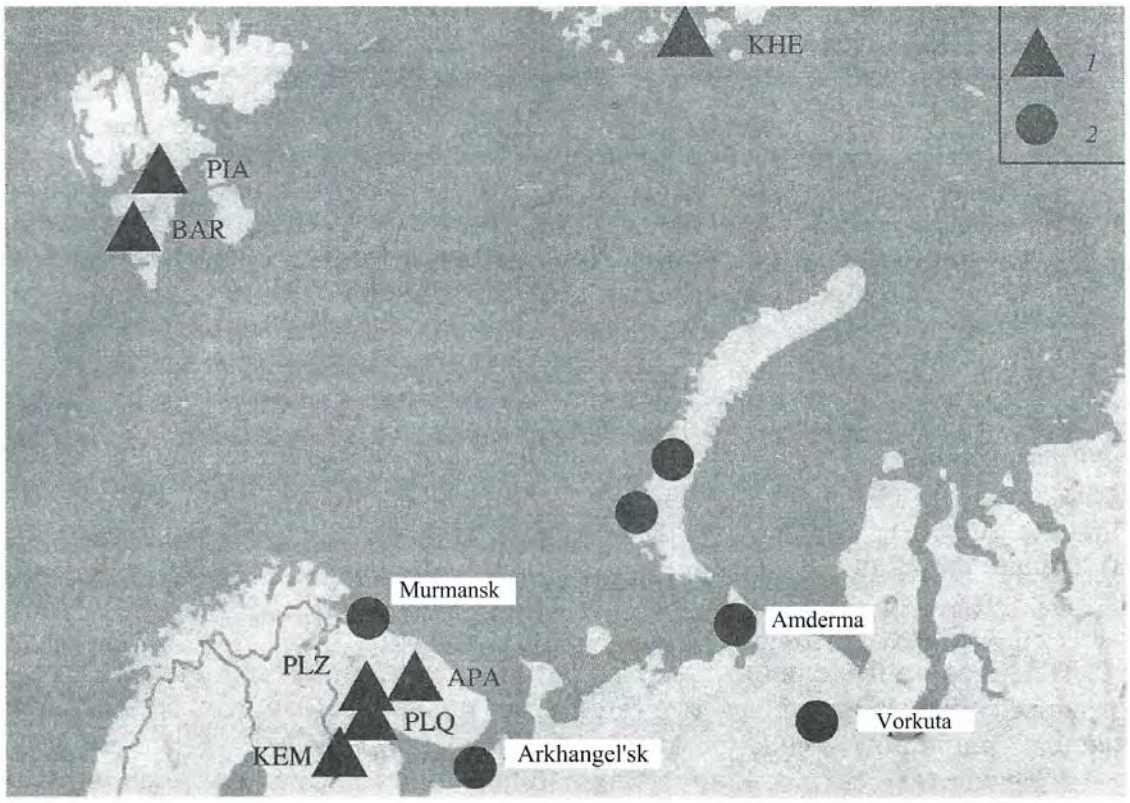

Figure 4.25. Map of seismic stations around Novaya Zemlya Test Site. The triangles show permanent stations, the circles show temporary stations.

The results of observations show that tectonic energy released during explosions is less than the energy of the explosion. Thus, 19 earthquakes were detected within 14 hours after a megaton class explosion conducted at NZ on 27 October, 1973 with body wave magnitude m_b = 6.9. The largest of these earthquakes had a body wave magnitude m_b = 4.8. Energy released by these aftershocks was at least three orders of magnitude less than the energy of the nuclear test that caused the seismicity. Therefore conducting nuclear tests did not cause catastrophic tectonic release; instead it resulted in stress release in the region as a series of induced smaller earthquakes.

Regional seismic observations within about 300 to 400 km were conducted in order to study the effect of emplacement conditions, geological structure, yield, and epicentral distance on seismic wave characteristics. These observational data were used to develop methods for developing TNT equivalent yield estimates for nuclear explosions at the NZ Test Site, for predicting seismic wave parameters needed in the preparation and conduct of nuclear tests, and for predicting seismic wave effects on equipment, electronics, and residences in the nearby towns.

Systematic seismic observations were initiated on the mainland during first megaton class nuclear tests at Novaya Zemlya, because these tests were felt along the north coast of the European Platform, in Finland, and even in Moscow. After yields were limited to 150 kt

beginning in 1976 the intensity of seismic oscillations observed on the mainland, Spitsbergen Island and Franz Joseph Land were considerably reduced. These events were no longer felt by people and did not affect buildings or other structures (Novaya, 1991).

On the mainland the seismic waves (from NZ explosions) can be detected only by using highly sensitive equipment. Figure 4.25 shows a network composed of permanent and temporary stations located on the mainland, which allowed recording of all seismic events. The USSO station network on the mainland is non-uniformly distributed. Due to seismic activity within the Kola Peninsula the network within this region is more dense. The nearest permanent stations USSO are: 1) Kheis (Franz Joseph Land) – 800 km; 2) Apatity (Kola Peninsula) – 1020 km; 3) Polyarnye Zori (Kola Peninsula) 1070 km; 4) Polyarnyi Krug (Kola Peninsula) – 1080 km; 5) Umba (Kola Peninsula) – 1080 km; Kem – 1200 km; 7) Barentzburg (Spitsbergen Island) – 1250 km (These distances are with respect to Area B).

Table 4.7. Temporary seismic stations (network) in the Northern European USSR.

Seismic Station	Distance, km	Seismic Station	Distance, km
Severnyi	5 – 15	Nar'yan-Mar	620
Povorotnyi	30 – 35	Vorkuta	720
Karmakuly	100	Murmansk	920
Belush'ya	200	Archangelsk	1100
Amderma	420		

Temporary networks were deployed at regional and teleseismic distances during nuclear testing, for each explosion. These stations recorded in digital format using magnetic tape (Table 4.7).

These temporary deployments during nuclear events provided broad coverage in both azimuth and distance. Therefore seismic wave parameters were obtained for each populated area for each explosion.

Basic features of seismic waves generated by explosions are similar to those from earthquakes. Seismic wave field is complex due to structural complexities and heterogeneities in the crust, generating numerous reflections and refractions, as well as conversion between different seismic phases.

Analysis of the registered parameters of seismic waves has shown that maximum amplitudes for 150 kt explosions (threshold yield according to the international treaty signed in 1974) can be approximated using a relationship:

$$v = \frac{62}{r^{1.05}}, \tag{4.24}$$

where v is in mm/s, and r is distance in km.

Comparison between (4.24) and other published data describing seismic wave parameters shows that the body wave amplitudes produced by explosions at Novaya Zemlya recorded at regional distances is 4 to 10 times lower than commonly observed for events of the same yield conducted elsewhere. It is interesting to note that the Lg phase is absent from records at continental stations, while it is recorded at distances beyond 100 km for stations located on the island. This is caused by low crustal *Q* in the region, and the absence of the granitic layer in the oceanic crust. Amplitude reduction is less pronounced at teleseismic distances where waves travel through the mantle and the core.

Table 4.8. Seismic intensities and associated seismic effects for underground explosions conducted at Novaya Zemlya.

Intensity level	Limiting velocity of oscillations *v*, mm/s	Radii of the zones with different intensity *r*, km
1	0.5	200
2	1.25	100
3	2.5	40
4	5	20
5	10	12
6	20	5.6
7	40	3

Epicentral distances where the wave intensities reach certain levels were estimated using recorded data for body and surface waves. Figure 4.20 shows different zone according to MSK-64 intensity scale[19] for 150-kt explosion conducted at Area B. Limiting ground velocities and radii for these zones are shown in Table 4.8.

According to MSK-64 scale, damaging waves start at intensity levels 7 and higher. Cracks in the building walls, damage to pipelines (near joints), rock falls and landslides are possible in this zone.

For explosions at Novaya Zemlya this zone is limited within 3 km radius around explosion epicenter. The radius of the zone with intensity level 5 is 12 km. This zone is characterized by shaking of the glass windows, damage to painted walls and ceilings, shaking and overturning of dishes. Intensity level 3 is the minimum intensity felt by people. The radius of this zone for Novaya Zemlya does not exceed 40 km.

[19] See: http://unesdoc.unesco.org/images/0015/001545/154508eb.pdf and the paper Medvedev S.W., W. Sponheuer and V. Karnik (1965). Seismic intensity scale version MSK 64, UNESCO/NS/SEISM/28/ Paris, May 7, 1965.

Table 4.9. Seismic ground velocities (v, μm /s) for explosions with different yields (q).

City/Town	Distance, km	v, μm/s	
		q = 50 kt	q = 100 kt
Amderma	450	28	60
Nar'yan-Mar	620	17	37
Vorkuta	730	14	30
Salekhard	890	11	25
Murmansk	920	11	25
Arkhangelsk	1100	8.5	18

Based on seismic observations and using Equation 4.24 the intensity levels for some of the populated areas were determined. Table 4.9 shows maximum P-wave amplitudes caused by explosions between 50 and 100 kt conducted at Area B for some of the large cities of the region.

Ground velocities produced by explosions are so low that they are comparable to noise. For example seismic background noise amplitudes at 3 Hz generated by traffic and industrial objects in the city of Vorkuta is approximately 10 μm/s. The amplitudes of the seismic waves from explosions are 50 μm/s, which exceed the background noise only by a factor of 5.

Seismic waves from 40 underground nuclear explosions conducted At Novaya Zemlya Test Site were recorded using a permanent network of both Russian and international stations located from regional to teleseismic distances including Antarctica. According to the International Seismic Centre (ISC) Bulletin the magnitudes for these explosions change between m_b = 4.3 to m_b = 6.9 when the yield change between q = 1.1 kt to q = 3.7 Mt.

Figure 4.26 shows the relationship between the magnitude m_b, determined using regional and teleseismic P waves, and the explosion yield q. Magnitudes of the explosions conducted in adits are shown with solid circles, while the explosions conducted in boreholes are shown with open circles. For explosions with $q \leq 150$ kt the relationship is

$$m_b = 0.76 \log q + 4.13 \qquad \text{for } q \leq 150 \text{ kt} \tag{4.25}$$

Explosions with yields $q > 150$ kt plot below the expression (4.25) and are better described by the relationship

$$m_b = 0.48 \log q + 5.10 \qquad \text{for } q \leq 150 \text{ kt} \tag{4.25}$$

In addition, the plot in Figure 4.26 shows that for the same yield the magnitudes of the explosions conducted at the southern testing area significantly exceed the magnitudes of the explosions conducted in tunnels at the northern testing area.

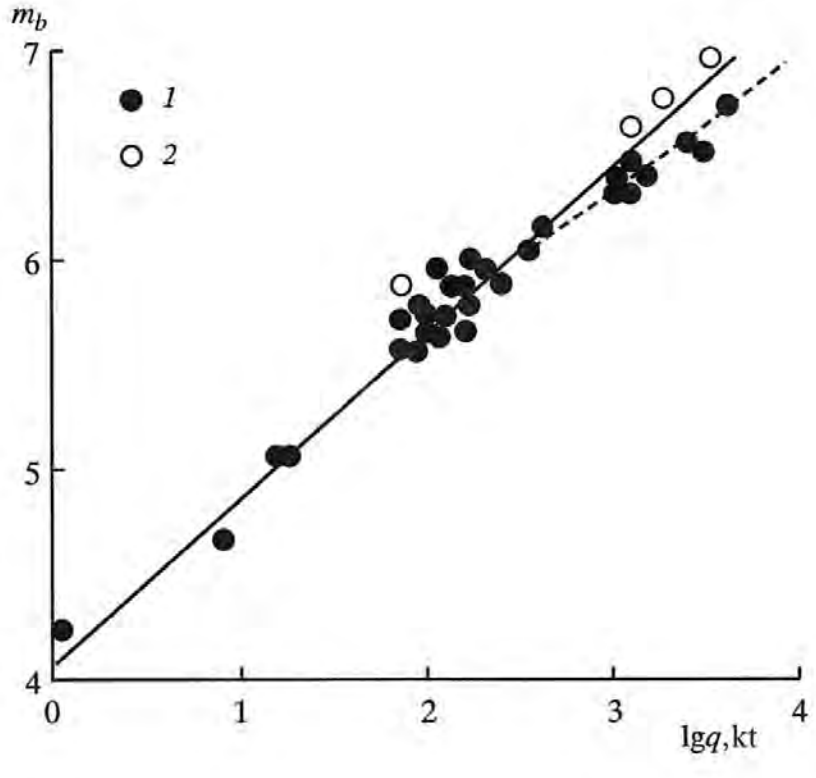

Figure 4.26. Relationships between seismic magnitude and yield for Novaya Zemlya: 1 – tunnel explosions; 2 – borehole explosions.

4.6. Observation of regional and teleseismic waves at the Borovoye Observatory (BRVK)

Most important studies of regional and teleseismic waves generated by nuclear explosions were conducted by using records from Station Borovoye (BRVK, coordinates lat 53°03′29″, lon 70°16′58″) located in the Kokchetav Region of Northern Kazakhstan. The seismic station is situated in the Kokchetav Anticlinorium formed by old granites, which form outcrops in some places. The granites are dense with few fractures below 5 – 10 m and seismic velocity of C_p = 5700 to 6200 m/s. The Moho boundary can be traced at a depth of 52 – 55 km with C_p = 5700 ÷ 6200 m/s.

The geological conditions at the Kokchetav Anticlinorium help good quality seismic records from various places around the world (Adushkin and An, 1993). For example Station BRVK show the best sensitivity to the explosions conducted at the NTS compared to other stations of ESSN. The low sensitivity threshold is m_b = 3.8, and all explosions greater than m_b = 4.2 are recorded by the station. Seismic and acoustic observations at Station BRVK started in 1954 and were conducted episodically. Continuous seismic recording was performed between 1961 and

1991, and digital recording began in 1966. At the present time Station BRVK records continuously with modern data storage[20].

In 1975 additional arrays were installed near Station BRVK, including "Treugol'nik" (Triangle), "Krest" (Cross) and "Ozherel'e" (Necklace) arrays (Figure 4.27) (Adushkin et al, 1996)[21].

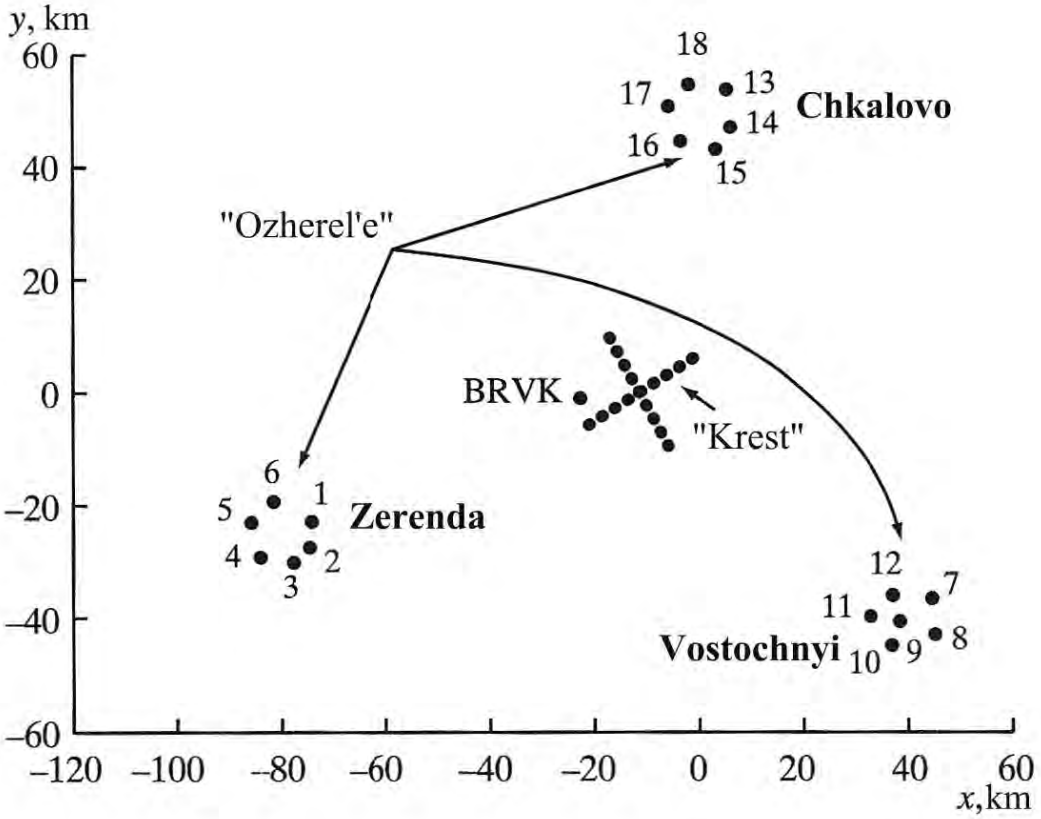

Figure 4.27. Map of the seismic arrays located near Station BRVK: "Treugol'nik" (Chkalovo, Zerenda, Vostochnyi), "Ozherel'e" (1 – 6; 7 – 12; 13 – 18), and "Krest.

The geological structure of the region in which BRVK and other seismic arrays are situated, is a complex juxtaposition of pre-Cambrian blocks with early Paleozoic orogenic zones covered with Mesozoic and Paleozoic structures. A system of deep faults with different orientations forms a complex tectonic "skeleton". The presence of sediments of different ages, and igneous rocks, suggest long term development of faults that were reactivated in the Mesozoic. The details of the crustal structure of the Kokchetav anticlinorium, based on seismic sounding data as well as on regional velocity profiles, can be summarized as follows:

[20] BRVK is a part of the Global Seismographic Network operated by the IRIS Consortium and the US Geological Survey.

[21] A new array, with code BVAR, has also been installed nearby, as an Auxiliary station of the International Monitoring System of the Comprehensive Nuclear-Test-Ban Organization.

1) The crustal thickness decreases from 55 km in the south (Temirtau) to 40 km in the north (Petropavlovsk).
2) In the central part of the structure where the Borovoye Observatory is located, the Moho is only weakly defined.

To record regional and teleseismic signals the Borovoye Observatory was equipped with short period (0.5 – 50 Hz) and long period (0.04 – 0.1 Hz) instruments. Maximum sensitivities were 10^5 and 10^3 counts per micron for the short-period and long-period channels respectively. The amplitude range was between 10^{-2} and $2 \cdot 10^4$ nm for the short period and between 1 and $2 \cdot 10^6$ nm for the long period channels.

Borovoye is in an aseismic region with low microseism levels from both natural and man-made origins. Power spectra over a broad frequency range are shown in Figure 4.28. Thus the noise level in the short-period band has amplitudes on the order of 1 – 10 nm, while in the long-period band it is 100 – 200 nm.

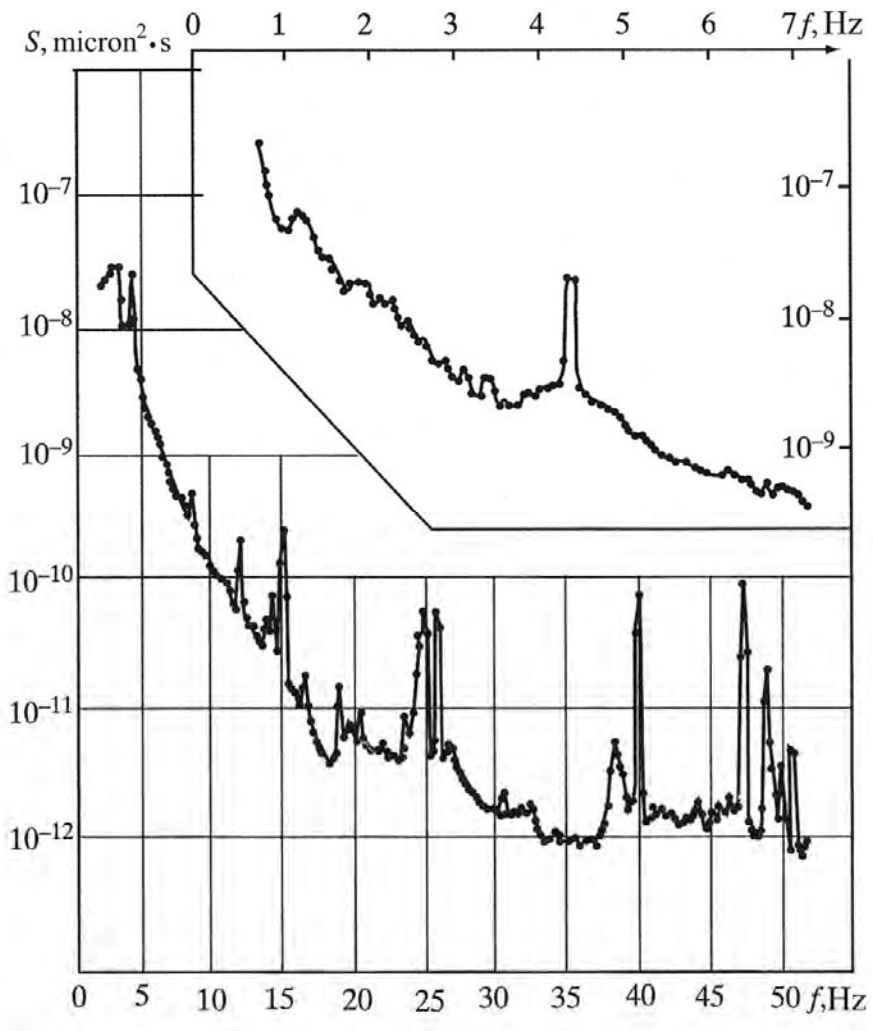

Figure 4.28. Spectral density of microseismic background noise at station BRVK.

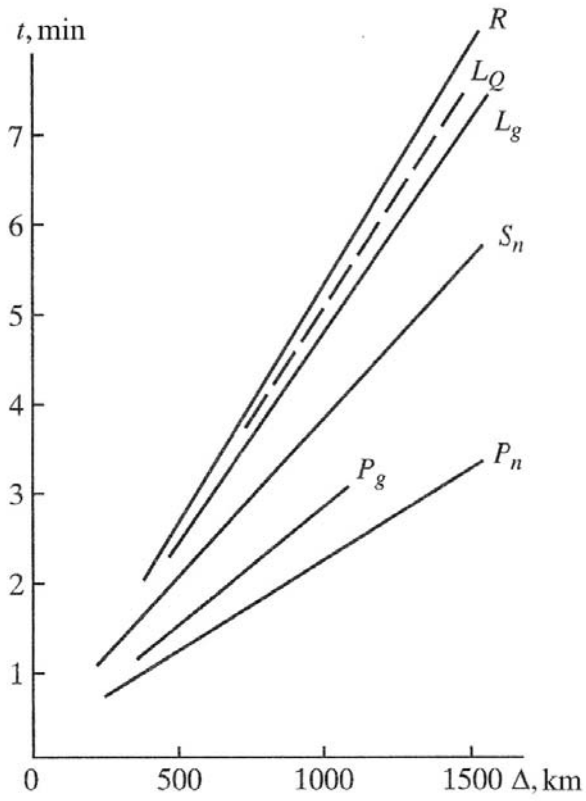

Figure 4.29. Travel time curves for different seismic phases. See explanations in the text.

A large volume of data from BRVK both analog and digital was collected between 1961 and 1992. The collection includes almost all large nuclear explosions (m_b > 4, q ≥ 5 – 10 kt) conducted at all nuclear test sites in the world, as well as peaceful nuclear explosions and large number of earthquakes. Seismic records obtained by BRVK can be divided into two groups: seismic signals from sources located between 500 and 3000 – 4000 km [regional], and teleseismic records from events over 10,000 km, including NTS explosions. This division is natural because the distance from BRVK to the STS is *r* = 550 to 750 km, distance to NZTS is *r* = 2100 to 2400 km, distance to Lop Nor in China is *r* = 1900 to 2100 km, and the distance range for most of the PNEs is *r* = 1000 to 3500 km. Numerous earthquakes that occurred in Northern Tyan-Shan, Eastern Kazakhstan, Pamir, Hindu-Kush Iran and Arctic zone have been located within 1000 – 4000 km from BRVK.

Seismic waves recorded from the sources in this distance range (500 – 3500 km) propagate mainly in the crust and upper mantle. Seismic waveforms at these distances are very complex because heterogeneities in the crust and upper mantle affect signals in both the time and frequency domains. Analysis of the waveforms is also complicated by the presence of the first shadow zone that falls in this distance range. Nevertheless the separation of different phases is clear and allows their identification.

Figure 4.29 shows travel time curves for *Pn* and *Pg* phases, as well as for the corresponding shear wave phases *Sn* and *Sg*. These phases are related to longitudinal and sometimes shear

energy refracted from the deep parts of the crust and the upper mantle. The crustal *Lg* phase is also prominent in this distance range. Rayleigh and Love waves are almost always observed. For observations of the surface waves at longer distances long-period channels with high sensitivity are needed.

The Borovoye Observatory has been particularly effective for detection and interpretation of seismic waves from Semipalatinsk Test Site. However in order to determine the yields of the explosion, a relationship between seismic magnitude and yield is necessary. Calibration explosions are necessary in order to create such relationship. There have been few calibration explosions, and relationships between magnitudes and yields are approximate. As information about nuclear explosions becomes available (Bocharov et al, 1988 a,b), these relationships have improving.

It is well-known that emplacement conditions of the nuclear charge (e.g. rock density, strength and elastic properties, the presence of ground water, depth and other factors) significantly affect seismic radiation generated by explosions. Therefore the relationships between seismic magnitude and yield are different not only for different test sites, but also for explosions detonated within each test site in different rocks. These relationships (between yield and magnitude) for the Semipalatinsk Test Site were determined using data from BRVK. The relationships for Rayleigh wave amplitudes were studied in more detail.

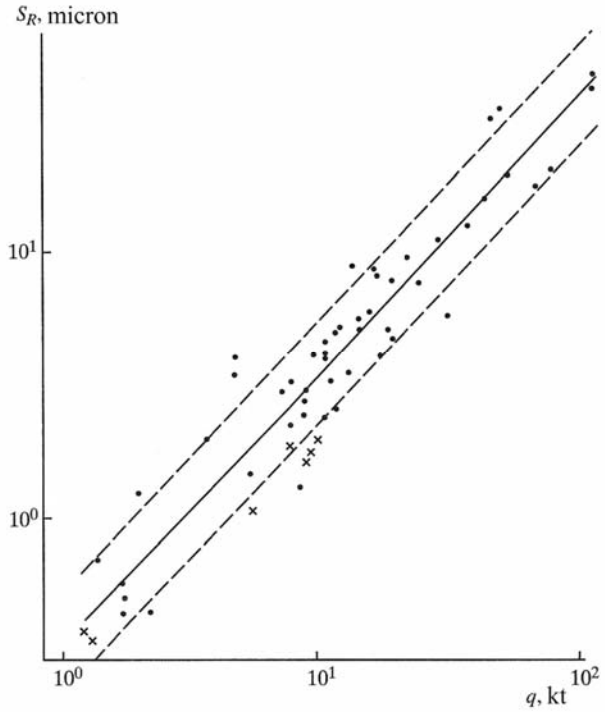

Figure 4.30. Relationship between the Rayleigh wave amplitude (S_R) and yield of explosions for Degelen Testing Area.

The relationships are different for explosions conducted in Degelen adits (Figure 4.30) and for shafts in Balapan (Figure 4.31). For Degelen explosions Rayleigh wave amplitude is proportional to $S_r \sim q^{1.05}$ with a standard deviation of $\sigma = 15\%$. For Balalpan this relationship is

$S_r \sim q^{0.98}$ with standard deviation σ = 16%. Thus in order to estimate yield of the explosion one needs to know the emplacement conditions. Methods of detection, identification, localization and yield estimation for explosions conducted at the STA down to the yields of 0.5 – 1 kt and even smaller were developed based on the analysis of the regional waveforms recorded at BRVK.

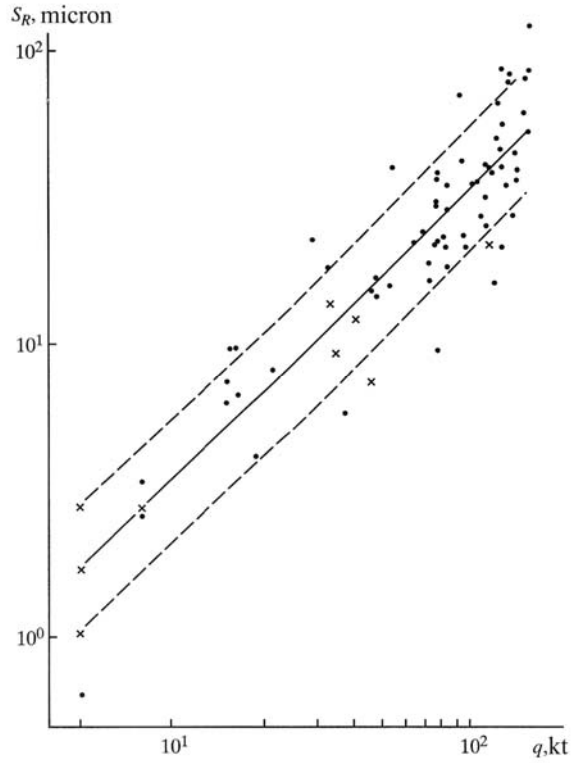

Figure 4.31. Relationship between the Rayleigh wave amplitude (S_R) and yield of explosions for Balapan Testing Area.

While seismic observations at BRVK were being developed, particular attention was given to teleseismic recordings in the distance range 90 – 120°, which included nuclear test sites belonging to foreign countries. Monitoring of nuclear explosions at teleseismic distances is usually conducted using the data from national networks. The capabilities of each individual stations of the network are very important.

Below we describe results of observations and analysis of teleseismic waves from explosions conducted at the NTS, recorded at the single well-calibrated BRVK Observatory. Despite large epicentral distance between BRVK and the NTS (10,000 km) this station was the most sensitive of the teleseismic stations with respect to the NTS events. It was determined that this is a characteristic property of the entire Kokchetav Anticlinorium.

At teleseismic distances the wavefield is relatively simple: the major phases including P, S and surface waves are well separated in time. Characteristic features that separate explosions from earthquakes at teleseismic distances include low surface wave amplitudes generated by explosions and simple P waveform with a characteristic shape.

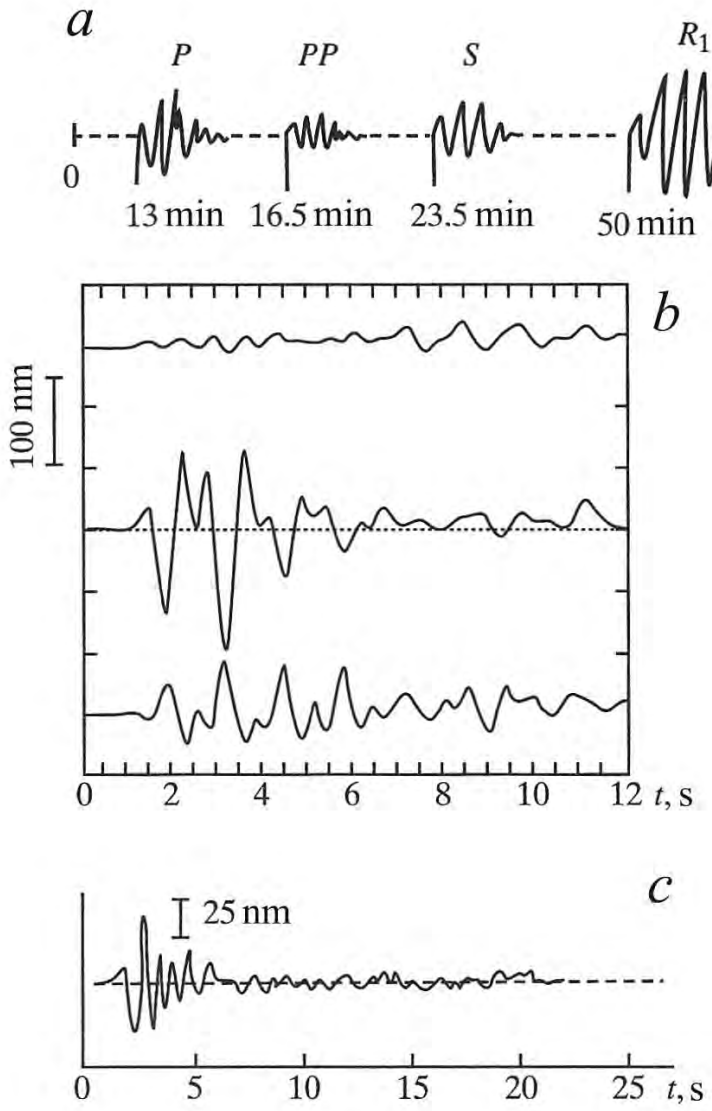

Figure 4.32. a) Schematic view [also used words in the text “morphology”, “structure”] of the teleseismic signals produced by NTS nuclear explosions recorded by Station BRVK. b) – c) P-wave recorded using short period channel.

Basic features of teleseismic signals coming from the NTS and observed at BRVK are shown in Figure 4.32a. The teleseismic P wave has a travel time of 13 minutes. Phases PP and PcP arrive 3.5 minutes later and have lower amplitudes. The S-wave arrives 7 minutes after that, followed by Rayleigh and Love waves 27 minutes later. The *P*-wave has a short impulsive arrival with maximum amplitudes on the vertical component. It decays to the level of $0.3 \cdot A_{max}$ within 15 – 20 s after the arrival. Characteristic shape of P-wave is shown in Figure 4.32 b,c.

The vertical component of motion shows the largest amplitude, while the analysis of the horizontal components shows the predominant motion is north-south. The P-wave is clearly seen

above a low threshold corresponding to m_b = 4.0 to 4.1. The period of oscillations corresponding to the maximum P amplitude ranges between 0.7 and 1.4 s,increasing by only 0.09 s per unit of magnitude in the interval m_b = 4.0 ÷ 7.0. The PP phase becomes visible for explosions with magnitudes m_b > 4.5 ÷ 4.7. The S-wave is observed only for large explosions with m_b > 6.3 ÷ 6.4. The Rayleigh wave is observed for magnitudes starting from m_b > 5.3 ÷ 5.5 and appears as two wavetrains with periods 19 – 21 s and 16 – 17 s following each other with an interval of approximately 2 min. For large explosions with m_b > 6.3 the number of different phases within the surface wave increases 7 – 9. The first of these phases has a period of 30 – 32 s and arrives approximately 8 – 9 min before the arrival with the period of 19 – 21 s. The largest ratio between the amplitude and the period is observed for the wave with the period of 16 – 17 s. The Love wave is not very clear and is observed only for the largest explosions (greater than 50 kt).

The recorded data were used to address the three main problems of nuclear monitoring: signal detection, particularly for small seismic signals; identification of the source as an explosion (rather than an earthquake), and estimation of explosion yield. Signal detection involved detailed automatic data processing using its spectral, polarization and amplitude characteristics. The measured features included time of arrival, amplitude, dominant period, azimuth, and takeoff angle. The amplitude and the polarization information were used for polarization filtering. After that the event coordinates, origin time and magnitude were estimated.

Large-base arrays (Treugol'nik and Ozherel'e) and Krest array played significant role in determining the event location (epicenter coordinates, depth and origin time) as well as for event identification (explosion or earthquake). Large-base arrays consisted of four points: central Station BRVK (Central Point or CP), and peripheral points located in Zerenda (PP1), Vostochnyi (PP2) and Chkalovo (PP3). Starting in 1978 each peripheral point included the sub-system called Ozherel'e, which consisted of 6 boreholes with a vertical seismometer located at depth between 30 and 200 m (depending on the depth needed to reach unfractured/monlithic granite).

Figure 4.33 shows fragments of the seismograms recorded by long-period channels of Treugol'nik array (4.33a) and vertical channels of sub-system "Ozherel'e" for three points PP1, PP2, and PP3 recorded for underground nuclear explosions (a) KASH (June 12, 1980) and (b) TAFI (July 25, 1980), both conducted at the NTS. Using seismic arrays helps to increase the signal-to-noise ratio, and to improve the quality of azimuth measurements and the wave apparent velocity, and thus to enable an estimation of the epicentral distance using the travel time curves for corresponding wave types.

Explosion and earthquake identification was performed using about ten criteria of different efficacy. The discriminants are based on differences between source mechanisms, size, and source duration, between explosions and earthquakes. Some discriminants can be directly observed from seismograms. For instance, earthquake wavetrains are significantly more complex and have longer duration than explosion wavetrains. Earthquakes are often accompanied by foreshocks and aftershocks. Explosion sources have spherical symmetry and small dimensions, therefore the major part of seismic energy is contained in *P*-waves. Shear and surface waves

produced by explosions have lower amplitudes than longitudinal phases. In addition the duration of each phase is shorter for explosions than for earthquakes.

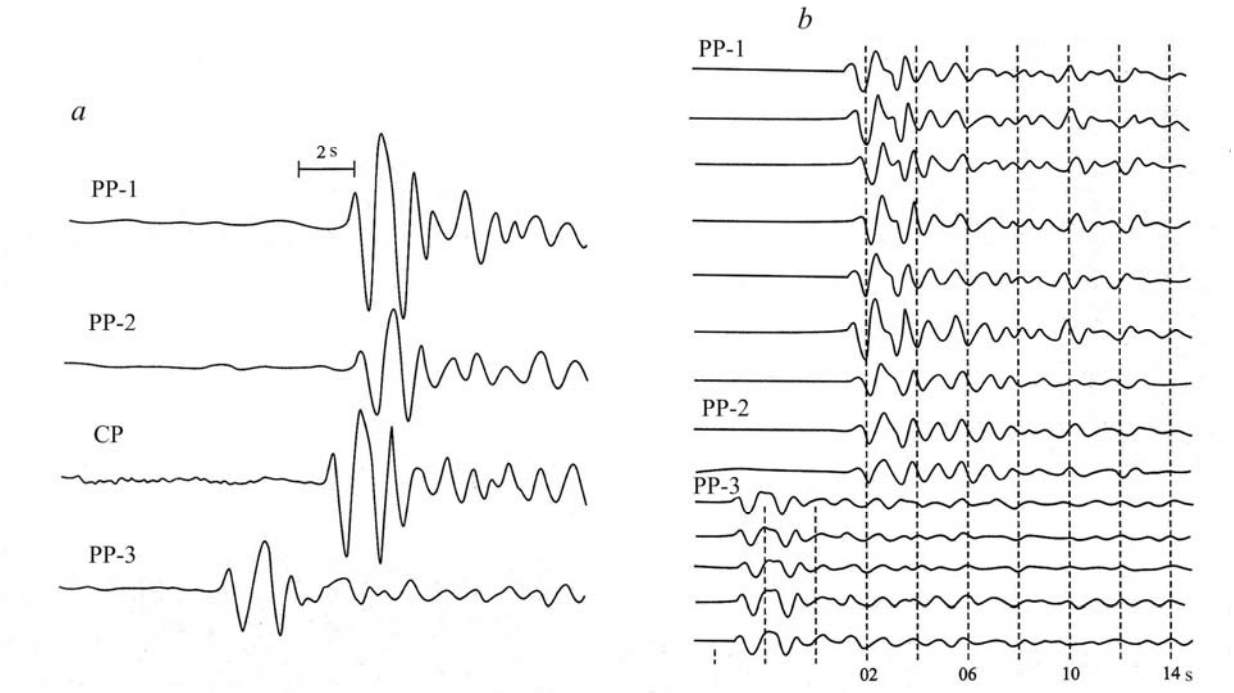

Figure 4.33. Examples of seismograms recorded by the large-base array for underground nuclear explosions: a) KASH (m_b = 5.6), and b) TAFI (m_b = 5.6).

The differences between the source types are usually quantified using a comparison between event magnitudes m_b and M_s computed using *P*-waves and Rayleigh waves respectively, determined using wave amplitudes and periods via

$$m_b = lg\left(\frac{A_p}{T_p}\right) + \sigma_p(\Delta), \qquad M_s = lg\left(\frac{A_R}{T_R}\right) + \sigma_R(\Delta), \tag{4.27}$$

where the values of the distance correction σ_p and σ_R for the BRVK station are shown in Figure 4.34 as a function of epicentral distance.

A comparison of the magnitude difference, $m_b - M_s$, as a function of the body wave magnitude m_b for explosions and earthquakes is shown in Figure 4.35. It is clear from the plot that the observations for explosions and earthquakes represent two separate families of points. This magnitude criterion is a robust method of identification: applying it to data from station BRVK, all explosions and 80% to 90% of earthquakes are correctly identified. However, usage of this criterion is limited by the fact that surface waves are difficult to detect from the long-period background for explosions smaller than several tens of kilotons. Small body wave amplitudes for smaller explosions makes other identification criteria difficult to use.

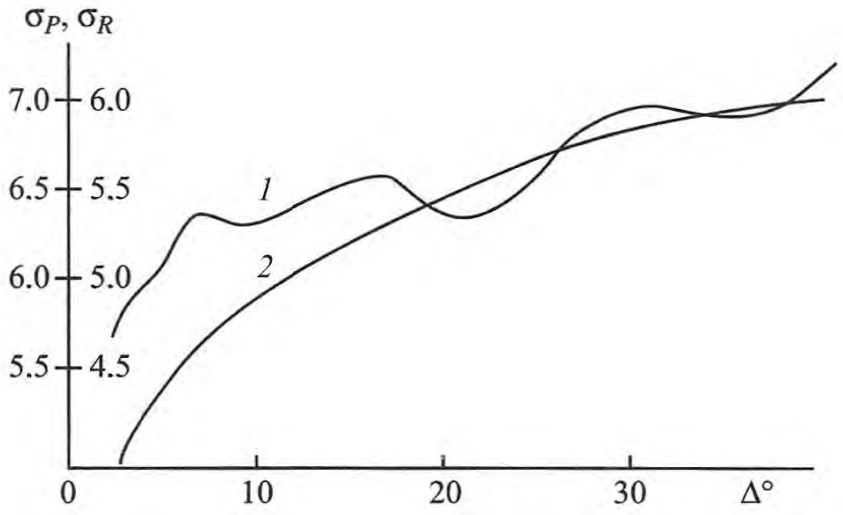

Figure 4.34. Calibration coefficients σ_p (line 1) and σ_R (line 2) for seismic Station BRVK depending on epicentral distance Δ°.

Another more effective identification criterion is based on spectral-temporal analysis of short-period body waves. The dominant period of body waves for explosions ranges between 0.5 and 2 s and is almost independent of the explosion yield. The dominant period for earthquakes is usually longer than that for explosions. Using spectral-temporal analysis, and applying conditional probability criterion calculated for eight 5-second long intervals using 5 different filter banks, the combined conditional probability of the event being an explosion is determined. Applying this method to seismic data of 38 NTS explosions and 19 earthquakes completely separated the two groups.

In order to discriminate between explosions and earthquakes, a criterion based on determining the event depth using depth phases (*pP*) is used in addition to the magnitude criterion. It uses the fact that the explosion depth is always less than 10 km. Other criteria such as event location (explosion is suspected if the epicenter is located in an aseismic region), as well as polarities of the first motions can be used. However determining first motion polarities for explosions smaller than 10 – 20 kt is difficult. The Nevada Test Site is not an aseismic region. Thus the depth phase criterion, alone, can be useful, and its efficiency can be improved by improving the methods of *pP* detection.

In addition to low microseism levels the main feature of BRVK records is increased efficiency of P-wave recording from various seismically active regions (Kamchatka, Japan, Philippines, North-Atlantic Ridge, etc), as well as the waves coming from nuclear tests conducted at the Nevada Test Site. Systematic error for magnitude determined using Station BRVK $\delta m_b = m_b^{BRVK} - m_b$ for 212 NTS explosions with published m_b is $\delta m_b = 0.7$ with a standard deviation of $\sigma = \pm 0.18$ (Table 4.10).

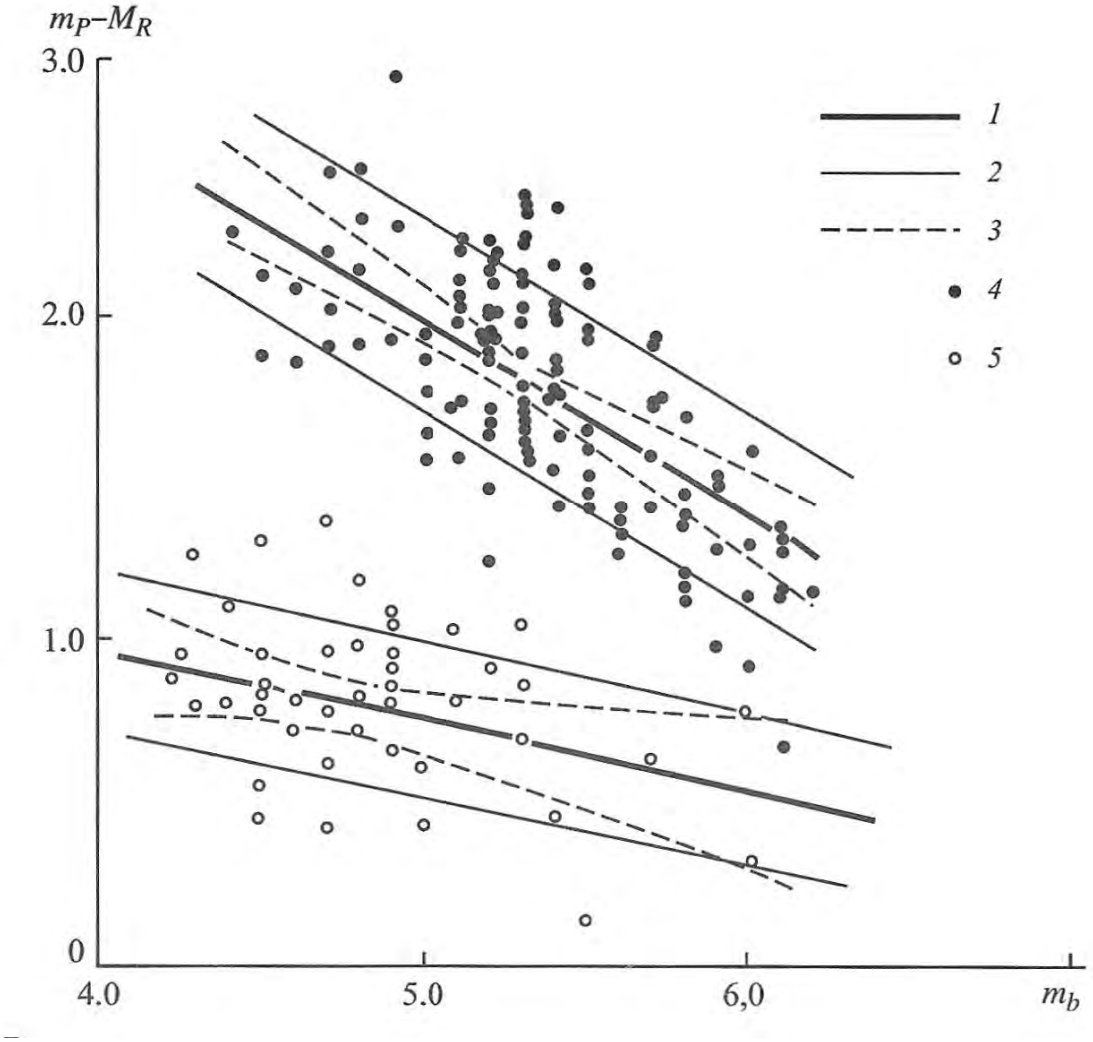

Figure 4.35. Difference between magnitudes estimated using P and surface waves using BRVK data for explosions and earthquakes as a function of *m_\mathrmb*. The lines and symbols show: 1 – linear regression line; 2 – standard deviation of the data points from the regression line; 3 confidence levels with a probability p = 0.9 for the regression lines; 4 – observed [individual] explosions; 5 – observed earthquakes.

As Table 4.10 shows the value of δm_b is practically independent of the testing area or the magnitude. High efficacy of seismic wave registration at the BRVK station is related to the geological structure of the region. Geological studies show that Kokchetav Anticlinorium is built with rigid blocks of old basement exposed at the surface at the present time. Deep seismic sounding shows strong attenuation of refracted waves due to reduced sharpness of Moho boundary, which can be seen along the profile within approximately 85 km. Evidently the old rocks forming Kokchetav Anticlinorium penetrate the entire crust down to 52 – 55 km and have their roots in the mantle. This feature improves the quality of registration of teleseismic waves from different regions around the globe.

Table 4.10. Magnitude error for the BRVK station.

Testing area	Number of explosions	m_b range	Magnitude error $\delta m_b \pm \sigma$
Pahute Mesa	56	4.8 – 6.4	0.61 ± 0.16
Rainier	18	4.8 – 5.3	0.61 ± 0.18
Yucca Flat			
north	45	3.9 – 5.8	0.77 ± 0.14
center	73	4.0 – 5.9	0.78 ± 0.17
south	20	4.3 – 5.9	0.59 ± 0.14

High quality data from the NTS and many years of data acquisition allow high-quality calibration of the ray path between Nevada and Borovoye. Due to the morphology of seismic waves (as shown for example in Figure 4.32) the problems of detection, epicentral location, identification, and yield estimation are solved using predominately P-waves recorded using short period three-component sensors. Detection of seismic signal arrival is performed by data filtering and determining the ratio between variances in short (~1s) and long (~20 s) time intervals (the STA/LTA method). After that, the Flynn polarization method is applied in order to determine the arrival azimuth, and angle, and polarization (whether linear or elliptical). The arrival angle and degree of polarization are used to determine the type of the wave.

The coordinates of the epicenter are determined using the azimuth (α_p) and angle (i_p) of the particle motion for the *P*-wave (sometimes, *PKP*). In order to determine the epicentral coordinates a correction for the systematic azimuth error is applied. The true azimuth between the BRVK station and the NTS was determined using the geographical coordinates for the announced explosions varies within $\alpha = 5.01 \div 5.43^{\circ}$ depending on the testing area (within the NTS). The observed average azimuth for P –wave is 353.04 ± 0.19^{0} (determined using 73 explosions with the largest yields). Therefore the systematic azimuth error for *P*-wave is 12.2°. The observed average arrival angle is 18.56 ± 0.13^{0}. The "true" angle $i = 14.66^{\circ}$ is calculated using Herrin's travel time tables (Bahghar) for P-wave for the distance of $\Delta = 90°$.

Thus the systematic angle error is 3.90°. We note that for the BRVK station the arrival azimuth and angle are determined as the direction of the long axis of the polarization ellipsoid for the first cycle of the *P*-wave. The error in azimuth calculations using three-component BRVK records is approximately 1°. This corresponds to the maximum epicentral error up to $100 - 150$ km in the azimuthal direction, and $300 - 400$ km in radial direction. The error in determining the epicenter location results in the origin time error reaching 20 s.

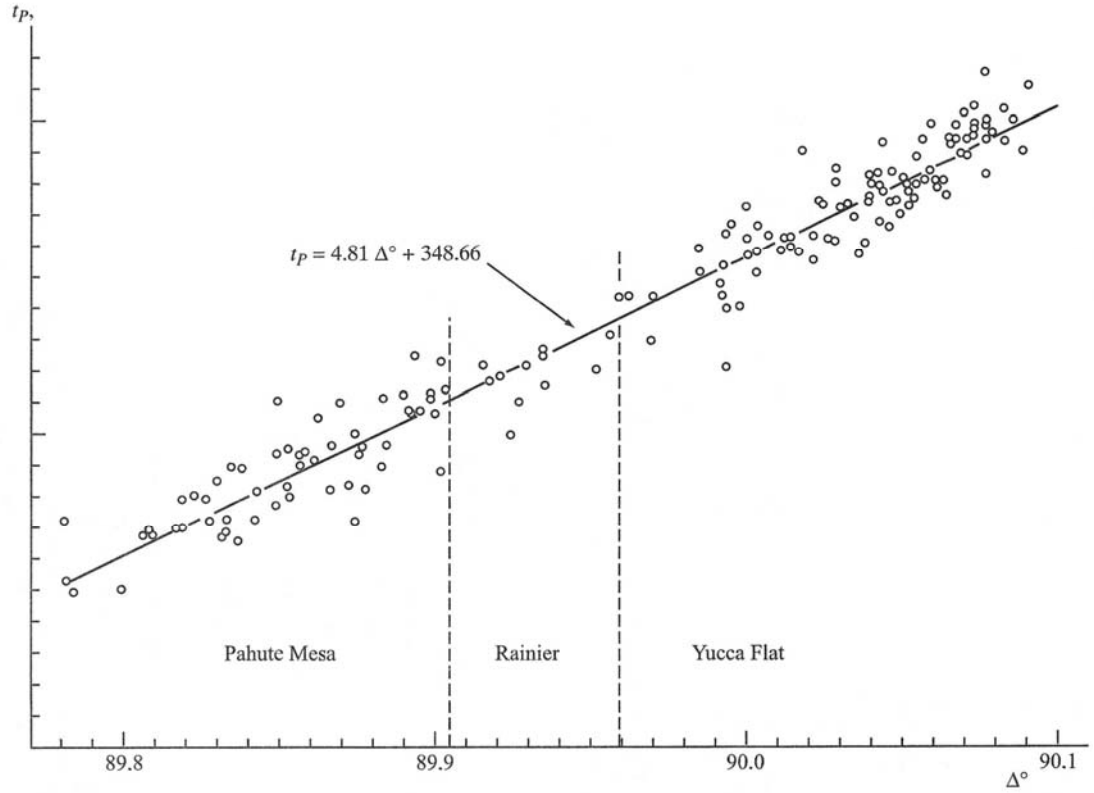

Figure 4.36. Local travel time curve for *P*-waves for sources at the NTS as observed from BRVK.

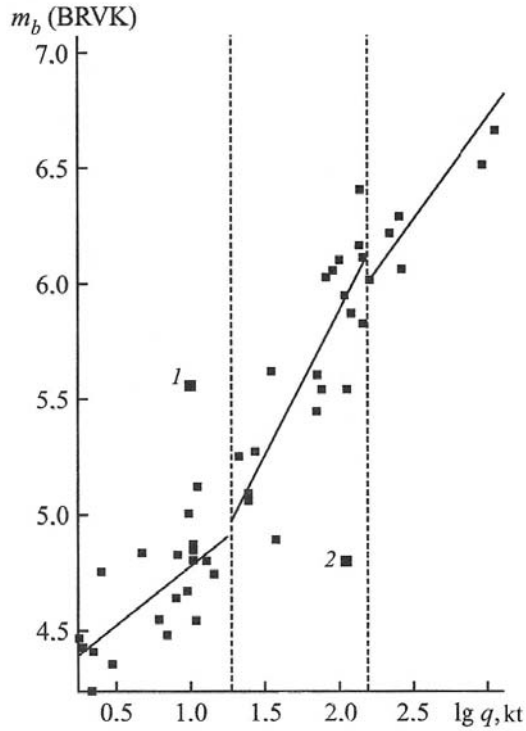

Figure 4.37. Magnitude m_b calculated using BRVK data plotted as a function of announced yield. Numbered dots show tests: 1 – BANEBERRY; 2 – SEDAN.

Figure 4.36 shows the travel time curve calculated using 167 explosions recorded by the BRVK station for the major testing areas of the NTS. The travel times are given by:

$$t_p = 4.81 \cdot \Delta^\circ + 348.66 \text{ (s).} \quad (4.28)$$

The travel time curve in Figure 4.38 is given with respect to the sea level using a velocity model for the NTS. The elevation of the BRVK station was not accounted for (h = 340 m). The observed *P*-wave travel times are different from Jeffreys-Bullen travel time tables for Δ=90° by 1.14 s, for Herrin tables the difference is 0.84 s, and for Kogan tables the difference is +0.54 s. Therefore the travel time table by S. Kogan for the source at the surface is the best (for this ray path). We note that the travel time is independent of magnitude for the range $m_b^{ISC} = 4.0 \div 6.4$.

Explosion yield estimates were performed using P-wave amplitudes. Since we present methods related only to one-station monitoring, we will use the magnitude parameter m_b^{BRVK}, based solely on relationships for the BRVK station. We noted earlier that the value of m_b^{BRVK} is higher than m_b^{ISC} by 0.7 magnitude units on average. The plot of m_b^{BRVK} as a function of yield for NTS explosions is shown in Figure 4.37. Only explosions with reported yield were used for the plot in Figure 4.37.

We note that explosions in alluvium, tuff and rhyolite have similar yield–magnitude relationships for Pahute Mesa, Rainier and Yucca Flat testing areas. The magnitudes for the explosions in granite are systematically higher by 0.4 – 0.8 magnitude units.

The magnitudes of explosions conducted in shale and sandstone in New Mexico and Colorado are somewhat lower than the main trend. The magnitude of the explosion SEDAN (marked as point 2) is also below the line, which can be explained by its shallow depth of burial with excavation (cratering) action –- which redirected a significant portion of the energy into formation of the crater and the air wave. The magnitude of the explosion BANEBERRY (point 1) is above the line, which may be explained by high water content in the source area.

One significant feature of the relationship between m_b^{BRVK} and log q is lack of linear dependency in the yield range between 1 and 1000 kt. Using the available data a piecewise approximation was obtained for three yield intervals:

$$m_b^{BRVK} = 0.52 \lg q + 4.78 \text{ for q < 20 kt} \quad (4.29)$$

$$m_b^{BRVK} = 1.071 \lg q + 4.13 \text{ for 20 ≤ q ≤ 150 kt}$$

$$m_b^{BRVK} = 0.531 \lg q + 5.48 \text{ for q > 150 kt.}$$

This character of the relationship between m_b^{BRVK} and q is probably related to the effect of the depth of burial on seismic efficiency, because the increase in depth corresponds to changes in physical properties and gas content of rock, which changes the seismic effects of the explosions. Evidently the increase in depth of burial leads not only to an increase in the lithostatic pressure, but also to changes in strength, density, porosity, elastic velocity and moisture content of the emplacement rocks.

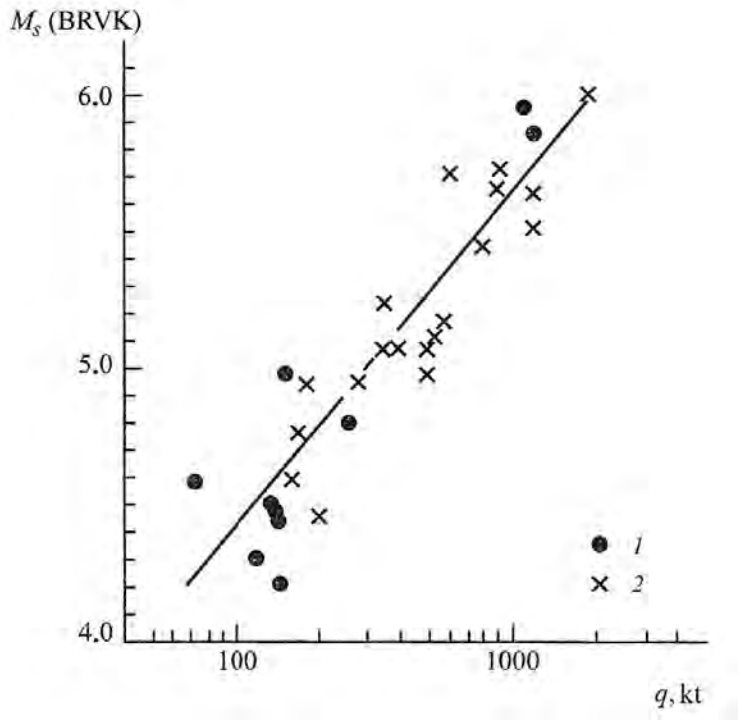

Figure 4.38. Magnitude (BRVK) as a function of yield of the underground nuclear explosions. The symbols show: 1 – announced yields; 2 – estimated yields.

The combined effect of these factors influences the distribution of the energy between the cavity, damage zones, plastic and elastic deformation, and seismic radiation. It follows from equations 4.29 that the NTS has two seismic boundaries determining the effect of explosions on the medium: 1) the explosions with yields greater than 20 kt are conducted below 200 – 250 m, and 2) the explosions with yields greater than 150 kt are conducted below depths of approximately 400 – 450 m.

Magnitude determined using Rayleigh waves (M_S^{BRVK}) has a scatter with respect to M_S^{ISC} up to ± 0.5 m.u. However there is a systematic error of approximately 0.2 m.u. in the values of M_S^{BRVK} compared to M_S^{ISC}. Figure 4.38 shows the relationship between M_S^{BRVK} and yield of explosions, which can be described as follows:

$$M_S^{BRVK} = 1.22 \lg q + 1.95. \qquad (4.30)$$

To improve accuracy of yield estimation the shape of the P-wave is commonly used, since it contains information about the conditions at the source affecting seismic efficiency of the explosion. This method was used earlier by a number of researchers (P. Basham, R. Horner, J. Everden; B.C. Bocharov, O.K. Kedrov). Here we provide a different method of yield estimate based on the shape of *P*-wave:

1. A "nominal" magnitude with symbol m_b^* is used instead of magnitude m_b^{BRVK}. It is determined from a vertical component of a short period channel using the amplitude and the period of the second half-period after the first arrival (negative extremum #2 in Figure 4.32 b). This "nominal" magnitude m_b^* is used because the value of m_b^{BRVK} is determined in the time interval of 25 seconds from the first arrival of *P*-wave. Therefore there is a possible interference between the direct *P*-wave and surface reflected *pP* (extremum #6 in Figure 4.32 b), determined not only by the explosion yield, but also by the phase shift between the two phases. In addition the apparent oscillation period changes with amplitude. It is possible that this interference is one of the reasons for the scatter of m_b^{BRVK} in comparison with m_b^{ISC}. Therefore the value of m_b^* is determined before the interference.
2. For NTS explosions the *P*-wave shape recorded at the BRVK station shows different coda decay. As a quantitative measure of *P*-coda decay we use parameter K determined as a ratio of the amplitude of oscillations within the interval between 1 – 3 s and 3 – 10 s after the first P-wave arrival.
3. The yield of an explosion is determined using the relationship obtained using regression analysis for explosions with declared yields:

$$\lg q\ (kt) = 0.747 m_b^* - 0.294K - 2.021\ . \qquad (4.31)$$

Table 4.11 shows some examples of yield estimated via equation 4.31 for several explosions with $m_b^* = 5.0\ to\ 6.4$ with yields ranging q = 20 to 150 kt. It can be seen from Table 4.11 that the maximum deviation for the estimated yield does not exceed 20%. So this method significantly improves on yield estimated via Equation 4.29.

Analysis of the data shows that the BRVK station records NTS explosions down to m_b = 3.8 to 4.2. This magnitude corresponds to the explosions with yields 1.2 to 1.9 kt (with a confidence level of 90%). For example BRVK recorded CABRIOLET with published yield of 2.3 kt (January 26, 1968), BEEBALM with yield of approximately 1 kt (May 1, 1970), as well as a number of small explosions with yields between 1 and 5 kt. Thus using optimal filtering methods (frequency, polarization, and spectral-temporal) allows robust detection, identification, and determination of the major parameters, of explosions down to approximately 1 kt for all testing areas of the Nevada Test Site.

Between 1961 and 1992 the BRVK station recorded 484 underground nuclear explosions conducted on USA territory. The lower detection threshold was m_b = 3.8, and starting from m_b = 4.2 almost all explosions were be detected (Hennet et al, 1996). Figure 4.39 shows the yield distribution of these explosions. The explosions with small yields corresponding to so-called secret tests[22] conducted at the NTS (Adushkin and An, 1996) were added to the distribution. Three yield maxima can be determined: 1 – 3 kt, 15 kt, and 90 kt, corresponding to research nuclear explosions, and refining charges for tactical and strategic weapons.

[22] In the United States, most nuclear tests—but not all—were announced at or shortly after they were conducted. A complete list of the unannounced tests was eventually released in the mid-1990s.

Table 4.11. Example of yield estimate for some nuclear tests conducted in the USA.

Date	Explosion	q, kt	m_b^{BRVK}	m_b^*	K	q_{BRV}, kt	Δq, %
05.23.1967	SCOTCH	155	6.5	6.25	1.37	176	14
05.26.1967	KNICKERBOKER	76	6.1	5.79	1.18	91	20
12.08.1968	SCHOONER	30		5.24	1.28	33	10
02.05.1970	LABIS	25	5.3	5.05	1.03	28	12
03.23.1970	SHAPER	-	6.4	6.01	1.61	99	-
05.26.1970	FLASK	105	6.3	5.98	1.77	84	-20
07.08.1971	MINIATA	83	6.4	5.79	1.94	74	-11
04.26.1973	STARWORT	90	6.4	5.92	1.58	86	-
09.06.1979	HEARTS	-	6.5	6.37	2.14	128	-
01.28.1982	JORNADA	-	6.5	6.30	1.71	152	-
08.05.1982	ATRISCO	-	6.4	6.34	1.68	166	-
09.01.1983	CHANCELLOR	-	6.1	5.76	0.89	105	-
07.17.1986	CYBAR	-	6.2	5.88	1.06	115	-
08.17.1988	KEARSARGE		6.0	5.80	1.08	99	-

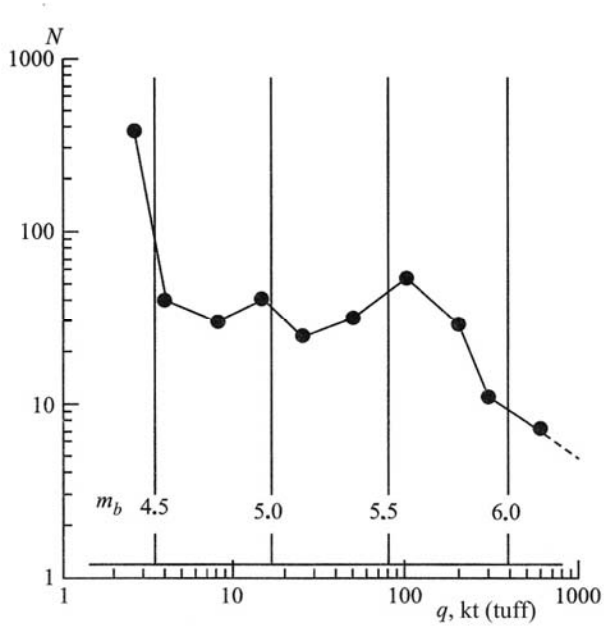

Figure 4.39. Yield distribution for underground nuclear explosion conducted in the USA.

4.7. Seismic waves from explosions in air-filled cavities (decoupling)

Nuclear test A-III-2 (8 kt) was conducted on March 29, 1971 at the Azgir site in a large air-filled cavity. This test is an example of a decoupled explosion, where the term decoupling refers to an amplitude reduction of the seismic signal due to conducting the explosion in a large underground chamber so that the cavity walls are not subjected to inelastic deformations. Test A-III-2 was conducted in a cavity created by a previous fully tamped explosion (test A-III; March 29, 1971). Test A-III had a yield of 64 kt and was conducted at a depth of 987 m in a salt dome of Eastern Azgir (Nuclear, 1997-2000). The scaled DOB for the tamped explosion was 247 m/kt$^{1/3}$.

The size of the cavity was determined using the laser distance measurement system Luch-2 [23] with an error of 5 – 8%. Horizontal and vertical radii were 38 and 33 m respectively. The average value of 38 m was used for calculations, with scaled radius of 9.7 m/kt$^{1/3}$, a value that agrees with measurements from other explosions taking into account depth of burial. For instance the nuclear test SALMON conducted at a depth of 828 m produced a cavity with an average radius of 17 m, corresponding to a scaled radius of 9.9 m/kt$^{1/3}$. Test A-II with a yield of 25 kt conducted at 600 m depth created a cavity with a scaled radius of 10.9 m (e.g. Kedrovskii et al, 1972). Murphy (1981) provides the following empirical relationship for the cavity radius as a function of the depth and yield:

$$r_0 = Cq^{0.29}/W^{0.11}, \tag{4.32}$$

where *C* is an empirical constant. The average value of C is 24. Radius estimates using Equation 4.32 have error on the order of 1 m. Applying (4.32) to A-III produces radius of 37.6 m, which is close to the measured value. Based on comparison of the radius measurement we conclude that the physical properties of salt are similar between A-III and Salmon.

The center of explosion A-III-2 had a depth of 987 m, which corresponds to a scaled depth of 494 m/kt$^{1/3}$. A geological cross-section in the plane of the charge is schematically shown in Figure 4.40. The top 210 m below the surface are represented by clay and sand with P-wave velocity 1800 – 2200 m/s. The second layer with thickness of 65 m is composed of anhydrite and gypsum. Below 275 m is rock salt with density 2170 kg/m^3, and P-wave velocity 4200 – 4500 m/s. The laboratory-measured compressive strength for this salt is 37 MPa.

Seismic waves from A-III-2 were recorded by a temporary seismic deployment at distances between 1 and 154 km. Seismic stations were located along two main profiles: northeast between 1 to 84 km, and north-northwest between 26 and 154 km. This network was in general similar to the network deployed to record A-III, so most of the stations were installed almost at the same locations.

Figure 4.41 shows the horizontal components of ground displacement as a function of distance for events A-III and A-III-2. The amplitudes decay faster for the decoupled than for the fully tamped explosion. This (faster decay) is due to higher frequency content of the decoupled

[23] "Ray-2" in English

explosion. For instance, the observed period of oscillations is 3-4 times shorter than for the tamped explosion. Figure 4.42 shows the ratios between the amplitudes of ground displacement and velocity with increased distance. The ratios increase with increased distance due to higher attenuation for high frequencies, characteristic for decoupled explosions.

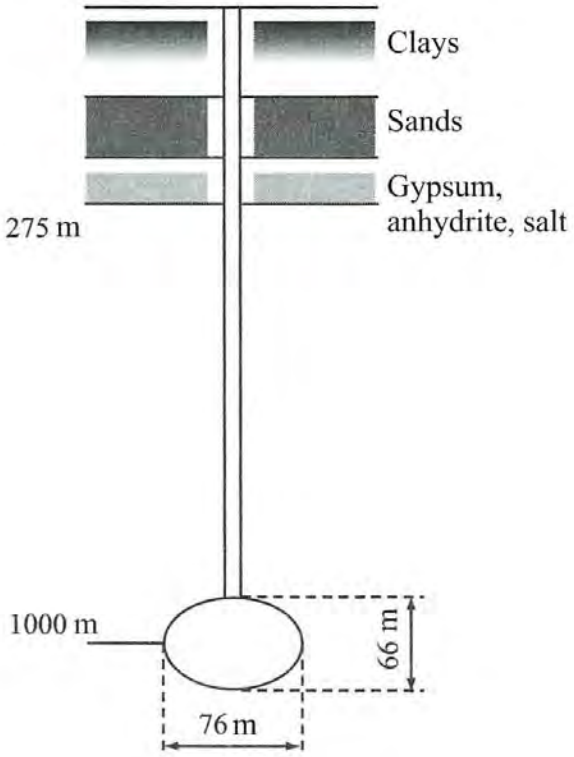

Figure 4.40. Schematic crossection through borehole A-III-2 according to drilling data. See explanations in the text.

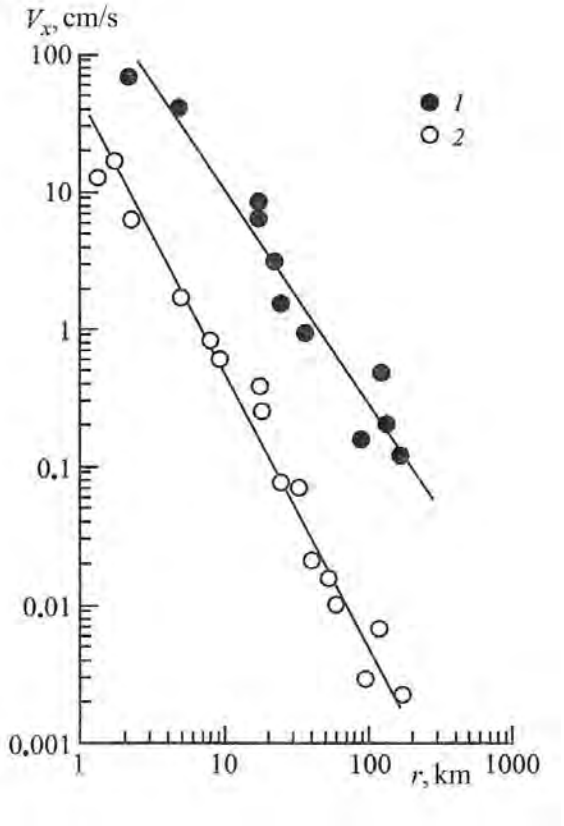

Figure 4.41. Horizontal component of the ground velocity of the seismic wave as a function of distance for underground explosions: 1 – A-III, 2 – A-III-2.

The decoupling coefficient was determined for explosions A-III and A-III-2 using the experimental data and applying different methods. The first estimate was made using statistical analysis of the relationship between the displacement and velocity amplitudes. The analysis was applied to data of tamped explosions [I think they mean other than A-III] conducted at Azgir. These results were compared with the observations for A-III-2 (Adushkin, 1991).

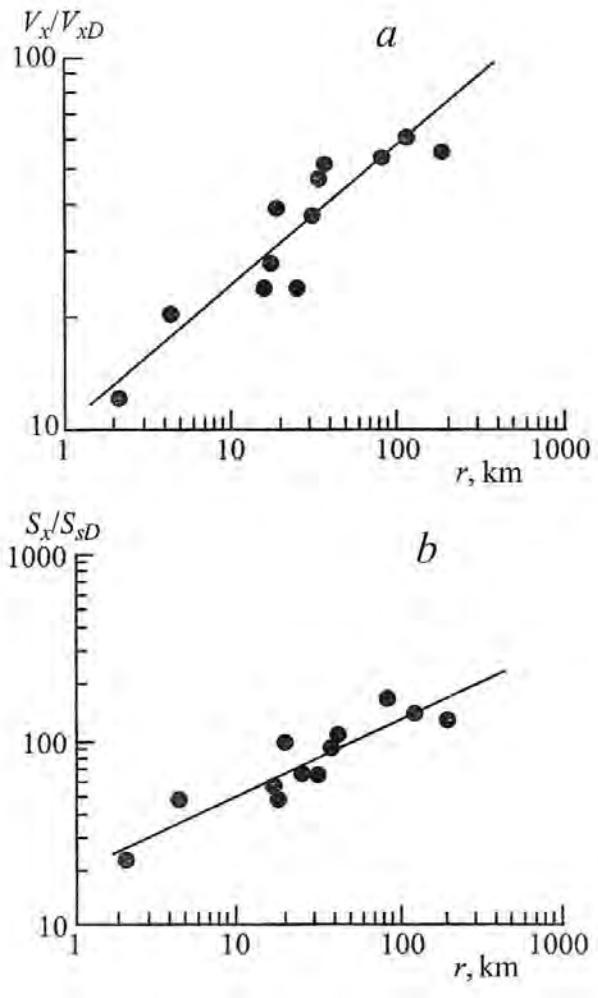

Figure 4.42. Ratio between maximum a) velocity and b) displacement amplitudes (amplitude decoupling coefficient) for explosions A-III and A-III-2 (index D) as a function of the epicentral distance.

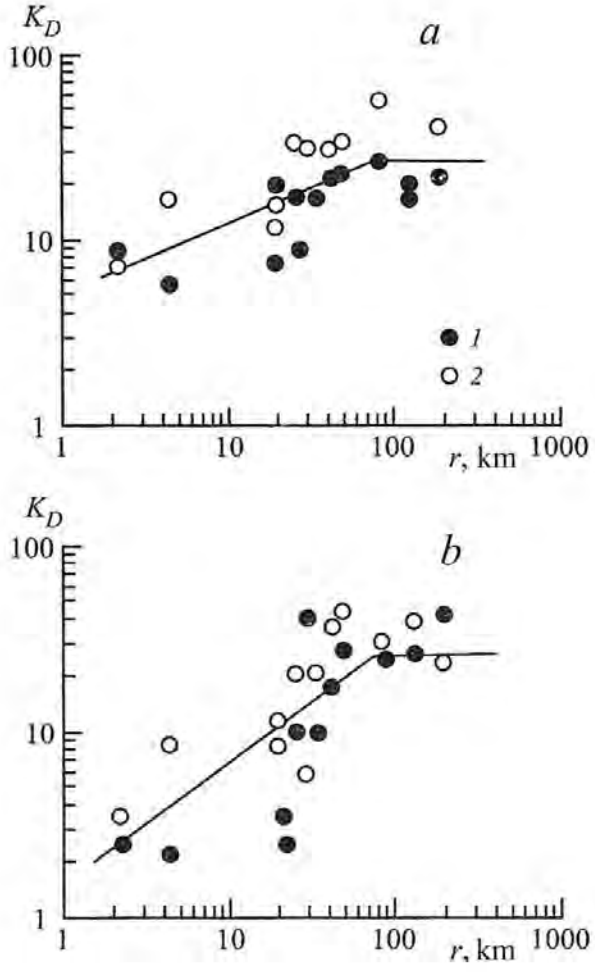

Figure 4.43. Changes in energy decoupling coefficient KD with epicentral distance determined using a) ground displacements, and b) velocities. The symbols correspond to components: 1 – vertical, and 2 – horizontal.

Relationships for different displacement and velocity components in the form $A_i = aq^{\alpha}r^{\beta}$ where A_i is the amplitude of the i^{th} component, α and β are the empirical constants, were obtained (Adushkin et al, 1993):

$$S_z = 10q^{0.8}r^{-1.7} \quad (\sigma=1.85), \tag{4.33}$$

$$S_x = 6q^{0.75}r^{-1.74} \quad (\sigma=1.77),$$

$$v_z = 19q^{0.8}r^{-1.8} \quad (\sigma=2.18),$$

$$v_x = 18q^{0.65}r^{-1.5} \quad (\sigma=1.78),$$

where S_z and S_x are the displacement amplitudes for z and x components (in mm), v_z and v_x are the corresponding velocity amplitudes (in mm/s), q is the explosion yield (in kt), r is the distance (in km), and σ is the standard deviation. Using these relationships and using the displacement and velocity amplitudes of the decoupled explosion the effective energy for the TAMPED explosion was estimated. The ratio of the actual energy and the effective energy is called the *energy decoupling coefficient* (as opposed to the amplitude decoupling coefficient described below). The average value of the effective energy of the tamped explosion was 0.27 kt, therefore the value of the decoupling coefficient obtained using this method is 30.[24]

Figure 4.43 shows the energy decoupling coefficient obtained using the described method as a function of distance. The estimate becomes stable beyond 30-40 km from the epicenter. This can be explained by the high frequency content of the explosion. The decoupled explosion generates higher frequency waves due to smaller effective size of the source (e.g. Glenn, 1993; Glenn et al, 1987). At distances less than 30-40 km the spectra of A-III and A-III-2 are very different, and the estimate of the decoupling coefficient is performed close to the spectral fall-off part, which reduces the amplitude ratios. Beyond 30-40 km the spectra become more similar due to high frequency attenuation, therefore the amplitude ratios are computed around 1.5 – 2 Hz, or in the flat part of the spectra.

This method has some disadvantages. First, the seismic amplitudes can vary depending on the recording site by a factor of two or more, which is reflected in the standard deviation. This amplitude variability reduces the precision of the yield estimate. Second, the range of yields of the tamped explosions used for the statistical analysis was between 1 and 64 kt, whereas the effective yield for the decoupled explosion was 0.27 kt, which is 4 times smaller than the minimal yield used to obtain the expressions. Such extrapolation in the low yield range is not experimentally justified. In addition the decoupled explosion was conducted at greater scaled DOB (1520 m/kt$^{1/3}$ estimated for the effective yield), therefore relationships 4.33 may underestimate the effective yield.

Two methods were used to estimate the *amplitude decoupling coefficient*. First method used the displacement and velocity amplitudes for A-III and A-III-2 at the same locations for different distances. The ratios between the tamped and decoupled explosions were calculated by rescaling of the tamped explosion with yield of 64 kt into 8 kt by multiplying by a factor 8/64. Decoupling coefficient was determined separately for each component by averaging the results between different stations between 2 and 113 km. The resulting estimates of the decoupling coefficient D are shown in Table 4.12.

The average value of the decoupling coefficient is 11.5 ± 8.3. If we convert the value of the amplitude decoupling coefficient into the energy decoupling coefficient, the value is 22 ± 14. This is smaller than the value of the energy decoupling coefficient obtained earlier. This can be explained by using stations close to the epicenter, where the decoupling coefficient is smaller (Figure 4.43). We also mentioned earlier that the effective yield of the decoupled explosion was

[24] Needs discussion with experts to improve clarity. Apparently the value 30 is obtained from 8 kt divided by 0.27 kt. Note added by translators.

underestimated, which becomes apparent after conversion from the amplitude to the energy decoupling coefficient. We note that this method[25] also has disadvantages because the amplitudes are measured for the signals with different frequency content.

Table 4.12. Amplitude decoupling coefficient D from local data.

Component	D	Component	D
X	8.42 ± 6.1	Y_{max}	15.9 ± 12
X_{max}	10.6 ± 6.6	Y	10.2 ± 9
Y	13.0 ± 8.8	Z_{max}	11.2 ± 6

The second method of determining the amplitude decoupling coefficient is by computing the ratios of the spectra in the low-frequency limit. The spectra were calculated by averaging each individual spectrum between 0.5 and 2 Hz, or up to the corner frequency of the tamped explosion. The ratio between the averaged values was then calculated.

Since the spectra are very similar, this technique has a very high precision. The amplitude decoupling coefficient was obtained by calculating the average ratio between the two spectra multiplied by the ratio of the yields (8/64). The resulting average value for the amplitude decoupling coefficient was 19.3 with the standard deviation of $\langle D \rangle = 6.8$. The results for the horizontal component show lower value of the decoupling coefficient of 16 and higher standard deviation $\langle D \rangle = 9.5$. These values are somewhat higher than the decoupling coefficient determined by the amplitude ratios because similar frequencies were used.

The main problem related to decoupling is the frequency dependence of the decoupling coefficient. Figure 4.44 shows the ratio of the absolute values of the spectral amplitudes for explosions A-III and A-III-2 averaged for all stations. The ratios of the absolute values represent the frequency-dependent decoupling coefficient. In the frequency range between 0.5 and 2 Hz the ratio is approximately 155, which (after multiplying by 8/64 to correct for the difference in yields) leads to a value of 19.3 for the low-frequency limit of the amplitude decoupling coefficient.

The small increase in spectral ratios for frequencies around 2 Hz is caused by a peak (overshoot) near the corner frequency for tamped explosions A-III. As frequency increases from 2 to 5 Hz the frequency dependent (spectral) decoupling coefficient decreases from 155 to 10, which means that the amplitude reduction is significantly lower for high frequencies than for low frequencies. The sharp decrease of spectral ratios with increasing frequency is due to decrease in spectral amplitudes for the tamped explosion and constant amplitude of the decoupled (cavity) explosion. Since the dynamic range of the seismic records was limited to 30-40 dB the spectrum for A-III can be reliably determined only up to 8-10 Hz. The spectral amplitude for A-III falls off

[25] the one used in Table 4.12

at high frequencies as f^{-2}, and for frequencies 8–10 Hz the amplitude is two orders of magnitude lower than at low frequencies. In this frequency range the spectral ratios approach 4–5, giving an amplitude decoupling coefficient close to 1. Such low decoupling coefficient at 8 – 10 Hz is probably due to a spectral peak at these frequencies for A-III-2 recorded at close distances. At lower frequencies (about 4 – 5 Hz) the amplitude decoupling coefficient should increase to 2 – 3.

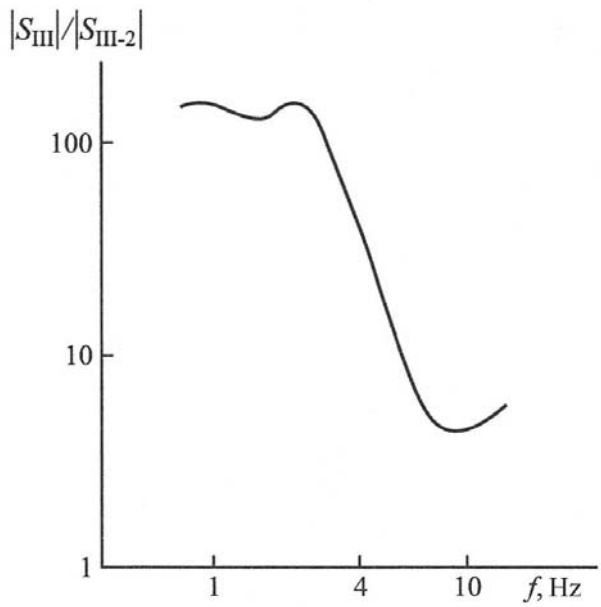

Figure 4.44. Average spectral ratio between explosions A-III / A-III-2 using vertical component records of the displacements in the distance range from 17.8 to 113 km.

Thus the main result of the analysis above is the rapid reduction of the decoupling coefficient beyond the corner frequency of A-III, which can be used for monitoring of underground nuclear explosions, including decoupled explosions at frequencies above 5 Hz.

An independent method to estimate the decoupling coefficient involves analysis of the theoretical and observed spectra at short distances from the explosions, where the spectra are not significantly distorted by the heterogeneities along the path. To estimate the decoupling coefficient we use a simple model of a seismic source developed by Sharpe (1942). According to Sharpe model the displacement spectrum at distance *r* is given by:

$$S(\omega) = \frac{\sigma_{el} R_0^3}{4\mu r}\left[\frac{C_p}{C_p^2 - 0.75R_0^2\omega + iC_p w R_0}\right], \qquad (4.34)$$

where ω is the angular frequency, R_0 is the elastic radius of the source, σ_{el} is the elastic limit at the cavity wall, μ is a shear modulus, and C_p is the *P*-wave velocity. The defining parameters of the model are R_0 and σ_{el}, because the radius where the pressure reaches σ_{el} depends on the initial pressure in the cavity as well as the attenuation of pressure with distance.. To find the parameters R_0 and σ_{el} we need to find the match between the theoretical and experimental source function using the corresponding spectra and the standard physical properties of salt (ρ = 2200 kg/m^3; σ_{tensile}=27 MPa; C_p = 4850 m/s).

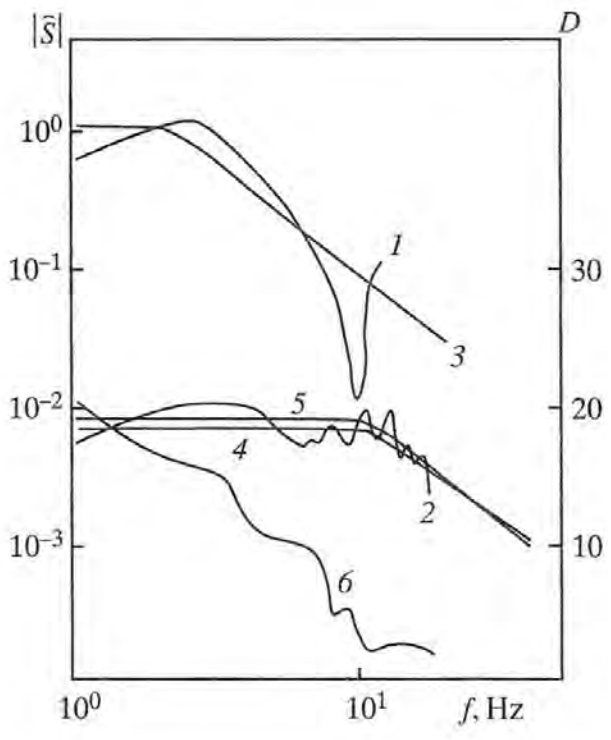

Figure 4.45. Theoretical and observed spectra for explosions A-III and A-III-2. The lines show: 1 – A-III at a distance of R = 2.3 km from the source; 2 – A-III-2 at R = 1.34 km; 64 kt explosion, R = 2.3 km; 4 – tamped 0.4 kt explosion at R = 1.34 km; 5 – 8 kt explosion at *R* = 1.34 km; 6 – decoupling coefficient.

Figure 4.45 shows the observed spectra computed for the displacement seismograms at a distance of 2.3 km from the epicenter of explosion A-III (line 1) and at a distance of 1.34 km from A-III-2 (line 2). Also shown are theoretical spectra calculated using Equation 4.34 for a tamped explosion with a yield of 64 kt at 2.3 km from the epicenter (line 3), for a tamped explosion with a yield of 0.4 kt at a distance of 1.34 km from the epicenter (line 4), and for a decoupled explosion with a yield of 8 kt conducted in a cavity with the radius of 38 m recorded at 1.34 km from the epicenter (line 5). The theoretical displacement spectrum for 64 kt at 2.3 km (line 2) agrees with the observed spectrum. Therefore the proposed model well describes the magnitude of the signal (in the low-frequency range) as well as the frequency fall-off.

This agreement allows modeling of the spectra for explosions in cavities. The modeling was performed by varying the effective yields of the tamped explosions between 0.1 and 0.6 kt. Comparison between the theoretical and observed displacement spectra at 1.34 km enables finding a yield for a tamped explosion (0.4 kt) that best matches the theoretical and observed spectra (lines 2 and 4) for the 8 kt explosion in a cavity with a radius of 38 m at 1.34 km distance (lines 2 and 5).

Based on this approach the decoupling coefficient was estimated as a ratio between the theoretical spectrum of an 8 kt tamped explosion and the measured explosion spectrum in a cavity of the 8 kt explosion A-III-2 at a distance of 1.34 km. The results are shown in Figure 4.45 as line 6, as a function of frequency $D(f)$. As the plot shows the decoupling coefficient has a strong frequency dependence: in the low frequency limit (0.5 – 2 Hz) the value is close to 20,

while the value at 10 Hz is approximately 2 – 3. Thus this method yields the estimate of the decoupling ratio similar to the value obtained using the spectral ratios method.

A similar analysis of seismic efficiency of decoupling explosions using theoretical source models was performed by Denny and Goodman (1990), Glenn et al (1987), and Glen and Goldstein (1994) using the experimental data for STERLING (q=0.38 kt) conducted in a cavity with a radius of 17 m left by a tamped explosion SALMON (q =5.3 kt; W=827.8 m) in a salt dome in Mississippi (USA). Related work includes estimating the efficiency of contained explosions as a function of scaled cavity radius (Terhune et al, 1970). According to Murphy and Muller (1974) the energy flux produced by a contained explosion is given by:

$$E_{el} = 8\pi\mu S_{res}^2 R_0 + \frac{4\pi\rho}{C_p}\int_0^\infty \left(\frac{d^2\varphi}{dt^2}\right)^2 dt \qquad (4.35)$$

Where μ is the shear modulus, S_{res} is the residual (permanent) displacement on the boundary of the elastic region, R_0 is the elastic radius, rho is the density, C_p is the P-wave velocity, and φ is the displacement potential.

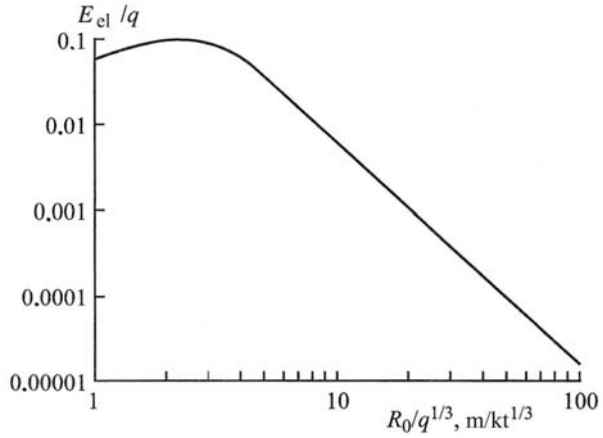

Figure 4.46. Radiated seismic energy as a function of the scaled radius for fully contained explosion.

The first term depends only on the magnitude of the permanent displacement and corresponds to a static energy of an elastic deformation caused by a cavity expansion. The second term depends on the nature of the displacement potential and corresponds to the radiated seismic energy. Figure 4.46 shows estimates of radiation efficiency of elastic energy as a function of the scaled radius of the cavity for the contained explosion HARDHAT, conducted in granite (ρ = 2670 kg/m^3; C_{p} = 5440 m/s; υ = 0.28; m = 0.027, η_ω = 0.01). The results show that for a change of the cavity from 0.1 m/kt$^{1/3}$ (point source) to 10^2 m/kt$^{1/3}$ (full decoupling), the radiated energy decreases from 6% to 0.002% of the total energy of the explosion. Thus the fraction of the radiated energy is reduced by a factor of 3000.

We note that if the scaled cavity radius is increased from 1 to 2.5 m/kt$^{1/3}$ the radiated energy increases slightly, from 6% to 8% of the total energy (because less energy goes into melting and vaporization, and more into seismic radiation). If the scaled radius is further increased to 10

m/kt$^{1/3}$, comparable to that for the cavity of A-III-2 (9.7 m/kt), the portion of energy radiated seismically reduces from 8% to 0.5%, i.e. by a factor of 16 – which agrees with previous estimates of the energy decoupling coefficient.

Table 4.13. Regional and teleseismic data for explosion A-III-2.

Seismic station	Distance, km	Amplitude, nm	Period, s	Magnitude m_b
Kirovobad	785	8	0.7	-
Mikhnevo	1065	20	0.4	-
Sverdlovsk	1230	23	0.4	-
Borovoe	1590	6	0.7	4.0
Hagfors	2220	9	0.4	4.4
Garm	2250	5	0.8	-
Talgar	2280	7	0.8	3.99
El'tsovka	2690	5	0.8	4.75
Bodaibo	4310	8.5	0.6	4.25

The seismic efficiency of the decoupled explosion A-III-2 was studied using seismic data recorded at both regional and teleseismic distances (Adushkin et al, 1993). This explosion was recorded with both Russian and international seismic stations. The stations with standard equipment recorded the event up to 2500 km, while the high quality stations recorded it up to 4300 km (Table 4.13).

According to the International Seismological Centre (ISC) catalog the magnitude of the event A-III-2 is m_b = 4.4. Using the relationship between magnitude and yield of the explosion (Equation 4.33) for the same salt dome the effective yield was determined for the decoupling explosion. The average value of the decoupling coefficient for A-III-2 determined using the yield estimate was 30, which in general agrees with the local data and the theoretical calculations.

The results of the analysis of seismic efficiency for the decoupling explosion A-III-2 can be summarized as follows:

1. The energy decoupling coefficient for this explosion is 20-30.
2. Seismic waves from this source are significantly enriched with high frequencies.
3. Decoupling coefficient is a frequency dependent quantity, which reduces with increased frequencies.
4. Experiment A-III-2 didn't produce full decoupling (for explosions in salt the amplitude reduction for full decoupling is at least 100). This is related to either insufficient size of the cavity, or the existence of a weaker (fractured) zone around the cavity walls.

5. The cavity size required for full decoupling and decoupling efficiency is discussed in a number of previous works (e.g. Kitov, 1992; Glenn, 1993; Murphy, 1981). The results of these studies suggest that full decoupling of 1 kt explosion can be reached using a cavity with a radius of 60 – 100 m. In these circumstances decoupling explosions between 1-10 kt would have magnitudes $2 < m_b < 3$. For these events regional discriminants are needed, because large numbers of earthquakes and rock bursts occur in this magnitude range.

4.8. Seismic waves from industrial explosions in quarries

Statistical information related to the number of chemical explosions in Russia and the amount of explosives used for these explosions is useful to determine the rankings of each region in terms of the environmental load, and for quantitative estimates of the environmental effect of mass usage of explosive technologies.

The total amount of explosives used in Russia for specific years is presented below:

Year	1992	1994	1996	1998	2000	2001	2002	2003	2004	2005
Mass of explosives, 1000s of tons	1100	800	550	550	640	700	705	795	810	980

Evidently after some reduction of the volume of explosive operations in the late 1990s, the amount of explosives has gradually grown. Currently the amount of explosives used annually exceeds 1 million tons.[26]

Over 90% of the total amount of explosives used in Russia, are used in about 15 out of the 40 districts of Rostechnadzor[27] in which explosive operations are conducted.

Table 4.14. Volume of explosive operations for districts with the largest usage of explosives (in % from the total amount during the period 1994 – 1998).

District	Amount of explosives					
	1994	1995	1996	1997	1998	1999
Kuznetskii	22.1	23.9	25.3	25.8	25.3	27.2
Ural'skii	7.1	8.5	7.9	8.6	11.2	8.1
Yakutskii	11.5	10.1	9.7	9.4	10.8	10.6
Murmanskii	7.4	9.7	8.8	9.8	10.4	9.5
Kursko-Belgorodskii	4.6	4.8	7.2	7.9	8.4	9.2

[26] Statement made in about 2006. Note added by translators.

[27] Federal Service for Ecological, Technological and Nuclear Supervision. Literally "Russian Technical Monitoring" This is an organization responsible for safety and monitoring of explosive operations.

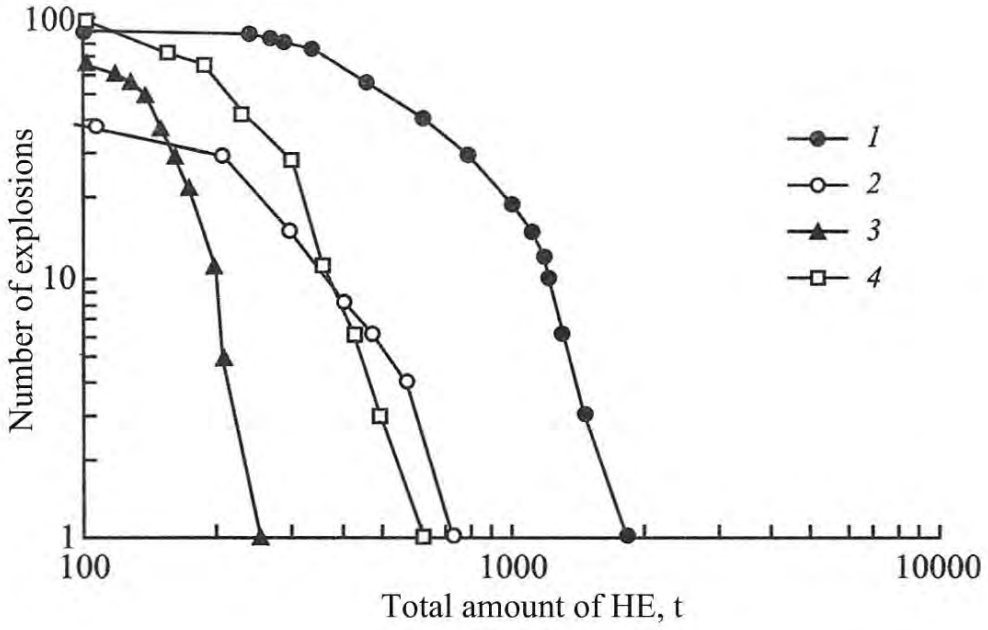

Figure 4.47. Cumulative number of chemical explosions with explosive yield [weight] exceeding a given weight. The lines show: 1 – Lebedinskii GOK (quarry) (1992 – 1994); 2 – Stoilenskii GOK (quarry) (1993 – 1994); 3 – Kachkanarskii GOK (quarry) (1993); 4 – Olenegorskii GOK (quarry) (1994 – 1996).

The amount of explosives used in the industry varies significantly between districts. For example in 1998 Chita (Chitinskii) district used 3000 t of explosives, while Kuznetzk (Kuznetskii) district used 138,700 t. Five districts using the highest volumes of explosives are shown in Table 4.14. According to Table 4.14 the largest amount of explosives is used in Kuznetzk Basin.

To evaluate the environmental effect of explosive operations one needs to know not only the total amount of explosives used in a particular quarry or mine, but also the amount of explosives used for each individual explosion (Figure 4.47). This amount determines the intensity of the environmental load on the surrounding territory (amplitudes of seismic waves and electromagnetic impulse, volume and mass of gas-dust cloud), as well as the area of influence of a specific mine (radius of the zone of acceptable seismic amplitudes, distances where the dust cloud can reach, based on meteorological conditions for the specific area).

Table 4.15 shows the numbers of chemical explosions with yields exceeding 100 t for the five main districts. According to the table the majority of large explosions with total mass of explosives exceeding 500 t are conducted within Kursk-Belgorod district. The majority of explosions are detonated in the higher ranges of yield (for chemical explosives). In this respect Kursk-Belgorod district is the most interesting for study of the environmental impact of large industrial explosions.

Table 4.15. Number of large explosions for five major mining districts in Russia with different explosive yield q.

District	$100 < q < 500$			$q > 500$		
	1994	1995	1996	1997	1998	1999
Kuznetskii	348	313	361	1	0	0
Ural'skii	84	72	87	0	0	0
Yakutskii	99	74	211	3	7	8
Murmanskii	194	172	188	0	0	0
Kursko-Belgorodskii	79	75	88	32	35	40

Table 4.16. Number of large explosions detonated within KMA (Kusrsko-Belgorodskii from Kursk-Belgorod district of Russia) with different explosive yield q.

GOK (Quarry)	$100 < Q < 500$			Average	$Q > 500$			Average
	1997	1998	1999		1997	1998	1999	
Lebedinskii	29	29	26	28	25	24	35	~25
Stoilenskii	20	34	26	~27	0	1	3	~1
Mikhailovskii	30	41	36	~36	7	10	12	~10

Let us now briefly describe the technology of explosive operations using the example of mines in the Kursk Magnetic Anomaly (KMA). Mining at KMA has been carried out since the 1950s. At present the major mines in this area (Lebedinskii, Stoilenskii and Mikhailovskii GOKs[28]) use the open pit method, which produces quarries of significant size. Thus the area of Lebedinskii Quarry is approximately 10 km^2 with a depth of approximately 250 m. The area of Stoilenskii Quarry is approximately 7 km^2. Mining is performed using large scale explosions accompanied by gas-dust clouds and seismic waves, which affect the environment, industrial structures, and people's houses.

The cyclical technology of quarry operations used by KMA mines provides a stable periodicity of large explosions (for example, each quarry conducts explosions every 2 weeks).

[28] GOK is an abbreviation for Gorno-Obogatitel'nyi Kombinat – Mining-Enrichment Facility (Note added by the translators).

The number of explosions conducted at KMA is shown in Table 4.16. The number of large explosions each year is similar. The largest number of explosions with yield over 500 t was conducted at Lebedinskii Quarry.

With a few exceptions, large quarry blasts are detonated using the delay-fire method, which involves sequential detonation of relatively small (between 100 and 1000 kg) borehole charges arranged in rows. Different groups of charges are detonated with 20 to 50 ms delays. This technique not only results in reduction of the seismic amplitudes, but also helps regulate rock fragmentation.

The charge boreholes have depths of 8 – 16 m and diameters between 160 and 250 mm. The commonly used explosive is emulsion "Tovan" prepared on the spot, and granotoluol. The amount of explosives placed in each borehole is 0.5 – 1.5 t. Charge boreholes are located in rows along the cliff of rocks. Groups of 3-5 boreholes are detonated simultaneously. The distances between the boreholes in each row is 5 m, the distance between the rows is 8 m.

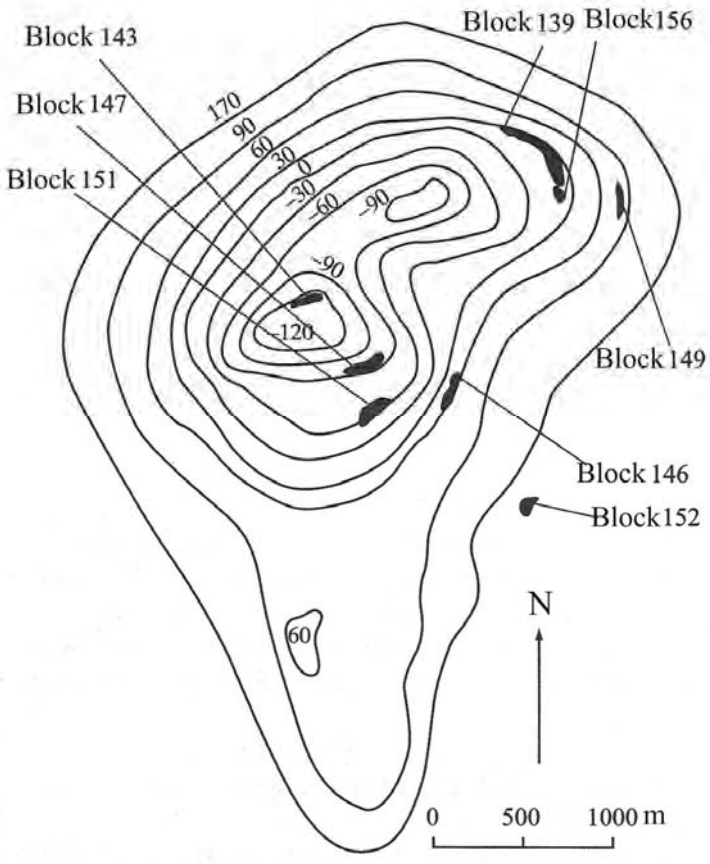

Figure 4.48. Schematic map of the blocks blasted on October 1, 1998 at Lebedinskii quarry.

To optimize preparation and detonation operations the blasts are conducted in blocks located in different parts of the quarry. As an illustration, Figure 4.48 shows locations of different blocks of rock blasted on October 1, 1998. The time interval between explosions in each block was between 1 and 10 s. Each block was blasted using between 80 and 300 t of explosives.

With this scheme the energy release during an explosion is non-uniform in space and time. Figure 4.49 shows a plot of energy release with time for one of the explosions. According to the plot sequential blasting of different blocks makes the rate of energy release quite variable.

Seismic safety during large quarry blasts is one of the most important considerations during open pit quarry mining operations. Due to constant increase in mining area, more stringent restrictions on ground vibrations, and higher requirements to maintain stability of quarry walls, the seismic effect of explosions is an open problem that requires continuing studies of seismic waves in quarries and improved seismic zoning, in order to chose the appropriate parameters of explosions for specific mining operations.

We note that seismic signals produced by large quarry blasts are very complex, due to the interference between seismic sources spread out in time and space, which creates interference between waves of different types.

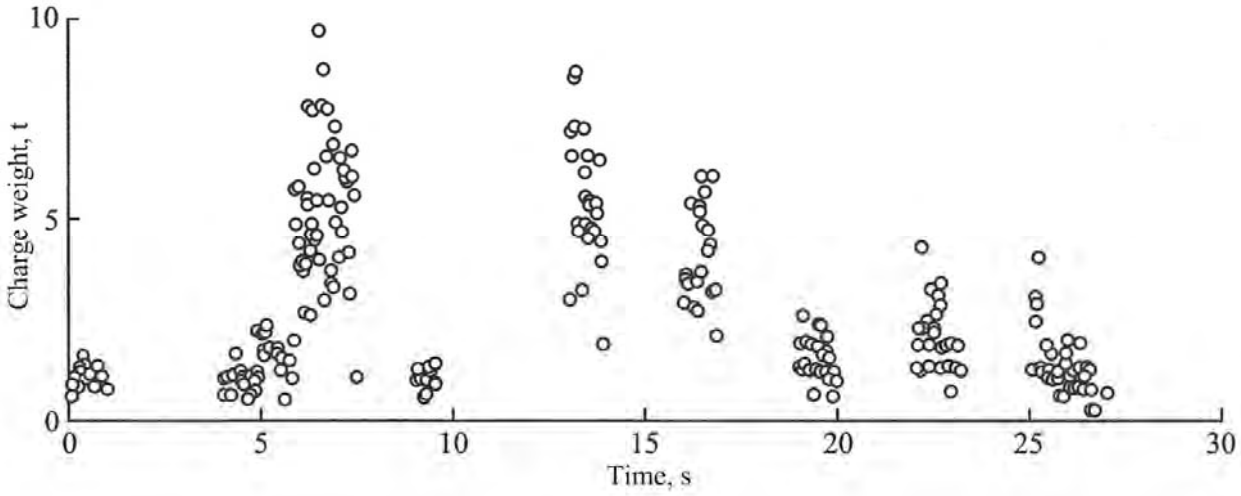

Figure 4.49. Timing of individual blasting of different chemical charges for a large explosion at Lebedinskii Quarry on August 24, 1995 (total weight of explosives – 834.6 t).

In this work we use seismic measurements from large quarry blasts recorded over a broad range of epicentral distances. Complex operational seismic measurements were performed using a combination of different methods, such as used in geophysical observatories. In particular, the observatory located in Mikhnevo (Moscow region), belonging to Institute of Dynamics of Geospheres) was used for complex geophysical observations of quarry blasting.

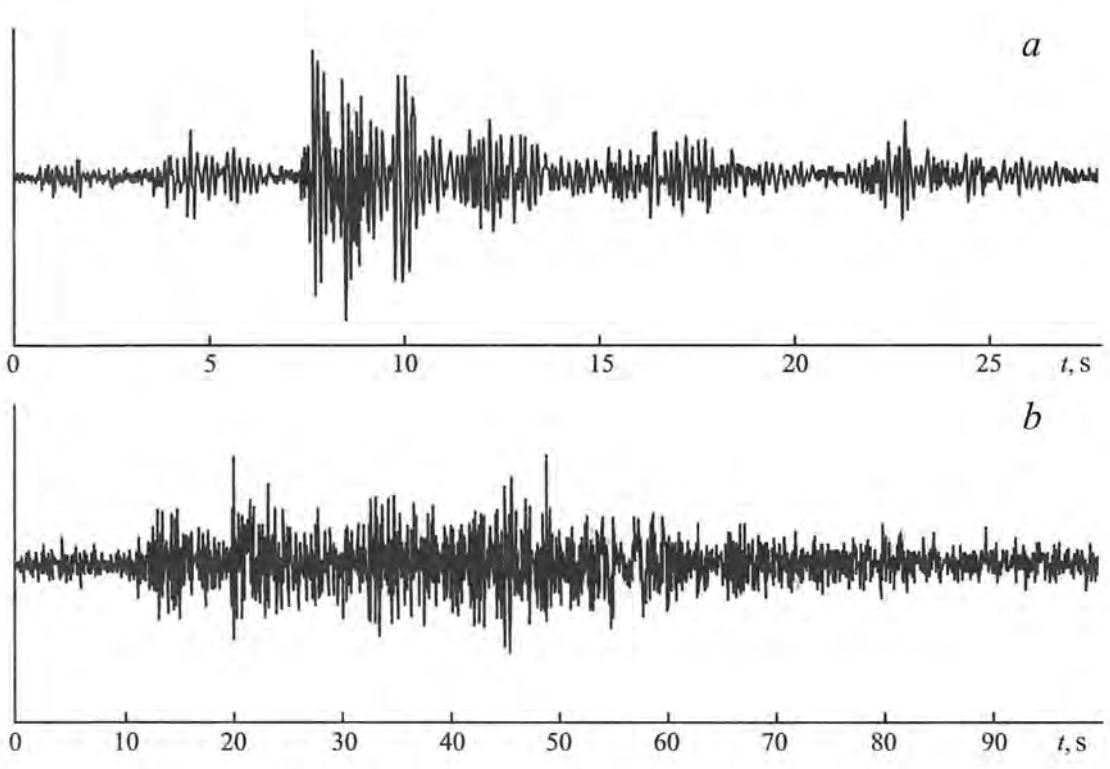

Figure 4.50. Velocity seismograms for large explosion at Lebedinskii Quarry on October 1, 1998. a) Seismic trace recorded at a distance of 1 km from the closest block. b) Seismogram recorded at a distance of 150 km from the quarry.

As an illustration we discuss seismic waves from explosion conducted at the Lebedinskii Quarry on October 1, 1998. The explosion was conducted in nine separate blocks. The main characteristics of each block are shown in Table 4.17. Figure 4.50 shows velocity seismograms recorded at different distances from the quarry. The seismogram recorded near the quarry shows separate wavetrains related to blasting of each block (Figure 4.50a). Starting from distances of about 15- 20 km, seismic oscillations from this explosion are represented by a continuous wavetrain (Figure 4.50b).

Analysis shows that unlike waves from earthquakes or single-fired explosions, seismic waves from delay-fired explosions propagate almost as a "packet" (with uniform wavetrain). This is due to interferences between different phases, created by different explosions in different boreholes and blocks.

It follows that amplitude characteristics of large quarry blasts should be determined by analyzing their envelopes. At close distances to the quarry, where seismic signals are potentially damaging for buildings and other structures, the amplitude of the seismic signal should be determined for each block separately. These estimates are performed separately for different azimuths.

Table 4.17. Block characteristics for the explosion conducted at Lebedinskii Quarry on October 1, 1998.

Block #	Horizon [Depth or height], m	Number of charge boreholes	Total weight of explosives, kg
143	-135	116	143,361
147	-105	96	159,509
151	-30	131	134,915
156	+30	40	2934
149	+75	94	85,665
146	+60	120	98,243
152	+175	40	5040
139	+30÷45	186	167,693
148	0	28	1649

The main characteristic of a seismic signal generated by an explosion is its amplitude. More precisely it is the amplitude of the vector of oscillations (determined from three components of motion) at a specific point. To obtain an overall understanding of the measurements performed using different layouts of source and station it is important to choose a correct underlying scale in order to be able to combine observations. Traditionally, the scaled distance $\bar{r} = r/q^{1/3}$ is used to describe seismic waves at different distances from the source, where r is the distance and q is the weight of explosives in kilograms. For delay-fired blasts consisting of large number of boreholes the parameter q is given by the weight of explosives in a group of boreholes detonated simultaneously.

Figure 4.51 shows ground velocities as a function of distances for multiple measurements of large blasts detonated at the Lebedinskii Quarry. The stations were located along a profile between city of Gubkin and Moscow.

The plot shows that the overall absolute value of seismic velocities $v_0 = |\vec{v}|$ is described by

$$v_0 = 3.93\left[\frac{q^{1/3}}{r}\right]^{1.5} \text{ (m/s)},$$

where parameters r and q are measured in meters and kilograms respectively.

Local amplitude increases due to specific reflections from different boundaries within the earth's crust were not observed.

The maximum amplitude of the vector of oscillations v_m at a specific distance from an explosion is given by

$$v_{0m} = 5.2\left[\frac{q^{1/3}}{r}\right]^{1.5} \text{ (m/s).}$$

This formula takes into account scatter in the experimental data, which is an important parameter for evaluation of seismic safety of buildings and other structures.

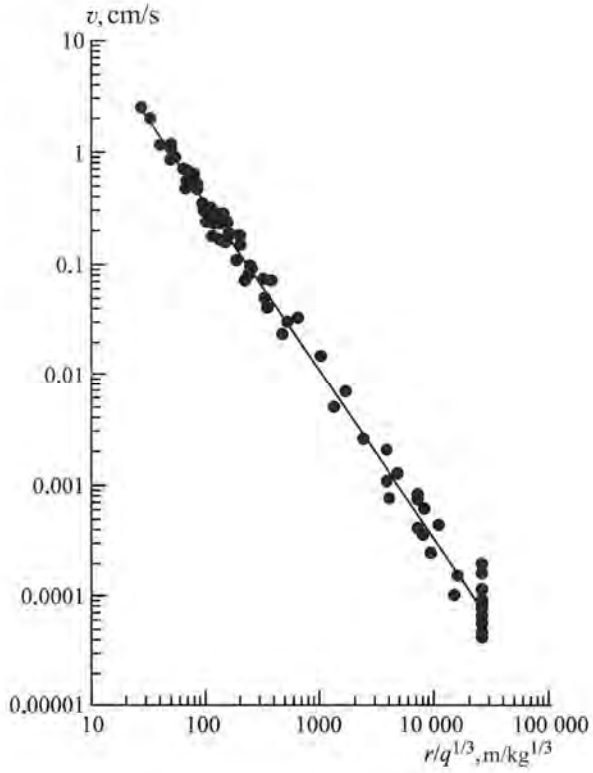

Figure 4.51. Maximum absolute value of the ground velocity as a function of the scaled distance R for large explosions conducted at Lebedinskii Quarry.

These relationships were obtained in order to determine the radius of potential damage to buildings and structures.

In order to evaluate the seismic effect on structures it is important to know spectral characteristics of seismic waves. The major damage to buildings and structures is caused by oscillations in the frequency range between 0.5 – 8 Hz. The dominant frequencies generated by single-fired shots are within this frequency range. However the delay-firde detonation generates higher frequency signals. Figure 4.52 shows a seismic spectrum produced by a delay-fired explosion. In addition to the main peak at approximately 20 Hz there are two additional peaks at 42 and 64 Hz.

Spectral modulation is a typical characteristic of delay-fired quarry blasts (e.g. Adushkin et al, 2000). As a result of modulation there is an increase in high frequency amplitudes. This example indicates the need to study effects of high frequency oscillations on different parts of buildings and other structures located close to open pit mines.

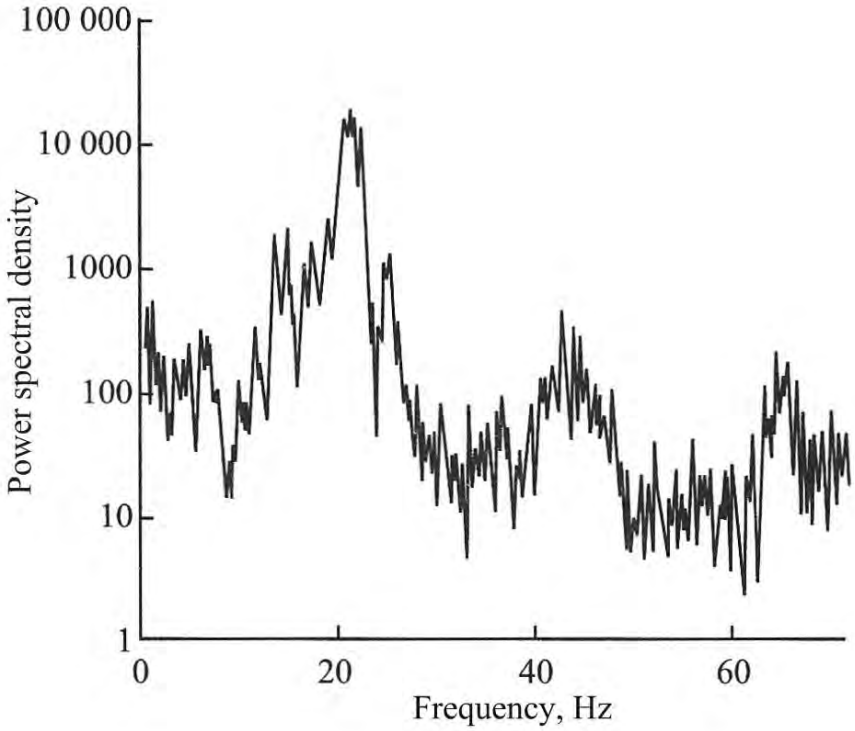

Figure 4.52. Power spectral density of seismic waves produced by a large explosion conducted at Lebedinskii Quarry on October 3, 1996.

4.9. Effect of seismic waves on buildings and other man-made structures

Characteristics of seismic waves produced by explosions need to be considered in order to evaluate seismic safety and potential damage. In particular seismic phases responsible for structural damage need to be considered. Buildings and structures respond to seismic waves as oscillation systems with characteristic frequencies.

The characteristic period of oscillations for one-storey buildings varies between 0.05 – 0.2 s, depending on the building materials; for three – five story building the periods are 0.2 – 0.5 s; for buildings higher than five stories, 0.4 – 1 s. Therefore the building response to ground motions significantly depends on wave period, resonance period of the building, and the total duration of the wavetrain. During the early days of explosive operations, blasts were conducted using smaller charges at shallow depths. For these explosions the duration of oscillation was not long and consisted of a few cycles of body waves and two or three cycles of surface waves.

In these circumstances the seismic motions most damaging to buildings are surface waves, because of their frequency content and slow decay with distance (so that they affect a wide area). Geological structure does not significantly affect surface wave amplitudes, though the period of surface waves strongly depends on the geology and is almost independent of yield. The most

robust criterion of seismic safety was therefore based upon consideration of a critical velocity of oscillations, taken to be 10 cm/s. An increase in explosive yield increases the duration of oscillations. In addition the periods of oscillations increase and can approach the natural periods of oscillations for the buildings. Thus in the near-source zone the dominant period of oscillations for P-waves is 0.15 – 0.45 s, while in the far field at distances 80 – 300 km the dominant periods for Moho-refracted body waves ranges between 0.2 and 0.5 s. The total duration of oscillations in this zone is 4 – 5 s.

As a result, structural damage can be sustained even from waves whose parameters were such that they were previously considered to be safe. An increase in the radius of the damage zone can be seen particularly clearly for nuclear explosions with yields exceeding 10 – 20 kt. For these explosions the zone of seismic damage extends to distances of 100 – 200 km and spans territories with different geological structure. For an increase in the area subjected to seismic waves, the number of buildings and other structures of different types with variable strength characteristics, also increases. This leads to lowering the ground velocity threshold that can cause structural damage in cases where the natural frequencies of the structure coincide with dominant frequencies of seismic waves.

The empirical method based on a critical value of particle velocity is effective for prediction of seismic effect on structures, but the geological structure and specific characteristics of structures should be taken into account. This is important because for large scale explosions the short-period body waves (0.1 – 1 s) are the most damaging at different distances from the explosions. Ground motion due to surface waves is less dangerous, because the oscillation periods are several times larger than the natural frequencies of the structures, and the ground velocity produced by surface waves is lower than for the body waves.

Table 4.18. Values of critical horizontal velocity (in cm/s) producing different degrees of damage (50% and 5%) to buildings.

Structure	50% damage		5% damage	
	Light	Moderate	Light	Moderate
Multistory brick buildings	2 – 5	5 – 10	0.3 – 0.6	0.6 – 1.2
Multistory panel buildings	-	-	0.5 – 1.0	1 – 2
Single story brick buildings	4 – 8	8 – 16	0.5 – 1.0	1 – 2
Single story wooden buildings	10 – 20	20 – 30	2 – 4	4 – 8
Clay buildings	4 – 8	8 – 16	0.5 – 1	1 – 2
Brick chimneys and wood stoves	2 – 5	5 – 10	1 – 2	2 – 4

Empirically determined values of critical horizontal velocity that can cause specific types of damage are shown in Table 4.18. Two damage "levels" are presented: the first level corresponds to damage of 50% of structures registered in the near-source and intermediate zones, and the second level corresponds to damage of approximately 5% of all buildings registered in the far field zone. To describe intensity of damage to buildings and structures the following classification has been used (Kostyuchenko et al, 1974):

- Light damage: peeled paint, thin fractures in the plaster, along the joints between concrete panels, fractures to brick chimneys.
- Moderate to significant damage: massive fractures in masonry walls and chimneys, fallen parts of plaster, fractures between concrete panels, structural damage to beams, damage to door and window frames, numerous broken windows.
- Severe: massive damage to plaster walls, deep fractures in masonry walls and chimneys, chimney collapse, structural damage to buildings, all windows are broken.

According to Table 4.18:

1. The increase in duration of oscillations results in the decrease of the critical velocity that can produce structural damage.
2. Estimates of potential seismic wave damage should take into account the possibility of light damage from very low ground velocities, up to 0.5 – 1 cm/s.
3. Reduction of the amount of damaged structures and buildings from 50% to 5% requires approximately an order of magnitude reduction in ground velocity.
4. The value of the critical velocity depends significantly on the building type.

Ground velocities over 20 – 30 cm/s may cause severe damage to the buildings.

Table 4.19 shows the effects of seismic waves from explosions on concrete panel apartment buildings as a function of horizontal velocity and epicentral distance.

In order to use the results from Tables 4.18 and 4.19 to estimate seismically safe distances we need to use the empirical relationships between ground velocities and epicentral distances. In addition the following factors need to be taken into account: rock type at the source of the explosion, seismic velocities along the ray path, and the rock type and seismic velocity at the site of the building. Thus, for a 1 kt explosion in hard rock, seismic effects can be observed up to 10 km radius, while moderate structure damage can be seen up to 3.5 km. For 100 kt explosions these distances increase to 100 – 200 km and 20 – 30 km respectively.

The damage data presented in Table 4.18 and 4.19 are similar to the description of damage caused by natural earthquakes. The seismic effects of earthquakes are typically quantified using an intensity scale. The intensity levels are determined using people's testimonials/descriptions/observations, movement of household objects, building damage, ground fracturing, landslides, etc. According to the MSK intensity scale, the damage described in Tables 4.18 and 4.19 corresponds to intensity ranging between 5 and 9. Aptikaev (1999) developed relationships between the intensity parameter J and the major parameters of seismic oscillations: maximum acceleration A, velocity v, and displacement S (Table 4.20).

Table 4.19. Effect of seismic waves on concrete panel buildings.

Damage intensity	Ground velocity v_x, cm/s	Radius of the damage zone, m/kt$^{1/3}$	
		In hard rock	In soft sediments
No significant damage	< 1.5–3	> 2000÷3000	> 1000÷1500
Small fracture to plaster and paint, some broken glass	3 – 6	2000 – 1500	1000 – 750
Damage to plaster, fractures in the ceiling and along seams	6 – 12	1500 – 1000	750 – 500
Fractures to masonry structures	12 – 25	1000 – 500	500 – 250
Large fractures in the walls and ceilings, significant damage to masonry structures	25 – 50	500 – 300	250 – 150
Partial or total structural damage	50 – 100	< 300÷500	< 150÷250

Table 4.20. Relations between the intensity parameter (2 – 9) and seismic amplitudes*

Parameter	2	3	4	5
A, cm/s^2	0.7 – 1.7 (1.1)	1.7 – 4.3 (2.8)	4.3 – 11 (7.0)	11 – 27 (18)
v, cm/s	0.029 – 0.086 (0.05)	0.086 – 0.25 (0.15)	0.25 – 0.75 (0.44)	0.75 – 2.2 (1.3)
S, cm	0.0006 – 0.003 (0.0013)	0.003 – 0.014 (0.006)	0.014 – 0.065 (0.03)	0.065 – 0.31 (0.14)

Parameter	6	7	8	9
A, cm/s^2	27 – 70 (44)	70 – 180 (110)	180 – 440 (280)	440 – 1090 (690)
v, cm/s	2.2 – 6.5 (3.8)	6.5 – 19 (11)	19 – 57 (33)	57 – 170 (98)
S, cm	0.31 – 1.5 (0.68)	1.5 – 7.1 (3.3)	7.1 – 34 (16)	34 – 164 (75)

* The median values of parameters are shown in brackets

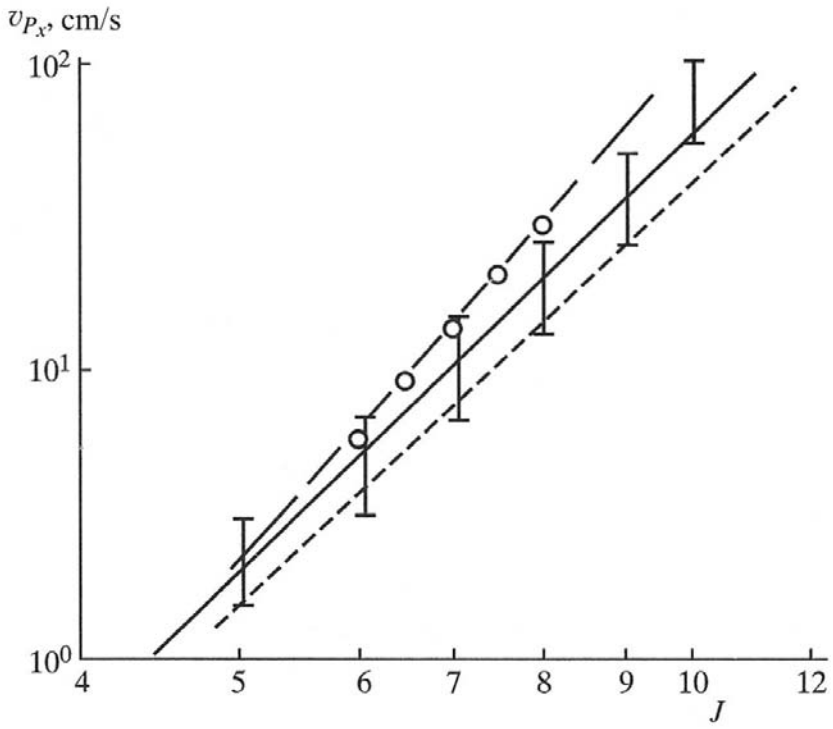

Figure 4.53. Relationships between horizontal velocity of the seismic wave and intensity.

Figure 4.53 shows relationships between the horizontal velocity and intensity (solid line) which corresponds to an empirical formula (based on work by Medvedev and Shebalin, 1969), namely

$$v_x = 6 \cdot 10^{-4} J^5 \text{ (cm/s)}. \quad (4.36)$$

The top dashed line is based on results by Aptikaev (1999), the lower line is after Medvedev and Shebalin (1969). Substituting expressions for velocity as a function of distance and yield (Figure 4.6) into Equation 4.36 we can estimate the size of zones with different intensity as a function of yield:

$$R = 2.8 \cdot 10^2 \, q^{0.33} J^{2.85} \text{ (km) for } q \sim 1 - 10 \text{ kt}. \quad (4.37)$$

$$R = 8.5 \cdot 10^2 \, q^{0.47} J^{3.35} \text{ (km) for } q \geq 10^2 \text{ kt}.$$

Dimensions of the zones of different intensity as a function of intensity parameter J is shown in Figure 4.54 for different yields ranging between a kiloton and a megaton. For this yield range the zones of the same intensity vary in size by two orders of magnitude. For explosions with yield $q = 10^2$ to 10^3 kt the size of the zone with shaking intensity $J = 5$ corresponds to distances of 70 – 100 km; the zone with intensity $J = 10$ extends to 7 – 10 km.

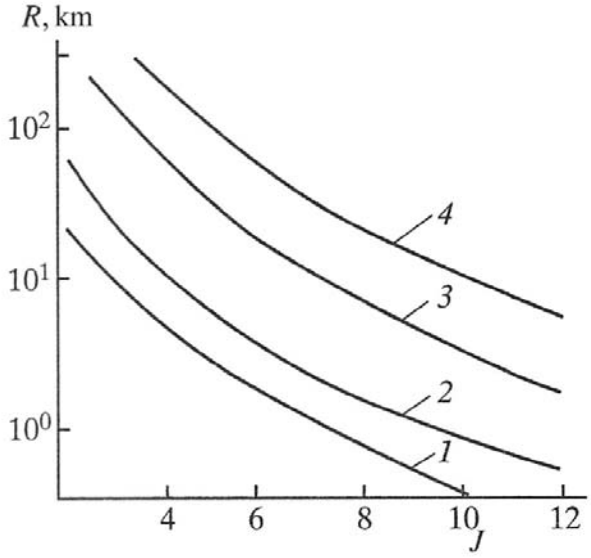

Figure 4.54. Sizes of different intensity zones for explosions with yield q: 1 – 1 kt; 2 – 10 kt; 3 – 10^2 kt; 4 – 10^5 kt.

The quantitative methods of seismic risk estimation for large explosions presented here don't describe the full picture of damage to different types of structures. Strength of materials also plays significant role (even for structures of the same type). These differences between different buildings may be random causing seemingly similar structures to have different degree of resistance to seismic waves. Because of this a statistical description of damage distribution is being developed. Within this framework the number of structures and degree of damage can be estimated/predicted in each particular case (e.g. Sadovskii and Kostyuchenko, 1974; Kostyuchenko, 1985).

According to this approach a distribution of relative number of damaged structures $n = N/N_0$ can be developed, where N_0 is the total number of structures, and N is the number of structures that are damaged due to a specific value of maximum ground velocity. The value of n is governed by a log-normal distribution:

$$n = 2\pi \int_0^t \exp\left(-\frac{t^2}{2}\right) dt\,; \qquad t = b\,log\,(v/v_0). \tag{4.38}$$

The coefficient b determines the distribution width, while v_0 is some characteristic value of ground velocity, which causes damage to 50% of the buildings.

The values of parameters b and v_0 are determined for each type of structure by analyzing previous damage observations. Figure 4.55 shows the analysis of data related to damage from nuclear explosions conducted as a part of the Peaceful Nuclear Explosion program for some common building types (Nuclear, 1997 – 2000). Solid lines in Figure 4.55 show theoretical results calculated using Equation 4.38. The following parameters required for Equation 4.38 were used: For light damage the average velocity was taken as v_0 = 9 cm/s, for moderate damage this parameter was v_0 = 18 cm/s, and for severe damage it was v_0 = 36 cm/s according to Table 4.19. Different symbols show explosions with different yield between 2 and 20 kt, detonated in

salt and in oil and gas deposits. Horizontal error bars for some experimental points correspond to scatter in measured maximum velocities.

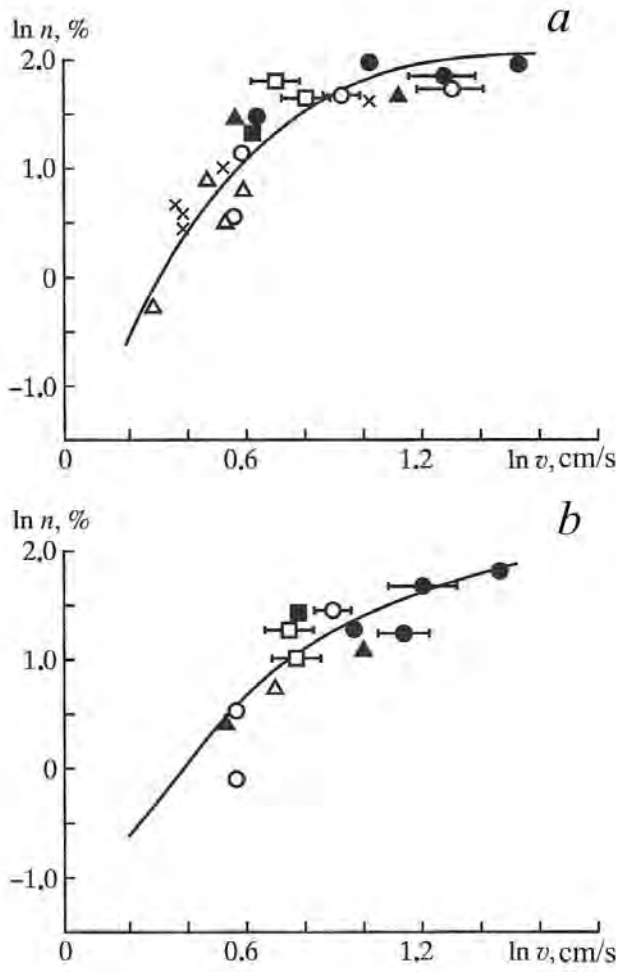

Figure 4.55. Percentage of single-story brick and panel buildings with a) light and b) moderate damage as a function of maximum ground velocity (according to V.N. Kostyuchenko).

For comparison, the crosses in Figure 4.55 show data points obtained for explosion RULISON (USA, q = 40 kt), which in general agree with the estimate using Equation 4.38.

The statistical approach to evaluation of building and structure damage due to seismic waves, helps to describe the problem of seismic risk within a single framework for both explosion operations and for strong earthquakes. The relationship between the relative number of damaged structures and maximum velocity, $n = n(v)$, according to Equation 4.38 is equivalent to a probability of damage (to certain types of structures). Using this relationship one can estimate the probability of different severity of damage for this type of structure using a selected value of ground velocity v_0.

An example of this estimate is shown in Figure 4.56. The probability of different degrees of damage (from light to severe) as a function of maximum ground velocity are shown for two and three story brick buildings. According to the plot the velocity amplitude

corresponding to 50% of moderate damage to structures is close to 10 cm/s, which agrees with earlier estimates by Sadovskii. This result is an important argument supporting the validity of statistical seismic risk analysis.

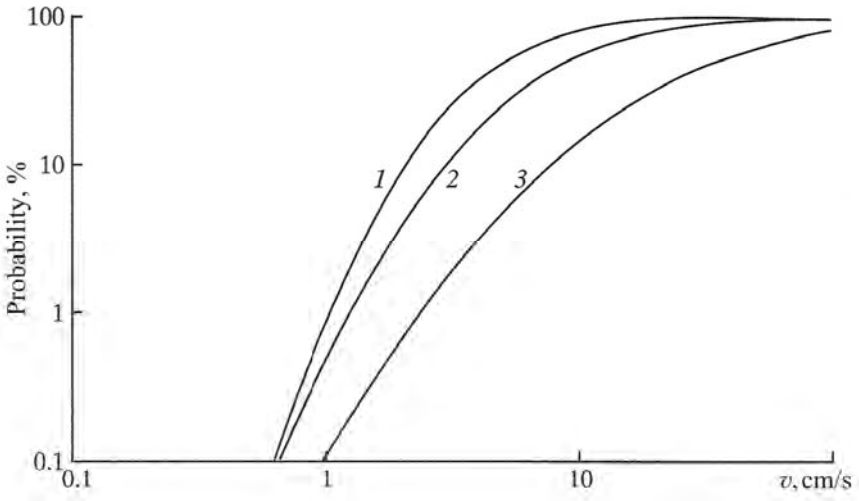

Figure 4.56. Probability of damage to two and three story brick buildings. The numbered lines show the degree of damage: *1* – light, *2* – moderate, and *3* – severe.

Chapter 5

Effects of an underground nuclear explosion on transport properties of the medium and on the hydrological regime

5.1. Changes to structure and transport properties of a rock massif due to rock damage

Quantifying the degree of rock damage is an important problem that needs to be solved while studying the effects of underground explosions on rock massifs. We briefly discuss structural features of the damage zones.

Any rock massif (including those in their undamaged original state) can be represented by a system of blocks, characterized by at least two parameters: fracture density λ and the average fracture opening $\langle\varepsilon\rangle$. To the engineer, fracture represents a space between block walls inside the rock massif.

The fracture content of a rock massif is the mix of all component fractures in the massif. Since fracturing is an inherent property of rock massifs, and because it determines the mechanical response of the rock massif, it should be studied on a case-by-case basis by accounting for a specific structure and its history of formation.

The total set of the fractures in a rock massif can be divided into systems of approximately parallel groups of fractures. The intersection between different groups of fractures results in a natural fragmentation of the rock massif. The average spacing between fractures determines the average fragment size.

There are several methods to determine specific [average?] fracture content of the rock massif. Planimetric measurements involve determining the number of fractures crossing a specific surface of a certain size [check]. If such direct measurements are difficult then the number of fractures can be estimated by visual analysis through a screen having measuring grid.. Photoplanimetric methods involve measuring fractures from imagery.

The major difficulty in application of these methods is separation of the visible fractures into natural and man-made. Man-made fractures include those made locally (for instance created during tunnel digging), and regionally (e.g., created by an underground explosion). The existing techniques are imperfect.

An acoustic method to determine relative fracture content involves comparison between the longitudinal velocities in the rock massif and in the rock fragment. The ratio of the squared velocities between the massif and the sample is called an *acoustic fracture index* [check]. Fractured rock massifs can be characterized by the values of their fracture indices.

In addition to methods of determining fracture density, there are methods to determine average fracture aperture $\langle\varepsilon\rangle$. Some of these methods involve direct measurements of the parameter $\langle\varepsilon\rangle$, while others determine some relative characteristics based on the measurements of rock permeability – the ability of rock to pass gas or fluid. Studies of the fracture surfaces caused

by natural phenomena and anthropogenic activity (for instance due to an explosion) have shown that such surfaces are characterized by waviness [???] and roughness. The changes in fracture aperture are less affected by the waviness than by roughness since the middle line of the fracture follows the wavy profile configuration. Extensive study of rock masses (Ruppeneit, 1975) shows that the average roughness of the fracture and fragment surfaces ranges in the interval $(4 – 6) \cdot 10^{-4}$ m, and the distribution of the deviation of the surface from the average is close to normal.

A fracture is represented by a cavity with walls that touch in some points (contact points). Intersection of different sets of parallel fracture systems results in formation of connected fracture networks (voids) within the rock massif. Together with the porosity of the rock matrix these fractures determine the porosity of the rock massif as a whole. The porosity of the massif is defined as $m=V_v/V$, where V_v is the total volume of void in a given volume V.

We note that the parameter m can characterize any medium regardless of the nature of the voids: fractures or pores. In this sense a medium with high fracture content can be considered porous, with separate structural blocks playing the role of grains, and fractures representing pores. We note however that porous rocks always show hydraulic permeability due to the presence of connected fractures. The permeability of porous rocks does not always increase with increased porosity: some rocks including tuffs and limestones may have “closed” pores resulting in low permeability.

We noted earlier the word “filtration” used to represent the ability of fluid to move through a solid medium with connected voids. The problem of fluid movement through porous medium was first described in the mid-19th century. At that time the relationship between the so-called hydraulic head, Δh, (that is, the difference in levels at different locations for a fluid moving through a porous medium) and the velocity of filtration v_f (amount of fluid moving through a unit of area in a unit time) was determined experimentally to be

$$v_f = \frac{i_f \Delta h}{\Delta l_f}, \tag{5.1}$$

where i_f is a filtration coefficient characterizing the medium on an interval with length of Δl_f for a specific fluid.

The latter equation (5.1) represents a linear relationship between the scalar speed of filtration and a spatial derivative of the hydraulic head. The underlying concept has widely used to solve numerous problems related to movement of different fluids and gases. Equation (5.1) has since been developed in a more universal vector form as

$$v_f = -\frac{k_1}{\mu} grad\, P, \tag{5.2}$$

where μ is the dynamic viscosity of the fluid, P is the fluid pressure and k_1 is a medium permeability coefficient independent of the properties of the filtering fluid.

Further analysis of fluid motion in rock pores has shown that the total pressure gradient in the fluid is influenced by hydraulic resistance and is obtained by adding the inertial and frictional losses:

$$grad\ P = -\frac{\mu}{k_1} v_f - \frac{\rho v_f}{k_2} \left|\overrightarrow{v_f}\right| sgn(\overrightarrow{v_f}), \tag{5.3}$$

where ρ is the density of the working fluid, and k_2 is a second permeability coefficient, which has dimensions of length (meter). The parameter k_2 has sometimes been called the turbulent permeability of the medium.

At present the filtration law in the form (5.3) is considered the best description of movement of fluid and gas through a permeable medium.

The first attempt to relate the parameters characterizing permeability with a medium's structural characteristics was made by Charles Slichter (1898). He considered fluid filtration through a simplified porous medium composed of spherical particles. According to Slichter the permeability coefficient is determined by the diameter of the spheres d_s, the porosity m, and the measure of the cross-sectional area of the pore K_s as follows:

$$k_1 = \frac{K_s d_s^2}{96(1-m)}. \tag{5.4}$$

Later other models of the geological media were considered, of which the following three are the most notable:

The capillary model describes the permeable medium as a series of parallel capillaries with a constant diameter a_c. For this medium the permeability is given by

$$k_1 = \frac{\pi N_c a_c^2}{128}, \tag{5.5}$$

where N_c is the density of the capillaries across the plane perpendicular to the fluid flow.

The Parallel fracture model describes the fractured medium as a massif divided into impermeable blocks with three sets of mutually perpendicular systems of planar parallel fractures having similar apertures $\langle\varepsilon\rangle$. For this medium the permeability is given by

$$k_1 = \frac{m\langle\varepsilon\rangle}{12} = \frac{\lambda\langle\varepsilon^2\rangle}{4}, \tag{5.6}$$

where λ is the specific fracture density.

The serial capillary model describes fluid movement through the porous medium represented as a capillary model in which every fluid particle passes through the entire pore space. For this model,

$$k_1 = \frac{m a_c^2}{96 T_c^2}, \tag{5.7}$$

where T_c is the tortuosity of the permeable channels in the medium.

We note that the parallel fracture model is the most appropriate for description of realistic fractured rocks. This model has been widely used to describe the parameters of fluid movement through rock massifs.

We note that rock permeability can be used as a characteristic of rock damage, because any mechanical deformation causes increase in size of existing fractures as well as formation of new fractures. In both cases the porosity of the rock massif increases. Then, according to any of the equations (5.5) – (5.7) the greater permeability coefficient would correspond to a greater degree of damage.

5.2 Methods of determining the transport properties of a damaged rock massif

Numerous methods and devices have been developed for determining the filtration properties of the subsurface using measurements based on different physical methods. However none of them permit measurements using small diameter boreholes and accurate determination of the second permeability coefficient k_2. We shall show that this parameter is an important characteristic of filtration properties of damaged rock massifs. For such a study we developed a special methodology and a device to perform *in situ* measurements within a rock massif (Spivak and Svintsov, 1982).

Using air as a working fluid in this method eliminates mechanical and chemical interactions of the fluid with rock. We note that formation of a fluid boundary layer precludes accurate determination of permeability as a characteristic of the rock itself. In addition using air allows for more cost effective and less labor-intensive measurements, making our method more efficient for use in the mining industry.

The measurements rely on a packer, that is, a device providing hydraulic isolation of part of a borehole, drilled either from a tunnel or from a rock outcrop. Air at pressure P_1 is pumped into this isolated (working) interval of an uncased borehole. The rate of flow G is measured after steady state flow conditions have been established, determined by reaching a constant air output. The measurements are conducted for several different values of the differential pressure $\Delta P = P_1 - P_0$, where P_0 is the atmospheric pressure.

Pressure measurements are also conducted at the same time at the top of the borehole (by sealing the borehole at the top) in order to control the quality of the hydraulic seal.

Both permeability coefficients of the fractured rocks, k_1 and k_2, are determined by analyzing of the flow rate G as a function of ΔP.

The method is implemented as follows. A sealing device is placed into a prepared borehole (two of them, if the given interval is otherwise not isolated). The device schematic is shown in Figure 5.1. The main element of the packer is a threaded connection, which consists of a locked (3) and movable (8) parts. The device is operated from the side facing the top of the borehole using a special key (10) or a pipe (duct) (11). The key has a notch to fit the stud (9) of the movable part (8). The key is assembled from 2-meter long metal rods with diameter of 20 mm. A

special non-threaded connection between the rods (Figure 5.2) provides the integrity of the connections during both screwing and unscrewing of the threaded element of the device.

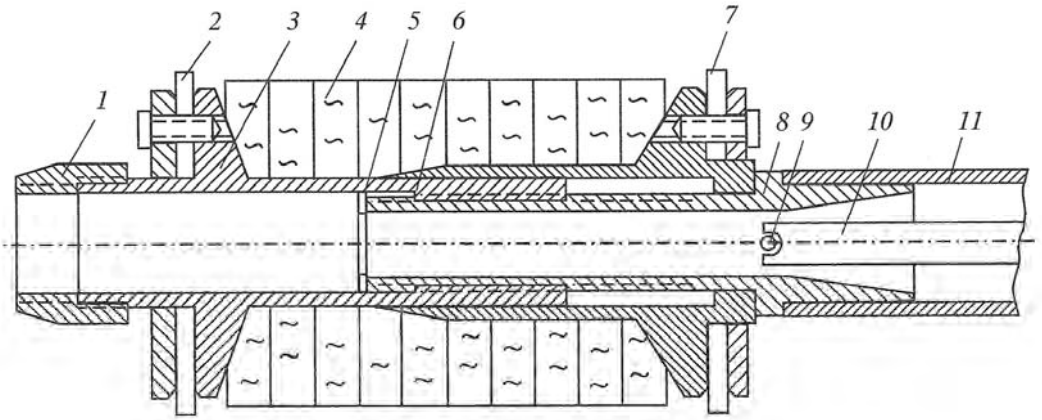

Figure 5.1: Schematics of the packer: *1* – nozzle extender; *2* and *7* – rubber washer (seal); *3* and *8* – locked and movable parts of the threaded connection; *4* – micro-porous rubber; *5* – lock washer; *6* – protruding part of the locked part; 9 – stud for the key; 10 – key; 11 pipe (duct).

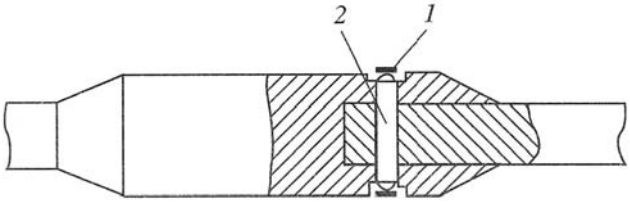

Figure 5.2. Non-threaded connection: *1* – stud; *2* ring spring (lock washer)

During twisting in of the threaded connector, its locked part and the device as a whole is kept from turning by using seals (2 and 7). The seals are cut out of heavy-duty rubber with thickness of 6 – 8 mm and a diameter exceeding the diameter of the borehole. These seals are added to increase coupling between the lock washers.

The space between the rubber seals is filled with micro-porous rubber (4, set of rings with thickness of 10 – 20 mm). Compression of the porous rubber using the threaded mechanism (connection) causes its expansion in the perpendicular direction to achieve the sealing effect. After measurements are completed, the threaded connection is twisted off and the packer is released.

To prevent complete untwisting of the threaded connection in its movable part a stop washer (5) is used, which is seated against the protruding part (6) of the locked part of the mechanism (3). The length of the working part of the packer should be at least three-four times longer than the diameter of the borehole.

The duct (11) (Figure 5.1) is made of either thick polyethylene pipe (in which case its construction doesn’t require any additional explanations), or pieces of duralumin pipe joined together taking into consideration the sealing and the rigidity of the connection (Figure 5.3).

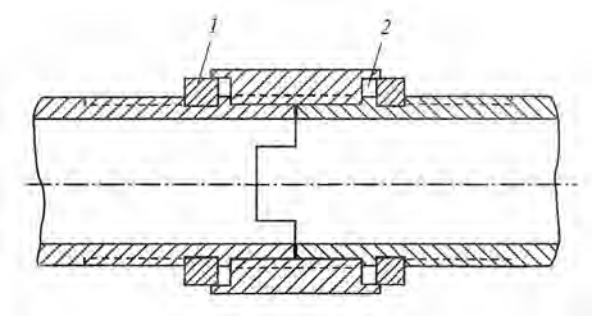

Figure 5.3: Duct joint (connector): 1 – lock washer; 2 rubber seal.

To determine permeability of rocks along the borehole (this need may arise when working in a very deep borehole or in a rock massif with a strong permeability gradient) two packers limiting the working interval of the borehole can be used as mentioned above. The packers are connected using a perforated duralumin pipe through a nozzle (1) (Figure 5.1). In this case the threaded connection of the packer more remote from the borehole entrance is operated using the key, while the threaded connector for the other packer is operated using the duct [pipe]. The difference in the additional packer located close to the entrance to the borehole is the absence of the stud used for the key (9) (Figure 5.1), and it is attached to the duct as shown in Figure 5.3. For measurements in small holes with diameter of 42 – 56 mm a simplified packer without the threaded connection can be used (Figure 5.4). In this case the porous rubber (2) is compressed before placement into the borehole using a movable washer (3) until the needed radial diameter is reached.

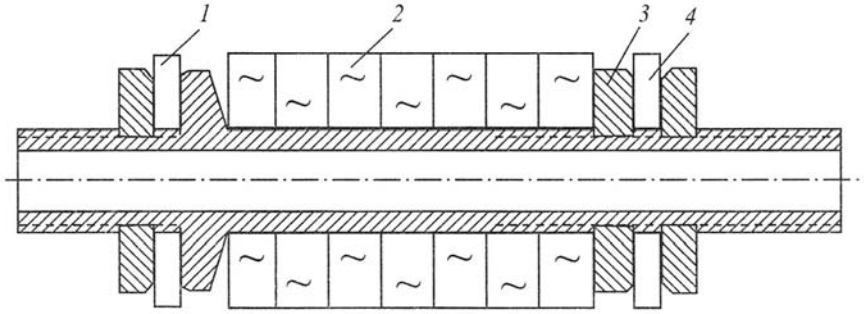

Figure 5.4: Packer for small holes: *1, 4* – rubber seals; *2* – micro-porous rubber, *3* – lock washer.

With the system shown in Figure 5.5, measurements are conducted in the following order. After sealing the working interval from the top of the borehole, air is pumped through the hose through the control valve (9), the expansion volume (8) and the flow meter (7). Air pressure P_2 at the exit from the flow meter (at the borehole entrance) is measured using a calibration control manometer (5). A U-shaped manometer (6), attached with a connector pipe to a plug (4), measures a possible rise of pressure in the borehole. In most cases the measurements show the absence of any pressure difference on both sides of the plug (4). The pressure increase in the borehole is insignificant (~10^2 Pa) during work in strongly fractured rock (significantly smaller than P_1 even for extended pumping of the working volume), which is naturally explained in this

case by air filtration through the rock massif. Air input and the output needed for maintaining a specific pressure P_1 in the borehole volume, is performed using a flow controller (9).

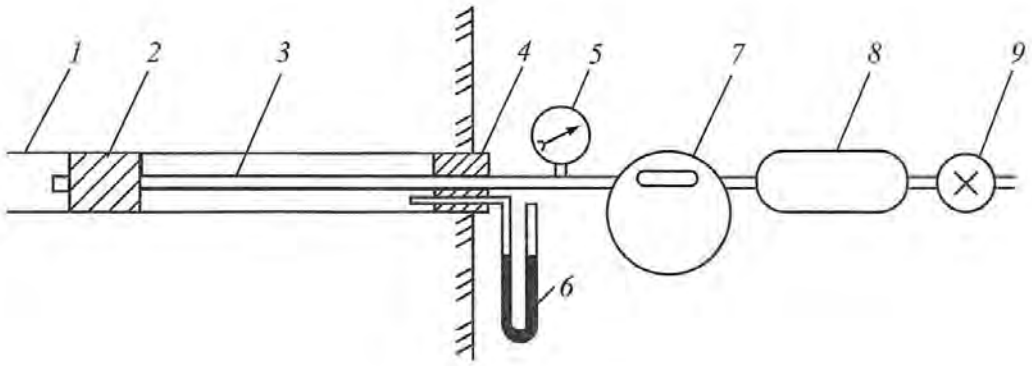

Figure 5.5: Recording system for in situ permeability measurements: *1* – working volume of the borehole; *2* – packer; *3* – pipe (duct); *4* – plug; *5, 6* – manometers; *7* – flow meter; *8* – expansion volume; *9* – flow control valve.

The volumetric air flow rate *G* is measured using gas flow meters (for example serial number RG-40 and RG-100), which operate in the range satisfying the parameters of the experiment.

The value of G significantly depends on the length of the isolated working volume of the borehole L_i. The choice of the value of L_i is determined by the fracture content of the rock: the length of the volume should exceed the size of fragments – the intervals between the fractures --- by at least a factor of 5 – 10. In this case the fracture permeability considerably exceeds the permeability of the rock matrix. To determine a minimal value of L_i a series of measurements can be conducted with increasing values. The value of L_i for which the measured parameters k_1 and k_2 remain constant with further increase in L_i, is determined acceptable. The results of numerous applications of this method show that for study of rock formations with natural fractures the length of the working interval should be at least 3 – 6 m. For studies in rocks damaged by a large explosion the length L_i can be reduced to 1 m. The method can then be used in small holes with depth up to 3 -- 5 m).

The pressure in the tunnel P_0 (atmospheric pressure) required for data processing is measured using an aneroid barometer.

Experimental data analysis is performed using the two terms of equation 5.3. To obtain a relationship for calculation of the permeability values k_1 and k_2 using gas volumes, we consider a problem of gas flow in elliptical coordinates. For simplification we replace the elongated cylindrical volume with diameter a_0 and finite length l (for $l \gg a_0$) with an ellipsoid of revolution with a length between the foci of *l* so that

$$\frac{x^2+y^2}{a^2}+\frac{z^2}{b^2}=1\,,$$

where a and b are semi-minor and semi-major axes respectively. For a strongly elongated ellipsoid,

$$b \cong l/2,\ a \cong \alpha a_0/2,$$

where $\alpha \cong 1.2$ is a correction coefficient obtained from the equality between the surface area of the ellipsoid with $b=l/2$ and the area of the side surface of the cylinder of the working volume of the tested borehole.

In elliptical coordinates the surface with q=const represents the surface of a constant pressure if the relationship $q=q(x, y, z)$ is written in a form:

$$\frac{x^2+y^2}{(l^2/4)sinh^2 q} + \frac{z^2}{(l^2/4)cosh^2 q} = 1\ ,$$

where $l\ sinh\ q$ and $l\ cosh\ q$ are semi-minor and semi-major axes of an ellipsoid with the same foci as the ellipsoid that represents the borehole filtration. Using the expressions for the axis of the ellipsoid trough which the flow of gas/fluid occurs we write the expression for its surface area as follows:

$$S = \frac{\pi l^2}{2} \dots .$$

Assuming that the gas flow is close to cylindrically symmetrical and using grad P = (dP/dq) grad q we obtain:

$$grad\ P \approx \frac{2}{l}\frac{dP}{dq}.$$

For the fluid (air in this case) we introduce the velocity u_1 averaged over the surface S so that $u_1 = G/\rho S$, where G is the mass volume of air passed through the surface, which in case of stationary flow is independent on parameter q. Assuming that the flow process is isothermic (then $P_0\rho_1 = P_1\rho_0$) we integrate equation (5.3) using expressions for S and grad P over the limits

$$\frac{\alpha a_0}{l} \le q \le \infty.$$

The relationship obtained as a result of integration can be used to determine the parameters k_1 and k_2:

$$\frac{P_1^2-P_0^2}{P_1 Q} = \frac{4\mu \ln(\pi l/2\alpha a)}{\pi^2 l k_1} + \frac{16\rho_1 P_1 Q}{\pi^2 l^3 P_0 k_2}\left[\frac{l}{a} - \frac{4}{\pi}\ln\left(\frac{\pi l}{2\alpha a}\right)\right] = A + (P_1 Q)\ B, \qquad (5.8)$$

where $Q=G/P_1$ is a volume of air that is measured experimentally and is the quantity needed for determining k_1 and k_2.

Indeed, the left hand side of Equation 5.8 ($(P_1^2 - P_0^2)/P_1 Q$) is a linear function of the quantity $P_1 Q$, therefore the experimental data points plot along a straight line. If the relationship

$Q = Q(P_1)$ is determined from experiments, the parameters k_1 and k_2 can be easily found from the linear relationship.

It follows from equation 5.8 that in order to find the values of k_1 and k_2 it is necessary to know the pressure in the working volume of the borehole P_1. The measurement of P_1 is technically complicated; however it is sufficient to measure the air pressure at the top of the borehole, P_2. In this case the value of P_1 needed for the computations can be easily obtained using a relationship between P_1 and P_2 in the form:

$$P_1 = P_2 - \Psi \frac{L}{d} \frac{\rho U^2}{2},$$

where $\Psi = \Psi(Re)$ is a resistance coefficient (Re is the Reynolds number), d is the diameter of the duct (for gas input), L is the distance between the top of the borehole and the working volume, ρ and U are the density and the velocity of the air through the duct respectively. The following relationship applies:

$$U = \frac{4G}{\pi d^2}.$$

The volume of air pumped through the working part of the borehole is measured during the experiment. The length of the working part of the borehole can be changed. In cases where the permeability changes along the borehole the measurements for each interval are determined assuming a linear superposition of the volume flow for each interval. If more accurate measurements are needed or if the borehole is intersected by a tectonic fault with permeability several times more than the permeability of other intervals, a similar device consisting of two packers can be used. In this case rock permeabilities are determined for each borehole interval using the described method.

5.3 Changes in hydraulic permeability of rocks and rock massifs as a result of an explosion

Rock damage near explosive sources significantly increases the permeability of the medium. Practical interest in studying the permeability of rocks (other than mining) has been driven by the possibility of using high yield explosions for oil and gas extraction, as well as by aspects of geothermal and mineral resource exploration. An important parameter is the radius R_p of the zone of increased permeability. The results for some underground explosions (in the USA) are shown in Table 5.1.

This Table shows the radius of increased permeability is approximately 7 times greater than the radius of the cavity, r_c. The radius of increased permeability can be accurately expressed as

$$R_p = B_p\, q^{1/3} \text{ m},$$

where q is the explosion yield, $B_p = 11.5$ for the silicate rocks with density 2.5-2.7 g/cm^3, and $B_p = 9$ for the dolomites and limestones with density about 2.8 g/cm^3. It is worthwhile to note, that

the radius of increased permeability approximately matches the radius of damage. Thus, the radius of the fracturing caused by an explosion, from different sources, is approximately between 5.3 and 10 r_c.

Table 5.1. Radius of the zones of increased permeability for some underground nuclear explosions (UNE)

UNE	Rock type	Yield, kt	R_p, m	R_p/r_c
HARDHAT	Granite	5	145	7.6
HANDCAR	Dolomite	12	128	6.2
SHOAL	Granite	12	182	6.9
PILEDRIVER	"	60	310	7.1

In our work we studied the permeability of a rock massif which was damaged by an industrial nuclear explosion having a yield of 2 kt[1]. The explosion was conducted on September 4, 1972 to assess a technology for extracting mineral deposits by crushing ore bodies (Rodionov et al, 1976a, Spivak, 1980b).

The explosion was conducted in the northeastern part of the Khibiny massif in the mount Kuelporr at a depth of 150 m (the "least resistance" depth or LLR was 121 m). The block to be destroyed was located on the edge of the ore body (apatite-nepheline ores) and was represented by a cube with a side of 50 m. The charge was placed in the middle of the upper horizontal side of the cube (Figure 5.6).

On the opposite side from the charge the block was surrounded by two areal unfilled gaps (also called screens or slots): one was vertical and another was horizontal gap. The gaps were used in order to localize the damage within the block. The rock was completely removed from the vertical gap before the explosion. The horizontal gap had an empty space of 0.5-1.2 m between the broken rock at the bottom and the roof.

Physical and mechanical properties of the apatite ore and the surrounding rocks (urtites) are close the properties of granites. Some physical properties of the rocks are shown in Table 5.2.

A wide range of the rock properties indicates the heterogeneity of the massif. The rock mass is characterized by high fracture density (the most common size of the blocks between the fractures is about 1 m).

The hydrological studies were conducted using the boreholes with diameter of 105 mm, also 56 mm core holes, and small drilled holes with diameter of 42 mm. There were total of 12 boreholes and 20 small holes crossing the horizon at 375 m, 26 small holes crossing the horizon at 355m (tunnel #22), and two core holes through the horizon at 310 m. The schematic view of the tunnels, boreholes through the horizon at 375 m is shown in Figure 5.7.

[1] The reported yield for this explosion (PNE Dnepr) is 2.1 kt (e.g. Mikhailov, 1996)

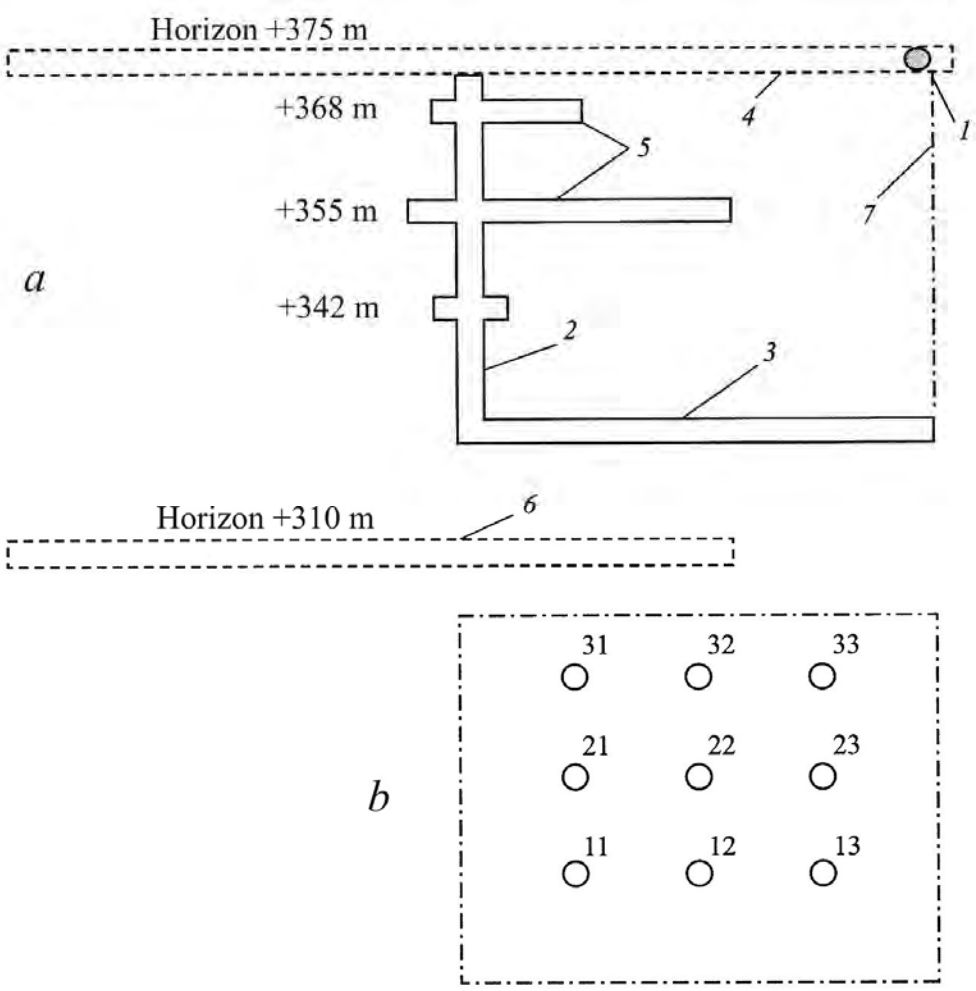

Figure 5.6: Schematic of the rock block subject to fragmentation during 2 kt nuclear explosion conducted on September 4, 1972 in Khibiny Massif: a) *1* – center of the explosion; *2* – vertical screen; *3* – horizontal screen (Russian – "podsechka"); *4* – Tunnel at the horizon at +375 m; *5* –observation tunnels; *6* – auxiliary tunnel for rock removal; *7* – projected boundaries of the fragmented block. b) Schematic location of the observation tunnels (view perpendicular to the vertical screen), numbers show the tunnel numbers.

The presence of an unfilled screen (gap) significantly affects the deformation and damage of the massif caused by an explosion. However, it will be shown in Chapters 6 and 7 that the zone of the influence of the screen is limited.

This section will describe the filtration characteristics of the rock mass without unfilled gaps. Figure 5.8 shows the amount of air Q flowing through the 105 mm boreholes as a function of the pressure change ΔP. The measurements were conducted in the parts of the massif with different degrees of damage.

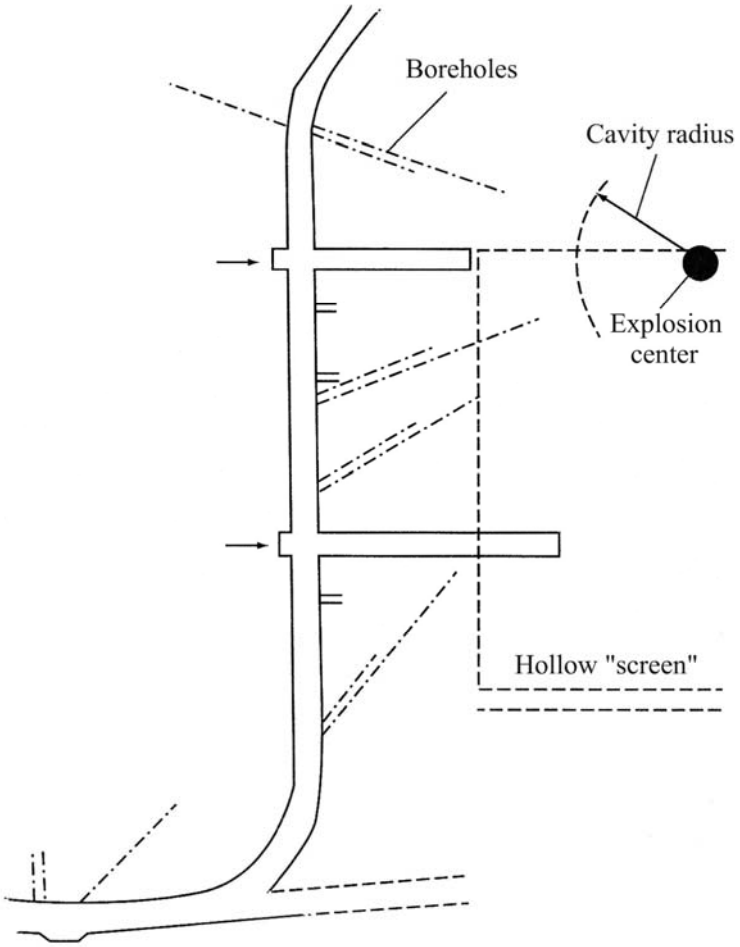

Figure 5.7: Schematic locations of the exploratory tunnels, boreholes (dash-dotted lines) and small holes (solid lines) within the horizon at +375 m.

Table 5.2. Physical properties of rocks (emplacement medium of the PNE in Khibiny – Dnepr 1)

Parameter	Rock type	
	Apatite ore	Rock matrix
Density ρ, kg/m^3	2900 – 3000	2700 – 3000
Porosity m, %	0.12 – 0.2	0.12 – 0.2
Moisture content ω, %	0.5 – 0.9	0.5 – 0.9
Compressive strength σ_*, MPa	70 – 200	100 – 250
Tensile strength σ_t, MPa	3 – 30	8 – 30
Seismic velocity C_p, km/s	5.0 – 5.6	5.0 – 5.6
Poisson coefficient υ	0.21 – 0.37	0.2 – 0.24

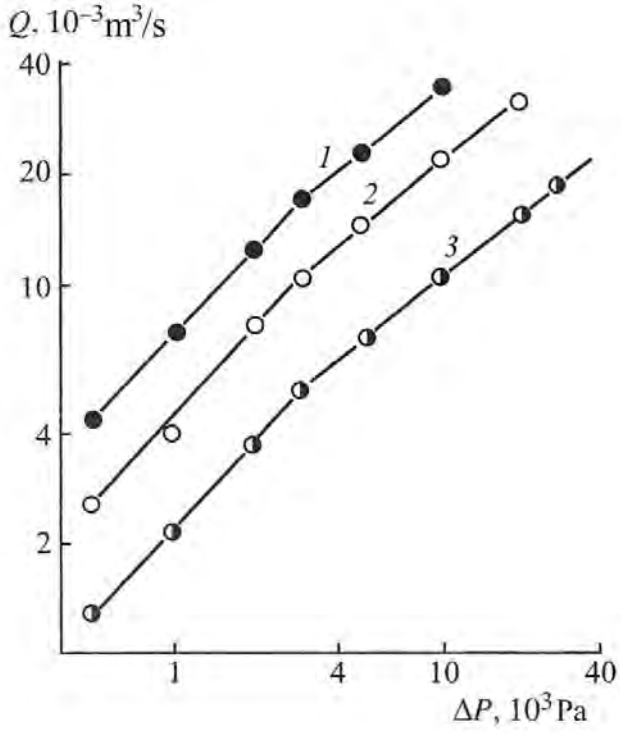

Figure 5.8: Changes in volumetric air flow as a function of the pressure change magnitude in the working volume of a borehole with length l_w ("working length") along the intervals with different degrees of damage: 1 – $k_1 = 1.85 \cdot 10^{-13}$ m, $k_2 = 2 \cdot 10^{-11}$ m [the exponents are definitely messed up in the text] (l_w = 6 m); 2 – $k_1 = 1.15 \cdot 10^{-13}$ m, $k_2 = 1.4 \cdot 10^{-11}$ m (l_w = 6 m); 3 – $k_1 = 2.85 \cdot 10^{-13}$ m, $k_2 = 10^{-11}$ m (l_w = 6 m).

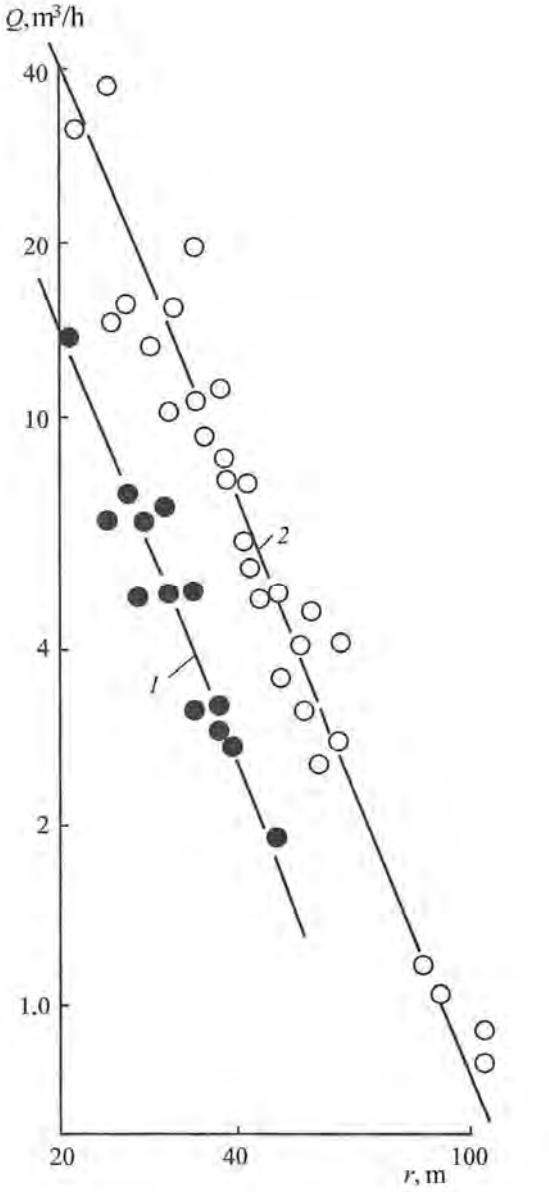

Figure 5.9: Changes in volumetric air flow through a borehole with diameter of 0.105 m as a function of distance to the explosion: 1 – ΔP = 100 kPa [typo in the book], 1 – ΔP = 30 kPa [of the same units as in 1].

The plots show that two regions can be separated based on the degree of change of Q as a function of ΔP: for small pressure changes ($\Delta P \leq 3$ kPa) the relationship Q (ΔP) is close to linear ($Q \sim \Delta P^{0.88}$), with the increase of ΔP the power becomes smaller ($Q \sim \Delta P^{0.55}$ for $\Delta P \geq 3$ kPa). One of the possible explanations for the observed effect is predominately turbulent flow of the air in the particular pore space when the pressure change reaches $\Delta P = \Delta P_* = 3$ kPa. This

feature of the flow curves provides an opportunity to study the gas flow in fractured medium for different flow regimes and allows obtaining information about the structure of the medium itself (fracture density and their aperture).

Study of the working intervals located at different distances r from the explosion allows us to determine the effect of distance r at different pressure changes ΔP (Figure 5.9) on the volume flow of gas per unit of length of the working volume Q_1. In particular, for ΔP = 3 kPa the relationship is given by:

$$Q_1 = 2.5 \cdot 10^{-4}\, r^{-2.5}\ \mathrm{m^3/h}, \tag{5.9}$$

where r is the distance in meters.

To determine the stability of the filtration properties of the rock massif with time the measurements were repeated after 0.5 and 1.5 years. The obtained data were similar to the original data with high degree of accuracy. We note that the data of stability of filtration properties of rocks with time were described in earlier publications. For instance, study of rock properties in the vicinity of the nuclear test HARDHAT (USA, February 15, 1962) has shown that the permeability remained constant one year after the explosion (Boardman, 1970).

The values of the parameters k_1 and k_2 as a function of scaled distance $r/q^{1/3}$ estimated using Equation 5.8 are shown in Figures 5.10 and 5.11. The relationships $k_1(r)$ and $k_2(r)$ in the distance range can be approximated using the formulas:

$$k_1 = 1.45 \cdot 10^{-7}\, r^{-2.5}\ (\mathrm{m^2}), \qquad k_2 = 1.6 \cdot 10^{-3}\, r^{-4}\ (\mathrm{m}),$$

where r is the distance in meters.

Initial permeability of the rock massif is approximated by the following relationships:

$$k_1 = (1.75 – 3.7) \cdot 10^{-13}\ (\mathrm{m^2}),$$

$$k_2 = (1.1 – 2.3) \cdot 10^{-11}\ (\mathrm{m}).$$

Figure 5.10 also shows [permeability] measurements for the underground nuclear tests HARDHAT (Boardman et al., 1964) and HOGGAR (Duncan et al., 1972) conducted in low-porosity granites. In these experiments the initial permeability values were: $k_1 = 4 \cdot 10^{-17}\ \mathrm{m^2}$ for HARDHAT and $k_1 = 2.7 \cdot 10^{-15}\ \mathrm{m^2}$ for HOGGAR. The important characteristic of permeable rock k_2 was not determined for HARDHAT and HOGGAR.

The results shown in Figures 5.10 and 5.11 demonstrate significant increase in rock permeability after underground explosions. The permeability of the damaged rocks decreases with distance from the explosion, which corresponds to decrease in intensity of the explosive damage with distance.

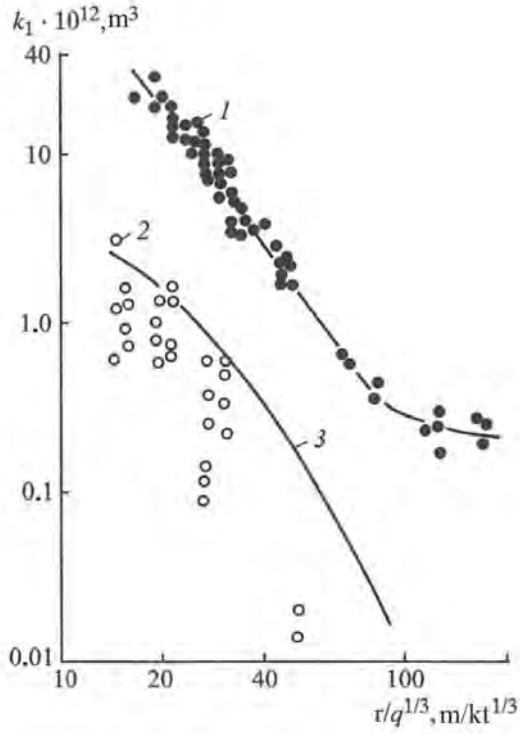

Figure 5.10: First permeability coefficient (k_1) in the damage zone created by underground nuclear explosions: *1* – 2 kt explosion (Dnepr 1), *2* and *3* – HARDHAT and HOGGAR respectively.

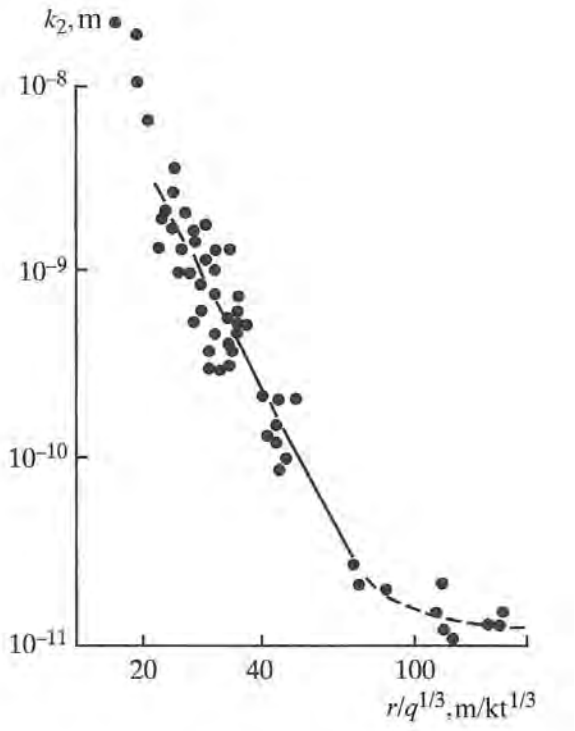

Figure 5.11: Second permeability coefficient (k_2) in the damage zone created by the 2 kt underground nuclear explosion (Dnepr1).

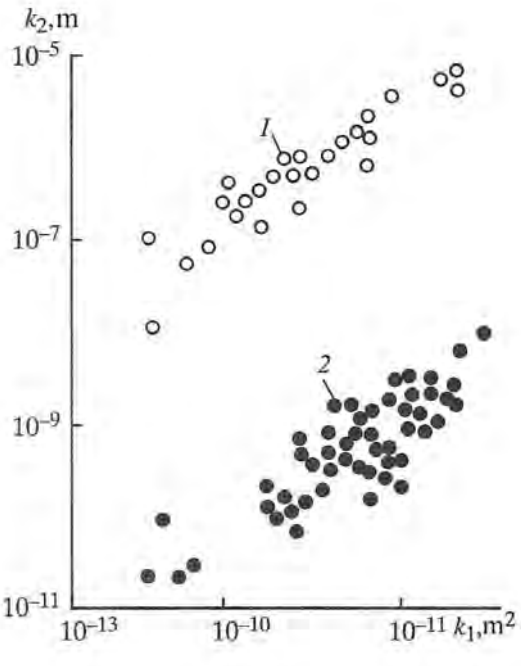

Figure 5.12: Empirical relationships between the first and the second permeability coefficients for: *1* – porous media, and *2* – fractured rocks.

Table 5.3. Percentage of the turbulent component of motion in the total hydraulic resistance as a function of a pressure change at the borehole filter

Permeability coefficient $k \cdot 10^{-12}$, m^2	Pressure change, ΔP, kPa			
	5	10	20	30
8.3	30	42	55	62
5.6	54	66	75	80
2.2	38	49	62	68

The relationship between the values of parameters k_1 and k_2 are of particular interest. Fractured rock with larger thickness of permeable channels has significantly different value of k_2 than porous medium for the same values of k_1. This is clearly seen in Figure 5.12 which shows both the results of this study for fractured rock massif and the data from Adushkin and Kaazik (1976) for permeability in porous materials with "regular" structure (e.g. granular rocks). The observed differences in the relationship k_2 (k_1) between the "real" rock massif and "generic" porous media are caused by an increased input from the turbulent component of the flow (the second term in Equation 5.3) into the total hydraulic resistance during flow through fractures compared to filtration through porous media. This happens due to differences in the Reynolds number *Re*, because the flow of air takes place in channels with different thickness and structure. Thus the second permeability coefficient k_2 represents an important parameter of the medium for the same values of the first permeability coefficient k_1. The parameter k_2 may be the only characteristic describing the thickness of the channels.

This feature of permeability in fractured rock massif causes significant increase in the second term of Equation 5.3 and its role in the total hydraulic resistance. Below we show the percentage of the second (turbulent) term from Equation 5.3 into the total hydraulic resistance φ_c for the areas with different permeability (for pressure difference ΔP = 10 kPa). The values of k_1 are also shown for illustrative purposes.

φ_c, %	44	42	66	49
k_1, 10^{-12}, m^2	27	8.3	5.6	2.2

With the increase in the differential pressure in the working volume of the borehole the contribution of the turbulent component of the gas flow to the total hydraulic resistance increases. This is illustrated in Table 5.3, which shows values of φ_c and ΔP for different parts of the rock massif.

The data presented in Table 5.2 suggest that both parameters k_1 and k_2 are important for the characterization of hydraulic permeability of the rock masses.

Rock characterization in the area surrounding large underground explosion shows that microscopic structure and, therefore, the mechanical characteristics of rocks are affected in the large volume of the rock massif. Thus petrographic studies (Short, 1964) shows that open micro-

fractures extend to distances up to four cavity radii, which is equivalent to a scaled distance of 40 $q^{1/3}$ (q is the explosion yield in kt). The changes in permeability are observed in approximately the same region (Hansen and Lager, 1968). Similar results are obtained for the rocks surrounding chemical explosions. For example Ostin and Leonard (1975) noted damage to mineral structure and micro-fracturing in diorite resulted from explosion stimulation of production borehole.

In order to obtain more detailed data about rock damage in the zone of irreversible deformations we studied rock samples collected at different distances from an explosion. Studies show that in the near zone of the underground explosion (up to distances 30 – 40 $q^{1/3}$ m/kt$^{1/3}$) rocks are characterized by increase in micro-fracturing, which can be observed from thin sections. Linear density of micro-fractures at a distance of $r/q^{1/3}$ = 25 m/kt$^{1/3}$ is on average 70 m^{-1}. There were no changes in micro-fracturing with distance before the explosion. No induced micro-fractures were observed at distances $r/q^{1/3} \geq 40$ m/kt$^{1/3}$.

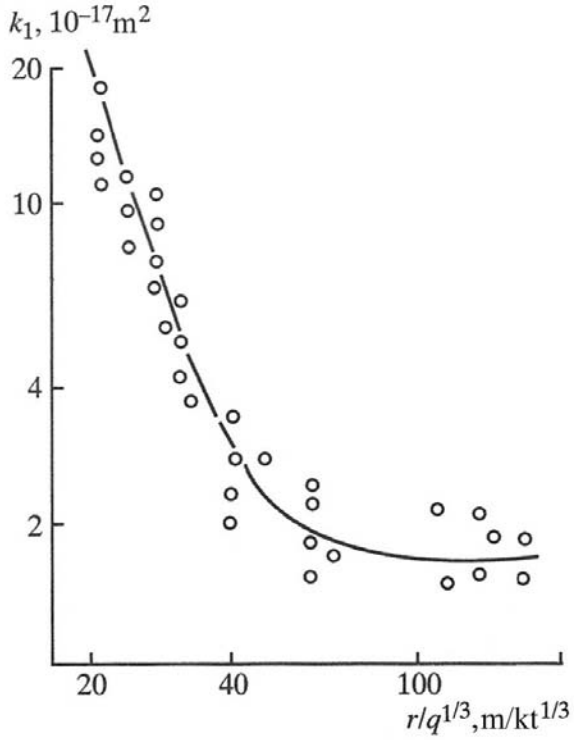

Figure 5.13: First permeability coefficient (k_1) in the damage zone created by the 2 kt UNE plotted as a function of distance from the explosion.

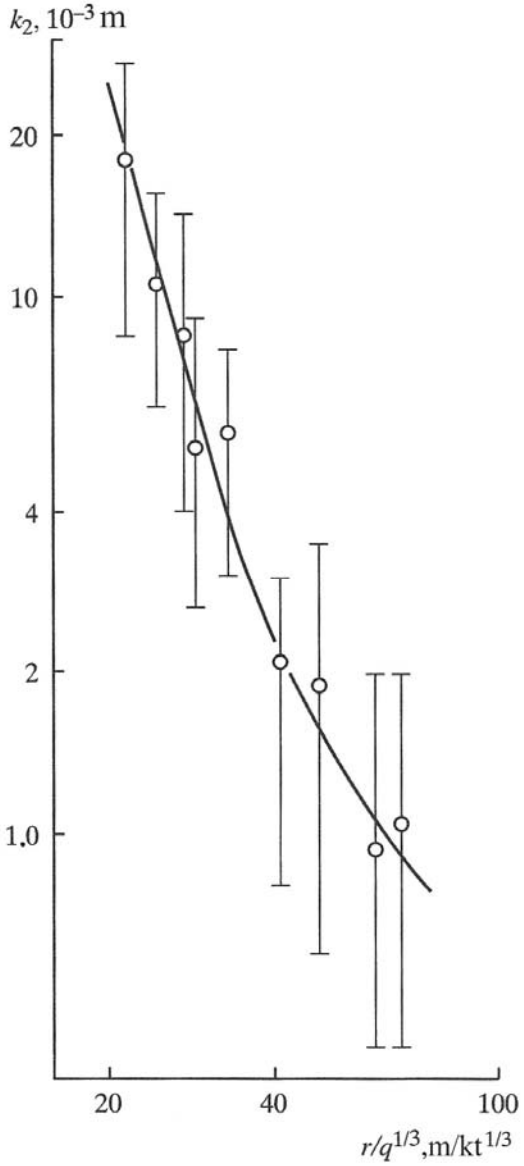

Figure 5.14: Second permeability coefficient (k_2) in the damage zone created by the 2 kt UNE plotted as a function of distance from the explosion.

Table 5.4. Permeability coefficients for tectonic fault zones of V order before and after the explosion

Fault zone order (rank)	Seismic amplitude, m/s	Permeability coefficient			
		k_1, Darcy		k_2, m	
		Before explosion	After explosion	Before explosion	After explosion
I	27	1.3	4	$3 \cdot 10^{-10}$	$5 \cdot 10^{-12}$
II	21	2.5; 4.7	11.2	$1.5 \cdot 10^{-9}$; $6 \cdot 10^{-10}$	$4 \cdot 10^{-10}$
III	8	0.8	7.6; 9.5	$2 \cdot 10^{-11}$	$8 \cdot 10^{-10}$; $3 \cdot 10^{-9}$
IV	4.2	3.6	11.8	$5 \cdot 10^{-11}$	$\sim 10^{-9}$
V	2.5	1.65	2.4	$2 \cdot 10^{-11}$	$5 \cdot 10^{-11}$

The results of the hydraulic tests are shown in Figures 5.13 and 5.14. The presented data show significant changes in permeability due to a large explosion. The permeability decreases with distance from the explosion and only at distances greater than 60 $q^{1/3}$ m/kt$^{1/3}$ the permeability reaches the initial values.

We note that the relationship between the parameters k_1 and k_2 is comparable to the results for the porous media of “regular” structure (Figure 5.12), which suggests predominately laminar flow regime in pore space and micro-fractures of rocks.

Comparison between the *in situ* filtration parameters of the rock massif and the laboratory measurements of the rock samples in the damage zone from an underground explosion shows that the permeability of the rock massif exceeds the permeability of the rock samples by several orders of magnitude. Therefore it is not necessary to account for gas/fluid flow through the rock when estimating rock damage during hydraulic testing. However changes in rock permeability as a result of an explosion have an important effect on the velocity of gas/fluid flow into a rock fragment during leaching. In this case permeability changes should be considered significant. [I think this means that for the purposes of fluid flow through the bulk rock massif permeability of each fragment is unimportant, but the fluid/gas can still get into those fragments to some extent].

Changes in permeability of tectonic faults due to underground explosions. Hydraulic studies conducted in the influence zone of an underground explosion showed anomalously high fluid discharge in some intervals of boreholes surrounding the explosion source. The discharge in these intervals was different (often by an order of magnitude) from the discharge in the adjacent intervals. The extent of these intervals did not exceed 0.2 – 1 m, which suggested that these intervals represented intersection of the borehole with tectonic faults. Geological survey of the rock massif and the tunnel supported the existence of tectonic faults of V order at the intervals with anomalously high permeability.

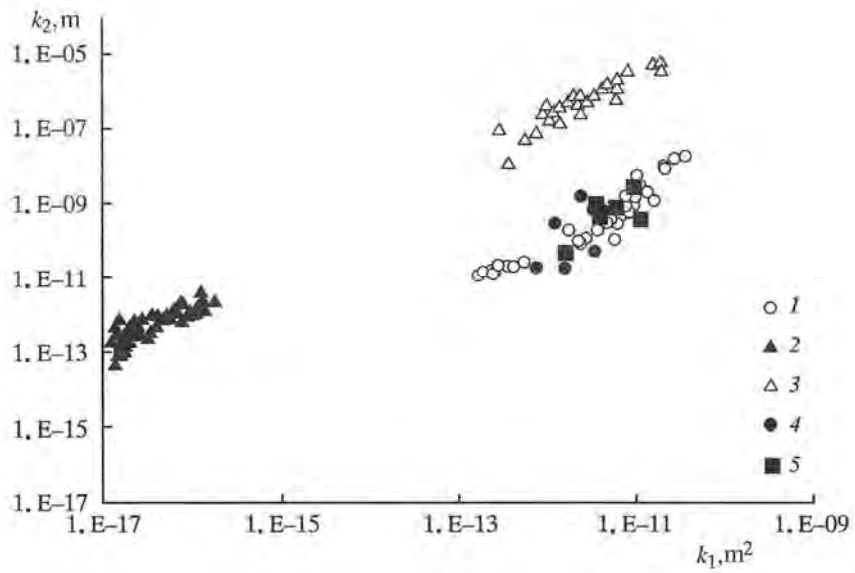

Figure 5.15: Empirical relationships between the laminar and turbulent permeability coefficients for: *1* – fractured rocks (before the explosion); *2* – rock samples collected at different distances from the explosion; *3* – porous media with "regular structure", *4* and *5* – tectonic fault zones before and after the explosion respectively.

The results of hydraulic testing in the intervals containing intersections with tectonic faults are shown in Table 5.4 as the values of permeability coefficients before and after the explosion. These values represent *in situ* permeabilities of the tectonic faults.

According to Table 5.4 the initial permeability of faults of the same order varies in wide range between 0.8 and 4.7 Darcy. After the explosion the rock permeability significantly increased.

Of interest are the relationships between the laminar (k_1) and turbulent (k_2) permeability coefficients of tectonic faults and their changes as a result of explosion. The values of k_1 and k_2 are shown in Figure 5.15 together with the data from hydraulic testing of rock massif and porous media of regular structure [I think they mean granular].

According to the data shown in Figure 5.15 the relationship between the laminar and turbulent permeability coefficients for tectonic faults, both before and after the explosion, agree with the relationships between the coefficients for the regular [granular] porous media. This is not surprising because tectonic fault zones [gouges] are filled with material similar to fragmented rock and sand.

Unlike fault zones the relationships between the laminar and turbulent permeability coefficients for rock samples agree with the relationships for fractured rocks. This leads us to an important conclusion: structural features of permeable channels for undamaged rock samples are close to micro-fractures. Thus, even rock subjected to considerable damage due to external dynamic loading is not well described in terms of packed granulated medium.

5.4. Estimation of structural characteristics of the rock massif based on fluid transport studies

In order to determine structural characteristics of damaged media (Spivak, 1980a; Rodionov et al., 1981) we use the simplest model of fractured medium – model of parallel type. According to this model the "real" rock mass (both undamaged and damaged by an explosion) is represented by impermeable blocks of rock separated by systems of planar fractures. Each individual fracture, which can be partially closed due to contacts between the surface imperfections, can be characterized using two parameters: average aperture $\langle\varepsilon\rangle$ and "overlap" coefficient *S*.

Let us consider the case when the medium is characterized only by one permeability coefficient k_1. In practice this situation is common because the majority of permeability measurements of damaged rocks are based on fluid filtration, in which case only one parameter k_1 can be accurately measured.

Fluid flow through an individual fracture with a constant opening is described by a well-known relationship between fluid flow per unit length q_f and the pressure gradient:

$$q_f = -\frac{\langle\varepsilon\rangle^3}{12\mu} grad\ P.$$

Using this equation and assuming that the permeable space consists of three systems of fractures, and fracture opening obeys linear function in the interval $(0,\varepsilon_*)$, where ε_* is the maximal fracture opening, we obtain the expression for fluid discharge per unit of fracture length in a form:

$$q_f = -\frac{(1-S)\varepsilon_*^3}{48\mu} grad\ P. \tag{5.10}$$

Taking into account that fluid flow occurs through two intersecting systems of fractures(to estimate porosity it is necessary to account for all three systems) and using Equation 5.10 we obtain the expression for the flow velocity:

$$v_f = -\frac{(1-S)\varepsilon_*^3\lambda}{24\mu} grad\ P, \tag{5.11}$$

where λ is the number of fractures per unit length within the rock massif [formation].

Comparing Equations 5.2 and 5.11 we obtain:

$$\lambda = \frac{24k_1}{(1-S)\varepsilon_*^3}. \tag{5.12}$$

We express the value of maximal fracture opening using the massif porosity:

$$m = \frac{3}{2}(1-S)\varepsilon_*^3. \tag{5.13}$$

Combining the last two equations we obtain:

$$\varepsilon_* = 6\left(\frac{k_1}{m}\right)^{1/2}. \tag{5.14}$$

Thus we expressed the unknown parameters of the rock massif ε_* and λ which cannot be measured directly using characteristics that can be measured: k_1 and m.

Equations 5.12 and 5.14 allow estimation of [structural] parameters λ and $\langle\varepsilon\rangle$ in case where the rock massif is characterized by fractures of the same aperture. In cases where fracture apertures are not the same, a combination of fractures with various apertures should be considered. We will introduce a distribution function $\varphi(\varepsilon_*)$, which determines the fraction of fractures with apertures in the interval $(\varepsilon_*, \varepsilon_* + d\varepsilon_*)$:

$$d\lambda = \lambda\varphi(\varepsilon_*)d\varepsilon_* .$$

Partial permeability of the massif through fractures with maximum opening ε_* according to 5.10 can be expressed as:

$$dk_1 = -\frac{(1-S)\varepsilon_*^3\lambda}{24}\varphi(\varepsilon_*)d\varepsilon_*.$$

From Equation 5.15 we obtain:

$$k_1 = -\frac{(1-S)\lambda}{24}\int_{\varepsilon_1}^{\varepsilon_2}\varepsilon_*^3\varphi(\varepsilon_*)d\varepsilon_*. \tag{5.15}$$

where ε_1 and ε_2 are the minimum and maximum value for ε_* respectively.

According to Equation 5.13 the value of ε_* is proportional to the dimensions of the fragment adjacent to the fracture (the average fragment size is $\langle x\rangle = \lambda^{-1}$). Therefore we can select a distribution function $\varphi(\varepsilon_*)$ based on the fragment size distribution. For example we can use Rosin-Rammler distribution (Equation 1.20). In this case the distribution function can is given by:

$$\varphi(\varepsilon_*) = \frac{n}{\varepsilon_0}\left(\frac{\varepsilon_*}{\varepsilon_0}\right)^{n-1}\exp\left[-\left(\frac{\varepsilon_*}{\varepsilon_0}\right)^n\right], \tag{5.16}$$

where ε_0 and n are the distribution parameters, where $n > 1$ for $\varepsilon_0 = 0$.

In case $\varepsilon_1 = 0$ and $\varepsilon_2 \to \infty$ Equation 5.15 can be easily integrated taking into account Equation 5.16. The result of integration is:

$$k_1 = -\frac{(1-S)\lambda\varepsilon_*^3}{24}\Gamma\left(1-\frac{3}{n}\right), \tag{5.17}$$

where $\Gamma\left(1-\frac{3}{n}\right)$ is the Gamma function of the corresponding argument.

We express the distribution parameter ε_0 in Equation 5.17 using the average value of the maximum fracture opening $\langle\varepsilon\rangle$ on the interval using the expression:

$$\langle\varepsilon_*\rangle = \varepsilon_0\Gamma(1-1/n).$$

Substituting the expression for ε_0 expressed using $\langle\varepsilon_*\rangle$ into Equation 5.17 we obtain the final expression:

$$\lambda = -\frac{24k_1[\Gamma(1-1/n)]^3}{(1-S)\langle\varepsilon_*\rangle^3\Gamma(1-3/n)}.$$

To estimate the degree of rock damage the value of $\langle\varepsilon_*\rangle$ can be chosen as the irregularity size of the fracture wall (surface of detachment). According to a work by Ruppeneit (1975) this parameter does not vary significantly for rocks of different types and is on average $5 \cdot 10^{-4}$ m.

We use a numerical example of determining structural characteristics for the rock massif after a 2 kt nuclear explosion. For a part of the massif with m = 1% and $k_1 = 1.9 \cdot 10^{-11}$ m^2 and assuming that $S = 0$ (area of contacts [between fracture walls?] approaching to zero) we obtain using Equations 5.12 and 5.14:

$\lambda = 26$ m^{-1} and $\varepsilon_* = 2.6 \cdot 10^{-4}m$.

Field measurements in this area yield $\lambda \sim 26$ m^{-1} and $\varepsilon_* = 3 \cdot 10^{-4}m$.

Simple relationship to estimate the average characteristics in the medium using hydraulic testing can be obtained by using Kozeny [-Carman] relationship:

$$k_1 = \frac{\xi^2 m^3}{S_s^2},$$

where S_s is the specific surface area of all fragments in the unit of volume of the damaged medium, ξ is a constant, and m – porosity, so that $m \approx 0.5S\langle\varepsilon_*\rangle$.

Assuming Rosin-Rammler fragment size distribution (Equation 1.20) we obtain:

$$S_s = -\frac{\Gamma(1+1/n)\Gamma(1-1/n)}{\langle x\rangle}.$$

From this expression we obtain $\langle x\rangle = \xi_1/k_1$, $\xi_1 = \langle\varepsilon_*\rangle^3\Gamma(1+1/n)\Gamma(1-1/n)/8$.

If we express the constant ξ_1 using permeability and fracture content of the un-damaged massif k_{10} and λ_0 we obtain the final expression:

$$\langle x\rangle = k_{10}/\lambda_0 k_1. \tag{5.18}$$

This expression produces reasonable estimates for λ as a function of distance from the explosion (Figure 5.16).

Now we estimate the degree of damage of a rock massif after an explosion using the method of hydraulic testing discussed earlier. In order to perform the estimate we use the original experimental data, namely: we chose pressure change ΔP (differential pressure) and the discharge of gas/fluid Q corresponding to this differential pressure as the main parameters.

We note that data analysis using filtration equations similar to Equation 5.3 requires high density of permeable channels in the vicinity of the working volume of the borehole, which is not always the case during studies of fractured media. In case of fractured medium the

permeability coefficients k_1 and k_2 can be considered as equivalent medium parameters describing porous medium. Because of this in order to estimate structural parameters of damaged medium we will use the initial data in a form of so-called discharge curve $Q(\Delta P)$.

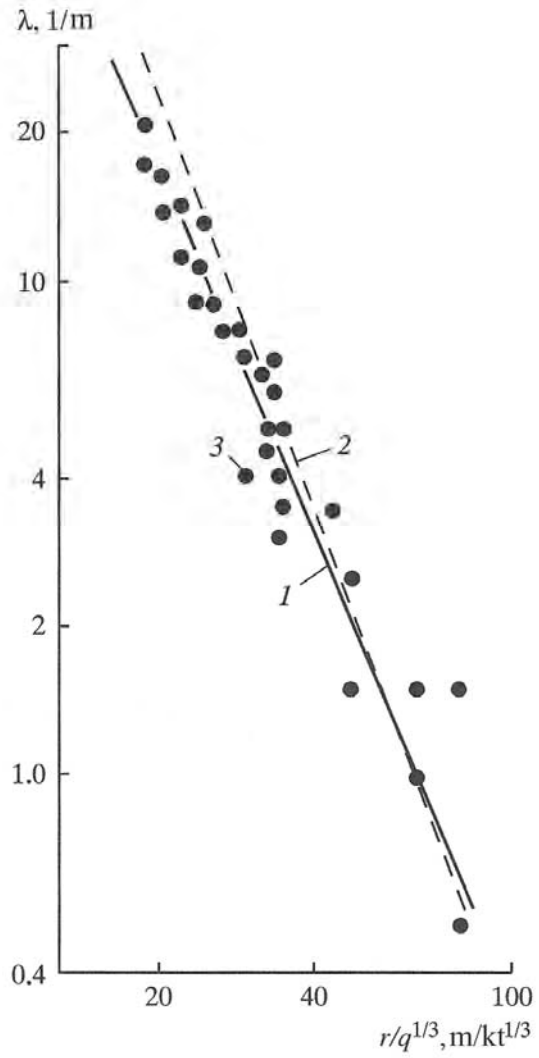

Figure 5.16: Specific fracture content for rocks damaged by an explosion: *1* –estimates using hydraulic testing; *2* – estimates using Equation 5.18; *3* – planimetric studies of the fragments.

To create a physical model of the experiment determining in situ rock permeability using a borehole we consider axisymmetric gas flow through a narrow gap perpendicular to the borehole axis. In order to further simplify this problem we assume the model of incompressible working body [gas/fluid].

Integration of the governing equation for incompressible viscous fluid using Stokes approximation (in cylindrical coordinates) yields an expression for the volumetric discharge of working fluid as a function of distance from the borehole axis r_1 in a form:

$$q_1^* = \frac{2\pi r_1 (\langle\varepsilon\rangle)^3}{\mu}\left(1 - \frac{2r_1}{\langle\varepsilon\rangle}\tan\frac{\langle\varepsilon\rangle}{2r_1}\right)\frac{dP}{dr_1}. \qquad (5.19)$$

Assuming that the fracture aperture $\langle\varepsilon\rangle$ is small compared to the borehole radius a_0 ($\langle\varepsilon\rangle \ll a_0 \leq r_1$) we obtain:

$$q_1^* \approx \frac{\pi r_1 (\langle\varepsilon\rangle)^3}{6\mu} \left|\frac{dP}{dr_1}\right| .$$

From this expression:

$$q_1^* \approx \frac{\pi r_1 (\langle\varepsilon\rangle)^3 (P_1 - P_0)}{6\mu \ln(a_p/a_0)} . \quad (5.20)$$

The distance $r_1 = a_p$ for which the fluid pressure becomes equal to an atmospheric pressure can be chosen equal to 1 m (in this case the overpressure in the working fluid drops by an order of magnitude compared to an initial pressure P_1).

It follows from the last expression that the amount of the fluid flowing out of the borehole per unit of time grows linearly with an increase of pressure P_1. At a certain differential pressure $\Delta P = \Delta P_*$ the flow velocity in the fracture can reach its critical value, at which the flow becomes turbulent. Here we need to differentiate between turbulent flow in each individual fracture (flow becomes turbulent if the Reynolds number *Re* reaches ~10^3) and the condition when linear filtration approximation Equation 5.2 breaks down (*Re* ~ 1). It is impossible to compare these conditions because breakdown of the linear filtration approximation and change of flow regime in channels have different mechanisms: the flow in channels becomes turbulent at high Reynolds numbers, while losses during filtration may appear [even] without turbulence.

Neglecting a possibility of existence of transitional regimes we assume that for $\Delta P \sim \Delta P_*$ flow of working fluid becomes turbulent in the entire flow region. Similar to the case of circular channels we assume that the resistance coefficient for the turbulent flow in the planar fracture ψ weakly changes with Reynolds number increase. Then the equation of motion can be written in a form:

$$\frac{dP}{dr_1} = -\psi \frac{\rho U_f^2}{2} , \quad (5.21)$$

where U_f is a physical velocity of flow in the fracture at a distance r_1.

Integration of Equation 5.21 in cylindrical coordinates yields:

$$q_1^* = \frac{\pi r_1 (\langle\varepsilon\rangle)^{3/2} \Delta P^{1/2}}{\rho^{1/2} \psi^{1/2} (1/a_0 - 1/a_p)} . \quad (5.22)$$

As a result we obtain a simplest model of permeable fractured medium. According to this model the relationship $q_1^*(\Delta P)$ is described using Equation 5.20 for small differential pressures ($\Delta P < \Delta P_*$) and using Equation 5.22 for large values of differential pressure ($\Delta P > \Delta P_*$).

We found earlier that the experimental relationships $Q(\Delta P)$ show two intervals with different power law for the change of air discharge Q as a function of the differential pressure ΔP. For ΔP

$\leq$ 3 kPa the power is close to 1, while for $\Delta P \geq 3$ kPa it is close to 0.5, which agrees with Equation 5.20 and 5.22. In this case the value of ΔP_* is 3 kPa.

We determine specific fracture content of the damaged rock massif λ and the average fracture aperture $\langle\varepsilon\rangle$ using the equations of the obtained model and the experimental results for determining air discharge Q as a function of ΔP.

We assume that at a fixed distance from the explosion fracture aperture can be characterized by some average value $\langle\varepsilon\rangle$ which depends on the distance to the explosion. Using Equations 5.20 and 5.22 and taking into account the condition

$$Q = (1 - S)q_1^*\lambda$$

we obtain the following relationships:

$$\langle\varepsilon\rangle^3\lambda = \frac{6\mu Q ln(a_p/a_0)}{\pi(1-S)\Delta P} \text{ for } \Delta P \leq \Delta P_*,$$

$$\langle\varepsilon\rangle^{3/2}\lambda = \frac{Q(1/a_0 - 1/a_p)^{1/2}}{2\pi(1-S)} \cdot \left(\frac{\rho\psi}{\Delta P}\right)^{1/2} \text{ for } \Delta P \geq \Delta P_*.$$

Existence of two flow regimes for small and large values of differential pressure point to two parameters, ΔP_* and Q_*, characterizing flow of working fluid through the damaged region of the rock massif with structural parameters λ and $\langle\varepsilon\rangle$. In this definition Q_* represents volumetric fluid discharge for the differential pressure $\Delta P = \Delta P_*$.

Substituting $\Delta P = \Delta P_*$ into the last two relationships and solving with respect to λ and $\langle\varepsilon\rangle$ in the assumption that $a_p \gg a_0$ we obtain

$$\langle\varepsilon\rangle = 5.24 \left(\mu \ln\left(\frac{a_p}{a_0}\right)\right)^{2/3} \left(\frac{a_0}{\rho\psi\Delta P_*}\right)^{1/3}, \quad (5.23)$$

$$\lambda = \frac{\rho\psi Q_*}{24\pi(1-S)a_0\mu\, ln(a_p/a_0)}. \quad (5.24)$$

Equation 5.23 shows that if other parameters stay the same the fracture aperture is determined by ΔP_*. In our case the value of the critical differential pressure is approximately equal for all studied intervals and is close to 3 kPa. This shows that the damage parameter $\langle\varepsilon\rangle$ is independent of the distance to the explosion. The specific value calculated using the experiment parameters is $3.3 \cdot 10^{-4}$ m.

The values of λ calculated using Equation 5.24 using S = 0.9 and $\psi = 0.12$ (resistance coefficient at $Re \sim 100$) and using the results of Equation 5.8 are shown in Figure 5.16 as a solid line. The relationship $\lambda(r)$ can be analytically expressed as

$$\lambda = 5.8 \cdot 10^4\, r^{-2.5}\ (\text{m}^{-1}),$$

where r is the distance in meters.

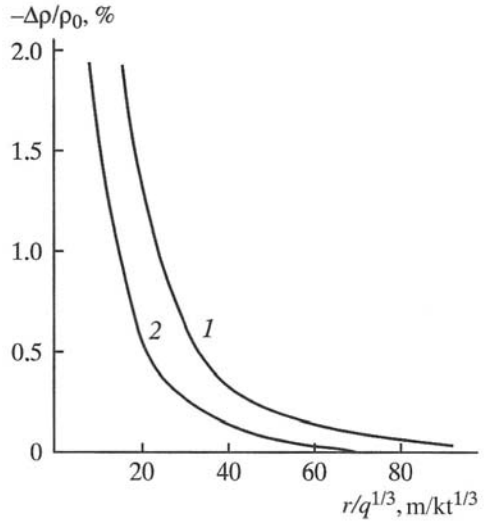

Figure 5.17: Bulking (dilation) for rocks damaged by an explosion: *1* – estimates using Equation 5.25; *2* – experimental measurements for HARDHAT.

The values of λ obtained from the direct measurements in the tunnel wall at the site of the hydraulic testing are also shown for comparison in Figure 5.16, as well as the calculation results using Equation 5.18 (dashed line). According to the plot the values of λ calculated from the hydraulic study data adequately describe the observed fracture density of the damaged rocks. In addition, in order to determine fracture content of the rock massif it is sufficient to calibrate the parameter *S* using the data from accessible areas.

The obtained results show some promise of using *in situ* hydraulic testing of to determine the degree of damage in the damage zone of underground explosions or in case of any other fractured formation/zone with structure close to isotropic.

The estimated structural parameters of the medium allow us to determine the final value of dilation (density reduction) of the rock massif around the explosion source, which is an important characteristic for evaluation of the mass of fragmented rocks.

In the described model of permeable medium (model with parallel fractures with three mutually perpendicular directions) the relative density reduction is related to the parameters λ and $\langle\varepsilon\rangle$ via a simple relationship:

$$\frac{\Delta\rho}{\rho_0} = -3\langle\varepsilon\rangle\lambda.$$

Using this equation and employing the relationship $\lambda(r)$ and the calculated value of $\langle\varepsilon\rangle$ we obtain:

$$\frac{\Delta\rho}{\rho_0} = -5.4 \cdot 10^3\, r^{-2.5}\ (\%), \tag{5.25}$$

where *r* is the distance in meters.

Figure 5.17 shows a graphic interpretation of Equation 5.25 (line 1). It also shows the residual displacements produced by the nuclear test HARDHAT (line 2). It is clear from Figure

5.17 that despite significant displacements during explosions the final dilation is not very high: he total volume of void created by a 2 kt explosion is ~10^4 m^3, while the final cavity volume is approximately $0.5 \cdot 10^4$ m^3. More accurate analysis produces the following value for the average dilation (bulking) coefficient

$$k_b = \left(1 + \frac{\Delta\rho}{\rho_0}\right)^{-1} \approx 1.12 \, .$$

Small values of dilation produced by the explosion may cause difficulties in rock extraction from the massif (the condition of unobstructed [unhindered] rock extraction from the mine is given by $k_b \sim 1.18 \div 1.25$). Because of this conduction of large contained explosions for the purpose of ore extraction requires preparatory work to provide additional rock bulking in the damage zone (creating of compensatory volumes etc).

5.5 The effects of underground nuclear explosions on ground water flow

Study of ground water behavior after large explosions is of interest for: a) industrial use of underground explosions; b) obtaining information about permeability of rocks and its changes due to explosions; c) most importantly in order to provide hydrological nuclear safety while using underground structures and aquifers [Adushkin et al, 1992; Adushkin and Spivak, 1993b).

The main mechanical expressions of large underground explosions, which disturb steady state ground water flow, are cause first by the action of the stress wave on aquifers, and second by formation of additional void space (explosive cavity, induced fractures, as well as void formed due to loosening of the ground) and by deformation of aquifers and the rock massif as a whole. Highly heterogeneous deformations to complex geological media do not allow for detailed study of ground water behavior as a result of explosions.

However the main characteristics of hydrodynamic processes caused by explosions can be easily found by using model formulation by Gorbunova and Spivak (1997). We consider an explosion of yield q conducted at a depth W in low-permeability medium containing sub-horizontal water-saturated layer. Wave processes following the explosion cause deformation of the surrounding medium. Note that the aquifer sustains greater deformations than the surrounding medium. This is caused by higher porosity and compressibility of water-saturated aquifers compared to other rocks (aquitards). Dynamic compression of the aquifer causes increase in the fluid pressure in some region, which creates either actual rise in the water table (plume) or the fluid pressure P increase corresponding to a hydraulic head rise according to Dupuit approximation:

$$\text{grad}\,(P) = \rho g \cdot \text{grad}\,(h),$$

where h is the absolute water table elevation, and ρ is the density of the fluid.

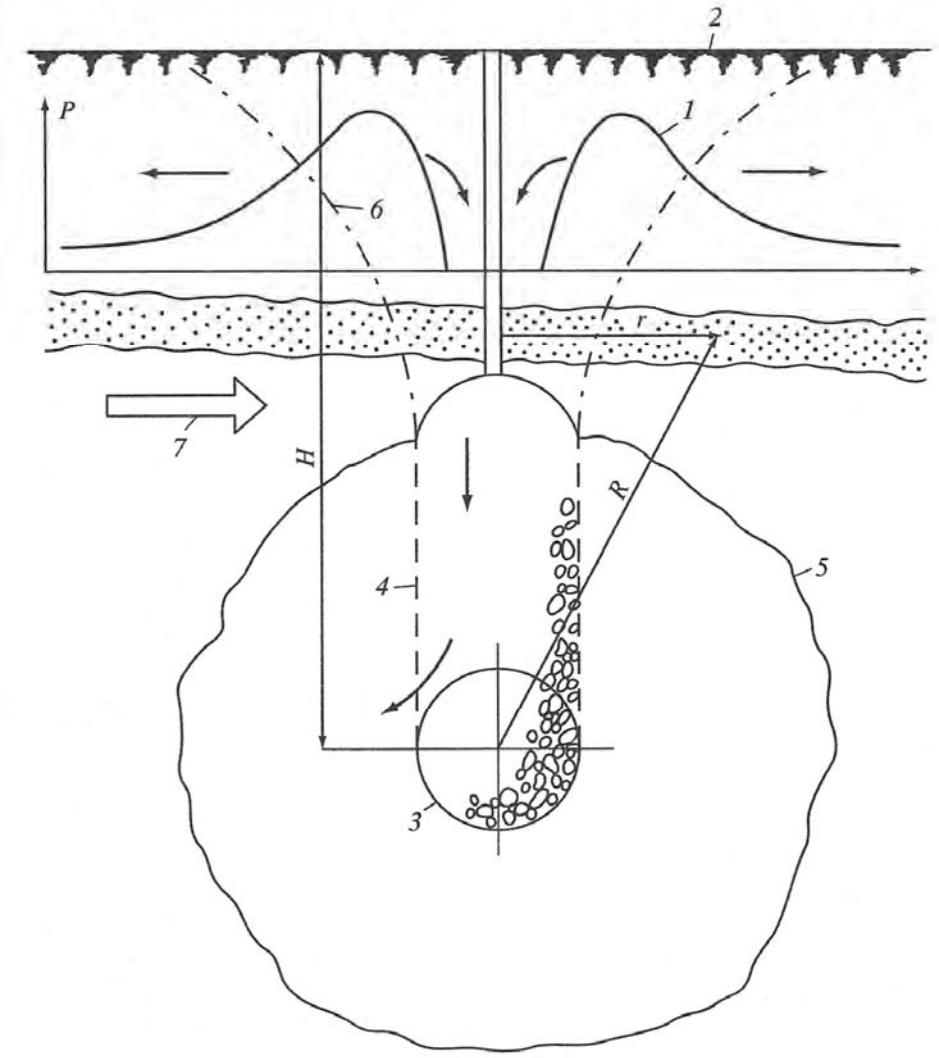

Figure 5.18: Schematic of the ground water flow in the vicinity of an underground explosion: *1* – fluid pressure in the layer (which represents the water table for an unconfined aquifer) in the epicentral area after cavity collapse (arrows show the direction of the water flow); *2* – ground surface; *3* – explosive cavity; *4* – chimney; *5* – boundary of the fracture zone; *6* – boundary of the epicentral surface damage zone; *7* – the direction of the regional flow of the ground water.

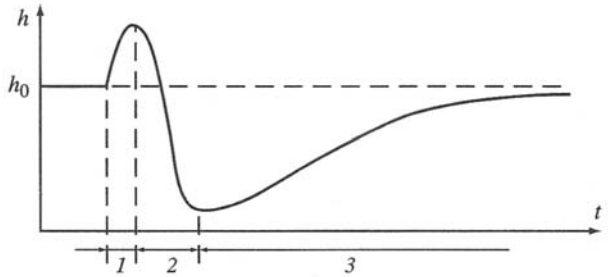

Figure 5.19: Quantitative curve showing the water level changes with time *t*: *1* – plume formation; *2* – void filing; *3* – water table return to the initial level.

This pressure increase is accompanied by water injection into pore space of surrounding rocks, as well as into pre-existing and newly-formed fractures. Formation and subsequent collapse of the explosive cavity creates a chimney filled with loose rocks, often extended all the way to the surface, causing a depression in the water table (Figure 5.18). Existence of the region of high pressure (or dome) of the ground water in the epicenter naturally causes the increase in the water table in the observational boreholes. Schematically the character of water level changes is shown in Figure 5.19.

The next stage in ground water movement is represented by flow into the newly-formed voids. High permeability of rocks in the chimney (permeability coefficient reaches 10^{-9} m^2) leads to fast release of the ovepressure and a subsequent drop below the level that existed in the epicenter before the explosion. The latter causes rapid decrease in flow to the regions of natural water migration (discharge areas) and a simultaneous formation of the depression cone. This results in sudden reduction in the water table in the zone of influence.

The final stage is restoring of the initial water level in the entire area after filling the voids created by the explosion.

We make a qualitative estimate. The value of hydraulic head (or overpressure in case of low-permeability overlaying layer) $\Delta h = h \div h_0$ (Figure 5.19) is determined by the intensity of the explosive loading, represented by the maximum particle velocity v_0 in the stress wave. Using the empirical relationship v_0 (r) on the distance from the explosion (Equation 1.8) we obtain:

$$\Delta H = \frac{A \cdot q^{1/3}}{[(H-b)^2+r^2]^{n/2}}, \tag{5.26}$$

where r is the distance from the explosion in meters, b is the depth of the lower aquitard, A and n are empirical constants ($n \approx 1.7$), and q is the explosion yield in kt.

The time t_1 from the explosion until the maximum head is reached at the epicentral distance r is given by:

$$t_1 = \frac{1}{C}\sqrt{(H-b)^2 + r^2}\,,$$

where C is medium seismic velocity.

In the future we will describe ground water movement using the linear equation:

$$\vec{v}_f = -\frac{k}{\mu}(grad\ P - \rho\vec{g}),$$

where P, μ and $\vec{v}_f$ are the pressure, viscosity and flow velocity of the fluid respectively, k is the permeability of the medium, and g is gravitational acceleration.

Volume of voids created by an underground explosion. To determine hydrodynamic characteristics during the second stage of the ground flow movement (filling the void space created by the explosion) we first determine the volume of the void space. The total volume of the void consists of the volume of the explosive cavity V_0, volume of void in the fracture zone V_1

and the volume of void in the chimney V_2. We note that the void within the chimney is formed due to filing of the cavity [moving of part of the material into the cavity]. This means that if we assume that the explosive cavity is a sphere with radius r_c, we can neglect the volume V_2. We can also neglect near-surface fracturing created by spall and assume that the fracture zone is spherically symmetric. Multiple experimental studies (e.g. Adushkin and Spivak, 2004) suggest that for the majority of rock types

$$r_c = 10\, q^{1/3}\ (\text{m}), \tag{5.28}$$

where q is the explosion yield in kt (of TNT equivalent), and therefore:

$$V_0 = 4.2 \cdot 10^3\, q\ (\text{m}^3).$$

We express the volume density ρ_m of rock with fracture density λ and the average fracture aperture ε as

$$\rho_m = \rho_0\,[1 - a\varepsilon\lambda(1 - s)], \tag{5.29}$$

where ρ_0 is the density of the rock, a is the coefficient determined by the number of fractures and the average tortuosity of individual fractures (for rock massif crossed by three fracture systems of nearly planar fractures $a \approx 3$), s – is the average value of the fracture overlap (in a simplest case it is the average ratio of areas of contact to the total length of the fracture).

We write the value of dilation coefficient of the rock massif using Equation 5.29

$$\eta = \frac{\Delta\rho}{\rho_m} = \frac{\rho_* - \rho_1}{\rho_1} = \frac{\alpha(1-s)(\varepsilon\lambda - \varepsilon_1\lambda_1)}{1 - \alpha(1-s)\varepsilon_1\lambda_1},$$

where ρ_* is the final density of the rock, index 1 defines the initial medium parameters before explosion (it is assumed that $a \approx a_1$, $s = s_1$).
If the initial medium had few fractures ($\varepsilon \to 0$, $\lambda \to 0$) then

$$\eta = -a(1 - s\varepsilon\lambda).$$

Based on the experimental results large explosions cause structural changes in the area with the radius [approximated as]

$$R_* = 100\, q^{1/3}\ (\text{m}). \tag{5.30}$$

The parameter describing the average fracture aperture is practically independent on the distance from the explosion:

$$\varepsilon \approx \text{const} = 3.3 \cdot 10^{-4}\ \text{m},$$

and the function [relationship] $\lambda(R)$ can be expressed in a form:

$$\lambda = 5.8 \cdot 10^4\, (r/q^{1/3})^{-2.5}\ (\text{m}^{-1}).$$

Using these expressions we obtain:

$$\eta = \eta_0 (q^{1/3} r)^{2.5}, \tag{5.31}$$

where η_0 is the initial void ratio of the rock.

We determine the total volume of void in the fracture zone created by an explosion [by integrating]

$$V_1 = 4\pi \int_{R_0}^{R_*} \eta r^2 dr \ .$$

Using Equations 5.28, 5.30 and 5.31 we obtain:

$$V_1 = 4\pi\eta_0 R_*^{2.5} \left(\sqrt{R_*} - \sqrt{R_0}\right) \approx 8.6 \cdot 10^6 \, \eta_0 q \ .$$

Thus the total volume of voids created by an explosion is given by:

$$V \approx 4.2 \cdot 10^3 \, q \, (1 + 2.04 \cdot 10^3 \, \eta_0). \tag{5.32}$$

Dynamics of filling of the pore space with ground water. Time required to fill the newly-created void with water is determined by fluid discharge Q_1 flowing through permeable channels into the chimney. To estimate the value of Q_1 we use the scheme shown in Figure 5.20. Ground water flow in water-saturated layer of thickness h and permeability coefficient k_0 is moving due to the pressure head with velocity u. At the moment $t = 0$ a vertical permeable channel of radius R_0 is created and part of the fluid starts flowing through the channel. At this moment the fluid flow becomes non-stationary.

Consider the fluid flow in the neighborhood of the drainage channel. The discharge Q of fluid through the cylindrical surface of radius r is given by:

$$Q \ = -2\pi K h r \frac{\partial h}{\partial r} \, ,$$

where K is the coefficient of transmissivity of the layer, h is the thickness of the water layer.

Taking into account mass conservation law

$$\frac{\partial Q}{\partial r} = 2\pi r m \frac{\partial h}{\partial r}$$

we obtain

$$\frac{\partial h}{\partial t} = \frac{1}{mr} \frac{\partial}{\partial r} \left(r h K \frac{\partial h}{\partial x} \right), \tag{5.33}$$

where m is the porosity of the aquifer.

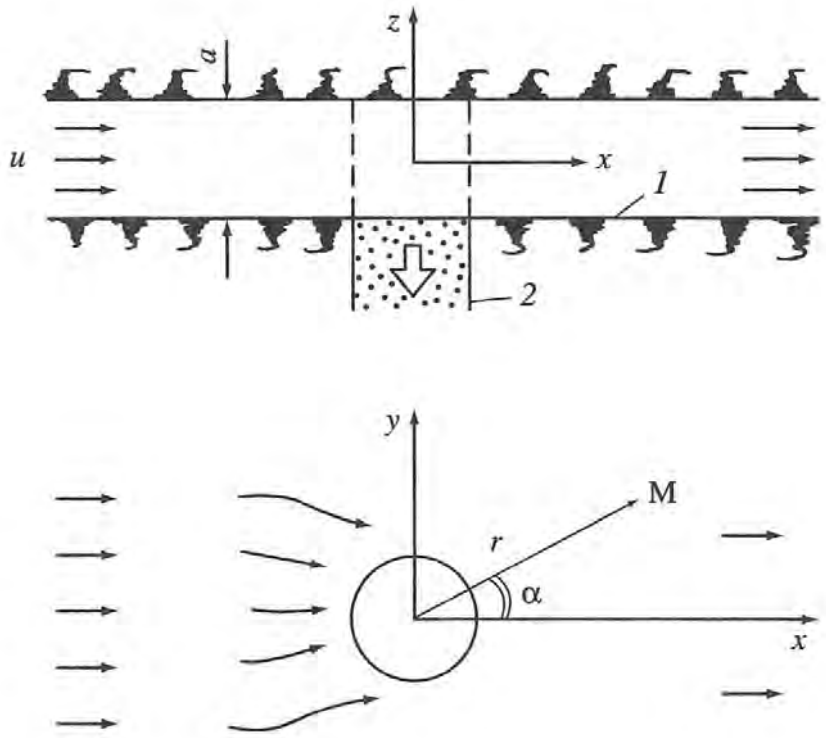

Figure 5.20: Schematic of the ground water flow in an aquifer: *1* – aquitard; *2* – chimney. Additional explanations are provided in the text.

Using Equation 5.28 we rewrite 5.33 as

$$\frac{\partial h}{\partial t} = -u\frac{\partial h}{\partial r} - \frac{uh}{r} + \frac{\rho g k_0}{\mu m} h \frac{\partial^2 h}{\partial r^2}, \tag{5.34}$$

where k_0 is the permeability of the aquifer.

We observe that the right hand side of Equation 5.34 is not defined in the vicinity of $r = 0$. Since

$$lim\left[\frac{1}{r}\frac{\partial h}{\partial r}\right] = \left.\frac{\partial^2 h}{\partial r^2}\right|_{r=0},$$

instead of Equation 5.33 we can describe the fluid flow in the aquifer in the vicinity of the point $r = 0$ using

$$\frac{\partial h}{\partial t} = \frac{2Kh}{m} - \frac{\partial^2 h}{\partial r^2}. \tag{5.35}$$

We assume that between the time of chimney formation ($t = 0$) and the time when quasi-stationary flow is established ($t = t_2$), fluid discharge through the cylindrical surface of radius R_0 is determined by the parameter Q_1. The boundary condition at $r = R_0$ is given by:

$$Q_1 = -2\pi R_0 h \frac{\partial h}{\partial r}.$$

From this expression we obtain for $r = R_0$:

$$h\frac{\partial h}{\partial r} = \frac{Q_1}{2\pi R_0 K} = const. \quad (5.36)$$

In case $r \to \infty$ we have: $h(t,r) \to h_0$, which is equivalent to $P \to P_0$.

The initial condition for solving Equation 5.33 is the effective fluid surface at the time $t = 0$ given by Equation 5.26:

$$h(t,r) = h_0 + \Delta h(r) \equiv \varphi(r). \quad (5.37)$$

Using the value of the permeability coefficient in the vertical channel k and using 5.27 and 5.28 we obtain:

$$Q_1 = \frac{\pi\rho g k_1 R_0^2}{\mu} \approx \frac{100\,\pi\rho g k_1}{\mu} q^{2/3}. \quad (5.38)$$

If $\rho = 10^3$ kg/m^3 and $\mu = 10^{-3}$ Pa·s the value of Q_1 is $3.08 \cdot 10^9\, k_1\, q^{2/3}$ m^3/s (where q is yield in kt).

As an illustration Figures 5.21 and 5.22 show the distribution of the hydraulic head as a function of epicentral distance r for different moments of time obtained using integration of Equation 5.33 and using Equations 5.27 and 5.35 – 5.38. Computations were conducted for the case: q = 20 kt, H = 600 m, b = 70 m. Initial spatial distribution $\varphi(r)$ was chosen according to Equation 5.26. The values of parameters used for the estimates were close to real characteristics of a permeable layer [not sure how to say it correctly]: a = 25 m, $k_0 = 10^{-11}$ m^2, P_0 = 0.5 MPa (h_0 = 25 m).

Figure 5.21 shows that the water table plume dissipates too fast and there is not enough time for water to migrate down the aquifer. Due to significant heterogeneity of the initial distribution $\varphi(r)$ the plume dissipation is achieved mostly by fluid flow down into the permeable chimney ($k_0 = 10^{-10}$ m^2). This means for instance that after the increase in hydraulic head during the explosion it doesn't grow any more at any distance r due to lateral flow. Thus we expect that the maximum water table increase at any fixed distance from the explosion is determined by the explosion amplitude and is reached at time t_1.

According to these calculations the time when the steady-state flow is established t_2 (complete leveling off of the water table rise and formation of the depression cone) doesn't exceed first tens of minutes.

At the moment of time t_2 flow regime changes because the volume of fluid reaching the drainage surface through the aquifer is no longer sufficient to provide flow due to difference in pressure head. The drainage occurs due to outflow of the fluid through the chimney wall at $r = R_0$.

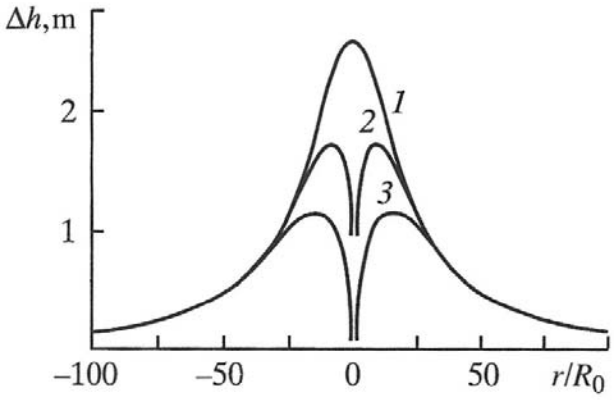

Figure 5.21: Ground water plume caused by an underground explosion q = 20 kt. Time from the explosion t, minutes: *1* – 0; *2* –3; *3* - 10.

In this case to determine a specific value of Q_1 and the spatial water level distribution we need to take into account the fact that cylindrically symmetrical fluid flow through the aquifer is superimposed on a quasi-one-dimensional fluid flow in the aquifer [I assume they mean the ambient fluid motion]. In the simplest case we assume that these modes of motion occur independently and a superposition principle applies.

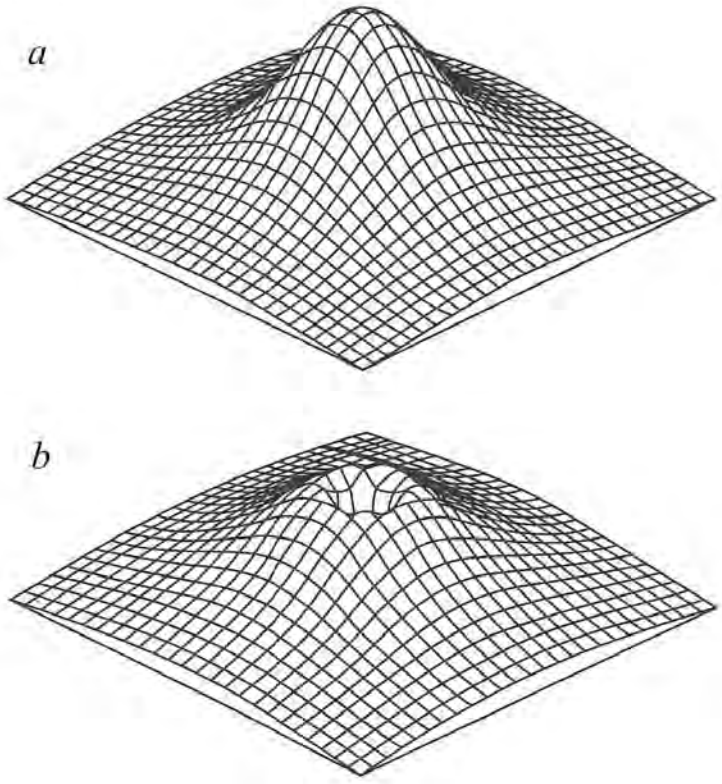

Figure 5.22. Ground water plume caused by an underground explosion q = 20 kt. Time from the explosion t: a) 0 min; b) 5 min.

Pressurized flow in water-saturated layer with a cylindrical [did they mean conical?] depression surface. As an example we consider pressurized fluid flow in a layer of thickness *a* containing a cylindrical depression surface with a radius R_0. The estimates will be performed for the case of a stationary flow using hydraulic approximation: all flow characteristics will be averaged across the layer thickness.

Using these assumptions the following model parameterization can be used. One-dimensional flow with a velocity *u* takes place in the plane (*x*, *y*) along the x-axis. At the moment of time $t = t_2$ the flow becomes complicated by initiation of a centrally symmetrical flow with velocity $u_r(r)$. In this case the resulting velocity $u_1(x, y)$ in an arbitrary point of the flow *M* (Figure 5.20) has the following magnitudes of x and y components:

$$u_{1x} = u - u_r \cdot \cos(\alpha),$$

$$u_{1y} = u_r \cdot \sin(\alpha),$$

where α is the angle between the *x*-axis and the direction to point *M*.

Applying the mass conservation law to the centrally-symmetrical flow component yields:

$$u_r(r) = \frac{Q_1}{2\pi amr}.$$

It follows from this equation that

$$u_r(R_0) = \frac{Q_1}{2\pi amR_0} = const = u_0 \text{ for } r = R_0$$

and therefore

$$u_r(R_0) = u_0 \frac{R_0}{r}.$$

Using the last two expressions and [rewriting them in Cartesian coordinates] using $\cos(\alpha) = x/r$ and $\sin(\alpha) = y/r$, where $r = \sqrt{x^2 + y^2}$, we obtain

$$u_{1x} = u[1 - \frac{\beta x R_0}{x^2+y^2}], \; u_{1y} = u[-\frac{\beta y R_0}{x^2+y^2}],$$

where the quantity β is given by

$$\beta = \frac{u_0}{u} = \frac{Q_1}{2\pi amuR_0}.$$

The equation for the flow lines

$$\frac{\partial y}{\partial x} = \frac{\beta y R_0}{x^2 + y^2 - \beta x R_0}$$

can be easily integrated and its solution is given by

$$x = y \cdot tan\left[\frac{C_1 - y/R_0}{\beta}\right],$$

where C_1 is an integration constant, which determines specific flow lines.

As an illustration Figure 5.23 shows the ground water flow lines in the vicinity of the cylindrical depression surface $r = R_0$ for several values of parameter β, which determine the relationships between the "natural" fluid discharge through unit area in the aquifer and the amount of fluid flowing into the cylindrical permeable channel. It is clear from Figure 5.23 that the flow lines in the vicinity of the depression surface are significantly curved, and the magnitude of the hydraulic head in an arbitrary point *M* determined by the flow velocity according to Equation 5.27 depends not only on the epicentral distance *r*, but also on the angle α. The last observation means that the water level in observational boreholes located at the same distance at different azimuths should be different.

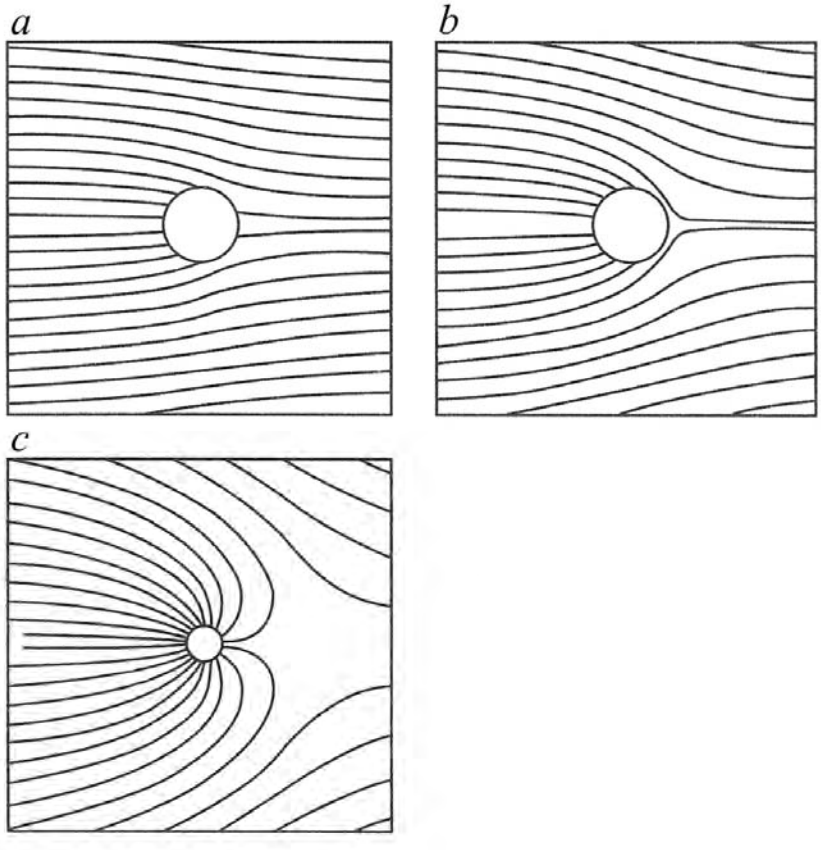

Figure 5.23. Isopiestic lines and the flow lines in the vicinity of the depression surface. The value of parameter β: *a* – 0.5; *b* – 1; *c* – 5.

The equation of the isopiestic lines (in our case the lines with the same pressure head values correspond to the pressure *P*) is given by

$$\frac{\partial x}{\partial y} = \frac{\beta y R_0}{x^2 + y^2 - \beta x R_0}.$$

It has a solution given by:

$$\frac{x}{R_0} - \beta \cdot ln\left[\frac{x^2+y^2}{R_0}\right] = C_2 = const\ .$$

Considering that the value of the constant C_2 is determined by the effective height of the aquifer h_0 we obtain the distribution of the ground water level in space in the form

$$h = \frac{\mu m R_0}{\rho g k_0}\left[\frac{x}{R_0} - \beta \cdot ln\left[\frac{x^2+y^2}{R_0}\right]\right] \cdot u + h_0\ . \qquad (5.39)$$

We note that the same solution as given by 5.39 can be also obtained by solving the stationary equation

$$\Delta h\ =\ 0$$

using the boundary conditions

$$r \to -\infty : \qquad \frac{\partial h}{\partial x} \to \frac{\mu m}{\rho g k_0} u\ ,$$ [not sure how *r* can go to minus infinity!]

$$r = 0 : \qquad \frac{\partial h}{\partial x} \to \frac{\mu m}{\rho g k_0} u_0\ .$$

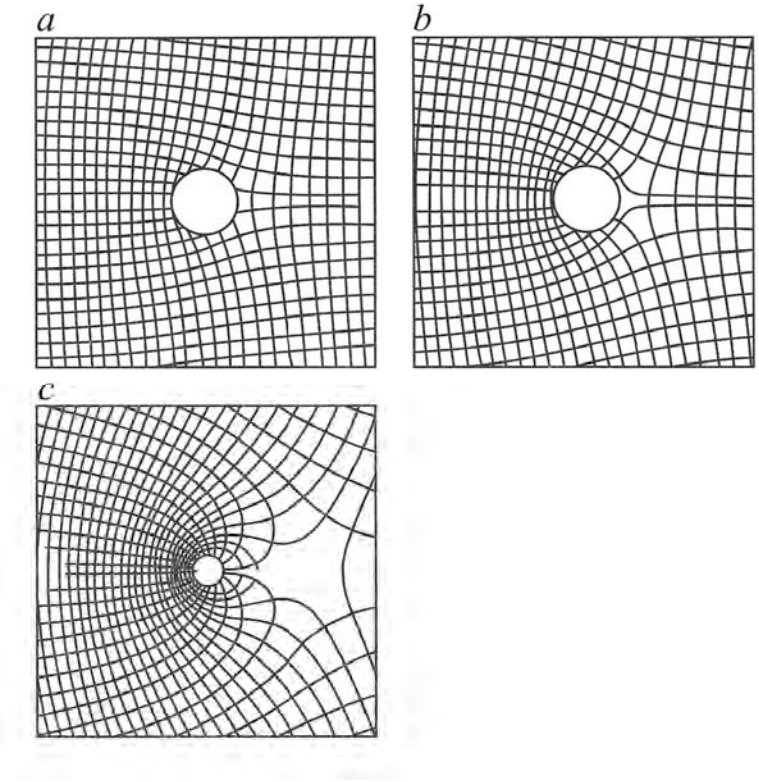

Figure 5.24. Isopiestic lines and the flow lines for ground water flow. See notation from Figure 5.23.

As an illustration Figure 5.24 shows isopiestic lines for several values of parameters. The solutions above suggest that the fluid flow in a layer with a depression surface $r = R_0$ is governed by a non-dimensional parameter $B = u/u_0$. In particular, if $\beta < 1$ the fluid flow in every point in space is predominately directed along the initial flow direction of the ground water ($u_{1x} > 0$). For $\beta = 1$ there is a point ($x = R_0$, $y = 0$) where the flow velocity is zero.

A case with $\beta > 1$ is the most interesting in practical applications. In this case there exists a region where flow $u_{1x} > 0$ (Figure 5.23). The exact value of parameter β is determined by the value of Q_1 for $t > t_2$.

In cases when either the additional hydraulic head created by an explosion is $\Delta h \ll h_0$, or when the time of the plume leveling off as a result of ground water flow is short compared to the time needed to fill the void created by an explosion, the parameter Q_1 can be estimated using the relationship:

$$Q_1 \approx \frac{2\pi a k_0 P_0}{\mu \ln(R_0/r_0)}, \tag{5.40}$$

which can be obtained by integration of Equation 5.27 in the region R_0 $r \leq r_0$, where is the radius of the recharge zone for the depression surface, and R_0 is the value of pressure in the unperturbed zone ($r \to \infty$).

In case where flow is without pressurization, instead of Equation 5.40 so-called Girinskii relationship should be used (the result of integration of Equation 6.2 in cylindrical coordinates)

$$Q_1 \approx \frac{\pi \rho g k_0 (h_0^2 - h_1^2)}{\mu \ln(R_0/r_0)},$$

where h_0 and h_1 represent values of hydraulic head for $r \to \infty$ and at the boundary $r = R_0$ respectively. In our case r_0 corresponds to distances where $u_{1y} \ll u_{1x}$.

The final stage of the water level evolution is defined by filling the voids formed by an explosion and returning to the original water table h_0. We can estimate the duration of this process using Equations 5.32 and 5.40. Indeed, if $k_0 = 10^{-11}$ m^2, $P_0 = 0.5$ MPa, $q = 100$ kt, and $\eta_0 = 10^{-3}$ the time required to fill the void space with ground water given by

$$t_3 \approx \frac{4.2 \cdot 10^3 \mu q \left(1 + 2.04 \cdot 10^3 \eta\right)}{2\pi a k_0 P_0} \ln\left(\frac{R_0}{r_0}\right), \tag{5.41}$$

is approximately 60 days.

In reality the time to restore the original water level could be significantly longer due to: a) formation of long fractures connecting to different horizons, b) colmatage or filling of the aquifer pores with suspended particles, or c) deformation of the pore structure.

Results of the field studies. Studies of the ground water reaction to large underground explosions were conducted for a long time (1983 – 1989) using a group of observational

boreholes at Balapan Testing Area of the STS. Sampling of the ground water levels was conducted periodically in 68 boreholes after 12 large-scale explosions with yields ranging between 8 and 150 kt at depths between 300 and 600 m (Table 5.5) (Adushkin et al, 1993a; Adushkin and Spivak, 1993b; Gorbunova and Spivak, 1997). During each experiment the boreholes located in the zone of influence of the explosion at distances between 0.3 and 10 km from the epicenter were studied in more detail. Figures 5.25 and 5.26 shows examples of the explosion and observational boreholes for two areas.

Table 5.5. Radius of the zones of increased permeability for some underground nuclear explosions

Test (Borehole #)	1308	1235	1414	1323
Date Yield, kt Depth, m	March 7, 1984 50 – 100 460	November 20, 1983 10 – 30 300	May 26, 1984 100 – 150 480	October 27, 1984 100 – 150 520

Test (Borehole #)	1411	1340	1348	1388
Date Yield, kt Depth, m	December 2, 1984 50 – 100 450	February 10, 1985 50 – 100 530	August 2, 1987 100 – 150 600	December 27, 1987 50 – 100 520

Test (Borehole #)	1350	1346	1352	1410
Date Yield, kt Depth, m	September 14, 1988 100 – 150 530	December 17, 1988 100 – 150 640	August 7, 1988 25 –50 550	September 2, 1989 5 – 15 400

Ground water, both pressurized and not pressurized, is abundant in the study region. Fluids occur in the zones of tectonic fracturing within the crystalline rocks of Paleozoic age. Fluid saturated horizons were uncovered at depths from 2.1 to 70 m (with hydraulic heads of 4 – 66 m).

The area of recharge for Balalpan Testing Area is located mostly in the southwest of the territory in the areas where the aquitard is exposed at the ground surface. The flow of ground water, which have a slope of 0.02 – 0.05, occurs predominately in the northeastern direction. Complex geological structure and existence of tectonic faults of different orders results in heterogeneities of rock permeability. Thus the structural blocks have transmissivity of 0.05 – 1.3 m^2/day, while in the areas near tectonic faults this value reaches 14 – 34 m^2/day.

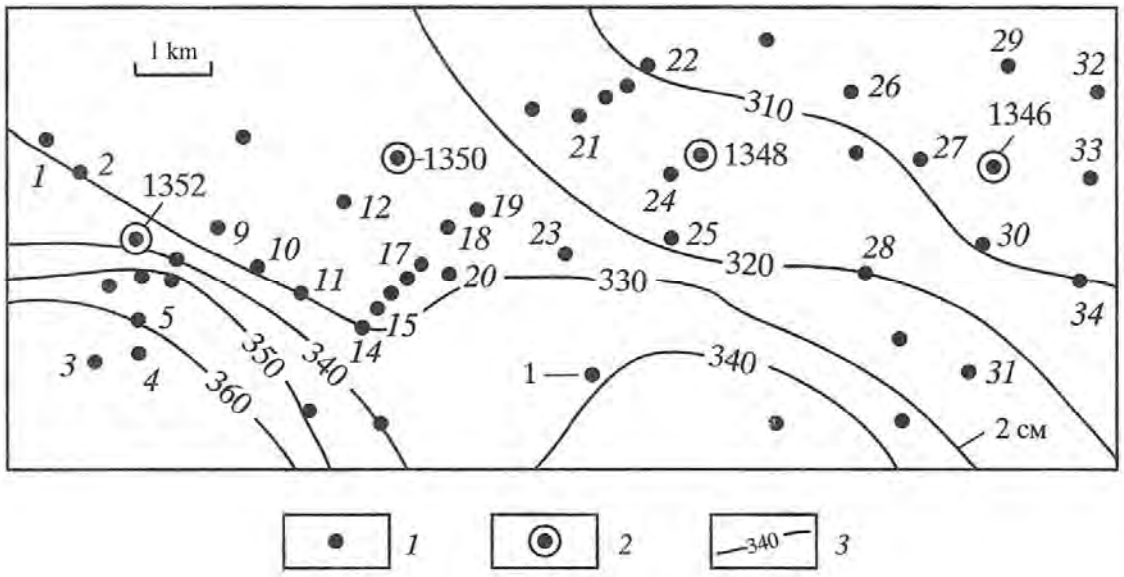

Figure 5.25: Map of the area of study: *1* – observational boreholes, *2* – charge boreholes, *3* – ground water table. Additional explanations are in the text.

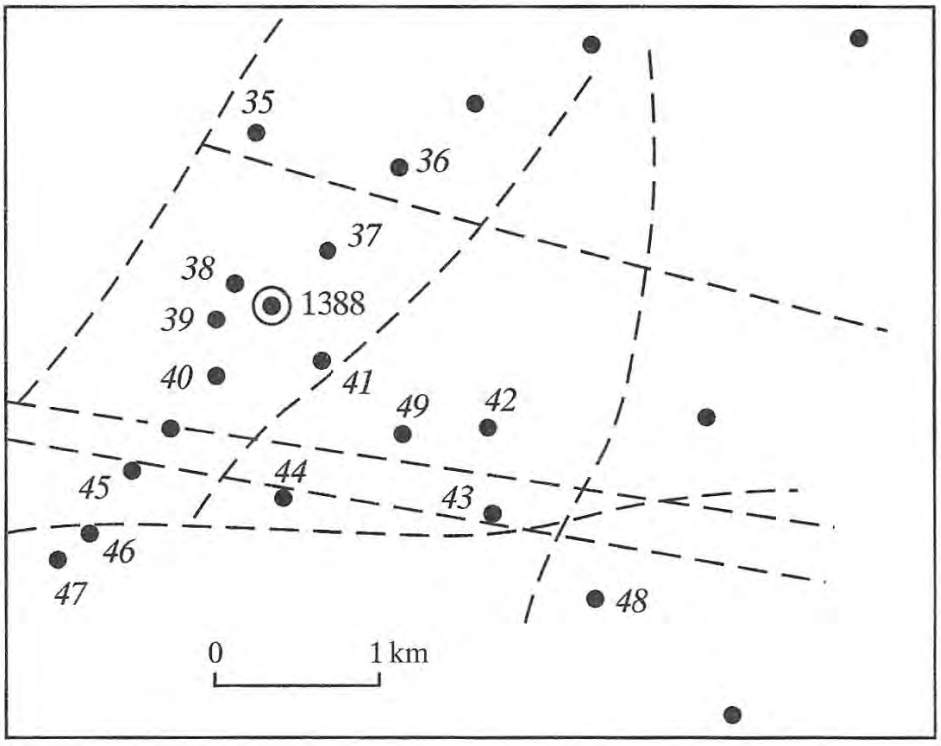

Figure 5.26. Map of the observations for testing Borehole 1388. See definitions from Figure 5.25. Dashed lines show tectonic faults.

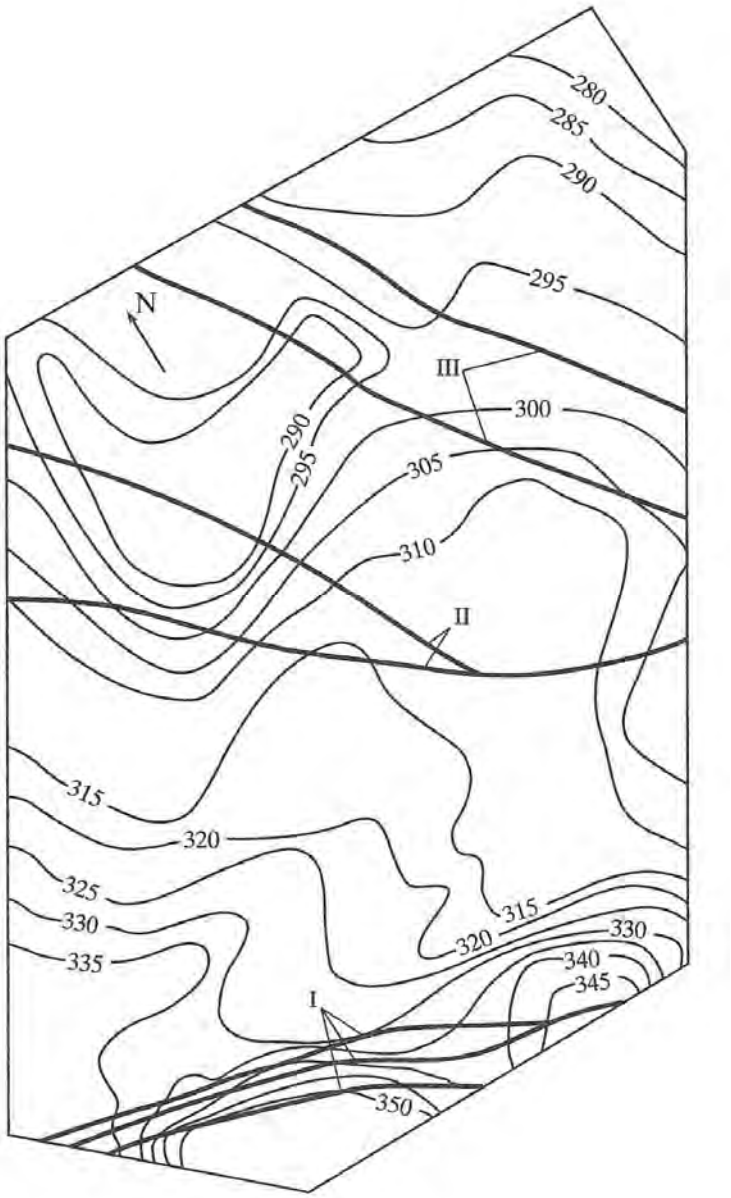

Figure 5.27. Map of the extent and flow of the ground water (isopiestic lines) for an area located at the STS. See definitions from Figure 5.25. Tectonic faults: I – Kalba-Chingiz, II – Chinrauz, III - Chagan.

According to the results of hydraulic testing the zone of near-surface fracturing contain the largest amount of water. Based on the drilling data the thickness of this zone ranges between 10 and 40 m. Based on our estimates, permeability coefficient for the structural blocks in this zone is $3 \cdot 10^{-15} \div 6 \cdot 10^{-14} m^2$.

The ground water regime is typical for plain regions. The value of the daily variations of the water table does not exceed 3 – 5 cm. Seasonal variations of the water table up to 1 – 2 m during spring and fall is common for this region.

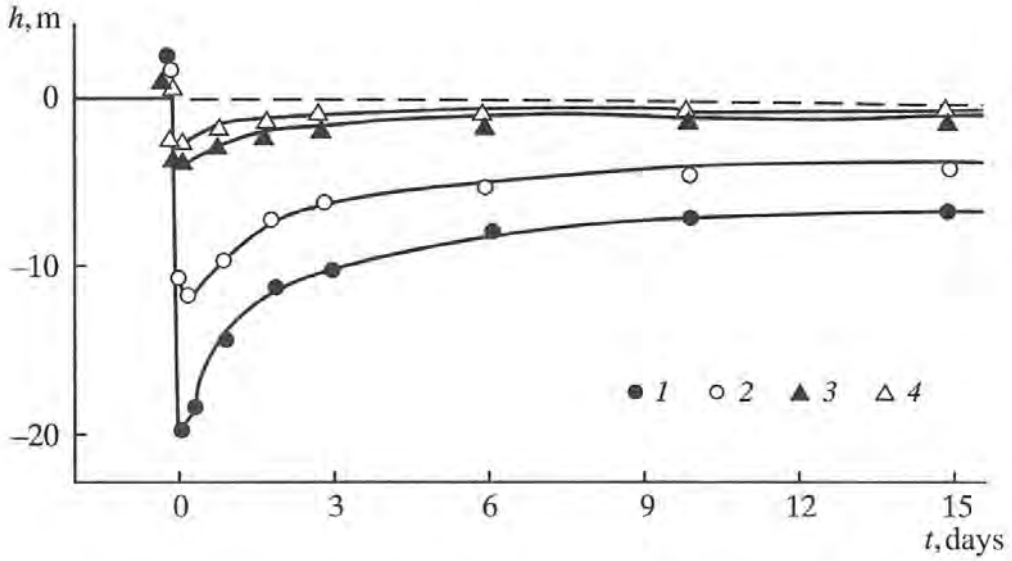

Figure 5.28. Changes of the ground water level in the observational boreholes after explosion in Borehole 1352. Epicentral distance *r* in km: *1* – 0.8; *2* – 0.5; *3* – 1; *4* – 1.57.

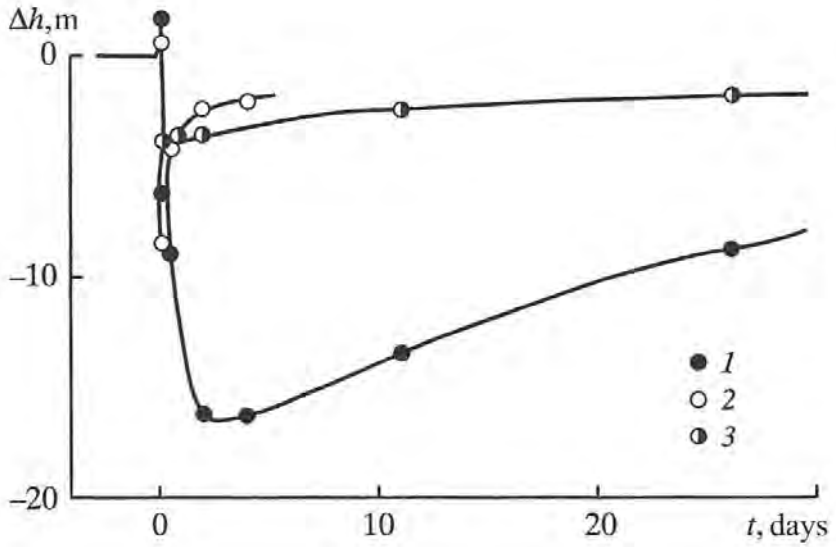

Figure 5.29. Changes of the ground water level in the observational boreholes after explosion in Borehole 1348. Epicentral distance *r* in km: *1* – 0.9; *2* – 0.93; *3* – 1.25.

A large-scale explosion causes significant changes in hydrodynamical ground water regime. Although the changes in the ground water level has complex spatio-temporal character, defined by the specific characteristics of the rock massif, distance between the observational borehole and the explosion epicenter, existence of nearby tectonic faults, the following common characteristics could be selected.

Immediately after the explosion a short-term uplift of the water table is observed in the boreholes (in some cases accompanied by water ejection). The uplift is followed by a short duration interval (0.1 – 3 day) characterized by water table reduction down to the original level or even lower. This phase is the most pronounced in close proximity to the explosion (r < 1 km), where the water level reduction may reach 40 m. This phase is followed by a stable rebound to the previous level lasting a long period of time (from 10 days to 6 months). This is illustrated in Figure 5.28 and 5.29 showing the water level changes in some of the observational boreholes following the [nuclear] explosions in boreholes 1352 and 1348.

The character of water level changes following the explosions in tunnels at Degelen is significantly more complex (Figure 5.30).

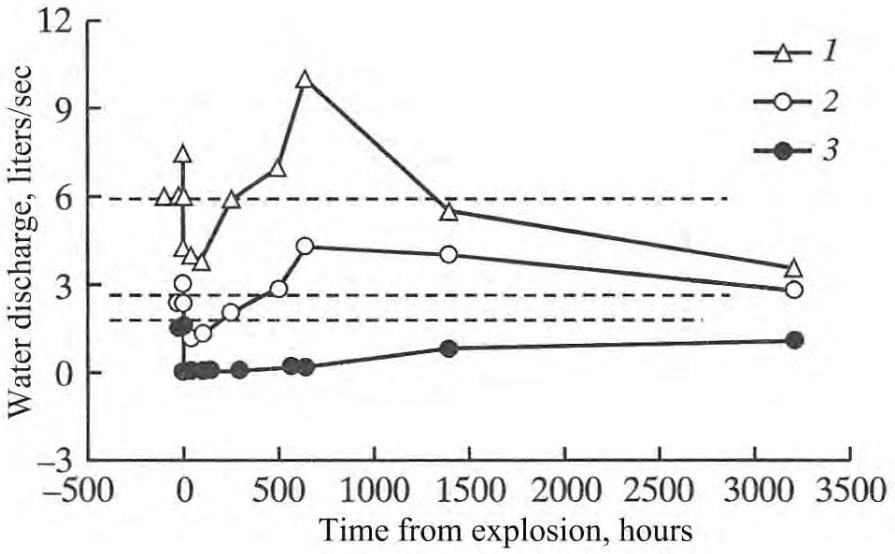

Figure 5.30: Changes of the ground water level after explosion in Tunnel 138 (June 6, 1977) conducted at Degelen Testing Area. Observations were conducted in the tunnels: *1* – #143; *2* – 504; *3* – 511.

Overall the character of water level changes in all boreholes at Balapan is similar. Amplitude of the changes is determined by the distance between the observational borehole to the explosion and azimuth α, while the specific features of the relationship $\Delta h(r, t)$ depend on the explosion yield and the structural and tectonic characteristics of the explosion site. Thus during first hours after the explosion in borehole 1352 there was 0.3 – 0.6 m decrease in the water table recorded in observational boreholes 20 and 23 located 2.2 and 3.6 km from the explosion epicenter respectively (Figure 5.25). No water level changes were observed in boreholes 13 and 17 located at distances 3.8 and 4.8 km. The water level stabilized during 30 days after the explosion (the deviation of the water level from the original level did not exceed 0.1 m).

Water ejection from observational boreholes 40 and 41 (Figure 5.26) continued for 7 hours after explosion in borehole 1388. These boreholes were located within the same structural-tectonic block as the test [explosion] borehole. In other boreholes located close to the epicenter –

36, 37, and 45 – the water level increase by 3.6 – 4.2 m was observed. During the following 24-hour interval the water level dropped to Δh = -60 m.

The variation of the piezometric surface after explosions in the observational boreholes depends on the location of the structural block containing the borehole with respect to explosion epicenters. Reaction of the aquifer to the explosion is different for the boreholes located within the epicentral structural block (in boreholes 37, 40, and 41) and the boreholes located within the zone of influence of a regional tectonic fault (boreholes 43 and 45) (Figure 5.26). Piezometric level practically didn't change in observational boreholes 36, 42 and 47 located outside of the epicentral structural block.

Table 5.6. Changes in ground water level

Borehole #	Distance *r*, km	Change in the water table level, m	
		During first 24 hours	After 6 months
30	0.96	–8.5	–1.6
29	1.28	–3.8	–0.9
33	1.29	–2.8	–0.8
32	1.65	–1.1	–0.4
34	1.73	–0.1	-
25	4.0	0	-

After explosion in borehole 1350 the maximum water level rise (Δh reached 2.5 m) was registered in observational borehole 17 (Figure 5.25). During the first hours after the explosion the water level dropped between 0.6 m (borehole 7, r = 3.3 km) and 4.4 m (borehole 12). Analysis of the water level changes after explosion in borehole 1350 suggests that the value of Δh is determined not only by the epicentral distance, but also by the hypsometric position [meaning the depth to the water table] of the [initial] level. For instance, among the boreholes (#2, 7, 9, and 13) located at similar epicentral distances from explosion IX [?] the largest drops in the water level by 6 and 10 m were observed in boreholes 2 and 9 corresponding to the lowest hypsometric position of the initial level.

During the explosion in borehole 1346 conducted 3 months after the explosion in borehole 1350 the highest increase in water level (approximately 3.4 m) was observed in borehole 26 located at the epicentral distance of r = 2 km. We note that the highest water level rise after the explosion in borehole 1350 was observed in the same borehole. Maximum water level increase in borehole 27 located within the same structural block as borehole 1346 was 1.6 m. In other observational boreholes the water level rise was insignificant (up to 0.2 m), with the exception of borehole 34 (r = 1.7 km) where the water level rise reached 1.0 m.

Maximum water level drop was observed within 24 hours from the explosion in borehole 1346 in all boreholes around the explosion epicenter (with the exception of boreholes 24 and 26

located in the zone of influence of explosion boreholes 1348 and 1350). The amplitude of the changes significantly depends on the distance *r* (Table 5.6).

During the explosion in borehole 1352 water level rose on average by approximately 0.4 m. The highest rise of the water table (1.2 m) was observed in borehole 7. The largest water level drop was detected in borehole 6 (Figure 5.25) located 0.5 km from the explosion. In other observational boreholes the maximum water level drop continued up to 24 hours after the explosion. The amplitudes of the water level changes are determined not only by the epicentral distances but also by the local structure and by specific aquifer (Table 5.7).

Table 5.7. Changes in ground water level after underground explosions

Borehole #	Epicentral distance *r*, km	Change in the water table level, m	
		During first 24 hours	After 6 months
Carboniferous Period aquifer			
8	0.5	–11.7	–1.2
2	1.0	–3.2	0.4
1	1.5	–2.3	0.4
9	1.0	–1.8	0.4
10	1.3	–0.2	-
11	2.3	–0.1	0.6
12	2.6	–0.4	0.8
13	2.9	–0.2	0.7
Cambrian Era aquifer			
5	1.1	–3.4	–1.5
4	1.5	–0.9	–0.7
3	1.6	–0.1	-
Late Paleozoic Era aquifer			
6	0.5	–15.9	–5.2
7	0.7	–19.7	–4.1

Long-term observations of the water table changes in the observational boreholes at distances over 3 – 5 km suggest disturbances to the hydrological regime over the large region. There is a strong tendency of water level to drop by 2 – 5 m after explosions, which is less pronounced in the vicinity of the recharge areas (boreholes 20, 23 in Figure 5.25).

Disturbances of the hydrological regime in the area of large-scale explosions is caused by significant changes of the rock massifs as a results of the explosions. Thus changes to hydraulic transmissivity of rocks were observed as a result of the repeated hydrological sampling (Table 5.8) after the explosion in borehole 1348. The largest changes were observed in the area with boreholes with lower water discharge. For instance the increase in transmissivity from 0.26 to

0.52 m^2/day was detected in borehole 23 (r = 2.1 km) drilled through andesite porphyrites. This corresponds to a porosity increase from 3.8% to 5.3 %. In boreholes 20 and 24 the transmissivity changed to a lesser degree (by 0.13 and 0.4 m^2/day respectively).

Table 5.8. Results of hydrological sampling before ($index_1$) and after ($index_2$) explosion

Explosion	Borehole #	Head H, m		Debit [discharge?] Q, m^3/day		Transmissivity (aK), m^3/day	
		H_1	H_2	Q_1	Q_2	$(aK)_1$	$(aK)_2$
BH 1348	24	44.4	24.2	28.5	28.5	3.9	3.51
	20	3.6	3.7	16.6	17.4	0.78	0.91
	23	19.0	17.4	7.7	4.3	0.26	0.52
BH 1388	48	-	-	34.5	35.4	3.0	3.0
	45	16.5	-	34.6	23.9	3.5	13.7
	47	61.7	61.6	19.8	16.9	1.69	1.43
	49	31.9	24.9	34.5	16.5	1.0	0.8
	42	-	-	6.8	6.2	0.16	0.16
	41	56.8	28.6	180	32.8	16.5	2.1
	40	53.2	34.6	18.0	16.4	0.7	3.38
	37	23.1	3.5	78.5	20.7	10.0	7.7
	36	14.3	22.8	31.1	50.1	3.0	6.0
BH 1350	9	12.7	9.4	27.6	27.6	1.82	1.95
	13	21.2	18.6	95.9	101.9	7.8	14.3
	12	62	57.8	9.5	9.5	0.39	0.39
	17	4.6	0.4	233.3	159.8	30	35.1
BH 1352	7	57	50.5	63.9	108	2.6	7.7
	6	53.4	46.5	1.04	0.03	0.02	0.0
	5	4.0	2.6	144.3	127.8	18.1	18.5
	9	9.4	9.1	27.4	36.0	1.5	2.1
	8	42.9	41.4	19.0	24.2	0.72	0.91
	1	27.1	29.1	190	173	27	24
	10	23.7	27.1	0.55	5.2	0.02	0.2
	11	58.3	59.5	0.17	0.28	0.01	0.01

After the explosion in borehole 1350 the transmissivity didn't change in borehole 12 located close to the epicenter (r = 0.8 km). This borehole was drilled through low-permeability tuff. Insignificant increase in transmissivity (by 15%) was observed in borehole 17 (r = 1.3 km) due to a formation of the new recharge zone in the depth interval 52 – 54 m according to the hydraulic testing results). The largest increase in transmissivity (by 83%) was observed in borehole 13 (r = 2.2 m). Based on the results of the hydraulic testing this increased is explained by significant permeability increase for the water-saturated tuffaceous sandstones caused by the explosion. The results of more detailed geophysical survey confirmed these rock property changes. For instance the apparent resistivity decrease by 38 % was observed during the geophysical survey.

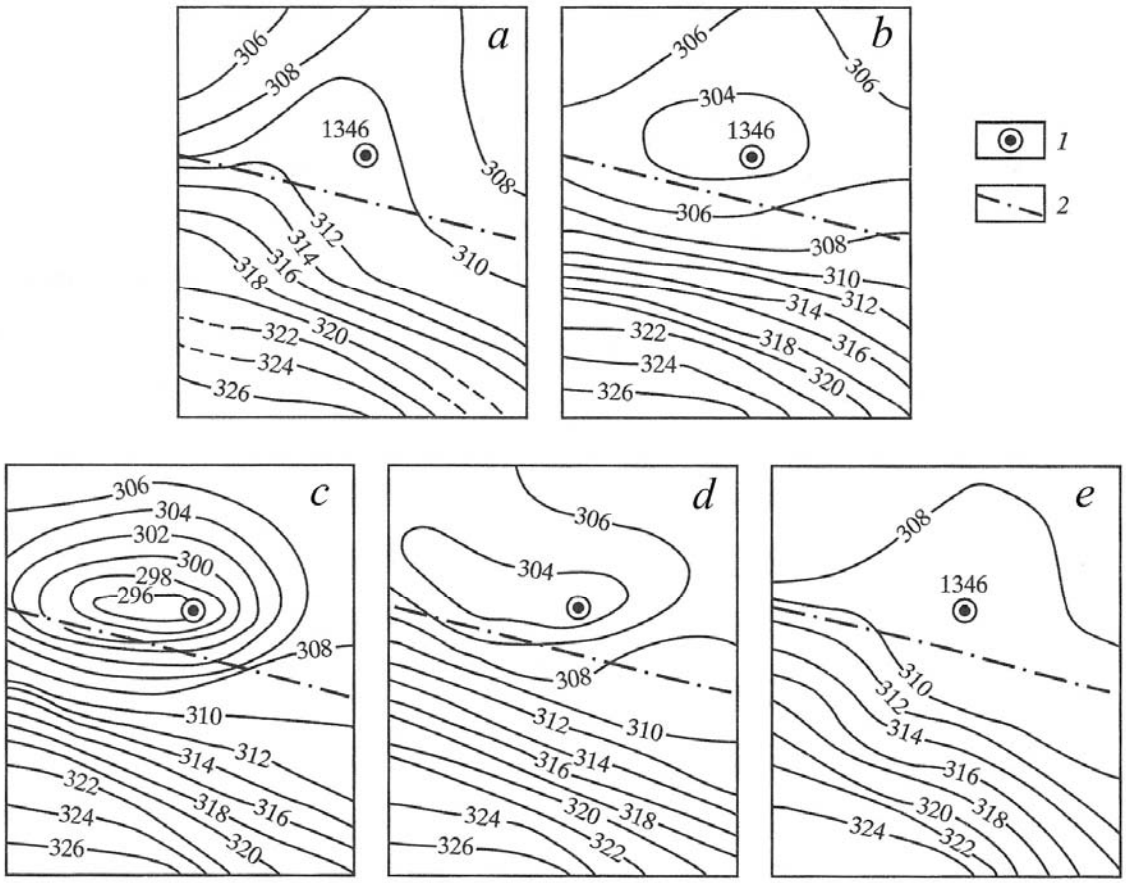

Figure 5.31. Map of the isopiestic lines in the area of the nuclear explosion in borehole 1346 (December 17, 1988): a) before the explosion; b) 5 hours after the explosion; c) 4 days after the explosion; d) 1 month after the explosion; e) 7 months after the explosion. *1* – explosion epicenter; *2* – deep tectonic fault.

Detailed hydrological survey of the observational boreholes have shown another effect: in addition to changing permeability of the water-containing rocks some boreholes also show shift in the recharge intervals. Thus after the explosion in borehole 1388 the main recharge was observed in the depth interval at 61 m (the initial recharge was registered in the interval 40.8 – 53 m). An additional recharge interval with transmissivity of 9.1 m^2/day was detected in the interval 73.5 – 77 m. These changes in the recharge horizons can be attributed to creating new hydraulic connections between closely located fractures within the zone of tectonic fracturing, or by formation of a direct fracture to the surface as a result of the explosion.

Overall the disturbances of the hydrological regime as a result of underground nuclear explosions can be observed up to distances of 10 km from the explosion epicenter. Depression cones can be clearly seen in the epicentral zone. Figure 5.31 shows an example of isopiestic lines for ground water levels for several moments of time after the underground nuclear explosion in borehole 1346.

Chapter 6.

Laboratory studies of irreversible deformation by explosions in solid media

6.1. The stress wave from a fully contained explosion

The inelastic deformation of the solid medium during explosions is one of the major manifestation of the explosion, the consequences of which include extensive irreversible changes to the medium in the vicinity of the explosive source, including formation of the cavity, the damage zone, etc.

For explosions in gas and liquid the parameters of medium motion are the defining characteristics of the explosion scale and intensity. Therefore study of the laws of motion produced by explosions in weakly cohesive (e.g. gas or fluid) media is the first priority. However, it is impossible to fully quantify underground explosions in solid media using only the parameters related to medium deformation, since there is the complication of inelastic deformations. Study of the kinematics of the motion in this case is useful only to determine seismic characteristics of the explosion source.

Nevertheless, in the study of explosion source processes, determining the characteristics of the deformation of the solid medium provides information (of both a qualitative and a quantitative nature) on relationships between the parameters needed to describe different effects of explosions, including damage to the emplacement medium. In addition, knowing the laws of the medium deformation allows us to describe the explosion source processes in a single framework using a small number of governing parameters. The latter significantly simplifies the description and prediction of the most important explosion phenomena in solid media.

An electromagnetic method to record the medium particle velocity was developed in the Institute of Dynamic of Geospheres [IDG] (Spivak, 1973; Spivak and Tsvetkov, 1973). This method allows for high precision measurements of the deformation parameters during laboratory experiments with chemical explosives.

Across the range of phenomena, a fully contained explosion with a large depth of burial (DOB) allows for the simplest description. In this case we assume that the event takes place in an infinite medium and spherical symmetry can be applied.

The development of a nuclear explosive source in time is accompanied by reduction of the material density in the cavity during cavity expansion. In addition, a shock wave of high amplitude propagates in the zone adjacent to the charge cavity, creating gas products that act as a working body, exerting mechanical work due to vaporization and chemical decomposition. Therefore, the charge cavity cannot be treated as the explosion source, as can be done for chemical explosions.

Determining the extent of the source is in this case related to analysis of the changes of explosive characteristics while varying the volumetric energy density. There are two ways to change the energy density of the charge during small scale experiments with high explosives

(HE): first, using HE with different energy content per unit volume; and second, placing HE into a cavity of fixed volume. The first case corresponds to use of fully tamped charges, the second case entails cavity decoupling. The effective charge density is determined similarly in both cases: $\rho_1 = q/V_0$, where V_0 is the volume of the charge cavity. However, the two cases are characterized by very different conditions of energy transfer (i.e., coupling) into the emplacement medium, even for the same values of the parameter ρ_1.

We note that study of the explosion source using microexplosions in rocks encounters numerous difficulties because the sensors have to be placed inside the rock samples causing damage to the rock. Therefore, rocks are rarely used to conduct small scale laboratory experiments (with HE). Usually some homogeneous material suitable for laboratory experiments is used for these purposes, with properties similar to those of rocks. Such materials include rosin, sodium thiosulphate and clear acrylic glass or polymethyl methacrylate (PMMA) known in Europe under its brand name Plexiglas.

Our experiments were conducted using fully tamped spherical PETN (Pentaerythritol Tetranitrate, $C_5H_8O_{12}N_4$) charges with weights between $1.7 \cdot 10^{-4}$ to $2.6 \cdot 10^{-4}$ kg. The density of PETN is 1500, 1000 kg/m^3 (compressed PETN), 400 kg/m^3 (loose PETN [pellet or powder?]) and 500 kg/m^3 (a different type of powdered PETN, double processed???).

Measurement results have shown that the deformation region can be divided into two distinct zones. At distances less than a certain value, $R_{*,}$ the material particles move predominately away from the source. A typical velocity record in the near-source zone is shown in Figure 6.1 a. At distances $r > R_*$ the returning motion becomes visible (Figure 6.1b). The amplitude of the returning motion grows, becoming more prominent with increasing distance. The characteristic radius R_* is 11 – 13 times the charge radius for sodium thyosulphate, and 4 – 5 times the charge radius for PMMA.

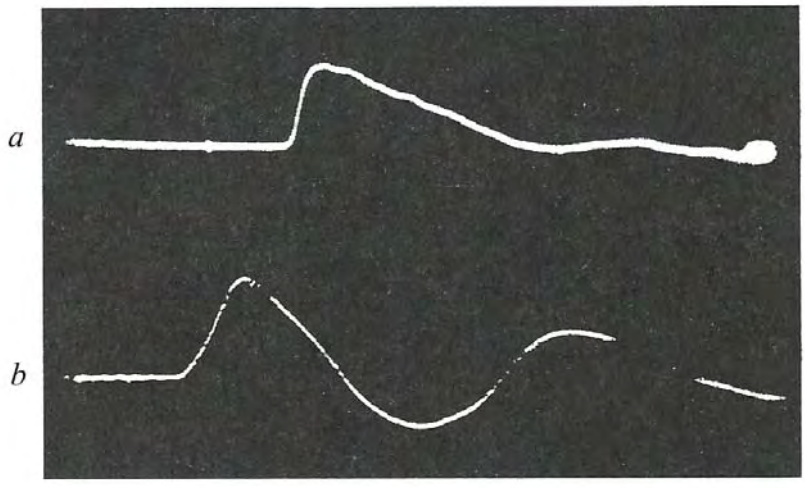

Figure 6.1: Records of particle velocities: a) in the near field, and b) in the far field.

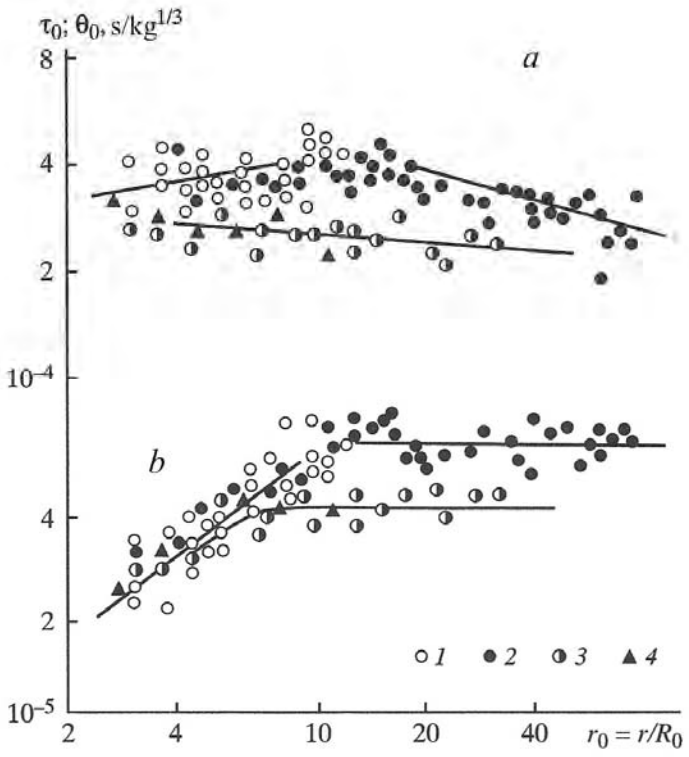

Figure 6.2: a) Duration of the positive phase and b) rise time in thiosulphate (symbols *1* and *2*) and PMMA (symbols *3* and *4*) for chemical explosions with the explosive density of 1500 kg/m^3. The charge weights are: 1 – 7.8·10^{-4} kg, 2 – 1.7·10^{-4} kg, 3 – 4·10^{-4} kg, and 4 – 2.6·10^{-4} kg.

Particle velocity records show that the positive particle acceleration exceeds the negative acceleration by a factor of 6 – 7. This is clearly observed in Figure 6.2, which shows the scaled rise times $\theta_0 = \theta/q^{1/3}$ (lines *b*) and the duration of the positive phase $\tau_0 = \tau/q^{1/3}$ (lines *a*) as a function of scaled distance $r_0 = r/R_0$, where R_0 is the charge radius. We note that the positive phase duration exceeds the rise time by almost an order of magnitude.

Despite the fact that there is a clear region of damage, velocity records do not show any evidence of irreversible damage of the material. This shows that either material damage does not break the continuity of motion, or the changes of parameters across the damage front (if it is observable) are negligible.

We shall use the following notation: $v_0(r)$ for the maximum particle velocity (it could also be called peak particle velocity or PPV) in the stress wave at distance r from the explosion, R for the radius of the wave front (the surface in which the medium particle reaches its maximum velocity at a given time), $u_0(r)$ for the maximum particle displacement in the stress wave at a distance r from the explosion, so

$$r_0 = r/R_0,\ r_* = R_*/R_0,$$

where R_0 is the charge radius.

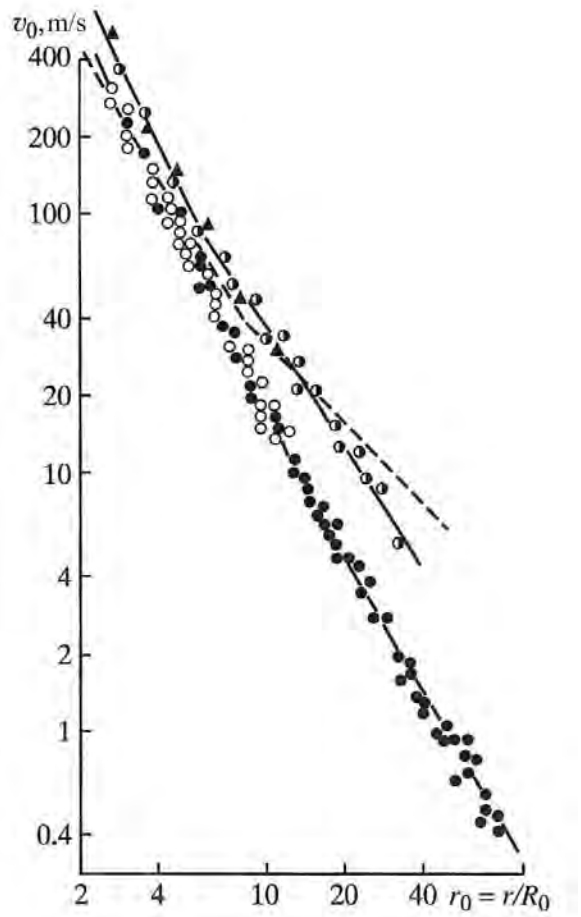

Figure 6.3: Maximum particle velocities in thiosulphate (symbols *1* and *2*) and PMMA (symbols *3* and *4*). The notations are the same as in Figure 6.2. Dashed line shows maximum particle velocities in rosin.

Figure 6.3 shows the maximum particle velocities as a function of distance for a charge with density 1500 kg/m^3. The figure shows that two zones with different wave attenuation as a function of distance are observed, for both sodium thiosulphate and PMMA. The attenuation is stronger in the near-source zone to distances $r_0 < 12.5$ for the first medium, and $r_0 < 5.5$ for the second medium, than it is further away from these sources. We note that the particle motions begin showing the returning motion at approximately the same distances. The proposed physical meaning of the boundary $r = R_*$ will be addressed later.

The following relationships for the maximum particle velocity as a function of distance were obtained as a result of analysis of the experimental data:

$$v_0 = \begin{cases} a_0 r_0^{-n_0} \text{(m/s) for } r_0 < r_* \\ b_0 r_0^{-p} \text{(m/s) for } r_0 > r_* \end{cases} \tag{6.1}$$

The values of the constants a_0, b_0, n_0 and p are provided below.

	a_0	b_0	n_0	p	F_0	S_0
Thiosulphate	2300	760	2.16	1.71	0.23	1.88
PMMA	3400	1250	2.14	1.57	0.17	1.57

The results in Figure 6.3 show that maximum particle velocity values, recorded for explosions with different charge weights, collapse to a single line in scaled coordinates. This observation once again supports the validity of the principle of geometrical similarity for estimation of wave motion from contained explosions of different sizes.

The measurements of the maximum velocity for explosions in rosin are also shown in Figure 6.3. Similar to other media the explosions in rosin produce two zones with distinct character of the relationship $v_0(r)$. We also note that despite significant differences in mechanical properties for these media, the magnitude of the velocity and the character of its change with distance in the near-source zone are very similar for all three media. Away from the sources, however, the character of the wave attenuation in these media is significantly different.

The lack of sensitivity of the amplitude and the decay rate in the near-source zone to the medium properties, limits the possibility of using the explosion characteristics to determine the degree of fragmentation for different materials. As we have just seen, the motion parameters for explosions in different media are almost the same (close to the source). However, to determine the energy and integral damage characteristics of the rock massif, knowledge of the parameters of deformation is very useful.

Waves propagating through the medium cause displacement of the medium particles from their initial position. Using velocity records one can find the displacement at every point in space and time:

$$u(\omega) = \int_0^{\omega} v d\omega,$$

where $\omega = t - r/c$ is the time of the wave arrival at a given distance r, and v is the particle velocity.

Figure 6.4 illustrates the displacement histories $u(\omega)$ for specific distances in sodium thiosulphate (charge density – 1500 kg/m^3). The experimental points are not shown for the time interval $\omega \leq \tau/4$ because they are well fit by the averaging curves, shown with solid lines.

Of particular interest is the joint analysis of the maximum u_0 and the residual displacements w in the medium, caused by an explosion. Since the returning motion for $r \leq R_*$ is negligible, the following relationship holds in the near-source zone:

$$u_0 = \int_0^{\omega} v d\omega = \int_0^{\infty} v d\omega = w.$$

For $r > R_*$ the residual displacement is smaller than maximum because of the returning motion. Maximum displacements in the medium obtained by numerical integration of the particle velocities are shown in Figure 6.5. They are described in the entire range by a single relationship:

$$u_0/q^{1/3} = F_0 r_0^{-S_0} \text{ (m/kg}^{1/3}\text{)}.$$

The values of the constants F_0 and S_0 were provided earlier.

The residual displacements from the explosions (w) are shown in Figure 6.5 for thiosulphate only. However the following relationship holds for both sodium thiosulphate and PMMA:

$$w = u_* \left(\frac{r}{R_*}\right)^{-2.7},$$

where u_* is the maximum displacement of the boundary $r = R_*$.

The values of v_0 and u_0 for sodium thiosulphate as a function of scaled distance recorded for explosive charges with density of 400, 500 and 1000 kg/m^3 are shown in Figures 6.6 and 6.7. The dashed lines show results for the wave amplitudes for a charge density of ρ_1 = 1500 kg/m^3. We note that amplitude of motion in the medium decreases as the charge density decreases, which follows from the solution of Riemann boundary problem.

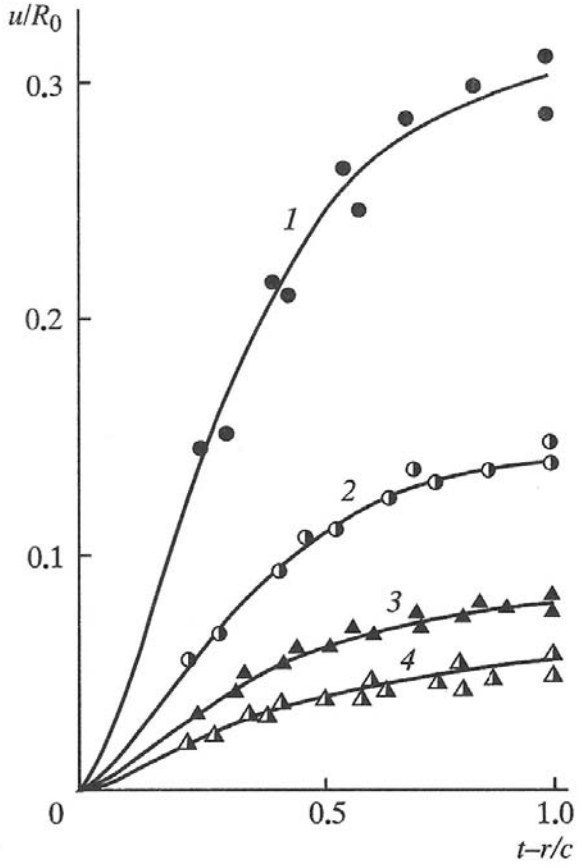

Figure 6.4: Relative particle displacement in the stress wave with time, measured at the following relative distances r/R_0: 4 (*1*), 6 (*2*), 8 (*3*), and 10 (*4*).

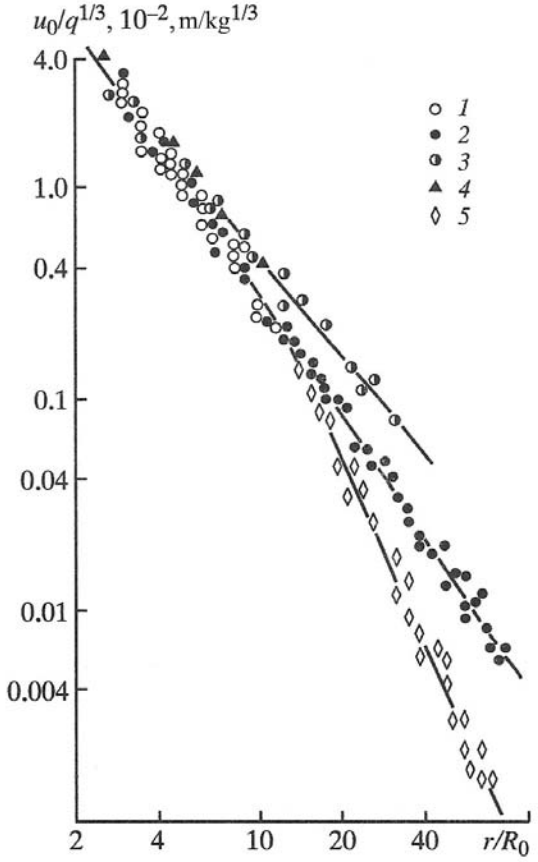

Figure 6.5: Scaled maximum (*1 – 4*) and residual (*5*) displacements caused by an explosion in the medium. Same notation as in Fig. 6.2.

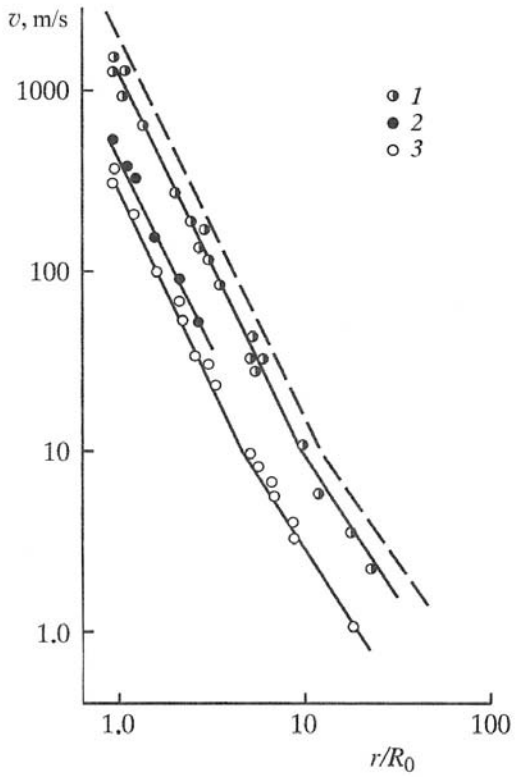

Figure 6.6: Maximum particle velocities in sodium thiosulphate for explosions of chemical charges with the densities: *1* – 1 kg/m^3, *2* – 0.5 kg/m^3, *3* – 0.4 kg/m^3. The dashed line shows the results for the explosives with the density of 1500 kg/m^3.

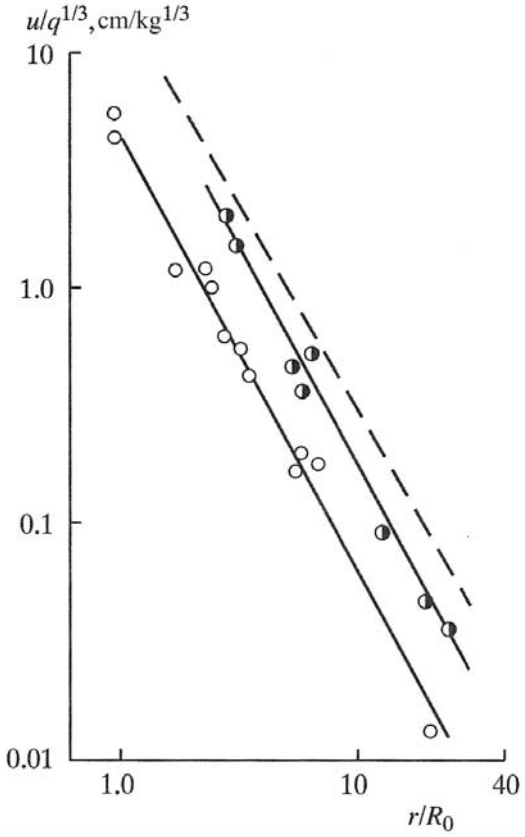

Figure 6.7: Scaled maximum displacements caused by an explosion with charges of different densities. Same notation as in Figure 6.6.

As we noted earlier, particle motion records do not show any discontinuities due to effects of medium damage. In other words, the motion of each individual element of the medium with time is smooth. However, this does not mean that the damage cannot express itself in spatial distribution of the explosive motion. Since each electromagnetic sensor inserted into the medium detects some averaged particle velocity along its spatial dimensions, the obtained velocity records cannot give the exact motion of each individual material fragment formed as a result of the explosion.

Thus the electromagnetic method measures only some averaged particle velocity at a fixed distance *r*. Additional averaging results from the fact that due to a small number of sensors we cannot record the motion of each particle, even though each sensor records the motion of the fragment to which it attached.

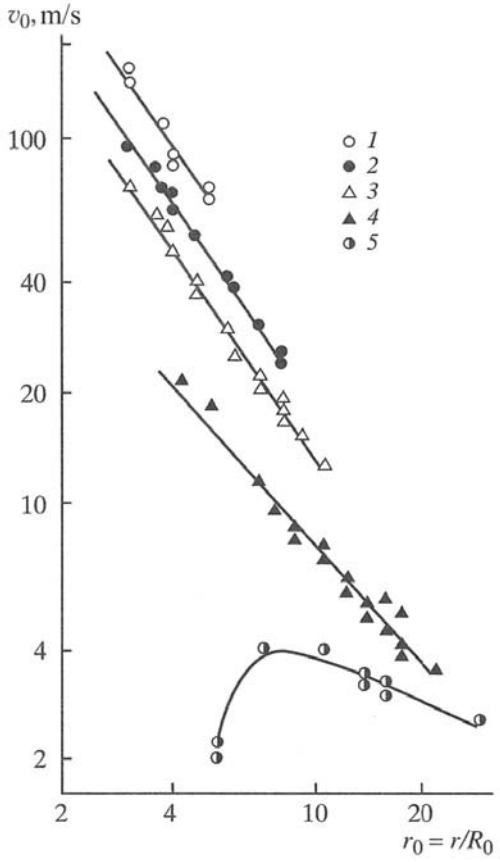

Figure 6.8. Distribution of particle velocities behind the wave front, recorded at the following relative distances r/R_0: *1* – 5, *2* – 8, *3* – 11, *4* – 22, and *5* – 27.

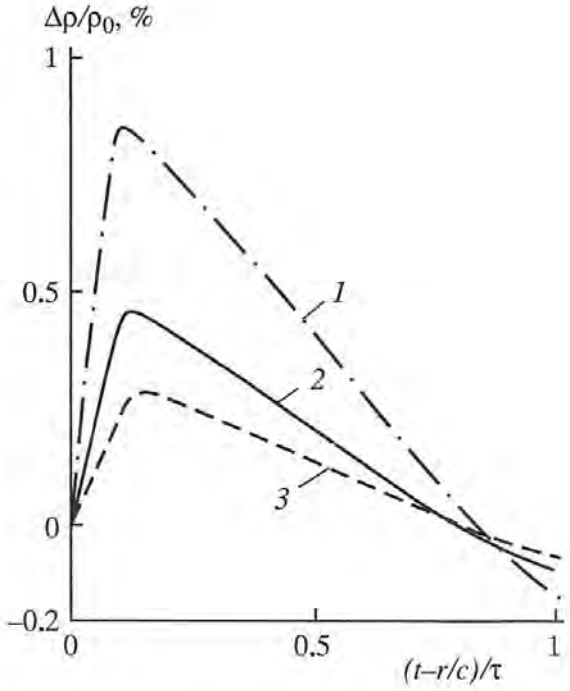

Figure 6.9. Density changes in the stress wave measured at the following relative distances r/R_0: *1* – 6, *2* – 8, *3* – 10. The measurements were conducted in thiosulphate with a density of 1500 kg/m^3.

Distribution of particle velocities behind the wave front can be plotted at each moment of time at different distances from the explosion. The results in Figure 6.8 for thiosulphate (charge density 1500 kg/m^3) show that the spatial velocity distribution does not have any significant features (such as inflections or jumps), which could be correlated to the location of the damage front at a given moment. The distribution *v(r)* is smooth (up to the measurement precision), and is given by the following relationship near the wave front:

$$v(r) = v_0(R)\left(\frac{r}{R}\right)^{-k_0}. \qquad (6.2)$$

Equation 6.2 is satisfied in the entire region where $R \leq 15R_0$. The exponent k_0 in this case is close to 1.4. For $R \geq 15R_0$ the value of the parameter k_0 decreases with increase of the wave front radius.

The loss off cohesiveness and formation of block structure due to an explosion in an initially continuous medium inevitably leads to changes in the medium density. The density change can be addressed using particle velocity data.

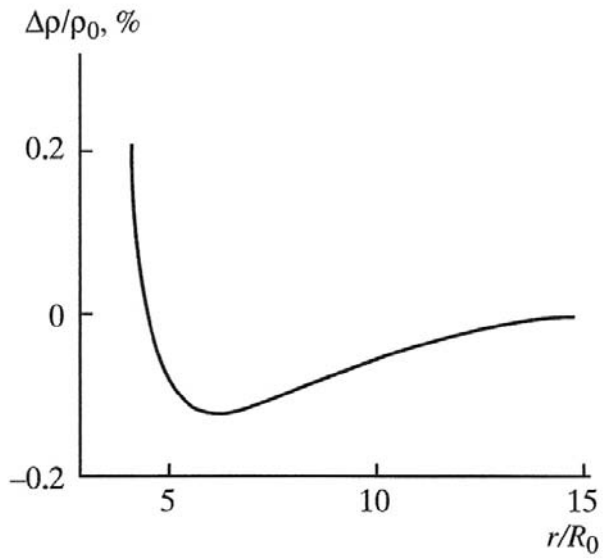

Figure 6.10. Residual density in thiosulphate after an explosion having an explosive density of 1500 kg/m^3.

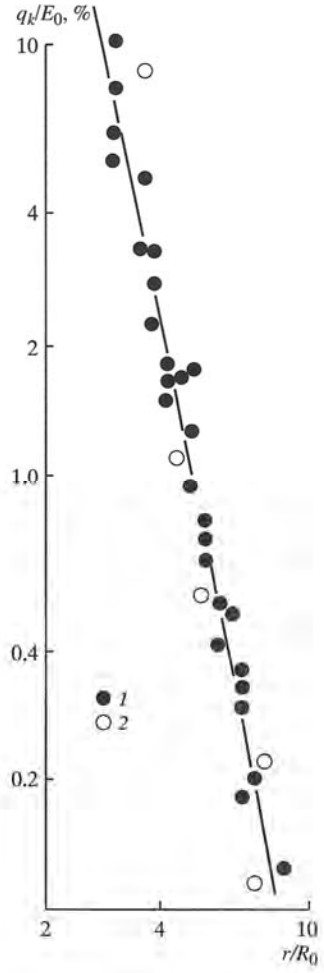

Figure 6.11. Kinetic energy flux during an explosion in thiosulphate (*1*) and PMMA (*2*) (explosive density – 1500 kg/m^3).

Using the known (measured) particle velocity field at each moment of time, it is easy to determine the material density $\rho(\omega)$ at a given distance from the explosion. From the mass conservation law we have:

$$\rho(\omega) = \rho_0 \left(1 + \frac{u}{r}\right)^{-2} \left(1 + \frac{\partial u}{\partial r}\right)^{-1}.$$

Figure 6.9 shows the variation of the quantity $\frac{\Delta\rho}{\rho_0} = \frac{\rho}{\rho_0} - 1$ with time for some distances r. We note that the maximum material compaction caused by explosion is reached for $\omega \sim \theta$, or at the moment when the maximum particle velocity is reached. Then the density drops, and by the end of the wave motion the material dilates. The final density distribution as a function of distance is shown in Figure 6.10, which shows that the medium dilates in practically the entire zone $r < R_*$

(taking into account the fact that the final cavity radius is $3R_0$). The degree of dilation decreases as we approach the boundary $r = R_*$.

Shock wave propagation inevitably leads to energy redistribution in space. Changes in the energy flux with increasing distance reflect the geometrical spreading of the wave (factor r^{-2}) , as well as the rate of energy dissipation near the source. The flux of kinetic energy of the shock wave through the surface characterizes the wave amplitude decay with respect to kinetic energy:

$$q_k = 4\pi r^2 \int_0^\tau \rho v \frac{v^2}{2} d\omega.$$

The quantity q_k, normalized to the total explosion energy E_0 and calculated using the velocity records assuming $\rho \approx const$, which as we saw earlier is not far from reality, is plotted in Figure 6.11. The value for both media – sodium thiosulphate and PMMA – is described by a single empirical relationship (for the charge density of 1500 kg/m^3):

$$\frac{q_k}{E_0} = 40 r_0^{-4.2} \ (\%).$$

6.2. The stress wave from underburied (shallow) explosions

The presence of a free surface close to the underground explosion source adds complexity to the wave motion analysis (e.g. Spivak, 1974). The rarefaction phase, forming when the stress wave reaches the free surface, causes weakening of the downgoing wave and produces a tangential component of motion in the near surface. Thus, explosions near the free surface produce both P and S waves (even in a homogeneous half-space). Nevertheless, it is possible to select a zone around a shallow explosion where the free surface does not play a significant role on the geometry of the deformation front. For a near-surface explosion, this zone is bounded by a conical surface with the vertex in the explosion center and an angle of π/2 (assuming that the compression and the rarefaction waves have the same speed).

The existence of the mentioned zone allows us to study the downgoing wave independently from processes that take place near the surface, where the longitudinal and transverse components of motion overlap. However this approach is valid only for shallow charge depth, for which the loading and unloading fronts are similar.

The presence of a free surface substantially changes the shape and the main parameters of the seismic signal propagating into the medium. This changes dissipation processes within the stress wave. We note that artificial creation of free surfaces close to the charge in laboratory experiments caused significant changes in the source parameters: the amplitude of the source remains the same, but the signal duration increases. The presence of a free surface near the source is just one example of a “strong” spatial heterogeneity, which in general influences the parameters of seismic waves. Allowing for the effect of heterogeneities is important in the estimation of explosion parameters.

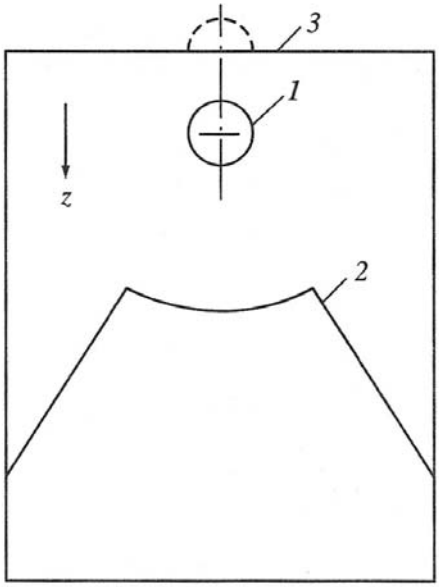

Figure 6.12: Experiment schematic: *1* – chemical explosive charge, *2* – electromagnetic sensor, *3* – free surface.

Table 6.1. Empirical coefficients for shallow explosions in laboratory experiments

Parameter	Sodium thiosulphate			PMMA	
η	-0.5	0	1	-0.5	0
a_1	2800	2700	2500	-	3500
b_1	440	600	700	870	1050
n_1	2.57	2.34	2.22	-	2.28
p_1	1.71	1.69	1.7	1.54	1.53
r_*	9	10.5	11.5	4	5

The study we have presented used small scale experiments to determine the effects of the free surface on the wave motion. The experimental design is schematically is shown in Figure 6.12. The HE charge was placed close to the free surface at different scaled distances $\eta = h/R_0$, where h is the distance from the charge center to the free surface.

The stress wave propagating into the medium was recorded inside the unloading cone above the source. Spherical PETN charges were used for most of the experiments, though semi-spherical surface charges ($\eta = 0.5$) were sometimes used.

The velocity records for shallow charges do not differ qualitatively from those for fully contained charges, and therefore are not shown here. We note that for an explosion at the free surface the returning motion phase is present throughout the medium, unlike the case of fully contained charges ($\eta \rightarrow \infty$).

Figures 6.13 and 6.14 show experimental values of the maximum particle velocities as a function of distance from the charges. The analytical expressions for these relationships are given by:

$$v_0 = \begin{cases} a_1 r_0^{-n_1} (\text{m/s}) \text{ for } r_0 < r_* \\ b_1 r_0^{-p_1} (\text{m/s}) \text{ for } r_0 > r_* \end{cases}.$$

The values of the constants a_1, b_1, n_1 and p_1 are shown in Table 6.1.

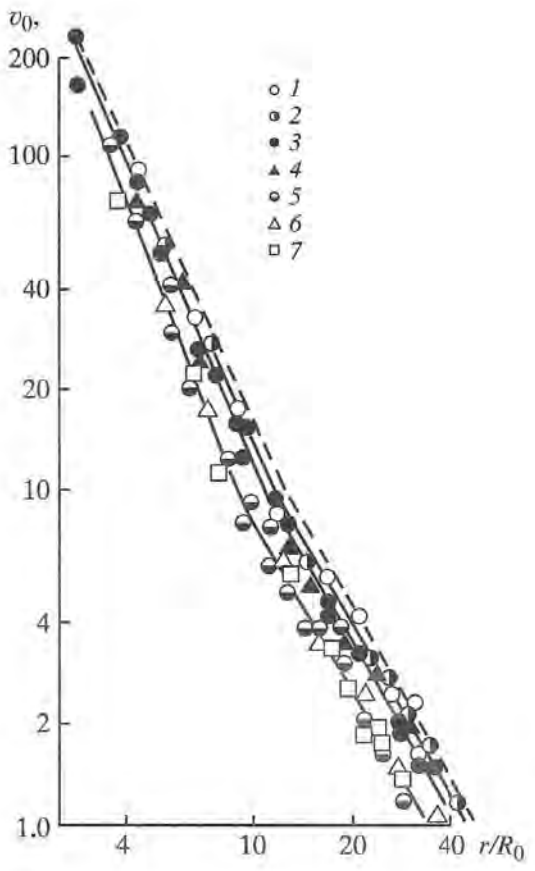

Figure 6.13. Maximum particle velocities for shallow (underburied) explosions in sodium thiosulphate as a function of the scaled distance. The weights of the charges are: 0.78 g for curves *1*, *3*, *5* (η = 1, 0, and –0.5 respectively); 0.4 g for curves *2*, *4*, 6 (η = 1, 0, and –0.5 respectively); and 2.6 g for curve *7* (η = –0.5). The dashed line shows the results for a fully contained explosion ($\eta \to \infty$).

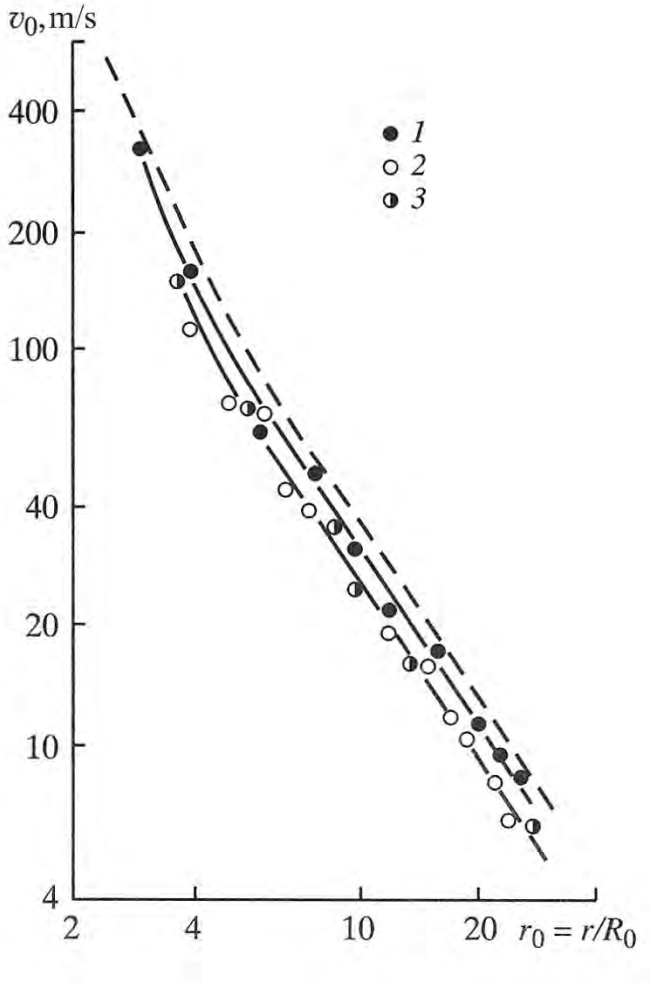

Figure 6.14. Maximum particle velocities for explosions in PMMA: *1* for η = 0, q = 0.78 g; *2* for η = -0.5, q = 0.78 g; *3* for η = -0.5, q = 0.4 g

We note that for underburied explosions the value of the coefficient a_1 does not correspond to a particle velocity at the boundary between the charge and the medium, because the distribution of the particle velocities regardless of their depth of burial coincides with the case

$\eta \rightarrow \infty$ in the region $r_0 < a_*$, where a_* is a function of the parameter η. Indeed, a shock wave forms as a result of a discontinuity at the boundary between the charge and the medium, and its amplitude is determined by the properties of the medium and the explosives.

Thus, before the moment of the wave arrival from the surface (rarefaction phase), the amplitude in the medium does not depend on the charge depth. The amplitude of the direct wave is equal to the amplitude generated by a fully confined explosion. Since the rarefaction wave reflected from the free surface propagates with the elastic velocity in the stressed medium (behind the compression front), which exceeds the elastic wave velocity in the un-stressed medium, we observe additional attenuation for the wave caused by the presence of the free surface beginning at a distance equal to a_*, compared to the case where $\eta \rightarrow \infty$. Particular values of the parameter a_* are determined by the depth of burial, and by the time of the reflected wave arrival at the boundary between the charge and the medium. The values of the parameter a_* calculated using the empirical relationships from Figures 6.13 and 6.14 are provided below.

	Sodium thiosulphate		PMMA		
η	-0.5	0	1	-0.5	0
a_*	1.6	12	2.8	–	1.4

The arrival of the rarefaction wave back to the explosion source causes significant reduction in the wave motion compared to the case $\eta \rightarrow \infty$. The closer the source is located to the free surface, the more significant is the effect of the reflected arrival on the signal duration. Thus, the amplitudes from explosions with different depths of burial in the region bounded by $r < a_*$ are similar, while the signal durations for the first peaks are different. Shorter waves correspond to shallower depths of burial (because the time delay between the direct and the reflected pulses is shorter in this case). Because of this the wave amplitudes from explosions with different depths of burial are reduced differently in the region $r < R_*$. As we expect, the short wavelengths attenuate faster than the longer wavelengths.

The relationships between the maximum particle velocities and distance are shown in Figures 6.15 and 6.16. The scaled durations of the positive phase are shown in Figure 6.17 and 6.18. Analysis of the experimental data shows that the free surface has a stronger effect on the wave duration than on the peak particle velocity. Assuming that the principle of “energetic similarity” applies to the explosion wavefield even if the free surface is present, we shall formally define the efficiencies of the shallow (underburied) explosion with respect to a fully contained explosion using separately the maximum particle velocity ω_1, the maximum particle displacement ω_1, and the duration of the positive phase ω_1. The values of the quantities ω_1, ω_2, and ω_3, determining the “contained” equivalent for the underburied explosions with respect to the corresponding parameters, are provided in Table 6.2.

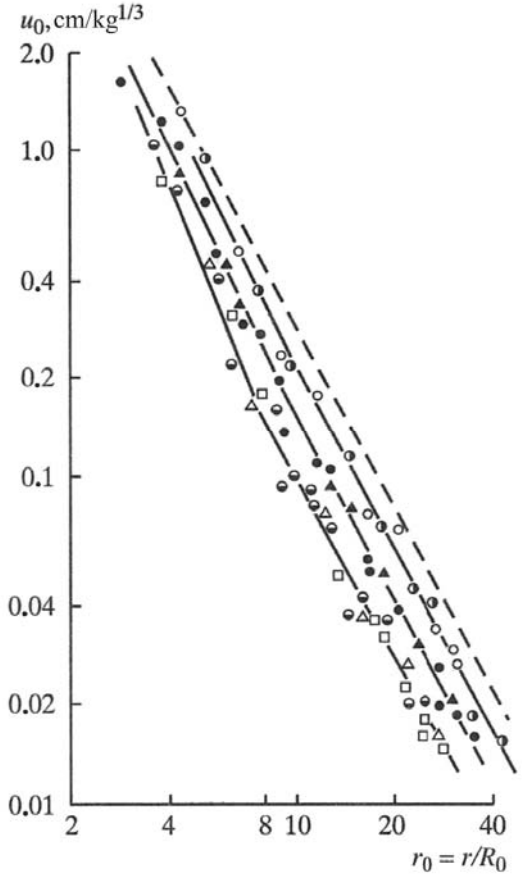

Figure 6.15: Scaled maximum displacements for explosions in thiosulphate. Same definitions as in Figure 6.13.

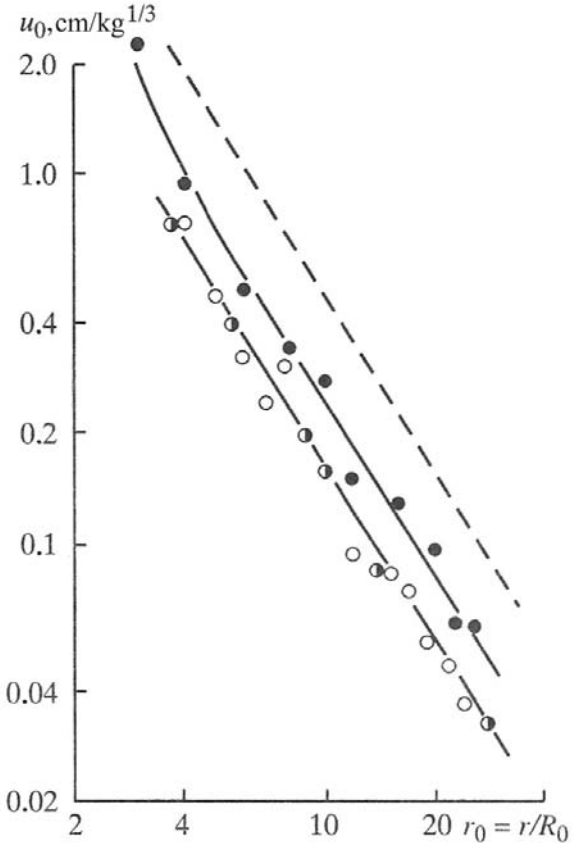

Figure 6.16: Scaled maximum displacements for explosions in PMMA. Same definitions as in Figure 6.13.

Table 6.2. Contained equivalents of shallow explosions

Medium	Parameter	Relative depth of burial η		
		-0.5	0	1
Sodium thiosulphate	ω_1	0.35	0.65	0.8
	ω_2	0.25	0.25	0.75
	ω_3	0.18	0.44	0.65
PMMA	ω_1	0.5	0.73	-
	ω_2	0.23	0.5	-
	ω_3	0.1	0.25	-

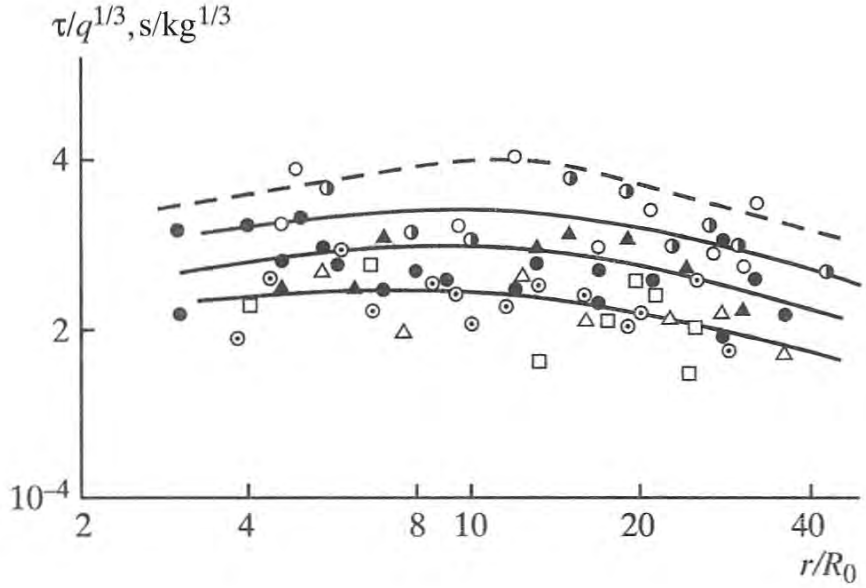

Figure 6.17: Scaled positive phase duration for the stress wave in thiosulphate. Same definitions as in Figure 6.13.

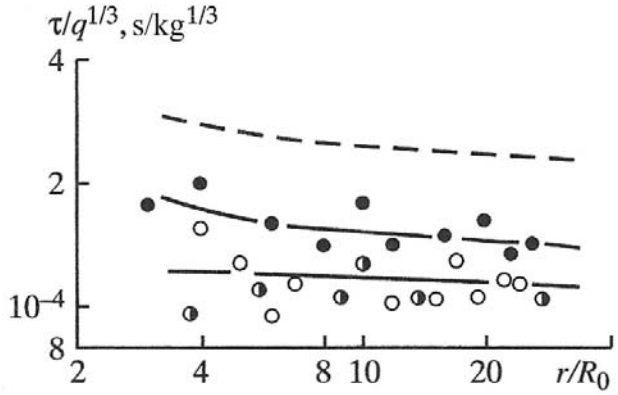

Figure 6.18: Scaled positive phase duration for the stress wave in PMMA. Same definitions as in Figure 6.13.

It can be seen from Table 6.2 that the "contained" explosion equivalents defined using the maximum velocity and the positive phase duration are significantly different. This is because the explosions with different values of the parameter η cannot be placed into a similarity group based on one of the explosion parameters. However, the explosions with different yields and the same values of the scaled depth of burial satisfy similarity criteria, as clearly seen from Figures 6.13 – 6.18. The similarity of the particle motion will be described later in more detail.

Going back to the results in Table 6.2, we note that the efficiency determined using the maximum displacements is the same for both media. This is understandable because the same effect from the free surface should lead to the same amount of relative energy lost to atmosphere, and due to generation of the surface and near-surface waves. The medium displacement in this

case is an equivalent to an explosion effect (in terms of energy), because neither wave velocity amplitude nor the wave duration alone determines the energy transferred to the medium. Study of the mechanical characteristics (effects) of explosions with a change of scaled DOB leads to the following conclusion: the presence of a strong heterogeneity in a form of a free surface does not significantly affect the near-source amplitudes. The effect of the heterogeneity becomes prominent with distance increase. Changes to the parameters of motion (due to a free surface) occur gradually rather than as a sharp jump. Thus the creation of medium heterogeneities due to fragmentation (creation of small fractures behind the wave front) cannot produce sharp changes to the wave behavior, and the damage front propagation cannot be observed from the particle motion records.

Because of the asymmetry of the wavefield for shallow explosions, there is a specific characteristic of the mechanical action – an impulse transferred to the medium in the positive z direction (e.g. Spivak, 1978) (Figure 6.12):

$$I = 2\pi \int_{R_1}^{R} r^2\, dr \int_{\pi/2}^{\pi} \rho v \sin\varphi_1 \cos\varphi_1\, d\varphi_1,$$

where R_1 is the radius of the charge cavity determined as the displacement of the boundary between the charge and the medium.

It is possible to plot the velocity distribution behind the wave front for different moments of time using the particle velocity records for explosions with different scaled depth of burial. Equation 6.2 holds immediately behind the front as in case $\eta \rightarrow \infty$, and with the value of the exponent in this case is $k \approx 1.4$ in the region $R < R_*$ for all values of the parameter η.

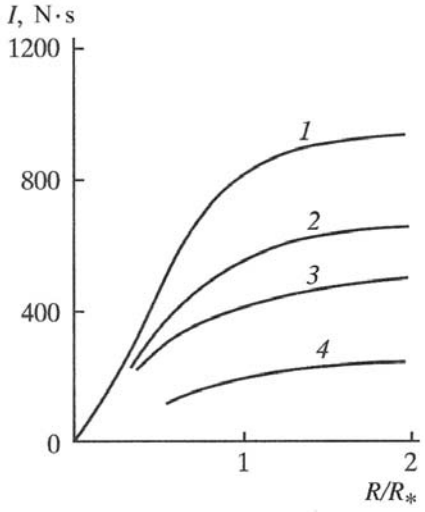

Figure 6.19: Impulse transferred to the medium in the positive vertical (Z) direction for explosions with different scaled depth of burial η: *1* for $\eta \rightarrow \infty$; *2* for $\eta = 1$; *3* for $\eta = -0.5$.

Taking into the account the power law distribution of the velocity as a function of radius and the condition $\rho = const$ we determine the impulse transferred to the medium for different time values (Figure 6.19). According to the plot, the value of the impulse transferred to the solid

medium grows with time as the wave develops and reaches its maximum I_0 for $R \sim R_*$. The values of I_0 are shown in Table 6.3. The table also shows the values of I_0 obtained from the direct experimental measurements for underburied explosions in sand (Ivanov, 1977). These estimates do not take into account the value of the impulse transferred in the negative z direction, which is present for η>0.

Table 6.3. Maximum impulse (in N·s) transferred into the medium by 1 kg explosion as a function of the scaled depth of burial η.

Medium	Scaled depth of burial η			
	-0.5	0	1	∞
Sodium thiosulphate	250	490	660	930
Plexiglas	180	390	-	550
Sand	-	370	500	-

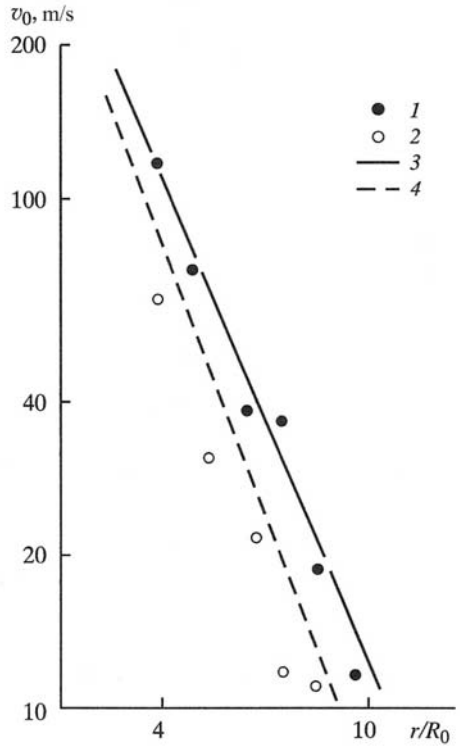

Figure 6.20: Maximum particle velocities in the stress wave observed at the free surface, for explosions with the following values of the scaled depth of burial: *1* – η = 0; *2* – η = -0.5; *3* and *4* same for the wave travelling into the medium (as opposed to the free surface), for η = 0 and η = -0.5 respectively.

In conclusion we note that in order to calculate the impulse we conducted the integration over a semi-spherical volume. To determine the parameters of radial motion near the free surface additional sensors were installed at the surface. Measurements show that the amplitudes of the

longitudinal wave propagating along the surface are similar to the amplitudes of the wave propagating into the medium (Figure 6.20).

The influence of the medium properties on the source processes of shallow (underburied) explosions is of particular interest. Laboratory experiments in metals (duralumin, aluminum) and PMMA were conducted to study this problem (Spivak, 1974; Kulikov, 1990).

Table 6.4. Physical and mechanical properties of modeling materials

Medium	Parameter						
	ρ, g/cm^3	C, km/s	ρC^2, MPa	σ_1, MPa	σ_2, MPa	σ_3, MPa	σ_*, MPa
Duraluminum	2.80	6.47	$11.7 \cdot 10^4$	127	143	238	135
Aluminum	2.70	6.44	$11.2 \cdot 10^4$	53	37	79	45
Plexiglas	1.17	2.70	$0.85 \cdot 10^4$	47.7	47	69	47.3

The main physical parameters for the materials used in the experiments are shown in Table 6.4. The parameters include: density ρ, the sound wave with velocity C (measured using ultrasonic defectoscope at a frequency of 2.5 MHz), incompressibility ρC^2, the uniaxial tensile σ_1 and compressive σ_2 strengths (determined for cylindrical samples using the apparatus "Instron-1196" for a constant deformation rate of $3 \cdot 10^{-4}$ c^{-1}), and σ_* is an average plastic limit. For ideal plastic medium it is known that $\tau = \sigma_*/2$.

Use of these materials facilitates experiments because of their homogeneity, absence of internal blocks structural elements, and porosity. These materials exhibit almost purely elastic behavior up to the limiting stresses σ_1 and σ_2. Above these limits the materials behave as purely plastic with a constant plasticity limit. Therefore, the number of parameters needed to describe these materials is minimal. In addition, comparison between the parameters in Table 6.4 shows that the materials differ only with respect to one parameter: either incompressibility or the plastic limit (yield strength), allowing us to study the separate effects of these parameters on the seismic waves.

In addition, extensive body of research exists for these materials including: a) numerous laboratory experiments with fully contained explosions (Rodionov and Sukhotin, 1971), and b) numerical calculations using elasto-plastic models with constant yield strength (Korotkov and Lobanov, 1973). These studies significantly simplify the new experiments related to the effect of the depth of burial on the explosion seismic effect and the resulting analysis.

In this study, the experiments were conducted using cylindrical samples with diameters of 200 mm and lengths ranging between 20 and 300 mm. The sample lengths varied in order to study wave attenuation with distance. The charges were made of compressed powdered PETN. The charges weighed $4 \cdot 10^{-4}$ kg and had spherical shapes with a radius of 4 mm. The detonation was performed using electrical current through a wire placed into the charge.

The charges were placed along the axis of the cylindrical samples at different distances from the free surface (the end of the cylinder). In order to do so, a 100 mm long hole was drilled on

the side of the cylinder; then a charge was placed into the hole and secured with epoxy. The holes were filled using sticks made of the same material as the sample (stemming). The length of the hole was an order of magnitude longer than the minimum distance to the free surface, which provided the integrity of the stemming and prevented leakage of the detonation products through the “stemming”.

The charge depth was determined as a distance between the charge center and the [nearest] end of the cylinder. The experiments were conducted using “depth” W equal to R_0, $2R_0$ and $3R_0$ (R_0 being the charge radius). Fully contained explosions are defined as $W = \infty$, however in reality these explosions are conducted using depth of $15R_0$ and $20R_0$. For surface explosions the charges were glued into a hemispherical depression drilled at the end of the cylinder. For “above ground” shots it was assumed that W<0, and the explosions were conducted with “depths” of $-R_0$, $-2R_0$ and $-3R_0$. For surface shots, hemispherical charges weighing 0.4 g were glued to the end of the sample. The depth of these charges was calculated as the distance from the surface to the center of the mass of the charge equal to 1.9 mm, or in relative units $W = -0.475\ R_0$.

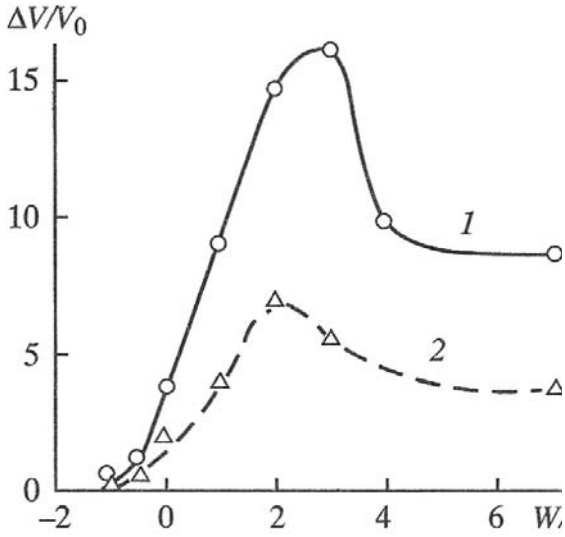

Figure 6.21: Relationships between the ratios of the volume of the medium displaced toward the surface and the volume charge and the charge scaled DOB in aluminum (*1*) and duralumin (*2*).

The volume of the displaced material was calculated as a volume of the craters ΔV for different charge depths. The relationships between the ratio of the displaced volume to the charge volume V and the charge depth for aluminum and duralumin are shown in Figure 6.21. The curves are similar qualitatively and each has a maximum at approximately $(2 – 3)\ R_0$. This result is expected because thin plastic layer above the charge provides less resistance to the detonation products, and they expand to smaller final pressure, than for a fully contained explosion. The radius of a fully contained explosion in duralumin is $1.67\ R_0$, and for aluminum it is $2.12\ R_0$, which is practically identical to the results of Rodionov and Sukhotin (1971).The difference between the cavity radii for the two media is due to the different yield strength for these materials.

A typical result of an explosion in PMMA is formation of a damage zone, consisting of planar radial fractures. Evidently it is related to a brittle nature of PMMA under tension. The damage zone is axially symmetric and can be represented by a spherical zone around the cavity and a conical zone extending to the free surface, related to spall. As a result, the volume of the damage zone for a charge with depth of (3 – 4) R_0 exceeds the damage zone for fully contained explosion by a factor of 1.5, where the radius of the damage zone is approximately 5.5 R_0. For explosions elevated above the sample surface, the damage occur only for surface explosions, or $W = -R_0$.

Medium oscillations for these experiments were detected and recorded using the capacitance method described in Rodionov and Sukhotin (1971), which involves recording the velocity at the free surface. The sensor was placed in the center on the opposite side of the sample, which allowed us to record the parameters below the explosion. The reflection from the free surface and the amplitude doubling compared to an infinite medium was taken into account.

Since the motion of a free surface is caused by a spherical rather than a plane wave, the resolution of the wave front depends on the sensor size. Sensors with diameter 10 mm were used for these experiments, so at a distance of 100 mm from the charge center the spatial resolution for the wavelength was 0.2 mm and the temporal resolution was about 0.03 μs. The explosion rise time for these experiments was about 1 μs. Thus the capacitance method provides good resolution of the wave fronts of spherical waves.

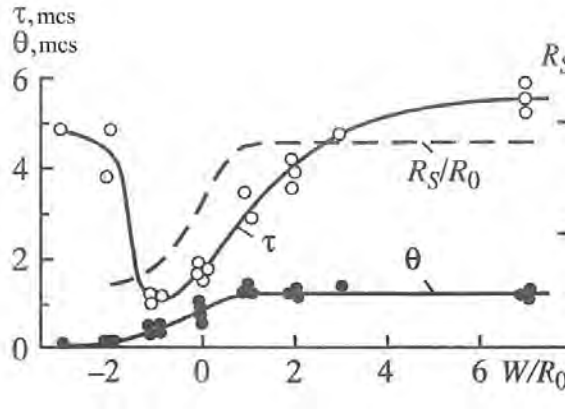

Figure 6.22: Rise time of particle velocity to its maximum, θ, the positive phase duration τ, and the relative radius of the elasto-plastic zone R_s/R_0, as functions of the relative depth of burial (expressed in terms of the charge radius), for explosions in duralumin.

Analysis of the motion of the free surface shows that at first an increase in the charge depth causes an increase in the rise time θ to its maximum value. While for “above ground” shots the wave fronts are practically shock waves, for surface shots the amplitude rise time θ is almost half the duration of the positive phase (Figure 6.22).

According to calculations using an elasto-plastic model (Korotkov and Lobanov, 1973), buried explosions with depth W > 0 in plastic materials commonly exhibit broadening of the wave front. In these media the velocity of the elastic precursor C is higher than the velocity of the plastic wave C_1. Using relationships between the rise time and the differences between

velocities C and C_1 we can estimate the radius of the elasto-plastic zone R_s for duralumin with different depths of burial, finding

$$\theta = (R_s - R_0)/C_1 - (R_s - R_0)/C.$$

The maximum value of R_s is $9.1R_0$, reached for fully contained explosions (Figure 6.22). The formation of such an extensive zone of plastic deformation for contained explosions is due to the fact that the pressure of the detonation products for a contained explosion reaches 10^4 MPa [10GPa], which exceeds the yield stress for duralumin by two orders of magnitude. For raised (above ground) explosions the shock wave formed in the air acts upon the solid medium with pressure of 10^2 MPa, exciting what is effectively an elastic wave in the medium. No pulse broadening occurs in this case.

A second feature of the stress wave is related to a continuous increase in the duration τ of the positive phase with an increase in the depth of burial, reaching 5.5 μs for a contained explosion. These changes in τ can be explained by the fact that the detonation products escape into the atmosphere for shallow explosions, reducing the duration of their action upon the medium compared to a contained explosion.

Raising the charges above the surface increases the duration of the positive phase of the wave, because the wave in this case has two fronts. The first is produced by a shock wave, and the second is caused by an expansion of the detonation products. Both events have short duration, but their combined duration is about 5μs.

We note that the data points in Figure 6.22 showing the values of θ and τ for duralumin were obtained at distances greater than $10R_0$, or in the elastic zone. The values of θ and τ vary initially with the distance at which the wave is recorded: θ increases with this distance and stabilizes at $R > R_s$, while τ decreases with the distance and also stabilizes at $R > R_s$. From this point on we use θ and τ to refer to parameters measured in the elastic zone, which do not change with the distance.

The values of θ and τ for explosions in aluminum are approximately double those for duralumin. Qualitatively the relationships $\theta(W)$ and $\tau(W)$ are similar for aluminum and duralumin. For example, for a fully contained explosion in aluminum and duralumin the rise time is 3.1μs and 1.2μs respectively, the duration of the positive phase is 11μs and 5.5μs respectively, and the radius of the elasto-plastic zone is $27.5R_0$ and $9.1R_0$ respectively. The factor of 3 difference for the plastic limits, and the values of σ_* between these materials, can explain these differences.

To compare the effects of explosions in three different media we show only the relationships between the duration of the positive phase τ and the depth of burial W (Figure 6.23). Qualitatively the character of the changes of τ with the depth is similar for all three media. The values of τ obtained here for duralumin and aluminum are practically identical to the results of Rodionov and Sukhotin (1971). The values of τ for explosions in PMMA are half those value obtained in Spivak (1974). This discrepancy can be explained by differences in the mechanical properties of the material, for instance by a 10% density difference.

We note that wave amplitudes for shallow (underburied) explosions are practically the same as those for fully contained explosions. However for charges placed above the surface, wave amplitudes decrease significantly with increasing height of burst. The relationships between the maximum particle velocity v_0 and the distance from the charge center to the surface, for duralumin, aluminum, and PMMA, are shown in Figures 6.24 a, b and c respectively. The depths [distance, or height of burst) relative to the charge radius are shown as the numbers next to the corresponding lines. Curves $v_0(r)$ are not shown for some experiments to prevent overloading the plot. Some curves, for instance for duralumin and aluminum, are shown using a limited number of points with the same slope, because the velocity decrease with distance for different depths (or heights) is the same. Establishing this fact allowed us to reduce the number of experiments significantly.

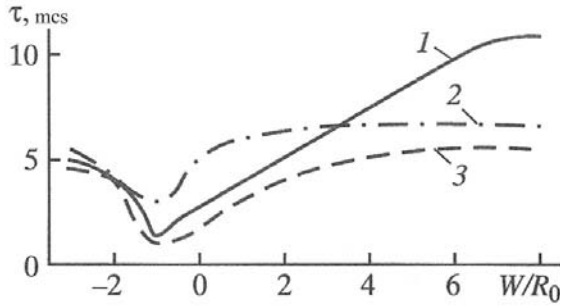

Figure 6.23: Positive phase duration τ as a function of the relative depth of burial (W/R_0) for explosions in aluminum (*1*), PMMA (*2*) and duralumin (*3*).

The slopes of solid lines in Figure 6.24 correspond to velocity v_0 decreasing as r^{-1}, which characterizes perfectly elastic media. This law of amplitude decay $v_0(r)$ in aluminum and duralumin was determined earlier during experiments with contained explosions (Rodionov and Sukhotin, 1971). The relationships $v_0(r)$ determined by Rodionov and Sukhotin (1971) are shown in Figure 6.24a and b with dashed lines. The amplitude decay as $v_0 \sim r^{-1}$ is confirmed by other experiments in duralumin for depths $W = -R_0$ and in aluminum for W = 0. However, the amplitude decay in aluminum in the near-source zone $r < R_s$ is even more rapid, due to energy dissipation in the plastic zone. Velocity amplitude decay in PMMA is proportional to $r^{-1.33}$ over the entire distance range, indicating that energy dissipation occurs even for stresses below the material strength.

According to Figure 6.24, the relationships $v_0(r)$ for shallow explosions in all three media are the same as the relationships for fully contained explosions. Even for surface explosions with detonation products ejected into the air, wave amplitudes are not significantly different from the amplitudes from fully contained explosions. Therefore, the initial effect of the source (the initial pressure of the detonation products) completely determines the maximum particle velocity at the wave front. The venting of detonation products from the cavity for shallow (unconfined) explosions, leading to unloading of the medium, have almost no effect on either the peak velocities below the source epicenter or the amplitude decay rate.

For explosions above the surface the maximum velocities are significantly lower than for fully contained explosions. From Figure 6.24 a, for an explosion in duralumin with $W = -3R_0$ the amplitude at the same absolute distances is reduced by a factor of 5 compared to that for a confined explosion. This is a significant amplitude reduction, because the equivalent contained charge has to have the weight reduced by a factor of 100 to produce the same signal as the above-ground signal.

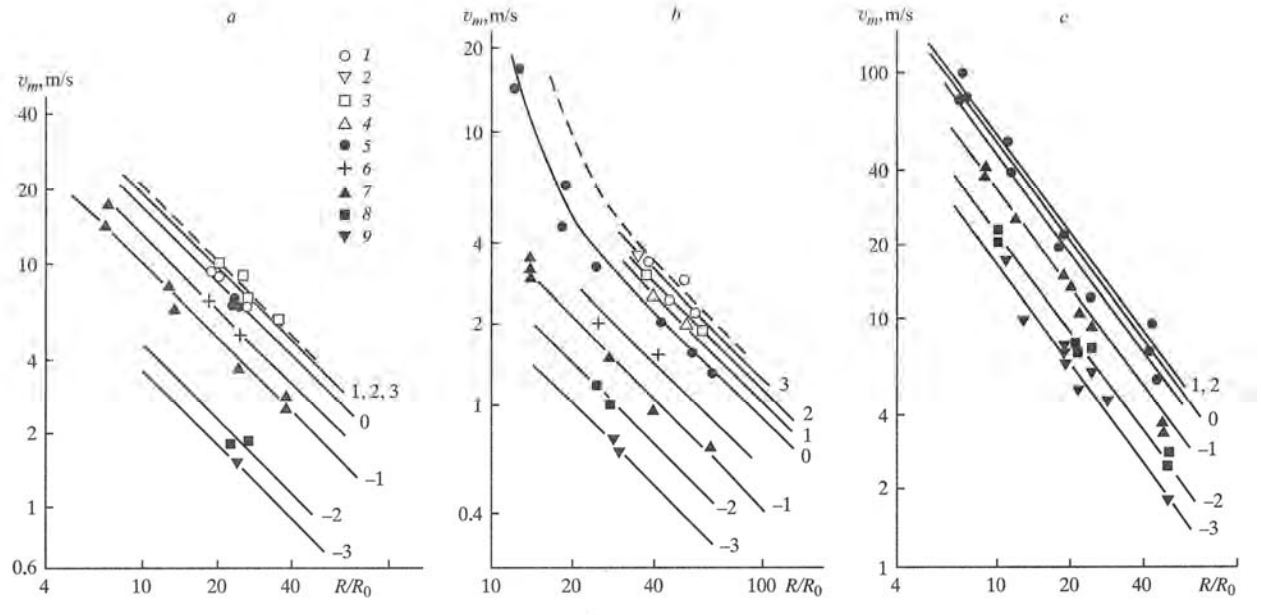

Figure 6.24: Peak particle velocities as a function of distance for explosions in duralumin (a), aluminum (b), and PMMA (c) for the following values of the relative depth of burial (W/R_0): *1* – ∞; *2* – 3; *3* – 2, *4* – 1; *5* – 0; *6* – slopes [no idea---is this about the effects of a sloped surface? And then, the remaining curves have a negative "depth of burial" so are they for explosions above the medium?], *7* – (-1); *8* – (-2); *9* – (-3).

Table 6.5. Characteristics of the laboratory explosions

Medium	Parameter			
	v_0, m/s	σ_r, MPa	P_{inc}, MPa	P_{ref}, MPa
Duraluminum	12	217	22	240
Plexiglas	83	2.62	22	240

We shall estimate wave parameters for above a ground source. For simplicity we consider experiments with depth of $W = -3R_0$ in duralumin and PMMA. The waves from these sources are practically shock waves (i.e. have negligible rise time), because no plastic zone is formed. Because of this the experimental curves $v_0(r)$ can be extrapolated to the free surface (using the

curves in Figures 6.24 – 6.25) assuming the attenuation remains unchanged, in order to determine the particle velocity at the free surface.

The values of v_0 obtained by extrapolation are given in Table 6.5. The radial stresses estimated at the free surface using the relationship for a shock wave $\sigma_r = \rho C v_0$ are also shown in Table 6.5. Even though the maximum particle velocities in duralumin and PMMA differ by a factor of 7, the radial stresses at the wave front are close. The pressure at the medium boundary is created by the shock wave in the air. The pressure at the shock wave front at a distance of $3R_0$ from the charge center is 22 MPa.

Calculation of the wave amplitude reflected from a rigid wall, taking into account the temperature dependence of the adiabatic constant for air, shows that the pressure at the boundary between the air and the medium increases to 240 MPa. Comparison between the values of σ_r and P_{ref}[1] shown in Table 6.5 shows that the characteristics of the waves excited in the medium by the explosion are determined by the pressure P_{ref} created by reflection of the wave from the free surface. The actual properties of the medium can be neglected, and medium is considered rigid.

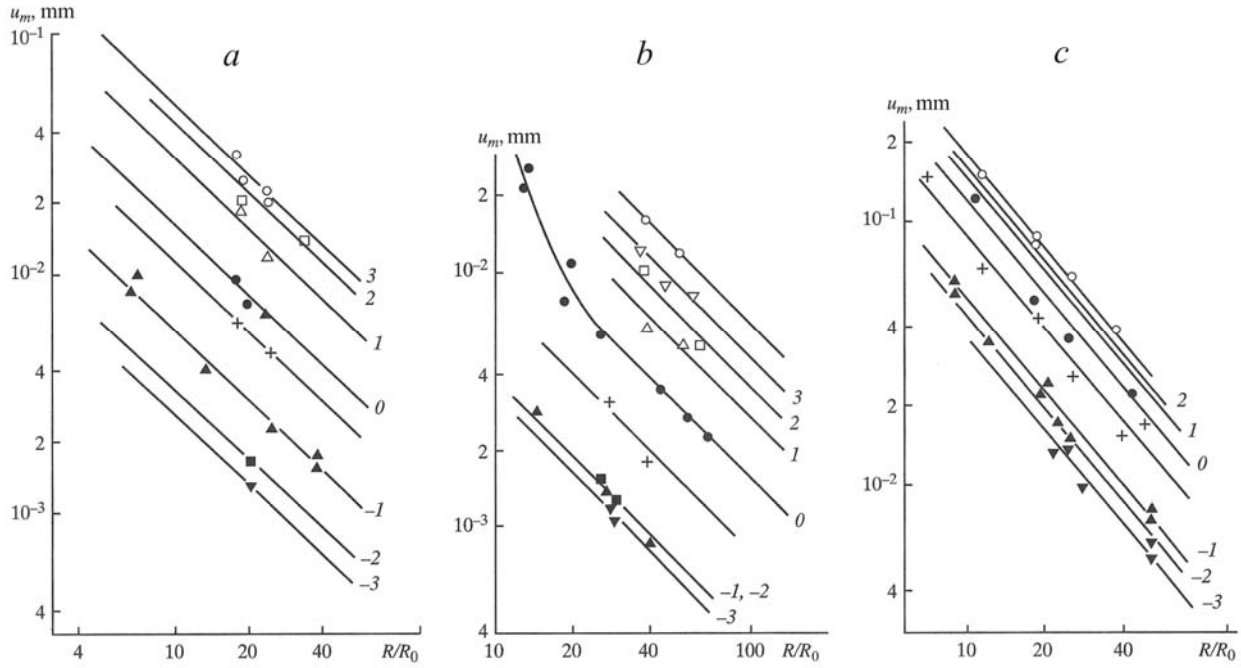

Figure 6.25: Maximum displacements as a function of distance for explosions in duralumin (a), aluminum (b), PMMA (c) for the different values of the relative depth of burial (W/R_0). Same definitions as in Figure 6.24.

Integration of the velocity recordings allows us to determine the maximum displacements in the medium. Displacements are shown in Figure 6.25 (solid lines) as a function of the distance r ($u_0 \sim r^{-1}$) for different depths of burial. The numbers next to the lines show the scaled depths of

[1] P_{inc} is P_{ref} in Table 6.5 indicate pressure amplitudes in the incident and reflected waves respectively

burial. The velocity recordings due to explosions in duralumin with depth $W = -R_0$, and in aluminum with depth of $W = 0$, were integrated to obtain these displacements. The results (Figure 6.25 a,b) confirm that for $R > R_s$ the maximum displacements decrease with distance according to the elasticity theory.

Table 6.6. Efficiency coefficient values for shallow explosion in duralumin

Scaled depth of burial, W/R_0	Parameter				
	k_v	k_u	k_τ	k_{Rs}	$k_{\Delta V}$
3	1	1	0.64	1	1.51
2	1	0.81	0.38	1	1.80
1	1	0.45	0.16	0.98	1.05
0	0.71	0.17	0.03	0.37	0.47
0.5	0.31	0.10	0.02	0.32	0.12
-1	0.136	0.037	0.006	0.067	0.03
-2	0.014	0.015	0.48	0.026	-
-3	0.007	0.01	0.66	-	-

Table 6.7. Efficiency coefficient values for shallow explosion in aluminum

Scaled depth of burial, W/R_0	Parameter				
	k_v	k_u	k_τ	k_{Rs}	$k_{\Delta V}$
3	1	0.64	0.166	0.69	1.9
2	0.66	0.42	0.094	0.54	1.72
1	0.50	0.29	0.047	0.34	1.05
0	0.31	0.125	0.015	0.11	0.44
0.5	0.09	0.046	0.006	0.11	0.12
-1	0.034	0.015	0.002	0.018	0.026
-2	0.011	0.015	0.06	0.014	-
-3	0.004	0.012	0.09	0.013	-

Table 6.8. Efficiency coefficient values for shallow explosion in PMMA

Scaled depth of burial, W/R_0	Parameter		
	k_v	k_u	k_τ
3	1	1	0.98
2	1	0.89	0.89
1	1	0.77	0.70
0	0.91	0.59	0.42
0.5	0.77	0.40	0.16
-1	0.64	0.19	0.09

-2	0.42	0.15	0.25
-3	0.31	0.11	0.56

In PMMA the attenuation with distance is $u_0 \sim r^{-1.2}$, meaning that amplitude decay is slower for displacements than for particle velocity. This can be explained by a change of wave profile with distance: the exponential decay of velocity behind the wave front changes into linear with the distance increase. (To avoid overloading, we ′do not show experimental values for $W = -2R_0$, R_0, $2R_0$, and $3R_0$.)

Comparison of the function $u_0(r)$ in three media demonstrates a common feature. While the relationships $v_0(r)$ for underburied explosions are similar to the relationships $v_0(r)$ for fully contained explosions, the maximum displacements are smaller for underburied explosions than for fully contained explosions. So the maximum displacements depend on the depth of burial not only for $W < 0$, but also for $W > 0$. The maximum displacements for underburied explosions reach the displacements for fully contained explosions only for $W = 3R_0$. This characteristic of u_0 as a function of W agrees with relationships between the positive phase duration and the depth shown in Figure 6.23 (Kulikov, 1990).

The seismic efficiency of explosions can be estimated using different methods. Note that the fraction of the explosive energy transferred into a seismic wave depends on the physical properties of the medium. Studies show that charge placement affects the wave parameters and consequently the seismic effect of the explosion. Therefore a natural way to estimate the seismic efficiency of explosions at different depths is to compare it with the efficiency of a fully contained charge in the same medium. We shall introduce the efficiency coefficient k, determined in the same way as the TNT equivalency for comparison of different types of HE. The efficiency coefficient can be estimated using different parameters of the wave. We assume that for all depths of burial the wave characteristics depend on the energy or mass of the charge, according to the following relationships:

$$v_m = A(kq)^{n/3}/R^n,$$

$$u_m/(kq)^{1/3} = B(kq)^{m/3}/R,$$

$$\tau = C(kq)^{1/3};\ R_s = D(kq)^{1/3};\ \Delta V = Ekq,$$

where A, B, C, D and E are constants independent of the depth of burial, and n and m are exponents determining the amplitude decay with distance. The values of the coefficient k using the experiments and the formulas above for duralumin, aluminum and PMMA are shown in Tables 6.6, 6.7 and 6.8 respectively. The efficiency coefficients in these tables have indices corresponding to the physical wave properties used for their estimation (i.e., velocity, displacement, or duration).

Comparison between the efficiency coefficients as a function of depth for each parameter shows that the depth decrease results in a monotonic decrease in efficiency. Comparison between the efficiency coefficients, determined using different physical wave properties, at fixed depths

of burial, shows broad range variations. The largest differences are noted between the coefficients k_v and k_τ, determined using the maximum velocity and the positive phase duration. The differences in these parameters show that the underburied explosions, surface explosions, and above ground explosions, are not similar geometrically to explosions having a normal depth of burial. This means, on the one hand, that it is impossible to find an equivalent charge for a normal DOB explosion that could recreate a wave with the same parameters as v_0, u_0, and τ simultaneously, for the non-fully contained explosion (meaning either underburied, or surface, or above ground). Therefore the way we have proposed, of defining the efficiency coefficients, is not entirely correct.

On the other hand, the lack of similarity of explosions in the different depth regimes, involving (in some cases) the ejection of detonation products into atmosphere, and unloading at the free surface, make the problem of prediction of the seismic effect of explosions with different depths of burial more difficult than is the case for fully contained explosions. The presence of a free surface makes the problem of a shallow explosion two-dimensional. The experimental data partially address the effect of unloading from the free surface, on the physical wave variables below the explosion epicenter. Since for distances $R > R_s$ in aluminum the wave decay is similar to that for a purely elastic medium, the wave motion in aluminum can be described using the elastic potential for a spherically symmetric source (Rodionov et al, 1971). The elastic potential for a surface explosion in aluminum was numerically computed using velocity records. Using the elastic potential the medium motion was then calculated at different distances from the source.

The calculations of the values of $u_0(r)$ and $v_0(r)$ and the velocity waveforms $v(t)$ calculated for $R > R_s$ showed good agreement with the experimental data indicating that the motion is spherically symmetric below the explosion epicenter, and also that the effect of the free surface is important only for early stages of the explosion, when the wave is in its plastic phase, during the formation of the elastic source. Evidently, these results are related only to the wave motion below the epicenter, and cannot describe the wave motion along the free surface.

Similar conclusions about the effect of the free surface can be made, even without such calculations, for explosions with different depths of burial in various media, by using the observation that the rate of decay of $u_0(r)$ and $v_0(r)$ is the same for both underburied and normally buried explosions.

Studies show that seismic wave amplitudes from explosions in duralumin, aluminum, and PMMA, depend on the yield stress and the elastic parameters of the medium. For example, duralumin and aluminum differ only in their yield stress. Experimental data for these media show that an increase in yield stress by a factor of 3 reduces the radius of the plastic zone by a factor of 3, the duration of the positive phase by a factor of 2, the rise time by a factor of 2.6, and the maximum velocity in the elastic zone by a factor of 1.5, while the maximum displacements are practically identical for both media.

A similar comparison between the physical wave variables for fully contained explosions in PMMA and aluminum, which differ only in their elastic moduli, shows that an increase in

compressibility by a factor of 13 reduces the maximum particle velocities by a factor of 3, and the maximum displacements by a factor of 2.5.

To analyze experimental results in all three media we shall use results obtained by Korotkov and Prosvirnina (1980) and Rodionov et al (1986). For instance, calculations show that fully-contained explosions are self-similar in the elasto-plastic medium model having a constant yield stress. The similarity parameter in this case is the radius of the elasto-plastic zone (i.e., the length of a plastic wave), which depends on the medium parameters as follows:

$$l \sim \sigma_*^{-0.6} (\rho C^2)^{0.3}.$$

Therefore the duration of the positive phase in the elastic wave is given by

$$\tau \sim l/C \sim \rho^{0.7} \sigma_*^{-0.6} (\rho C)^{-0.4},$$

the maximum velocity is given by

$$v_0 = \frac{\sigma_m}{\rho C} = \frac{1}{\rho C} \frac{\sigma_*}{r} \sim \left| \frac{\sigma_*}{\rho C} \right|^{0.4},$$

and the maximum displacement is

$$u_{m0} \sim v_0 \tau \sim \rho^{-0.4} \sigma_*^{-0.2} (\rho C)^{0.8}.$$

The above formulas can be used to obtain transformation coordinates for straightforward comparison of wave characteristics. The experimental values of v_0, u_0, and τ at a distance of $30R_0$ from the charge center are shown with open symbols in Figure 6.26. The slopes of the line through the symbols and the origin depend on the charge radius and the initial pressure of the detonation products or on the explosion energy (Korotkov and Prosvirina, 1980). The scatter of the experimental points in Figure 6.26 does not exceed 40%. These relationships can be recommended for predicting the explosion parameters for contained explosions in plastic media having different values of ρ, C, and σ_*.

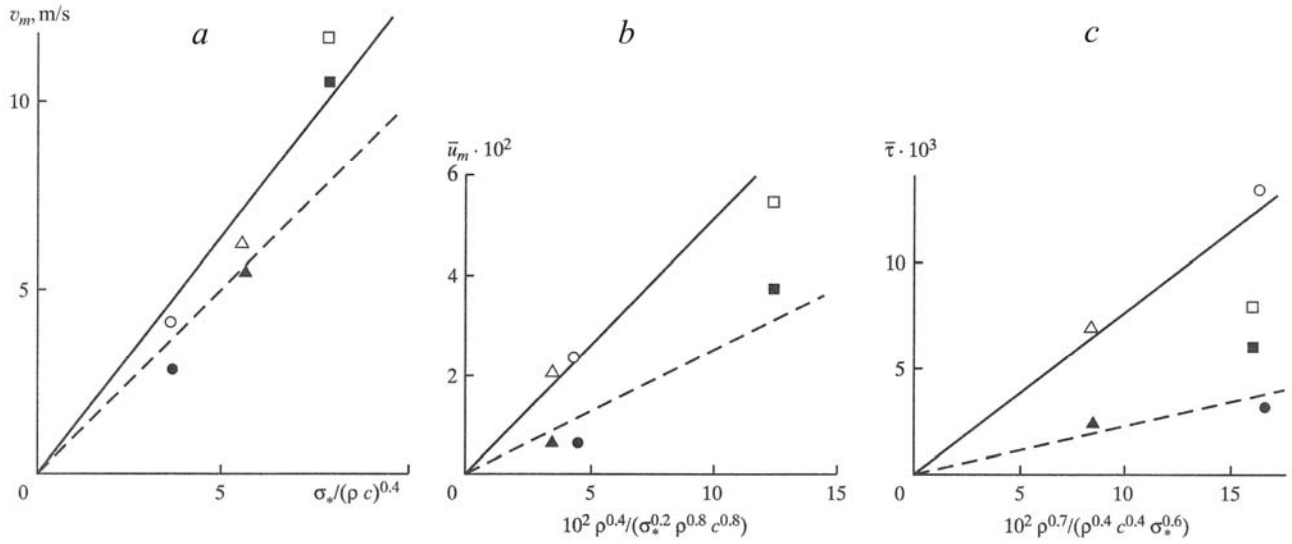

Figure 6.26: Relationships between wave characteristics and medium parameters measured at a distance of $30R_0$ for: $a - v_m$, $b - u_m$, $c - \tau$.

Applying the above formulas to surface explosions we obtained the relationships shown in Figure 6.26 with dashed lines. The experimental points for surface explosions are shown in Figure 6.26 with solid symbols. These relationships can be used to predict the explosion parameters for surface explosions in different plastic media.

The slopes of the dashed lines in Figure 6.26 are different from those of the solid lines because of the lack of similarity (in a scaling sense) between the surface and fully contained explosions. The experimental data show that deviation from similarity is determined by the yield stress. For example, the efficiency coefficient for a contact explosion in duralumin k_v is greater than k_u by a factor of 4.2, while in aluminum it is greater by the factor of only 2.5. Thus the decrease in yield stress leads to an increase in the degree of similarity, in which case the coefficients become closer.

The experimental studies were conducted in order to determine qualitative relationships and, to some extent, space-time characteristics, of the damage process due to an explosion close to a free surface (Adushkin and Sukhotin, 1961; Spivak, 1981). These experiments involved the detonation of small PETN charges that were detonated in a 15 cm × 18 cm × 18 cm block of solid PMMA. Mechanical characteristics of the PMMA used in these studies were the same as for the material described earlier (e.g. Table 6.4) that was used to determine the physical wave characteristics from explosions.

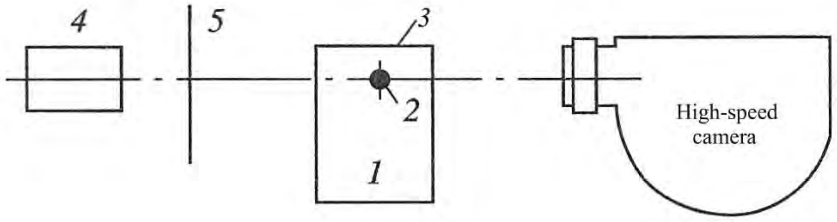

Figure 6.27: Experiment schematic: *1* – the model material block, *2* – the chemical explosive charge, *3* – the free surface, *4* – a light source, *5* – scattering screen.

Figure 6.27 shows schematically the apparatus used to perform the experiments. The damage was detected with transmitted light using a high-speed photo-recorder (LPR?), which could record in both snapshots and continuously. With reference to this Figure, block (*1*) with HE charge (*2*) was placed so that not only the charge but also the free surface was recorded. The light source was represented by either a flash-light, or by an explosive source using powdered hexogen and aluminum shavings. A scattering screen made of thin paper (5) was used instead of a condenser [???].

The photographs in Figure 6.28 show snapshots of the main stages of the development of a damage zone. Figure 6.29 shows a continuous photographic record of the same process in time along an axis perpendicular to the free surface and crossing the charge center.

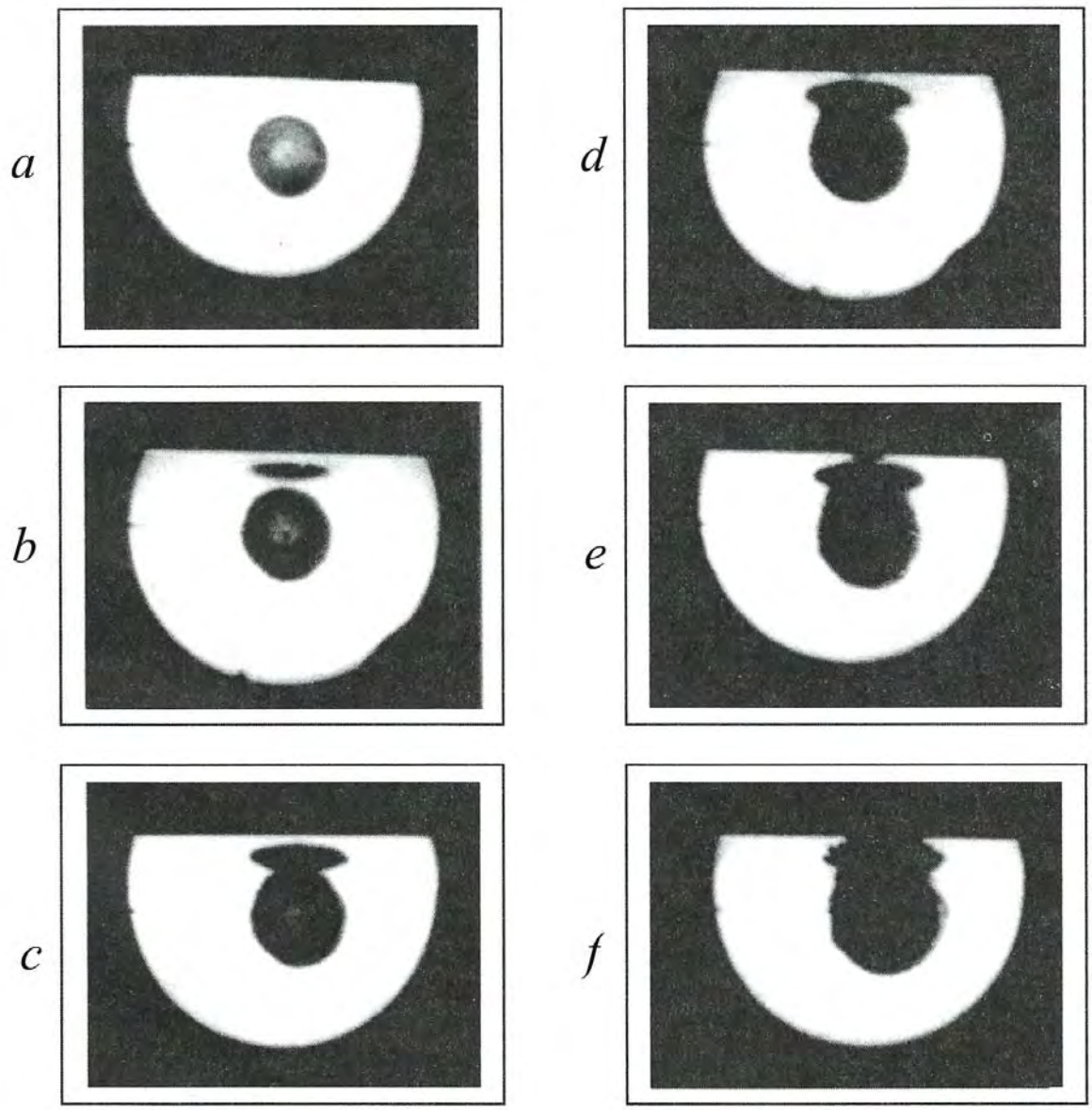

Figure 6.28: Snapshots showing the development of the damage zone in PMMA at the following moments of time (after detonation) in 10^{-6} s: *a* – 7, *b* – 8, *c* – 9, *d* – 10, *e* – 11, *f* – 14.

The processed results of the experimental data are shown in Figure 6.30. Solid lines correspond to a $7.8 \cdot 10^{-4}$ kg charge at a depth of $h_0 = 5R_0$, and dashed lines to a similar charge at $h_0 = 3R_0$.

The pictures show that unlike the case of a fully contained explosion, explosions close to a free surface, in addition to a central (spherical) damage zone close to the source, create a damage zone close to the free surface. This causes "elongation" of the damage zone along the z direction, at later time during the source development. Compared to the deep source case (when $\eta \to \infty$), additional damage is caused by a well-known spall phenomenon, or, more precisely, by multiple spalling, in which each newly-formed free surface becomes the source of subsequent spalls.

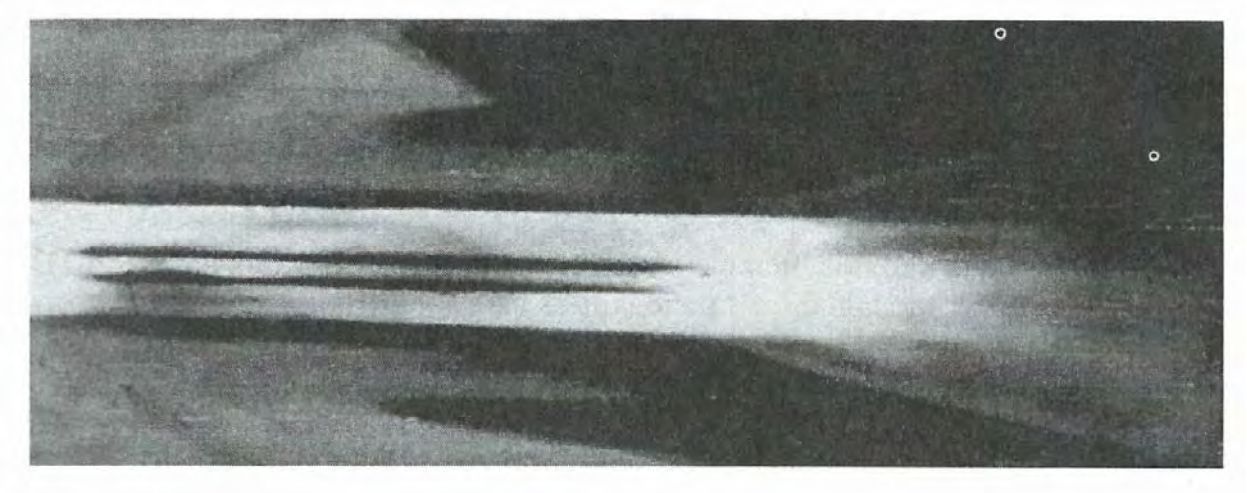

Figure 6.29: Continuous photo-chronogram of the process shown in Figure 6.28.

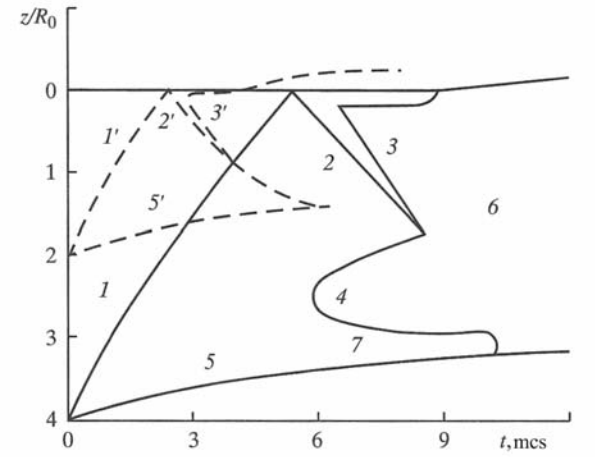

Figure 6.30: Travel-time curves for the stress wave: direct wave – 1, 1′; reflected wave – 2, 2′; damage front (central zone – 4 and spall zone – 3, 3′); 7 – motion of the cavity wall; 6 – zone of the fragmented material, 5, 5′ – cavity wall.

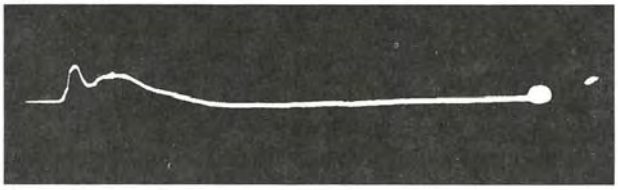

Figure 6.31: Vertical component of the velocity at the free surface.

Figure 6.28 – 6.30 show that the zones of spall and central damage move towards each other, and then merge. Only after they merge, a "neck" of damage forms in the material below the free surface. This is caused by an intense motion of the damaged medium toward the free surface.

Figure 6.31 shows the particle velocity (vertical component) at the free surface along the z direction obtained by using an electromagnetic method of velocity recording.

Joint analysis of the different stages of damage development and of the particle velocities shows that, in addition to the first maximum corresponding to the wave front reaching the free surface, there is a second maximum with smaller amplitude. The second maximum coincides with the moment when the "neck" of damage begins to form, or the damage reaches the free

surface. The moment when the velocity begins to grow between the two maxima corresponds to the creation of the spall zone.

6.3. Explosions in air-filled cavities

Investigation of possible ways to control the mechanical effects of explosions leads to consideration of different explosion source scenarios. One of the most effective ways to influence the coupling of nuclear explosions is by placing the nuclear device into a sufficiently large cavity. The artificial reduction of the intensity of the initial disturbance leads to redistribution of the charge energy between the emplacement medium, and the explosive by-products remaining in the cavity (e.g. Spivak, 1974; Adushkin et al, 1991).

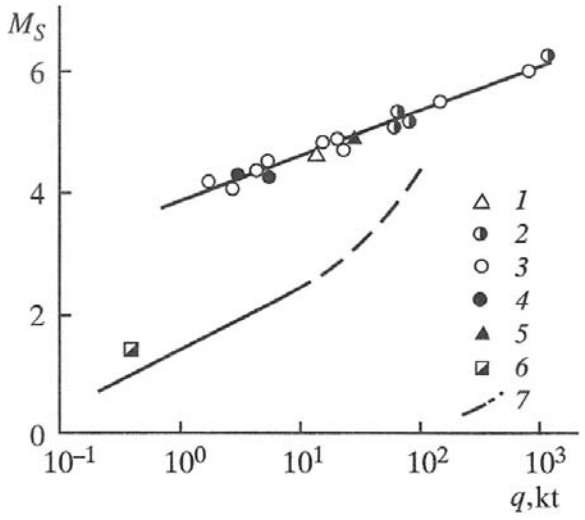

Figure 6.32: Magnitude-yield relations for tamped explosions: *1* – granite, *2* – rhyolite, *3* – tuff, *4* – salt, *5* – clay; and for decoupled explosions: *6* – STERLING (salt), 7 – theoretical decoupling for an artificially created cavity: full, and partial (above 10 kt).

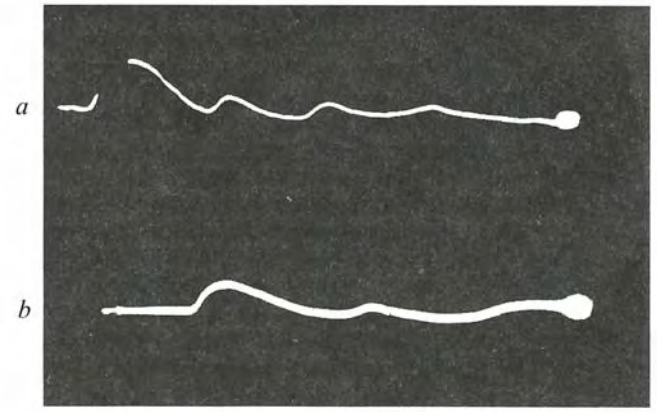

Figure 6.33: Oscillogram record of particle velocities for explosions conducted in air-filled cavities with two different relative volumes, ξ: *a* –2; *b* – 2.

Theoretical studies, and measurements for nuclear explosions in cavities formed as a result of previous explosions, have shown that the presence of a cavity significantly changes seismic signals and reduces the seismic effects of underground explosions. This is shown with data in Figure 6.32, demonstrating the importance of the effect of a cavity on seismic magnitude from explosions (Rodin, 1974). In this study the cavity radius R_c varied from $1.5R_0$ to 18 R_0 to provide a broad range of charge energy densities and initial loading amplitudes. Characteristic velocity recordings from a small explosion in a cavity are shown in Figure 6.33 for different relative

cavity radii $\xi = R_c / R_0$. It is clear that unlike waves from a fully tamped explosion, the waveforms consist of several phases with different amplitudes v_i (I = 0, 1, 2, …).

Comparison of the time delay between the first and the second arrivals $\Delta\tau$ with travel time for a shock wave across the cavity diameter shows that the secondary phases are caused by multiple reflections from the cavity walls. More careful analysis shows that the delay $\Delta\tau$ does not change with the distance and is determined by the linear dimensions of the cavity. As an illustration, Figure 6.34 shows the value of $\Delta\tau$ plotted against cavity radius for charges of different size.

Velocity records such as shown in Figure 6.33 indicate that the first phase makes the largest contribution to maximum particle displacement, amounting to 58, 65 and 78% for cavities with relative radii of ξ = 2, 3 and 4 respectively.

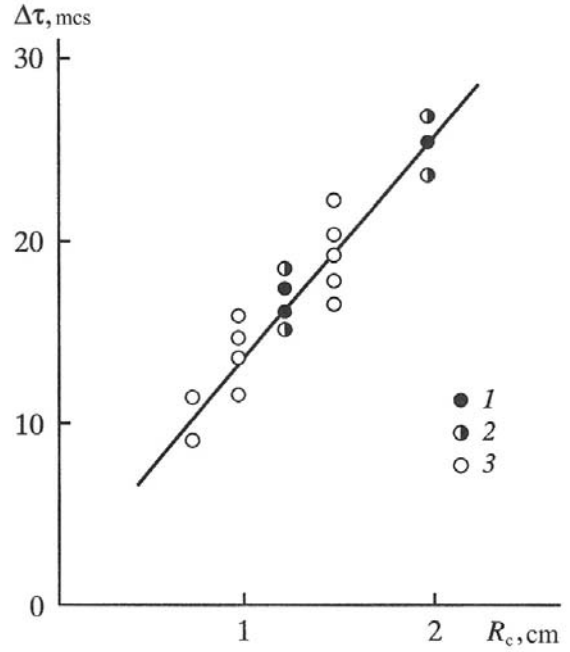

Figure 6.34: Delay time for the second maximum of the wave as a function of the radius of the decoupling cavity. The charge weights are: *1* – 0.17 g, *2* – 0.4 g, *3* – 0.78 g.

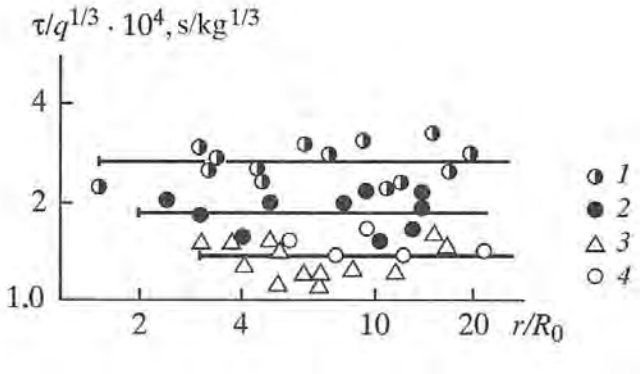

Figure 6.35: Scaled duration of the positive phase of the stress wave for explosions conducted in air-filled cavities with three different relative volumes, ξ: *1* – 1.5; *2* – 2; *3,4* – 3.

Figure 6.35 shows the scaled duration of the first phase τ as a function of r for several values of cavity size. In addition we note that for a $7.8 \cdot 10^{-4}$ kg charge in a cavity with the size of $\xi = 4$ the duration of the first phase is approximately $9.5 \cdot 10^{-6}$ s.

According to Figure 6.35 the duration of the first phase is independent of the distance from the charge, within experimental error, and decreases with an increase in the relative cavity size. A fit to these observations is given for $\tau(\xi)$ by:

$$\frac{\tau}{q^{1/3}} \cong 4 \cdot 10^{-4} \xi^{-0.88} (\text{s/kg}^{1/3}) \text{ for } 1 \leq \xi \leq 4.$$

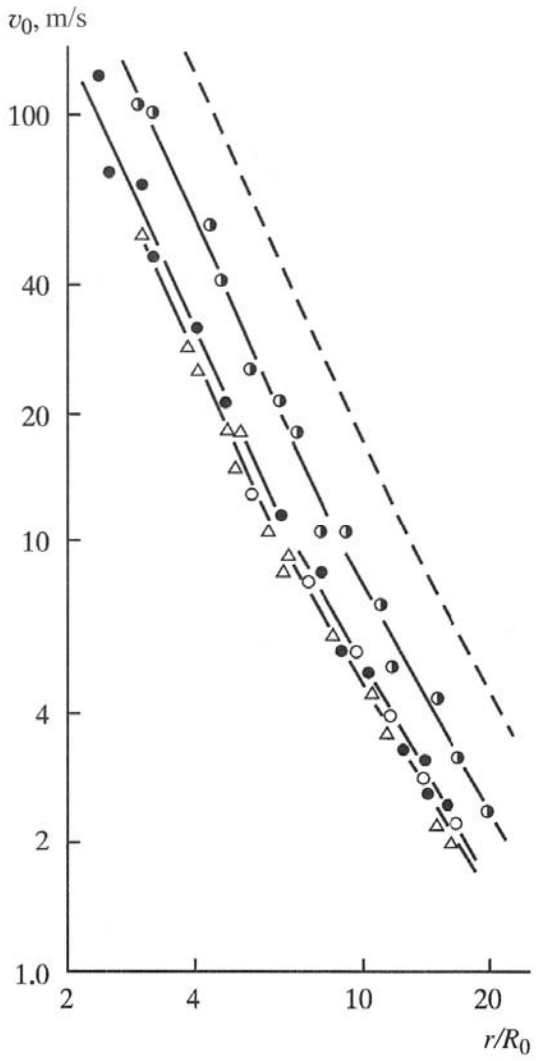

Figure 6.36: Maximum particle velocities for the stress wave: *1, 2, 3* – q = 0.78 g (ξ = 1.5, 2, 3); and *4* – q = 0.4 g, ξ = 3.

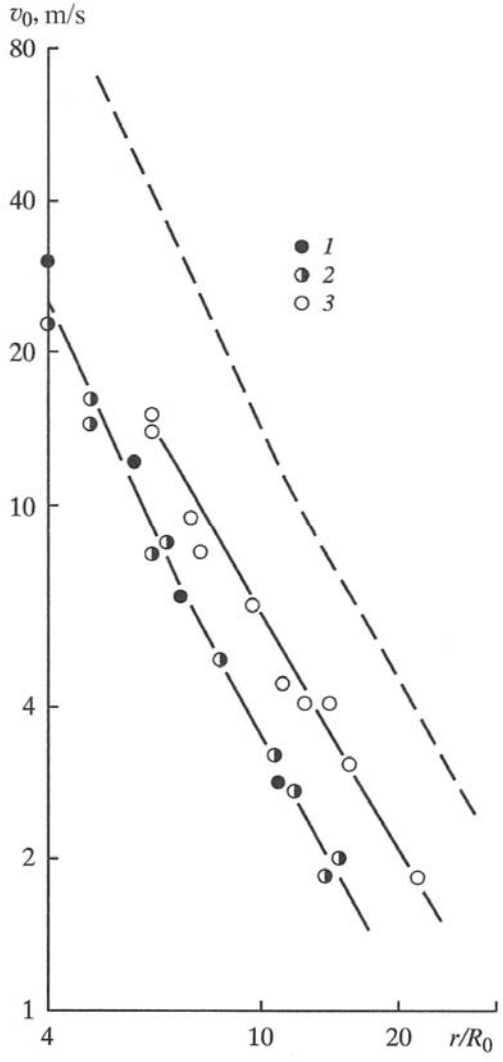

Figure 6.37: Maximum particle velocities for the stress wave: *1* – q = 0.78 g (ξ = 4); *2* – q = 0.17 g (ξ = 4); *3* – q = 0.17 g (ξ = 6.7).

The wave amplitude v_0 (maximum particle velocity) is shown in Figures 6.36 and 6.37. Just as was found for the case ξ = 1, these Figures show that for $1.5 \leq \xi \leq 4$ there are two zones with different rates of the amplitude decay with distance.
The empirical relationships are described by the formulas

$$v_0 = \begin{cases} a_2 r_0^{-n_2} (\text{m/s}) \text{ for } r_0 < r_* \\ b_2 r_0^{-p_2} (\text{m/s}) \text{ for } r_0 > r_* \end{cases}.$$

The values of the constants a_0, b_0, n_0 and p as well as the characteristic size of the zone r_* are provided in Table 6.9.

Table 6.9. Empirical coefficients for explosive charge in air-filled cavity (decoupled)

Relative cavity size ξ	Parameter						
	a_2	b_2	n_2	p_2	r_*,	F_2	S_2
1.5	1100	370	2.22	1.72	8.8	0.22	1.88
2	620	220	2.23	1.63	6.8	0.45	1.97
3	530	190	2.21	1.6	6.3	0.11	1.86
4	500	240	2.24	1.76	6.5	-	-
6.7	-	320	-	1.7	-	-	-

The relationships for the maximum displacements are shown in Figure 6.38 and are given by:

$$\frac{u_0}{q^{1/3}} \cong \mathrm{F}_2 r_0^{-S_2} (\mathrm{m/kg}^{1/3}).$$

The values of the constants F_2 and S_2 are also given in Table 6.9.

Measurements of the particle velocities using sensors placed at the cavity walls provided the relationship between the maximum velocity of the cavity wall and the radius $v_c(R_c)$. Figure 6.39 shows this relationship (line *1*), the velocity of the cavity wall calculated using the reflection of the shock wave (line *2*), and the pressure of the detonation products during their isentropic expansion from the initial cavity for the tamped explosion with varying isentropic constant (line *3*).

Comparing the lines in Figure 6.39 we conclude that for cavities with relative sizes $\xi \leq 3$ the cavity wall velocities are determined by the action (pressure) from the detonation products, while for the cavities with $\xi \geq 3$ the wall velocities are determined by reflection of the shock wave. This determines different mechanisms of energy transfer (also called coupling) into the emplacement medium for cavities of different sizes. For explosions in cavities with $\xi \geq 3$ the work of the explosive products can be described by using only quasi-static relationships for gas expansion, while for $\xi \leq 3$ the energy transferred to the medium has to be calculated using dynamic relationships.

The detailed analysis of experimental data suggests that the decoupling coefficient k_d (for the amplitudes) is not a monotonic function of the cavity radius since we find pairs of values as follows:

$\xi = R_c / R_0$	1.0	1.25	1.5	2	3	4	6.7	10	17
k_d	1.0	0.73	2.7	6.0	7.7	7.2	4.1	6.0	29

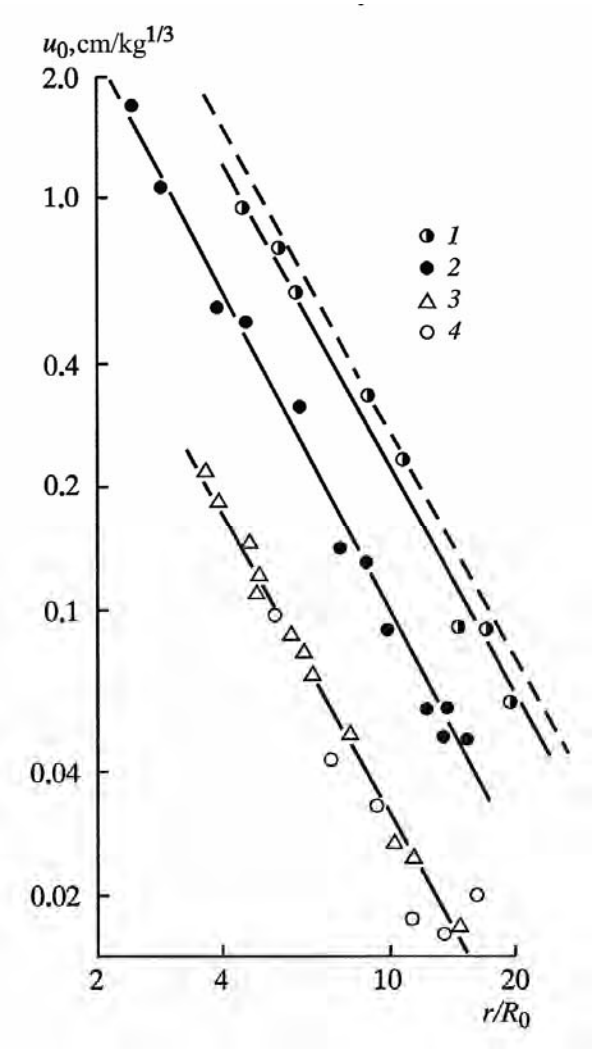

Figure 6.38: Scaled maximum particle displacements in the stress wave. Same notation as in Figure 6.35.

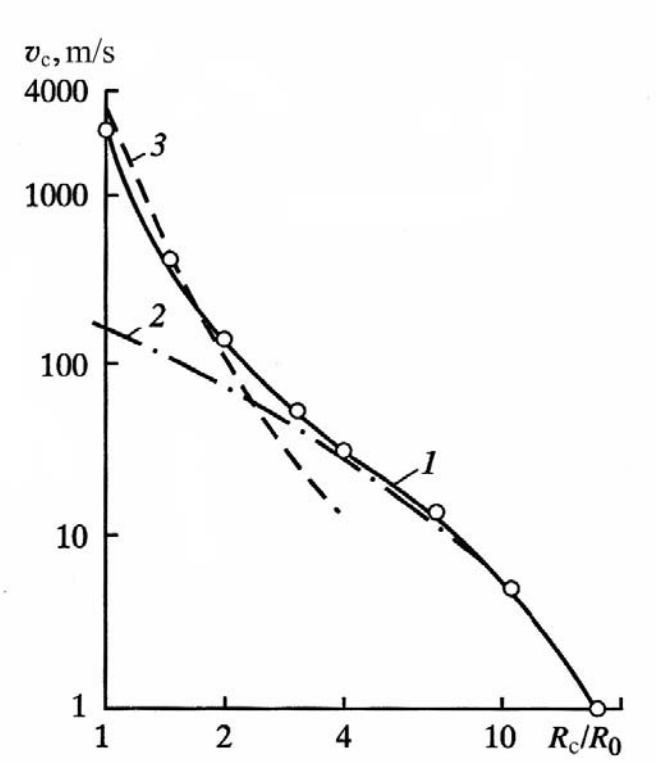

Figure 6.39: Velocity of the cavity wall as a function of radius (*1*); calculated from the reflection of the shock wave off the wall (*2*); calculated using the model of isentropic expansion of cavity gas (*3*).

According to these experimental data, an increase of the relative radius of the air-filled cavity ξ from 1 to 3 results in an increases of the amplitude weakening effect, then in the interval $4 \le \xi \le 10$ the decoupling coefficient decreases somewhat, and for $\xi \ge 10$ the decoupling coefficient k_d continues to increase. The maximum reduction of the wave amplitude in the interval $1 \le \xi \le 10$ is reached for $\xi = 3$. This effect is likely to be related to peculiarities of chemical explosions in the air. As was noted earlier, the cavity wall velocity (and subsequently the velocity amplitudes in the medium) is determined by the shock wave amplitude. It was determined by Adushkin and Korotkov (1961), that, for a monotonic reduction of the shock wave amplitude in air with the distance, its impulse shows significant increase in the interval between 6 to 10 times the charge radius.

6.4. The effect of the initial charge energy density on deformation of a solid medium

Changes of parameters of an explosion source, such as its total energy and energy density, cause significant changes in explosion effects in a solid medium (Spivak and Kondrat′ev, 1979)′. Variability of the explosion conditions and the usage of non-equivalent charges create some difficulties in the quantitative prediction of explosion effects.

Using empirical relationships is a common method to help classify and predict explosion parameters. Empirical relationships can also help us establish similarity groups of explosions based on one of the source parameters.

Thus, the most commonly used geometrical similarity principle states that the parameters of explosions of the same HE type, at the same scaled distances, are similar. This principle sometimes is called the energy similarity principle (Gubkin, 1978), assuming that for explosions of the same HE (for the same charge density) the charge weight and therefore the explosion energy are proportional to the source dimensions. In particular, for a spherical charge the following is true: $q \sim R_0^3$. In this case comparison between explosions of different size is performed by using a "dimensionless" variable, $r/q^{1/3}$. We note that even though the principle of geometrical similarity is not universal, it is widely used for estimation and prediction of explosion parameters.

The principle of energy similarity is based on the fact that for high energy concentration the parameters of the stress wave are determined by the integral action of the source, which diminishes the role of the initial conditions of the source. We note that for chemical explosions the energy density may not be sufficiently high, therefore the wave parameters will depend not only on the total energy, but also on the specific features of the explosion. Changes of the main parameter – energy density ρ_1 – result in a similarity violation.

Thus, for an explosion in an air-filed cavity located in a solid medium, the wave amplitude v_0 and maximum displacement u_0 at the same scaled distance $r/q^{1/3}$ from the source decrease as a function of the relative cavity radius ξ. In particular, the function v_0 (r) in the range $1 \le \xi \le 2$ (energy density $0.19 \cdot 10^3$ kg/m^3 $\le \rho_1 \le 0.19 \cdot 10^3$ kg/m^3) is given by the expression:

$$v_0 = \frac{a}{\xi^{1/8}}\left(\frac{r}{q^{1/3}}\right)^{-p_1} \text{ (m/s)}, \tag{6.3}$$

where a = 4.5, p_1 = 2.1 for $r/q^{1/3} < 0.6/\xi$, and a = 5.2, p_1 = 1.7 for $r/q^{1/3} > 0.6/\xi$.

We note that stress waves from explosions of different sizes conducted in cavities with the same value of ξ remain geometrically similar, as follows from Equation 6.3.

Changes in the HE density may result in significant differences in energy release, which also affects the total energy E_0. We note that PETN, used for the experiments, has constant energy content within a large energy density range ρ_1.

The analysis of the experimental data in Figure 6.6 and 6.7 shows that neither maximum particle velocities, not displacements remain the similar for the same scaled distances $r/q^{1/3}$ for

explosions with different energy density. For example, the function v_0 (r) is described by a relationship:

$$v_0 = b\rho_1^{0.8}\left(\frac{r}{q^{1/3}}\right)^{-p_2} \text{ (m/s)},$$

where b = 3.3, p_2 = 2.1 for $r/q^{1/3} < 0.55\rho_1^{0.3}$, and b = 4.5, p_1 = 1.7 for $r/q^{1/3} > 0.55\rho_1^{0.3}$. The dimension of the charge density in the later relationship is given for convenience in g/cm^3.

Thus, changing the energy density, either by using an air-filled cavity or by reducing the charge density, significantly complicates the analysis and prediction of explosion effects in a solid medium.

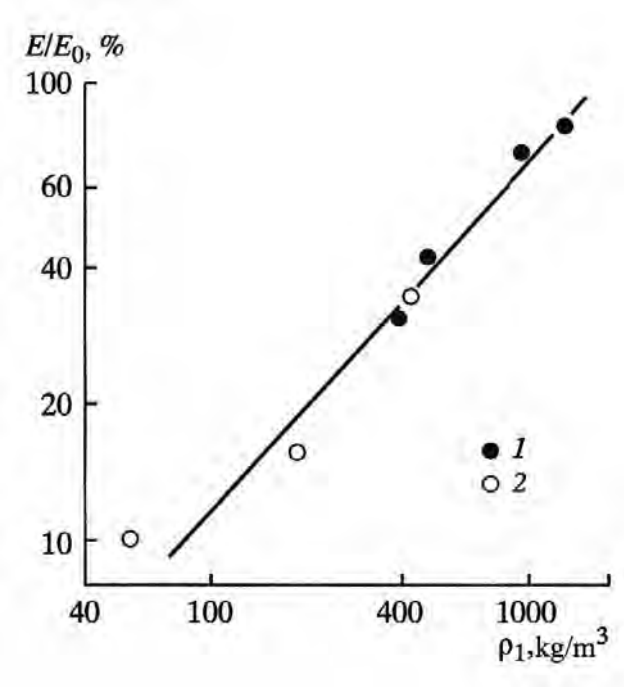

Figure 6.40: Energy transferred into the medium from an explosion, for: *1* – a tamped explosion; *2* – a cavity decoupled explosion.

Reduction in the intensity of a blast wave in a solid medium, due to reduction in the energy density and the depth, is related to the redistribution of energy between the detonation products and the medium. Thus, the energy remaining in the detonation products increases with the decrease in charge density. If we know the law of motion of the cavity wall and the law of expansion of the detonation products we can calculate the energy E transferred into the solid medium during the explosion. The estimates for the energy E for explosions in sodium thiosulphate are shown in Figure 6.40. Analytically the relationship $E = E(\rho_1)$ (the solid line in Figure 6.40) is given by:

$$\frac{E}{E_0} = 0.36\rho_1^{3/4} \text{ (\%)}. \qquad (6.4)$$

The energy transferred by exploding a fully tamped charge with a density of 1500 kg/m^3 into PMMA is approximately 70% of the total energy of the explosion (Spivak and Kondrat′ev, 1970).

Let us consider an underground explosion conducted near a free surface. Since in this case part of the energy can escape with the detonation products into the atmosphere, sometime after the explosion, the energy transferred into the solid medium is reduced as the explosion center becomes more shallow.

Table 6.10. Energy transferred to the medium during explosions with different charge depths

Medium	Relative depth of burial η			
	-0.5	0	1	∞
Thiosulphate	21	42	60	80
Plexiglas	18	36	-	70
Sand	22	35	47	-

Using the efficiencies of shallow explosions with respect to a fully contained explosion from Table 6.2 one can calculate the values of energy E for different depths of burial. Since neither the maximum particle velocity nor the positive phase duration can individually be measures of the work of the explosive detonation products, we will use the ground displacements ω_2 to estimate the efficiencies of shallow explosions. Taking into account that fully contained explosions transfer 80 and 70 % of their total energy to the emplacement medium (for thiosulphate and PMMA respectively), we can calculate E using the parameter ω_2 from Table 6.10 (the parameter ω_2 was defined in the discussion to Table 6.2). For comparison, Table 6.10 also provides the value of E for sand with density of 1600 kg/m^3 obtained by Alekseenko (1967). The results in Table 6.10 are given in % with respect to the total energy of the explosion E_0.

The value of energy E transferred to the solid medium during an explosion is distributed between the major energy sinks—which have different capacities′. Suppose that the change of energy E resulted from the changes to the explosion parameters is proportional to the changes in characteristics of explosion effects on the medium. For instance we can compare the size of the explosive damage, which represents a parameter that can be directly measured, with the value of energy transferred to the medium. The estimates for explosions conducted in an air-filled cavity show that, despite the presence of a void space in the medium, the value of R_* is quite accurately proportional to $E^{1/3}$. This shows that most of the damaged material resides in the zone adjacent to the boundary $r = R_*$. To illustrate this, Table 6.11 provides the values of R_*/R_{*0} and the values of $[E(\xi)/E(\xi{=}1)]^{1/3}$, where R_{*0} is the size of the damage zone for a fully contained explosion. Studies of the shallow explosions lead to a similar relationship: $R_* \sim E^{1/3}$ (Table 6.12).

Table 6.11. Relative size of the damage zone and relative energy transferred to the medium for explosions in cavities of different sizes

Scaled cavity size ξ	Parameter	
	R_*/R_0	$[E(\xi)/E(\xi=1)]^{1/3}$
1.5	0.7	0.74
2	0.54	0.58
3	0.5	0.5

Table 6.12. Relative size of the damage zone and relative energy transferred to the medium for explosions with different scaled depth of burial

Scaled depth of burial η	Sodium thiosulphate		Plexiglas	
	R_*/R_{*0}	$[E(\eta)/E(\eta\to\infty)]^{1/3}$	R_*/R_{*0}	$[E(\eta)/E(\eta\to\infty)]^{1/3}$
-0.5	0.72	0.63	0.51	0.61
0	0.84	0.80	0.66	0.79
1	0.92	0.91	-	-

Thus, a satisfactory agreement between the volume of the fragmented material and the energy transferred into the medium, both for explosions in air-filled cavities and for explosions conducted near the surface, can be achieved without considering the question of the absolute energy expenditures needed to fragment a unit of volume of material.

Changes in energy transfer due to changes in explosion parameters affect the energetic relationships in the stress wave. Using the power law for particle velocity with distance, equation (6.2), we determine kinetic energy of the medium as a function of the front location via

$$E_k = \frac{2\pi\rho_0 v_0^2 R^3}{3-2k_0}\left[1-\left(\frac{R_1}{R}\right)^{3-2k_0}\right],$$

where R_1 is the radius of the cavity for a fully contained explosion—which can be estimated by an approximation of the relationship *u(r,t)* at the boundary between the charge and the medium. The value of E_k relative to the total energy of an explosion is shown in Figure 6.41 for different charge densities ρ_1. The Figure shows that for $R \le 3R_0$ the kinetic energy of the medium increases with the increase of mass of the moving medium (expansion of the wave front). But then for $R \ge 3R_0$ the increase of the mass involved in the wave motion cannot compensate for the velocity decrease along the wave front. As a result, the value of E_k drops with further expansion of the wave front.

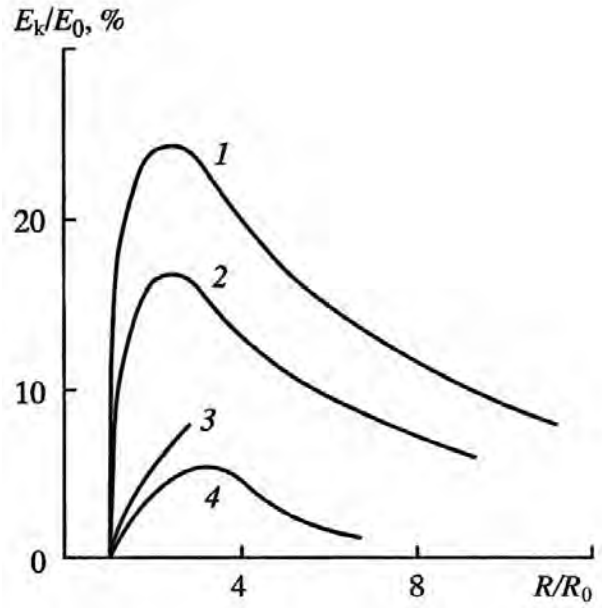

Figure 6.41: Kinetic energy as a function of the wavefront location for the following values of loading density in kg/m^3: *1* – 1500; *2* – 1000; *3* – 500; *4* – 400.

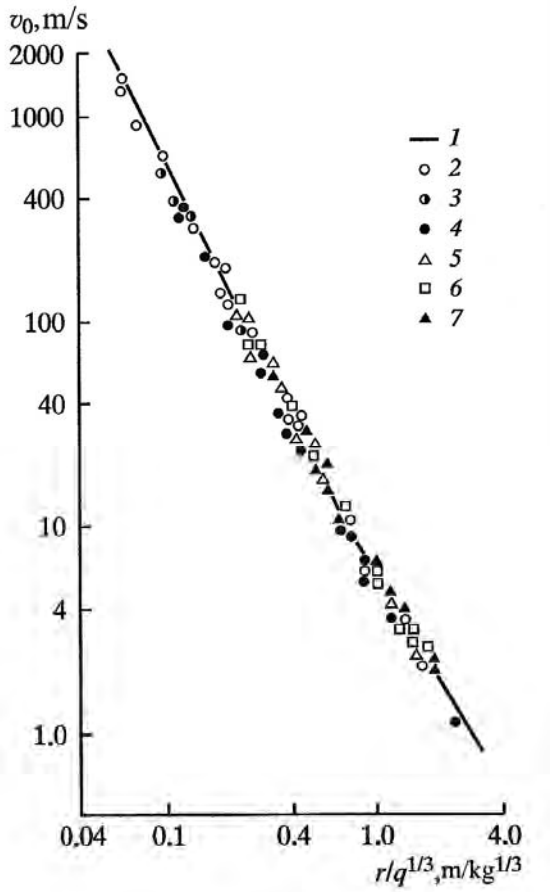

Figure 6.42: Maximum particle velocities during explosions: *1–4* – tamped explosions (density of the explosives 1500, 1000, 500 and 400 kg/m^3 respectively); *5–6* –explosions with density of the explosives 1500 kg/m^3 in cavities with ξ = 1.5, 2 and 3 (loading density 440, 190 and 55 kg/m^3 respectively).

The above calculations show that changes of the explosion source parameters first affect the energy relationships determining explosion effects. Assuming the isentropic law of expansion of the detonation products with a constant exponent n_n, we obtain an expression for the work performed by the detonation products:

$$A_p = \frac{E_0}{\xi^{n_n-1}}\left[1 - \left(\frac{\rho_*}{\rho_{HE}}\right)^{n_n-1}\right],$$

where ρ_* is the final density of the detonation products in the cavity, [and ρ_{HE} is the initial density of the explosives].

We note that the formula above is valid only for cavities with $\xi \geq 1.5$, because for $1 \leq \xi \leq 1.5$ the gas dynamics of air in the cavity is more complicated.

It follows from the last equation that the "useful" work of the detonation products (the energy transferred into the medium) decreases with a decrease of the charge density or with an increase in the relative cavity radius ξ. These conclusions are supported by analysis of experimental data (Figure 6.40).

A change of energy transfer due to variations of the charge density leads to a violation of similarity laws describing the explosively-caused motion. It is not the total energy E_0, but the energy transferred into the medium, E, that determines the explosion effects in the medium. To verify this proposition we introduce the coefficient of efficiency of an explosion,

$$\alpha_e = \frac{E}{E_0};\ \alpha_e < 1$$

and consider the parameters of the explosively-caused motions using scaled coordinates $r/q_0^{1/3}$, where $q_0 = \alpha_e q$. The results of this analysis using the values of α_e calculated from Figure 6.40 are shown in Figures 6.42 – 6.44 (for the maximum particle velocity, positive phase duration and maximum displacement respectively, as a function of scaled distance).

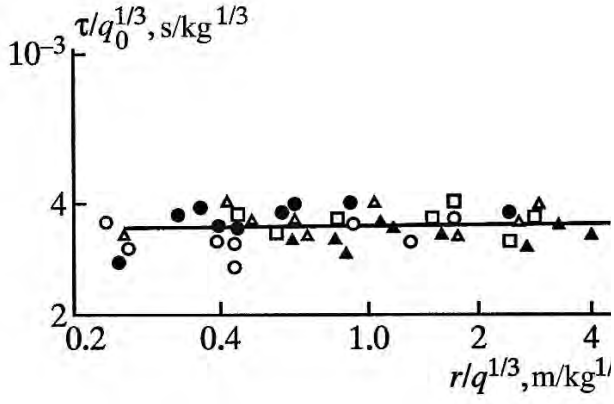

Figure 6.43: Duration of the positive phase. The notation is the same as in Figure 6.42.

The last three figures show that, regardless of the way the charge density is changed (e.g. using a different density of explosives, or placing the charge in a cavity), the experimental data are grouped into universal relationships. This suggests that the principle of energy similarity holds with respect to the wave characteristics for explosions with different energy density. The similarity parameter in this case is the energy E transferred into the medium during an explosion. We specifically note the fact that the only parameter determining the energy E for a particular medium, for both tamped and decoupled explosions, is the energy density of the source. This permits joint study of explosions with varying charge densities (Spivak, 1980c).

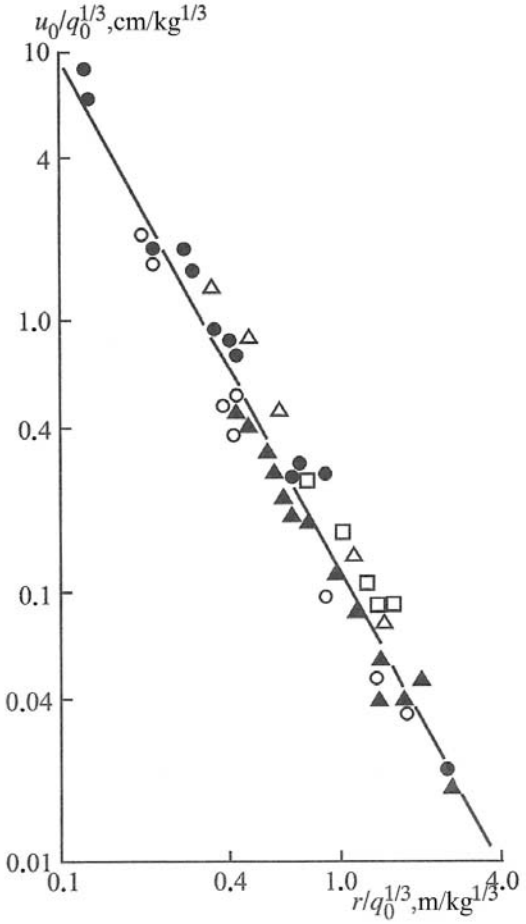

Figure 6.44: Scaled maximum displacements in the medium during explosions. The notation is the same as in Figure 6.42.

.

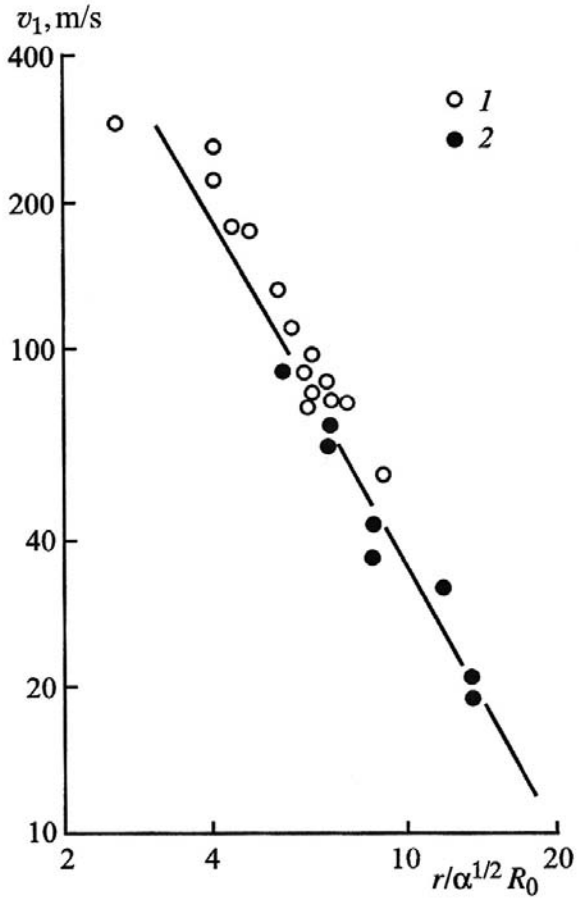

Figure 6.45: Maximum radial velocity component for tamped cylindrical charges in salt. The density of the explosives is: *1* – 1500 kg/m^3, and *2* – 500 kg/m^3.

For additional verification of the proposed method to form similarity groups for explosions with different energy densities, we apply this scheme to a cylindrical explosion, assuming that the value of E for such an explosion has the same value for a spherical charge of the same density. The same type of HE is used in both cases.

We use results obtained by Pavlov and Sudakov (1976) for fully tamped cylindrical charges in salt. We chose the correction coefficient α_e according to the averaged relationship in (6.4) obtained for spherical-charge explosions in sodium thiosulphate (the properties of rock salt and thiosulphate are similar).

Figures 6.45 – 6.47 show the maximum radial velocity component v_1, the maximum longitudinal velocity component v_2, and the duration of the positive phase in the radial direction $\tau/\alpha_e^{1/2}$, as a function of the scaled distance $r/\alpha_e^{1/2}R_0$, where R_0 is the cylinder radius.

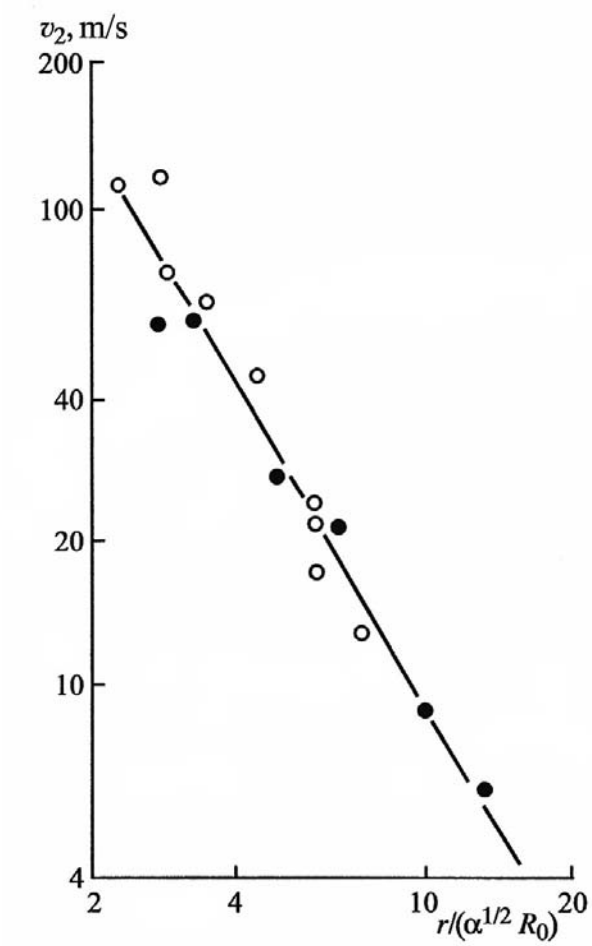

Figure 6.46: Scaled maximum longitudinal velocity component for cylindrical charges in salt. The notation is the same as in Figure 6.45.

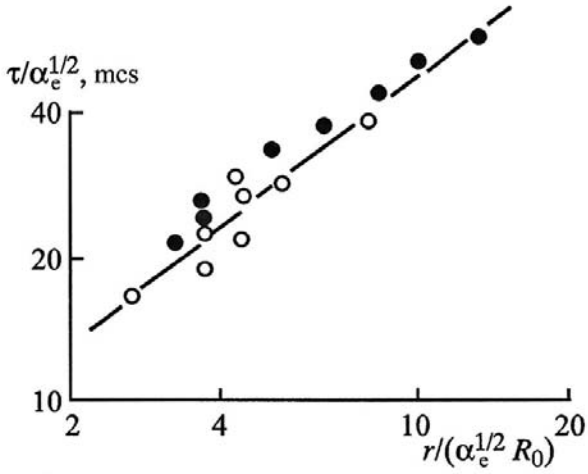

Figure 6.47: Scaled positive phase duration for cylindrical charges in salt. The notation is the same as in Figure 6.4

The last three figures show that for the proposed scaling scheme the experimental data obtained for cylindrical charges are grouped around the universal relationships with good accuracy.

Thus, we assume that the similarity principle, based on using the energy transferred into the medium, applies for cylindrical charges of different energy density.

Analysis of data from shallow (underburied) explosions shows that the problem of similarity for these explosions is complicated. Using either amplitude or signal duration separately, does not result in a common similarity parameter—because the efficiencies computed using amplitude ω_1 and the duration of the positive phase ω_3 are different. However a more detailed analysis shows that the efficiencies ω_1 and ω_3 become closer as rock strength is reduced. Table 6.13 shows the ratio ω_1 / ω_3 for different values of the medium strength, obtained by detonating spherical shallow explosions with η = 0. The relative (scaled) size of the damage zone for a fully

contained explosion was used as a parameter characterizing the medium strength. The results in Table 6.13 show that for low-strength media, for which radius of the damage zone for a fully contained explosion exceeds $20R_0$ the similarity principle applies. On the other hand, for explosions in strong media ($R_* \leq 20R_0$) the similarity with respect to each of the physical wave variables separately should be considered.

Medium	R_*/R_0	ω_1 / ω_3
PMMA	5.5	2.9
Sodium thiosulphate	12.5	1.5
Rosin	25	1

Table 6.13. Ratio of efficiencies for shallow explosions as a function of material strength.

Table 6.14. Relative volume displaced by the explosion source as a function of relative energy transferred to the medium by explosions

Scaled depth of burial η	Sodium thiosulphate		PMMA	
	$[\Delta V(\eta)/\Delta V(\infty)]$	$[E(\eta)/E(\infty)]$	$[\Delta V(\eta)/\Delta V(\infty)]$	$[E(\eta)/E(\infty)]$
-0.5	0.31	0.27	0.3	0.26
0	0.47	0.52	0.49	0.51

Regarding the averaged characteristics of shallow (underburied) explosions, as shown in Table 6.12 the size of the damage zone is proportional to the cube root of the energy transferred into the rock ($E^{1/3}$). The same is true for the volume displaced into the elastic zone ΔV, which (according to estimates) is in good agreement with E (Table 6.14).

The data presented in this section suggest the similarity of effects of an explosive source, in the presence of a free surface, with respect to the averaged parameters: R_* (determining the amount of the damaged (fragmented) material), and ΔV (determining the amplitude of the seismic signal). The energy transferred into rock during these explosions represents the similarity parameter in this case.

6.5. The effect of pre-stress on damage characteristics of a solid medium during explosions

The medium damage produced by a deep fully contained explosion is affected by the ambient stress field. Most obviously there is an increase with depth in the vertical component of the ambient stress due to the overburden pressure $P_h = \rho gh$. The horizontal stress components depend on the Poisson coefficient. The magnitude of the overburden pressure can be comparable to the strength characteristics of the rock. Calculation of explosion source properties in these conditions is a complicated problem. Specifically we are interested in the loading magnitude

which changes the mechanical efficiency of the explosion and the processes of fracture formation. For this purpose we conducted an experimental study of fully contained explosions in a block of PMMA subjected to hydrostatic compression.

The experiment used a high-pressure apparatus schematically shown in Figure 6.48. Its main element is a cylindrical steel chamber with 5 cm thick walls, an inner diameter of 22 cm, and a length of 1.5 m. The pressure in the chamber was changed using an air compressor.

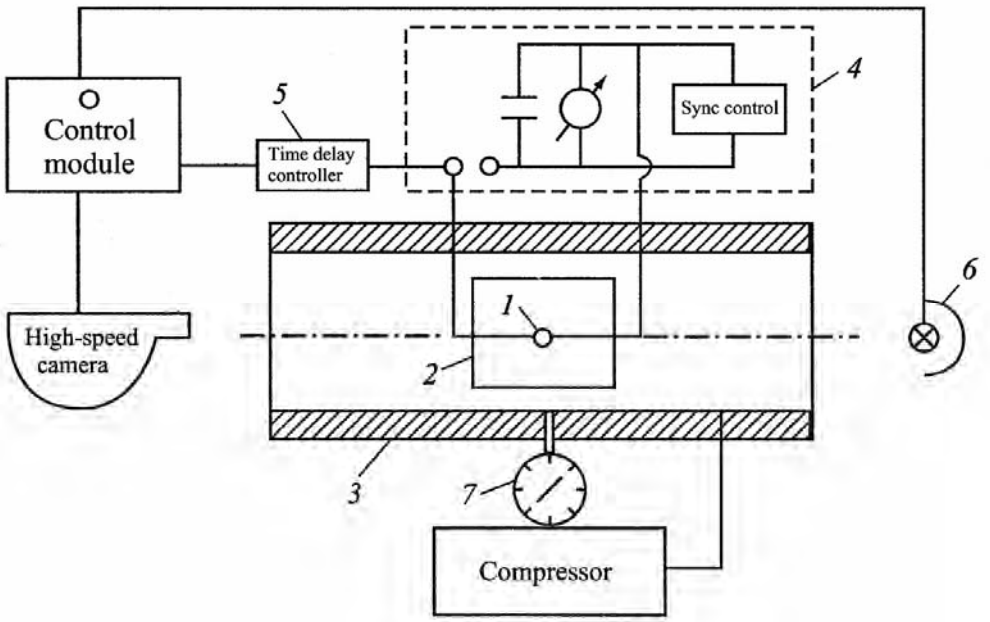

Figure 6.48: High-pressure apparatus schematic: 1 – [chemical] explosive charge, 1 – PMMA sample, 3 – high-pressure chamber, 4 – detonation controller, 5 – relay controlling time delay, 6 – impulse light source, 7 – manometer.

Windows with diameter of 12 cm were placed at the ends of the cylinder to permit video recording. A block of PMMA with a spherical HE charge in the center was placed into the high-pressure chamber. The explosive detonation and the impulse lighting were synchronized from a control center using the high-speed camera SFR-2M. These experiments were conducted under hydrostatic compression at 50 MPa pressure.

The most interesting and significant observation from the explosion was the absence of any visible damage inside the block. Evidently in these conditions the tension stresses from the explosion were cancelled by the external compression. We note that the magnitude of the hydrostatic compression corresponded to the elastic limit for PMMA and was less than the yield stress (plastic limit), so that the material stayed solid and did not change into a quasi-liquid state. In addition to the absence of a central damage zone, there was none of the spall damage common for a limited-size block. The absence of spall deformations for this experiment can be explained by changes in the reflectivity of the free surface. Indeed, the density of air at 50 MPa is only

about a factor of two lower than the density of PMMA, while at atmospheric pressure the density of air is a thousand times lower than the density of PMMA.

The cavity development was observed during the entire recording time (10^{-4} s). The maximum cavity radius $r_m = (1.85 - 1.9)\, r_{ch}$ was recorded after 8 – 10 μs after the explosion. After that a returning motion of the cavity wall was detected. After 20 – 25 μs the cavity radius was reduced to $r_c = (1.5 - 1.6) r_{ch}$ and did not change significantly at later times. However the final cavity radius measured after the experiment was $r_f = 1.3 r_{ch}$, which is the same as for an explosion without the applied stress.

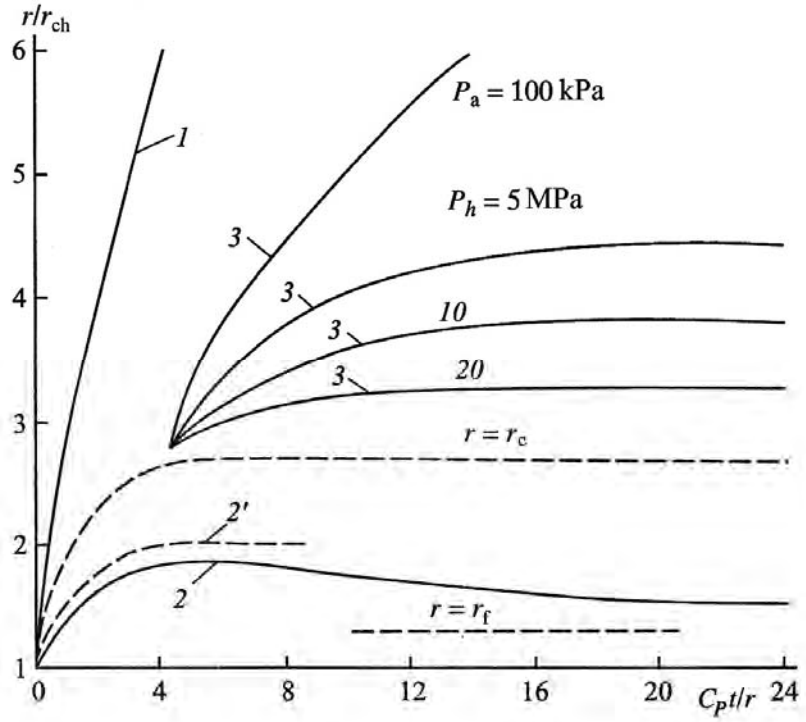

Figure 6.49: Diagram of the explosion development in PMMA under hydrostatic compression: *1* – stress wave front; *2*, *2′* – cavity boundary with and without the applied pressure; *3* – damage front for the specified magnitude of the compression.

A space-time picture of the explosion development in the PMMA block under external loading is shown in Figure 6.49. No differences in the wave front velocity between the experiments with external loading and atmospheric pressure were detected, within the measurement accuracy (line *1*). The maximum expansion of the cavity in the sample compressed to 50 MPa (line *2*) was lower than for the atmospheric pressure experiment (line 2′). Measurements showed that the maximum cavity volume in the compressed sample was 17% lower. Based on this result, Figure 6.50a illustrates the relationship between maximum cavity volume and hydrostatic compression, which can be expressed to first order as:

$$\frac{V_p}{V_m} = 1 - 0.77\frac{\rho g h}{\sigma_*},$$

where V_p and V_m represent the maximum cavity volume in compressed and un-compressed samples respectively, and σ_* is the compressive strength. These values for PMMA are $\sigma_* = 120\ MPa$ and $\frac{\rho g h}{\sigma_*} = 0.42$ for the experiment conditions. It follows from the last equation that with an increase in the confining pressure there is an increase in both the mechanical work of the explosion and the energy of the explosion products remaining in the cavity.

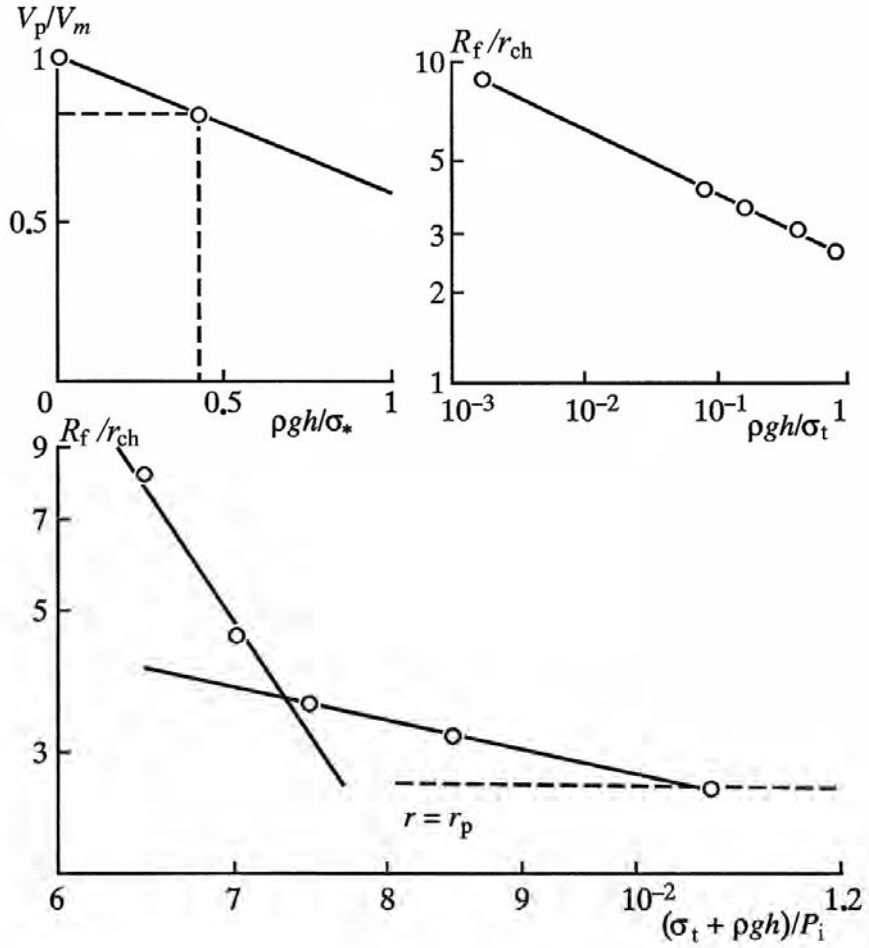

Figure 6.50. The effect of the confining pressure on the cavity size (a) and fracture zone extent (b and c). The explanations are in the text.

The propagation of the damage front in the PMMA block under atmospheric pressure is shown in Figure 6.49 (line *3*). There was no damage in a sample with an external compression of 50 MPa. In order to show a more complete picture of fracture formation under different levels of compression, Figure 6.49 shows the propagation of the damage front for compression of 5, 10 and 20 MPa (Chernikov, 1967). It shows that an increase in the external compression reduces both the size of the central damage zone and the velocity of its formation. Figure 6.50 shows the

radius of the damage zone R_{fr} as a function of confining pressure divided by the material tensile strength (σ_*), because the damage in PMMA was typically represented by radial fractures produced by radial tensile stresses. The relationship is given by an empirical formula:

$$\frac{R_{fr}}{r_3} = 2.7\left(\frac{\sigma_t}{\rho g h}\right)^{0.18}.$$

It is useful to express the relationship between the radius of the damage zone as a function of the confining pressure and the material strength. The sum of the stresses resisting the damage is normalized by the initial pressure in the chamber P_i which is of the order of gigapascals (GPa).

Two zones with different behaviors are seen in Figure 6.50. For distances $r > 4r_3$ the dependency is very strong:

$$\frac{R_{fr}}{r_{ch}} \sim \left(\frac{\sigma_t + \rho g h}{P_i}\right)^{-4}. \tag{6.5}$$

For distances $r < 4r_3$ the dependency becomes weaker:

$$\frac{R_{fr}}{r_{ch}} \sim \left(\frac{\sigma_t + \rho g h}{P_i}\right)^{-1.1}. \tag{6.6}$$

These different degrees of dependency of the fracture zone, on the sum of the tensile strength and overburden pressure, correspond to two different stages of fracture formation around the cavity. First, numerous fractures form in the zone with $r < 4r_3$ due to tensile stresses from the passing stress wave. Second, the individual radial fractures propagate as a result of a predominately quasi-static pressure from the cavity, and form in the zone with $r > 4r_3$. The zone with the strong dependency (6.5) shows that in order to change the extent of the radial fractures to distances of $r > 4r_3$ a small addition to the rock strength from the confining pressure is sufficient. The region with weak dependency (6.6) represents a zone ($r < 4r_3$) in which a significant increase in the external pressure ($\rho g h \sim \sigma_t$) is necessary in order to stop the nucleation of radial fractures

These experiments with hydrostatic compression produced the practical conclusion that even a small value of confining pressure, not exceeding the rock tensile strength, can significantly affect the explosive damage to the rock. Therefore for rocks at large depth subjected to triaxial compression the damage from explosions can be reduced and even disappear. Obviously, the experiments with PMMA are very specific and can only provide qualitative conclusions. The quantitative effects of the overburden pressure, on damage zone size, will depend upon specific physical properties of the rock.

There are on-going attempts in the mining industry to develop new technologies for rock breakage using non-traditional approaches (thermal damage, using radiation and high-energy particles), but chemical explosions remain the main method of rock fragmentation. It is likely in the next decades that the industry will continue to be dominated by explosion technology.

Improving this technology (for example by increasing the efficiency of explosions and the quality of explosive fragmentation) remains the most important problem of the mining industry.

One way to improve methods of fragmentation by explosives involves utilizing the geomechanical properties of the rock massif, in particular its stress-strain distribution. In real conditions, rock fragmentation takes place in the presence of external stresses due to overburden pressure as well as tectonic stresses (Kropotkin, 1996; Leonov, 1996). For blasting along rock benches using holes on the order of 10 m deep, the stresses at the bottom of the boreholes can reach 0.3 MPa and can be considered as one of the factors affecting rock damage. This factor significantly increases with increasing depth. We note that rock fragmentation occurs predominately along pre-existing fractures where strength is significantly lower than the strength of the intact rock (Adushkin and Spivak, 1993).

The stresses in a rock medium determine not only the magnitude of the stored elastic energy, which can be used to regulate the fragmentation parameters, but also the conditions under which the fragmentation takes place. The latter is related to a) changes in physical rock properties with stress increase (Kuliev, 2000), and b) uneven stress concentrations at structural discontinuities, which significantly increases the probability of local deformation as a result of release of the loading, and creation of a network of initial centers of damage.

The importance of the effects of rock stress on rock damage (fragmentation) becomes most obviously apparent for deep mining operations, which in some cases now reach down several kilometers.

Below we provide results of laboratory experiments, including those conducted at large scale, and our analysis of the damage characteristics of pre-stressed media.

The amount of elastic energy stored in a medium is determined by the stress acting upon that medium due to external loading. This energy can contribute to the mechanical processes taking place during explosive loading. It was determined experimentally (Spivak, 1982; Adushkin and Spivak, 1993a) that media (including rocks) with a large amount of stored elastic energy are capable of spontaneous fracturing via processes that include rock bursts or rock bumps. An increase in the stress level in the medium increases the volume V that determines the value of the released elastic energy, which also contributes to rock damage. For instance, the following relationship was determined during experiments in rosin, which adequately represents brittle failure of rocks (Spivak, 1982):

$$\frac{V}{V_{50}} \approx 5.33 \cdot 10^{-16} \sigma_0^2,$$

where σ_0 is the value of the applied stress in Pa, V_{50} is the volume for the applied stress of 50 MPa. In this case the shape of the damaged zone is close to hemispherical, which is common for the explosion of a surface charge.

It follows from the last relationship that if for $\sigma_0 < 50$ MPa additional energy is released (due to external compression) during explosion in the volume equal to the volume of the damage zone, the increase of the external pressure to 150 MPa would result in an increase of the volume (where the energy is released) exceeding the volume of the damage zone by up to a factor of 12.

While analyzing the possible contribution from the static external compression to the rock damage during explosions, it is necessary to compare the energy stored in the medium as a result of the pre-stress with the energy of the explosion that is supposedly spent on rock damage. The value of this energy E_d can be estimated as follows (Adushkin and Spivak, 1993a). It is known that the amount of energy remaining in the cavity with the detonation products is approximately 20% of the explosion energy E_{TNT}. Approximately 70% of E_{TNT} dissipates as heat. Other 1 – 3 % of E_{TNT} propagates as the seismic wave. Thus, approximately 5% of E_{TNT} is spent on the rock damage.

Analysis of stress amplitudes as a function of depth shows that an increase of the volume of fragmented rock is impossible to achieve by using a single explosion. As an illustration, Figure 6.15 shows approximate values of the principal compressive stress at different depth S_h, specific elastic energy of the rock massif E_e with the relative elastic compression energy in the volume V (damage zone of a TNT charge with energy E_{TNT} was determined using experimental relationships in Adushkin and Spivak, 1993a). According to the figure, the possible contribution of the elastic energy stored in the medium due to pre-stress, is small compared to the explosion energy (the condition $V = V_{50}$ is reached at a depth of h = 1780 m).

Therefore, we cannot count on the release of stored energy in order to significantly improve the volume of fragmented rock. In addition, considering that the energy spent on formation of new free surfaces is small, we expect that the quality of fragmentation can be improved by smarter use of stored energy. It will be shown later that this proposition is supported by experiments.

The following experimental data were used to study the effect of stress [pre-stress? PGR] on fragmentation characteristics of the rocks due to explosions. The data were obtained by explosion loading of solid medium samples across a broad range of sizes.

Laboratory experiments. Medium damage was studied using samples of clear PMMA. The sample sizes were 30 x 30 x 30 mm and 100 x 140 x 140 mm [and had different configuration – not sure I understand this one]. The sources included: 1) laser beam (1 J with the impulse duration of 30 ns), and 2 spherical PETN charges with the density of 1500 kg/m^3 and weights of 0.2, 0.4 and 0.8 g. As an illustration, Figure 6.51 shows photographs of the damage zone development for a spherical charge explosion in the center of a sample that was subjected to external compression in order to produce different types of stress-strain configuration (Figure 6.51 b, c and d). The loading schematic is shown to the left of corresponding photographs.

The damage characteristics and the magnitude of the released energy were studied using sodium thiosulphate and rosin samples with sizes of 100 x 100 x 100 mm. This experiment was a study of explosive and spontaneous damage of the medium, subjected to spherical-charge explosions of 0.2 g, under static compression of different magnitudes.

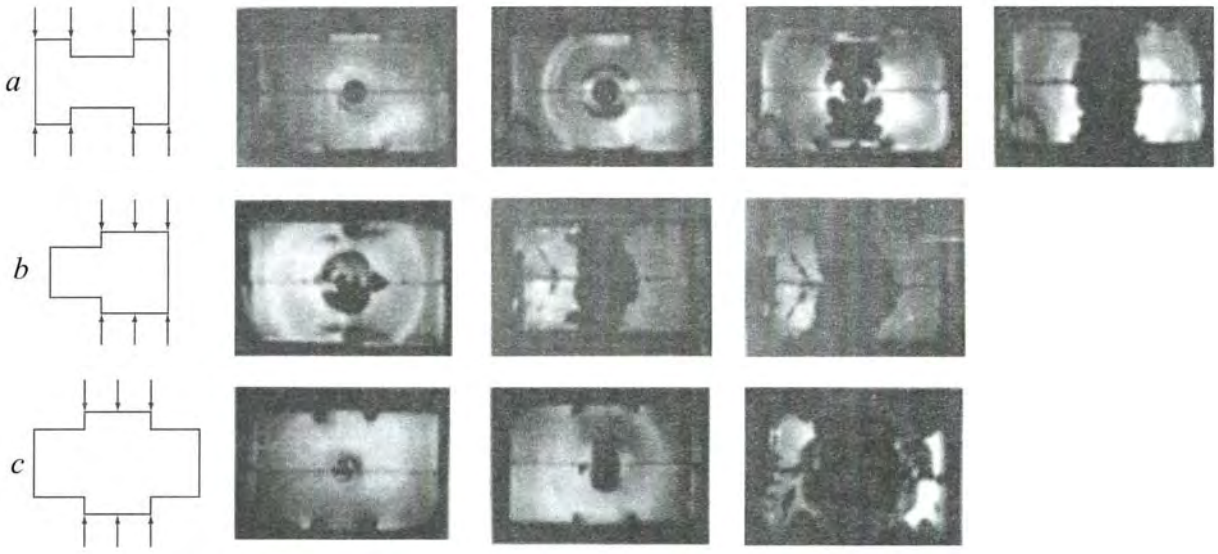

Figure 6.51: Snapshots showing the development of the damage zone during the detonation of PETN charges in PMMA for different experimental scenarios: $a - \sigma_0 = 50$ MPa; $b - \sigma_0 = 45$ MPa; $c - \sigma_0 = 70$ MPa. Loading schematics for the samples are shown on the left ($a - c$).

Figure 6.52: Matrix used to study self-sustained medium damage in a planar (2D) case.

The quality of fragmentation (the average size of the fragment in the damage zone) and the values of the maximum particle velocities were studied using rosin samples with sizes of 100 x 100 x 100 mm for explosive and spontaneous damage.

The loading of the samples was performed using screw and hydraulic presses. To study the spontaneous damage and explosive damage of the solid medium under static stress, custom made devices (matrices) were used (Figure 6.52).

Enlarged laboratory experiments. Damage characteristics of solid media and particle velocities under pressure [stress] were studied using 0.4 g spherical charges in granite blocks (1 m cubes) and concrete blocks of 500 mark [this is like concrete #500, whatever that means, it is a Russian thing] with sizes of 0.55 x 0.55 x 0.65 m. The loading of the blocks was performed using a hydraulic press HKMZ-500, which can create pressure up to 50,000 t of force per square meter (Figure 6.53)

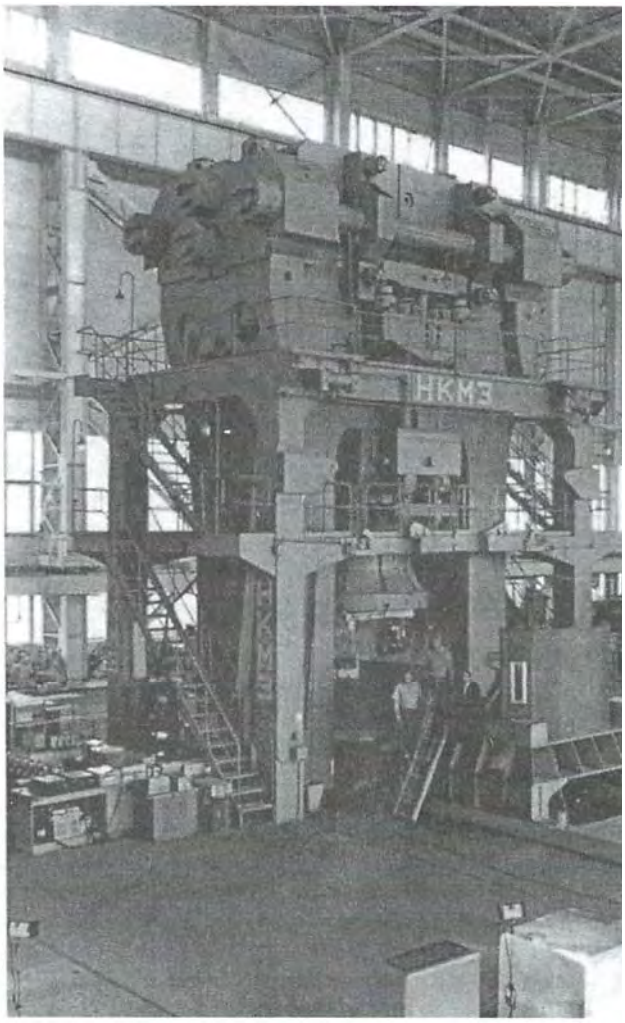

Figure 6.53: Press HKMZ-500 capable of exerting a pressure of 50,000 tons per square meter.

In order to determine the effect of the scale of the experiment on material damage, smaller samples with sizes of 4 x 4 x 4 cm were also used. Some characteristics of the experimental materials are provided in Table 6.16.

It is known from practice that large magnitude elastic energy stored in the solid medium (for instance due to external compression) can cause spontaneous material damage (rock bursts are a good example). Brittle homogeneous rocks with few pre-existing fractures are particularly susceptible to spontaneous bursts.

Table 6.16. Physical and mechanical properties of experimental materials

Experimental medium	Density, kg/m^3	Longitudinal wave velocity, m/s	Compressive strength, mPa	Young modulus, MPa
Concrete-500	2390	-	40	$3.8 \cdot 10^5$
Granit (from Yartsevo)	2610	5150	150	$5.6 \cdot 10^5$
PMMA	1180	2670	65	$5.35 \cdot 10^3$
Rosin	1080	2370	20	$3.2 \cdot 10^3$
Sodium thiosulphate	1650	3000	30	$1.65 \cdot 10^4$

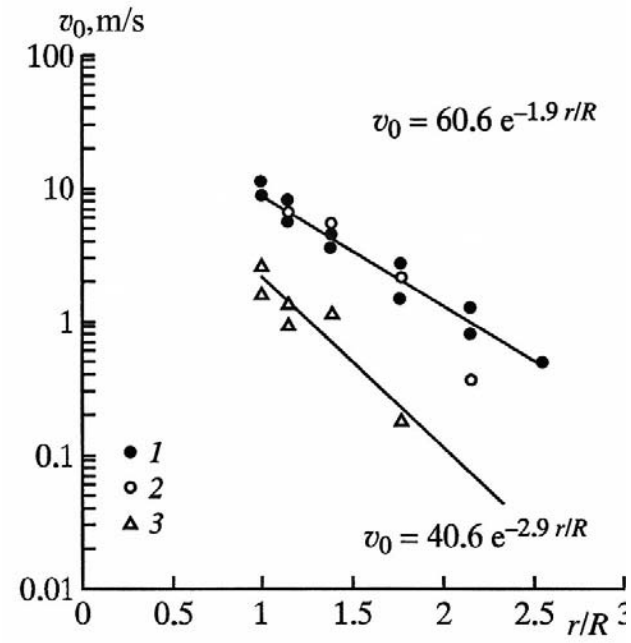

Figure 6.54: Maximum velocities of the flying fragments during self-sustained deformation (under a pressure of 50 MPa): *1*, *3* – induced damage (*1* – rosin, *3* – sodium thiosulphate); *2* – self-induced damage (rosin); *R* is the radius of the cylindrical emplacement cavity.

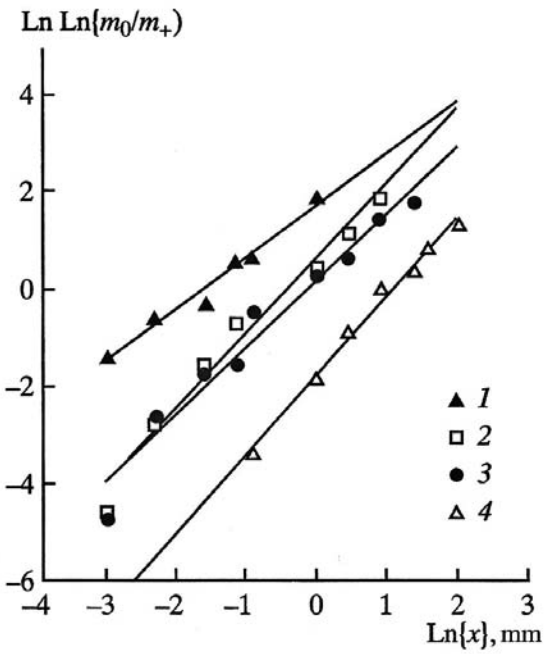

Figure 6.55: Fragment size distribution in the damage zone for rosin measured at the following distances from the explosion R/R_0: *1* – 2(5); *2* – 3(7.5); *3* – 5(12.5); *4* – 7(17.5).

Rapid explosion-like release of elastic energy with material damage and flying debris is possible with rapid changes of stress-strain conditions.

Laboratory experiments show that each material has a threshold value, above which a spontaneous burst is possible, leading to loss of mechanical equilibrium with rapid energy release. The value of this stress exceeds the material strength.

Material damage occurs as a damage wave, spreading from the free surface into the material. The velocities of flying fragments in this case are not very large (Figure 6.54). Self-sustained damage takes place when the deformation rate reaches approximately $(0.1 – 3) \cdot 10^2$ s^{-1}.

Simple estimates based on measuring the velocity of the flying fragments (to determine the kinetic energy) and residual temperature (to determine the dissipation losses) allow us to determine the energy spent on medium damage during spontaneous bursts. This energy was estimated to be approximately 50% of the total stored elastic energy, while the kinetic energy was 1 – 2%, and heat losses accounted for 35 – 45%.

The main characteristics of solid medium damage during explosions. The damage taking place within the solid medium occurs within the stress wave front formed as a result of expansion of the explosion products in the cavity (Tsvetkov et al, 1977; Adushkin and Spivak, 1993a). Without describing details of the damage zone evolution due to explosions, we consider some of the characteristics of the final state of the medium.

An explosion turns an initially quasi-homogeneous medium into a agglomeration of fragments having a broad range of sizes. As before, we use the Rosin-Rammler distribution (Eq 1.20) to describe particle sizes.

For this distribution the average particle size $\langle x \rangle$ is determined via an analytical relationship:

$$\langle x \rangle = x_0 \Gamma\{1 + 1/n\}, \tag{6.7}$$

where $\Gamma\{1 + 1/n\}$ is a gamma function [of the corresponding argument].

In loglog vs log coordinates, as shown in Fig 6.55 for the Rosin-Rammler distribution, the transformed fragment size distribution is represented by a straight line, which is convenient for analysis. This Figure shows an example of the results of laboratory experiments with rosin, at different distances from the source *r*. It is clear that the average fragment sizes increase with distance. This observation is associated with a shock wave amplitude decrease with distance due to geometrical spreading and energy dissipation in the medium.

The results of numerous laboratory investigations show that the parameters of the explosive deformation in the solid media are geometrically self-similar and can be described by universal analytical relationships $\langle x \rangle(r)$ if the argument is given by: a) a scaled distance $r / q^{1/3}$, or b) a relative distance r / R_0, where q and R_0 are the charge weight and radius respectively. In particular, the average fragment size as a function of distance for rosin damaged by spherical explosions of different sizes is well described by the relation:

$$\langle x \rangle = 0.0012(r/R_0)^{1.84} \text{ (cm)}. \tag{6.7}$$

The strain rate is an important parameter characterizing damage under external loading. In case of explosive damage the strain rate ε changes considerably with distance and significantly exceeds the strain rate that occurs during spontaneous rock bursts (see below).

r / R_0	2.5	5	8.75	13.75
ε, s^{-1}	$5 \cdot 10^4$	$8 \cdot 10^3$	$2 \cdot 10^3$	$6 \cdot 10^2$

The conditions of the explosion significantly affect the damage characteristics. This is not surprising, since the damage of the solid medium significantly depends on the parameters. In particular, Tsvetkov et al (1979) determined that the degree of fragmentation increases (that is, fragment size becomes smaller) with increasing strain during deformation. Additional fragmentation in this case occurs if certain conditions of additional deformation beyond the elastic limit are met.

The conditions (such as depth of burial of an explosion affect the parameters of the medium damage. For instance, the wave of unloading (a rarefaction) for a blast near the free surface reduces the degree of medium fragmentation, thus increasing the fragment size (Figure 6.56).

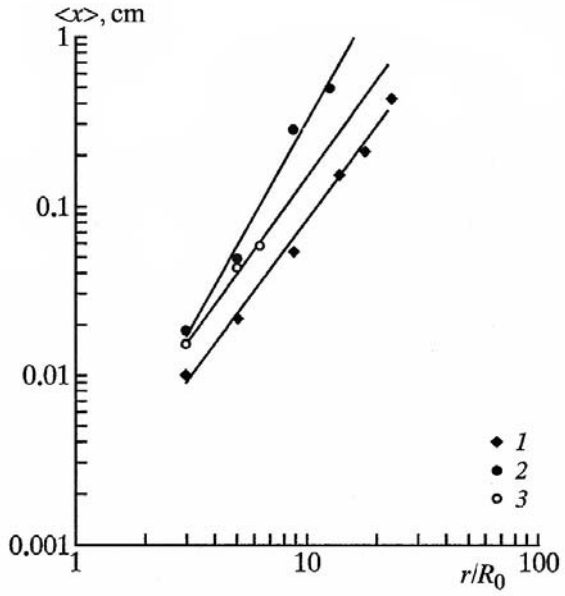

Figure 6.56: Average fragment size in rosin damaged by a PETN explosion (0.4 g): *1* – contained explosion; *2* – explosion at the free surface; *3* – explosion at the surface of the material under stress of 150 MPa.

Effect of the pre-stress. Damage of the solid medium due to stress waves from explosions takes place upon reaching certain conditions between the principal stresses. Depending on the explosion geometry and rock properties, these conditions may include: Coulomb-Mohr criterion for shear deformations, the condition when the tensile stresses reach the rock tensile strength, or other conditions. If these conditions are met, the material can lose its cohesiveness.

Obviously the presence of pre-existing (external) stress changes the relationships between the principal stresses produced by an explosion, and causing changes to the damage characteristics.

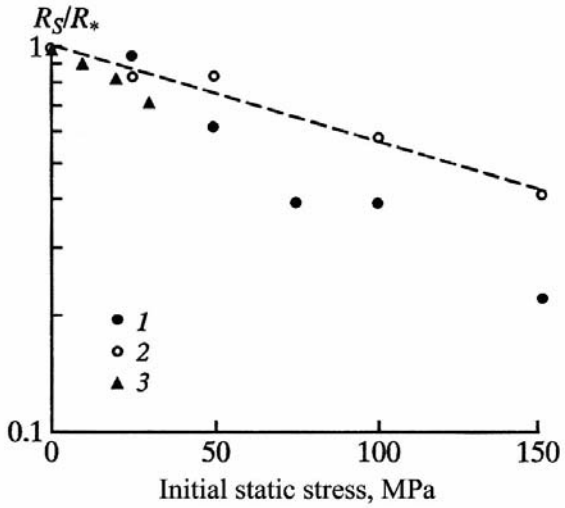

Figure 6.57: Ratios between the radii of the damage zone in pre-stressed and un-stressed media: *1*, *2* – contained explosion in media under hydrostatic compression (*1* – rosin, *2* – PMMA); *3* – spherical charge at the surface of the medium (rosin) with an artificial barrier.

For example, stresses close to hydrostatic compression (the values of the horizontal and vertical stresses are close to each other) cause significant reduction of the volume of the damage zone (Adushkin and Spivak, 1993a). Figure 6.57 shows the relative radius of the damage zone R_s/R_* for different values of initial stress (where R_s and R_* are the radii of the damage zones in stressed and un-stressed media respectively). For a fully contained explosion the relationship $R_s(P)$, where P is the initial static pressure, is given by

$$\frac{R_s}{R_*} = 1.01exp\{-0.0058P\}.$$

Reduction of the volume of damaged material suggests an increase in energy needed to induce medium damage E_0. In particular, for rosin the relationship between E_0 and P (Figure 6.58) is given by:

$$E_0 = 3.3 \cdot 10^4 exp\{0.03P\}.$$

It is important to note that the ratio between the specific energy of the static compression and energy needed to induce the damage of the solid medium is not a monotonic function of the external compression (Figure 6.59).

Comparison between the particle size analysis for a stress-free sample and a sample under complex stress-strain conditions shows that the latter case is more favorable for rock fragmentation. Indeed, as shown in Figure 6.56 the average fragment size in a pre-stressed medium is significantly smaller compared to the stress-free medium. The difference increases with the distance from the center of the explosion (when approaching the boundary of the damage zone). This observation suggests that the conditions favorable to initiation of self-sustained damage develop near the boundary $r = R_s$.

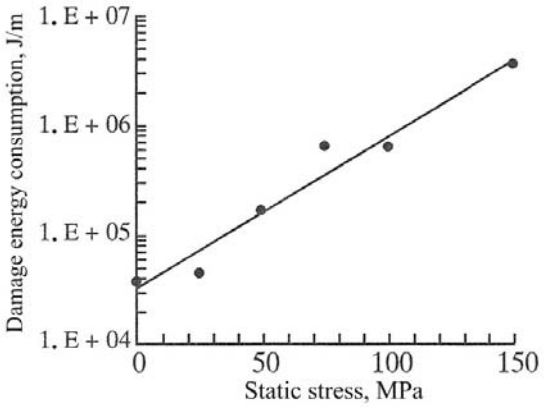

Figure 6.58: Energy needed to induce medium damage, as a function of the increase of static compression.

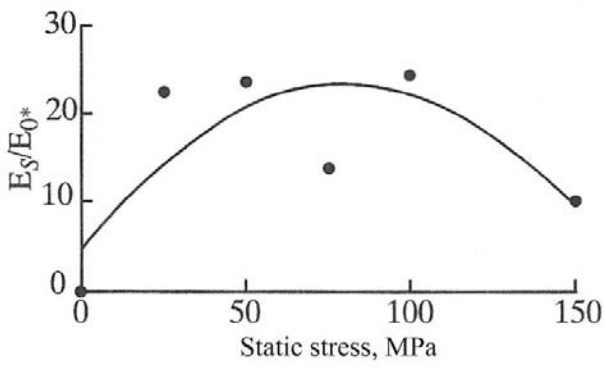

Figure 6.59: Ratio between the specific energy of static compression and the energy needed to damage of medium (rosin), under hydrostatic compression.

The analytical formula for the average radius of the damage zone in a complex stress environment is given by:

$$\frac{R_s}{R_*} = 1.02exp\{-0.01\sigma_0\}$$

as shown in Figure 6.57 for rosin.

Improvement of the quality of fragmentation. It is easier to analyze the process of the explosive damage in brittle media, where the material damage occurs as a result of fracture formation.

Characteristics of fracture formation are determined by imperfections in the material as well as by the loading conditions. The medium structure (the existence of the fracture nuclei) and the strength play major roles at the stage of fracture nucleation, while the loading conditions are more important during accelerated fracture growth.

A standard type of fracture initiation and propagation arises if the energy released during fracture propagation is equal to the energy required to create new surfaces. But in the presence of high initial stresses this standard fracture formation regime does not occur and the fracture propagation becomes unstable. In such cases of “excess” energy (where the energy of the elastic deformation E_e released during fracture propagation exceeds the surface energy E_s needed to create new free surfaces) a regime of self-sustained damage begins, with cascading fractures. This regime is characterized by bifurcation of fractures at irregularities in the medium. The

higher the ratio E_e/E_s becomes, the higher the probability of self-sustained damage (fracture bifurcations occur more often, leading to decreased fragment sizes).

We can express this regime using the following relationships. Additional stress at the defects created during static loading of the medium is given by:

$$\Delta\sigma = k\sigma_0,$$

where k is the coefficient of stress concentration ($k \sim 2\ to\ 10$ depending on the material properties).

The additional (excess) energy in the unit volume is:

$$E_e \sim (\Delta\sigma)^2 N,$$

where N is the average number of irregularities per unit volume.

The analysis of experimental data shows that the average fragment size for a fully-contained explosion in un-stressed medium (for example, rosin) is given by:

$$\langle x_0 \rangle = 4.6 \cdot 10^{-3} \{r/R_0\}^{2.2}.$$

Since $v_0(r) = 1.33 \cdot 10^3 \{r/R_0\}^{-1.6}$ (m/s) and $\sigma_f \sim \rho C v_0$, then

$$\langle x_0 \rangle = 90 \{\rho C\}^{1.375} {\sigma_f}^{-1.375}.$$

In the case of a pre-stressed medium we have:

$$\langle x_0 \rangle_f \sim 90 \{\rho C\}^{1.375} \{\sigma_f + k\sigma_0\}^{-1.375}.$$

We choose to define a coefficient of improvement of the fragmentation "quality" for a pre-stressed medium:

$$K = \frac{\langle x_0 \rangle}{\langle x_0 \rangle} = \{[\sigma_f + k\sigma_0]/\sigma_f\}^{-1.375}.$$

Table 6.17 shows the values of parameter K for the case of a static stress σ_0 = 150 MPa (for an explosion in rosin). This Table also shows the value of the parameter K_e obtained from analysis of the experimental data.

It follows from Table 6.17 that, accounting for the experimental error, a good agreement with the experiment is observed for $k < 1$, or in case when only a portion of the elastic energy from pre-stress is spent on medium damage. Indeed, residual stresses develop in the medium as a result of applied stress, which prevent a complete release of the stored energy.

More complete energy release can be achieved only when the conditions promote self-sustained damage [Spivak, 1982].

Indeed, certain conditions promote self-sustained release of stored energy. In this case the release of energy may occur even without having an explosion. Thus if the abrupt change in the

state of stress occurs as a result of an explosion (for instance due to removal of a support) we may expect additional energy release resulting in formation of new surfaces.

Table 6.17. Coefficient of improvement of fragmentation quality for an explosion in pre-stressed medium (σ_0 =150 MPa)

Distance r, cm	r/R_0	v_0, m/s	σ_f, Pa	K			K_e
				k = 1	k = 0.5	k = 0.4	
1	2.5	307	$7.86 \cdot 10^8$	1.27	1.13	1.1	~1
2	5	101	$2.58 \cdot 10^8$	1.88	1.42	1.3	~1
3.5	8.75	41.5	$1.06 \cdot 10^8$	3.36	2.08	1.85	~2

The experimental data provided above suggest that while pre-stress can have a negative effect on damage/fragmentation (i.e. a reduction of the amount of damaged material), it can also have some positive effect under certain conditions, which then improve fragmentation quality of the material. As we noted earlier, this can be explained by additional fragmentation as a result of the release of stored elastic energy.

It can be inferred that explosive fragmentation of a statically pre-stressed medium occurs in two stages. During the first stage the dynamic fragmentation of rocks occurs due to the passing shock wave. The loose material formed during this phase has low strength, which provides specific conditions for unloading of the pre-stressed medium (i.e. the medium surrounding the crush zone).

The second stage involves additional damage of already damaged material due to a release of the stored energy. It is possible that this additional damage takes place near the boundary of the damage zone, where the undamaged medium can unload due to the lack of resistance from the debris formed earlier.

We estimate the value of this additional deformation, to which an already-damaged medium is subjected due to a release of the stored elastic energy. We use the work of Tsvetkov et al (1979) which determined the value of additional fragmentation for a solid material (rosin) subjected to stresses beyond its strength limits. The average fragment size after the additional fragmentation L is described using the relationship:

$$\frac{L}{L_0} = exp\{-14e_a\},$$

where L_0 is the average fragment size during the initial fragmentation, and e_a is the value of an additional deformation of the damaged medium.

The value of e_a for the pre-stressed medium is provided in Table 6.18. Using the values of e_a it is easy to estimate the volume of the material V_s, which contributes to the additional damage during unloading. Assuming that approximately 50% of the released elastic energy is spent on the self-sustained damage we obtain:

$$V_s \sim (0.8 \div 1.0) V_*,$$

where V_* is the volume of the damage zone.

Table 6.18. Value of additional deformation of material dispersed [fragmented?] by the pressure wave as a result of energy release due to pre-stress[2]

Scaled distance, r/R_0	Parameter	
	$\langle x \rangle_{150} / \langle x \rangle_0$	e_a
3	1.06	$4.4 \cdot 10^{-3}$
5	1.4	$2.4 \cdot 10^{-2}$
6.25	1.58	$3.2 \cdot 10^{-2}$

In conclusion we note that the explosively-caused damage occurring in pre-stressed media takes a number of different forms, depending on different loading:

- under triaxial compression (quasi-hydrostatic) the volume of the damage zone decreases with the increased load;
- under uniaxial compression the damage develops along the direction of principal compression, and the volume of the damaged material can be substantial;
- under a compressional load exceeding the strength limit of the material, additional damage to the medium may occur due to the release of stored elastic energy following the explosive damage;
- in the case of inhomogeneous field of static stresses it is possible to control the explosion damage by placing separate borehole charges and controlling the order of their detonation; in this case the volume of the damaged medium can be increased.

If conditions are met for the release of stored elastic energy during the explosion, the quality of fragmentation increases, and thus a reduction in the number of large fragments occurring during mining operations.

In order to develop recommendations for optimal rock fragmentation under high applied stress, other factors have to be considered. One of the most important, is the quantitative relationship between the principal static stress and the strain rate and their effect on the average fragment size.

[2] 1. Explosion charge q = 0.4 g on the surface of rosin with a barrier for σ_0=150 MPa; 2. $\langle x \rangle_{150}$ and $\langle x \rangle_0$ are the average size of fragments produced by an explosion in pre-stressed and stress-free media respectively

6.6. Explosions in compressible media

The process of compaction is the main mechanism of cavity formation during explosions in porous rocks (e.g. clays, loess etc). The magnitude of compaction mainly depends on the porosity and fluid content in the pores. Below we show the effects of porosity and moisture content on the elastic properties and strength of the medium (emphasizing sediments) and on the mechanical explosion results.

The measurements of linear dimensions and volume of the cavity and their relationship to the density and moisture content were investigated experimentally for fully contained explosions. To conduct the experiment, sand was placed into a steel cubic container (called a "bomb"). The length of each side of the cube was 30 cm, the wall thickness was 2 cm. The walls of the container were bolted together to prevent the escape of the explosive products into atmosphere. The container was placed on a scale to determine the average volume and weight of the sand.

The measurements showed that oscillations of density did not exceed 3%. Spherical charges made of compressed PETN with density of ρ=1400 kg/m^3 and the mass of $m_{ch} = 0.2\ to\ 0.8\ g$. The charges were placed either in the center of the sample or near the wall close to the steel plate. No residual deformations of the container walls were observed. After each detonation the container was opened, the sample was cut and the cavity sizes were measured. In order to determine the volume of the cavities they were filled with liquid paraffin or plasticine and the volume of the cast was determined by placing it into water. Experiments with different charge sizes showed that the cavity volumes were proportional to the charge sizes, i.e. the cavity size satisfies the geometrical similarity principle. Therefore the size of the container was sufficiently large and it did not interfere with the cavity development.

6.6.1. The main characteristics of the material. The sand used had homogeneous grain sizes from 0.2 to 0.5 mm, with 80% of the particles measuring 0.28 – 0.35 mm, and did not contain clay particles. The density of the dry sand used in the experiment varied in the range $1400 \le \gamma \le 1700$ kg/m^3, for moist sand the densities varied in the range $1400 \le \gamma \le 1700$ kg/m^3. To moisten the sand glycerin was added with γ_ω = 1260 kg/m^3. The moisture content, defined as the ratio between the mass of the fluid to the mass of the solid particles, was ω = 0.02, 0.1, and 0.2. Glycerin was used instead of water in order to keep the moisture content constant for a long time (preventing evaporation). The porosity of sand is equal to the ratio of the pore volume to the total sample volume:

$$m = 1 - \frac{\gamma}{\gamma_s(1+\omega)},$$

where γ is the volume weight of the material as a three-component medium (mixture of sand, moisturizer and air), γ_s = 2650 kg/m^3 – volume weight of the skeleton (sand matrix). The air porosity is equal to the ratio of the volume of air to the total volume of the sample mixture:

$$m' = 1 - \frac{\gamma(\gamma_\omega + \omega\gamma_s)}{\gamma_s\gamma_\omega(1+\omega)}.$$

In dry conditions ω = 0, m = m′, and the expression is simplified:

$$m = 1 - \frac{\gamma}{\gamma_s}.$$

During the experiments the porosity varied in the range $0.34 \leq m \leq 0.62$ and air porosity measured in the range $0.15 \leq m' \leq 0.54$.

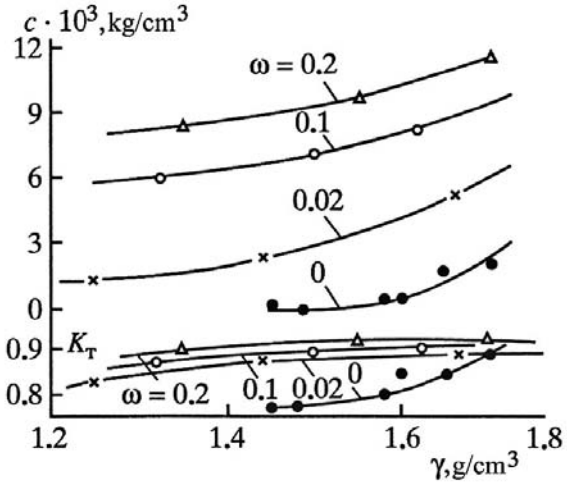

Figure 6.60. Relationship between the material cohesion and the coefficient of internal friction (for unconsolidated materials).

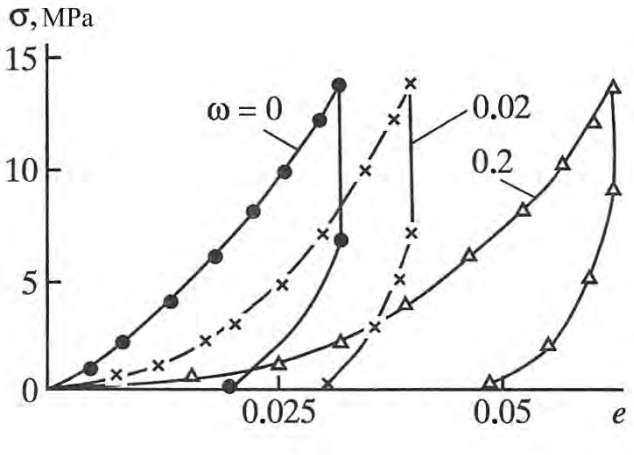

Figure 6.61. Static compression curves for sand with different moisture content (γ = 1630 kg/m^3).

The main strength-related characteristics of sand used in the experiments were determined. Figure 6.60 shows the cohesion c and the coefficient of internal friction K_f as a function of the volume weight of sand. Measurements were performed for dry sand and for different values of the moisture content. Cohesion increases with increasing volume weight, particularly for moist sand (for instance from 10 MPa for $\omega = 0$ to 1 kPa for $\omega = 0.2$). The internal friction coefficient has only a weak dependence on both volume weight and moisture content.

Additional data on static compression of sand was obtained using samples confined in a cylindrical vessel 2 cm in diameter and 8 cm long. There was no drainage. Figure 6.61 shows typical relationships between the compressional stresses σ and the volumetric strain ε. The figure shows that the deformations are irreversible. The increase in moisture content with other conditions being equal led to an increase in irreversible deformation, while the free porosity of sand decreased simultaneously ($m' = 0.38$ for $\omega = 0$, $m' = 0.27$ for $\omega = 0.2$). Thus the presence and the increase of the amount of fluid reduced compressibility of sand for static loading.

To characterize dynamic compressibility the velocity of longitudinal waves was measured as a function of the volumetric weight and moisture content (Figure 6.62). The measurements were

conducted using an ultrasound apparatus KUB-1 and frequency of 60 kHz. The P-wave velocity grows with the increase in the volumetric weight. This relationship is linear for dry sand:

$$C_p = 540\ (\gamma\text{-}1)\ \text{m/s for } 1400 \le \gamma \le 1700\ \text{kg/m}^3.$$

The increase in moisture content with fixed volumetric weight reduced the P-wave velocity, with the exception of a low-density medium at low water content (the sound velocity in glycerin is 1930 m/s).

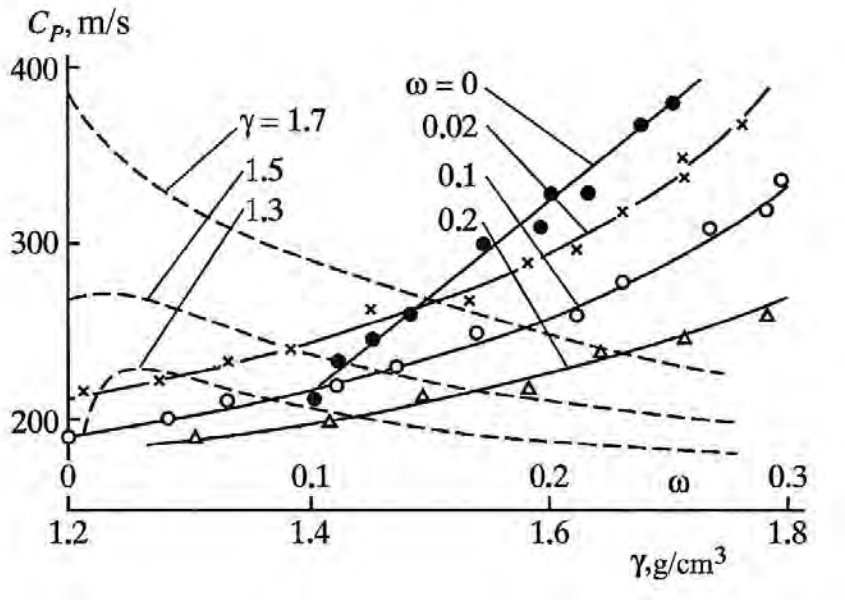

Figure 6.62. P-wave velocities as a function of the volumetric weight and of the moisture content (dashed lines) of the material.

6.6.2. The results of the experiments. The cavities in sand were not spherical, and their surfaces were covered with conical fractures. The depths of the fractures and their apertures depended on the volumetric weight and moisture content. Using measurements of the cavity volume V_c the values of the so-called "overshoot parameter" $\Pi = V_c/q$ were measured for different values of the volumetric weight and moisture content (Figure 6.63). The spread of the experimental values is approximately 10 – 15% for moist sand and 15 – 20% for dry sand. The increase in the volumetric weight results in a strong decrease in the "overshoot parameter" according to the formula:

$$\Pi = B\gamma^{-n}\ (\text{m}^3/\text{t}) \text{ for } 1200 \le \gamma \le 1900\ \text{kg/m}^3.$$

The values of the empirical constants B and n are shown in Table 6.19.

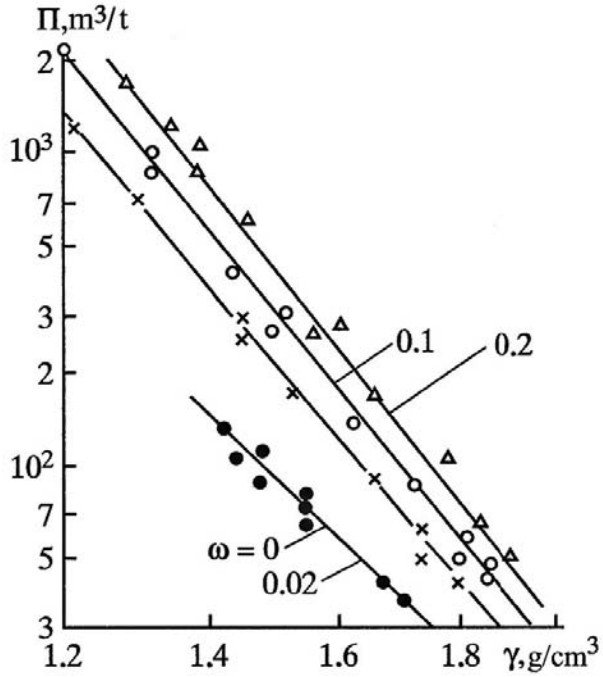

Figure 6.63: Overshoot parameter as a function of the volumetric weight of the material.

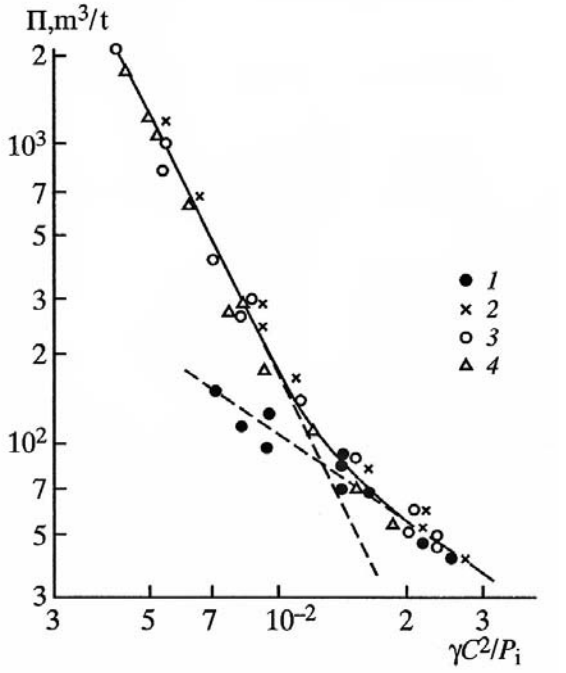

Figure 6.64: Overshoot parameter as a function of material compressibility for the following values of moisture content: *1* – 0; *2* – 0.02; *3* – 0.1; and *4* – 0.2.

We note that the increase in volumetric weight from 1400 to 1700 kg/m^3 causes the decrease in the overshoot parameter by a factor of 4 – 5 in dry sand, and by a factor of 7 – 8 in moist sand. The increase of the moisture content from 0 to 20% with fixed volumetric weight the "overshoot parameter" increased by a factor of 3 – 5.

The measurements of the "overshoot parameter" show that the volume of the cavity for a fully contained explosion is determined mostly by the dynamic compressibility. This is illustrated in Figure 6.64, which shows the relationships between the "overshoot parameter" and the incompressibility modulus γC_p^2 divided by the average pressure in the cavity P_c = 10 GPa. All experimental data points (with the exception of the values for dry sand) are situated around the same line. The relationship is particularly strong for low values of densities $\gamma \leq 1.6$ *to* 1.7 g/cm^3:

$$\Pi = 1.63 \cdot 10^{-10} \left(\frac{\gamma C_p^2}{P_c}\right)^{-3} \text{ (m}^3\text{/t) for } \frac{\gamma C_p^2}{P_c} \leq 1.2. \qquad (6.8)$$

If the density and consequently incompressibility (γC_p^2), increases, this relationship becomes weaker: [Something is very wrong here. I think they did cut and paste here, and forgot to change the symbols.][indeed, lots wrong --- I get 10^{-8} not 10^{-10} and the slope changes where the x-axis is about 10^{-2} not 1.2]

$$\Pi = 108\left(\frac{\gamma C_p^2}{P_c}\right)^{-1} \text{ (m}^3\text{/t) for } \frac{\gamma C_p^2}{P_c} \geq 1.2.$$

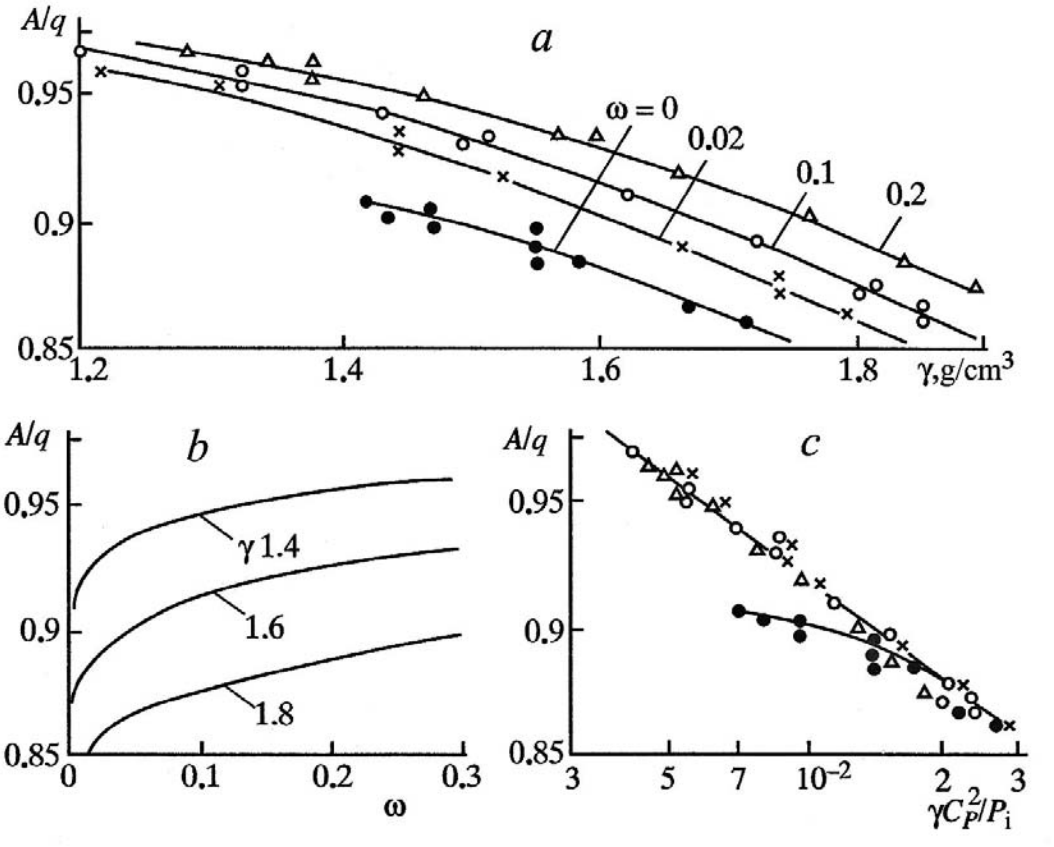

Figure 6.65: Work performed by explosions as a function of (a) material density, (b) moisture content and (c) compressibility. The notation is the same as in Figure 6.64.

Using the measurements of the cavity volumes we determined the work of a fully contained explosion:

$$A = \int_{V_i}^{V_c} P(V)dV,$$

where V_i is the initial volume of the charge cavity, and V_c is the final cavity volume. The isentropic exponent for the detonation products with ρ_{ch} = 1400 kg/m^3 was used to perform the integration. The calculation results (Figure 6.65a) show that the increase in the volumetric weight of sand causes the decrease in the work, which for this experiment varied in the range $0.85q < A < 0.97q$. The work increases with the increase in moisture content if the volumetric weight remained fixed and the rate of increase also increases with increase of the volumetric weight (Figure 6.65b). The dependency of the explosion work on the medium compressibility is shown in Figure 6.65c and corresponds to the empirical formula:

$$\frac{A}{q} = 0.45 - 0.13lg\left(\frac{\gamma C_p^2}{P_c}\right).$$

The case of dry sand represents an exception for $\gamma \leq 1550$ kg/m^3, which can be explained by the escape of the gaseous products into the pore space during the cavity expansion.

Determining the radius of the cavities was difficult due to the presence of deep fractures on their surface. Therefore the radius was calculated from the measured volumes using

$$r_c = \left(\frac{3V_c}{4\pi}\right)^{1/3}.$$

Figure 6.66 shows the relationship between the cavity radius and the volumetric weight of the material. For this experiment ($1200 \leq \gamma \leq 1900$ kg/m^3 and $0 \leq \omega \leq 0.2$) the radius of the cavities ranged $r_c/q^{1/3} \leq 2 \div 8$ m/t$^{1/3}$ (or $r_c \leq 3.6 \div 1.4 r_{ch}$).

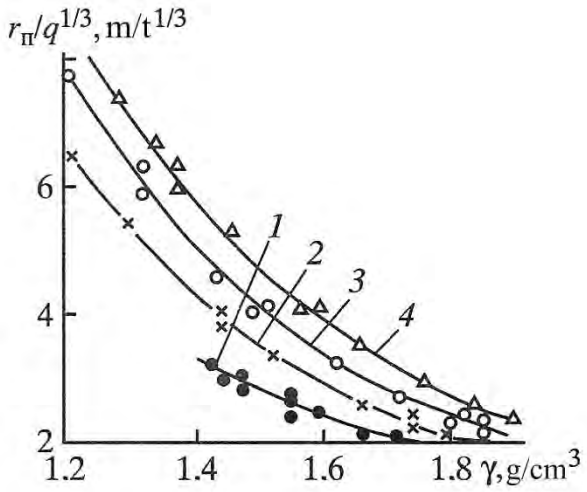

Figure 6.66: Cavity radius as a function of material volumetric weight (mass density) for different values of moisture content. The notation is the same as in Figure 6.64.

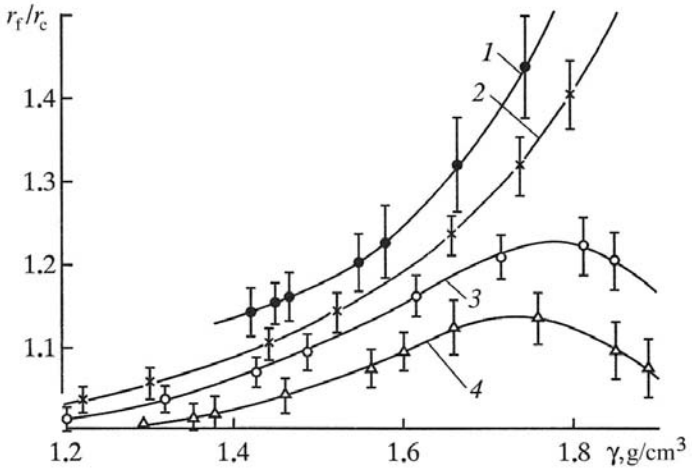

Figure 6.67: Cavity radius as a function of material volumetric weight for different values of moisture content. The notation is the same as in Figure 6.64.

It is interesting to note that the radial fractures formed on the surface of the cavity had their aperture approximately equal to the fracture depth. Figure 6.67 illustrates the cavity radius combined with fracture depth r_f (this is the radius from the center to the end of the fractures rather than the surface of the cavity) divided by the cavity radius r_c as a function of the volumetric weight of the material. The bars show the variation of the fracture sizes. The fractures in dry sand had the greatest size variations. The relative fracture depths and their variations grew with the volumetric weight increase. This pattern changed with an increase in the moisture content and the changes occurred sooner for higher moisture content.

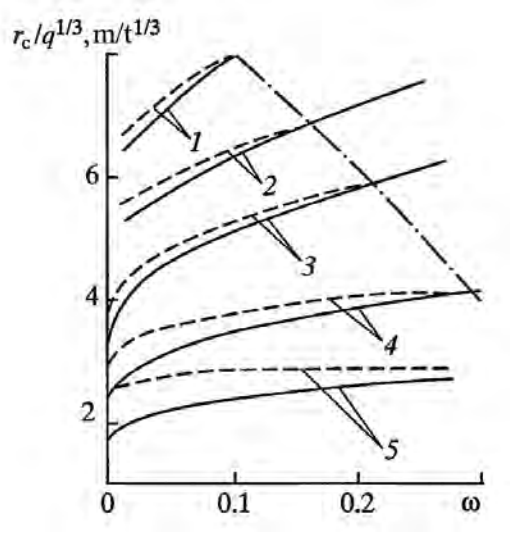

Figure 6.68: Cavity radius (r_c) as a function of material moisture content ω for the following values of density in kg/m^3: *1* – 1200; *2* – 1300; *3* – 1400; *4* – 1600; *5* – 1800. For further explanations see the text.

The increase in moisture content caused simultaneous decrease of the volumetric weight and the fracture size. Figure 6.68 shows the scaled cavity radius r_c (solid lines) and the cavity radius combined with the fracture depth r_f (as a function of the moisture content). For explosions in sand with $\gamma \leq 1300$ kg/m^3 and $\omega \leq 0.1$ the cavity has a smooth surface and the fracture sizes are comparable to the grain sizes (this behavior is marked in Figure 6.68 with dash-dotted lines). Thus, the volume and the moisture content of granular materials have a significant effect not only on the final cavity sizes, but also on the size of the radial fractures, in some cases making the radial fractures disappear.

Other experimental studies (Altshuler et al, 1970; Isakov, 1976) have reported the effect of cavity fracturing during explosions in soft sediments. Calculations of the stress field created by an explosion in a visco-plastic medium (Koshelev, 1975) noted that tensile stresses were present even during the cavity expansion phase, which created the system of radial fractures. However, this experiment has shown that only a few fractures develop further. It also follows from the calculations that the radial fracturing of the cavity surface should not occur with an increase in the explosion scale, because the material is under uniform compression and the tensile stresses appear at later stages.

6.7. Explosions with cylindrical charges

Explosions with cylindrical charges of variable lengths. When the charge becomes longer, the symmetry of the explosion changes, which may affect energy transfer into the emplacement medium (e.g. Adushkin, Koschii, 1979). Therefore we need to determine:

- whether the cavity volume will change with change of the charge geometry;

- the ratio between the charge length to its diameter at which the transition from spherical to cylindrical symmetry will occur;
- effects of physical and mechanical properties of the rock medium.

These problems were solved experimentally by measuring the "overshoot parameter" in PMMA, sodium thiosulphate, sand, and plasticine (clay). The selected materials allowed us to study brittle damage, volumetric compaction, and plastic deformation that can occur in solid media.

The experiments with sand, plasticine and sodium thiosulphate (ST) were conducted in a steel cube. Experiments with PMMA involved blocks measuring 12 x 15 x 20 cm^3. The sand had a density of 1850 kg/m^3, fluid content ω = 0.1 (the fluid being glycerin), porosity m'=0.18, and the velocity of stress waves C_p = 360 m/s.

The plasticine had a density of 820 kg/m^3, C_p = 1000 m/s, and a Poisson ratio of 0.33. Solidified after melting ST had a density of 1700 kg/m^3, uniaxial compressional strength of 20 MPa, C_p = 4500 m/s, and a Poisson ratio of 0.28. The density of PMMA was 1180 kg/m3, uniaxial compressional strength was 120 MPa, C_p = 2800 m/s, and its Poisson ratio was 0.35.
To conduct the explosions the cylindrical charges made of either pressed (density of 1400 kg/m3) or loose (density of 1000 kg/m^3) PETN, with a diameter d = 3 – 6 mm. The mass of the charges was m_c = 0.2 – 4 g, charge density of q_l = 0.2 – 0.3 g/cm, the aspect ratio or caliber varied between $1 \le l \le 50$. The explosion initiation was done by using lead azide. The scaled length of the charges is related to the *caliber* by the relationships:

$$\frac{l}{q^{\frac{1}{2}}} = 0.92\,\frac{l}{d}\ (\mathrm{m/(t/m)^{1/2}}) \text{ for } \rho_{ch} = 1400\ kg/m^3,$$

$$\frac{l}{q^{\frac{1}{2}}} = 1.13\,\frac{l}{d}\ (\mathrm{m/(t/m)^{1/2}}) \text{ for } \rho_{ch} = 1000\ kg/m^3.$$

After the explosions the samples were cut and measurements of the radius, length and the volume of the cavities were made. The volumes of the cavities in plasticine were measured using water. Cavities in sand and ST were filled with gypsum or melted plasticine and the volume of the cast was determined by placing in water. The errors of the cavity measurements depending on the medium type were 2 – 5%, and the errors in the linear measurements were 1 – 8%.

Cavities in plasticine and ST were smooth, with hemispherical end surfaces. The cavities in sand were covered with V-shaped fractures predominately along the axis with depths of about 0.2 r_c. The ends of these cavities had conical (frustum) shapes. The variation of the cavity shapes in plasticine with the length increase is shown in Figure 6.69. The charge caliber varied in the range $1 \le l/d \le 44$, and the ratio of the cavity length to the diameter for these charges was $1 \le l_c/2r_c \le 4.5$. The cylindrical part of the cavity was formed for the charges with ratios of $l/d \ge 4$. However the cavity radius increased until it reached the limiting diameter for charges with $l/d \ge 16$.

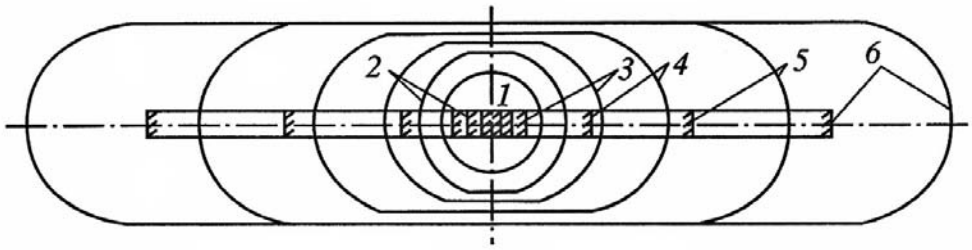

Figure 6.69: Changes of the cavity shape in plasticine with increases in charge length, *1 – 6* denote the charge and the corresponding cavity created by the explosion of that charge.

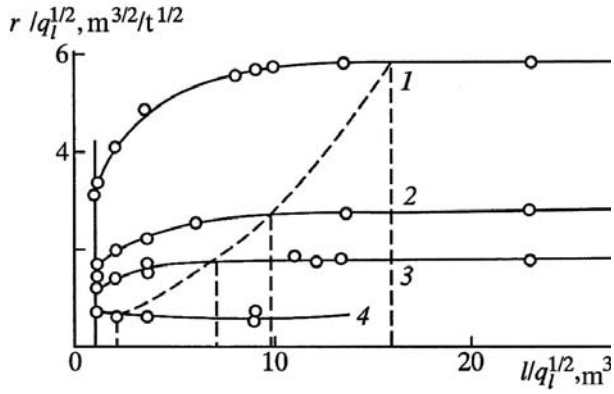

Figure 6.70: Relative radius of the cavity as a function of the scaled charge length: *1* – plasticine, *2* – sand; *3* – sodium thiosulphate; *4* – PMMA.

For these two types of media, relationships were obtained for the radius (Figure 6.70) and the length (Figure 6.71) of the cavity as a function of the scaled charge length. For explosions in plasticine, sand and ST, gradual change from spherical to cylindrical symmetry [is this right?] led to an increase in the cavity radius. In PMMA, however, the cavity radius decreased with the scaled length increase. For small values of *l/d* the cavity length was increasing faster than the charge length. In all media a characteristic charge length $l = l_*$ was observed, beginning from which the cavity radius remained constant and its length was proportional to the charge length. This length is different for the different media types as shown with vertical dashed lines in Figures 6.70 and 6.71. The linear dimensions of the cavities for $l \geq l_*$ are described by the following empirical relationships:

In plasticine:

$$\frac{r_c}{q_l^{1/2}} = 5.9\frac{m^{3/2}}{t^{1/2}}; \qquad \frac{l_c}{q_l^{1/2}} = 12 + \frac{l}{q_l^{1/2}}\frac{m^{3/2}}{t^{1/2}}; \qquad \frac{l_*}{q^{\frac{1}{2}}} = 13\frac{m^{3/2}}{t^{1/2}};$$

In sand:

$$\frac{r_c}{q_l^{1/2}} = 2.7\frac{m^{3/2}}{t^{1/2}}; \qquad \frac{l_c}{q_l^{1/2}} = 4.0 + \frac{l}{q_l^{1/2}}\frac{m^{3/2}}{t^{1/2}}; \qquad \frac{l_*}{q^{\frac{1}{2}}} = 8\frac{m^{3/2}}{t^{1/2}};$$

In thiosulphate:

$$\frac{r_c}{q_l^{1/2}} = 1.75\frac{m^{3/2}}{t^{1/2}}; \qquad \frac{l_c}{q_l^{1/2}} = 2.0 + \frac{l}{q_l^{1/2}}\frac{m^{3/2}}{t^{1/2}}; \qquad \frac{l_*}{q^{\frac{1}{2}}} = 5.7\frac{m^{3/2}}{t^{1/2}};$$

In PMMA:

$$\frac{r_c}{q_l^{1/2}} = 0.59\frac{m^{3/2}}{t^{1/2}}; \qquad \frac{l_c}{q_l^{1/2}} = 0.5 + \frac{l}{q_l^{1/2}}\frac{m^{3/2}}{t^{1/2}}; \qquad \frac{l_*}{q^{\frac{1}{2}}} = 1.6\frac{m^{3/2}}{t^{1/2}}.$$

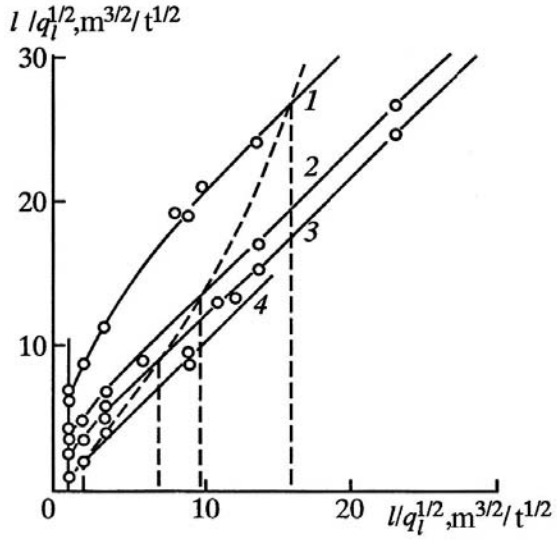

Figure 6.71: Relative length of the cavity as a function of the scaled charge length: *1* – plasticine, *2* – sand; *3* – sodium thiosulphate; *4* – PMMA.

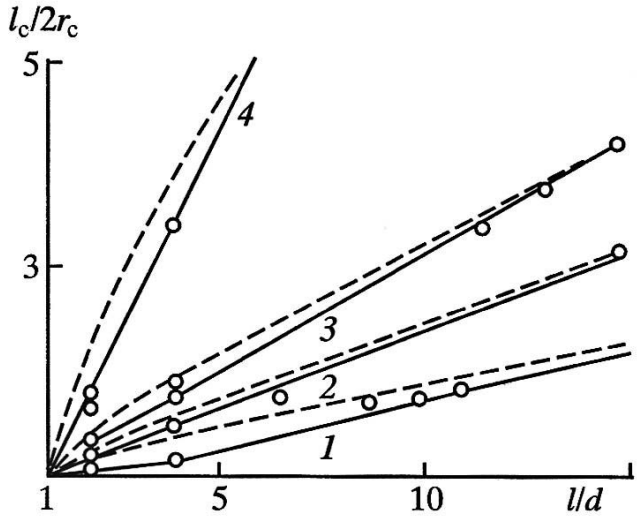

Figure 6.72: Ratio between the length and diameter of the cavity as a function of charge caliber: *1* – plasticine, *2* – sand; *3* – sodium thiosulphate; *4* – PMMA.

As it turns out, the relationship between the linear dimension of the charge and the cavity (Figure 6.72) is sensitive to physical properties of the emplacement medium. In hard media the ratio between the length and the diameter of the charge and the cavity remained practically constant. For soft media the increase in the ratio between the cavity length and its diameter became slower with caliber increase. Thus for an explosion in plasticine with l/d = 13 the cavity length was twice its diameter. Using simple geometrical relationships we obtain the relationship between the charge caliber $K_{ch} = l/d$ and the cavity $K_c = l_c/2r_c$:

$$K_{ch} = 1 + \left[\frac{(K_c-1)^3}{K_c}\Pi_c\rho_{ch}\right]^{1/2}, \ldots$$

where ρ_{ch} is the charge density, and Π_c is the "overshoot parameter" for cylindrical symmetry ($l \gg l_*$). The fit between this relationship and the experimental data improves with the increase of the charge caliber (dashed line in Figure 6.72).

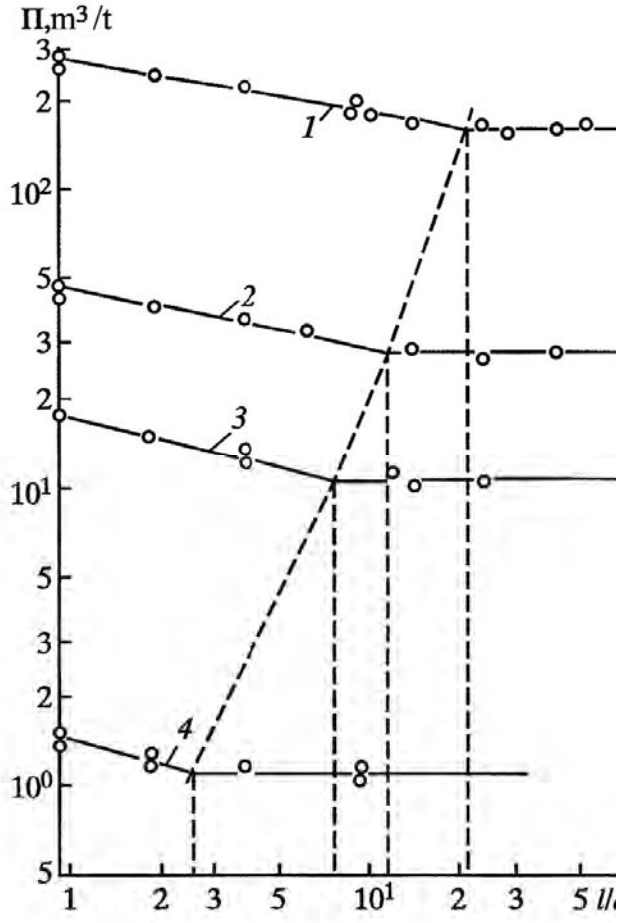

Figure 6.73. Overshoot parameter as a function of charge caliber (aspect ratio) for the following materials: *1* – plasticine, *2* – sand; *3* – sodium thiosulphate; *4* – PMMA.

The measurements of the "overshoot parameter" as a function of the scaled length and the charge caliber are shown in Figure 6.73. For *l/d* = 1 the "overshoot parameter" corresponds to the spherically symmetrical case ($\Pi_c = \Pi_s$). An increase in the aspect ratio causes a decrease in the "overshoot parameter" according to the formula:

$$\Pi_c = \Pi_s \left(\frac{l}{d}\right)^{-0.2}, \Pi_c = \Pi_s \left(\frac{l}{q_l^{1/2}}\right)^{-0.2} \text{ for } l \leq l_*. \text{ [not sure if this is correct]}$$

It follows from the last relationship that in the early stages of elongation (that is, for smaller aspect ratios) the reduction in the "overshoot parameter" is determined only by the geometrical dimensions of the charge and not by the medium properties. For an increase of the charge length above the characteristic value $l \geq l_*$ the "overshoot parameter" becomes constant, which corresponds to a transition from central to axial geometry (from spherical to cylindrical symmetry). Based on the experimental measurements of the "overshoot parameter" the characteristic length was:

In plasticine:

$$\frac{l_*}{q_l^{1/2}} = 21;$$

In sand:

$$\frac{l_*}{q_l^{1/2}} = 11.4;$$

In thiosulphate:

$$\frac{l_*}{q_l^{1/2}} = 7.6;$$

In PMMA:

$$\frac{l_*}{q_l^{1/2}} = 2.5.$$

where $l_*/q_l^{1/2}$ is in $m^{3/2}/t^{1/2}$.

According to these relationships the characteristic length of the charges is approximately 10 – 30% higher than inferred from the linear dimensions of the cavities, which can be explained by effects on the final cavity lengths. It was determined from an analysis of data shown in Figure 6.73 that for any solid medium the characteristic length of the cylindrical charge $l = l_*$ is related to the "overshoot parameter" $\Pi = \Pi_s$ via an empirical formula:

$$\frac{l_*}{q_l^{1/2}} = 2.3\Pi_s^{0.4} \text{ or } \frac{l_*}{d} = 2.4\Pi_s^{0.4},$$

where $[l_*]$ is in meters, $[q_l]$ is in t/m [ton/meter], $[\Pi_s]$ is in m^3/t.

The "overshoot parameters" for cylindrical and spherical symmetries are related via a formula:

$$\Pi_c = 0.76\Pi_s^{0.9} \text{ for } l \geq l_*.$$

We can express the radius of the cavity for a cylindrical charge of any caliber using the "overshoot parameter" Π_c and other parameters of the explosion:

$$r_c = 0.56\left(\frac{\Pi_c q_l l}{l_c}\right)\left(\frac{l}{d}\right)^{-0.1} \text{ for } l \geq l_*,$$

$$r_c = 0.49\Pi_s^{0.45}\left(\frac{q_l - l}{l_c}\right)^{0.5} \text{ for } l \geq l_*. \text{ [There must be an error]}$$

The work of explosions for both cylindrical and spherical symmetry was determined based on the measurements of the "overshoot parameter" (Table 6.20).

Table 6.20. Characteristics of cylindrical explosions

Medium	Symmetry type	Parameter			
		r_c/r_{ch}^3	Π, m^3/t	A/q	E_c/E_s
PMMA	Sphere	1.3	1.4	0.45	1.17
	Cylinder	1.25	1.1	0.36	
Thiosulphate	Sphere	3.0	17.5	0.82	1.21
	Cylinder	3.6	10.4	0.78	
Sand	Sphere	4.2	47	0.87	1.23
	Cylinder	5.5	27.5	0.84	
Plasticine	Sphere	7.5	280	0.94	1.26
	Cylinder	12.5	157	0.92	

The results show that the work performed by the explosion (that is, the energy used to carry out the mechanical damage of the emplacement medium) significantly depends on the mechanical properties of the medium, and increases with increasing values of the "overshoot parameter" (e.g. the "overshoot parameter" in plasticine is 200 times greater than in PMMA, while the work of the explosion is greater by a factor of 2). It turns out that the transition from central to axial (spherical to cylindrical) symmetry, while keeping everything else the same, reduces the mechanical work of an explosion. Therefore, the residual energy of the gas remaining in the cavity $E = q - A$, which determines the efficiency of the crater formation, increases. The ratio of the residual energy between the cylindrical (E_c) and the spherical (E_s) explosions are shown in the last column of Table 6.20 and in Figure 6.74 as a function of the charge aspect ratio. The residual energy for the cylindrical explosion is greater than for the spherical symmetry. The ratio E_c/E_s depends on the properties of the medium and increases with an increase in the "overshoot parameter" Π_s according to:

$$E_c/E_s = 1.16 + 0.04 \log \Pi_s \text{ where } l \geq l_*$$

Thus, the change in symmetry for the contained explosion from central to axial (spherical to cylindrical) results in the decrease of both the "overshoot parameter" and the mechanical work of the explosion on the emplacement medium. Therefore, spherical charges are more efficient for damage (i.e. fragmentation) of hard crystalline rocks and for compaction of porous rocks, while using cylindrical charges is more effective for excavation. The aspect ratio for which the transition between the spherical and cylindrical symmetry occurs depends on the mechanical and physical properties of rocks, and grows with an increase in the "overshoot parameter".

[3] I think r^3 in the text means "radius zaryada" or charge radius. It is confusing, because earlier they used R_0 as the charge radius.

Chapter 7

Explosive deformation and damage in media with artificial and natural discontinuities

7.1. Reducing seismic amplitudes from an explosion source by using unfilled gaps or voids

Several techniques can be used to control mechanical and seismic effects of explosions. One of the methods involves utilizing specific geological features of the emplacement medium. Conducting an underground explosion with considerations for surrounding faults, fractures, layers, and morphology of ore deposits, can to some degree affect the spatial distribution of explosive damage.

Other methods to control damaging effects of chemical explosions are based either on improving the design of the explosive charges and their placement, or by creating artificial heterogeneities in the rock massif where the detonation takes place (the emplacement medium). Placing explosive charges in specific patterns or creating some constructions (for example by using air-filled gaps) can significantly modify the effect of the explosives on rock fragmentation (in mining for instance). The possibilities of improving the design and charge placement for nuclear explosions are limited. Thus in order to obtain specific fragment size and its spatial distribution using nuclear explosions, secondary chemical explosions (with liquid explosives) can be used. Alternatively, artificial voids can be created to compensate for the rock dilation.

One of the important technological means to change the deformation processes and to reduce seismic coupling effect is the creation of so-called “screens” or extended voids surrounding the explosion in specific directions (Bronnikov and Spivak, 1981a; Spivak and Spungin, 1990)[1]. We note that existing modifications of explosive technology (including nuclear explosions) allow use of artificial unfilled voids to control damage from explosions over a wide range of parameters.

The presence of a screen in the deforming medium (either natural or artificial, including large fractures or tectonic faults) can complicate the analysis and prediction of explosion effects. The following problems need to be solved: determining amplitude reduction for the wave passing through a large natural discontinuity or an artificial screen, determining the diffraction pattern of the wavefield, as well as determining parameters of additional medium fragmentation.

We consider the main characteristics of the medium deformation in a presence of an unfilled gap with a constant aperture ε.

During laboratory experiments the role of the gap was played by a uniform gap between two separate blocks of the medium (sodium thiosulfate). Blocks were installed on a foam base covered with porous rubber. This design eliminated signal travelling around the gap thus allowing the separation of the effects of the gap from the direct signal.

[1] Spivak (1996) calls these “shields”.

Particle velocities behind the gap were measured using electromagnetic detectors. The delay in starting of the recording equipment by the time needed to pass through the gap Δt_w was performed when necessary by using a square impulse generator. A cut-off (as in Spivak, 1996) gap with a width of $0.014\ \mathrm{m/kg^{1/3}} \leq \varepsilon/q^{1/3} \leq 0.08\ \mathrm{m/kg^{1/3}}$ was created at different distances (l) from explosions ($l < R_*$), where R_* is the radius of the damage zone for an explosion in a homogeneous medium (for sodium thiosulfate $R_* = 0.68\ \mathrm{m/kg^{1/3}}$).

We will use parameters $v_0(r)$ and $\theta(r)$ to characterize maximum (peak) particle velocity as a function of distance and the rise time to reach v_0, for an explosion in a homogeneous medium, and parameters $v_1(r)$ and $\theta_1(r)$ to characterize maximum velocity and the rise time on the opposite side of the screen.

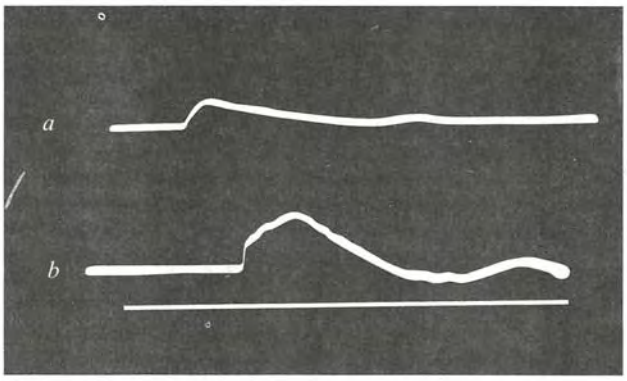

Figure 7.1: Examples of oscillograms of particle velocities: a) in the medium on the explosion side of the screen (shield), and b) on the other side of the screen.

Typical velocity records in the medium separated from the explosion by a cut-off screen are shown in Figure 7.1. The top plot (a) shows typical particle velocity for screens with $l/q^{1/3} \leq 0.4\ \mathrm{m/kg^{1/3}}$. The bottom plot (b) shows velocity for $l/q^{1/3} \geq 0.4\ \mathrm{m/kg^{1/3}}$ (for $\varepsilon/q^{1/3} \leq 0.05\ \mathrm{m/kg^{1/3}}$). The sharp (almost shock-like) initial rise of the velocity for $l/q^{1/3} \geq 0.4\ \mathrm{m/kg^{1/3}}$ is probably related to a spall-like character of damage in the medium before the gap.

A possible explanation is spallation of mass (separated/detached by the explosion), from the side closer to the explosion, hitting the wall on the opposite side as a projectile. Further velocity increase and the peak velocity value are determined by material damage. If the screen is located closer to the explosion the spall deformation of material starts practically from the free surface, which produces a smooth velocity behind the gap.

Analysis of the (temporal) velocity records obtained using different values of l and ε shows that the delay time due to the screen thickness is well described by

$$\Delta t_w = \frac{\varepsilon}{2v_0(l)}. \tag{7.1}$$

This expression suggests the damage is similar to spall deformation, observed when the wave reaches a free surface of the screen.

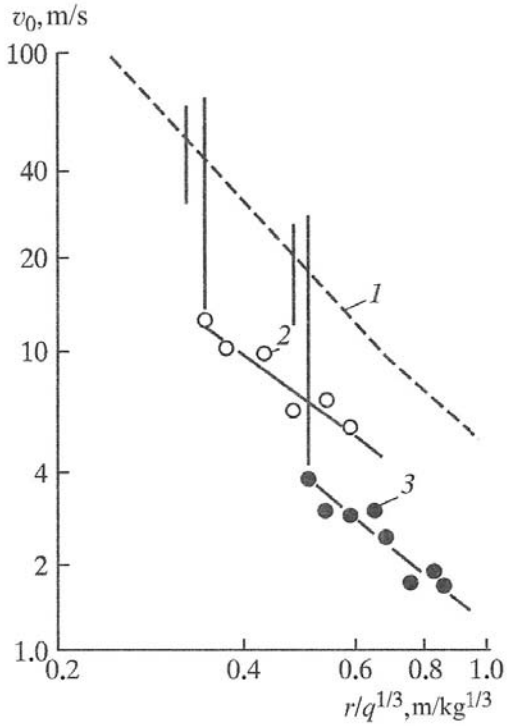

Figure 7.2: Maximum particle velocities behind the screen with thickness $\varepsilon/q^{1/3} = 0.027$ m/kg$^{1/3}$, for explosions: *1* – without a screen, *2* and *3* – with screens located at distances of 0.32 and 0.49 m/kg$^{1/3}$ respectively.

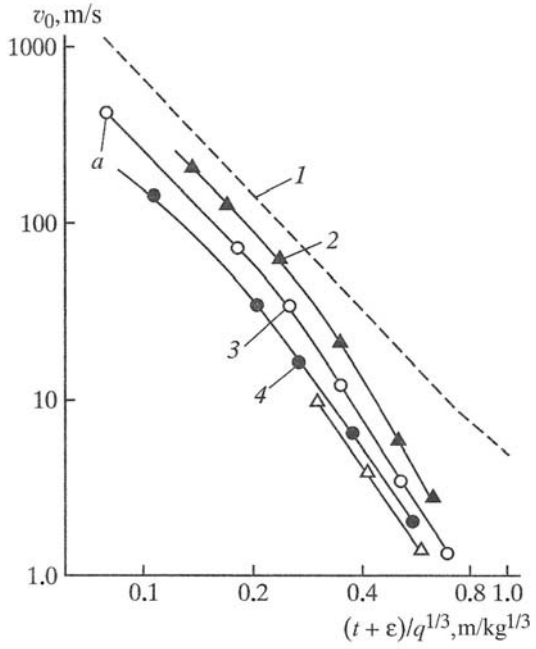

Figure 7.3: Maximum particle velocities of the opposite wall of the screen: $\varepsilon/q^{1/3} = 0.027$ m/kg$^{1/3}$: *1* – without a screen; *2–4* – explosions with screens with thickness $\varepsilon/q^{1/3}$: *2* – 0.013, *3* – 0.027, *4* – 0.055; *a* – screen "touches the explosion" – explosion in an air-filled cavity.

Analysis of the velocity records behind the screen shows that the duration of the positive phase after the wave passes the gap does not change much within the experimental error. The presence of a screen however significantly affects the velocity rise time. The effect of the gap opening to a value θ_1 can be expressed analytically as:

$$\frac{\theta}{\theta(l)} = 55(\varepsilon/q^{1/3}) \text{ for } 0.014 \leq \varepsilon/q^{1/3} \leq 0.05\ ,^{2}$$

where ε is the gap width (in m), and q is the mass of the charge (in kg).

It is worth noting that the screen position has almost no effect on the rise time (the relative coordinate $l/q^{1/3}$ varied in the experiments between 0.22 and 0.65 m/kg$^{1/3}$).

Changes in the wave amplitudes after passing the gap are shown in Figure 7.2. The presence of the gap significantly influences explosion effects on the media for distances $> l + \varepsilon$. Figure 7.3 shows velocities of the gap wall, opposite from the explosion, as functions of l and ε. The

[2] Should θ_1 be in the numerator? (Note added by the translators)

amplitudes ($v_0(r)$) in homogeneous media (Chapter 6) are also plotted in Figure 7.2 and 7.3 for comparison.

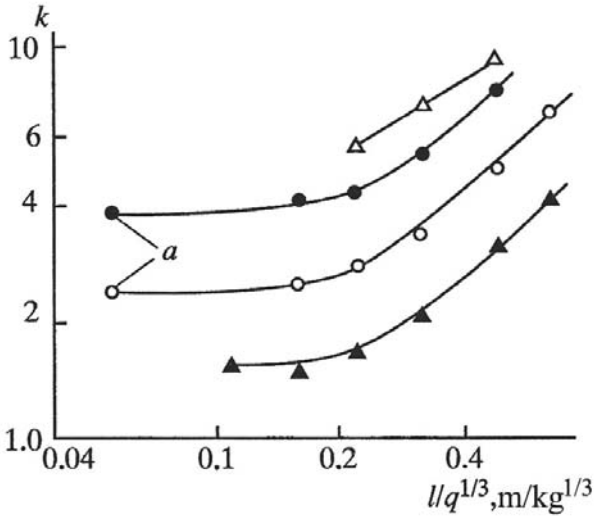

Figure 7.4: Screening coefficient (shielding factor) for the compressional wave, for explosions with screens. The notation is the same is in Figure 7.3.

The wave amplitude reduction factor due to a screen, also called a "shielding factor" (e.g. Spivak, 1995), defined as $k = v_0(l+\varepsilon)/v_1$ is shown in Figure 7.4. The value of $k(\varepsilon, l)$ can be expressed analytically as

$$k = 80\left(\frac{\varepsilon}{q^{1/3}}\right)^{0.6}\left(\frac{l}{q^{1/3}}\right)^{0.9} \text{ for } \begin{cases} 0.14 \le \frac{\varepsilon}{q^{1/3}} \le 0.05 \text{ m/kg}^{1/3} \\ 0.25 \le \frac{\varepsilon}{q^{1/3}} \le 0.7 \text{ m/kg}^{1/3} \end{cases}$$

$$k = 22\left(\frac{\varepsilon}{q^{1/3}}\right)^{0.6} \text{ for } \frac{l}{q^{1/3}} \le 0.2 \text{ m/kg}^{1/3}$$

Thus the presence of a screen substantially changes parameters of the wave produced by an explosion. First it causes the amplitude reduction of the pressure wave, which is important for reducing seismic effects of explosions. In addition, the screen acts as a low-pass filter. Indeed, a significant increase in the rise time effectively removes high frequencies from the wave spectra.

Passage of energy across an infinite gap occurs if the medium is damaged when the wave reaches the free surface, with a subsequent impact on the opposite wall if it is hit by broken rock. In rare cases energy can be transferred to the opposite wall by an acoustic wave (travelling through material in the gap).

To quantify this process we assume that the bulk of the material filling the gap after the explosion consists of material coming from a layer with thickness Δl located just before the gap. Then the density of the "projectile" ρ_p (material impacting the opposite (or non-moving) wall of the gap) can be estimated from

$$\rho_p = \frac{\rho_0 \Delta l}{\Delta l + \varepsilon},$$

where ρ_0 is the initial density of the medium (we neglect the medium compaction due to pressure wave).

Assuming that 1) the particle velocity doubles when the wave reaches a free surface, and 2) the material of the projectile can be described as a continuous medium, we obtain an expression for an acoustic approximation:

$$v_1 = \frac{2C_p\,\Delta l\,v_0(l)}{C+C_p},$$

where C and C_p are the acoustic velocities of the medium and the projectile material respectively.

Assuming that the loss of cohesion of the projectile is proportional to a time that material moves in the empty space between the screen walls, an approximate expression for the wave transfer through the gap is proportional to the particle velocity (before the screen):

$$C_p = 2B_* v_0(l).$$

Using the three last relationships we obtain:

$$k = \frac{1}{2}\left\{1 + \frac{C}{2B_* v_0(l)}\left(1 + \frac{\varepsilon}{\Delta l}\right)\right\}. \tag{7.2}$$

In order to estimate the parameter k we choose the thickness of the spalled (detached) material as the value of Δl. In this case:

$$\Delta l = \frac{\tau\,|\sigma_s|}{2\rho_0 v_0(l)}, \tag{7.3}$$

where τ is the duration of the positive phase of the pressure wave, andσ_s is the tensile strength of material.

Equation 7.3 is valid for a vertical (cut-off) gap. For a horizontal screen located below the block of rock (needed to be fragmented)[3] the value of $\sigma_s - \rho_0 g(W + l)$ should be used instead of σ_s, where W is the explosion depth.

Using 7.2 and 7.3 we obtain:

$$k = \frac{1}{2} + \frac{C}{4B_* v_0(l)} + \frac{\rho_0 C\varepsilon}{2B_*\tau\,|\sigma_s|}. \tag{7.4}$$

Table 7.1 shows the values of k for different distances from the explosion, estimated using Equation 7.4 and the following parameter values: ρ_0=1800kg/m^3, C=4500m/s, $|\sigma_s| = 10^7 Pa$, $B_* = 20$, and $\varepsilon/q^{1/3} = 0.027$. For comparison the experimental values of parameter k_s are also given in Table 7.1.

We note a good agreement between the results of laboratory experiments and a 2 kt nuclear explosion (in Khibiny) described in Chapter 5. For this explosion ($l/q^{1/3} \approx 0.44$ m/kg$^{1/3}$) the screening coefficient for the ground velocity ranged between 4 and 6. The variation is for

[3] Such horizontal screen is called “podsechka” in Russian, in Spivak (1996) it is called “undercut gap” in English

stations at different locations with respect to the screen. This value is in good agreement with the results of experiments presented in Table 7.1.

Table 7.1. Shielding factors for ground [particle] velocity depending on the distance between the screen and the explosive source

Scaled distance between the charge and the screen, $l/q^{1/3}$, $\mathrm{m/kg^{1/3}}$	Parameter		
	v_0, m/s	k	k_s
0.22	90	2.7	2.7
0.33	38	3.44	3.4
0.49	19	4.77	4.9
0.65	10	7.3	6.8

7.2. Damage caused by an underground explosion in the presence of a screen

The explosive wave propagating in the medium with a presence of a screen causes an increase in damage of the rocks in the area surrounded by the screen, compared to experiments without a screen. There is the possibility of additional damage to the rock by filling the gap, and also from collision of the flying debris with the side of the gap opposite to the explosion (i.e. causing more intense damage to the rock in the area surrounding the gap). To illustrate this, Figure 7.5 shows a photograph of the wall of Tunnel #22 (see also Figure 5.6), which crossed the screen created during the industrial nuclear explosion with yield of 2 kt (see Chapter 5). The boundary between the area behind the screen (with less damage), and the crushed rocks filling the gap as a result of the explosion, can be seen very clearly.

The existence of an empty gap (or screen) provides opportunities for rock fragmentation resulting from the explosion. The density reduction in each part of the massif is determined by the distance to the gap. Density reduction due to rock dilation causes changes in the rock permeability, with higher degree of density reduction corresponding to higher permeability.

As an illustration, Figure 7.6 shows measurements of the permeability of the massif in the area between the explosive charge and the screen (in the zone of influence of the latter), after the 2 kt explosion. For comparison, Figure 7.6 also shows the permeabilities for the same explosion in the area where the screen was absent[4]. It is worthwhile to note, that the data from Figure 7.6 confirm the results of earlier estimates of the "zone of influence" of the screen with parameters ε and l (ε is the width of the gap and l is the distance between the charge and the gap).

[4] We understand the screen was on one side from the explosion, so the other side was the area where "the screen has no influence"

Figure 7.5: Photograph of the tunnel wall crossing a cut-off screen, after the 2 kt explosion. Broken rocks on the left filled the screen (gap) as a result of the explosion, while the rocks on the right are only slightly deformed. The boundary between the zones is the opposite wall of the screen (the wall that is further away from the explosion source).

Referring to Figure 7.6, we note that in addition to increased damage inside the block, the screen also reduces the intensity of oscillations behind the screen. According to the data shown in Figure 7.6, the opposite side of the screen acts as the boundary, beyond which the rock permeability is significantly lower than after the explosion without screens. In addition, the screen represents a barrier for the propagation of individual fractures, which also improve the isolation of the block that is being fragmented. The isolating action of the screen increases if it is used in the direction parallel to the direction of preferential migration of gases and fluids (large fractures, tectonic faults, and areas with more fractures and higher permeability).

Studies of the frequency-size distribution of the fragments for explosion with a screen were conducted for the nuclear test Dnepr-1 (September 4, 1972) (Nuclear … , 1997 – 2000).

One of the laboratory experiments with a screen involved a spherical explosive charge with mass $4 \cdot 10^{-4}$ kg detonated in rosin, which in this case was placed in a special shell in order to prevent flying debris. Study of the frequency-size distribution was conducted using sieves and microscope analysis. The preliminary analysis indicates that both methods produced similar results. The study shows that the average size of the fragment $\langle x \rangle$ as a function of distance to the explosion r is not a monotonic function, unlike the fragment size distribution in homogeneous medium.

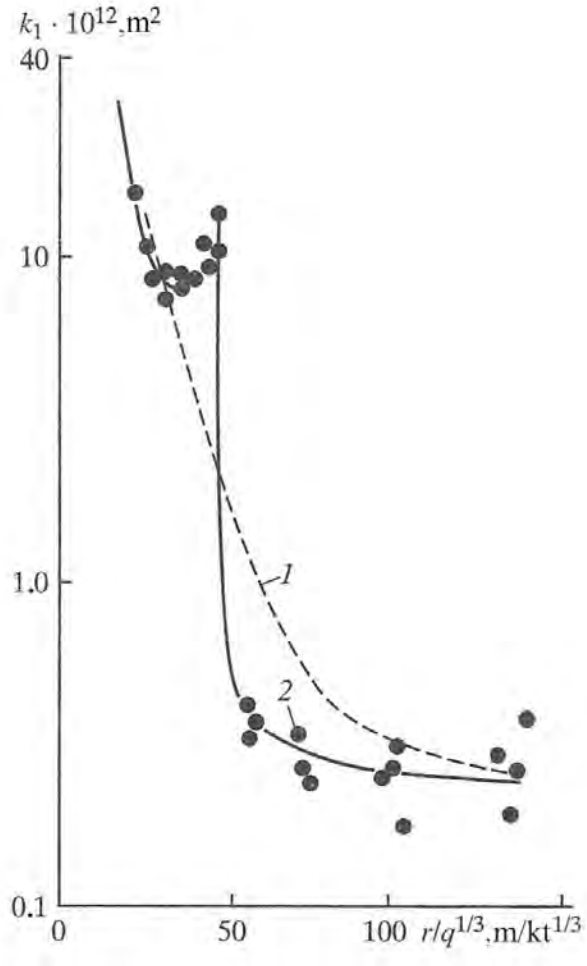

Figure 7.6: Permeability of the rock massif as a function of distance for the 2 kt explosion with a screen with thickness of $\varepsilon/q^{1/3} = 0.025$ m/kg$^{1/3}$, located at a distance of $l/q^{1/3} = 0.44$ m/kg$^{1/3}$ from the explosion source.

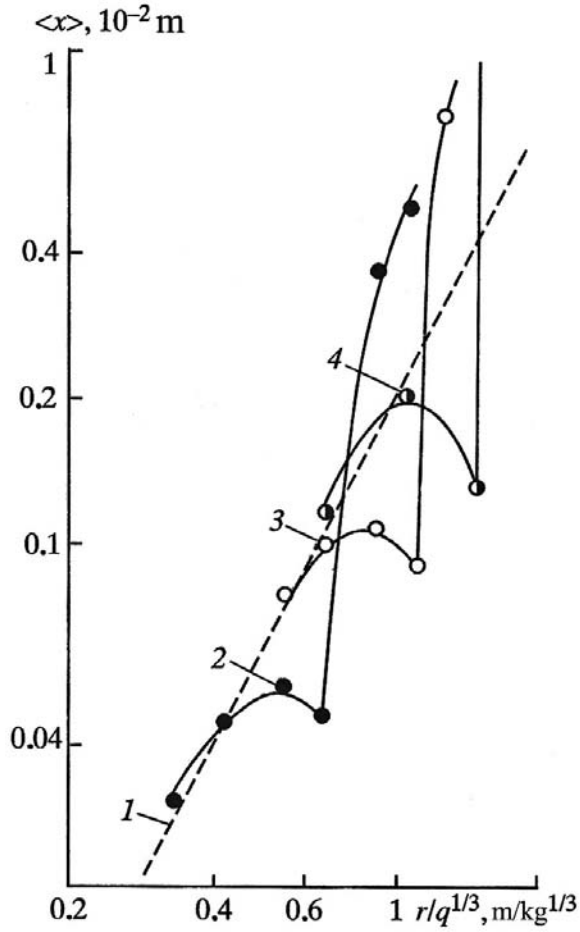

Figure 7.7: Average fragment size for the laboratory explosions: *1* – data for the explosion with no screen; 2–4 – explosions with screens with distances $l/q^{1/3}$: *2* – 0.65, *3* – 1.0, *4* – 1.3.

Figure 7.7 shows the results of these experiments, where this effect is clearly demonstrated. For instance the plot shows that the average fragment size first grows as the distance increases, then starts to decrease with a local minimum at the gap location. The presence of smaller fragments near the gap can be explained by additional damage due to the presence of a free surface, and due to collision of the material on the explosion side (acting as a projectile) on the opposite wall.

Using the relationship $\langle x \rangle(r)$ shown in Figure 7.7 one can estimate the zone where the characteristics of the broken material for the explosion with a screen agree with characteristics of the explosion in a homogeneous medium. The radius of the zone where a screen does not affect the medium r_m is shown in Table 7.2 for both laboratory and field experiments. Also shown are

the relative size of the zone where the screen affects rock damage $(l - r_m)/q^{1/3}$, and the average dilation coefficient K_d. [5]

Table 7.2. Dimensions of the zone affected by the presence of the screen and the average coefficient of dilation (?) for explosions with screens

Parameter	Laboratory experiment				Field test, ($l/q^{1/3} = 0.025$ m/kg$^{1/3}$)
$l/q^{1/3}$, m/kg$^{1/3}$	0.44	0.65	0.98	1.3	0.44
$r_m/q^{1/3}$, m/kg$^{1/3}$	0.27	0.4	0.6	0.85	0.24
$(l - r_m)/q^{1/3}$, m/kg$^{1/3}$	0.17	0.25	0.38	0.45	0.2
K_p	1.28	1.19	1.29	1.11	1.22

It is interesting that despite the differences in explosion scale, the dilation coefficient and the relative sizes of the zone of influence of the screen are close to each other, for the laboratory and the field experiments.

Table 7.2 shows that for a more distant screen location the zone of influence is larger. It happens because at larger distances a larger zone has to be involved in fragmentation to fill the gap.

Relaxation (i.e. expansion of material) into the unfilled gap reduces the intensity of the explosive action (wave amplitude) behind the screen. As a result, fragment sizes for $r > l$ exceed fragment sizes created by an explosion in a homogeneous medium.

The presence of a screen causes reduction of the size of the damage zone. For instance, for the void with opening (thickness) $\varepsilon/q^{1/3} = 0.027$ m/kg$^{1/3}$ the radius of the damage zone in the direction of the screen can be expressed as

$$R_s = R_* \left(\frac{l}{R_*}\right)^{1/3},$$

where R_* is the radius of the damage zone in a homogeneous medium, and the value $R_*/q^{1/3}$ for rosin is 1.36 m/kg$^{1/3}$.

Wave amplitude behind the screen is a monotonic function of the screen width ε. It is natural to assume that the degree of fragmentation in the immediate vicinity of the screen also changes monotonically as a function of the width of the screen, due to energy losses of the explosion wave.

[5] Alternatively “expansion coefficient”

However, the experiments have shown more complex relationships between the average fragment size taken from the gap filled due to an explosion, and the width of the gap. Samples were taken at the minimal distance from the charge to the screen. Figure 7.8 shows the relationship $\langle x_l \rangle(r)$ for screens located at different scaled distance $l/q^{1/3}$ from the explosion. Parameter $\langle x \rangle$ is the average fragment size at distance $r = l$ in a homogeneous medium (the vertical axis shows the normalized fragment size $\langle x_l \rangle / \langle x \rangle$). Figure 7.8 shows that for a screen located at a fixed distance from the explosion, a minimum fragment size is reached for an optimal screen width $\varepsilon = \varepsilon_{op}$. The relationship between ε_{op} and l can be expressed analytically as:

$$\varepsilon_{op}/q^{1/3} = 0.012(l/q^{1/3})^{-1.6}\text{m/kg}^{1/3},$$

where l is in m, and q is in kg.

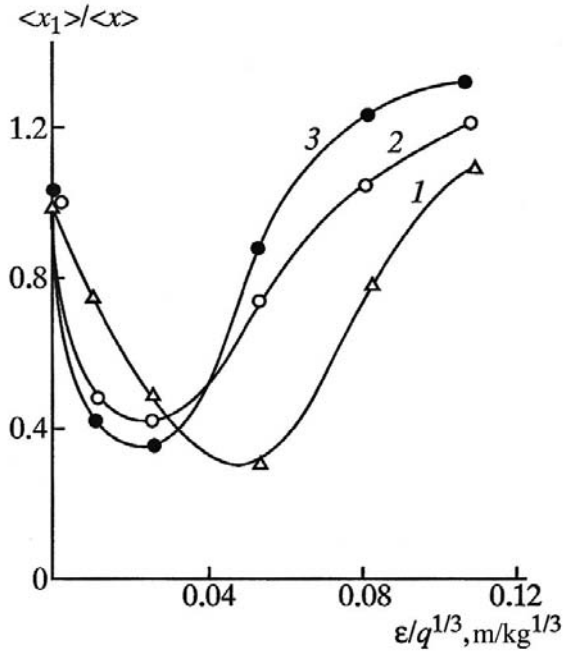

Figure 7.8: Average relative (scaled) fragment size for the material filling the gap after the explosion, as a function of the scaled thickness of the screen. The lines show data for different scaled distances from the screen $l/q^{1/3}$ m/kg$^{1/3}$: *1* – 0.44; *2* – 0.65, *3* – 0.98.

Thus the relationship between ε_{op} and l is similar in character to the relationship between the particle velocity and distance r. This seems natural since the time during which the additional deformation of the material takes place, during filling of the gap, is inversely proportional to v_0 as follows from Equation 7.1.

Some qualitative considerations help to explain the existence of an optimal width of the screen (for purposes of achieving better fragmentation). For thin screens, the dilation of the material is limited by the volume of the screen. Components of the stress tensor are not equal to 0, and thus deformation is "constricted". An increase in the degree of fragmentation (damage) with increase of the screen width, leads to an increase in fragmentation quality.

For larger screen thickness, the damaged material can dilate without restriction. The larger the thickness of the screen, the greater the role of “free deformation” (inertial motion of the material at the free surface of the screen) in the material damage. The role of additional deformation in the volume reduces in this case.

Thus we conclude that an increase in screen thickness from small absolute values increases the degree of damage in the material (giving a reduction in average fragment size). On the other hand, for thick gaps, an increase in thickness decreases the degree of damage, which increases the average fragment size.

The relationships obtained between the average fragment size and the distance to the explosion, enables calculating the average fragment size in the volume between the charge and the screen. We use $\langle x_2 \rangle$ for the average fragment size between the charge and the screen, and $\langle x_0 \rangle$ for the average fragment size in the same volume in a homogeneous volume. Analysis of the experimental data shows that using a screen increases uniformity of the fragment sizes in the volume (Figure 7.7), and the degree of damage increases (that is, the fragment size decreases). Table 7.3 shows the ratio $\langle x_2 \rangle / \langle x_0 \rangle$, which characterizes the degree of fragmentation for the explosion with a screen having scaled width $\varepsilon / q^{1/3} = 0.027$ m/kg$^{1/3}$.

Table 7.3. Relative average fragment size as a function of the distance to the screen with a scaled thickness of $l/q^{1/3} =$ 0.027 m/kg$^{1/3}$

Parameter	Value of the parameter			
$l/q^{1/3}$, m/kg$^{1/3}$	0.44	0.65	0.98	1.3
$\langle x_2 \rangle / \langle x_0 \rangle$	0.75	0.65	0.64	0.56

The results in Table 7.3 show that the degree of damage in the volume between the charge and the screen depends on the placement of the screen (or its distance from the charge). More detailed analysis shows that the optimal distance, in order to obtain fragments with fixed (uniform) size, is $l \approx (0.7 - 0.9) R_*$.

Figure 7.9 shows the fragment size distribution from the damage zone of the 2 kt nuclear industrial explosion (PNE in Khibiny, September 4, 1972). The average fragment sizes were estimated in this case based on filtration properties (porosity and permeability of the massif) using methods described in Chapter 5. Figure 7.9 also shows the results of direct fragment size measurements in the area between the charge and the screen. Added dilation (fragmentation) of the medium for explosions with screens simplifies the sampling of the material in this zone (because the rocks are loose).

Figure 7.10 shows rocks crushed by the explosion piling inside the hollow screen (also shown in Figure 5.6). The screen was crossed by the exploratory tunnel #33 after the explosion. The fragment size distribution obtained by measuring the fragment sizes at different distances

from the 2 kt explosion is shown in Figure 7.11 using characteristic coordinates for Rosin-Rammler distribution (Equation 1.20).

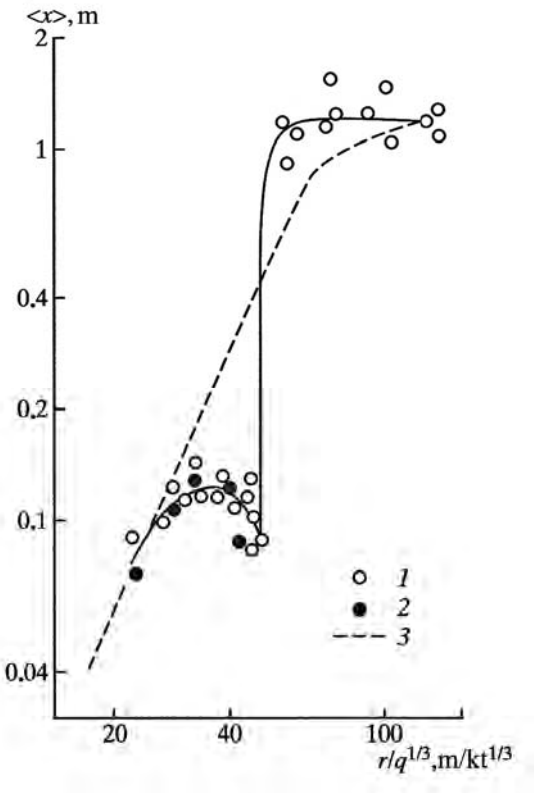

Figure 7.9: Average fragment size for the 2 kt explosion (PNE in Khibiny): *1* – estimates using permeability changes; *2* – estimates using fragment sizes measurements, *3* – in the area not subjected to the effects of the screen.

Figure 7.10: Photograph of loose rocks taken in adit #33 that crosses the cut-off screen as shown in Figure 5.6.

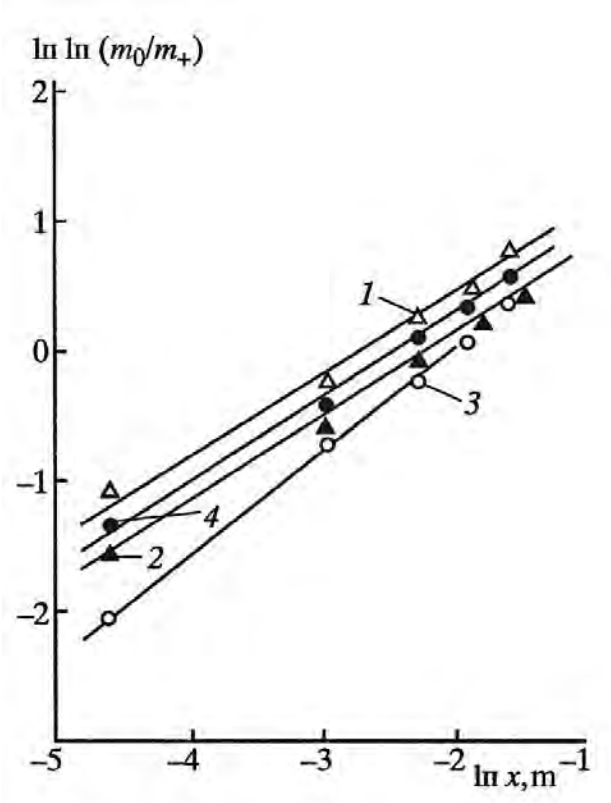

Figure 7.11: Frequency-size distribution of rock fragments for the (2 kt) explosion with the screen for different distances from the source (parameters m_0 and m_+ plotted along the vertical axis are explained in Chapter 1 Equation 1.20): *1* – 29 m; *2* – 36 m; *3* – 41 m; and *4* – 54 m.

Data shown in Figure 7.9 as well as the results of laboratory experiments suggest more uniform rock fragmentation in the areas where screens are used. The presence of a screen also increases the volume of rocks broken into very small fragments. Table 7.4 illustrates relative volume of rock broken by a large explosion into fragments, 50% of which have dimensions smaller than x.

To perform the estimate it was assumed that the fragment sizes follow the Rosin – Rammler distribution (1.20).

We use the surface area of the fragmented rocks as our measure of explosion efficiency (coefficient of efficiency), for purposes of describing rock fragmentation. Then using the results from Figure 7.9 we estimate that for a screen surrounding the explosion on four sides the fragmentation efficiency of the explosion increases by a factor of 1.35. If the screen is located only on one side of the explosion, the efficiency increase is approximately 10% of the explosion energy.

The increase in fragmentation efficiency for explosions with screens is due to partial use of energy that is wasted during the deformation in a confined medium. For example, the temperature between the charge and the screen is significantly lower than for explosions in homogeneous media.

In conclusion we note that it is possible in principle to control damaging energy of explosions by creating a series of unfilled gaps surrounding the explosive charge in a certain

way. Creating these screens is very labor-intensive, which can pay off only in the case of large explosions designed specifically for rock fragmentation.

Table 7.4. Volume of rock crushed by a large explosion for which 50% of fragments do not exceed size x.

Fragment size *x*, m	Volume of fragmented rocks, 10^3 m^3/kt		
	V_m/q *	V_{s1}/q **	V_{s4}/q ***
0.03	15	28	93
0.05	30	59	205
0.08	55	110	387
0.1	74	150	530
0.15	92	190	685

* V_m is a volume of rock for explosion in homogeneous medium
** V_{s1} is a volume of rock for the medium with a screen
*** V_{s1} is a volume of rock for the medium surrounded by screens on four sides

7.3. Deformation of the medium due to the stress wave interaction with a free-surface

Study of free surface effects on a medium can be simplified by subtracting the effect of the direct pressure wave from the combined wave in the medium with a screen present. This can be achieved by employing an approach, which is also used to study dynamic effects of explosions in pre-stressed media.

This approach can be implemented by using the following experimental procedure. A limited (or confined) volume is subjected to static stress, causing it to store mechanical energy. Then during a short time interval a free surface is created in the material. Creation of a new surface causes an unloading wave in the volume. The wave amplitude is determined by the amount of energy stored in the volume. Unloading leads to explosion-like motion and to subsequent material damage. The observed processes are similar to the effects of the wave interaction with a free surface.

In this case the direct pressure wave can be modeled as a step pressure increase with zero velocity, while the unloading wave is similar to the reflected wave. This experiment can help separate the effects of the free surface.

Explosion-like motion and subsequent medium damage is related (similar) to spontaneous fracturing which occurs naturally in the form of rock bursts. Study of this process in the laboratory is simplified by the choice of medium material. The material should be prone to rapid

damage/destruction due to step-like loading or changes in stress. It is also important to know what effects are determined by energy stored in the medium itself, as opposed to energy stored in under- or overlying layers. These effects can be separated in laboratory experiments.

The advantages of laboratory experiments include an ability to study dynamic processes of medium damage in a controlled environment, using electromagnetic methods to measure particle velocities as well as changes in electrical conductivity with time (Spivak, 1982).

Materials capable of spontaneous explosion-like destruction, due to step changes in stress, include rosin and pressed sodium thiosulfate (density about 1600 kg/m^3, compressional velocity about 3500 m/s).

The experiments were conducted in flat and cylindrically symmetrical settings. A cylindrical version of unloading was chosen, due to stable symmetry of the particle velocity field as well as higher intensity of damage processes and ballistic motion of the fragments.

Before conducting measurements, optimal parameters were determined to provide intense damage to the sample on unloading. The parameters included: 1) the size of the sample (its linear dimensions in rectangular or flat cases; its height, outer radius b and radius of the inner cylindrical cavity a, in cylindrical cases), and 2) the threshold pressure P_t above which the spontaneous material failure (loss of stability) was possible. In the flat case, explosion-like failure of rosin samples was achieved at 20 MPa, even though the volume of damaged material was not significant. For experiments in cylindrical configuration P_t was 50 MPa for rosin and 20 MPa for sodium thiosulfate.

Studies of explosion-like destruction were conducted for both spontaneous as well as artificially induced (forced) processes. The initiation process included use of a barrier holding material (together), which can be destroyed at a specific stress value (Spivak, 1982). The majority of the experiments were conducted using forced failure in order to stabilize the process with respect to the value of the applied stress and to simplify synchronization of the recording equipment.

After release of the barrier the material moves toward the axis of the symmetry and fills the cylindrical void in the center. The intensity of the process was determined by the energy stored during loading, namely

$$e_0 = \frac{V_s P_t}{2\rho_0 C^2},$$

where ρ_0 is the density of the material, and V_s is the volume of the sample.

Measured maximum particle velocities in the unloading wave v_0 are shown in Figure 7.12 as a function of distance r. Several experiments allowed measurement of v_0 without the holding barrier (spontaneous results). It turns out that the values of velocities are approximately the same: in both cases the break-up was achieved at loading pressure of P_t = 50 MPa.

The experimental relationship $v_0(r)$ is described well by the formula

$$v_0 = v_{10}(a/r)^3, \tag{7.5}$$

where $v_{10} = 10\ m/s$ for rosin and $v_{10} = 2\ m/s$ for sodium thiosulfate.

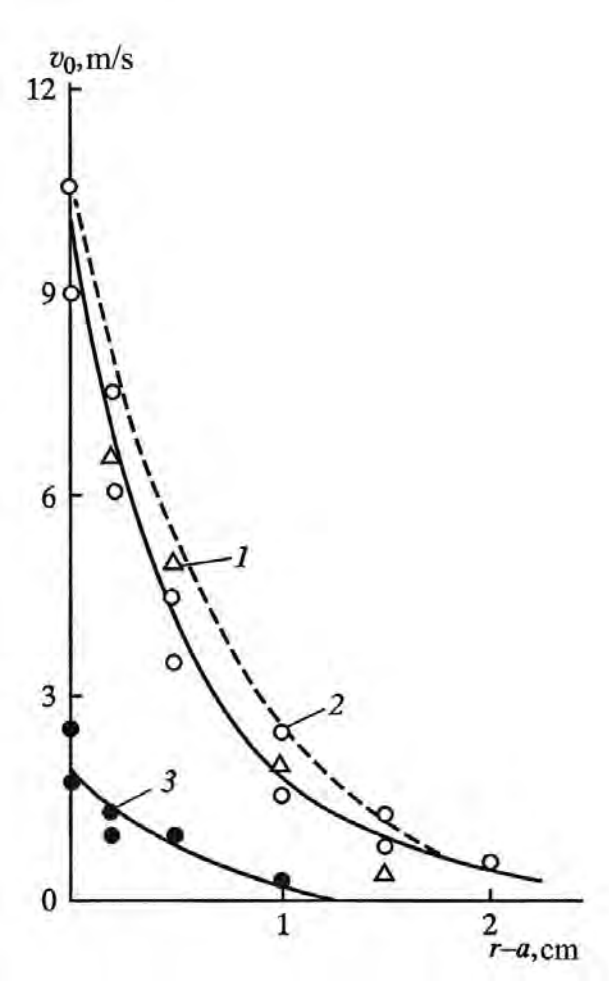

Figure 7.12: Maximum particle velocity in rosin (*1,2*) and sodium thiosulfate (*3*): *1* – spontaneous deformation; *2–3* – initiated wave of deformation; dashed line shows the results obtained with using soft cushions.

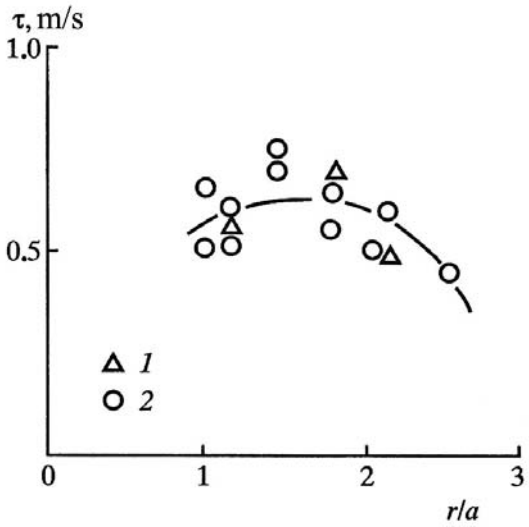

Figure 7.13. Duration of the wave of unloading (τ), for (*1*) a spontaneous, and (*2*) for an initiated wave of deformation.

The duration of the wave of unloading is on average $5 \cdot 10^{-4} s$ and is shown in Figure 7.13. Since the duration of the wave substantially exceeds the travel time within the medium (on the order of 10^{-5} s) we can assume that the velocities as a function of radius also can be described by Equation 7.5. Then the kinetic energy, at the moment when the maximum velocity is reached, is given by:

$$E_k = \frac{\rho_0 a^2 v_{10}^2 V_s}{4(b^2-a^2)} \left[1 - \left(\frac{a}{b}\right)^4\right], \tag{7.6}$$

and is approximately 1 – 2 % of the stored energy e_0.

To study the effect of rigidity of the under- and overlying layer, on the movement of material, experiments were conducted involving a rosin block placed between two solid rubber layers with thickness of $4 \cdot 10^{-2} m$. The measured velocities obtained at 50 MPa are shown in Figure 7.12 (dashed line). These results show that using soft cushions does not significantly affect the wave amplitudes.

Study of the propagation of the wave front during the unloading was conducted using contact sensors. Figure 7.14 shows the results of the experiment. The plot shows that the damage front is

delayed with respect to the front arrival, and we can tell with high precision that the maximum velocity is reached during material damage. The velocity of front propagation N_f decreases, as the front advances into the medium. However the main part of the damage front moves with a constant velocity, close to 500 m/s within the experimental error.

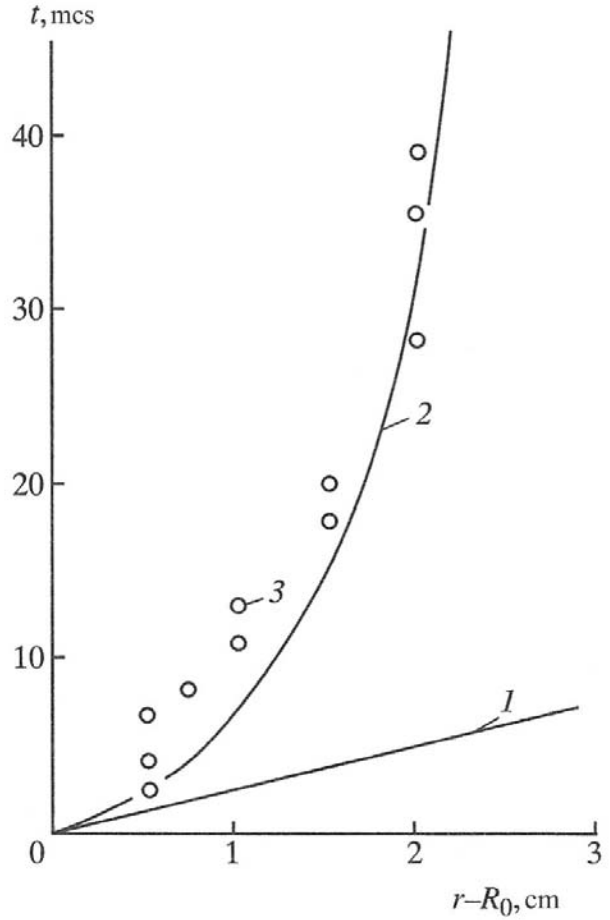

Figure 7.14. Travel times for (*1*) the wave of unloading and (*2, 3*) the front of deformation (damage), for spontaneous deformations of the medium (*2* – estimate, *3* – experimental data).

In order to parameterize this phenomenon we assume that during deformation the material reaches a limiting strain value ε_*. The time when this limiting strain is reached is given by

$$T_* = (r - a)/N_f.$$

To further simplify the estimate we assume that in the initial moment of damage the radius of the damage front R_d coincides with the radius of the inner (void) cylinder. The radial deformation can be expressed as a power law,

$$\varepsilon_r(r) = \varepsilon_* \left[\frac{b_* - r}{b_* - a}\right]^n, \tag{7.7}$$

where b_* is some limiting size (dimension) of the damage zone. In particular, during laboratory experiments the outer radius of the cylindrical sample can be used as b_*. Since deformations are localized near the free surface the power *n* should be sufficiently high.

This description reflects the fact that material located deep inside the sample (material) is energetically further away from the damage than the material near the free surface.

We write the energy balance equation in a form:

$$e_k = \alpha_{cp} e_0 - e_1, \tag{7.8}$$

where $e_k = 0.5\rho_0 v_0^2$ - kinetic energy in the unit of volume at the time of failure $t = t_*$; α_{cp} is the portion of the initial energy e_0 that is spent on processes not related to dissipation; and e_1 – is the energy reduction due to elastic deformation of the medium.

Using Equation 7.8 and applying Equation 7.7 we obtain

$$v_0(r) = \left\{\frac{\alpha_{cp}P^2}{\rho_0^2 C^2} - \frac{[\varepsilon_* C(1+\nu)/(1-2\nu)]^2}{1-\nu}\left[1 - \left(\frac{b_*-r}{b_*-a}\right)^{2n}\right]\right\}^{1/2}, \tag{7.9}$$

where ν is a Poisson coefficient of the medium.

It follows from Equation 7.9 that the velocity at the free surface (r=a) is

$$v_{10} = \frac{P}{\rho_0 C}\sqrt{\alpha_{cp}}, \tag{7.10}$$

On the other hand the parameter can be determined using a condition along the stationary deformation (damage) front without stress (the stress wave reaches the free surface with zero mass velocity).[6] We write:

$$v_{10} = -\frac{\sigma_{rf}}{\rho_0 C},$$

where σ_{rf} is a stress normal to the unloading front:

$$\sigma_{rf} = -\frac{\nu P}{1-\nu}. \tag{7.11}$$

Comparison between Equations 7.10 and 7.11 yields:

$$\alpha_{cp} = -\left(\frac{\nu}{1-\nu}\right)^2. \tag{7.12}$$

The results of the estimates of particle velocities using Equation 7.9 and 7.12 are shown in Table 7.5. The estimated values v_{10} and measure velocities v_0 are shown for different distances *r* (*P* = 50 MPa for rosin and *P* = 20 MPa for sodium thiosulfate). The value of ε_* was set to 0.69% for rosin and 0.05% for sodium thiosulfate. For the exponent we used the value of *n* = 5.

[6] Stress free boundary does not mean zero velocity. This is more like a rigid boundary!

Table 7.5. Maximum velocities for flying fragments

Parameter	Value of the parameter		
$r - a$, m	0	$5 \cdot 10^{-3}$	10^{-2}
Rosin (P = 50 MPa)			
v_{10}, m/s	5.2	2.4	
v_0, m/s	9 – 10.5	3.5 - 5	1.5 – 2.5
Sodium thiosulfate (P = 20 MPa)			
v_{10}, m/s	1.6	0.7	0.3
v_0, m/s	1.7 – 2.5	0.85	0.25

Table 7.5 demonstrates that Equation 7.9 adequately describes the maximum material velocity for different distances from the free surface, which justifies the simplifying assumption made earlier.

We studied the main characteristics of damage for a plane wave of unloading. For instance we determined the frequency-size distribution of fragments for rosin, and the effect of the prestress magnitude (or value) on the fragment size. Figure 7.15 shows fragment sizes for several values of P. The figure shows that the increase in prestress causes increase in damage (decrease in average fragment size) and more uniform fragmentation. We note that the data in Figure 7.15 correspond to equal volumes of material from areas adjacent to the free surface. This is important because an increase in the total volume of fragmented material leads to creation of larger fragments far away from the boundary, which impairs the quality of the integral characteristics of the medium.

For example, Figure 7.16 shows the volume of the damage zone V_* (or damaged material) relative to the volume of damage zone for P = 50 MPa. At this pressure the volume of the damaged material is exactly equal to one half of the spherical volume with the center located in the center of the detachment fracture and the radius equal to the radius of that fracture that is formed in the medium.

The average value of fragment size, using the “variability parameter” n as a function of stress P, can be expressed as

$$\langle x \rangle = 2.4 \cdot 10^{-2} P^{-0.5} \text{ (m) for } n = 0.052 P^{0.17},$$

where P is pressure in Pa.

The effects described in this section show qualitatively and quantitatively the effects of the void gap on the fragment size distribution of the material. The depth of fragmented rocks determines the characteristic size of the zone of fragmented rock, for explosions carried out in the presence of a screen – and hence the zone of influence of the screen.

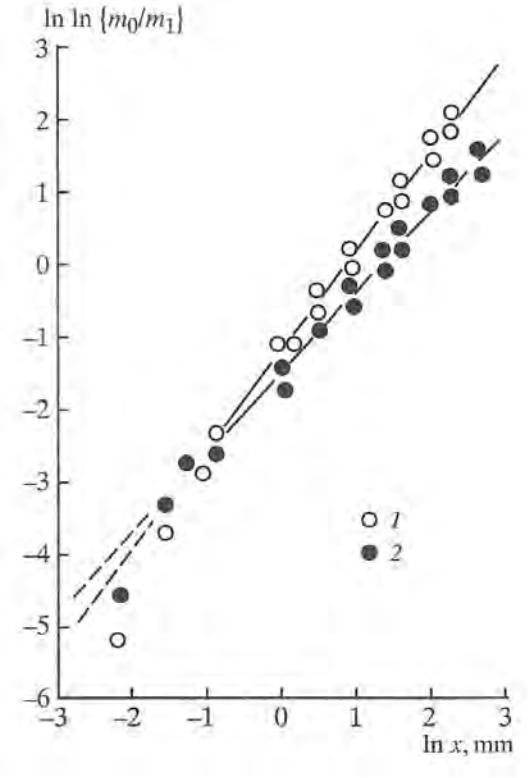

Figure 7.15: Frequency-size distribution of rosin fragments created by a plane unloading wave, for different initial pressure P values: *1* – 150 MPa; *2* – 50 MPa. Parameters m_1 and m_2 plotted along the vertical axis are explained in Chapter 1 Equation 1.20.

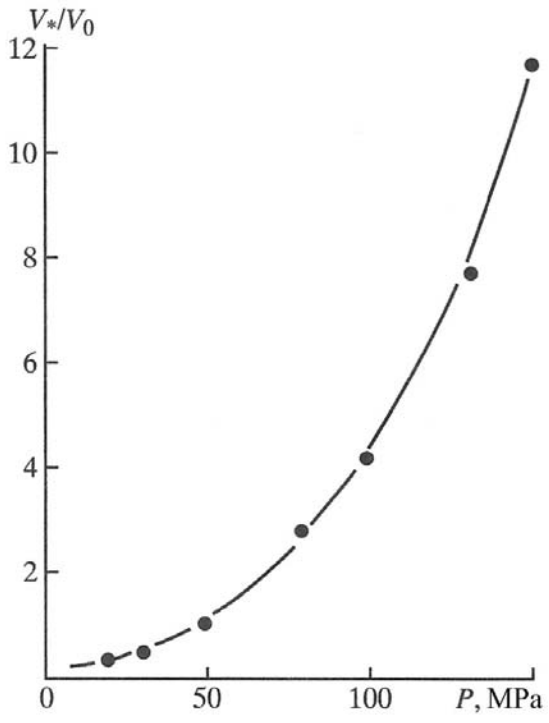

Figure 7.16: Relative volume of the fragmented medium (rosin) as a function of initial pressure.

7.4. Effect of the initial porosity on damage from explosions

The results of studies of the effects of explosions on media, presented here as well as historical data, show that the damage characteristics (including hydraulic permeability) of rocks increase as a result of explosion. With a reduction in the intensity of the explosion amplitude (for instance due to distance increase from the source), the degree of damage monotonically decreases. However, we note that: 1) most of the studies of rock damage due to underground explosions were conducted in media with little initial damage, and 2) only the average characteristics were studied. The experimental data were studied assuming monotonic parameter changes. The

variability of results was attributed to experimental errors and the effects of random heterogeneities.

Careful studies show that initial damage (fracturing?) in the emplacement medium has a significant effect on rock damage and deformation due to explosions.

Laboratory experiments were conducted in order to study the behavior (under explosion loading) of solid media with different degrees of damage. The experiments involved measurements of (hydraulic) permeability of the samples after subjecting them to loading with different intensity. The experiments were conducted as follows. A flat sample made of concrete with sand (diameter of 0.06 m and height of $1.5 \cdot 10^{-2}$ m) was placed into a cylindrical shell and subjected to a shock wave (loading) on one side.

The shock waves were initiated by spherical charges of chemical explosives with weight of $27 \cdot 10^{-3}$ kg located at different distances from the sample surfaces. The permeabilities of the samples before and after the explosions were compared.

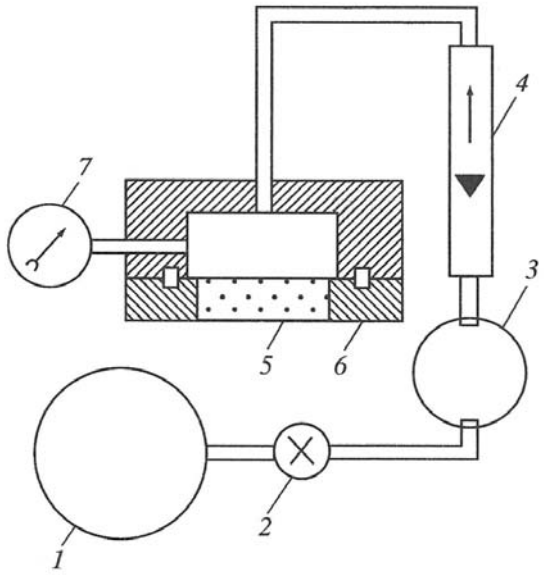

Figure 7.17: Schematics for the apparatus used to study permeability of samples: *1* – container filled with gas; *2* – switch; *3* – expansion joint; *4* – gas flowmeter; *5* – tested sample; *6* – shell; *7* – pressure gage.

The experiment design (for determining rock permeability) is schematically shown in Figure 7.17. The samples had initial porosities (denoted *m*) of 10, 14, 18, and 22%, which were kept for several months. For each series of experiments the porosity variation did not exceed 10%. The average values of hydraulic permeabilities are shown below (the variations of the permeability coefficient varied up to 30% for each series, with a mean standard deviation of 15%):

m,%	10	14	18	22
k, 10^{-14} m^2	0.7	4.3	13	31

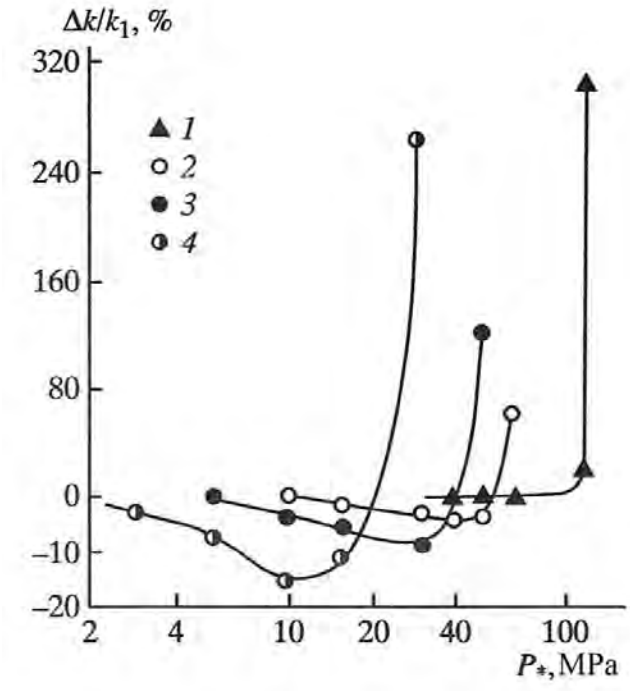

Figure 7.18. Changes in permeability of samples as a result of explosion loading for different values of initial porosity: *1* – 10 %; *2* – 14 %; *3* – 18 %; *4* – 22 %.

The results of the experiments are shown in Figure 7.18 as functions $\Delta k/k_1(P_*)$, where Δk is change in permeability due to the shock loading, k_1 is the initial permeability, and P_* is the pressure in the reflected shock wave.

The results in Figure 7.18 show that the changes in permeability with an increase in loading intensity are monotonic. Despite the qualitative character of this experiment we conclude that loading stresses smaller than a certain critical value can cause compaction in porous media. Figure 7.18 also shows that for less dense (more porous) media, the degree of compaction can be higher.

The nature of non-monotonic changes in permeability for media with high porosity under dynamic loading is probably caused by differences in mechanisms of deformation of the matrix for small and large stresses. Thus, small stresses can cause deformations of the matrix without destroying its structure, while stresses above a certain threshold can cause destruction of the rock matrix. In the first case the existing pores become narrower (smaller), leading to permeability decrease. In the second case new pores (channels, fractures) are created, due to matrix deformation, leading to an increase in permeability.

A study of the effect of initial porosity of the rock massif on damage from an explosion was conducted during an experiment in adit (Tunnel) 160 (Semipalatinsk Test Site) (Adushkin, Spivak, 1993). The rocks were from a volcanic complex (diabase porphyrites, linarite porphyrites) of Early Carboniferous Age. Numerous fractures of different scale (sizes) (both tectonic fractures and petrogenic joints related to magma cooling) were observed. The rock massif is broken by fractures and joints into smaller structural blocks of different sizes and

hierarchical orders. The smallest blocks were determined by petrogenic joints. Their average size in virgin rocks is about 0.2 m^3, and approximately 0.04 m^3 in the weathered zone. These blocks are merged into the next structural (hierarchical) level – larger blocks separated by tectonic fractures. The average size of these blocks is close to 100,000 m^3.

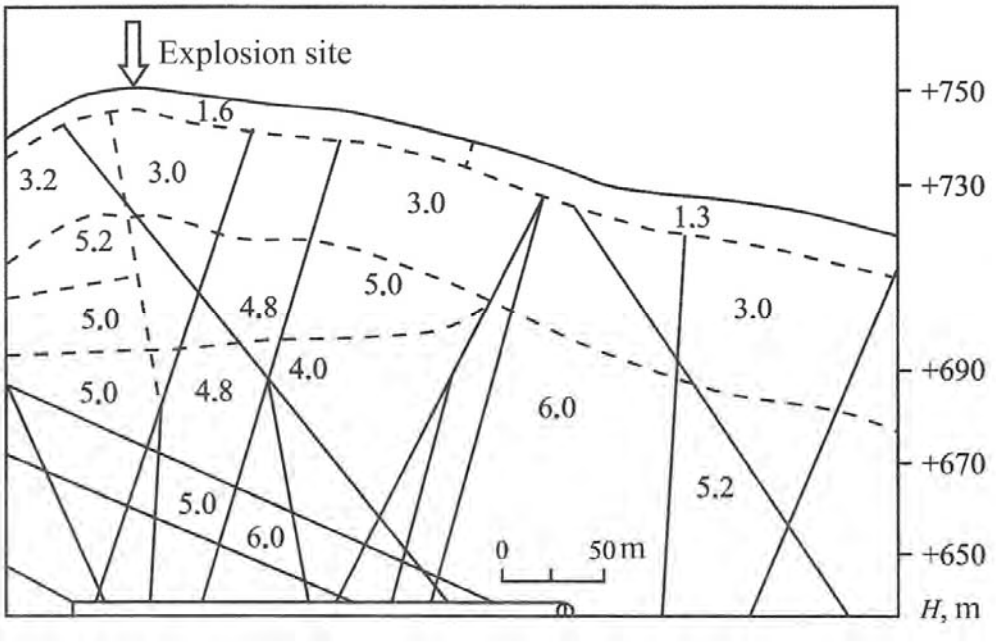

Figure 7.19. Results of seismic imaging of the rock massif in the vicinity of Tunnel 160 before the explosions. Solid lines show the boundaries between blocks, dashed lines show the velocity (refractive) boundaries; numbers specify seismic velocities of rocks (in km/s).

The experiment was conducted in two stages: first – a semi-spherical chemical charge (500 t, average density of explosive – 790 kg/m^3) was detonated on the surface of an undamaged rock massif, second – a similar charge was detonated at the bottom of a crater created by the first explosion. The purpose of the experiment was to study the mechanical effects of the explosion on the rock massif. Seismic imaging was conducted before and after each of the explosions. The size and configuration of the zones with different seismic velocities was determined as a result of the imaging (Figure 7.19, 7.20). The magnitudes of velocity changes in each zone (locality) can help estimate the degree of damage (porosity) of different portions of the rock massif, before and after each explosion. The porosity is determined using the relationship:

$$\eta = \frac{C_1}{C_0 - C_1}\left(\frac{C_0}{C} - 1\right),$$

where C_0, C_1, and C are the wave velocities of the rock, the fill between the blocks, and the massif, respectively. In this case parameter C determines the degree of rock damage.

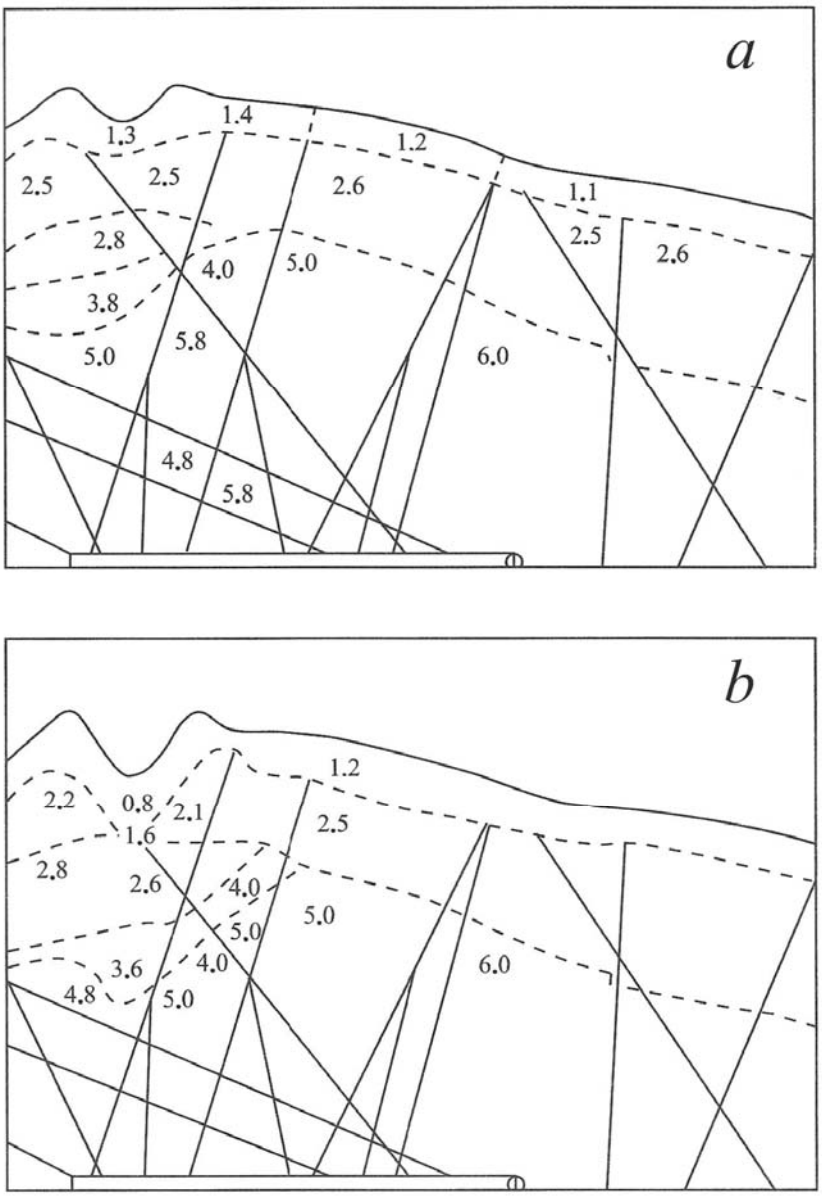

Figure 7.20. Results of seismic imaging of the rock massif in the vicinity of Tunnel 160; a) after the first explosion, and b) after the second explosion. The notation is the same as in Figure 7.19.

In order to determine the effect of the initial rock damage (for the second explosion, the conditions caused by the first explosion were used as an initial state) it is necessary to account for the changes in wave intensity as a function of distance from the source *r*, which determines the magnitude of the changes in the rock. It is known that the magnitude of inelastic deformations caused by the explosion is determined by the rock deformation. For instance, the magnitude of residual deformations for a point source is given by

$$\varepsilon_{r0} \sim \frac{v_0(r)\tau(r)}{r},$$

where v_0 and τ are the maximum velocity, and the duration of the positive phase of the pressure wave.

Therefore we can assume that changes in the non-dimensional parameter are given approximately by

$$\Delta\tilde{\eta} = \frac{r}{v_0(r)\tau(r)}\frac{\Delta\eta}{\eta_0},$$

where $\Delta\eta = \eta$ to η_0, is determined only by the initial degree of damage (porosity) of the medium η_0.

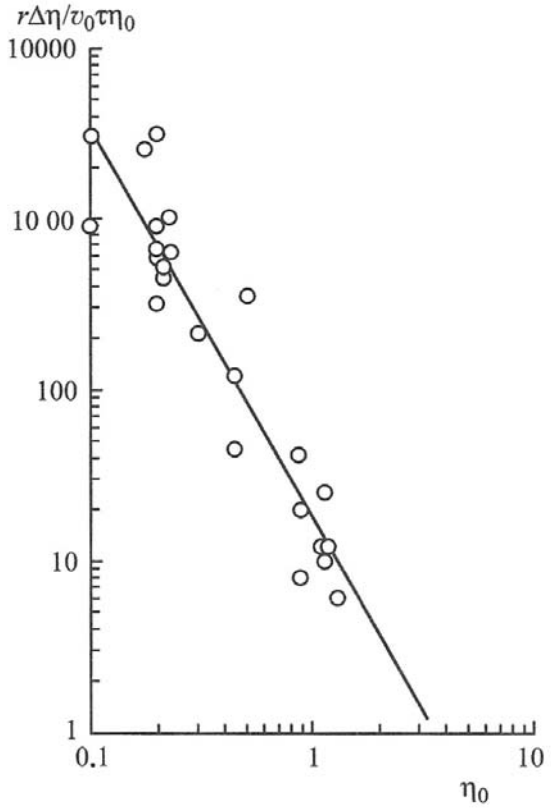

Figure 7.21: Changes in porosity as a result of explosive loading as a function of the initial porosity.

Figure 7.21 shows the analysis of the imaging results in a form $\Delta\tilde{\eta}(\eta_0)$. Using linear regression, we have

$$\Delta\tilde{\eta} \sim \eta_0^{-2.3},$$

and therefore

$$\Delta\eta \sim \eta_0^{-1.3}.$$

This relationship suggests that initial porosity of rocks plays an important role in changes in mechanical properties in the rock massif caused by an explosion.

To summarize: parts of a rock massif with different fracturing will be affected by explosions in different ways. For instance, from the last relationship, the mechanical effects of an explosion depend on the structure of the real medium.

7.5. Description of block deformations

We will treat the real rock massif as a combination of hierarchically-structured elements (blocks) separated by spatially extensive zones of weakness. The boundaries between the blocks can be represented by either void (unfilled) tectonic faults/fractures, or by lineaments (in this context, filled fractures and faults), characterized by higher compressibility and lower strength than rock. In both cases the medium within each hierarchical level can be represented as a combination of juxtaposed zones of volume V_i ($i = 1,2,3$ ...), with different physical properties.

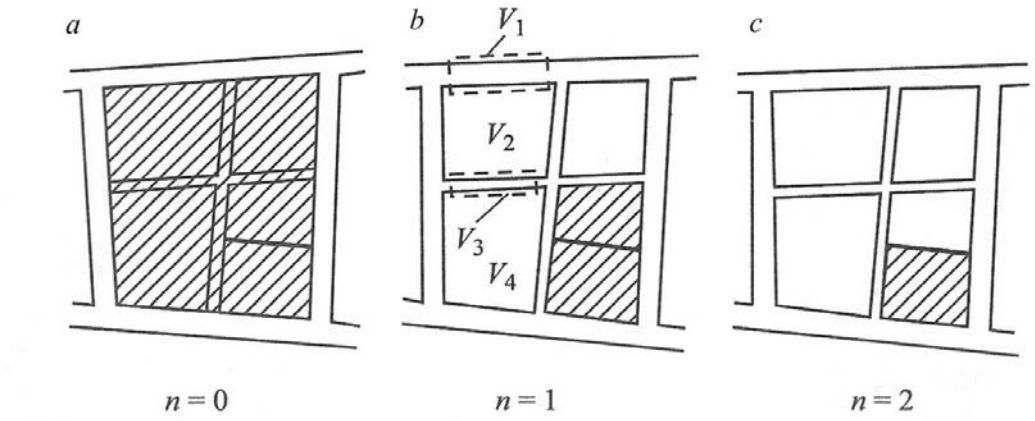

Figure 7.22: Schematics showing structural elements of different ranks: a, b, c – ranks of different hierarchical levels (explanations are provided in the text).

Ranking of structural elements can be based on the positions of faults, and fractures separating these blocks. The largest structural block, within which we will consider the largest irreversible changes, is referred to as zero rank ($n = 0$). The blocks composing these zero rank blocks, separated by the largest (within-the-block) structural discontinuities, form rank 1 blocks ($n = 1$) etc (Figure 7.22). Thus every structural element of the medium can be assigned its rank $n = 1,2, \dots N$, where N is the total number of ranks. Each cluster in this hierarchical structure with ranks $n + 1, n + 2, \dots N$, represents a separate structural block of rank n, and at the same time it is a structural element for block with rank $n - 1$.

Thus the hierarchical model of a real medium includes blocks with ranks $n = 0,1,2, \dots, N$, and the zones of weakness separating the blocks with different ranks. The medium within each

cluster can be heterogeneous and includes zones (blocks) V_i with different mechanical (physical) properties (including blocks, clusters of higher rank, and the space between the blocks). .

No mathematical formalism is available at this time to describe deformation processes within complex block structure. Methods involving spatial averaging of deformation (homogeneous continuous medium approximation) cannot describe local movement within the medium deformed by explosions. Thus, special methods have to be created to describe the motion within a real rock mass subjected to external forces.

The main features of the deformation of block structure, including deformation of an arbitrary element with rank *n*, are determined by 1) its mechanical properties (including strength) of its parts (smaller blocks and the space between these blocks), and 2) by the character of changes within each cluster. Depending on the parameters of the external action the changes in configuration of the blocks can be conforming or non-conforming. Depending on this the state of a cluster can be described as consolidated and unconsolidated.

At smaller deformations, rock massif can be in a consolidated state at all levels. We define the following stages in deformation of a structurally inhomogeneous medium.

Stage 1 – involves reversible deformation of the structural blocks. At this stage, the deformation of each part of the structure takes place with conformity and within elasticity limits without breaking continuity. The stress concentration caused by such deformations is completely determined by the external stresses. After removing such stresses the medium (system) returns to its initial state.

Stage 2 – involves irreversible conforming deformations of the structural blocks. At this stage the conformity between the structural elements is achieved by formation of zones of plasticity along the boundaries of the blocks V_i with different mechanical properties (Figure 7.23). Deformation occurs without breaking continuity of the medium due to plastic deformations within weaker elements (lineaments filled with softer material), compensated by elastic deformations within the stronger zones. Stresses created within the medium, unlike stress concentration along the boundaries, remain after the external stresses are removed. Therefore it creates conditions for force moments inside the medium, acting upon structural elements or the entire clusters.

Stage 3 – involves non-conforming deformations of the structural blocks. At this stage, the deformation of the structural elements is accompanied by a break in continuity of the medium.

Several methods can be employed quantitatively to describe the qualitative deformation model. Stage 1 is easily described in terms of classical elasticity theory. Below, we provide a technique that allows description of the deformations for stages 2 and 3 of the deformation of a hierarchically heterogeneous medium. This method is based on the elements of a theory of deformation of a composite medium (e.g. Panin et al, 1985; Rybin and Zusman, 1986).

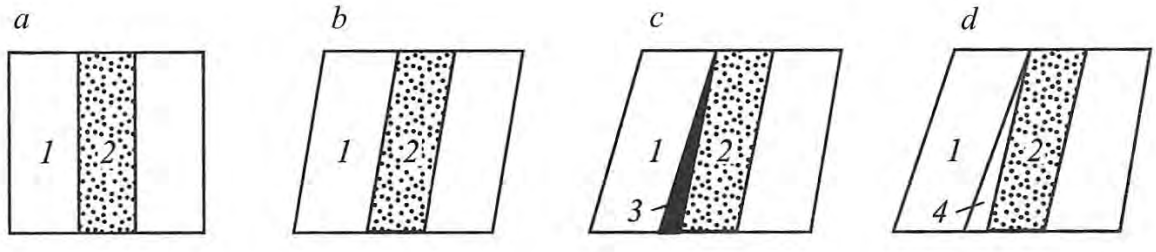

Figure 7.23. Different stages of deformation of a structural element: a) initial state; b) – d) – changes of the blocks: b) reversible, c) irreversible continuous (conforming); d) irreversible discontinuous (non-conforming). The numbers show: *1* – a single block, *2* – space between the blocks, *3* – plastic non-conformity; *4* – discontinuity.

We will characterize the deformation of the *i*-th structural element of an arbitrary cluster of *n*-th rank by a tensor of local deformation,

$$\varepsilon^{(n)} = \varepsilon^0 + \varepsilon^*,$$

where ε^0 and ε^* are elastic and plastic components of the tensor, respectively. We also define a tensor of volume averaged deformation

$$\varepsilon_i = \overline{\overline{\varepsilon^{(n)}}} = \varepsilon_i^0 + \varepsilon_i^*,$$

which characterizes deformation of the i-th element as a whole. In this equation, $\varepsilon_i^0 = \overline{\overline{\varepsilon_i^0}}$, $\varepsilon_i^* = \overline{\overline{\varepsilon_i^*}}$, and the double bar means averaging over the volume V_i.

We consider fluctuations of elastic and plastic properties with respect to the average properties of the total volume V (it can be a volume of a cluster of rank n):

$$\Delta\varepsilon_i^0 = \varepsilon_i^0 - \varepsilon_v^0$$

$$\Delta\varepsilon_i^* = \varepsilon_i^* - \varepsilon_v^*,$$

where $\varepsilon_v^0 = \overline{\varepsilon_i^0} = \overline{\varepsilon^0}$, $\varepsilon_v^* = \overline{\varepsilon_i^*} = \overline{\varepsilon^*}$ (the bar means averaging over volume *V*). The condition of cluster continuity

$$\varepsilon_i^0 + \varepsilon_i^* = \varepsilon_v^0 + \varepsilon_v^*$$

can be written as

$$\Delta\varepsilon_i^0 + \Delta\varepsilon_i^* = 0. \qquad (7.13)$$

The last relationship means that in the case of plastic non-conformities ($\Delta\varepsilon_i^* \neq 0$), the continuity of the medium can be preserved only by adding elastic deformation with magnitude $\Delta\varepsilon_i^0 = -\Delta\varepsilon_i^*$. If condition 7.13 is not satisfied (the magnitude of elastic deformations is

insufficient to compensate for plastic deformations), the deformation occurs with loss of continuity of the medium: a cluster becomes disjoint[7] at some level along weaker areas. We note that breaks in continuity at rank *n* relax its deformation as a whole. This leads to a delay in formation of plastic non-conformities at level $(n-1)$ and lower, and these non-conformities appear at stronger deformations.

A process of "disclination" (discontinuous motion) at certain levels of the rock massif can be viewed as one of the possible mechanisms producing "dissipation structures"--- structural elements of rank n_*, whose deformation to some degree determines global deformation of the medium in the presence of external forces.

We note that the tensors $\Delta\varepsilon_i^0$ and $\Delta\varepsilon_i^*$ which we have described, characterize deformation of the *i*-th element with respect to deformation of the total volume (the cluster as a whole). This allows description of the deformation of each structural element in terms of the fluctuations $\Delta\varepsilon_i^0$ and $\Delta\varepsilon_i^*$ separately, independently of deformation of the neighboring elements.

Explosive deformation of the medium is one of the most important practical applications of large underground explosions. Thus the description of motion of different structural elements of the medium is important, regardless of the peak stress magnitudes, because they (stress magnitudes) do not always determine the magnitudes of the residual deformations.

We define stress tensors σ_i, similar to the description of tensors ε^0, $\Delta\varepsilon_i^0$ and $\Delta\varepsilon_i^*$, averaged over the *i*-th element of a cluster with rank *n*, and their fluctuations with respect to the background stresses σ_v:

$$\Delta\sigma_i = \sigma_i - \sigma_v$$

where

$$\sigma_i = S_i \cdot \varepsilon_i^0,\ \sigma_v = \overline{\sigma_i}, \tag{7.14}$$

S_i – is a generalized module of deformation, averaged over the element *i*. As before, index *i* characterizes some element of the volume. Therefore, to multiply a matrix S_i by a tensor ε_i^0 we used operation $(\cdot)$. We can expand Equation 7.14 as

$$\begin{bmatrix}\sigma_{11}^i\\ \sigma_{22}^i\\ \sigma_{33}^i\\ \sigma_{12}^i\\ \sigma_{23}^i\\ \sigma_{31}^i\end{bmatrix} = \begin{bmatrix}\lambda_i+2G_i & \lambda_i & \lambda_i & 0 & 0 & 0\\ \lambda_i & \lambda_i+2G & \lambda_i & 0 & 0 & 0\\ \lambda_i & \lambda_i & \lambda_i+2G & 0 & 0 & 0\\ 0 & 0 & 0 & G_i & 0 & 0\\ 0 & 0 & 0 & 0 & G_i & 0\\ 0 & 0 & 0 & 0 & 0 & G_i\end{bmatrix}\begin{bmatrix}\varepsilon_{11}^i\\ \varepsilon_{22}^i\\ \varepsilon_{33}^i\\ \varepsilon_{12}^i\\ \varepsilon_{23}^i\\ \varepsilon_{31}^i\end{bmatrix} \tag{7.15}$$

where λ_i and G_i are the elastic moduli for the *i*-th element.

[7] The authors used the term that can be loosely translated as "disclination"

We denote a matrix of fluctuations of the generalized deformation module with respect to the background volume $S_0 = \overline{S_i}$ as ΔS_i, and then we can write expressions for σ_v and $\Delta\sigma_i$ using Equations 7.13 – 7.15 as follows:

$$\sigma_v = S_0 \cdot \varepsilon_v^0 - \overline{\Delta S_\iota \cdot \varepsilon_v^*}\,,$$

$$\Delta\sigma_i = -S_i \cdot \Delta\varepsilon_i^* + \Delta S_i \cdot \varepsilon_v^0 + \overline{\Delta S_\iota \cdot \varepsilon_v^*}\ . \tag{7.16}$$

The value of the residual deformations (after removing the external stresses: $\sigma_v \to 0$) is readily determined from these expressions:

$$\Delta\sigma_i = S_i[S_0^{-1} \cdot (\overline{\Delta S_\iota \cdot \varepsilon_v^*}) - \Delta\varepsilon_i^*]. \tag{7.17}$$

It follows from Equations 7.16 and 7.17 that plastic non-conformities (discontinuities) cause internal stresses, which remain in the medium even after the external stresses are released. The magnitude of the internal stresses (whether they are residual or irreversible) is determined not only by the deformation fluctuations, but also by differences in the deformation modules ΔS_i between different parts (elements) of the cluster.

To describe variability of real geological media caused by either natural or man-made processes, the parameter ΔS_i can be used as a measure of weakening or damage of a specific part of the medium. In this case Equations 7.16 and 7.17 can be used to predict the behavior of real heterogeneous media during explosions. Indeed, according to 7.16 and 7.17 the areas with higher damage (or weaker zones) will sustain higher permanent deformations, even with the same intensity of explosive loading.

Chapter 8

The influence of faults, joints, and fractures, on mechanical effects of underground nuclear explosions

Our understanding of the main effects of underground explosions was long based on empirical data, interpreted under the assumption that rock massifs can be treated as a continuous medium. But serious difficulties then arise in explaining phenomena related to the deformation of real media, because commonly-used elastic or elasto-plastic models of the rock medium are inadequate for the solution of the dynamical problems related to explosion deformations and explaining the processes accompanying underground explosions. Using continuum models of the medium without accounting for residual deformations leads to a significant misrepresentation of explosion processes.

Disagreement between the results obtained using continuum models to describe the results of underground explosions attracted attention to the structural heterogeneities—discontinuities, faults, joints and fractures—of real geophysical medium (Adushkin and Spivak, 1983; Adushkin et al, 1993b). It is impossible to describe the main features of the rock medium using a model that does not account for the influence of structural discontinuities.

In the following sections we describe the major geological characteristics of rock massifs at the nuclear test sites in Russia with emphasis on their structure. Further description of the mechanical effects of underground nuclear explosions, in contrast to their common features, is given taking into account the effects of discontinuities.

8.1 Geological structure of the Semipalatinsk Test Site

The Semipalatisnk Test Site was founded in 1948. It is composed of several separate areas. The main testing areas are Balapan, Degelen and Murzhik (Figure 8.1). The Test Site is located between the Chagan and Tundyk rivers in the eastern part of the Central Kazakh upland area. The latter represents a low mountain massif with absolute elevations ranging mostly between 500 and 1100 m. The highest mountains in the area exceed 1300 m. Erosion topography is relatively gentle, varying mostly between 50 and 200 m, though in some cases reaching 500 m.

Despite the presence of some planar features in the regional morphology, overall the region belongs to the low mountain type with considerable block differentiation. This agrees with the crustal structure, close to the structure of the mountain systems rather than platforms. The crustal thickness varies between 46 and 55 km.

Geologically and structurally this region belongs to the eastern part of the Central Kazakhstan Uplift formed within the Caledonian Central Kazakh Fold System. Only the north-east corner of the test site lies within the Hercynian Zaisan Fold Belt. The boundary between areas of different ages corresponds to the deep Kolba-Chingiz fault (Figure 8.1).

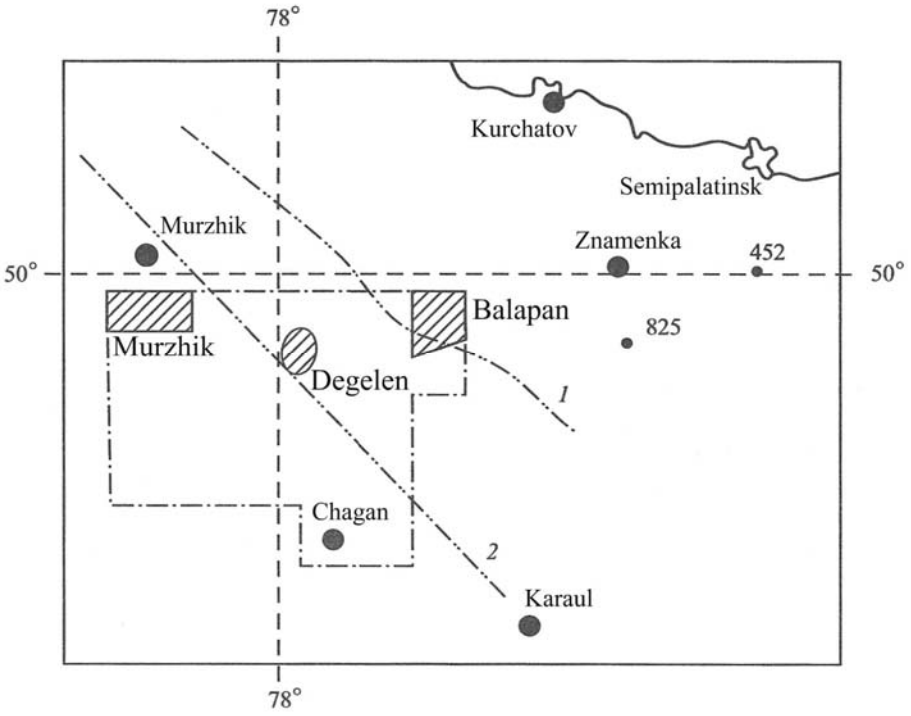

Figure 8.1: Map of the Semipalatinsk Test Site: *1* – Kalba-Chingiz Fault, *2* – Chinrauz Fault. Absolute elevation in meters is given at two points[1].

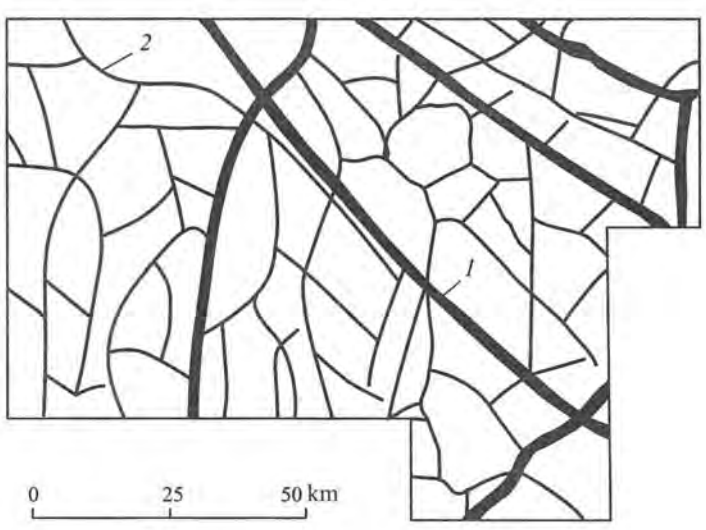

Figure 8.2. Morphological structure of the Semipalatinsk Test Site (the area shown in Figure 8.1 with dash-dotted line): *1* – deep tectonic faults (structures described in the text), *2* – tectonic structures of the second order.

[1] A detailed map of the Semipalatinsk Test Site boundary is available at http://www.LDEO.columbia.edu/~richards/Semi.boundaries.html

The main morphological feature of the area is its block structure (Figure 8.2). A block is a fragment of the upper part of the Earth's crust separated by faults with independent character of motion within the background macrostructure. Topographically, blocks are expressed as mountains, uplifts, massifs, steps within the slopes and valleys, individual valleys, widening of the bottom of the valleys, and water divides.

Shapes and sizes of the blocks reflect to some degree the character of regional stresses. Block shapes change depending on their proximity to structural discontinuities (sutures or faults). Elongated blocks are observed along structural discontinuities, while equidimensional (isometric) blocks are common for the central parts of the uplifts. A decrease in block sizes is observed close to areas of high deformation, suggesting that the blocks originated in geodynamical settings of regional compression and extension within the upper layers of the crust.

8.1.1. Geological features of the Balapan Testing Area. Geological structure of Balapan is represented by Devonian, Carboniferous, Triassic, Jurassic, Neogene and Quaternary rocks (Figure 8.3).

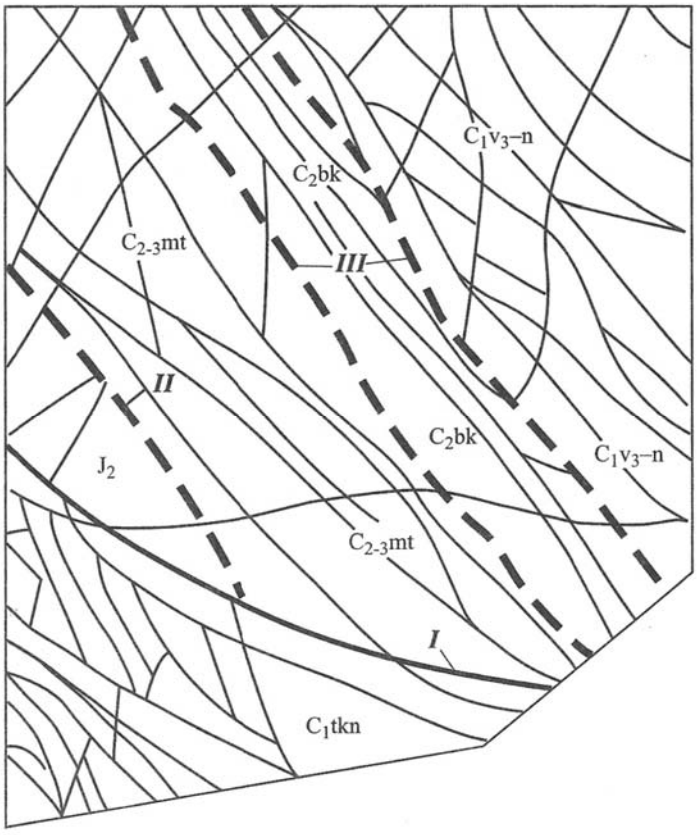

Figure 8.3. Tectonic structure of the Balapan Testing Area. Deep tectonic faults: I – Kalba-Chingiz, II – Chinrauz, III – Chagan.

Koyandinskaya formation (series) (C_1tkn). Siliceous, flinty, and chloride-sericite slates, with interlayers of quartzitic sandstones, conglomerates and limestones, are common in the lower part of the cross-section. The upper part of the cross-section is represented by coaly and clay shales with layers and lenses of siltstones and sandstones. These deposits are spread through the southwestern part of Balapan and are about 2300 m thick.

Kokpektinskaya formation (series) (C_1V_3–n) is represented by tuffs with basic and intermediate composition (in silica content). In the lower part of the cross-section the tuffs are interbedded with tuff-sandstones and less often with coal- and siliceous shales. These rocks have thickness of about 3000 m in the northeastern part of Balapan Testing Area.

Bukonskaya formation (series) (C_2bk) is represented by shales and sandstones, replaced with conglomerates in the lower part of the section. These rocks occupy the central part of the area, extending northwest with a width of 3000 m and thickness of about 2000 m.

Maityubinskaya suite (series) (C_2mt) is represented by molasse[2]. The lower part of the cross-section is composed predominately of conglomerates with lenses and beds of sandstones and siltstones. The upper part is occupied by sandstones, siltstones, and coaly clay shales with conglomerate lenses. The sediments contain zones of rock fragmentation, foliation and cataclasts. These sediments extend as a band in the central part of Balapan extending in the northwest direction as a tectonic block.

Intrusive rocks commonly occurring throughout the area are represented by complexes varying in morphology, composition and age:

- granitoids of Upper Paleozoic age;
- granitic intrusion of Upper Carboniferous age;
- Lower Carboniferous Verhnevizeiskii-Namyurskii complex of small sub-volcanic intrusions;
- Sub-volcanic Upper Carboniferous intrusions of basic and intermediate porphyrites;
- Dikes of andesitic porphyrites of Permian age.

Ground water is observed through the entire area in the boreholes at depths 5 – 96 m (more commonly at 20 – 40 m) depending on the thickness of Neogene clays.

The following types of ground water based on their origin and circulation type are observed:

- Fracture water occurring in the weathering fracture zone in Paleozoic and Mesozoic sediments; its thickness is 40 – 120 m, occasionally reaching 150 m.
- Fracture-vein water confined to the zones adjacent to the tectonic faults and fragmented zones.
- Pore water observed in the Quaternary and Neogene sediments.

The widely distributed ground water is fracture-related in the upper part of Mesozoic and Paleozoic rock massifs. This type of ground water is often pressurized. Neogene clays act as an aquitard filling the irregularities in the hard rock basement. Piezometric levels (heads water levels) are at depths between 5 and 33 m creating head up to 87 m.

[2] From Wikipedia: “The term "molasse" refers to sandstones, shales and conglomerates formed as terrestrial or shallow marine deposits in front of rising mountain chains.”

Table 8.1. Physical and mechanical properties of rocks at Balapan Testing Area

Rock type	Density, g/cm^3	Porosity, %	Water saturation [?], %	Uniaxial compression strength, MPa	
				Dry	Saturated
Tuff	2.76	1.9	0.11	96	113
Tuff sandstone	2.74	1.4	0.25	71	68
Tuff shale	2.72	2.2	0.1	98	84
Slate	2.72	0.7	0.24	86	49
Sandstone	2.74	0.8	0.27	80	54
Porphyrites	2.70	2.2	0.2	96	104
Metasomatic rocks	2.74	0.9	0.2	64	38
Granite	2.66	1.1	0.28	96	106
Granite-porphyrites	2.63	1.5	0.17	94	88
Granodiorite	2.66	2.3	-	-	-
Basalt porphyrites	2.76	3.5	0.35	-	66

Rock type	Seismic velocity, km/s		Young modulus, GPa	Poisson coefficient
	P	S		
Tuff	5.6	3.25	71	0.25
Tuff sandstone	5.54	3.33	71	0.25
Tuff shale	5.69	3.38	78	0.26
Slate	5.58	3.02	65	0.39
Sandstone	5.53	3.0	65	0.29
Porphyrites	4.9	3.2	70	0.29
Metasomatic rocks	4.99	2.82	56	0.26
Granite	5.56	3.22	68	0.23
Granite-porphyrites	5.1	-	-	-
Granodiorite	4.6	2.85	53	0.18
Basalt porphyrites	4.8	2.97	57	0.24

Rocks of the Balapan rock massif have low water content. Debits in the water wells vary between 1 – 10 to 1.21 – 10 m^3/s with level changes of 14.7 and 13.7 m respectively. The rocks are characterized by low permeability. The filtration coefficients vary between $5.8 \cdot 10^{-11}$ to $3.9 \cdot 10^{-7}$ m/s, in some cases (in the fracture zones and in limestones) increasing from $0.35 \cdot 10^{-5}$ to $7 \cdot 10^{-5}$ m/s.

Pore water is common for loose Cenozoic sediments. In watershed areas separating drainage basins [not sure what the proper term is—I tried a rewrite (PGR)] this type of water is related to lenses and beds of sand, sandstones and conglomerates at the bottom of the Neogene clays. These water-saturated sediments occur sporadically at depths of 11 – 84 m, their thickness does

not exceed 20 m. Pore water is pressurized. Debits in the water wells vary between $1.6 \cdot 10^{-3}$ to $7.7 \cdot 10^{-3}$ m^3/s with level changes of 18 and 7.9 m respectively. The filtration coefficient is approximately 2 – 20 meters per day.

From the engineering geology standpoint the Balapan sub-area is represented by a two-tier structure due to the presence of a hard rock Paleozoic/Mesozoic basement, covered by loose Cenozoic sediments. The sediment thickness varies from several meters to 100 meters. All basement rocks are weathered in the upper part of the cross-section. The thickness of the upper intensely weathered zone varies between 40 and 120 m. Based on seismic data, the bottom of the intensely weathered rocks is represented by a third refraction boundary. Seismic velocities for the rocks below the boundary range between 4.3 and 6.2 m/s. The values of 5.6 – 6.2 km/s correspond to the effusive and intrusive rocks. The velocities between 2.8 and 3.2 km/s correspond to the zones of faults and fractures.

Typical values for physical, mechanical and other parameters for Balapan rocks are presented in Table 8.1.

Close to 100 nuclear explosions were conducted in boreholes of the Balapan Testing Area, as well as 7 Peaceful Nuclear Explosions (during the period 1965 – 1968) conducted for the purposes of determining explosion parameters for explosion excavation in order to create ejection craters[3]. One of these explosions consisted of three nuclear charges placed in a row to create an elongated trench.

8.1.2. Geological features of the Degelen Testing Area are determined by its location, which is mostly confined to a rounded intrusive rock massif with a diameter of about 20 km. Based on geological studies, the intrusive massif represents a crustal ledge surrounded by a subsided caldera composed of sedimentary and effusive formations.

In the larger western part of the testing area intrusive rocks are exposed at the surface and are represented by Upper Paleozoic granites and syenites, and Lower Carboniferous granite-porphyrites (Figure 8.4). The rocks surrounding the intrusion are observed only in the upper part of the cross-section. These rocks are represented by acidic effusive rocks. The thickness of these effusive rocks increases in the significantly smaller eastern part of the testing area and along the southern and northern boundaries of the intrusion. In the eastern part the effusive rocks form a continuous cover and are represented not only by acidic, but also by basic effusive rocks of Lower Carboniferous System.

Granites of Upper Paleozoic age are subjected to tectonic faulting, and such faults can be traced also in the effusive formations in the eastern part of the testing area, forming a wide system of structural-tectonic blocks (Figure 8.4).

[3] When the texts of the Threshold Test Ban Treaty and the Peaceful Nuclear Explosions Treaty were negotiated between the USSR and the USA in the 1970s, a "Peaceful Nuclear Explosion" was defined as a nuclear explosion conducted off the territory of a recognized nuclear test site. By that definition, there could be no PNEs at Balapan. Nevertheless, since the primary purpose of a number of nuclear explosions in the Balapan sub-area of STS was evaluation of a civil engineering capability, and was not weapons-related, these explosions are often characterized as PNEs (note by translators).

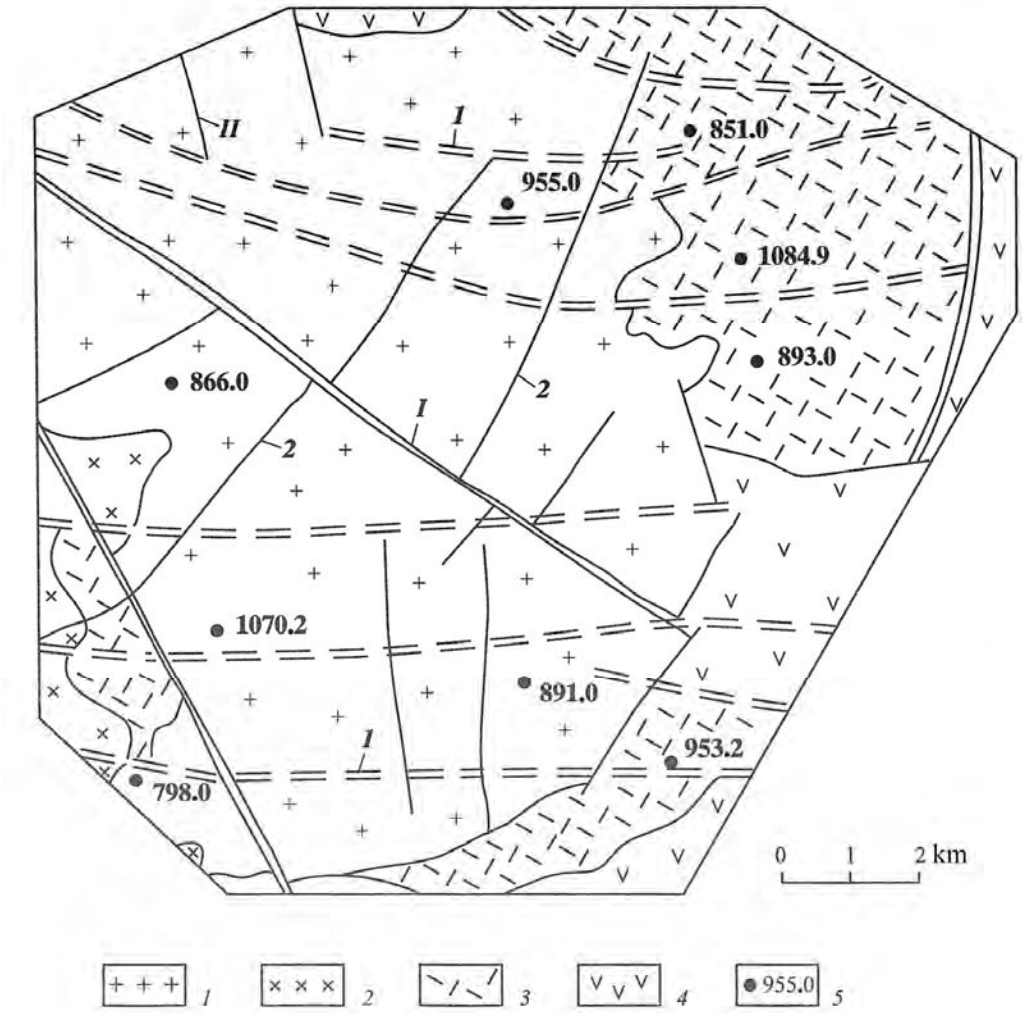

Figure 8.4. Geological map showing fault zones in the Degelen sub-area of the Semipalatinsk Test Site. Fault zones: *I* – major, *II* – secondary. Geological formations: *1* – granitoids of the Upper Paleozoic Era, *2* – granitoids of the Lower Carbon, *3* – acidic effusive rocks of Early Carboniferous age, *4* – basic and intermediate effusive rocks of Lower Carbon, *5* – absolute elevation marks.

In addition to large tectonic faults, there are many small faults of different orientations (especially in granites). Development of faulting deformations in the granite massif is likely due to a stress release caused by the uplift during the caldera subsidence.

The granites are crossed by dikes of porphyrites and micro-granite and, less often, by quartz veins. The thickness of the dikes and veins varies between 0.2 and 5 m. The common dip is 20 - 60 º with azimuthal directions ranging over 220 – 290º. The contacts between the dikes and the surrounding rocks are sharp, without significant rock alteration. The rock-forming minerals are: feldspar – 65–75 %, quartz – 25–30 %, and biotite 1 – 3 %.

Table 8.2. Physical and mechanical properties of rocks at the Degelen Testing Area

Rock type	Density, g/cm^3	Porosity, %	Water saturation, %	Uniaxial compression strength, MPa	
				Dry	Saturated
Granite	2.56	3.42	0.3	119	129
Quartz porphyrites	2.66	2.11	0.22	148	110
Andesite porphyrites	2.89	-	0.09	210	130
Diabase porphyrites	2.76	3.5	0.35	-	66

Rock type	Seismic velocity, km/s		Young modulus, GPa	Poisson coefficient
	P	S		
Granite	4.9	2.8	51	0.26
Quartz porphyrites	5.2	2.8	56	0.29
Andesite porphyrites	5.7	3.0	66	0.29
Diabase porphyrites	5.0	2. 7	55	0.29

Table 8.3. Classification of the structural blocks, faults and fractures

Order of the block structure	Classification of the faults and fractures		
	Order of discontinuity	Discontinuity length	Thickness of the fault damage zones (gouges) and fractures
I	I order, deep seismogenic faults	Hundreds to thousands of kilometers	Hundreds to thousands of meters
II	II order, deep seismogenic and non-seismogenic faults	Tens to hundreds of kilometers	Meters to tens of meters
III	III order faults	Kilometers to tens of kilometers	Meters to tens of meters
IV	IV order faults	Hundreds to thousands of meters	Tens of centimeters to meters
V	Small faults and large fractures of V order	Tens to hundreds of meters	Tens of centimeters
VI	Medium size fractures of VI order	Meters to tens of meters	Millimeters to centimeters
VII	Small fractures of VII order	Centimeters to meters	Fraction of a millimeter to millimeters
VIII	Thin fractures of VIII order	Less than 10 cm	Less than 2 mm

All rock massifs within the Degelen Testing Area are composed of similar intrusive and effusive magmatic rocks of high mechanical strength (Table 8.2).

According to a classification provided in Table 8.3, the Degelen massif is built predominantly with structural blocks of III – VIII orders. Tectonic faults defining the blocks of III, IV and, in many cases, V orders can also be reliably identified on aerial photographs and by visual inspection of the massif surface.

The location of tectonic faults can be determined with high accuracy for areas in which tunnels were constructed, and the shapes and sizes of structural blocks can be determined by examining the tunnel walls[4].

Blocks of the III order have sizes of a few tens of kilometers. As a rule, the tunnels used for nuclear tests are located entirely within a single III order block, or (more rarely) in two adjoined blocks of III order, so that no more than one III order fault is crossed by the tunnel.

Blocks of IV order have areas from (200 – 300) × (300 – 600) m^2 to (450 – 600) × (800 – 1500) m^2 in map view. The vertical extent of the blocs is thought to be comparable with the maximum depths of the tunnels.

Blocks of V order measure (15 – 150) × (40 – 400) m^2 in map view and (30 – 300) m in depth. The shapes of these blocks are close to irregular parallelepipeds or prisms. Their sizes vary significantly within the same rock massif. As a rule, their sizes increase with depth.

The average linear dimensions of blocks of V order vary from 12 to 243 m for different parts of Degelen (Table 8.4).

The structural blocks of VII and VIII orders represent the lowest hierarchical level of the Degelen structure. They can be determined only by mapping them in the tunnel walls in the tunnels or if they are exposed at the surface. The size of these elementary blocks varies from 0.1 × 0.2 × 0.3 m^2 to 1.3 × 1.5 × 2 m^2. As an illustration, Figure 8.5 shows the average linear dimensions of the blocks along the tunnels # 4 and 5 (Table 8.4), obtained by averaging the block sizes in the 5-m long tunnel intervals.

The boundaries between order III structural blocks are often represented by long (10 km or more) tectonic faults. These faults are often expressed on the surface as small valleys or steps in topography with depths up to several meters. The thickness of the affected zones for the order III faults is 2 – 4 m. There are 50 – 100 fractures per meter in these affected zones. Seismic data show that the thickness of the affected zones for the order III faults is even greater, and can reach 6 – 15 m for Tunnel #4 (inside the tunnel) and 15 – 40 m at the ground surface.

The boundaries of the IV order are represented by tectonic faults with lengths on the order of 1 km and the gauge zone thickness ranging from centimeters to several tens of centimeters. The inner structure of the IV order fault zones is variable. It can be a single thick fracture filled with clay and rock fragments, e.g. the zone in Tunnel #3 (the thickness of the fill is up to 30 cm and the affected area up to 2 – 4 m). In some cases these zones are represented by two closely spaced

[4] In mining practice is sometimes useful to distinguish between adits and tunnels—the former having only one point of entry (serving also as the exit), the latter having two. With such a convention, almost all underground openings at Degelen were adits—though they are commonly referred to as tunnels (note by translators)

fractures, e.g. the zone in Tunnel #7 with opening of 2 and 3 cm and the combined affected zone with a thickness of 15 m. Another common type of fault zone is a fracture “healed” by a dike of granodiorites (e.g. Tunnels # 4, 5 and 7). The dike thicknesses reach 2 – 3 m, and the affected zones are 15 – 20 m.

The boundaries of the blocks of IV order can be represented by either tectonic faults or tectonic fractures of short length (tens to first hundreds of meters). The thickness of the fill is commonly 1 – 2 cm, sometimes reaching 5 cm. The thicknesses of the affected zones are 0.15 – 0.5 m. The fracture index in the affected zones reaches 10 – 30 fractures per meter.

Table 8.4 Average size (A) of the structural blocks of V order for different parts of the Degelen Testing Area

Explosion [test] #	Tunnel #	Test date	Tunnel length, m	*A*, m
1	200	October 18, 1984	211	12
2	160	June 27, 1985	170	17
3	K-85	October 16, 1987	209	52
4	168	July 17, 1987	1238	88
5	169/1	November 23, 1988	745	106
6	215	May 30, 1983	788	113
7	190	April 15, 1984	1290	116
8	704	April 22, 1988	485	243

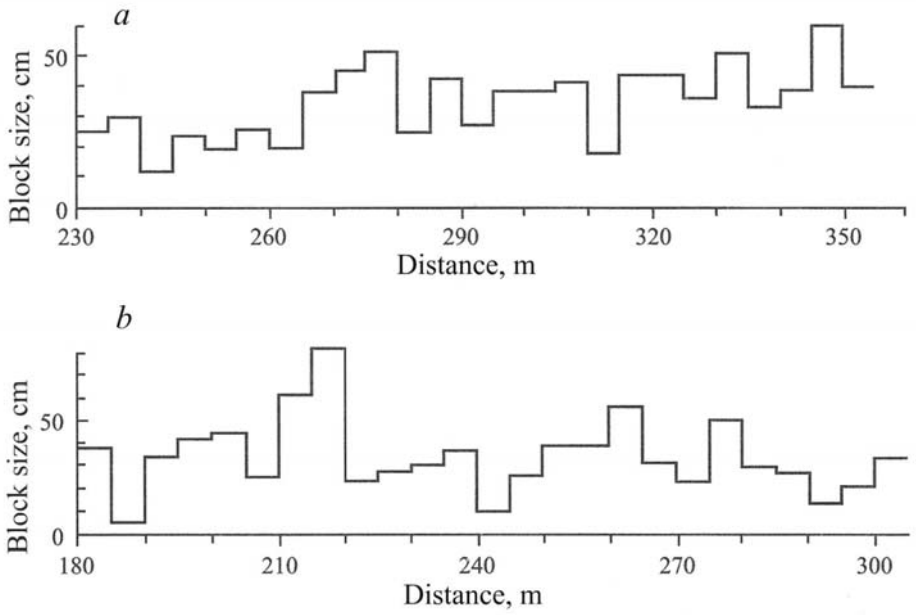

Figure 8.5. Average linear dimensions of elementary structural blocks along the tunnels: a) – 168 (UNT 07.17.1987), b) – 169/1 (UNT 11.23.1988).

Table 8.5. Fracture systems within the Degelen mountain

Fracture orientation		Explosion [test] number (from Table 8.4)
Azimuth	Dip	
0 – 30	70 – 80	7
15 – 25	5 – 20	7
80 – 125	60 – 80	5, 6, 8
105 – 140	50 – 80	3, 6, 7
120 – 130	25 – 30	8
150 – 180	45 – 70	1, 3
175 – 210	70 – 80	4, 7
180	25 – 30	7
180 – 240	75 – 85	5
205 – 240	50 – 80	1, 5, 6, 7
230 – 260	45 – 65	3, 8
260 – 285	50 – 70	1, 4, 8
310 – 350	10 – 35	5
310 – 350	40 – 70	1, 3, 6

Figures 8.6 and 8.7 show examples of tectonic structures along some profiles crossing the tunnels.

The boundaries between the smallest blocks are represented by tectonic and lithological fractures with lengths between tens of centimeters and a few tens of meters. The thicknesses of these fractures observed in the tunnels are between fractions of a millimeter and 1 – 2 mm.

Three to five fracture systems, often intermixed, coexist within a single block of V order with intervals on the order of several tens of centimeters. Less commonly, three to four fracture systems are observed with intervals amounting to several meters.

Table 8.5 describes the fracture systems characteristic for the Degelen massif, and shows that the most common fractures have NNW and NW strike directions, dipping to the SW.

Approximately 200 nuclear explosions were conducted in tunnels of the Degelen massif between 1961 and 1989. Below we present some examples of the geological structure of Degelen tunnel sites.

Tunnel 215 (UNT May 30 1983). The rock massif surrounding Tunnel 215 is represented by an effusive formation of Early Carboniferous Period. The lower part of the massif is built of andesite porphyrites, while the upper part is composed of quartz porphyrites.

In some places these rocks are broken by thin vein-like formations of granite porphyrites and quartz porphyrites of approximately Paleozoic age.

The basement rocks have the following values of compressional strength: quartz porphyrites – 119 – 130 MPa, andesite porphyrites – 123 – 140 MPa. The elastic velocities for these rocks are 4.9 – 6.8 km/s.

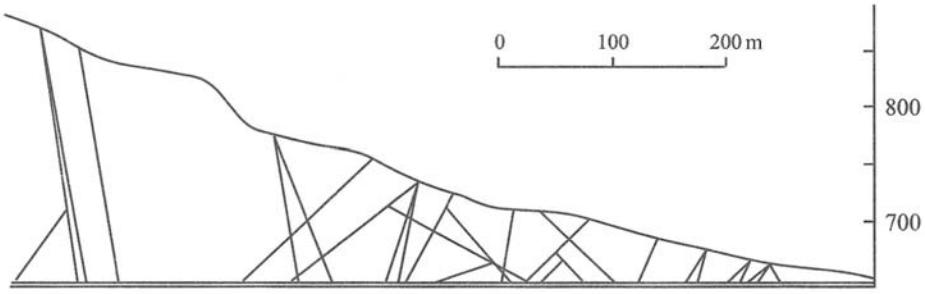

Figure 8.6. Structural geological cross-section through Tunnel 215. The lines show tectonic discontinuities (faults) of V order.

Seismic surveys show high seismic velocities (the major part of the massif is characterized by P velocities of 4.5 – 6.0 km/s). However there are zones with relatively low velocities (4.0 – 4.5 km/s) due to the presence of weak rocks, and zones with high velocities (5.0 – 6.0 km/s) related to dense lava formations. In addition, there are small zones with significantly reduced velocities (2.4 – 3.9 km/s) corresponding to tectonic fault zones. The massif in this particular area has a complex system of tectonic faults (Figure 8.6).

Tunnel 200M (UNT October 18 1984). The tunnel is located in the southeastern part of the Degelen massif on the southern slope of a mountain with elevation 875 m. The absolute elevation varies from 621 m at the tunnel entrance to 727 m at the end chamber, where the elevation above the chamber is 106 m. The tunnel length is about 200 m (Figure 8.7).

The rocks around the tunnel are represented by an effusive formation (quartz porphyrites) of Early Carboniferous age. The rocks are felsic cryptocrystalline (aphanitic), having no foliation or porphyritic texture, that is they are homogeneous (massive) with compressive strength of 180 MPa, porosity of 0.74 %, and moisture content of 0.21 %.

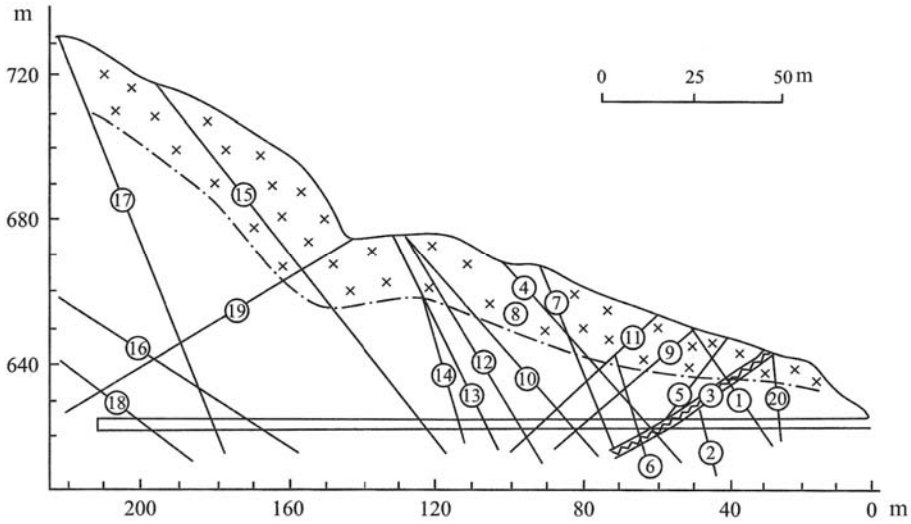

Figure 8.7. Structural and tectonic scheme (cross-section) through Tunnel 200M. Solid lines show tectonic faults with their numbers shown in circles.

There are two types of fractures observed along the tunnel: petrogenic (joints caused by cooling or unloading), and tectonic fractures. The first type of fractures can be traced along the entire tunnel. They are characterized by small openings with aperture up to 0.5 mm that are discontinuous and curvilinear, with varying strike and dip. The fracture index varies from 3 to 14 fractures per meter. Maximum values of the fracture index are related to the fault zones. The second type of fractures is observed in the intervals 30 – 46, 59 – 61, 64 – 72, 80 – 82, 91 – 95, 105 – 112, and 166 – 179 meters from the tunnel entrance. All these fractures have steep dips, with similar strikes and thicknesses, and can be clearly traced in the tunnel walls. These tectonic fractures are normally thin (0.01 – 0.2 m).

The complex system of tectonic faults breaks the massif into separate structural and tectonic blocks (Figure 8.7) with fractures having specific features within each block. Seventeen such blocks separated by tectonic faults, and different systems of petrogenic fractures (joints) and common fracture indexes, were identified within the tunnel. The characteristics of the tectonic faults and structural tectonic blocks (STB) are shown in Table 8.6.

Seismic studies in the area of Tunnel 200M were conducted in order to determine seismic velocities of the rock massif. The following surveys were performed: surface seismic profiling along four profiles, seismic profiling in the tunnel in the interval between 60 and 157 meters from the tunnel entrance, and seismic imaging. The results of these studies are presented in Figure 8.8. Relatively low seismic velocities suggest a high degree of pre-existing rock deformations in Tunnel 200M, which can be explained by this tunnel's shallow placement.

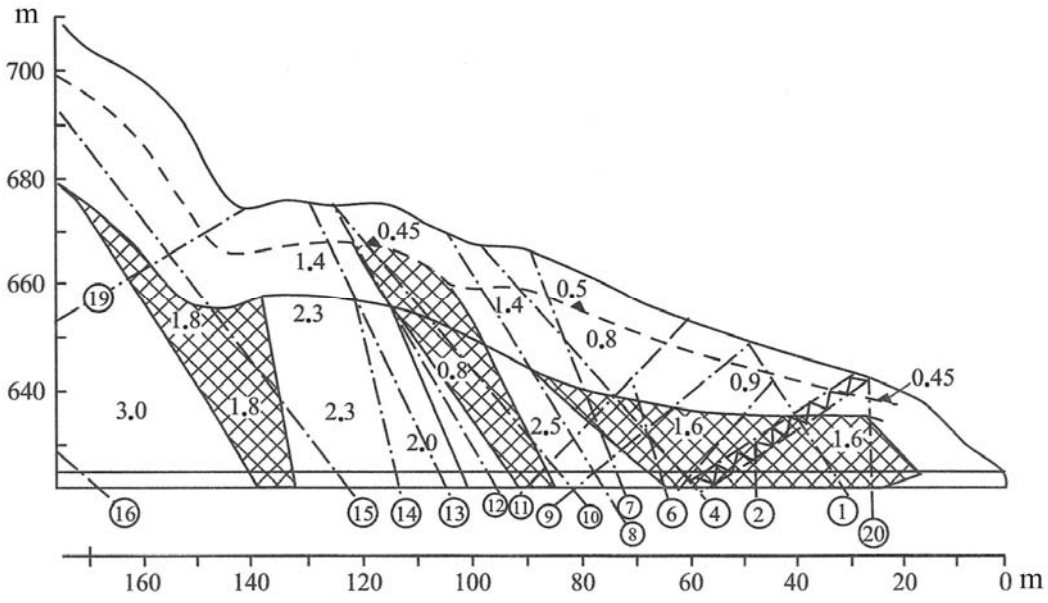

Figure 8.8. Results of the seismic imaging through Tunnel 200M. Numbers in the cross-section show longitudinal seismic velocities in km/s, numbers in circles show the faults (as in Figures 7.19 and 8.7).

Table 8.6. Characteristics of fractures [discontinuities] and structural blocks in Tunnel 200M

Fracture #	Distance from tunnel entrance, m	Thickness, m		Fracture type	Block #	Distance from tunnel entrance, m	Fracture index [?]
		Shifted [slipped/] zone	Influence zone				
1	30	0.1	0.5	Medium fault/fracture	1	27 – 30	15.75
2	46	0.04	None	Small fault/fracture	2	30 – 46	8.33
3	59	0.25	1.5	Damage zone	3	46 – 59	11.45
4	59	0.02	0.2	Medium fault/fracture	4	59 – 61	8.0
5	61	0.04	0.5	“	5	61 – 64	7.0
6	64	0.03	None	Small fault/fracture	6	64 – 72	6.88
7	72	0.01	0.5	Medium fault/fracture	7	72 – 75	5.67
8	75	0.19	0.8	“	8	75 – 80	8.25
9	80	0.15	0.6	“	9	80 – 82	6.33
10	82	0.03	0.3	“	10	82 – 91	10.0
11	91	0.2	1.0	“	11	91 – 95	9.8
12	95	0.03	0.25	“	12	95 – 105	8.8
13	105	0.05	1.5	“	13	105 – 112	9.25
14	112	0.08	0.2	“	14	112 – 122	12.4
15	122	0.02	0.1	“	15	122 – 166	7.24
16	166	0.15	None	“	16	166 – 179	7.0
17	179	0.01	0.15	“	17	179 – 197	4.9
18	197	0.03	None	“	18	197 – 211	5.27

Tunnel 168 (UNT July 17 1987). The tunnel is located in the southwestern part of the Degelen massif (the tunnel length is 1238 m and the line of least resistance, or LLR is 251 m). The rocks are represented by granitoids of approximately Upper Paleozoic age (γPZ_3). The rocks are composed of quartz and feldspar and have crystalline texture.

Four different rock complexes are observed at the site, associated with different features from a geological-engineering perspective:

- An anthropogenic complex (tQrv) with a thickness of 2 – 3 m, represented by boulders and gravel.
- A sedimentary proluvial-deluvial complex of Quaternary age, represented by sandy clay with some gravel, with a thickness of 0.5 – 1 m (up to 8 m in the valleys) and seismic velocity of 0.5–1.4 m.
- A complex of intrusive rocks of upper Paleozoic age (γPZ_3), represented by granites. A weathered zone with a thickness of 5 – 42 m and seismic velocities of 0.6 – 3.2 m/s is observed within this complex. The zone of rocks weakened during tunnel digging has a thickness of 0.5 – 7 m and is characterized by seismic velocities of 2.4 – 3.3 m/s.

- A dike complex of upper Paleozoic age (γPZ_3), represented by diorite porphyrites. The rocks of this complex are characterized by higher velocities, densities and strength.

Numerous tectonic faults and fractured zones are observed and located in the rock massif (Figure 8.9). The fracture index in the zones affected by tectonic faults reaches 10 – 50 fractures per meter. Based on geological surveys in the tunnel, the thickness of zones affected by tectonic faults is 0.1 – 2 m, while according to seismic profiling at the surface the zone thickness is 6 – 15 m. The fracture index in tectonically weakened (fractured) zones is 10 – 30 fractures per meter. The thickness of these zones reaches 6 m (6 – 23 m according to the results of seismic profiling).

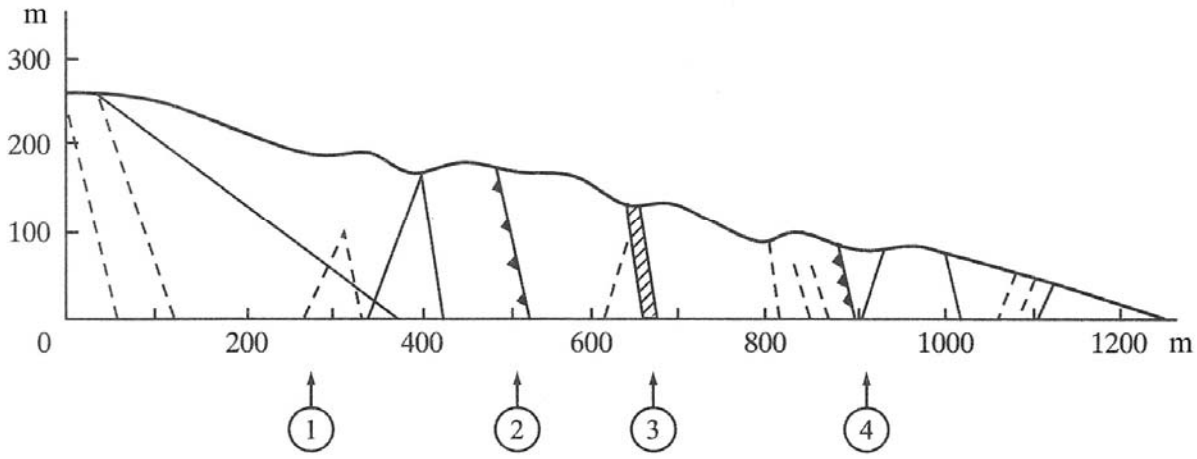

Figure 8.9. Structural and tectonic scheme (cross-section) through Tunnel 168. Lines show tectonic faults of different orders; their numbers are shown in circles (as in Figure 8.7).

The velocity of seismic waves in zones around the faults and in tectonically weakened zones ranges between 3.0 and 4.3 km/s.

Rocks within a vadose zone (associated with runoff ground water) are situated about 15 to 20 m below the tunnel floor. Water enters the tunnel through the roof and the walls mainly in areas of tectonic fractures and weakening deformation. In winter the water entry rate is 0.03 – 0.16 m^3/day; in the spring, 7 m^3/day. All water entering the tunnel is filtering through the floor into the deeper zone with water of vein type.

Tunnel 160 (UNTs June 27 1985 and June 29 1987). The rock mass surrounding Tunnel 160 is represented by volcanic formations (diabase porphyrite and rhyolitic porphyrite of Early Carboniferous Age (C_1v_3 – n). The rocks are cut by a quartz sienite intrusion of approximately Early Carboniferous Age ($\mu\varepsilon\ C_1v_3$ – n) and by granitic veins ($\gamma\pi\ PZ_3$).

The effusive rocks have porphyritic texture. The major part of diabase porphyrites are made of microliths of plagioclase and chloritized glass. The bulk of rhyolitic porphyrites is made of small crystals of feldspar, quartz and biotite.

Weathered porphyrites have high compressive strength (86 MPa), low compressibility (*P*-velocity is 5.39 km/s, elastic modulus is $6.2 \cdot 10^4$ MPa), and a fracture index of 11 fractures per meter.

Un-weathered porphyrites (with intermediate fracture content) are hard rocks with a discontinuous network of fractures. Un-weathered porphyrites are characterized by the following physical parameters: density – 2800 kg/m^3, porosity – 0.74%, water content – 0.26 %; the compressive strength for dry rock is 10^4 MPa and 98 MPa for water saturated rock, P-wave velocity – 5.03 km/s [why is the velocity of unfractured rocks is lower than for the fractured?], S-wave velocity – 2.69 km/s, elastic modulus – $5.5 \cdot 10^{10}$ MPa[5], fracture index – 5-6 fractures/meter, fracture porosity – 0.4%. The velocity of P-waves in the rock massif is 4.5 – 6.4 km/s.

Based on the data of seismic imaging (Figure 7.19) the massif is subjected to weathering down to depths of 20 – 45 m. The weathered zone consists of two layers: an upper (boulder) zone with a thickness of 20 – 12 m (P-velocity – 1.0-1.4 km/s), and a lower zone with highly fractured rocks having a P-velocity of 1.8-3.0 km/s. The velocity of the intact sienites is 4.4 – 6.0 km/s.

The ground water level becomes lower down the valleys. In the northeast of the area the slope of the water table is on average 6º. The water table in the slopes and the upper parts of the valleys is the deepest — 14 – 39 m. In the middle parts of the valleys the depth is 2.9 – 7.5 m. The ground water is unpressurized. The amplitude of natural water table oscillations in the wells in the spring-summer period reaches 0.25 m/day. The water is not abundant and is characterized by specific debits for the wells in effusive rocks between 0.0006 and 0.152 liters/s, and for intrusive rocks between 0.11 and 0.25 liters/s.

8.2. Disjoint block motion and deformations driven by explosions

Tectonic deformations including faults, fissures and fractures are widespread in the crust. The practice of building of underground structures shows that no rocks are monolithic geological formations. Tectonic deformations occur on different scales: from barely noticeable fractures to tectonic faults that can be traced not only in underground tunnels, but also on the surface (Figure 8.10). The presence of tectonic faults results in considerable redistribution of the ambient stresses and the strains produced by these stresses.

Tectonic faults of orders III – V with lengths between 10 and 10^5 meters have the most influence on medium deformation and damage due to an underground nuclear explosion. The presence of these structural discontinuities leads to strongly non-uniform deformation processes in rock massifs during underground explosions, with the most significant irreversible deformations being localized close to the medium discontinuities. Moreover, it is impossible to explain significant irreversible deformations observed at large epicentral distances from underground nuclear explosions without taking into a consideration large tectonic faults.

[5] The units should probably be Pa, not MPa (note by translators)

For example, studies performed after the underground nuclear test CANNIKIN (yield 5 Mt) determined that spatial deformations within the Earth's crust were strongly heterogeneous along fault zones (e.g. Dickey et al, 1972). Significant residual displacements reaching 1 – 3 m were observed along some faults.

Figure 8.10. Photograph from the Degelen Testing Area. The structural faults of V order can be easily identified.

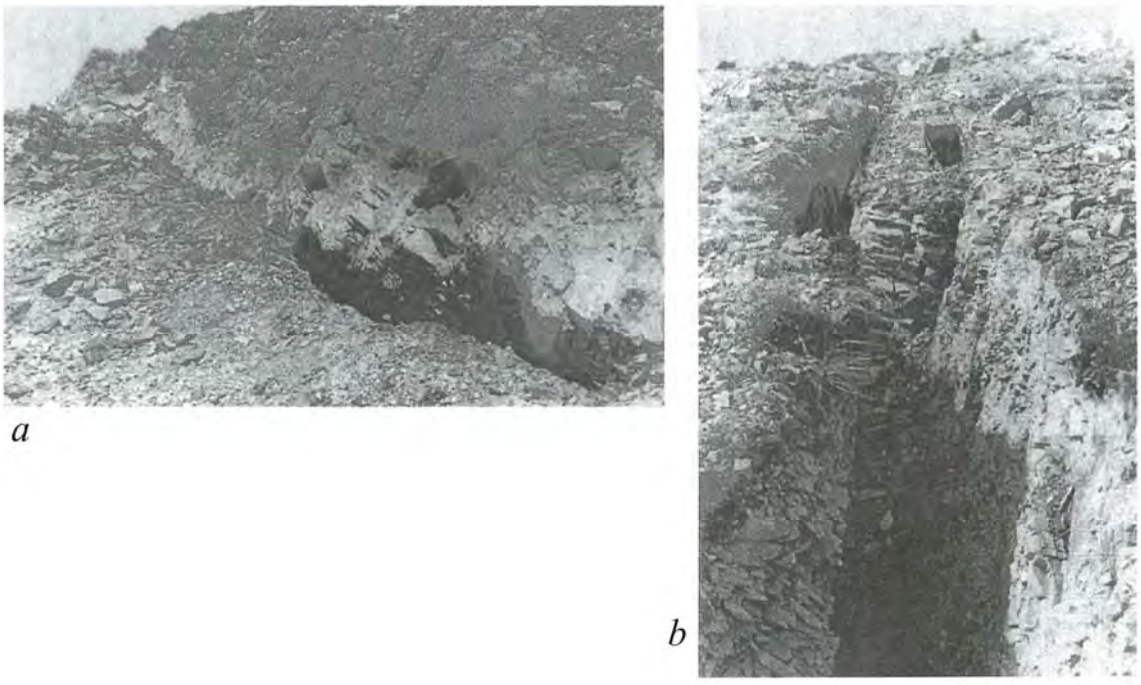

Figure 8.11. Photographs of residual deformations at the surface along the tectonic faults of V order: *a* – vertical throw, and *b* – fissure.

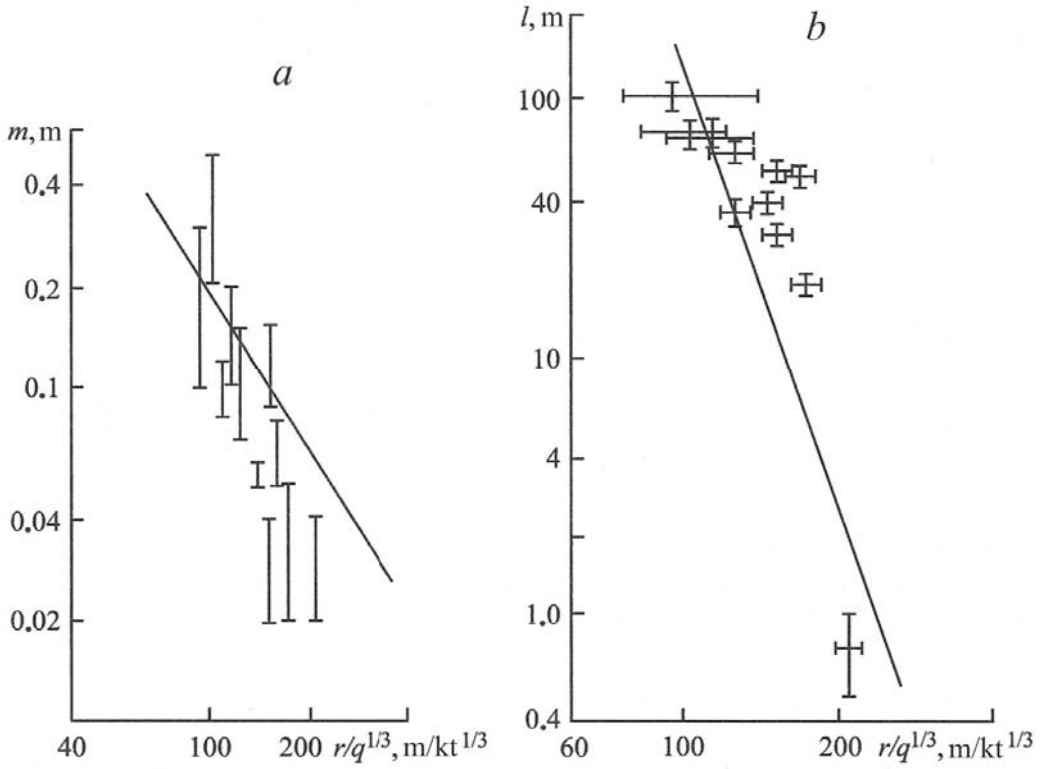

Figure 8.12. (*a*) Opening (aperture) and(b) length, of fractures observed at the surface following the underground test K-85 (10.16.1987).

Localization of the deformations along large faults is illustrated in Figure 8.11, which shows the photographs of the residual deformations at some tectonic faults (the vertical displacement reaches 1.7 m, the horizontal fracture opening is 0.7 m) during the nuclear test in Tunnel K-85.

Characteristics of the large fractures created by this explosion (mostly in the immediate vicinity of the tectonic faults) are presented in Figure 8.12.

The existence of pre-existing tectonic discontinuities not only causes heterogeneous medium deformations, but also significantly increases the area of the influence of underground nuclear explosions. For instance, during the test in Tunnel 200 considerable deformation of the rail near a tectonic fault was observed in the neighboring tunnel at a scaled distance of 743 m/kt$^{1/3}$. The relative displacement of the different sides of the fault was estimated (chord of the rail curve being about 1.5 – 2.0 m, with the maximum deflection of the rail reaching about 0.8 – 1.2 m) to be about 0.5 m.

The main features of the deformation of the medium due to an underground nuclear explosion can be determined using a simple estimate. Let us consider an arbitrarily oriented tectonic discontinuity (fault, block boundary) *BCKFF'B'* (Figure 8.13 a) characterized by a dip α and a strike azimuth φ_s, which intersects the test tunnel *ON* with the azimuth of φ_0 at a distance from explosion of l_0 (point φ_0).

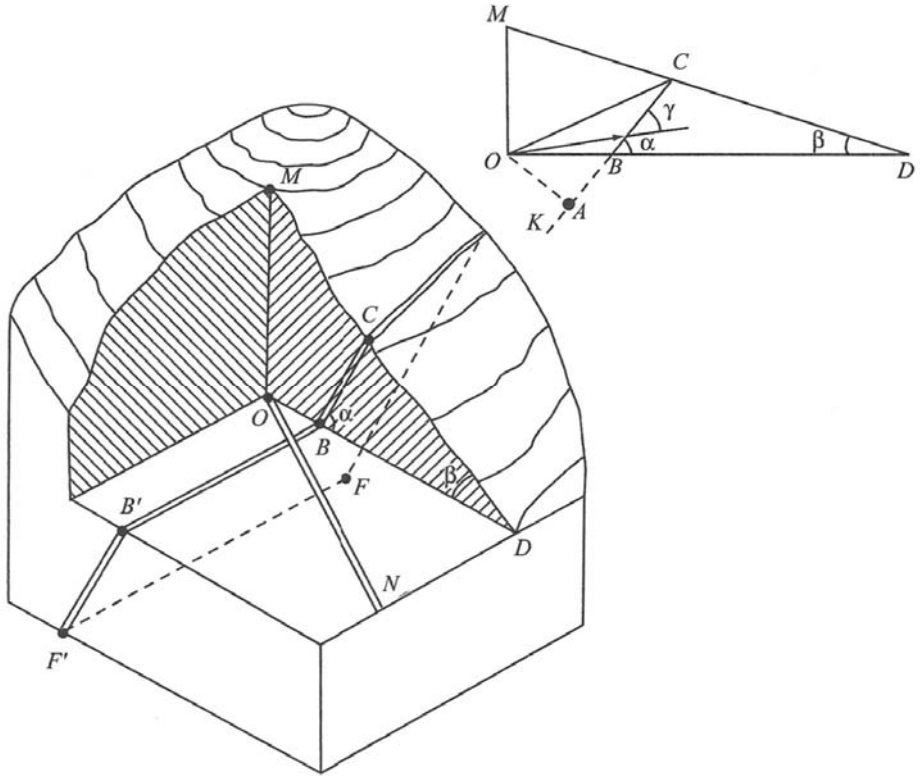

Figure 8.13: Schematic of an explosion in an underground tunnel: *ON* – tunnel, *OM* – the depth of the charge, F′B′BCKF – plane of a tectonic fault.

Further analysis will be conducted in the plane OMD, which is normal to the plane of the fault (See schematics in Figure 8.13). It is obvious that

$$OB = l = l_0\cos(\varphi_0 - \varphi_s + \pi/2),$$

$$OD = L = L_0\cos(\varphi_0 - \varphi_s + \pi/2),$$

where L_0 is the distance between the end chamber and the tunnel entrance.

We assume for simplicity that the main characteristic determining the medium behavior in the immediate vicinity of a discontinuity (such as a fracture) under dynamic loading is the deformation normal to the fracture plane ε_n. We also assume that the mechanical property of the rock and the material filling the fracture are identical. It follows from Figure 8.13b that the value of ε_n in any arbitrary point along the fault can be expressed as:

$$\varepsilon_n(r_1, t) = \varepsilon_r(r_1, t)\sin^2\gamma_1 + \varepsilon_\varphi(r_1, t)\cos^2\gamma_1, \tag{8.1}$$

where r_1 is the distance from the explosion to the point N, ε_r and ε_φ are the radial and tangential (azimuthal) deformations of the medium in the stress wave, and γ_1 is the angle between the wave vector and the fault plane at the point under consideration.

The particle velocity at a distance *r* from the explosion is given by:

$$v(r,t) = \begin{cases} v_0(r)\varphi(t) & \text{for } 0 \le t \le \tau \\ 0 & \text{for } t < 0 \text{ and } t > \tau \end{cases}, \tag{8.2}$$

where t is the time of the wave arrival at a distance r, $v_0(r) = Aq^{n/3}r^{-n}$ is empirically determined maximum particle [mass] velocity for an explosive charge with the yield equal q, $\varphi(t)$ is a function of time satisfying the condition $\varphi(0) = \varphi(\tau) = 0$.

We obtain:

$$\varepsilon_n(r_1,t) = \frac{v_0(r,t)}{C}[\varphi(t) - \varphi(0)] + \frac{dv_0(r)}{dr}\int_0^t \varphi(t)dt, \tag{8.3}$$

$$\varepsilon_\varphi(r_1,t) = \frac{u(r,t)}{r}, \tag{8.4}$$

where $u(r,t)$ is the particle displacement in the stress wave:

$$u(r,t) = v_0(r)\int_0^t \varphi(t)dt.$$

Defining the shortest distance between the explosion and the discontinuity [fault] plane *OA* as *a* with the main interest in the residual motion parameters in the stress wave ($t \to \tau$), we obtain using (8.1):

$$\varepsilon_n(r_1,t) = \varepsilon_{n0}(r_1) = \frac{v_0(r_1)}{r_1}\left\{1 + \left(\frac{a}{r_1}\right)^2\left[r_1\frac{dlnv_0(r)}{dr} - 1\right]\right\}\int_0^\tau \varphi(t)dt, \tag{8.5}$$

where

$$r_1 = \left\{a^2 + \left[\arctan\alpha + \frac{L - a\csc a}{\sin(\alpha+\beta)}\right]^2\right\}^{1/2}. \tag{8.6}$$

In this equation we use $\sin\gamma_1 = a/r_1$, the derivative $d\ln v_0/dt$ is calculated at the point *N*, and *OD = L*.

Using relationship (8.5) one can determine the value of normal deformations at the surfaces of structural blocks whose exteriors are arbitrarily oriented in space. For example, Figure 8.14 shows the variation of the quantity ε_{n0} along the sides of a cubic structural block with a side length of 50 m, located at a distance of 75 m from a 1 kt explosion, calculated for $\varphi(t) = \sin(\pi t/\tau)$. The plot shows that the deformations within the spherical wave significantly distort the initial shape of the structural element. We also note that the character of the shape change here corresponds to a restricted rotation of the block. In sections 8.4 and 8.5 we provide the computational scheme and the experimental evidence supporting this conclusion.

According to Figure 8.14, the value and the character of the deformation normal to the surface of the structural element depends on the spatial orientation of the specific side. For example, the normal deformation is positive along the side AB suggesting an extension, while it is negative along the sides AD and BC.

In the first approximation we assume that the angle of each individual fault determines the predominant character of deformations in the zone immediately adjacent to it. To perform the

calculations we use the explosion schematically shown in Figure 8.13 (assuming that $OD = L$ is the distance from the explosion to the free surface along the horizontal direction in the plane perpendicular to the fault plane, DM is the free surface, and β is the slope of the surface).

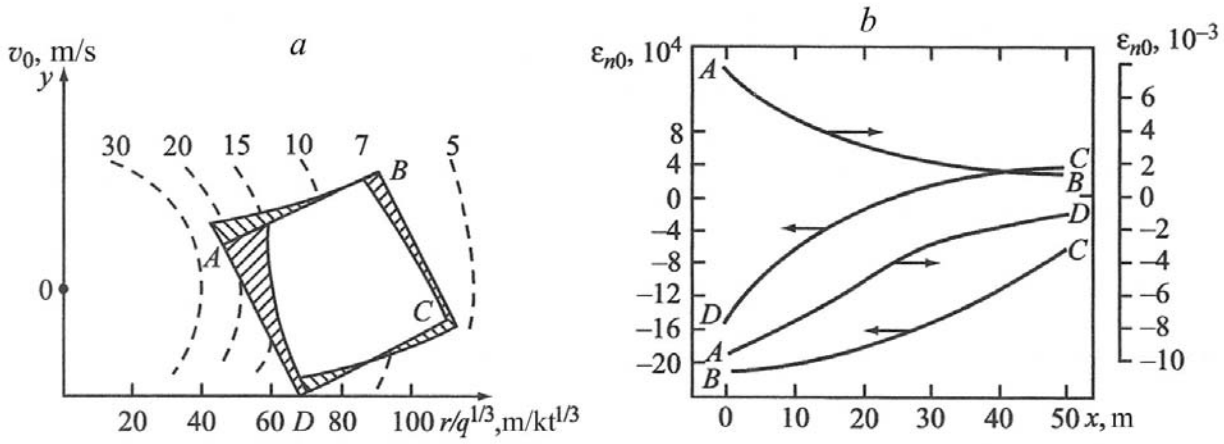

Figure 8.14: (*a*) Position of the block, and (b) the residual strain normal to a surface (side) of the block, due to a 1 kt explosion.

For a specific form of the source time function, namely

$$\varphi(t) = \sin\frac{\pi t}{r},$$

the residual deformation ε_{n0} normal to the fault surface BC at a point located at a distance r from the explosion is given by:

$$\varepsilon_{n0}(r) = \frac{2\tau v_0(r)}{\pi r}\left[1 - (1+n)\left(\frac{a}{r}\right)^2\right]. \quad (8.7)$$

In this case $r_1 \le r \le r_2$, where r_2 is defined using Equation 8.6, and

$$r_1 = \begin{cases} OB = l & for\ l > R_* \\ R_* & for\ l < R_* \end{cases},$$

where R_* is the radius of the region of explosive damage in the medium.

The behavior of a tectonic discontinuity (i.e. a fault) as a whole, loaded by a stress wave, can be characterized in terms of deformation averaged over the fault plane. From a practical point of view, the most important part of the fault is the side BC facing the free surface. The deformation ε_{n*} averaged over the line BC is determined using the expression

$$\varepsilon_{n*} = \int_{r_2}^{r_1} \varepsilon_{n0} dr.$$

The most interesting cases of positive deformation (in which tectonic faults open due to explosions) are presented in Figure 8.15. The figure shows that for each individual value $OB = l = a/\sin\alpha$ the relationship $\varepsilon_{n*}(\alpha)$ is non-monotonic: the maximum value of ε_{n*} is reached for specific values of dip angle of the tectonic fault:

$$\alpha = \alpha_*(l, \beta) \, . \tag{8.8}$$

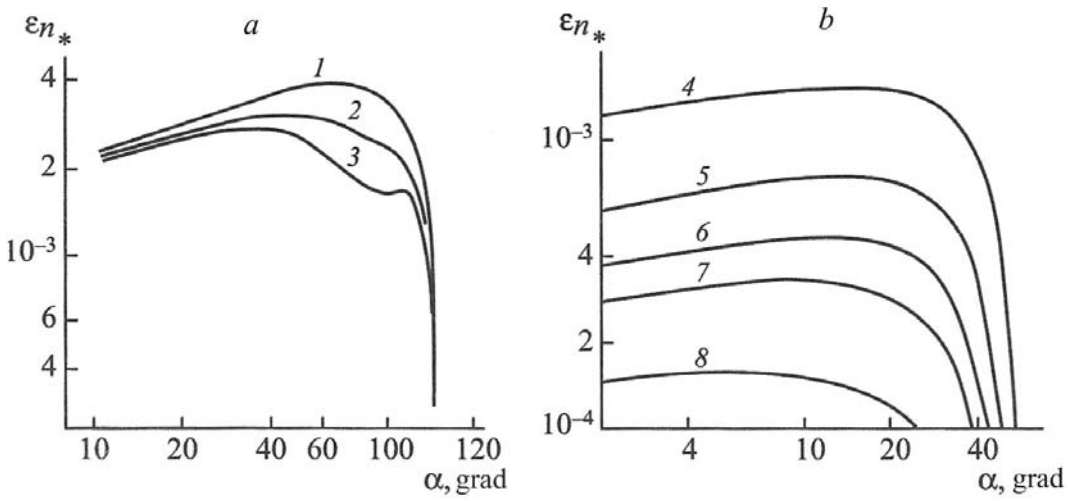

Figure 8.15: Residual tangential strain in the plane of the fault: *a*) for $l < R$, β = 25, q = 1kt; *b*) for $l > R$, β = 25, q = 1kt; lines *1 – 8* correspond to l/L = 0.04, 0.08, 0.1, 0.2, 0.3, 0.4, 0.6 and 0.8.

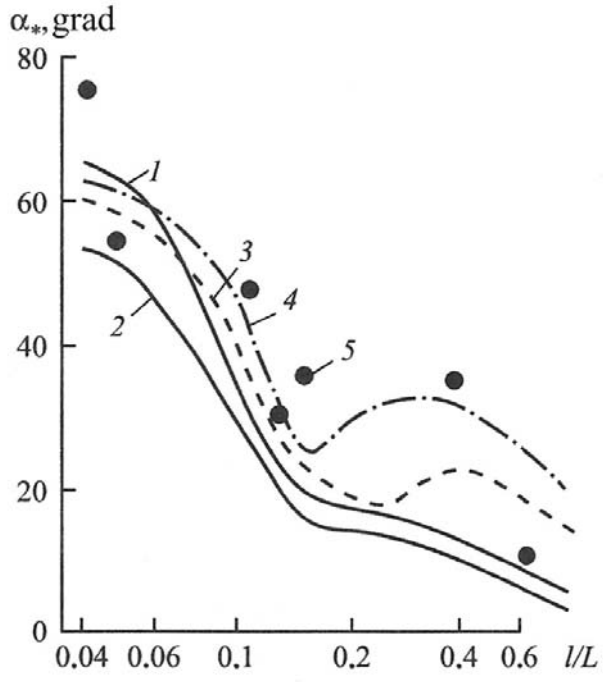

Figure 8.16: Dip angle of the fault with maximum irreversible deformations as a function of the ratio l/L: *1* – β = 25, h = 0; *2* – β = 35, h = 0; *3* – β = 25, h = 50; *4* – β = 25, h = 10; *5* – experimental data.

As an illustration, Figure 8.16 shows the results of computation using Equation 8.8 for ε_{n0} with solid lines for specific explosion conditions. A similar relationship, obtained by taking into account the effect of the free surface on the value of ε_{n0}, is shown for comparison. The effects related to the free surface reflection were accounted for by doubling the value of the velocity component normal to the surface *MD* in the layer of thickness h (Figure 8.13b).

This technique allows us to categorize tectonic faults based on the magnitude of the displacement normal to their surfaces (i.e. opening). Indeed, among all the faults with different orientations and distances from an explosion, it is possible to find the ones with the largest openings using the relationships shown in Figure 8.15. The same value of transverse deformation ε_{n*} can be reached for faults close to the source with smaller values of angle α and for remote faults with large α, indicating a tradeoff between angle and distance. If all other characteristics of the faults with different distances from the explosion are equal, higher deformations are expected at more shallow faults, located closer to the source.

Thus, among the faults crossing a tunnel at similar distances the most problematic (dangerous) are those with greater dip angle. Simpler estimates can be performed for the function $\alpha_*(l)$.

Studies were performed in regions of tectonic faulting subjected to explosive deformations, in order to verify the proposed technique. They involved examining the internal surfaces of rock massifs in order to find the areas (for specific faults) with the largest irreversible deformations (based on the length, opening of the fractures, and magnitude of the shear displacement). In addition, observations of gaseous emissions were performed. The second technique is based on the effect of predominant filtering of gaseous products of nuclear explosions along the most significant (most damaged) faults.

Results of the field observations are presented in Figure 8.16. It is clear that, despite the extreme simplicity of the calculations, the proposed approach produces a practical approximation for predicting the zones of irreversible deformation that are most significant (from the mechanical point of view). This is very important for estimating the stability of specific parts of the rock massif, and of the structures built in those areas. It is also important for estimating breakthrough times of the explosion products for specific experiments.

8.3 Deformations of discontinuous media during an underground explosion.

The presence of tectonic faults in a real geological medium determines the complex character of deformation of the structural blocks (Spivak, 1999 a, b). For instance, Figure 8.17 shows calculated residual deformations along boundaries of the structural elements of the rock massif. The calculations were conducted using the method presented in Section 8.3. Figure 8.17 shows that complex deformation of each structural element may cause disjoint motion of the adjacent blocks, which may violate the spatial continuity of the medium and its deformation.

Below we present the experimental results from a study of block motions during underground explosions at the Semipalatinsk Test Site (Spivak, 1999a; Garnov and Spivak, 2004). The measurements conducted during explosions, which focus on block motions, shed light on both qualitative and quantitative features of the deformation of block-hierarchical structures.

8.3.1. Methods of conducting field measurements. In order to solve practical problems the measurements were designed for determining linear dimensions of the actively deforming blocks, the relative displacements between the blocks, and the most probable places for their

occurrence. The displacements and deformations were divided into the residual displacements inside the blocks and along the boundaries between them, the motion of the blocks as a whole, and the differential displacements— i.e. the motions of adjacent blocks relative to each other. It was expected that anomalous mechanical effects would be observed with higher probability along the medium discontinuities (both faults and fractures). Because of this the following methods were used to conduct the experiments.

Measurements of displacements along the stress wave front were conducted by using velocity sensors of several different types with different frequency ranges. The sensors were installed as close as possible to each other on different sides of the faults and large fractures around the explosion, and at distances on the order of tens of kilometers in order to determine seismic effects of the explosion). Field data provided not only the magnitudes and intensities of the stress, but also the differences in displacements between blocks separated by structural discontinuities (faults). The displacements were calculated by integrating velocity seismograms.

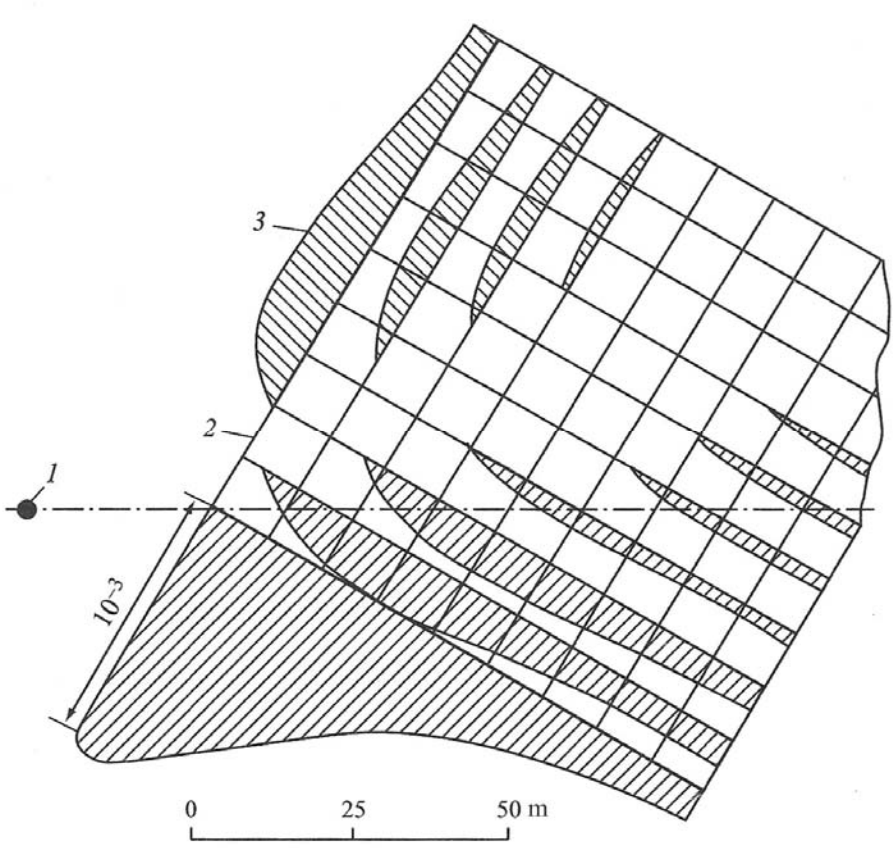

Figure 8.17. Tension deformations along the sides of structural blocks due to a 1 kt explosion (block size is 10 × 10 m): *1* – explosion source [center], *2* – block boundaries, *3* – deformation curves.

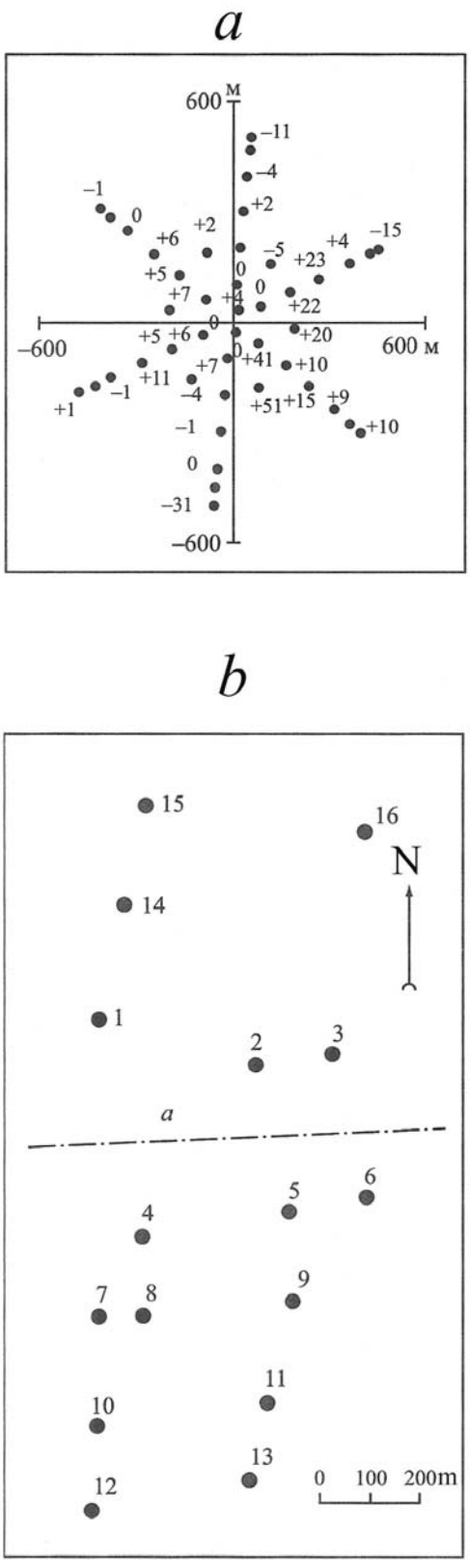

Figure 8.18: Map of the locations of geodetic reference stations at (*a*) area #1, and (*b*) area #2.

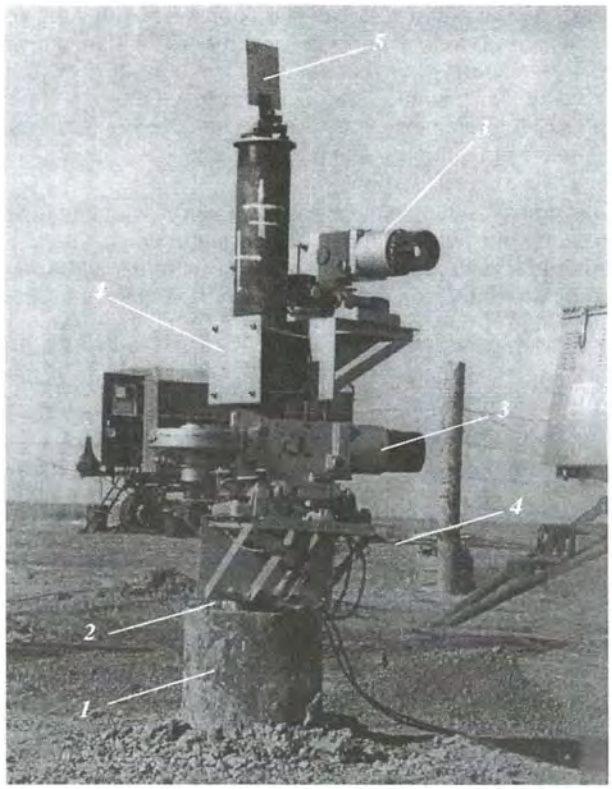

Figure 8.19: Equipment deployed at a deep geodetic reference station: *1* – borehole collar; *2* – metal pipe; *3* – photo-detectors FRD [?]; *4* – plates for the geodetic measurements; *5* – reflector of the quartz geodimeter.

Measurements of rock strains within the blocks were performed using "point" sensors (strainmeters) DDP[6]. These measurements allowed us to estimate the stresses and strains inside blocks with preserved integrity (not broken into pieces), which did not preclude having some other type of deformation. The measured strains were in the range from 10^{-6} to $5 \cdot 10^{-3}$ (non-dimensional units of strain).

Measurements of the relative residual displacements in the rock massifs were performed in the tunnels using wire strainmeters with different base lengths. The strainmeters with bases from 1 to 15 meters were installed on structural discontinuities of different scales, and within individual blocks.

Registration of absolute and relative displacements of geodetic reference stations. The reference stations were installed in underground tunnels (leveling along the tunnel walls), and at the surface. The most detailed studies of block motions were performed at the surface. In this case both linear and angular (rotational) block motions were detected using systems of geodetic reference stations installed in areal groups (arrays). Figure 8.18 a-b shows examples of the placement of sets of deep reference stations for two areas (area #2 is located at the deep Kalba-Chingiz tectonic fault).

Figure 8.19 shows a photograph of a deep geodetic reference station equipped with special optical devices designed for the registration of angular (vertical and horizontal) and linear displacements of distant benchmarks. The reference stations were built using metal pipes placed coaxially inside a larger pipe. The pipes were cemented [to the ground] at depths of 7 – 8 meters. Base plates used for placing the equipment were attached to the pipes. The equipment included the recorders, laser strainmeters using light reflectors, high-quality theodolites, and other geodetic devices.

The distances between the reference stations and their changes caused by explosions were recorded using traditional geodetic measurements (linear measurements), as well as using quartz [light] distance meters [geodimeters? I'd call them "quartz geodimeters] SKD-2 and SKD-8 (the maximum distance is up to 2 km, the accuracy of the distance measurements at a distance of 1 km is 4 mm).

To determine inclination and azimuthal rotation photo-registration equipment was used, including photo-recorders FRD (focus distance – 3.6 m, angular resolution – approximately 1 second of arc) and high-speed cameras RFK-5 (focus distance – 1 m, angular resolution – approximately 3 seconds of arc in rapid—single-shot—mode) working together with the laser geodimeter reference stations.

The residual linear and angular displacements were compared with the results of traditional theodolite surveys.

Measurements of the residual block rotations were conducted in underground tunnels at different distances from the explosion. Recording of the absolute inclination before and after the explosion was conducted using an optical device, specifically named KO-10, with an angular

[6] ДДП (DDP) - Датчик Деформации Привариваемый (literally "Deformation Sensor Welded") – tenso-resistor strain sensors made by Tenzo-M (http://www.tenso-m.ru/tenzodatchiki/specialnogo-naznachenija/239).

resolution of approximately 5 seconds of arc) and electrolytic dip-meters (ЭНЖ – ENZh). We note that because the main feature of the block medium is the ability of each block to move independently, the value of angular deformations should be considered as the most informative parameter for the description of behavior of the block medium.

8.3.2. Localization of deformations along structural discontinuities. The relative linear block motion can be determined by measuring explosion-related changes to the widths (openings) of the structural discontinuities. Figure 8.20 shows the values of the relative displacements between the sides of the tectonic faults resulted from the passage of waves from explosions with different amplitudes. The figure shows the absolute values of the displacements, because explosions could either increase or decrease the distances between adjacent blocks.

It is worthwhile to note that the magnitudes of the linear differential displacements at the block boundaries can significantly exceed the amplitudes of displacement directly associated with the stress waves. This means that the medium displacements in the stress wave are not monotonic: small deformations within the blocks alternated with significantly larger deformations at the block boundaries.

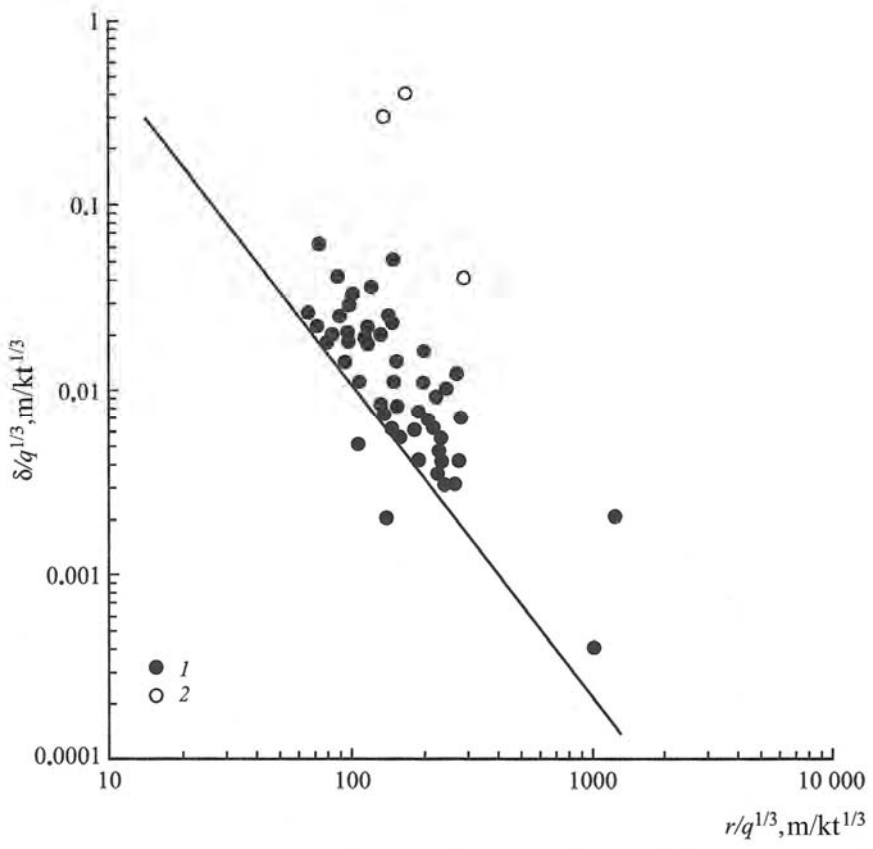

Figure 8.20. Relative displacements of the opposite sides of tectonic faults, caused by underground explosions in tunnels: *1* – measurements; *2* – estimates using the curvature of rails in the tunnels, associated with a high degree of rock deformation.

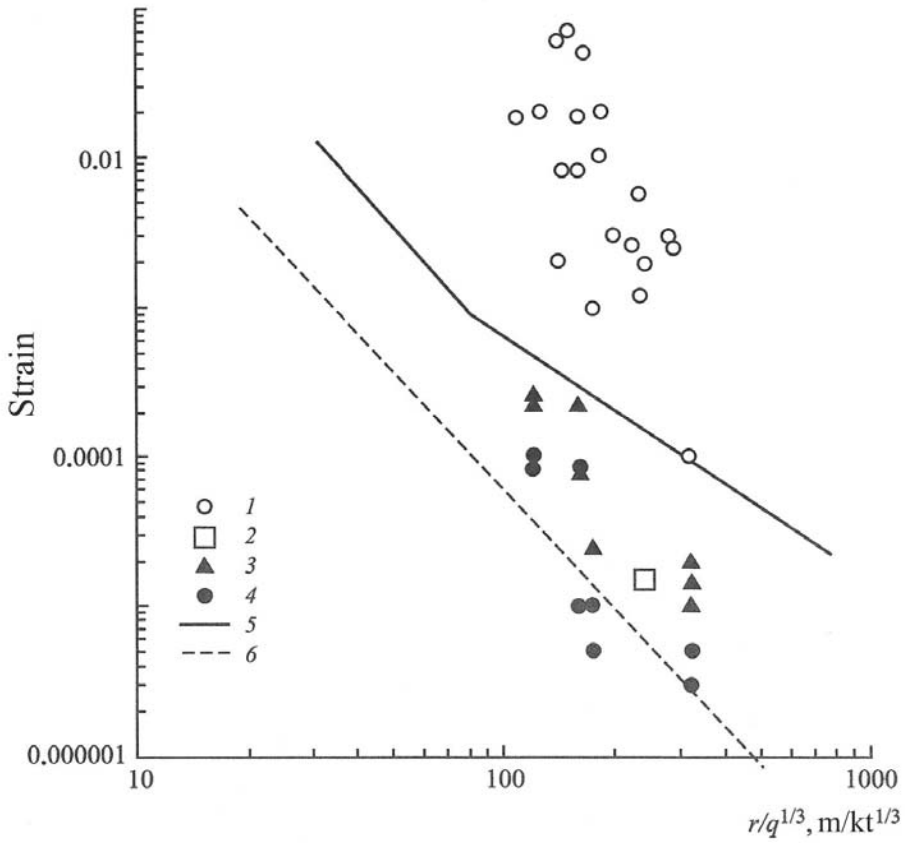

Figure 8.21: Relative strain measurements: *1* — measurements along long bases (6 – 12 m) across tectonic faults; *2 – 4* — measurements within the same block: *2* — zero-base (point measurement), 3 — base with the length of 1 m, *4* — base – 5 mm; *5*, *6* – maximum strain and the residual strain for the compressional wave.

The comparison between strain measurements near discontinuities (faults) and in regions with low fracture content (within the blocks) indicates (Figure 8.21) that strain measurements, using either short or long base strainmeters located in the unbroken parts of the mass, coincided with good accuracy with residual strains calculated from the compressional wave.

The strain amplitudes obtained using long-base measurements from parts of the massif deformed by large fractures, or in areas with faults, significantly exceeded not only the residual deformation, but also the maximum deformations observed in the pressure wave. It follows from Figure 8.21 that differential block motions are significantly higher than predicted for the stress wave. In some cases such displacements can pose a danger to the integrity of underground structures.

8.3.3. Independent angular displacements (rotations) of blocks. Rotational motions of underground blocks were determined by measuring the inclination of the tunnel walls. The measurements of the residual angular deformations for different blocks for explosions of different sizes suggest significant angular deformation due to explosions. As an illustration Figures 8.22 and 8.23 show the residual angular deformations of the tunnel wall for two nuclear

experiments at the Degelen rock massif at the Semipalatinsk Test Site (UNT October 18, 1984 (Tunnel 200) and June 27, 1985 (Tunnel 160)). These measurements are plotted as a function of the distance to the explosion source.

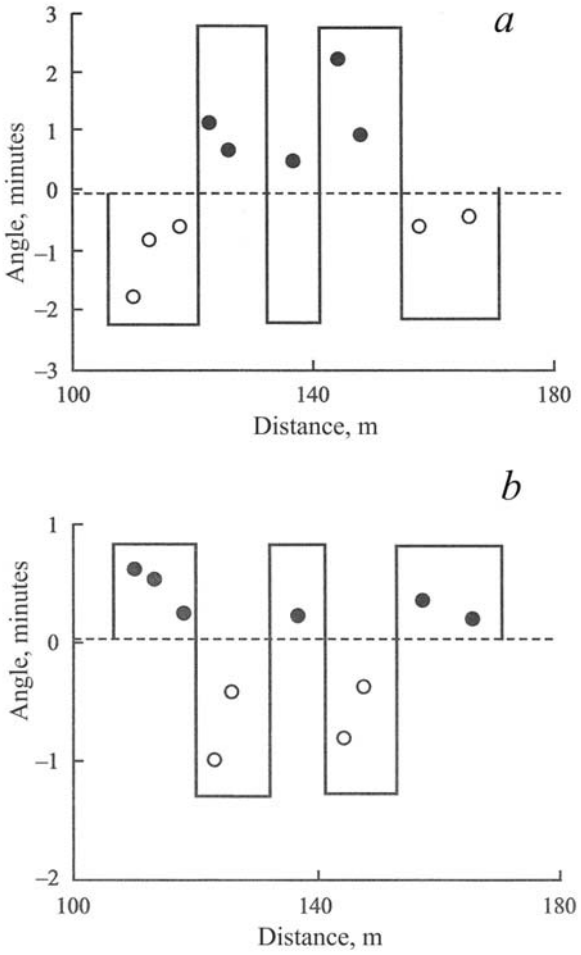

Figure 8.22. Residual inclination of the tunnel wall, (*a*) along and (*b*) across the tunnel axis, for the UNT conducted on October 18, 1984. Open and solid circles correspond to inclinations (rotations) with opposite signs.

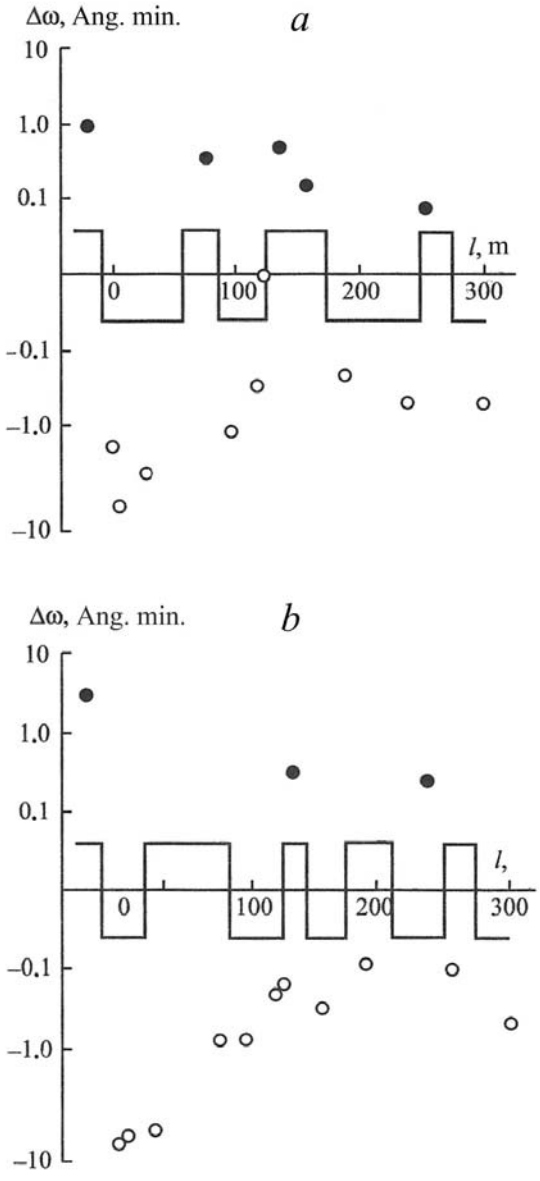

Figure 8.23. Residual inclination of the wall for Tunnel 160, (a) in the plane perpendicular to the tunnel axis and (b) parallel to this axis. Open and solid circles correspond to inclinations (rotations) with opposite signs.

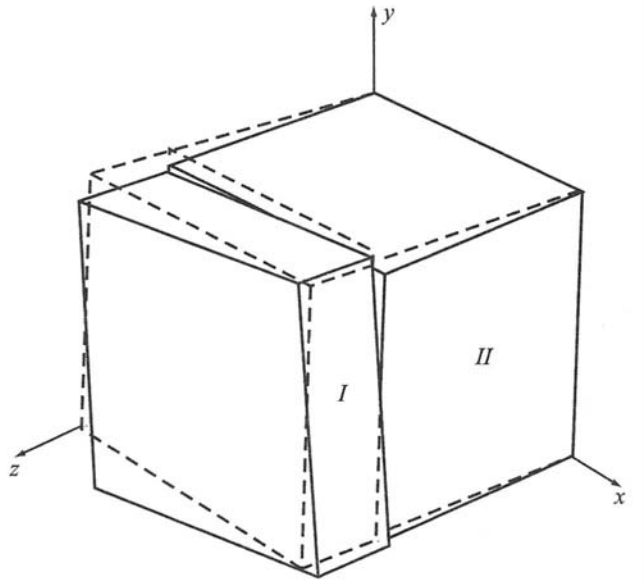

Figure 8.24. Schematic of the rotations of a composite structural block (dashed line shows the initial position of the block). Explanations are given in the text.

It is clear from Figures 8.22 and 8.23 that the explosions caused significant rotations of structural blocks both in the plane perpendicular to the tunnel axis and along the tunnel. We note that the angular changes to the tunnel walls are not monotonic function of the distance to the explosion. Instead, the observations show alternating areas with opposing directions of rotation. This feature can be interpreted as quasi-independent motion of the structural elements of the rock massif. Using the measurements of block rotation about two different axes simultaneously, and assuming that neighboring points with similar angular deformations belong to the same blocks, we can approximately estimate the sizes of the independent blocks. The results of these estimates are shown in Figures 8.22 and 8.23 with solid lines.

We note that coinciding signs of angular changes of the tunnel walls, and block sizes based on using rotations in the same direction are not unique interpretations of the observations. Indeed, it is conceivable that the sizes of structural elements within the same area of the rock massif subjected to rotations in different planes can be different. This can be seen from the schematic shown in Figure 8.24. The structural element composed of the structural blocks I and II is subjected to a rotation in the *yx* plane as a single element. At the same time, blocks I and II can be rotated separately in the plane *xy*, and the deformation can be different not only in magnitude, but also in direction.

8.3.4. Surface observations during explosions conducted in boreholes at the Balapan Testing Area. It is possible to determine the character of motion of blocks forming the rock massif, caused by waves of different amplitudes from explosions, by using the results of observations conducted at several arrays of reference stations. Block structure of the medium results in different inclination of deep reference stations, and different magnitudes of the relative horizontal and vertical displacements, both linear and rotational. We note that the recorded data

are difficult to analyze. Figure 8.25 shows an example of a vector diagram of the inclination (rotation) of geodetic reference stations for just one of the areas.

By making a joint interpretation of all recorded motion characteristics of the geodetic reference stations (taking into the account the gradients and the signs of linear and rotational motions) one can determine the block boundaries, their sizes, and the relative deformation amplitudes in the block ensembles with sufficient accuracy for all practical purposes, for external forces of different magnitudes. Figure 8.25 shows the results of such analysis for the most probable block boundaries with dashed lines. This configuration of blocks and structural discontinuities provides the best agreement between the model and the data obtained from independent measurements.

The analysis of block motions was performed with the addition of long-term observations, in an approach where block boundaries were determined by taking into account the gradient of changes in measured quantities. In this case linear and rotational displacements were practically constant within some blocks, while the displacements in other blocks varied significantly.

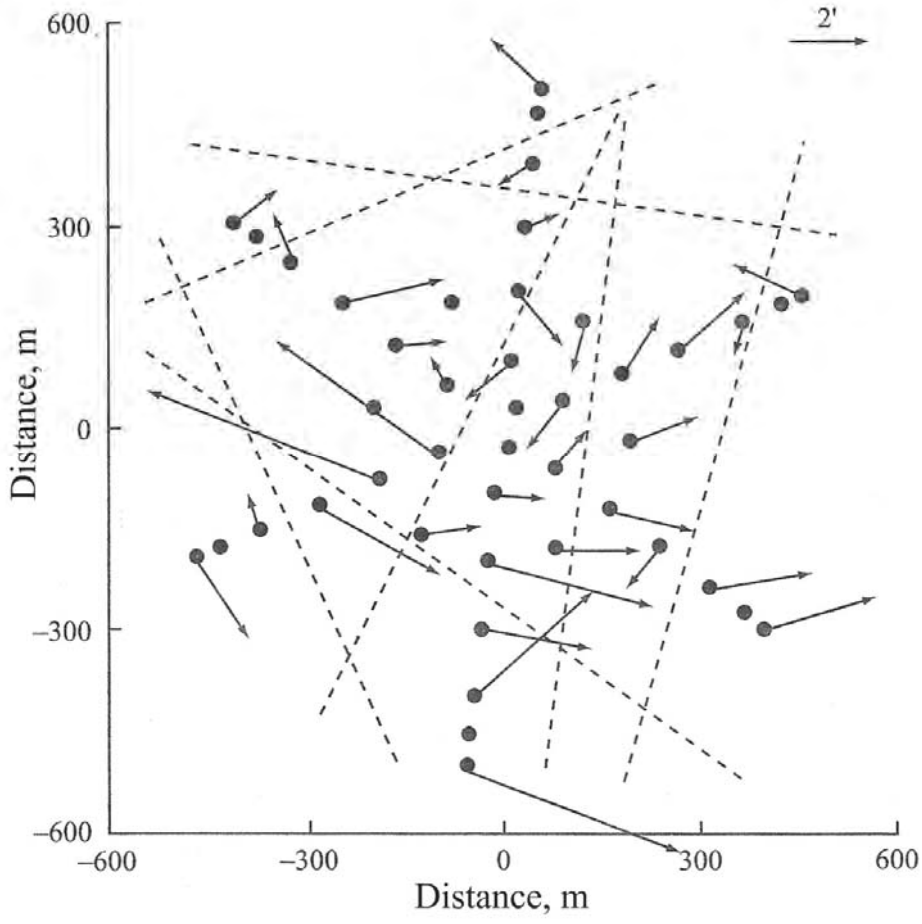

Figure 8.25. Vector diagram of the inclinations of the geodetic reference stations at area #1 for the explosion on October 12, 1980 (circles show locations of the reference stations).

8.3.5. Differential block movements in the zone of influence of a deep-seated tectonic fault. Geodetic studies were performed in the reference areas denoted as #3 and #4, located in the influence zone of the deep Kalba-Chingiz fault, in order to estimate differential linear block movements accurately. This is particularly important for determining the mechanical stability of the rock massifs subjected to external dynamic loading. It was assumed that the structure of this tectonic fault (just like any other regional level fault) is composed of a number of blocks and the fractures separating them, and the blocks have increased ability to move independently. The results of our studies confirmed these assumptions.

The measurements in areas #3 and #4 were conducted for several underground nuclear explosions, providing a generalized picture of explosion effects on a structure composed of blocks.

The locations of the geodetic reference stations for areas #3 and #4 are shown in Figure 8.26 with respect to Kalba-Chingiz tectonic fault and some of the test boreholes of the Balapan Testing Area.

An additional reason to survey areas #3 and #4 was to verify the position of the Kalba-Chingiz tectonic fault. According to the previous studies, the fault was mapped to the north from the test boreholes 1 – 4 (Figure 8.26) along the Chagan River.

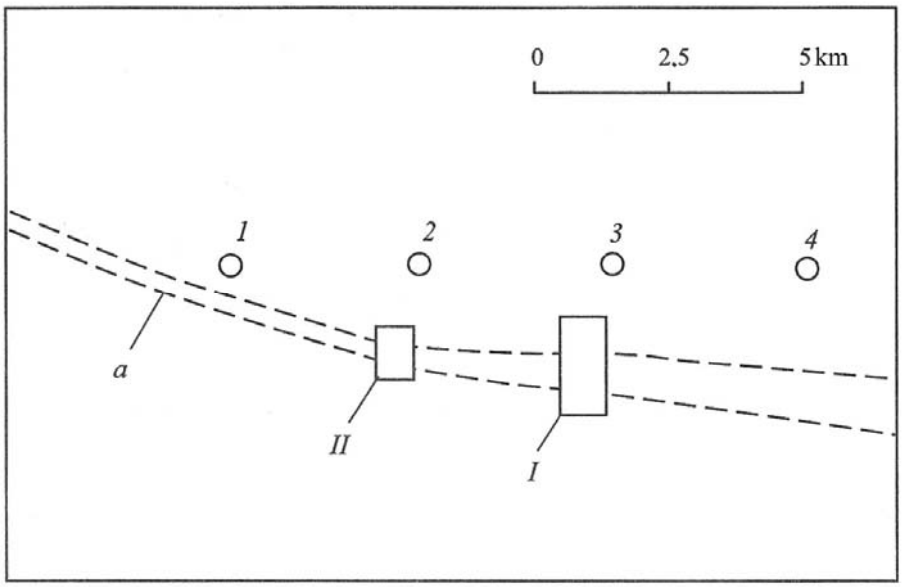

Figure 8.26. Locations of the reference areas #3 (I) and #4 (II) with respect to the deep Kalba-Chingiz Fault (*a*) and the epicenters of the underground nuclear explosions in the following boreholes: 1352 (*1*), 1350 (*2*), 1348 (*3*) and 1346 (*4*).

Brief description of Kalba-Chingiz fault. The Kalba-Chingiz fault separates the Chingiz-Tarbagay mega-anticline (formed during Caledonian tectogenesis, composed of coarse clastic sediments of Middle Cambrian Period) and Zaisan mega-syncline of Hercynian age (represented

by terrigeneous rocks of Early Carboniferous age). Both structures are characterized by intense folding that occurred during different periods, and faulting that determines complex block structure of the rock massif. Based on geological and geophysical observations the width of the zone of influence of the fault is estimated to be around 500 m, increasing somewhat toward the east.

The observations were conducted in the areas measuring 550 × 1450 m (#3) and 700 × 600 m (#4) equipped with the network of geodetic reference stations. Periodically the region was subjected to seismic waves coming from explosions at different azimuths.

The measurements of the absolute distances between the deep geodetic reference stations were performed. Since establishing the line of sight between the stations was not always possible, the distance measurements between stations were performed using *ad hoc* patterns of connectivity. An example of such a pattern for the area #3 is shown in Figure 8.27.

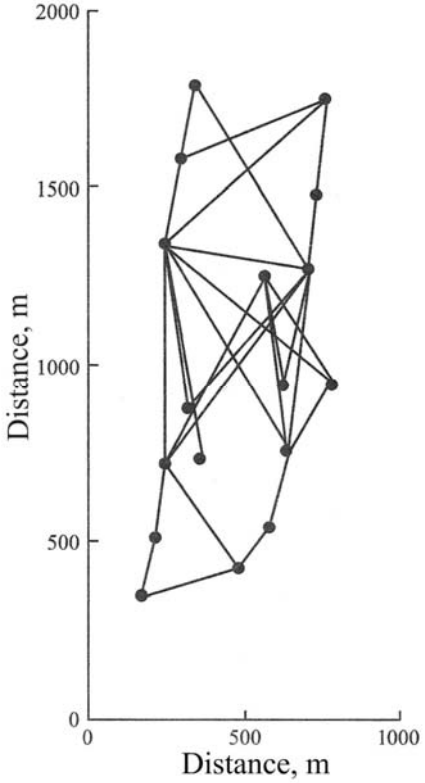

Figure 8.27. Scheme of connectivity used for distance measurements between the geodetic reference stations for area #3.

Both areas were located in a region with exposed bedrock (in the form of a ledge), which allowed us to interpret the measurements as a result of block movement in the zone of stress release due to motion on a tectonic fault.

The initial measurements were conducted for the entire network of geodetic reference stations two days before the explosions. Measurements were repeated on the days following the explosions, and control measurements were conducted 1 – 2 months after the explosions. Stations #10 – 12 from area #3, which were the most remote from both the explosion epicenters and the fault zones, were used as reference stations in order to evaluate the methodology.

Table 8.7. Results of the geodetic measurements [for inter-block spaces?] for the site [area?] #3 after the explosion in BH 1348 (August 02, 1987)

Baseline[7]	*D*, mm	Number of intervals			Average value of *d*, mm
		With $d > 0$	With $d < 0$	Total	
1 – 3	+25	2	1	3	+25
1 – 4	–4	2	2	4	–
1 – 6	–98	–	6	6	–16.5
1 – 7	–46	2	4	6	–23
1 – 8	–37	2	4	6	–18.5
1 – 14	–34	–	2	2	–17
1 – 15	–28	1	3	4	–14
1 – 16	–42	–	3	3	–17
2 – 4	–26	2	3	5	–26
2 – 5	–19	1	2	3	–19
2 – 6	–15	1	2	3	–15
2 – 7	–62	2	5	7	–20.5
2 – 9	–53	1	4	5	–17.5
3 – 4	–12	2	3	5	–12
3 – 5	–21	1	2	3	–21
3 – 6	–26	1	2	3	–26
3 – 7	–116	2	5	7	–23.5
3 – 9	–59	1	4	5	–19.5
5 – 9	–42	–	2	2	–21
2 – 14	+16	2	1	3	+16

All distance measurements between each pair of stations were performed twice, with the light source and reflector exchanged (for the second measurements). The results of the control measurements are in a good agreement with measurements conducted immediately after the explosions, indicating an irreversible character of block movements as a result of a single disturbance. The amplitudes of slow block motions (between the measurements) were within the measurement error.

As an illustration, Tables 8.7 – 8.9 show data for the light distance measurements between the geodetic reference stations (*D*) conducted in area #3 for several nuclear explosions.

The analysis of the results from area #3 and #4 shows a complex pattern of distance changes between the stations. Significant discrepancies were noted between relative displacements between the remote stations and the stations located along the lines between those stations (non-monotonic distance changes).

[7] The numbers for the geodetic points [and lines] in Tables 8.7 – 8.9 refer to the points shown in Figure 8.18 b

Table 8.8. Results of the geodetic measurements [for inter-block spaces?] for the site [area?] #3 after the explosion in BH 1350 (September 14, 1988)

Baseline	*D*, mm	Number of intervals			Average value of *d*, mm
		With $d > 0$	With $d < 0$	Total	
1 – 3	–15	1	2	3	–15
1 – 4	–18	1	3	4	–18
1 – 6	+21	4	2	6	+10.5
1 – 7	–24	2	4	6	–12
1 – 8	–28	2	4	6	–14
1 – 14	+3	1	1	2	0
1 – 15	–19	1	3	4	–9.5
1 – 16	–6	1	2	3	–
2 – 4	–16	2	3	5	–16
2 – 5	–13	1	2	3	–13
2 – 6	–11	1	2	3	–11
2 – 7	+10	4	3	7	+10
2 – 8	+12	4	3	7	+12
2 – 9	–33	1	4	5	–11
2 – 14	–30	–	3	3	–10
3 – 4	+14	–	2	5	+14
3 – 5	–9	3	2	3	–9
3 – 6	–12	1	2	3	–12
3 – 7	+16	1	2	7	+16
3 – 9	–35	4	3	5	–11.5
3 – 15	–10	1	4	3	–10
3 – 16	–21	1	2	4	–
3 – 17	–8	–	4	3	–
5 – 9	–28	1	2	2	–14
7 – 10	–9	–	2	1	–9
7 – 12	–11	–	1	1	–11
8 – 10	–8	–	1	1	–8
9 – 11	+2	–	1	2	0
9 – 13	–27	1	3	3	–9
10 – 12	–2	–	–	0	0
11 – 13	–7	–	1	1	–7

Table 8.9. Results of the geodetic measurements [for inter-block spaces?] for the site [area?] #3 after the explosion in BH 1352 (July 08, 1989)

Baseline* [?]	*D*, mm	Number of intervals			Average value of *d*, mm
		With $d > 0$	With $d < 0$	Total	
1 – 3	–9	1	2	3	–9
1 – 4	+16	3	1	4	+8
1 – 6	–9	1	5	6	–7
1 – 7	+22	4	2	6	+11
1 – 8	+24	4	2	6	+12
1 – 14	–2	1	1	2	–
1 – 15	–28	–	4	4	–7
1 – 16	–7	1	2	3	–7
2 – 4	–31	1	4	5	–10.3
2 – 5	–	–	3	3	–8
2 – 6	–	–	3	3	–7
2 – 7	–30	2	5	7	–10
2 – 8	–18	2	5	7	–6
2 – 9	–24	1	4	5	–8
2 – 14	+9	2	1	3	+9
2 – 16	+3	2	2	4	–
3 – 4	–24	1	4	5	–8
3 – 5	–21	–	3	3	–7
3 – 6	–18	–	3	3	–6
3 – 7	–24	2	5	7	–8
3 – 9	–18	1	4	5	–6
5 – 9	–3	1	1	2	–
7 – 10	+11	1	0	1	+11
7 – 12	+9	1	0	1	+9
8 – 10	+10	1	0	1	+10
9 – 11	–16	–	2	2	–8
9 – 13	–24	–	3	3	–8
10 – 12	+1	–	–	0	–
11 – 13	–6	–	1	1	–6
14 – 15	–12	–	2	2	+6
14 – 16	–5	–	1	1	+5

This can be explained only by an intersection of the line between the stations with several block boundaries, with large distances between intersections.

The apparent disagreements between separate measurements can be explained only by differential motions with opposite signs. In this case a relative displacement between the structural elements (*D*) separated by distance *L* is determined along the fixed direction as a

superposition of the distances (thicknesses of the apertures, gaps) between structural elements, which can be expressed as:

$$D = \sum_{i=1}^{M} a_i d_i,$$

where M is the number of gaps between blocks documented with geodetic stations, d_i are the changes in the thickness of the spaces between blocks, and parameter $a_i = \pm 1$ determines the sign of the thickness change.

Detailed analysis has shown that a good agreement between the measurements in each experiment and the proposed block boundaries is reached if $d_i = d \approx const$. As it turns out, the value of d does not vary significantly as a function of the amplitude of the seismic signal. This agrees with the results of previous studies (Adushkin and Spivak, 1993a; Kocharyan and Spivak, 2004) of cyclical behavior of damage zones of rock masses under repeated dynamical loading.

As an example, Figure 8.28 shows the block structure of the area #3, determined as a result of data analysis from all experiments, which provides the best fit for long-baseline results. We note that the same inter-block spaces may behave differently for different experiments: the gap may increase after some experiments, and decrease after others.

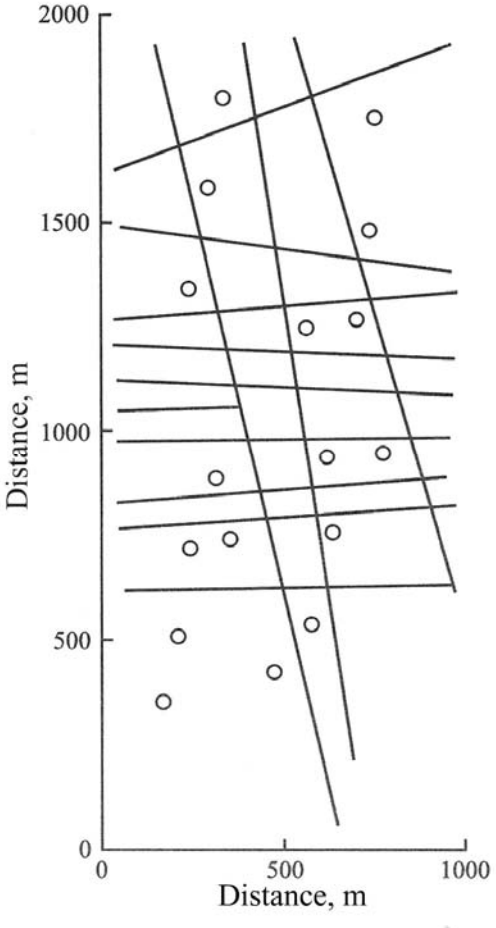

Figure 8.28. Map of the block structure for area #3 based on the light distance measurements using geodimeters (Fig. 8.19).

The sizes of block structures activated by explosions are approximately 180 m for area #3 and from 60 to 200 m for area #4.

The method for determining structural boundaries is easy to understand from Tables 8.7 – 8.9, which list, among other variables, the number of structural discontinuities with either increased or decreased apertures between blocks. Figure 8.28 shows structural discontinuities for area #3.

The following approach was used to identify active boundaries between adjacent blocks. A most probable number of active boundaries between each pair of stations was determined using the following conditions:

1) The boundaries can be represented as straight lines crossing the whole area or parts of the area;
2) The variance of changes of inter-block gaps (apertures) is minimized;
3) The set of block boundaries is the same for all experiments (nuclear tests). This condition does not preclude the possibility that different parts of a block boundary are activated during different experiments;
4) For each experiment each boundary shows displacements of the same sign along the entire boundary;
5) The changes of the average width of the inter-block gaps are determined by the number of boundaries having a common sign of thickness change (it is assumed that the total contribution from an equal number of boundaries with either increase or decrease of the gap width, is equal to zero).

The first condition appears to be very rigid, however it significantly simplifies the process of finding active block boundaries. We note that the map of block boundaries we have derived is not unique. It is probably possible to find more precise boundary positions. However at this stage and taking into consideration the generally non-deterministic nature of geophysical phenomena and processes, the approximation we have achieved appears adequate. This conclusion is supported by the discussion provided below.

One of the important problems related to the motion of specific structures subjected to external dynamic loading is determining the linear dimensions of the active blocks. The analysis of experimental data from explosions conducted in the tunnels and boreholes of the Semipalatinsk Test Site shows that the decrease of the wave amplitude (due to a distance increase) causes an increase of contributions from active blocks. Figure 8.29 shows the relative block sizes moved by the compressional wave as a function of the relative distance from the explosion source. The data are from nuclear explosions conducted in both the USSR and the USA.

The calculation results for the differential displacements for areas #3 and #4 are presented in Tables 8.10 and 8.11 respectively. In addition these tables show the peak particle velocity v_0 due to explosions at the reference stations. The value of v_0 was determined using the empirical relationship between the velocity and the distance to the explosion, obtained for explosions of different sizes conducted at Balapan. Since the complete picture of the differential displacements

is complex and the amplitude of the differential displacements was determined as the average value for the entire area, the amplitude of the explosion effect was characterized by a single value for each explosion, namely the maximum particle velocity at the geometrical center of the area.

This approach allowed us to construct the generalized relationship between differential block displacements and the amplitude of the external explosive loading for all reference sites #1 – 4. The combined data for all reference sites are shown in Figure 8.30. The results indicate significant differential displacements within geological media, produces by large-scale explosions.

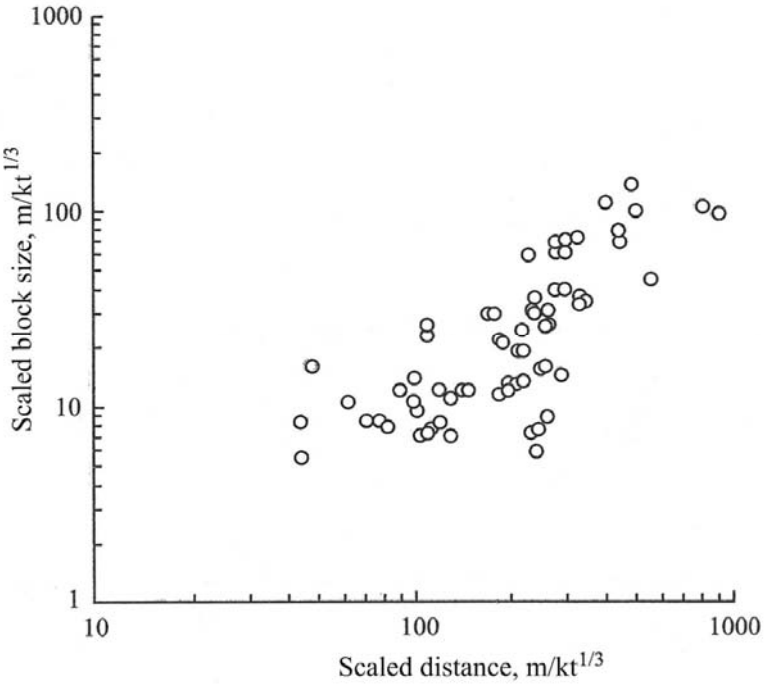

Figure 8.29. Scaled sizes of the blocks activated by a nuclear explosion.

Table 8.10. Results of light distance measurements at Site #3

Test (BH)	Test date	Epicentral distance, m	$r/q^{1/3}$, m/kt$^{1/3}$	v_0, m/s	Absolute differential displacement of the blocks S, mm	$S/q^{1/3}$, mm/kt$^{1/3}$
1348	August 02, 1987	1700	398	0.67	19.5	4.56
1350	September 14, 1988	3500	674	0.28	12	2.31
1346	December 17, 1988	3900	890	0.175	14	3.19
1352	July 08, 1989	5700	1743	0.05	8	2.45
1410	September 02, 1989	~7000	4000	0.014	2	1.07

Table 8.11. Results of light distance measurements at Site #4

Test (BH)	Test date	Epicentral distance, m	$r/q^{1/3}$, m/kt$^{1/3}$	v_0, m/s	Absolute differential displacement of the blocks S, mm	$S/q^{1/3}$, mm/kt$^{1/3}$
1348	August 02, 1987	3700	866	0.18	6.66	1.56
1350	September 14, 1988	1450	279	1.21	19.7	3.8
1346	December 17, 1988	6650	1518	0.072	5	1.14
1352	July 08, 1989	2900	887	0.176	3.5	1.07

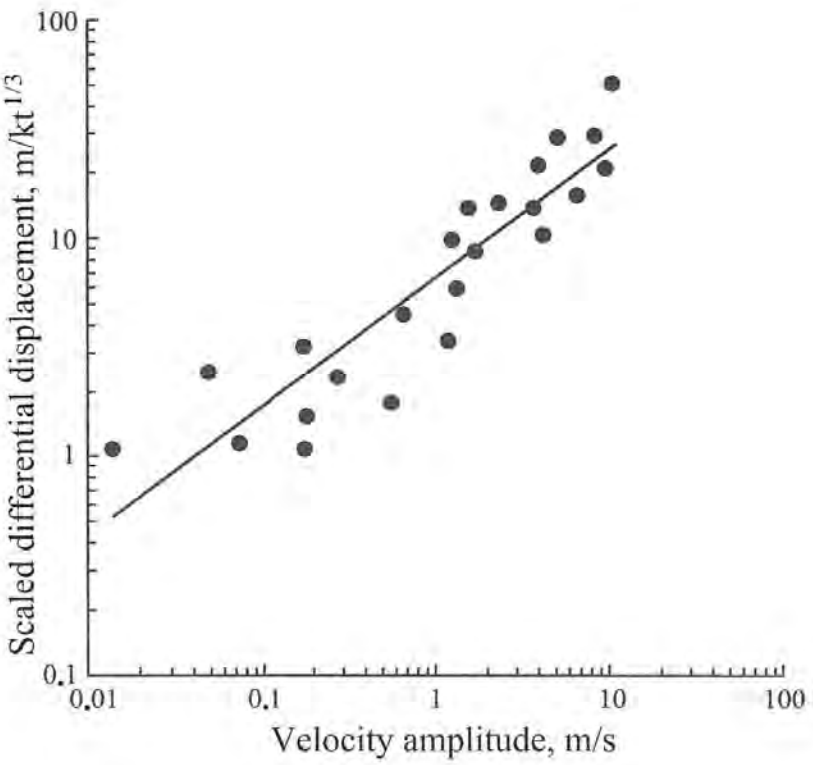

Figure 8.30. Scaled differential displacements of blocks due to seismic waves of different amplitudes generated by explosions.

8.4 Numerical modeling of the block movement

In this section we attempt to describe the process of medium deformation due to large scale explosions (with energies from 0.5 to 100 kt TNT equivalent) based on treatment of the medium as a combination of structural elements. Such elements are represented by independent zones limited by structural discontinuities (faults, fractures), of both natural and anthropogenic origin.

Rock massifs will be described as a combination of structural elements of different scales. The gaps between them are represented by meaning long fractures filled with loose material (compared to rock).

Without loss of generality, we assume that structural elements of different scales mostly behave similarly, during the medium deformation, and at each stage of the deformation the structural elements of a specific scale make their dominant contribution into the macro-deformation of the medium. This specific scale is determined first by the hierarchy of structural levels of the rock massif, and second by the character and the magnitude of the perturbing mechanical force.

From now on we shall describe the process of deformation of structures in the medium, based on the following concept: a point source explosion with yield q is conducted in the medium, which has some microstructure and a network of weak surfaces represented by several systems of oriented fractures and faults. Each system determines a corresponding size of structural elements L_i $(i = 1, 2, 3$ ...). For a small perturbation, when the stresses do not exceed the strength of the material filing the spaces between the blocks, the rock massif behaves as a homogeneous continuum. Its behavior can be described using the equations of continuum mechanics. But macrodeformations of the medium in general are determined by deformation of microstructural elements.

An increase in stress intensity causes heterogeneities of the stress field on a micro-level; so the structurally heterogeneous rock massif has to be described as a non-equilibrium system, which allows for formation of dissipation structures – macroscopic structural elements of the deformation (based on the general representation of the non-equilibrium system behavior (Nikolis and Prigozhin, 1979).

It is most probable that the linear size of a dissipation structure L_* corresponds to one of the sizes of the natural rock block in the massif L_i. In addition, the specific size of the structure L_* is determined by the spatial scale and the magnitude of the medium loading, meaning that it can change in time and space. The formation of dissipation structures can be described as follows. When a certain limiting magnitude of stress is reached, at one or more boundaries filled with softer filler material, there occurs an avalanche-like separation of the continuous medium into structural elements.

The motion of the newly formed macro-structures can be independent from each other, which allows for the possibility of formation of torques and, as a consequence, block rotation. In this case the rock massif can be represented as a Cosserat pseudo-continuum (Morozov, 1984). Features of this continuum will correspond to the displacement (u) and rotation (ω) fields, so that:

$$\vec{\omega} = \frac{1}{2}\nabla \times \vec{u}. \tag{8.9}$$

The deformation process at this stage can be described in terms of moment theory with limited rotation. The most important proposition of this theory is: a relationship (8.9) is fixed, according to which the tensor of generalized deformations coincides with the tensor of classical

deformations, and therefore is symmetrical; the existence of moment stresses determines the asymmetry of the stress tensor (the relationships between the stress and strain tensors are determined using the classical elasticity theory).

The field of macro-displacements in the medium U is determined by restricted rotations of dissipation structures having linear dimensions L_* and can be represented as:

$$\vec{U} = \frac{1}{2} L_*^2 \nabla \times \vec{\omega}. \tag{8.10}$$

The latter relationship reflects the fact that the displacement of material particles during medium deformation occurs along curvilinear trajectories, unlike classical elasticity theory, according to which motions can be represented by a superposition of linear motion and rotation.

We estimate deformation of the structured medium using the above representation for a specific case of explosive loading. Using a point charge as a source of spherically symmetric waves we determine the radial particle velocity in the medium as

$$v(r,t) = v_0(r) \sin\left(\frac{\pi t}{\tau}\right) \text{ for } 0 \le t \le \tau, \quad v = 0 \text{ for } t < 0 \text{ and } t > \tau, \tag{8.11}$$

where $v_0(r)$ and τ are the maximum particle velocity in the stress wave, and the wave duration at the distance r from the source.

Assuming that the deformation process has the predominant direction of the rotation vector, and the rotation itself is irreversible, we obtain for each structural elements (within the limits of each element):

$$\omega = \vec{\omega} = \pm \frac{2 v_0(r) \tau}{\pi L_*} \left(1 - \cos\frac{\pi t}{\tau}\right). \tag{8.12}$$

The rotation direction (the sign before the second additive term) is determined by the direction of the torque acting upon a specific structural element as a result of a sequential transfer of the wave disturbance from one block to another, as well as upon the initial spatial orientation of the structural element. Thus, given the rotations around both axis normal to U (defined in Equation 8.10) are interchangeable (equivalent), we allow for the rotation of the structural elements in different directions.

This motion of the structural elements (under the assumption

$$\frac{\partial \omega_i}{\partial x_k} = const \tag{8.13}$$

along the sides of each element) leads to a change in the effective width of the inter-block gap by the amount

$$\Delta\varepsilon \approx \pm \frac{v_0(r) \tau}{\pi} \left(1 - \cos\frac{\pi t}{\tau}\right), \tag{8.14}$$

where x_k are Cartesian coordinates (k = 1, 2, 3).

The combined displacement of structural elements Δl separated by a distance l along some fixed line $\Psi(x_k)$ is determined by the superposition of changes in the gaps between structural elements along the line.

It can be assumed approximately that for $v_0 = 0$ the residual displacement given by $\Delta l_* = \Delta l\ (t \to \tau)$, as it follows from (8.14), is given by $\Delta l_* = n_0|\Delta\varepsilon|$, where n_0 is the integer coefficient.

We move the coordinate axis x_1 to coincide with the line $\Psi(x_k)$ and denote boundaries between the structural elements as x_j, so that:

$$x_{j+1} = x_j + L_j,\ j = 1, 2, 3\ldots$$

In this case the relationship $\omega(x_j)$ is represented by a piecewise-smooth function defined on the interval (x_j, x_{j+1}). In particular, the value of residual rotational deformations of the structural elements $(t \to \tau)$ along the line $x_2 = x_3 = 0$ can be written as

$$|\Delta\omega(x_1)| = \frac{4v_0(x_j)\tau}{\pi L_j}\left(1 + \frac{x_j - x_1}{L_j}\right) \tag{8.15}$$

for each interval (x_j, x_{j+1}) which from (8.15) has a saw-tooth configuration. The envelope of the maximum rotations can be interpolated via:

$$|\Delta\omega(x_1)| \approx \frac{4v_0(x_j)\tau}{\pi L_*}. \tag{8.16}$$

The relationship (8.15) thus obtained defines the value of the rotation of the side of a specific block, provided its size is known. Conversely, the linear dimensions of blocks can be determined using measurements of angular rotations.

This model can be applied to interpret data on measurements of angle [rotation?]. As an illustration, Figures 8.31 and 8.32 show data-processing results. The data was obtained during the nuclear tests in Tunnel 168 (Figure 8.9) and Tunnel 200M (Figure 8.8). The figure shows that despite its simplicity, the model provides accuracy, adequate for practical purposes, in its description of the rotations of block structures during nuclear explosions.

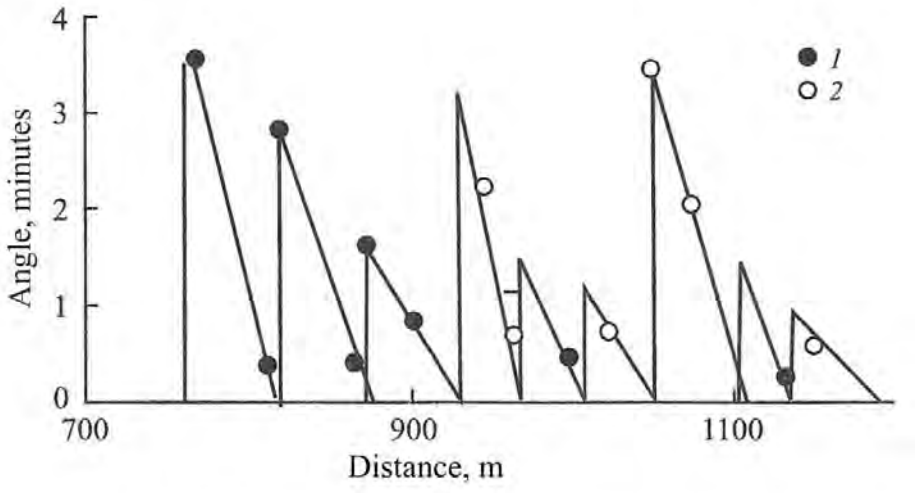

Figure 8.31. Residual inclination measurements for the wall of Tunnel 168 due to an explosion: *1* and *2* show inclinations of different signs.

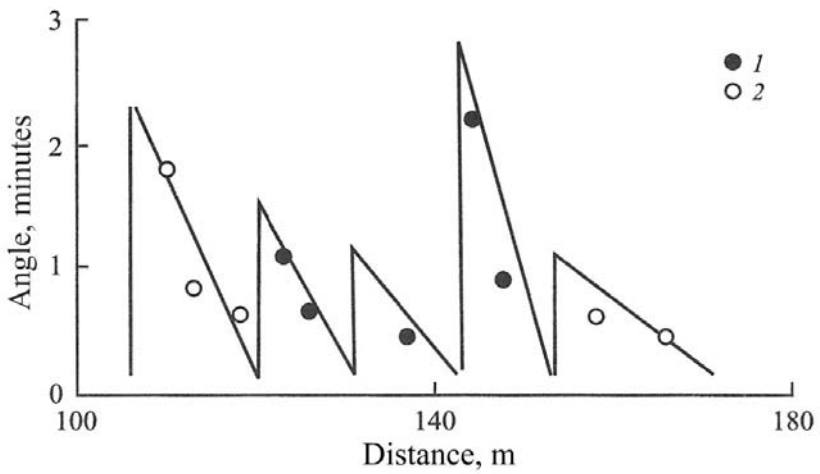

Figure 8.32. Residual inclination measurements for the wall of Tunnel 200M due to an explosion: *1* and *2* show inclinations of different signs.

Comparison between experimental results and estimates using the model we have developed, suggests that the model can be used in principle to estimate absolute displacements of the tunnel walls during underground explosions.

Study of the motion created in the rock mass subjected to dynamic loading indicates that the residual displacements are non-monotonic with increasing distance from the source *r*. This phenomenon can be explained by the existence of the block structure within real rock massifs, as well as by the existence of moments of forces in structured media, which rotate structural elements of different sizes.

The data we have obtained allow us to determine the scale of rheological changes created in the medium under external dynamical loading. This helps to determine the value of plasticity (creep or fluidity), and residual deformations, playing an important role in assessing rock site stability due to anthropogenic influences.

8.5. Sizes of zones of irreversible changes in structurally heterogeneous medium

The size of the zone of irreversible deformations (damage), caused by underground explosions, is of particular interest from the perspective of determining the stability of the medium and of structures built in the area. The character of these changes is determined by physical and mechanical properties of rocks that compose the medium in which the explosion is emplaced.

Studies of structure conducted during multiple nuclear tests show that the scaled damage zone has radius $R_d/q^{1/3}$ of about 35 – 45 m/kt$^{1/3}$, while newly created fractures can be traced up to the scaled distances amounting to $R_f/q^{1/3} \sim 70 - 100$ m/kt$^{1/3}$. This latter distance is generally accepted by the geophysicists as the radius of the damage zone, related to the duration of the far field signal at large distances *r*. Detailed studies conducted during the PNE DNEPR have shown that it is impossible to determine the position of the damage/crush zone inside the fracture zone

using geophysical instrumentation: the parameters of the medium damage (fracture density λ and permeability coefficient k) are smooth functions of the distance r all the way up to $r = R_f$, where they reach their original (undisturbed) values. This suggests that existing ambiguities in estimates of the damage zone require relating the term "damage" to a technological property or quantity that needs to be specifically addressed, for instance the size of the zone that represents a source of shear waves.

For instance, in the case of mining operations the main goal of conducting explosions is to produce fragmented rock mass, so the size of the damage zone coincides with the extent of loose rocks that can be easily removed from the rock formation. Based on the available data (Kornev et al, 1979) the loosening coefficient (or coefficient of dilation) k_m should be in this case no lower than $k_m^* = 1.18$. The scaled radius where the condition $k_m \geq k_m^*$ holds for an underground nuclear explosion is 30 – 35 m/kt$^{1/3}$. For geotechnical rock preparation (for purposes of metal leaching, and coal and shale gasification) the radius of the zone with sufficient damage is determined by the medium permeability and the extent of permeable channels, and is approximately given by 60 m/kt$^{1/3}$. The limiting permeability coefficient in this case is $k \geq 0.1\ Darcy$ and the average particle size is $\langle x \rangle \leq 0.25m$.

The radius of the zone of inelastic deformations produced by explosions is approximately 80 – 100 m/kt$^{1/3}$. This radius determines the size of a seismic explosion source and can also be viewed as the extent of the damage zone.

We note that in all cases mentioned so far, in order to define the extent of the deformation zone, it is sufficient to provide an average value. It is more difficult to estimate the extent of a damage zone in circumstances where even a small probability of irreversible deformations has to be taken into the consideration. One example is determining safe distances from an underground explosion to ensure the safety and structural integrity of buildings and other structures. In these cases it is sometimes necessary to estimate the maximum possible distances where the irreversible deformations are possible, including anomalously-large ground displacements, opening of tectonic faults, and fractures, etc.

Two questions arise in this respect: whether the rock damage zone has a spatial symmetry, and the possibility of significant irreversible effects (with an influence on structural stability) due to underground explosions, at distances up to a certain value of R_{**}, which exceed the traditionally accepted radius of the damage zone (~100 m/kt$^{1/3}$).

Regarding the first question, it is well known that the extent of the zone of intense fracturing is determined by the angle between the stress wave direction and the directions of the pre-existing fracturing or the boundaries between different rocks. The fractures created by explosions develop predominately in the direction of the ambient fracturing.

Regarding the range of the explosion-related deformations, a significant volume of experimental data has been collected to date (including the material presented in this book) suggesting that irreversible deformations exist at distances significantly exceeding 100 m/kt$^{1/3}$. The magnitude of such irreversible effects can in some cases be very significant. These effects of underground explosions include opening of tensile fractures (with width up to 10 mm),

anomalously large (up to 10 mm) local displacements, and angular deformations of the rails, as well as rock falls of significant volume, in underground tunnels.

We also note significant changes of hydrological conditions at large distances from explosions (see Chapter 5). Another important feature included in the range of explosion effects is related to the fact that during repeated explosions within the same area, local effects arise at smaller stresses compared to those associated with initial explosions. For example, during repeated explosion in diabase porphyrites (Tunnel 160), rock falls took place in a tunnel at a distance of 750 m/kt$^{1/3}$, while during the first explosion of the same yield, rock falls were observed only up to distances of 470 m/kt$^{1/3}$. During other repeat explosions, significant deformation to the rails at the tunnel entrance was observed.

One of the most probable causes for the amplification of mechanical effects of explosions at greater distances during repeat explosions, is accumulation of residual stresses or small strains from previous explosions, in areas of rock weakness. In this case repeat explosions can cause significant residual displacements even in areas where such displacements were not predicted (based on the prediction of seismic amplitudes). This feature of repeat explosions significantly complicates the stability analysis of structures and rock massifs due to intense dynamic loading.

The non-equilibrium state following underground explosions, expressed by the phenomena of aftershock zones, is observed in volumes significantly larger than the damage zone. Such a lack of equilibrium has been observed during for large underground nuclear explosions including BENHAM (Nevada, USA), MILROW and CANNIKIN (Amchitka, USA), as well as during some underground nuclear explosions at the Semipalatinsk Test Site, where aftershock zones were interpreted as zones of local explosion effects (Spivak, 1993; Adushkin and Spivak, 1996).

Recording and detection of aftershocks for explosions of different size allow us to estimate the resulting zone size R_{**} of local irreversible deformations, and the velocity amplitude v_{**} at these distances:

$$\frac{R_{**}}{q^{1/3}} = 650 - 1400 \text{ m/kt}^{1/3},\ v_{**} = 0.05 - 0.15 \text{ m/s}.$$

Tectonic deformations of the rock massif can lead to a significant increase of the scale of local irreversible deformations from explosions. Thus, during MILROW (USA), significant residual deformations were detected along pre-existing fault zones. The displacements observed at the surface along fault scarps reached 1 – 1.2 m in the vertical direction and 0.15 m horizontally. The lengths of the reactivated faults were between 0.3 and 8 km. Similar displacements along tectonic faults were observed after BENHAM (USA).

Numerous observations conducted during large-scale underground explosions allow us to determine the characteristic size of near-surface spall zones. In particular, for explosions with scaled depths of burial in the range $W/q^{1/3} = 80 - 120$ m/kt$^{1/3}$ the spall along pre-existing fractures reaches on average 800 – 900 m/kt$^{1/3}$. The maximum particle velocities at these distances are 0.15 – 0.2 m/s, which is also a limiting value for observable mechanical effects of the explosions.

The occurrence of local irreversible deformations in the medium at large distances from the source is determined by the block structure of rock massifs. In this case the average spatial deformation has contributions from block deformation and from the deformation of filler material between the blocks. The deformation of block structure takes place along block boundaries and in weak zones of the blocks, so irreversible deformations are localized in the vicinity of block boundaries.

Depending on specifics of the hierarchical structure and on the strength of inter-block connections, localized damage may occur at distances up to 10^3 m/kt$^{1/3}$ (Sadovskii et al, 1989). The documented scales of structural heterogeneities suggest that there no rock masses exist in nature that do not have hierarchical structure. For example, a rock mass without tectonic faults still has zones of weakness at lower hierarchical levels. It is also natural that the spatial scale of irreversible local deformations is consistent with the hierarchical scale of the structure itself.

In any case the prediction of possible deformations in a rock massif as a result of an underground explosion has to take into account the possibility of localized damage in zone up to a radius of 10^3 m/kt$^{1/3}$.

We estimate the radius of localized irreversible deformations R_{**} via the following steps. We represent the rock massif as a combination of elements having a characteristic linear dimension L. As before, structural elements are the individual blocks making up the rock massif, elements which can move in space more or less independently. We assume that the explosion does not produce irreversible effects if the strain caused by the explosion does not exceed some critical value ε_*. Maximum deformations in the block medium are reached along surfaces of weaknesses, therefore the measure of critical stress can be taken as $\varepsilon = u_0 L$, where u_0 is the relative displacement between sides of the adjacent structural elements (across the gap between the blocks).

Writing the field of macro-displacement in the medium using Equation 8.10 and using the expression for the particle velocity according 8.11, also taking into account (8.12) and $u_0 \approx 0.5\omega L$ for $t \to \tau$ we obtain:

$$\frac{R_{**}}{q^{1/3}} \cong \left(\frac{2AB}{\pi\varepsilon_* CL}\right)^{1/(n-m)} q^{1/3(n-m)}.$$

To obtain the numerical value (for the radius of irreversible deformations) we need to fix the value of ε_*. If we consider a real rock massif as a long-lived non-stationary system, we can choose the minimal value of ε_* as an ambient strain due to background crustal deformations. Numerous measurements of tidal and tectonic motions suggest that ε_* is approximately $(1 – 2) \cdot 10^{-5}$. We note that rock damage occurs for strains of 10^{-4}. Using an explosion with q = 1 kt in a medium with the block size of L ~ 100 m we obtain

$$R_{**} = 1000 - 1400 \text{ m}, \; v_{**} = 0.1 \text{ m/s}.$$

Some possible causes of the irreversible deformations along tectonic faults and inter-block spaces include: damage to the inter-block contacts or the filling material during the explosion; weak cohesion between the adjacent blocks (low friction coefficient); changes in the water

saturation along faults and large fractures at the time of the explosion; and the presence of tectonic stresses. In practice, damage to the filling material is the major cause of these deformations.

In this case the estimated value of R_{**} can be used to determine strength properties of the material filling inter-block spaces (or the rock of higher degree of fracturing, if the zones of weaknesses are represented by large tectonic faults). Indeed, the size of the damage zone is determined by material strength. It is easy to imagine that the blast wave, whose amplitude decay with distance is determined by rock characteristics, damages weak inter-block filling material at greater distances than damage is generated to the rock itself. By rearranging Equation 1.5 we obtain (Rodionov et al, 1971):

$$r_c \approx 0.61 \frac{q^{1/3}}{(\rho C^2 \sigma_*)^{1/9}},$$

Using Equation 1.18 the radius of the damage zone is given by (Rodionov et al, 1971):

$$R_d \approx r_c \left(\frac{\rho C^2}{4\sigma_*}\right)^{1/3}.$$

Assuming that the damage to the filler material is the only reason for localized irreversible damage at large distances, and substituting R_{**} instead of R_d into the previous expression we find that the strength of the inter-block filling material is

$$\sigma_{1*} \sim 0.01\sigma_*.$$

In these relationships r_c and R_d are the radius of the explosive cavity and the damage zone respectively, ρ and C are the density and the velocity of the undamaged rock, and σ_* is the medium compressive strength. The estimate of the value of σ_{1*} appears to be reasonable.

Everything discussed so far suggests that our knowledge of explosion effects on real rock massifs requires further development, especially the study of localized deformations. The radius of this zone is approximately 1000 m/kt$^{1/}$ depending on the specific characteristics of the massif. The irreversible localized deformations in the medium occur if particle velocities in the seismic wave exceed 0.1 – 0.15 m/s. The last condition allows us to delineate zones of localized deformation using kinematic parameters of the blast wave.

Table 8.12 shows some characteristics of the zones of irreversible deformation due to explosions, including velocity amplitudes on the outer boundaries of each zone (v_1) and the average volumetric energy density (E) for each zone

$$E = 3E/4\pi R^3,$$

where R is the radius of the corresponding zone.

We note that the volumetric energy density from explosions in the area of localized irreversible deformation (100 J/m^3) is similar to the density of seismic energy in earthquake sources (Sadovskii et al, 1983), which indicates similarities between processes of the seismic wave generation for earthquakes and explosions.

Table 8.12. Sizes of the zones of irreversible deformation of the medium during explosions

Zone	Parameter		
	R, m/kt$^{1/3}$	v, m/s	E, J/m^3
Cavity	7 – 12	200 – 500	10^9
[Damage] zones			
Crush zone	30 – 40	20 – 50	10^7
Fracture zone	80 – 120	2 – 5	10^5
Local irreversible deformations	800 – 1100	0.1 – 0.15	10^2

The existence of regions of localized inelastic deformation and the problems they pose for the stability of rock massifs and structures located in those rock masses, require further study related to the effects of large scale explosions on complex structures. This requires development of special methods and techniques for the diagnostics of the rock masses, in order to determine their initial and final state related to the geological structure, the heterogeneities of its physical properties, and the state of stress of the rock massif.

(THIS PAGE INTENTIONALLY LEFT BLANK)

Chapter 9.

Transport of radioactive gas from underground explosions

Conditions for carrying out underground nuclear tests, particularly with reference to the depth of burial, should satisfy the following requirements:

- The cavity gas, which contains primary explosion products, should not vent into the atmosphere;
- There should be safe operating conditions in the region of the nuclear testing;
- The requirements of the Limited Test Ban Treaty of 1963 should be observed, prohibiting radioactive debris outside national territorial borders[1].

According to a definition of "radiation containment", the concentration of secondary radioactive aerosols (fine particles) forming in the atmosphere should be limited and should not exceed global background values outside of the national territory[2]. Thus one of the criteria for choosing the depth of burial of nuclear charges is to control the resulting concentration of secondary aerosols (explosion by-products) in the atmosphere, in view of the specific yield of the explosion, the rock type, and the test site location (e.g. Adushkin and Spivak, 2000).

The problem of evaluating the pressurized transport of gas from the explosive cavity through damaged rock needs to be solved (in Cartesian and spherical coordinates), in order to determine gas release time at the surface as a function of charge depth and other parameters (e.g. Adushkin and Spivak, 1983). A solution in Cartesian coordinates was used to determine the pressurized flow of cavity gas through partially deformed (damaged) elements of the stemming structure, and deformation of its contacts with the rock massif, for tunnel and borehole explosions. A method for predicting the time of breakthrough[3] of radioactive gas, and its intensity and duration of gas escape through damaged rocks, was developed using a solution in spherical coordinate. This method also enables the determination of appropriate depths of burial, depending on rock gas content, strength and elastic properties, as well as the explosion yield. Particular attention was paid to determine the effects of geology and tectonic deformations of the rock massif on gas transport processes.

9.1. Quantification of gas transport through damaged rock

Quantification of pressurized gas flow through broken (fractured) rock is based on a model of non-stationary spherically-symmetrical transport (Adushkin and Kaazik, 1976; Adushkin and

[1] This chapter was written to describe the era of active underground nuclear testing in the USSR, prior to the 1990s.

[2] It appears there is disagreement on what, exactly, is banned; and specifically whether radioxenons are banned from crossing borders.

[3] Breakthrough times are the times when the gas first appears at the surface

Spivak, 1983). Since fully-contained (camouflet) explosions are conducted at significant depth and mainly in low-permeability rocks, we assume that the process of gas transport starts from the moment when the cavity reaches its maximum size. At that time the rock damage is finished, and the porosity and permeability of the medium do not change. If the radius of the damage (deformation) zone exceeds the cavity radius by more than an order of magnitude, a spherically symmetrical approximation of the transport processes can be used. Obviously the spall zone will add complexity to the gas transport processes at later stages, however the spreading (outward moving character) of the gas transport will be preserved.

In this problem, formulation of the non-stationary spherically symmetric gas flow can be described using the principle of mass conservation:

$$m\frac{\partial \rho}{\partial t} + div(\rho v) = 0 \tag{9.1}$$

as well as the filtration equation 5.3. In these equations, m is medium porosity, ρ is the density of gas, and v is gas velocity.

The equation of state for the gas is usually written as a power law with an exponent n:

$$\rho = AP^n, \tag{9.2}$$

where P is the gas pressure.

Neglecting heat exchange between the gas and the rock medium, and assuming that the mass of gas with a low condensation temperature does not change during transport, we write the condition on the cavity boundary in the form:

$$\frac{\partial \rho}{\partial t} = -(\rho v)\frac{S}{V}, \tag{9.3}$$

where S and V are the surface and the volume of the cavity respectively.

At the initial moment of time the pressure distribution is given by

$$P(r,0) = \begin{cases} P_* & \text{for } r = r_c \\ P_a & \text{for } r > r_c \end{cases}, \tag{9.4}$$

where P_* is the partial pressure of non-condensable gas in the cavity, and P_a is the initial air pressure in fractures and pores of the broken rocks.

By combining Equations 9.1 and 9.2 and eliminating ρ and v we obtain a single kinetic partial differential equation of second order with respect to r:

$$\frac{\partial P^n}{\partial t} = \frac{k_1}{m\mu}\left[\frac{d}{dr}\left(P^n\frac{dP}{dr}\right)\frac{1}{\Phi} + \frac{\mu^2 k_2}{r k_1^2 A\delta}(\Phi - 1)\right], \tag{9.5}$$

with a boundary condition for $r = r_c$:

$$\frac{\partial P^n}{\partial t} = \frac{S}{V}\frac{\mu k_2}{2Ak_1\delta}(\Phi_1 - 1), \tag{9.6}$$

where $\delta = -sgn\, v = sgn \frac{\partial P}{\partial r}$; $\Phi(P) = \sqrt{1 + \frac{4k_1^2 A\delta}{\mu^2 k_2} P^n \frac{dP}{dr}}$

$$\Phi_1 = \Phi(P) \text{ for } r = r_c.$$

In this equation, k_1 and k_2 are the first and the second permeability coefficients respectively, and μ is the gas viscosity.

It follows from 9.5 and 9.6 that the transport processes of the explosion gas products can be described by a set of non-dimensional variables, defined as

$$x = \frac{r}{r_c},\ \bar{P} = \frac{P}{P_*},\ \bar{P}_a = \frac{P_a}{P_*},\ m,$$

$$\alpha = \frac{Ak_1^2 P_*^{n+1}}{\mu^2 k_2 r_c},\ \tau = \frac{k_1 P_* t}{m\mu r_c^2}. \tag{9.7}$$

We write Equation 9.5 using non-dimensional variables from Equation 9.7:

$$\frac{\partial \bar{P}^n}{\partial \tau} = \frac{1}{\Phi}\frac{d}{dx}\left(\bar{P}^n \frac{d\bar{P}}{dx}\right) + \frac{4\bar{P}^n}{x(\Phi+1)}\frac{d\bar{P}}{dx}, \tag{9.8}$$

$$\Phi = \sqrt{1 + 4\alpha P^n \left|\frac{d\bar{P}}{dx}\right|}$$

Equation 9.8 can be numerically integrated using the boundary conditions

$$x = 1:\ \frac{\partial \bar{P}^n}{\partial \tau} = \frac{6m}{\Phi_1 + 1}\bar{P}^n \frac{d\bar{P}}{dx},$$

and initial conditions

$$\tau = 0: \bar{P}(x) = \begin{cases} 1 & \text{for } x = 1 \\ \bar{P}_a & \text{for } x > 1 \end{cases}.$$

The integration yields gas pressure and the transport velocity through the damaged rock, as a function of time and distance from the explosion source. Here we present the calculation results for a broad range of non-dimensional parameters ($10^{-3} \le \bar{P}_a \le 10^{-1}$, $10^{-2} \le \alpha \le 10^2$, $0.01 \le m \le 0.45$) for n = 1 (isothermal process). The results show the effects of the computational parameters on gas flow in a permeable medium. In order to choose the main parameters of the problem we used empirical data for the cavity size, the pressure of the non-condensable gas, the porosity and permeability of the damaged rock massif, as well as for the gas properties such as chemical composition, molecular weight, and viscosity.

Typical functions for the gas pressure in time and space are shown in Figure 9.1. The parameters used for these calculations ($\bar{P}_a = 10^{-2}$, $\alpha = 1$, $m = 0.01$) correspond to conditions created by a nuclear explosion in hard rock with high gas content ($\eta = 0.3$ to 0.4). The line for

x=1 shows the pressure change on the cavity wall, which decreases by approximately a factor of 2 when the front of flowing gas reaches a distance of ~8r_c.

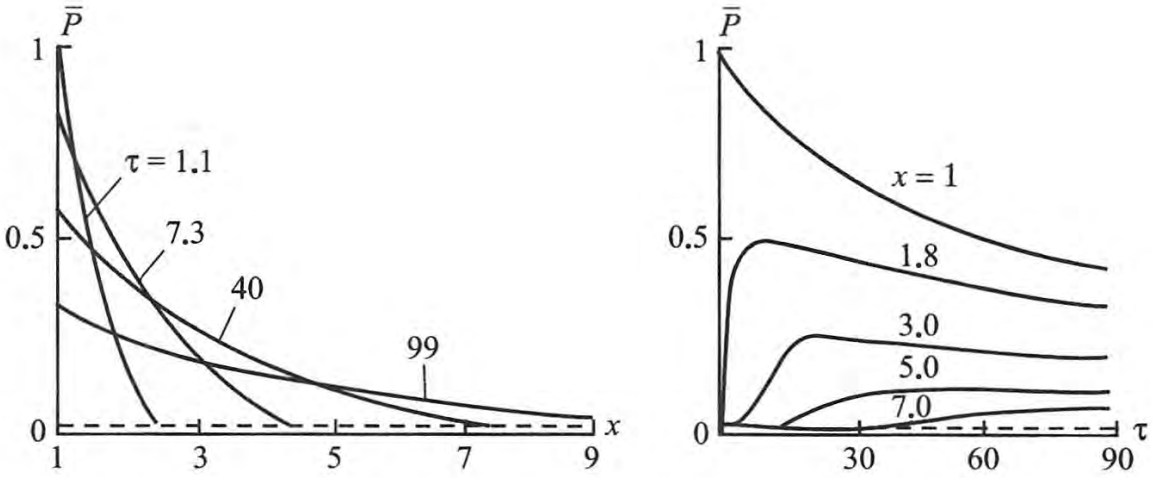

Figure 9.1: Gas pressure as a function of a) distance, and b) time, for $P_* = 10$ MPa and m=0.01. Scaled time τ and distance x are plotted along the axes

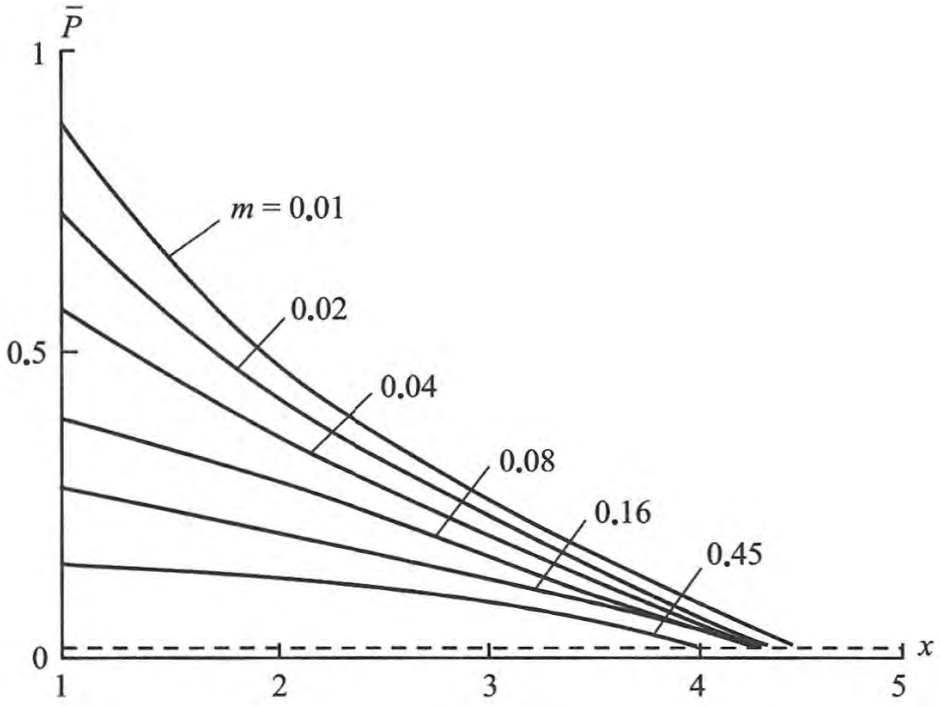

Figure 9.2: The effect of porosity on the pressure of moving gas for τ =10 and $P_* = 10$ MPa. A number shown near each curve) gives the porosity value.

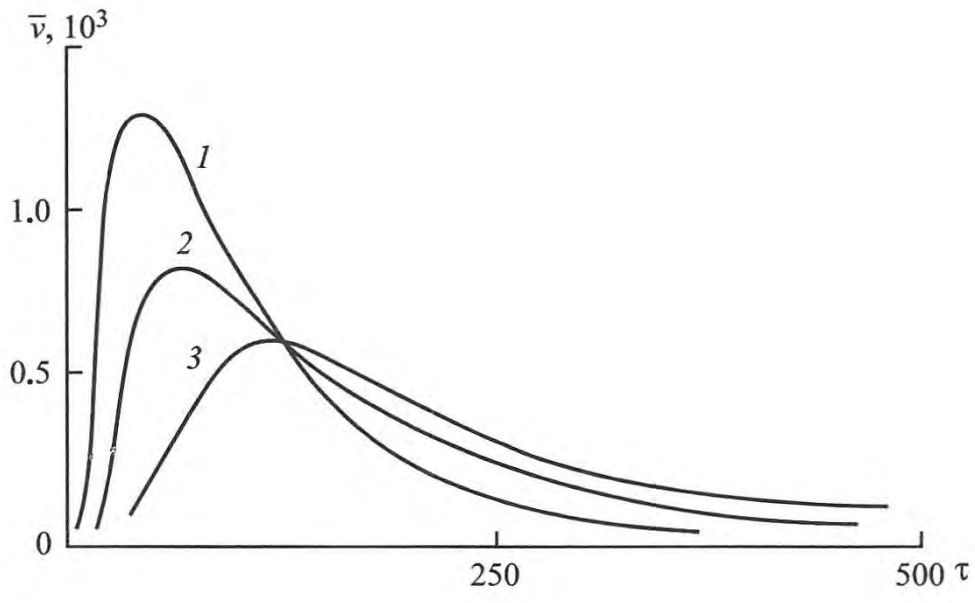

Figure 9.3: Effect of initial pressure on gas flux (Darcy velocity), for $m = 0.04$ at a scaled distance of $x = 7.5$. Values of the scaled (or normalized) pressure $\bar{P}$ are: *1* – 0.1; *2* – 0.04; *3* – 0.01.

Porosity has a significant effect on pressure distribution in the medium (Figure 9.2). For values of porosity $m < 0.04$ the sign of the expression d^2P/dx^2 is always positive. This determines the character of the non-dimensional flow velocity through a porous medium, and we use

$$\bar{u} = \frac{\mu r_c}{k_1 P_*} u \,, \tag{9.9}$$

where *u* is the actual velocity of gas flow through permeable channels.

For $m < 0.04$ the velocity of the gas flow decreases monotonically with distance, while for $m \geq 0.04$ the velocity profile has a maximum, which gets further away from the cavity as the time progresses. This change in velocity of the gas flow is explained by the rapid pressure decrease in the cavity.

The value of the gas flux[4] is given by

$$\bar{v} = \frac{\mu m r_c}{k_1 P_*} v \,, \tag{9.10}$$

which represents the average velocity of gas movement through a porous network, and is related to the total cross-section of the flow $\bar{v} = m\bar{u}$. Figure 9.3 shows an example of flux changes with time for different initial cavity pressure values. The effect of a distance from the explosion on gas flux is shown in Figure 9.4.

[4] Similar to Darcy flux in western literature, the authors call it "velocity of filtration"

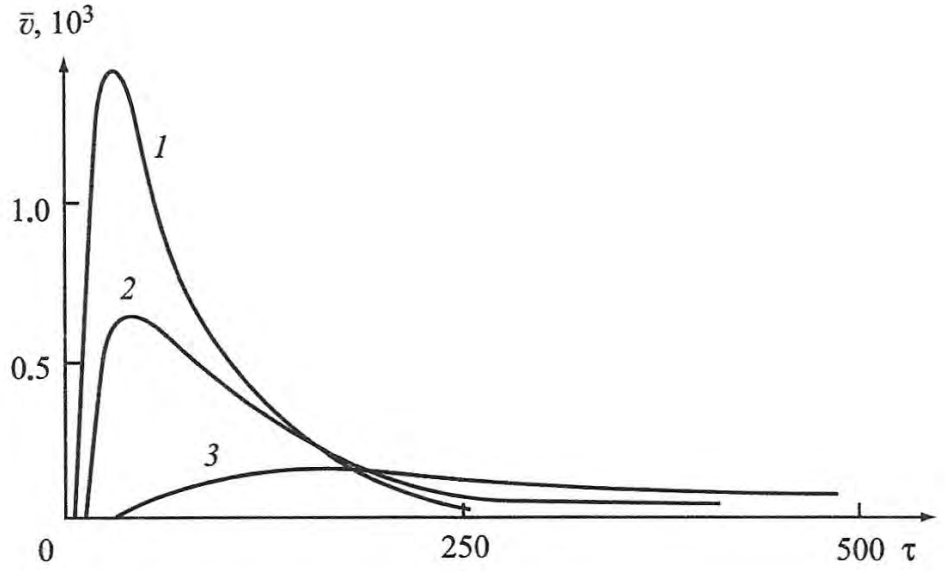

Figure 9.4: Scaled (normalized) flux of gas by-products, at different scaled distances *x*: *1* – 6; *2* – 7.5; *3* – 12 (for $m = 0.04$ and $\bar{P} = 0.1$).

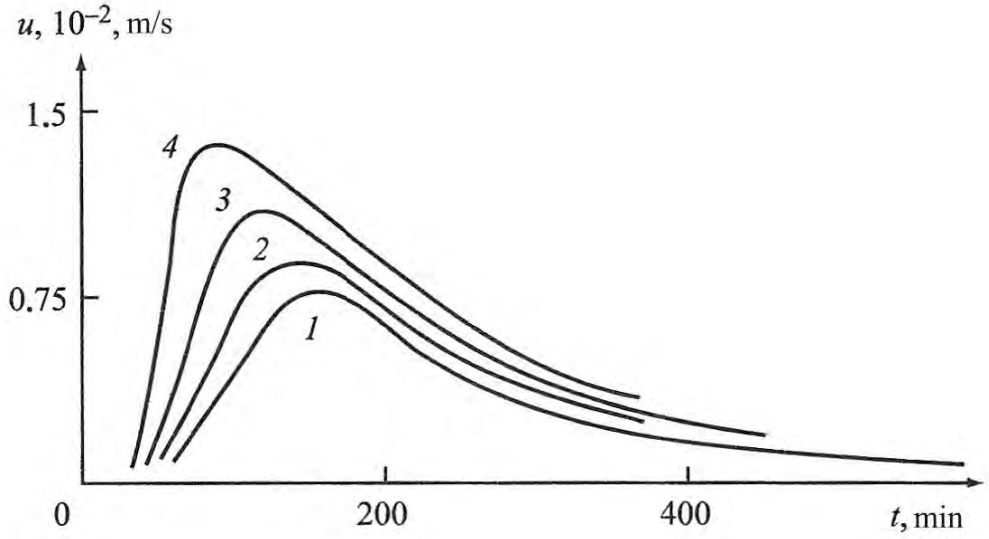

Figure 9.5: Flow velocity of gas in permeable channels, for the following values of porosity *m*, %: *1* – 3; *2* – 4; *3* – 5; and *4* – 10.

Of interest is the study of specific scenarios of gas transport through damaged media, for certain explosion parameters and geological conditions. Thus Figure 9.5 shows the effect of porosity of the damaged rock massif on the physical gas flow velocity *u*, for an explosion with yield of 100 kt (at a scaled distance of 90 m/kt$^{1/3}$). The effect of the explosion yield on the velocity of gas flow in granite is shown in Figure 9.6.

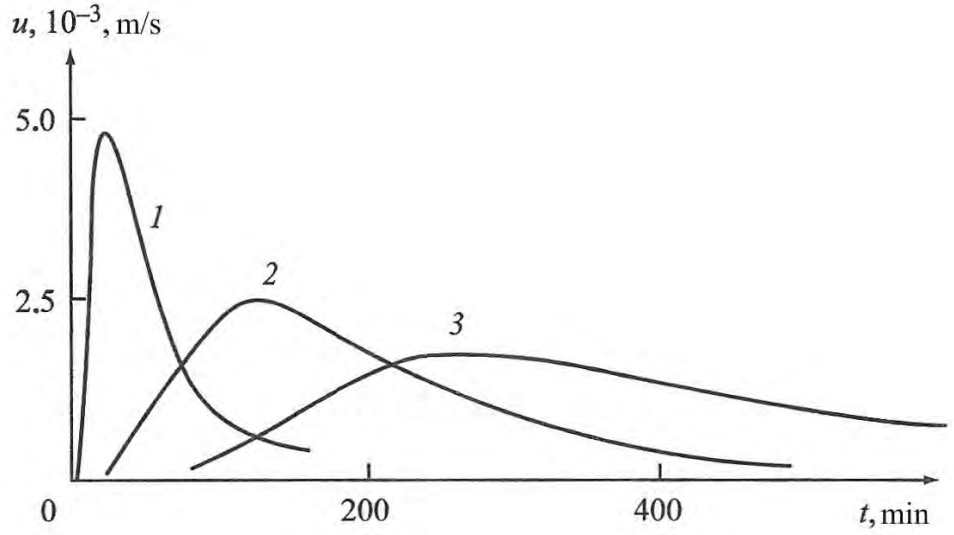

Figure 9.6: Gas flow velocity for explosions of different yield in granite ($m = 0.05$, scaled distance from the explosion is 120 m/kg$^{1/3}$). Yield q in kt is: *1* – 1; *2* – 10; *3* – 100.

Using a spatial distribution of gas pressure and flow velocity, we can determine the time of arrival of cavity gas at different distances from the cavity, in case where cavity gases and pore gases become completely mixed in the gas flow zone. Pressure at each point increases gradually with time, and it is difficult to determine the beginning of the pressure increase. Therefore, the initial moment of the arrival of the gas front at a certain distance was set to the point of intersection between the straight line, corresponding to the maximum of the derivative during pressure increase time interval, and the line corresponding to initial (background) pore pressure.

Figure 9.7a shows the calculated travel time curves for the gas front arrival for different values of parameter α (defined in Equation 9.7) varying in the range between 10^{-2} and 10^{2}. The initial pressure in the cavity was set to $P_* = 10\ MPa$ and the medium porosity – to $m = 0.04$. For $\alpha < 1$ the value of this parameter doesn't significantly affect the front movement. When α becomes greater than 1, it starts affecting the front propagation more significantly. The effect of parameter α is easier to visualize if we find a limit $\alpha \to 0$ in for the expression for the gas flux (flow)

$$\rho u = \frac{\mu k_2}{2Ak_1\delta}\left(1 - \sqrt{1 + 4\alpha P^n \left|\frac{d\bar{P}}{dx}\right|}\right). \tag{9.11}$$

In this case, instead of 9.11 we shall obtain a relationship similar to the linear (Darcy) equation (5.2) in the form:

$$\frac{\partial P}{\partial t} = -\frac{\mu}{k} v\ . \tag{9.12}$$

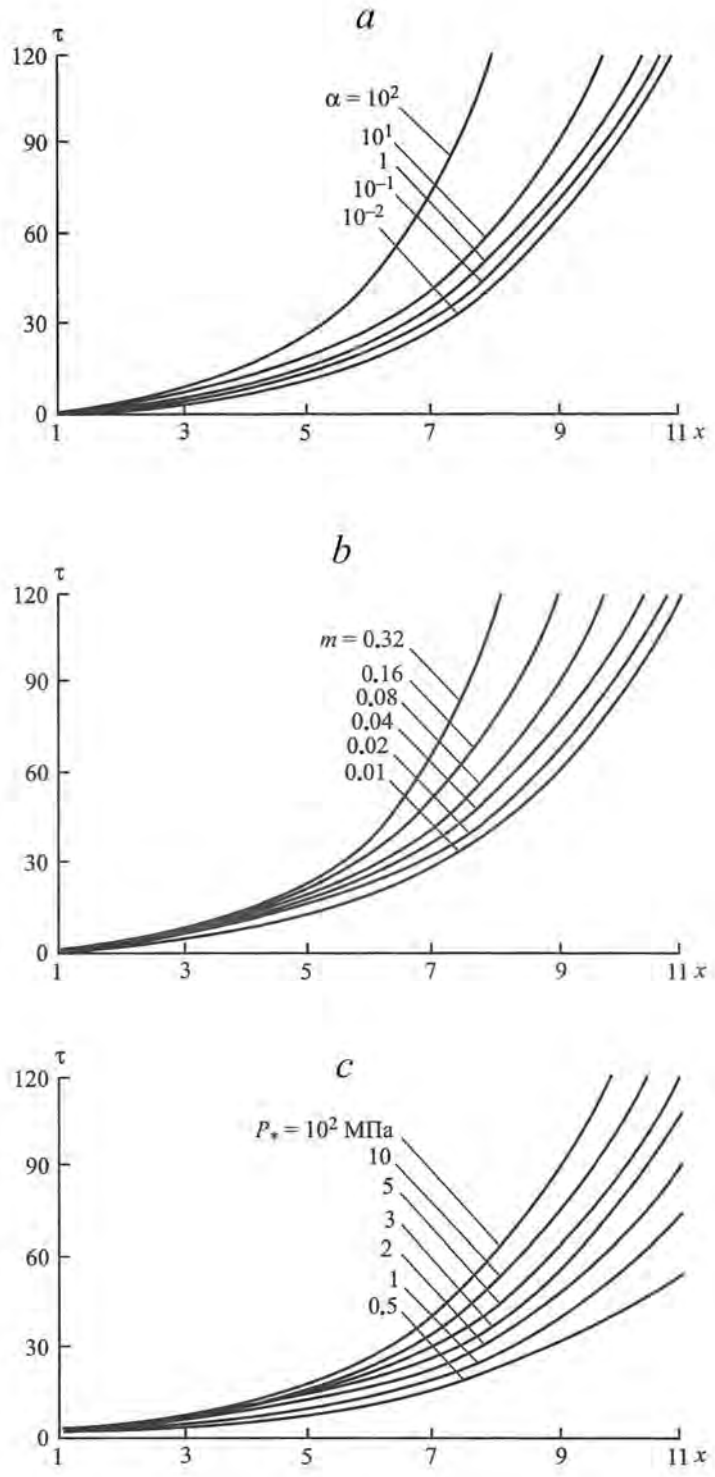

Figure 9.7: Gas front position (scaled distance vs scaled time – these are travel time curves for the gas front): a) effect of parameter α for $m = 0.04$; b) effect of porosity for $P_* = 10$ MPa; c) effect of the cavity pressure for $m = 0.04$.

Therefore if we reduce parameter α the flow becomes laminar[5] and the travel time curves in Figure 9.7 become almost identical. In the opposite limit, when $\alpha \to \infty$, we neglect the terms equal to 1, and retain only the quadratic term. Therefore for large α the flow becomes turbulent. According to Figure 9.7a the quadratic term has a significant effect [on gas flow] for $\alpha > 1$. In this case an increase in α causes an increase in the arrival of the front due to a non-linear increase of the resistance forces with the increase of the gas velocity.

The value of $\alpha = 1$ can be used to describe a broad range of flow parameters. To show this we will estimate the spatial and temporal distributions of the laminar and turbulent flow regimes. Substituting Equation 9.11 into 9.5 we obtain the expression for the Reynolds number:

$$Re = \frac{AP_2^2}{2\alpha\mu^2 r_c}\left(\frac{k_1}{m}\right)^{3/2}\left(\sqrt{1 + 4\alpha P^n\left|\frac{d\bar{P}}{dx}\right|} - 1\right). \qquad (9.13)$$

It follows from this expression that both flow regimes coexist for an extended period of time (up to τ ~10). The laminar regime starts in the entire space only after τ > 60, at which point the flow front reaches the distance of $6r_c$.

Let us determine the most suitable value of α for this problem. Field measurements have shown that the values of permeability in the crush zone (3 – 5 r_c) are on the order of $k_1 = 10^{-1}$ to 1 Darcy, and in the fracturing zone (5 – 10 r_c) the value is $k_1 = 10^{-2}$to 10^{-1} Darcy. Based on historical data (Leibenson, 1947) and on the results obtained in Chapter 5 we write the relationship between the first and the second permeability coefficients in the form:

$$\lg k_2 = 5.66 + 1.33 \lg k_2 .$$

The initial porosity in relevant areas of the Semipalatinsk and Novaya Zemlya Test Sites is $m = 0.01$ to 0.03. Drilling into the rock massifs after conducting nuclear tests, and using geophysical methods, have shown that porosity increases in the chimney zone by a factor of 2 – 8, in the crush zone by a factor of 1.8 – 4, and in the fracture zone by a factor of 1.25 – 3.5. Therefore it makes sense to use a factor of 2 – 2.5 or $m \approx 0.04$ for a significant volume of damaged rocks. The dynamic viscosity coefficient for a gas depends on temperature and pressure. To perform calculations we used a published value $\mu = 2 \cdot 10^{-4} Pa \cdot s$, which is similar to a viscosity of carbon dioxide at temperature $T \approx 40$℃ and $P = 6MPa$ and/or a viscosity of water vapors at $T \approx 100$℃ and $P \approx 1MPa$. The cavity radius for most rocks is approximately $\bar{r_c} \approx 10\, m/kt^{1/3}$ (Chapter 1). Using these parameters we find that the typical (characteristic) value is $\alpha \approx 1$. This reasoning assumes that cavity collapse takes place on a longer time scale longer than the gas flow.

The effect of the porosity of a damaged medium and the initial cavity gas pressure on propagation of the flow front, is shown in Figure 9.7 b,c. For small values of porosity $m = 0.01$ to 0.04 the effect of porosity on the gas front travel times is insignificant. For higher

[5] (Translator's footnote) A flux (flow) described by a linear function between the flow velocity and the pressure gradient is equivalent to laminar flow, similar to a laminar flow of ideal fluid through straight channels.

porosities, $m = 0.08$ to 0.32 the front propagation slows down. The value of the initial pressure has a significant effect on the gas front propagation, and the smaller the pressure in the cavity, the stronger its effect on the front propagation. Overall, using the results of the solution to the flow problem, it was determined that the flow front of gas can be described by an interpolation formula:

$$\tau = B(x-1)^b \,, \tag{9.14}$$

where the exponent (b) changes in the range $2.5 \le b \le 3.3$, the cavity pressure varies between 10 to 0.5 MPa, and the porosity varies between 0.01 and 0.32. The value of the coefficient B under these conditions varies in the range $0.1 \le B \le 0.21$. In particular, for some values of the initial pressure and medium porosity, Equation 9.19 is given by:

$$\tau = 0.16(x-1)^{2.6} \text{ for } P_* = 1\ MPa, m = 0.04 \,,$$

$$\tau = 0.2(x-1)^{2.9} \text{ for } P_* = 10\ MPa, m = 0.04 \,,$$

$$\tau = 0.18(x-1)^{2.7} \text{ for } P_* = 5\ MPa, m = 0.04 \,.$$

9.2. Initial state of flowing (transported) gas

Earlier in Chapter 1 we showed that the maximum size of the explosive cavity for contained nuclear explosion scales with the yield of explosion, and varies depending on physical and mechanical properties of the emplacement rocks in the range 7 – 15 m/kt$^{1/3}$. The time of cavity expansion is 0.05 – 0.1 s/ kt$^{1/3}$.

At the moment when the cavity reaches its largest value, the gas pressure inside the cavity is on the order of 100 – 500 atmospheres, and the temperature is 4000 - 5000°. At the end of the cavity expansion, gas products (filling the cavity) rapidly cool due to radiation and to heat transfer into the melt and into the emplacement rocks. Rocks containing water or carbonates release significant quantities of gas during an explosion, due to water evaporation and/or chemical decomposition of the rocks. When the cavity gas pressure becomes lower than the pressure of the gas released by the emplacement medium, intense gas release takes place into the cavity (from the walls) in form of an implosion. The existence of such an implosive process was confirmed by drilling into the cavities left from borehole testing at the Semipalatinsk Test Site. Study of the cores has shown that all the melt formed after the explosion is in a finely dispersed state. None of the explosions have shown a “lake” of solidified melt at the bottom of the cavity.

Including the additional mass into the energy exchange, as well as convective heat exchange with the melt inside the cavity, also promotes faster cooling and a pressure drop. On the other hand, condensation of the parts of melt with high melting temperature, and melt solidification, releases heat due to the latent heat content of evaporation and melting. Thus the gas temperature inside the cavity stabilizes at the melting temperature of the emplacement rocks. The solution of

the problem of cooling of the cavity material, considering molecular heat conduction, condensation of rock gas and additional increase of the amount of melt, shows that the characteristic time required to end condensation of the rock vapors and to equalize the cavity pressure, is 1 – 10 s/ $kt^{1/3}$. After that the cavity material gets into dynamic equilibrium, when the gas in the cavity is uniformly mixed, the temperature is close to the melting temperature, and the cavity pressure stabilizes at the level of pressure of non-condensable gases.

Experiments supporting the hypothesis of gas temperature stabilization in the cavity include cratering explosions conducted at the Semipalatinsk Test Site. During these experiments, measured temperatures of the light-emitting areas of gas venting were in the range of 1500 – 2100° C.

Table 9.1. Melting temperatures for some rock types

Rock type	Melting temperature, °C
Slate, Porphyrite	1220 – 1450
Granite	1340 – 1680
Quartzite, Sandstone	1400 – 1750
Shale, Argyllite	1120 – 1170

Analysis of samples taken after underground nuclear explosions from Novaya Zemlya Test Site to determine gas chemical composition, also showed that the non-condensable gas in the cavity was formed at temperatures between 1400 – 1700 °C. These temperatures are close to the melting temperatures of rocks characteristic for these test sites (Table 9.1).

The initial state of gas for the problem of gas flow is set to the state in the cavity after condensation of high-temperature components. Assuming conditions of dynamic equilibrium one can calculate the pressure of non-condensable gas using the formula:

$$P_* = \frac{M}{\mu_{cp}} \frac{RT_p}{V}, \tag{9.15}$$

where M is the mass of the non-condensable gas, T_p is the temperature of the equilibrium state (equal to the rock melting temperature), V is the cavity volume, and μ_{cp} is the average molecular weight of the gas mixture. Depending on chemical composition:

$$\mu_{cp} = \frac{\eta}{\mu_{cp}}, \tag{9.16}$$

where η_i is the mass fraction [specific content] and μ_i is the molecular weight of i-th component of the gas mixture, and N is the number of the components in the gas mixture.

The mass of the non-condensable gas released by the rock is:

$$M = \eta G q \ , \tag{9.17}$$

where G is a specific mass of rock participating in gas production per unit of yield.

The nature of gas release depends on physical and chemical properties of rocks. Silicates and carbonates differ significantly. Gas production in silicate rocks (e.g. quartzite, tuff, alluvium) is determined by free water content in pores and fractures. It was determined experimentally that dry granites and quartzites produce 300 ± 100 t/kt of melt, water-saturated tuff produces 500 ± 150 t/kt of melt, while wet alluvium produces 650 ± 50 t/kt of melt (e.g. Underground…, 1962). Using these data and taking into account the effect of water saturation, gas pressure and cavity size on the amount of melted rock, the pressure of water vapor was determined as a function of water content and cavity radius (Figure 9.8). The data are described by an empirical function:

$$P_* = 7.8 \cdot 10^5 \frac{\eta_\omega q}{r_c^3}, \ (\text{kgf/cm}^2) \tag{9.18}$$

where r_c is the cavity radius in meters, and q is the explosive charge in kt, and kgf (kilogram force) is a unit of force.

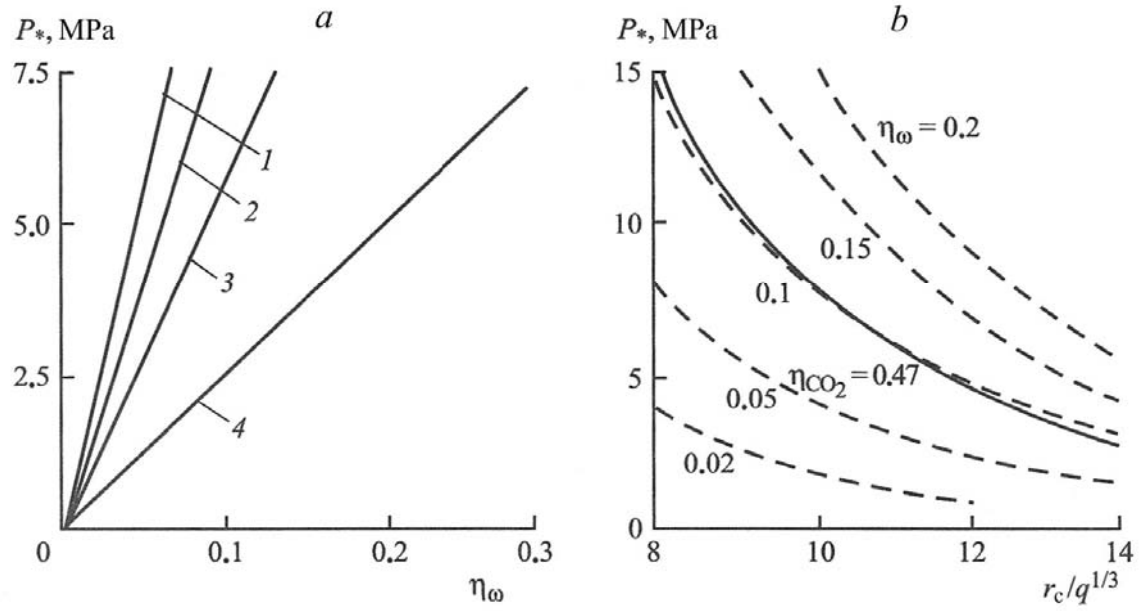

Figure 9.8: Partial pressure of water vapor in the cavity as a function of a) moisture content for $r_c/q^{1/3}$ of: *1* – 8.8, *2* – 9.6, *3* – 11.1, *4* – 15; and b) cavity radius, where rock gas content is shown by numbers next to the curves.

For these calculations the temperature of gas in the cavity was assumed equal to the melting temperature of granite, $T_p \sim 1600$ K. With an increase in strength of the rock and a decrease in

cavity size, the pressure and its rate of increase for given water saturation intensifies. Expression 9.18 is in a good agreement with historical experimental data. For example, during an explosion in alluvium with $\eta_\omega = 0.12$ the measured pressure in the cavity was 3.5 MPa (e.g. Olsen, 1967). For an explosion in tuff with $\eta_\omega = 0.153$ it was determined that the melt was crystallizing at a pressure of 4 MPa (e.g. Higgins, 1970).

The pressure using Equation 9.18 for these alluvium and tuff explosions yields 2.8 and 3.0 MPa respectively. For nuclear explosions at the Degelen Testing Area of the STS conducted in granite and quartzite, where water content is close to $\eta_\omega \approx 0.01$, the water vapor pressure in the cavity does not exceed 1 MPa. An increase in the water content of granite to $\eta_\omega = 0.03$ to 0.05 causes an increase in water vapor pressure to 3 – 5 MPa.

Explosions in carbonate rocks (e.g. limestone, dolomite, calcite) cause thermal (chemical) decomposition of the rock in addition to melting and evaporation. The non-condensable gas in these rocks is mainly represented by carbon dioxide. Dolomite and calcite decompose at similar temperatures of approximately 825 – 900° C at atmospheric pressure.

Calculations show that the mass of dolomite chemically decomposing during nuclear explosions is 180 t/kt, while the equilibrium temperature of material (gas) in the cavity is 2200° C. Higher temperatures for carbonate rocks is justified by the fact that the molecular weight of carbon dioxide (μ = 44) is higher than the molecular weight of water vapor (μ = 44), therefore the temperature of its release into the cavity is higher. However the equilibrium temperature of CO_2 in the cavity is significantly lower than melting temperatures for CaO and MgO (2570 – 2580° C). Therefore we expect that there is small amount of melt in the cavity, which can absorb some radioactive material. The dispersed state of the oxides as well as the presence of carbon dioxide[6] promotes spreading of radioactive isotopes into the surrounding rock, and their subsequent release into the atmosphere.

For dry dolomite $CaMg(CO_3)_2$ with $\eta_{CO2} \approx 0.47$ and T_p = 2200° K, the effect of cavity radius on the pressure of carbon dioxide is approximately the same as for silicate rock with a water content of $\eta_{CO2} \approx 0.1$ (Figure 9.8b). Therefore the efficiency of non-condensable gas in dolomite is approximately 4.7 times lower than the effect of water content in silicate rocks. It is mainly caused by reduction of the size of the gas-producing zone, and by the differences in molecular weights between carbon dioxide and water. Using this result and applying Equation 9.18, we obtain a relationship between non-condensable gas pressure in the cavity created by a nuclear explosion in dry carbonate rock:

$$P_* = 1.66 \cdot 10^5 \frac{\eta_{CO2} q}{r_c^3}, \text{ (kgf/cm}^2\text{)} \qquad (9.19)$$

where r_c is the cavity radius in meters, and q is the explosive charge in kt.

[6] Carbon dioxide does not condense, even after it cools down while moving through fractures of the broken rock

Table 9.2. By-products of thermal decomposition of rocks

Test	Rock type	η, %	Chemical complex									
			SiO_2	MgO	Al_2O_3	FeO	CaO	K_2O	CO_2	H_2O	C	S_2
Tun. A-1	Slate	10.24	57.4	11.1	10.5	6.3	1.8	3.9	5.3	4.5	0.2	0.8
Tun. A-2	Quartzite	5.0	78.7	0.9	12.0	4.6	1.3	0.6	2.1	2.8	-	-
Tun. A-3	Slate	11.3	50.2	11.3	12.8	4.6	7.4	4.7	7.4	3.8	0.06	0.0
Tun. A-4	"	4.7	58.3	8.2	14.4	7.9	1.0	5.5	0.77	3.8	0.03	0.1
Tun. A-5	"	8.5	57.7	10.7	11.8	4.8	2.4	4.7	3.8	3.9	0.1	0.7
Tun. A-7	Sandstone	7.8	85.2	4.0	5.2	1.3	0.14	2.6	3.6	3.9	0.15	0.2
Tun. A-9	Limestone	43.3	3.9	16.9	3.0	-	34	1.3	42.3	0.4	0.16	0.5
BH 1003	Shale	5.4	70.7	8.4	8.5	-	6.7	-	3.6	1.8	-	-
BH 101	Sandstone	12.8	48.6	23.2	7.0	-	8.4	-	6.0	6.8	-	-

It follows from 9.19 that for hard limestone, for instance as in the Southern Testing area at Novaya Zemlya (ρ=2.75 g/cm^3, C_p = 5700 m/s, $\sigma_* = 140\,MPa$, $\bar{r}_c = 9.3\ \mathrm{m/kt^{1/3}}$), carbon dioxide pressure in the cavity will be 9.7 MPa. For porous limestone, for instance in the case of the explosion KRYSTALL (ρ=2.22 k/cm^3, C_p = 3500 m/s, $\sigma_* = 70\,MPa$, $\bar{r}_c = 12.3\ \mathrm{m/kt^{1/3}}$), the cavity pressure will be 4.2 MPa.

The rocks at the Novaya Zemlya Test Site (Northern testing area), and Balapan and Murzhik Testing Areas near Semipalatinsk, have a mixed nature of gas-production. They contain both free water, and minerals that can chemically decompose.

Rocks at Novaya Zemlya are represented by shales, sandstones and quartziitic sandstones with limestone inclusions. The shales, which are most widespread, have the following mineral composition: 15 – 35 % of sericite $KaAl_3Si_3O_{10}(OH)_2$, 15 – 25 % of chlorite $Fe_2Al_3Si_3O_{10}(OH)_8$, 10 – 30 % of quartzite SiO_2, 3 – 30 % of talcum $Mg_3Si_3O_{10}(OH)_2$, 2 – 25 % of dolomite $CaMg(CO_3)_2$ and calcite $CaCO_3$, 0.1 – 3 % of pyrite FeS_2, and 0.05 – 0.8 % of free water.

At the Balapan and Murzhik Testing Areas the rocks are represented by siltstones, sandy tuffs, argillites, porphyries and carboniferous shales, which are composed of the following minerals: 20 – 50 % of quartzite, 5 – 15 % of dolomite, 1 – 45 % of chrysolite $Mg_3Si_2O_5\,(OH)_4$, 10 – 30 % of anorthite $CaAl_2Si_2O_8$, 1 – 20 % of talcum, and 0.8 – 1.2 % of free water.

The rocks for both test sites have a complex mineralogical composition. Almost all these minerals contain hydroxyl and carbonate groups. Chemical and thermal decomposition of these rocks leads to formation of oxides (SiO_2, MgO, Al_2O_3 etc) with high melting temperatures, as

well as gas components (CO_2, H_2O, S_2, H_2S etc). Table 9.2 shows the results of thermal decomposition of rocks in mass fractions (%) taken from locations of nuclear charges for some nuclear tests from adits of Novaya Zemlya Test Site. Thermal decomposition was conducted by heating rocks in a flow of argon. The results show that the largest fraction among all gas (volatile) components is from carbon dioxide and water vapor. The total fraction of all other gases combined does not exceed 1%.

Many of the rock forming minerals at the Semipalatinsk and Novaya Zemlya Test Sites contain water in hydroxyl form as well as water present as molecules within the crystalline structure of some minerals. The latter releases when rock is heated to about 300° C. Hydroxyl water is formed from ions OH- and H+ that are part of the crystalline structure of some minerals. It releases when rock is heated between 500 and 1300° C. In practice gas-forming properties of rocks are determined by heating in an atmosphere composed of inert gases, and are based on the loss of weight. Then the amount of free water (for T = 105° C), the joint amount of free water and water contained in crystalline structure (for T = 600° C), and the total water content (for T = 1100° C), are determined.

Performing calculations for slates at the Novaya Zemlya Test Site have shown that the formation of gas (volatile) components under thermal decomposition involves a mass of rock amounting to G = 300 t/kt. The equilibrium state of gas in the cavity is achieved due to vapor pressure, formed by decomposition of the mineral sericite, which provides the highest vapor pressure among all minerals composing slates. To simplify the calculations we can take into account only the formation of carbon dioxide and water vapor. The molecular weight of the gas mixture can be determined using the relationship:

$$\mu_{cp} = \frac{\eta}{\frac{\eta_{CO2}}{\mu_{CO2}} + \frac{\eta_{H2O}}{\mu_{H2O}}}.$$

We assume that the equilibrium temperature of gas in the cavity is equal to the melting temperature of slate (T_p = 1500° C). Since the molecular weight for carbon dioxide is 2.4 times higher than for water, we obtain the following relationship using Equations 9.15 – 9.16:

$$P_* = 2 \cdot 10^5 q \frac{2.4\eta_{H2O} + \eta_{CO2}}{r_c^3} \text{ (kgf/cm}^2\text{)}, \quad (9.20)$$

where r_c is the cavity radius in meters, and q is the explosive charge in kt. This formula determines the pressure of the major components of non-condensable gases in the cavity formed by thermal decomposition of rocks, not accounting for free water in the rock massif. We use Equations 9.20 and 9.18 to account for pressure created by water vapor for silicate rocks. In the general case, the pressure of non-condensable gases depends on the amount of the main gas components as follows:

$$P_* = 2 \cdot 10^5 q \frac{3.9\eta_{\omega} + 2.4\eta_{H2O} + \eta_{CO2}}{r_c^3} \text{ (kgf/cm}^2\text{)}, \quad (9.21)$$

where r_c is the cavity radius in meters, q is the explosive charge in kt, η_ω is the weight fraction of water originally present in rock, and η_{H2O} and η_{CO2} are the weight fractions of water vapor and carbon dioxide respectively formed during thermal decomposition of rock. Total gas content of rocks is given by $\eta = \eta_\omega + \eta_{H2O} + \eta_{CO2}$. Figure 9.9 shows an example of pressure estimated for a non-condensable gas in a cavity with $\bar{r}_c = 11.1$ m/kt$^{1/3}$, as a function of gas content of rocks, for different ratios between different gas components. The amount of free water was 1% ($\eta_\omega = 0.01$). An increase in water content leads to an increase of gas pressure in the cavity. Replacing carbon dioxide with water vapor causes pressure to increase by a factor of 1.5 – 2.2. The highest pressure in the cavity is reached if all the gas content of the rock comes from free water ($\eta = \eta_\omega$), if all other parameters are kept the same.

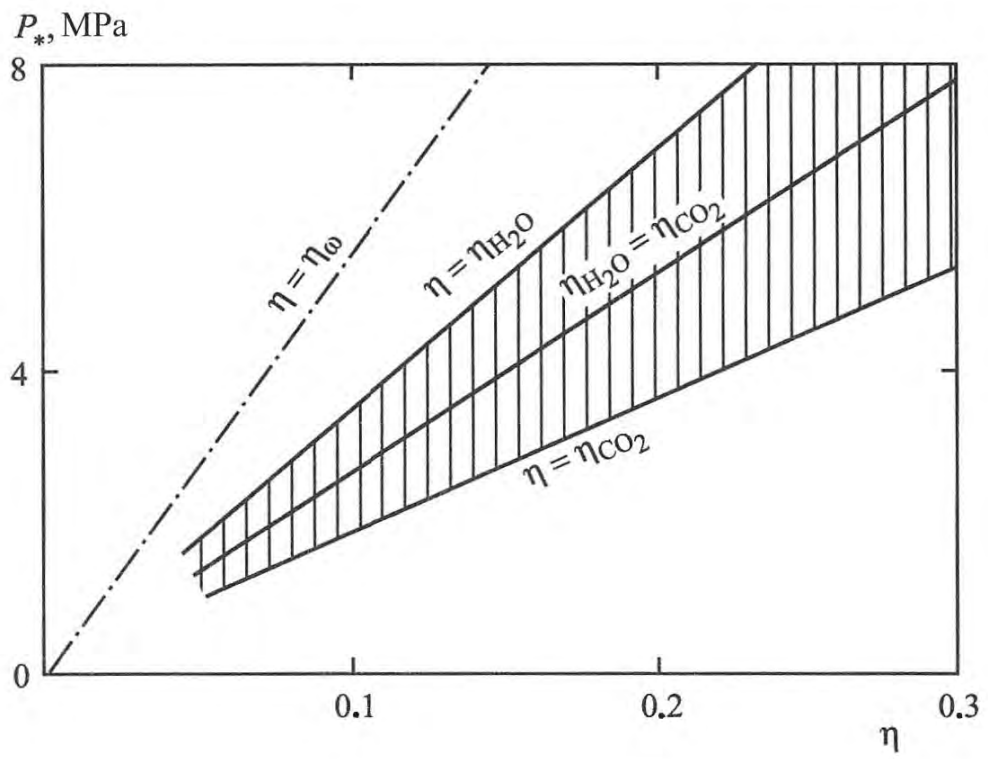

Figure 9.9: Effect of rock gas content and the ratio of the main gas components, on gas pressure in the cavity with $\bar{r}_c = 11.1$ m/kt$^{1/3}$, for moisture content of 1% (shaded area). Dash-dot line corresponds to Equation 9.18 when gas content of the rock comes only from free water.

In cases when gas is not registered after rock is heated above 300° C, the amount of hydroxyl water remains unknown. In this case, if there is a mix of gases, equivalent gas content can be used:

$$\eta_e = \eta_\omega + 0.21\eta_{CO2}.$$

where η_ω is the weight fraction of free and crystalline water, $\eta_{CO2} = \eta - \eta_\omega$, and η is the total gas content of the rock. Cavity pressure can be estimated using the formula:

$$P_* = 8.4 \cdot 10^5 \frac{\eta_e q}{r_c^3}, \text{ (kgf/cm}^2\text{)} \quad (9.22)$$

where r_c is the cavity radius in meters, and q is the explosive charge in kt.

9.3. Transport properties of damaged rock

Practical use of the solution to the filtration problem, developed in the previous subsection, requires knowing the gas permeability around the explosion source. Measurements of permeability have been obtained in granitic rocks after the explosions HARDHAT and HOGGAR (Boardman, 1970; Duncan et al, 1972), apatite-nepheline rocks (Spivak, 1980b), and for the excavated rocks from explosions at the Semipalatinsk Test Site (Atomic…, 1970). However, the range of permeability coefficient changes is very broad; so it was difficult to apply the results of these studies to the Semipalatinsk and Novaya Zemlya Test Sites.

Therefore, the filtrational parameters (characterizing permeability) were inferred, by comparing the solution of the non-stationary filtration problem with the results of the measurements of the venting times for the radioactive gases to the atmosphere. The registration of the time and place of radioactive gas breakthroughs was conducted at the entrance to each tunnel or borehole, and also from helicopters and planes equipped to perform radionuclide surveys. For some explosions the emergence of radioactivity into the atmosphere was also determined by the ratios of radioactive isotopes in the samples collected in places of the venting. Using known venting times for the radioactive products t_0, a combination of filtration parameters gives a "combined transport parameter" which is a function of both porosity, viscosity and permeability, similar to hydraulic conductivity.[7] This was determined using Equation 9.7:

$$\frac{k_1}{m\mu} = \frac{\tau r_c^2}{P_* t_0}, \quad (9.23)$$

where the value of τ is determined by solving the transport problem (9.14) using r = W, or x = W/r_c, using the corresponding values of the pressure and medium porosity; and r_c and P* are the cavity radius and the pressure of non-condensable gases respectively. The venting time t_0 is known from observations at both Novaya Zemlya and Semipalatinsk Test Sites.

At Novaya Zemlya the presence of radioactive gases was registered after all 42 underground nuclear tests. Of those, 36 explosions were conducted in tunnels at the northern testing area near Matochkin Shar Straight, and 6 explosions were conducted in boreholes of the southern testing area. Several distinct groups of explosions can be selected, associated with different levels of containment, based on the character of the radioactive gas escape into atmosphere:

1. For a significant number of the explosions, gas escape into the atmosphere took place in the epicentral area (above the explosion) of the rock massif, and the venting times were t_0 = 15-

[7] In fact the authors simply used the definition of non-dimensional parameter τ from 9.7 and rearranged it

40 min. In addition there was later escape of the radioactive gases through the tunnels (approximately 1 hour or more). The exact values of t_0 are shown in Table 9.3.

2. Another significant group of explosions was characterized by early venting times (t_0 = 5-12 min) through the damaged rocks (in the epicenter) and later gas escape (venting) through the tunnel (hours, sometimes days). The values of t_0 for these explosions are shown in Table 9.4.
3. A small group of explosions was accompanied by an early release of radioactive products into the atmosphere through tectonic faults ($t_0 = 1 \div 3$ min), and relatively early release of gases through the tunnel t_{tun} (Table 9.5).
4. Late escape of the radioactive gases into the atmosphere through the damaged massif was recorded for two of the tunnel explosions: A-27 (t_0 = 1 h) and A-13H (t_0 = 6 h 54 min), and also for 2 borehole explosions: Yu-1 (t_0 = 2 h) and Yu-5H (t_0 = 2 h 40 min).

Using the venting times the non-dimensional quantity $k_1/m\mu$ (Eq. 9.23) can be calculated. Other parameters needed for the calculations, such as the cavity radius rc and the pressure P^* can be determined using the relationships 2.21 and 9.21 and the mechanical properties of the emplacement medium measured for each explosion. To calculate P^* a typical fluid content should be used: 0.1% for the tunnel explosions, and 1% for the borehole explosions.

The estimated values of the non-dimensional parameter $k_1/m\mu$ for Novaya Zemlya as a function of the scaled depth are shown in Figure 9.10. Two groups of events can be seen. The best fitting function is shown with a solid line. Despite the scatter ($\sigma = 1.5 - 1.8$), there is a systematic increase in $k_1/m\mu$ within the scaled depth range of 60-95 m/kt$^{1/3}$ (small scaled depths). Overall, the dependence of $k_1/m\mu$ on depth for Novaya Zemlya can be expressed as

$$k_1/m\mu = 3 \cdot 10^4 \text{ (D/cP)}^8 \text{ for W/q}^{1/3} > 95 \text{ m/kt}^{1/3} \quad (9.24)$$

$$k_1/m\mu = 4.3 \cdot 10^6 \, exp(-0.05W/q^{1/3}) \text{ (D/cP) for W/q}^{1/3} < 95 \text{ m/kt}^{1/3}.$$

Table 9.3. Gas release times for explosions with different depths of burial (at NZTS)

Parameter	Tunnel number											
	B	A-1, A-2	A-4, A-5	A-3	A-9	A-8	A-10	A-17	A-25	Yu-3	Yu-7	Yu-6H
$W/q^{1/3}$, m/kt$^{1/3}$	163	65	71.6	84.7	71.4	67.7	73.3	84.2	80	1940	88	102
t_0, min	38	16	20	33	25	16	38	16	25	39	22	18

[8] D – Darcy (unit of permeability), cP – centipoise (unit of viscosity)

Table 9.4. Gas release times for explosions with different depths of burial (at NZTS)

Parameter	Tunnel number											
	A-6	A-16	B-1	A-14	A-21	A-24	A-26	A-40	A-37	A-30	A-32	Yu-4
$W/q^{1/3}$, m/kt$^{1/3}$	62.7	81.4	69.1	84	87	200	129	95	100	126	114	152
t_0, min	10	7	8	7	8	10	6	5	12	7	7	4

Table 9.5. Gas release times for explosions with different depths of burial (at NZTS)

Parameter	Tunnel number								
	G	A-11	A-23	A-37A	A-18	A-12	A-20	A-19	A-7p
$W/q^{1/3}$, m/kt$^{1/3}$	121	121	168	103	91.4	79.4	85.3	118	100
t_0, min	1-9	1.1	3	1.3	3	7-8	7	10	-
t_{un}, min	6	7	52	-	2	30	1	6	1

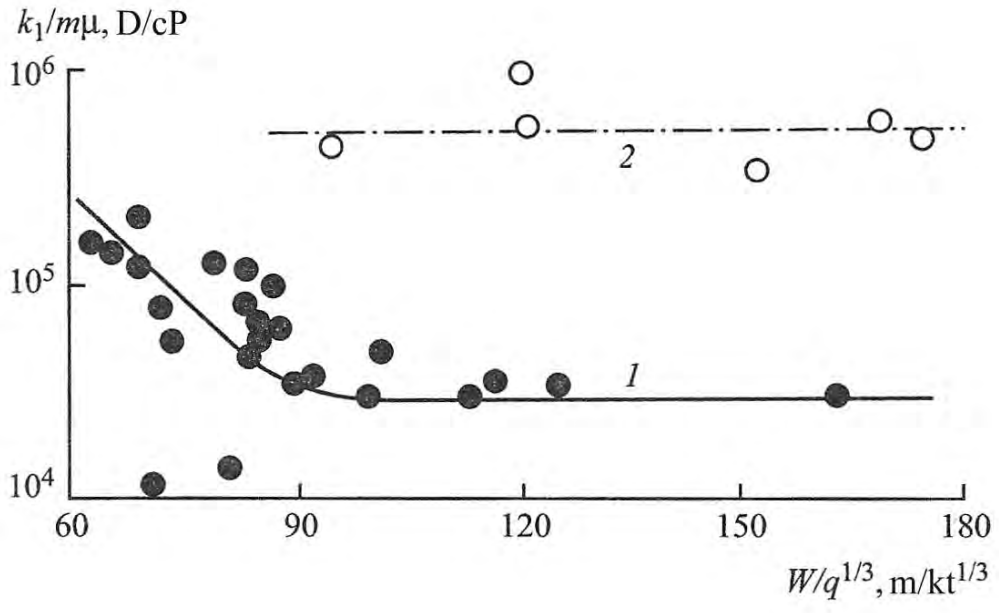

Figure 9.10: Gas transport parameters as a function of scaled DOB, for the NZTS.

Table 9.6. Gas release times for explosions with different depths of burial (at STS)

Parameter	Borehole number										
	102	111	128	1304	1054	1064	1050	1069	1077	2803	1223
$W/q^{1/3}$, m/kt$^{1/3}$	118	108	133	92	95	109	960	450	117	162	94
t_0, min	2.5	0.5	3.5	10	20	0.117	2.7	0.5	18	9	17

Table 9.7. Gas release times for explosions with different depths of burial (at STS)

Parameter	Borehole number								
	110	1061	1010	1214	1206	1400	1225	1201	1062
$W/q^{1/3}$, m/kt$^{1/3}$	119	89	120	114	157	124	109	145	152
t_0, hours	0.4	0.5	0.9	1	2	3.3	6.7	7.5	10

The second group of explosions plots above the line (9.24) and is shown in Figure 9.10 as the dashed line. The breakthrough times for these explosions are shown in Table 9.5, corresponding to gas escape through tectonic faults. Such escape of gases through permeable tectonic faults, either due to lack of cementation or opened during the explosion, can be described using the function $k_1/m\mu = 5 \cdot 10^5$ (D/cP).

A similar analysis was performed for underground nuclear explosions of the Semipalatinsk Test Site, where 225 explosions were conducted in tunnels of the rock massif Degelen and 138 explosions were conducted in boreholes, of which 112 were conducted at Balapan, 21 in boreholes at Murzhik, and 5 as a part of the peaceful nuclear explosion program, including cratering (excavation) explosions.

The tests in boreholes can be divided into three groups based on the breakthrough or venting times:

1. Early gas venting t_0 between 10 s and 20 min was observed for 30 borehole tests with a broad range of scaled DOB – between 70 and 960 m/kt$^{1/3}$. Table 9.6 shows the values of gas escape for some explosions of this group. The total gas content of rocks varied between 4.5 and 18%. This group includes 4 events classified as emergencies with very early venting times. The first test of this group conducted in Tunnel 1204 ($W = 72$ m/kt$^{1/3}$) produced gas venting through a dome after 12 s. The second test in Tunnel 1204 (W=118 m/kt$^{1/3}$) emplaced in coal-bearing slate created gas venting accompanied with fire 20 s after the explosion. During tests in BH 1303 ($W = 364$ m/kt$^{1/3}$) and in BH 1069 ($W = 450$ m/kt$^{1/3}$), stemming and borehole casing were blown out. All other explosions in this group led to gas escape through

artificial (man-made) channels (e.g. sampling ways, tubing casing annulus and inter-cable space, emplacement and core holes, etc).

2. Delayed escape of radioactive gases ranging between 25 and 60 minutes was observed in 40 borehole explosions, between 1 hour and 5 hours — in 30 explosions, and between 5 and 25 hours — in 10 explosions. The scaled depth of explosions of this group ranged over wide limits (88 – 236 m/kt$^{1/3}$), and the gas content of the rock was 2.6 – 14.4%. These parameters (characterizing conditions under which the explosions were conducted) were practically the same as for the preceding group. In this most numerous group of 80 borehole shots, radioactive gases were transported for a rather long time inside the rock mass through cracks and gaps between blocks, without encountering direct channels allowing exit to the atmosphere.
3. In the third group of 23 explosions, there was no emission of radioactivity into the atmosphere. The normalized depth of explosions of this group ranged widely: from 96 to 225 m/kt$^{1/3}$, and the gas content of the host rock reached 4 – 12%. With respect to these parameters, the explosions of this group were practically the same as for the first and second groups. In our opinion, the reason that gases did not escape into the atmosphere in this group of explosion was the sealing action of the upper sand-clay layer, along with a high-quality stemming system and the sealing of other components in the epicentral zone. Indeed, the only difference between these explosions and the first two groups was the presence of a thick layer of drift sediments, ranging from 25 to 90 m. For the explosions with release of radioactive by-products into the atmosphere, the thickness of the drift sediments was 3-30 m, with the exception of 10 shots for which this layer was 40-70 m thick. It is possible that sealing properties of this layer were disrupted for these explosions. Another possibility is lower quality of the stemming in these detonations.

The non-dimensional parameter $k_1/m\mu$ was estimated for a set of explosions at the Novaya Zemlya and Semipalatinsk Test Sites, using the measurements of breakthrough times t_0. The value of this parameter is plotted as a function of scaled DOB in Figure 9.11. The results can be divided in two groups: the values $k_1/m\mu = 5 \cdot 10^3$ to $7 \cdot 10^4$ D/cP, which correspond to a late/delayed gas release, and the values $k_1/m\mu = 10^5$ to 10^6 D/cp which correspond to an early gas release. Using the first more numerous group (~70% of all data points), we obtained empirical relationships as

$$k_1/m\mu = 7 \cdot 10^3 \text{ (D/cP) for W/q}^{1/3} \geq 120 \text{ m/kt}^{1/3}, \quad (9.25)$$

$$k_1/m\mu = 4.5 \cdot 10^6 \, exp(-0.05W/q^{1/3}) \text{ (D/cP) for W/q}^{1/3} < 120 \text{ m/kt}^{1/3},$$

shown in Figure 9.11 as a solid line. This group also includes the values $k_1/m\mu = (3 \text{ to } 7) \cdot 10^4$ D/cp, corresponding to the time of release (breakthrough of 10 – 20 min. The relationship 9.25 is very similar to the relationship 9.24 for the Novaya Zemlya Test Site for explosions with a scaled DOB in the range 90 – 120 m/kt$^{1/3}$.

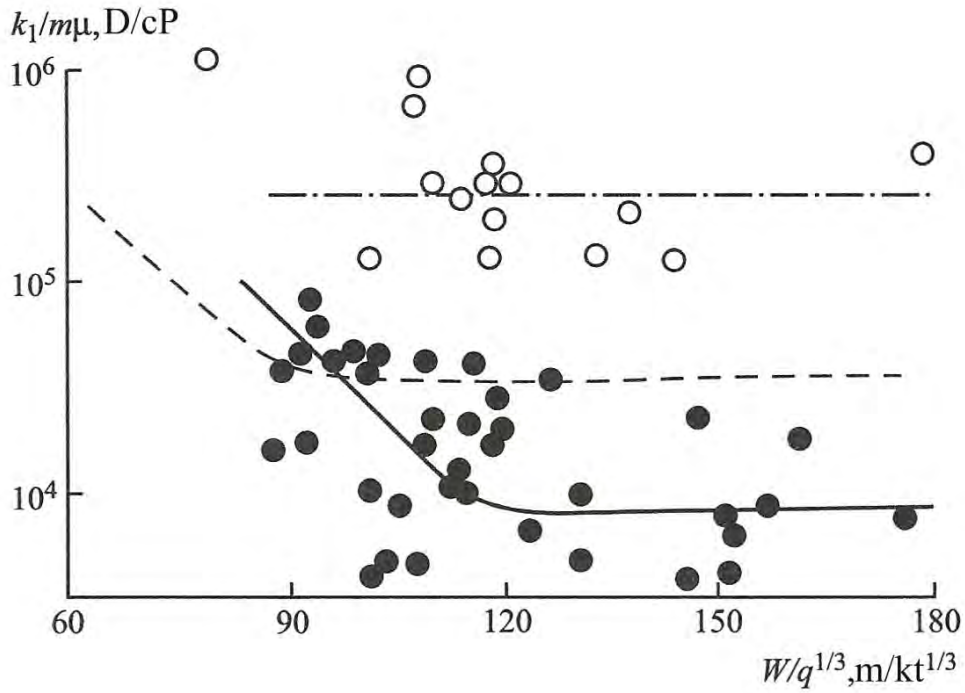

Figure 9.11: Gas transport parameters as a function of scaled DOB, for explosions conducted in boreholes at the STS (dashed line show the same relationship for NZTS).

For explosions with sDOB over 120 m/kt$^{1/3}$ the value of $k_1/m\mu$ for Semipalatinsk explosions is lower than for Novaya Zemlya explosions by almost an order of magnitude. This reduction in transport parameter is probably caused by the presence of a thick layer of drift sediments, ranging between 3 and 90 m. The sediments are mainly represented by pliable clay with low permeability, covered by sandy clays with a thickness of 2 – 5 m. For explosions with sDOB exceeding 120 m/kt$^{1/3}$ the ground uplift is insignificant, reaching 5 – 10 % of the DOB. For these explosions the sediment layer keeps its sealing properties and covers all geological discontinuities and fault zones. In these circumstances the release of radioactive gas occurred along man-made breaks (discontinuities) in the sediments (tubing casing annulus and inter-cable space, emplacement, and core holes, etc).

The second group of data points shown in Figure 9.11 was interpolated by the expression $k_1/m\mu = 2.5 \cdot 10^5$ (D/cP) and is shown as a dash dot line. This group corresponds to an early release of radioactive gases into the atmosphere (10 s – 5 min), which occurred mainly due to man-made discontinuities (pathways). It is hard to determine a correlation with the sDOB for this group. The transport parameter varies between 10^5 – 10^6 D/cp. At the Novaya Zemlya Test Site, similar values in the range $3 \cdot 10^5$ – 10^6 D/cp were characteristic for explosions with open tectonic faults and fractures, independent of the sDOB. Evidently, values in the range $k_1/m\mu \sim 10^5$ to 10^6 D/cp characterize gas transport through open artificial (man-made) channels (pathways) or through open tectonic faults. The possibility for this type of radioactive gas release should be considered separately from the transport through porous medium.

Table 9.8. Gas breakthrough times for explosions with different depths of burial (at STS)

Parameter	Tunnel number						
	13	A-5	B-2	17	1	A-p	11
$W/q^{1/3}$, m/kt$^{1/3}$	61	62	65	67	68	68.5	68
t_0	12 min	1.5 h	9 min	3.5 h	4.1 h	1 h	8 h

Parameter	Tunnel number						
	Z-5	14	Zh-3	Zh-1	19	Z-1	E-1
$W/q^{1/3}$, m/kt$^{1/3}$	70	70.5	72	72	72	74	59
t_0	14 h	2.5 h	3.3 h	3.5 h	5 h	18 h	24 h

Table 9.9. Gas breakthrough times for explosions with different depths of burial (at STS)

Parameter	Tunnel number					
	A-4	A	Zh-2	A-III	B-1	Z-3
$W/q^{1/3}$, m/kt$^{1/3}$	87	91	92	93.5	97	133
t_0	130 h	30 h	Several days	14 h	3.5 h	18 h

No pressurized gas release (venting) was observed during nuclear tests conducted at the Degelen Testing Area of the Semipalatinsk Test Site. This is probably due to the extremely low gas content of the granites and quartzite porphyries comprising the main rock mass at Degelen. For these rocks, gas can form only by evaporation of free water contained in pores and cracks of the rock mass. The moisture content of these rocks is generally low, ranging from 0.03% to 1.7%. Therefore, despite relatively small cavity sizes ($\bar{r}_c = 7$ to 9 m/kt$^{1/3}$), the excess pressure from water vapor in the shot cavity after condensation of rock vaporized by the nuclear explosion reached 1.2 – 3 kgf/cm^2 (1.2 to 3 atmospheres), and the water vapor could be accommodated by the fractures and pore space. Flow of vapor is also accompanied by its condensation due to cooling.

Only the first few experiments located on the mountain slopes with sDOB of 60 – 75 m/kt$^{1/3}$ resulted in craters of considerable size (radius of 0.3 – 0.4 *W*, and depth of 0.15 – 0.2 *W*). This

significantly reduced the thickness of rock above the charge; therefore the time before arrival of radioactive gases was between 10 min and several hours (Table 9.8). There were no more than 10 tests like this.

In later experiments at Degelen the scaled DOB were greater than 75 m/kt$^{1/3}$ to prevent crater formation. Times t0 of emergence of radioactive gases under these conditions were on the order of hours or days, and for some tests there was no radioactive gas release at all (Table 9.9).

Evidently the excess pressure of water vapor in the shot cavity was insufficient for pressurized flow, and radioactive gas transport was due to thermal diffusion. In such a situation, slow displacement of warm gases upward through cracks in the rock mass was aided by a "furnace effect" due to the difference in atmospheric pressure on the level of the tunnel and the upper section of the slope. In many cases, emergence of radioactive gases into the atmosphere was due to a change of atmospheric pressure. In this case the first occurrence of radioactivity was noted either in the epicenter (at ground zero) of the explosion or at the mouth of the tunnel.

The transport parameter $k_1/m\mu$ (see 9.25) for both the Novaya Zemlya Test Site (9.24) and the Semipalatinks Test Site, represents an integral characteristic of transport properties through hard rock deformed by a contained explosion. Using empirical values of the parameter $k_1/m\mu$ via (9.24) and (9.25), we determined corresponding values of the permeability coefficient k1 for typical values of porosity $m = 0.04$ and gas viscosity $\mu = 2\cdot10^{-4}$ Pa·s. The value of permeability thus obtained is $k_1 = 1\text{to}\ 10^2$ Darcy (we note that $k_1 = 10^3\text{to}10^4$ Darcy corresponds to gas movement through open faults and fractures and man-made pathways of the rock mass). For $k_1 = 1\text{to}\ 10^2$ Darcy we can determine the value of the turbulent permeability $k_2 = 10^{-3}\text{to}10^{-5}$ Darcy and the non-dimensional parameter $\alpha = 0.1$ to 10 using Equation 9.7. Therefore the value of $\alpha = 1$, used earlier to solve a transport problem, agrees with the data for gas movement for contained explosions.

Figure 9.12 shows resulting values of the permeability coefficient, compared with permeability measurements of rock massifs damaged by explosions. The permeability measurements for apatites and rock piles, for boreholes 1003, 125 and T-3, are lower by one or two orders of magnitude than theoretical values derived from Equations 9.24 and 9.25. For explosions HOGGAR and HARDHAT the measured permeability is three to five orders of magnitude lower than theoretical values. These differences could be caused by the fact that for these two explosions the permeabilities were measured locally on a small scale, so the effect of large faults and fractures were not taken, into account.

In this section we have obtained an overall permeability, determined on a scale equal to the explosion depth. For explosions with scaled DOB over 90 – 120 m/kt$^{1/3}$ the overall permeability is nearly a constant. For larger depth of burial the intensity of damage near the surface is reduced, and instead of a system of small chaotic fractures, large open channels along tectonic faults or artificial pathways are formed. As a result, gas transport changes, in this part of the rock massif, becoming a direct flow of gas into the atmosphere. Therefore, a further increase in sDOB of nuclear charges is ineffective for achieving an increase in the time of gas release to the surface.

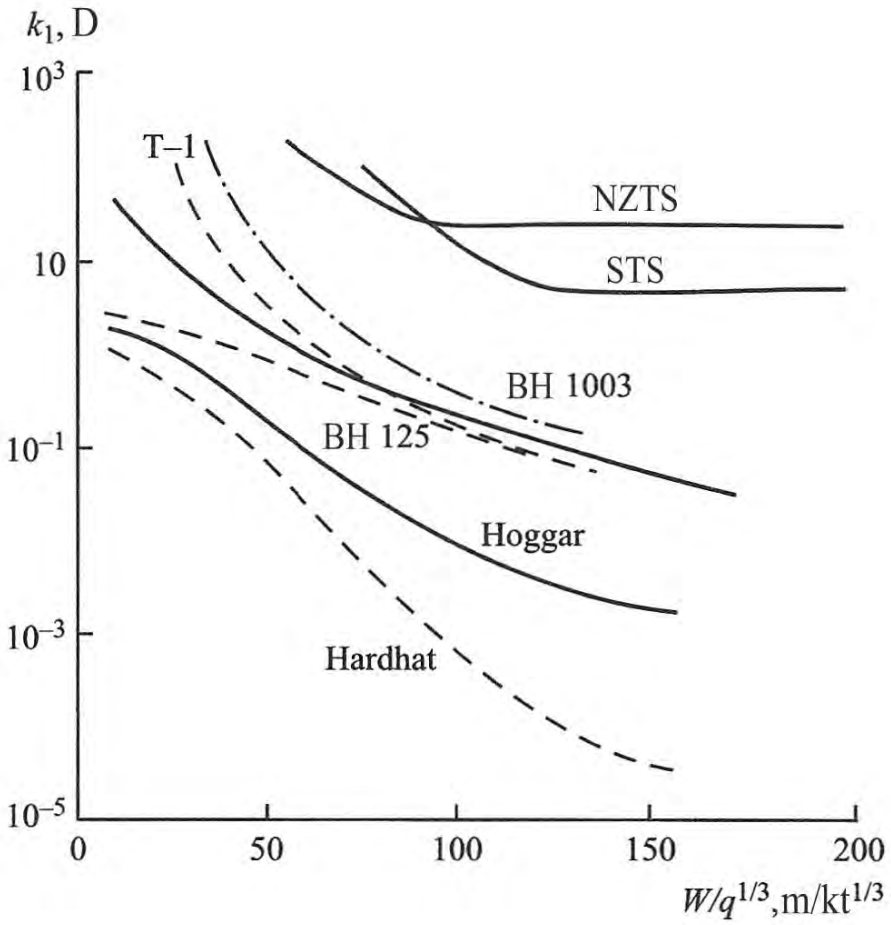

Figure 9.12: Changes in permeability coefficient with distance from the center of explosion. (See text for explanations.)

9.4. Effect of the explosion size and rock properties on gas breakthrough times

By solving the problem of non-stationary gas transport, we have obtained an estimate of the time it takes for radioactive gas to reach the surface — depending on the explosion yield and depth, for different emplacement conditions. To make this estimate it is necessary to know the cavity size, the excess pressure of non-condensable gas, and the porosity and permeability of the rocks involved. For NZTS, where rocks are represented by shales, sandstones and quartzites with gas content varying between 2 and 12%, the range of pressure of non-condensable gases in the explosive cavity is 0.5 – 3 MPa. In this case, assuming the average porosity is $m = 0.04$, it follows from the solution to the transport problem 9.14 that

$$\tau = 0.16(x-1)^{2.6}\ . \qquad (9.26)$$

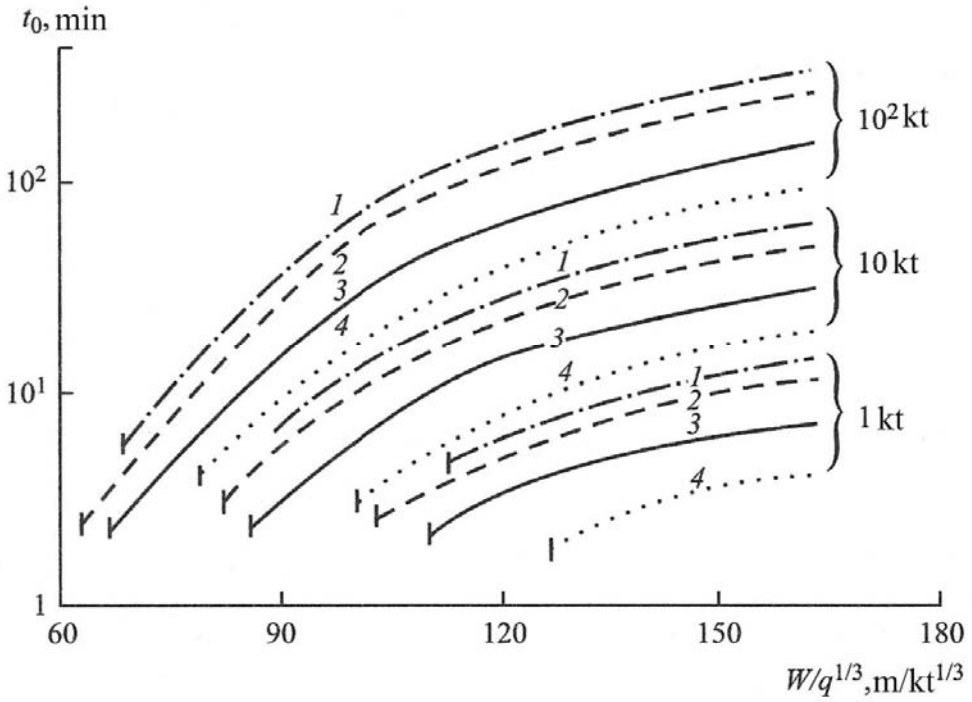

Figure 9.13: Effect of the explosion yield on gas breakthrough time for NZTS for the following rock types: *1* – quartzite, *2* – sandstone, *3* – shale, *4* – limestone.

In cases where nuclear charges were placed in limestones with gas content of 40 – 44 %, the excess pressure of carbon dioxide varies between 5 and 15 MPa. In this case Equation 9.14 can be written as

$$\tau = 0.2(x-1)^{2.9}\,. \tag{9.27}$$

After substitution of non-dimensional parameters 9.7 into Equation 9.26 and 9.27, we obtain the relationship between gas venting time and the yield and depth for the explosion in shales, sandstones and quartzites:

$$\frac{t_0}{q^{2/3}} = 26.7\,\frac{m\mu}{k_1 P_*}\left(\frac{r_c}{q^{1/3}}\right)^2\left(\frac{W}{r_c}-1\right)^{2.9}\,. \tag{9.28}$$

For limestones this expression is

$$\frac{t_0}{q^{2/3}} = 33.3\,\frac{m\mu}{k_1 P_*}\left(\frac{r_c}{q^{1/3}}\right)^2\left(\frac{W}{r_c}-1\right)^{2.9}\,, \tag{9.29}$$

where t_0 is time in minutes, q is yield in kt, r_c is in meters, k_1 is in Darcy, μ is in cP, and P_* is in kgf/cm^2. The parameter $k_1/m\mu$ is determined by the explosion sDOB according to (9.24). The cavity radius r_c and the excess gas pressure are determined by the rock properties including elastic moduli, strength, and gas content. Figure 9.13 shows gas release times as a function of

sDOB and yield of explosions, for major rock types at NZTS. The physical and gas-forming properties of rocks are shown in Table 9.10.

Table 9.10. Characteristic rock properties at the NZTS

Rock type	Parameter					
	ρ, g/cm^3	C_p, m/s	σ_*, MPa	η	$\bar{r}_c$, m/kt$^{1/3}$	P_*, MPa
Shale	2.7	5200	70	0.08	11.1	1.02 – 2.35
Sandstone	2.7	4000	90	0.04	11.1	0.83 – 1.19
Quartzite	2.7	5400	180	0.02	8.8	0.58 – 1.23
Limestone	2.75	5700	140	0.43	9.3	8.95

Variations of pressure P_* for a fixed cavity radius and gas content are due to a change in the chemical composition of non-condensable gases, from carbon dioxide to water vapor. Plots in Figure 9.13 are presented assuming equality between the major components of gas formation ($\eta_\omega + \eta_{H2O} = \eta_{CO2}$), for shales, sandstones and quartzites. The water content for each rock was 0.1%. The most favorable conditions for increase of the gas release times are for quartzites and sandstones. For explosions in quartzites and sandstones, the gas release times are twice as long as for explosions in limestone, if other emplacement conditions are the same. An increase in the explosion yield by an order of magnitude while keeping other parameters the same results in an increase in gas release times by a factor of 5.

For explosions with sDOB $W/q^{1/3} \geq 95$ m/kt$^{1/3}$ at NZTS, the parameter $k_1/m\mu = 3 \cdot 10^4$ D/cp, and so relationships 9.28 and 9.29 can be simplified for the rocks shown in Table 9.10. Thus for shales and sandstones we have

$$t_0 = 10.9 \cdot 10^{-2} \frac{q^{2/3} m\mu}{P_*} \left(\frac{W}{r_c} - 1\right)^{2.6},$$

for quartzites:

$$t_0 = 6.9 \cdot 10^{-2} \frac{q^{2/3} m\mu}{P_*} \left(\frac{W}{r_c} - 1\right)^{2.6}, \tag{9.30}$$

and for limestones:

$$t_0 = 9.6 \cdot 10^{-2} \frac{q^{2/3} m\mu}{P_*} \left(\frac{W}{r_c} - 1\right)^{2.9}.$$

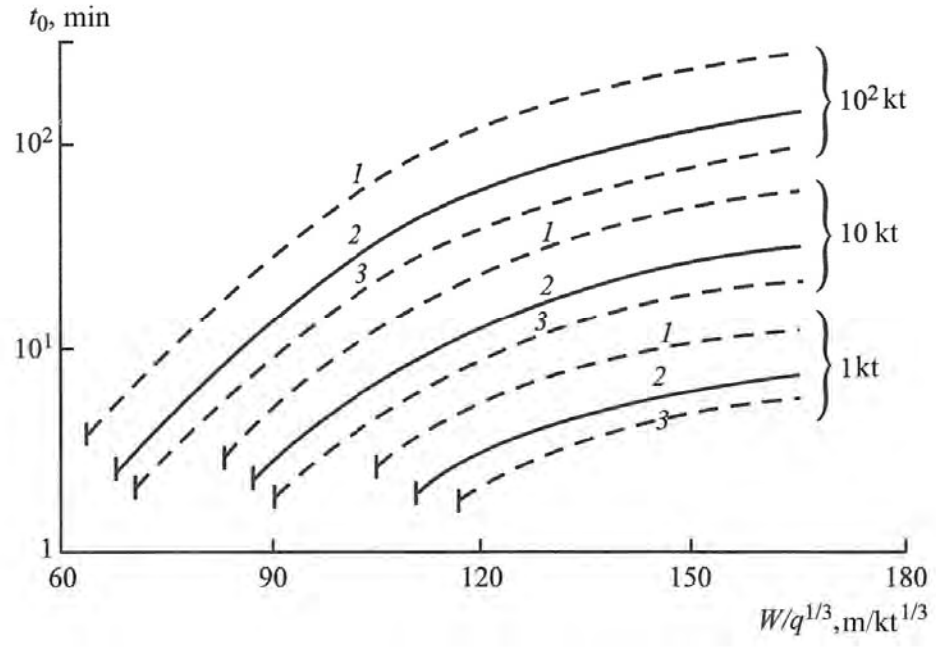

Figure 9.14: Effect of shale gas content on gas breakthrough time for NZTS, for the following values of gas content η: *1* – 0.04, *2* – 0.08, *3* – 0.12.

Shales are the most common rocks at NZTS. The gas content for shales depends on their mineralogical composition and varies over a wide range, from 3 – 4 % (clay-rich and mica-rich shales) to 15 – 20 % (carboniferous and carbonate-rich shales). The effect of shale gas content on the venting times for explosions of different yields is shown in Figure 9.14. For fixed rock properties and explosion yield, a reduction in gas content from 8 to 4% causes an increase in venting time by a factor of 2. Increasing the gas content from 8 to 12% reduces the time by a factor of 1.5. We obtain the relationship between gas venting time and explosion yield and DOB, for nuclear explosions in shales, using Equation 9.30 and substituting Equation 9.22:

$$t_0 = 1.76 \cdot 10^{-4} \frac{q^{2/3} m \mu}{\eta_e} \left(\frac{W}{r_c} - 1\right)^{2.6}, \tag{9.31}$$

for $\bar{r}_c = 11.1$ m/kt$^{1/3}$, $m = 0.04$, and $\mu = 2 \cdot 10^{-4}$ P.

It follows from 9.31 that the venting time is inversely proportional to rock gas content. Moreover, an increase in gas content increases the effect of the proportion of each gas component, on gas venting times.

The testing areas Balapan and Murzhik of the STS are characterized by a wide range of mechanical and gas-forming properties of rocks. The density varies between 2.5 and 2.85 g/cm^3, compressive strength between 10 and 200 MPa, P velocities between 3 and 6.5 km/s, and gas content between 1 and 20 %. Therefore the cavity radius varies in the range 8 – 14 m/kt$^{1/3}$, while the excess gas pressure changes between 1 and 8 MPa. In these circumstances the following

relationship (based on Equation 9.14) should be used to estimate gas venting venting times using a rock porosity value of $m = 0.04$:

$$\tau = 0.18(x-1)^{2.7} . \tag{9.32}$$

Substitution of non-dimensional parameters 9.7 yields:

$$\frac{t_0}{q^{2/3}} = 30\frac{m\mu}{k_1 P_*}\left(\frac{r_c}{q^{1/3}}\right)^2\left(\frac{W}{r_c}-1\right)^{2.7} , \tag{9.33}$$

where t_0 is time in minutes, q is yield in kt, r_c is in meters, k_1 is in Darcy, μ is in cP, and P_* is in kgf/cm^2.

In Equation 9.33 the parameter $k_1/m\mu$ depends on explosion sDOB according to relationship 9.25. To determine a cavity radius and excess gas pressure in it we select three main types of rocks (out of a wide variety of rock properties) in which the explosions were conducted at the STS (Table 9.11).

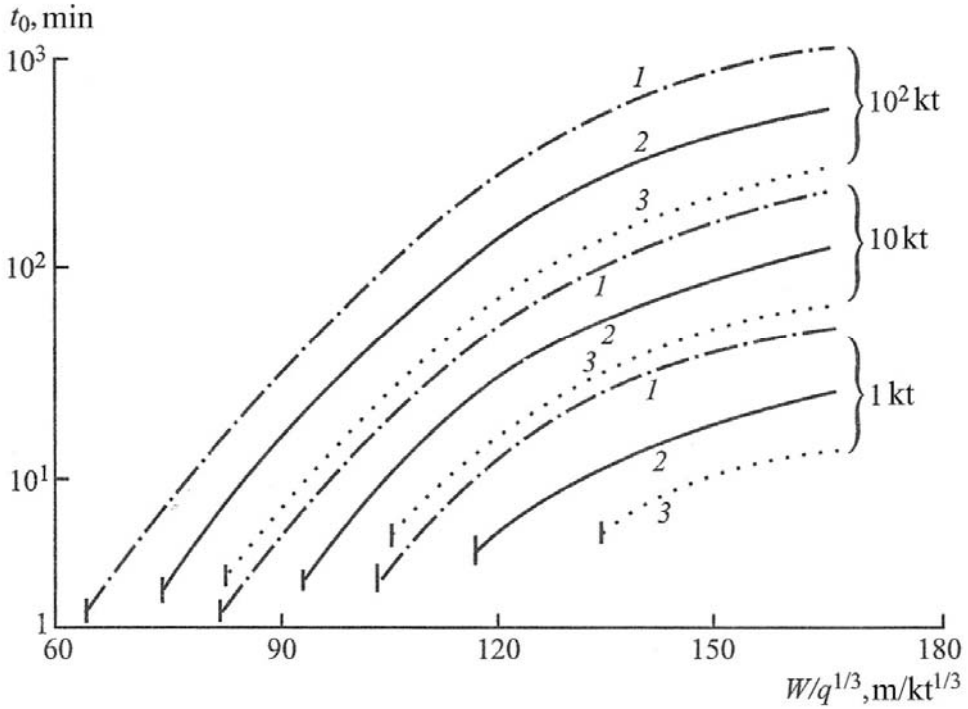

Figure 9.15: Effect of the explosion yield on gas breakthrough time for Balapan and Murzhik testing areas of the STS, for the following rock types: *1* – conglomerate, *2* – alevrolite (shale), *3* – tuff-sandstone.

The names of the rocks in Table 9.11 are somewhat general (i.e., not precise). The first type (conglomerate) includes rocks with relatively low strength and low gas content. The properties for rocks that belong to the second type (shale) are the most common for the area. The third type (tuff-sandstone) includes rocks with high strength and high gas content. Figure 9.15 shows breakthrough times as a function of sDOB and yield of explosions, for rock types shown in Table

9.11 assuming that the content of carbon dioxide and of water vapor are equal ($\eta_\omega + \eta_{H2O} = \eta_{CO2}$), and that moisture content is 1%. For explosions in rocks with low values of strength and gas content, the breakthrough times are 2 – 2.5 times longer than in rock with the most typical properties. For explosions in rocks with high strength and high gas content, the breakthrough times decrease by a factor of 1.5 – 2 compared to the (most) typical rocks.

Table 9.11. Characteristic rock properties at the STS

Rock type	Parameter					
	ρ, g/cm^3	C_p, m/s	σ_*, MPa	η	$\bar{r}_c$, m/kt$^{1/3}$	P_*, MPa
Conglomerate	2.6	4500	50	0.06	12.3	0.87 – 1.49
Alevrolite (shale)	2.6	5200	70	0.12	11.1	1.9 – 3.77
Tuff-sandstone	2.6	5400	150	0.18	9.3	4.4 – 9.39

For explosions with sDOB W/q $^{1/3} \geq 120$ m/kt$^{1/3}$ in STS boreholes, the parameter $k_1/m\mu = 7 \cdot 10^3$ D/cp, therefore relationships 9.33, after taking into account the results from Table 9.11, can be simplified. For conglomerate we have:

$$t_0 = 0.76 \frac{q^{2/3}}{P_*} \left(\frac{W}{r_c} - 1\right)^{2.7},$$

for shales:

$$t_0 = 0.53 \frac{q^{2/3}}{P_*} \left(\frac{W}{r_c} - 1\right)^{2.6}, \tag{9.34}$$

and for tuff – sandstone we have:

$$t_0 = 0.33 \frac{q^{2/3}}{P_*} \left(\frac{W}{r_c} - 1\right)^{2.9}.$$

To estimate the gas breakthrough times for explosions with sDOB of $W/q^{1/3} \geq 120$ m/kt$^{1/3}$ conducted in STS boreholes, it is convenient to transform Equation 9.33 by substituting expression 9.22 for the excess gas pressure and using the porosity $m = 0.04$ and viscosity μ = $2 \cdot 10^{-4}$ P:

$$t_0 = 5.1 \cdot 10^{-9} \frac{q^{2/3}}{\eta_e} \left(\frac{r_c}{q^{1/3}}\right)^5 \left(\frac{W}{r_c} - 1\right)^{2.6}. \tag{9.35}$$

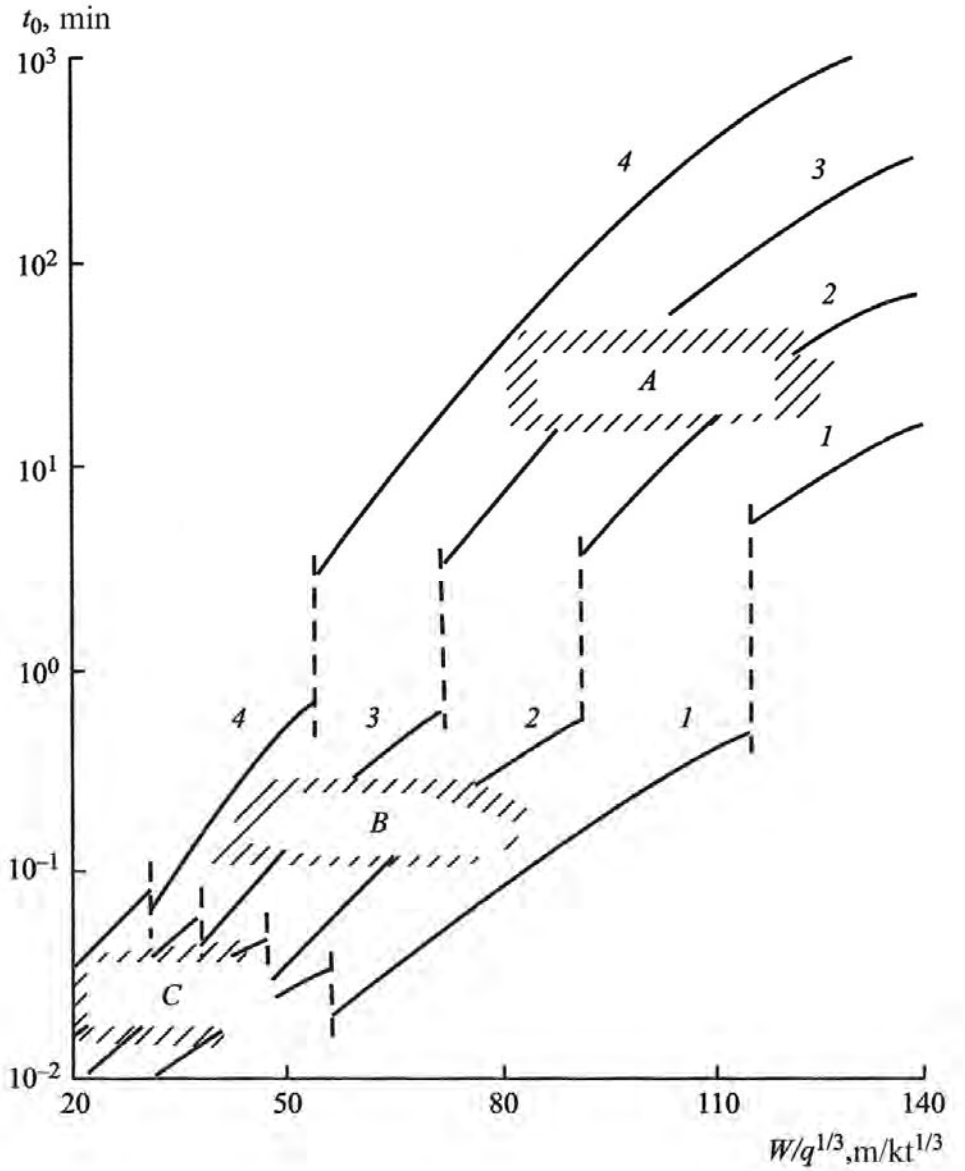

Figure 9.16: Gas breakthrough times as a function of sDOB for explosions conducted in shales at the STS, for fully contained explosions (A), partially contained explosions (B), and cratering (ejection) explosions (C). The lines correspond to explosions with different yields q in kt: *1* – 1, *2* – 10, *3* – 100, *4* – 1000.

It follows from 9.35 that breakthrough times are inversely proportional to rock gas content, but decrease significantly when cavity radius is reduced. It follows that radiation effects from explosions in rocks with high strength and high gas content require special attention.

Other types of explosion conducted in the Balapan and Murzhik testing areas of STS included cratering — that is, excavation explosions and partially contained explosions. Let us consider the time of gas appearance at the surface, for a broad range of sDOB. This relationship is shown in Figure 9.16 for explosions with different yields, for rocks with typical properties

(shales from Table 9.11). Vertical dashed lines show the boundaries between the sDOB values for fully contained, partially contained, and excavation explosions.

Notice that the functions have discontinuities at the boundaries between the explosion types, due to different mechanisms of gas transport: venting through the uplift for the excavation explosions, "floating" of the cavity upward for the partially contained explosions, and filtering through damaged rocks due to excess pressure in the cavity for fully contained explosions.

The common thread for all transport regimes is the effect of the yield of explosion on the breakthrough times. We also note a significant decrease in breakthrough times (by a factor of 4 to 10 for the yield range $1 \le q \le 10^3$ kt), with the change of transport regime from fully to partially contained explosions. This regime change can probably explain early gas venting for some explosions conducted in vertical shafts at the STS, which were planned as fully contained, but ended up as partially contained due to high rock gas content and the large scale of these explosions.

9.5. Minimal and minimum allowed depth for fully contained explosions

For the range of fully contained explosions two characteristic (scaled) depths can be selected: the minimum depth which separates fully and partially contained explosions, and the minimum allowable depth which provides sufficient containment to fulfill the requirements of radiation containment (the Limited Test Ban Treaty of 1963). To determine a minimal depth W_c needed to provide full containment, we use a previously-determined relationship, Eq. 3.3, to find this depth as a function of explosion yield, q:

$$(\rho r W_k + P_a) = 0.86 \frac{\xi q}{r_c}. \tag{9.36}$$

Replacing the coefficient of efficiency via $\xi = A/q$ from Equation 2.36, and denoting the specific weight of rock above the charge as $\gamma = \rho g$, we rewrite 9.36 in a form useful for practical calculations:

$$(\gamma W_c + 10) W_c^2 = 1.8 \cdot 10^8 \left(\frac{r_c}{q^{1/3}}\right)^{-1.84} (1 + 5.8 {\eta_e}^{0.7}) q^{0.67} \ , \tag{9.37}$$

where W_c is depth in meters, q is yield in kt, γ is in g/cm^2, r_c is in meters, and η_e is gas content.

If $\rho r W_c \gg P_a$ then Equation 9.37 can be simplified:

$$\frac{W_c}{q^{1/3}} = \frac{565}{q^{1/9}} \left(\frac{1 + 5.8 {\eta_e}^{0.7}}{\gamma} \left(\frac{r_c}{q^{1/3}}\right)^{-1.84} \right)^{1/3} \ , \tag{9.38}$$

It follows from Equations 9.36 – 9.38 that the minimum depth needed)for full containment does not satisfy the "law of geometrical similarity" (that is, the $q^{1/3}$ scaling law). The relationships between minimal depth W_c and the explosion yield and rock gas content, are shown in Figure 9.17 a-b. Figure 9.17a also shows the boundary between the fully and partially

contained explosions, marked as W_*. The exponent for the minimum DOB decreases with yield increase (according to $W_* \sim q^{0.24}$, $W_c \sim q^{0.22}$), and increases with an increase in rock gas content, particularly for smaller values of gas content up to 5 – 10 %.

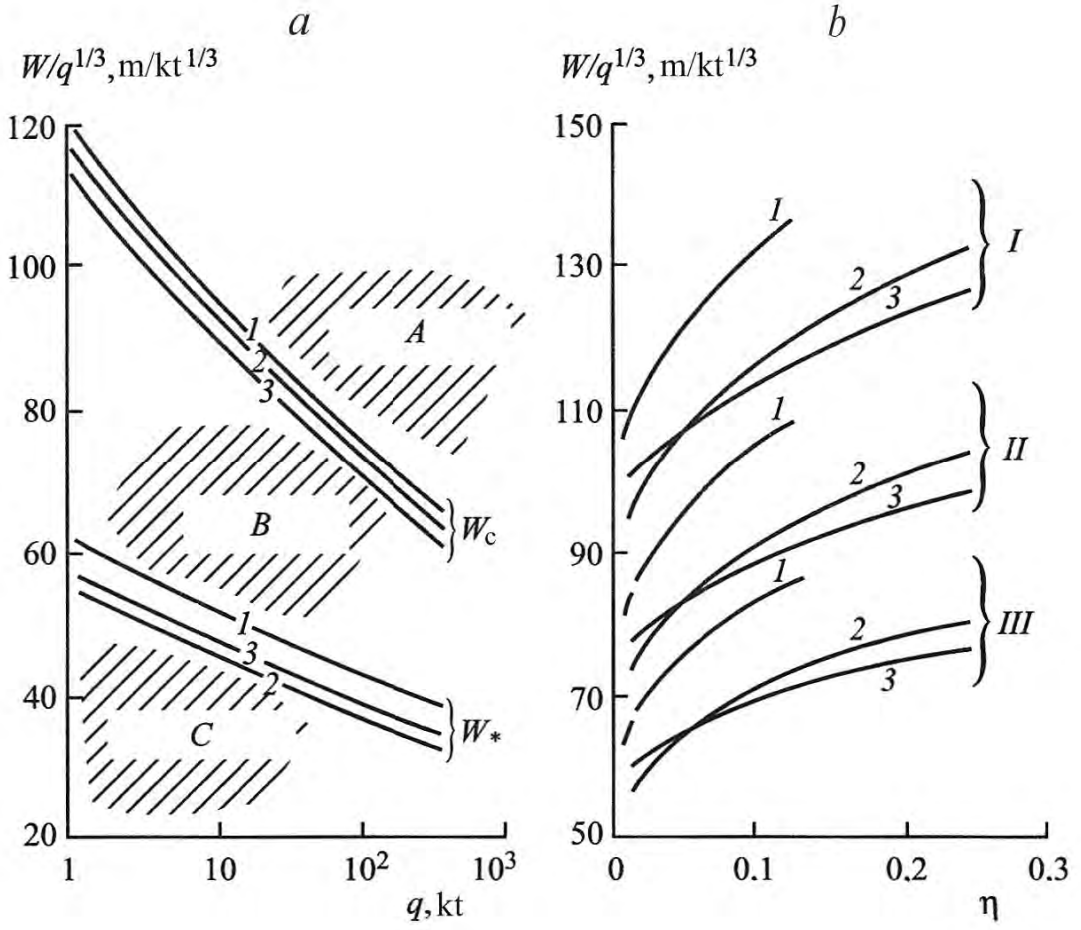

Figure 9.17: Minimal depth required for explosions to be fully contained, as a function of a) yield, and b) rock gas content for the following rock types: *1* – alluvium (γ = 1.6 g/cm^3, $\bar{r}_c = 15$ m/kt$^{1/3}$, η_ω=0.12); *2* – granite (γ =2.67 g/cm^3, $\bar{r}_c = 8.8$ m/kt$^{1/3}$, η_ω=0.03); *3* – alevrolite (shale?) (γ =2.6 g/cm^3, $\bar{r}_c =$ 11.1 m/kt$^{1/3}$, η_ω=0.12, $\eta_{H2O} = \eta_{CO2}$). The explosion yields are coded using roman numerals: I – 1 kt, II – 10 kt, and III – 100 kt. The letters A-C are used in same way as in 9.16.

The minimum allowed depth is determined in order to make sure that the concentration of long-lived radionuclides in the atmosphere after the explosion does not exceed global background values outside of national borders. In order to fulfill this requirement, the rate of escape, depending on the initial time of breakthrough, and the total amount of radionuclides, depending on the yield of the charge, should not exceed a certain limit (threshold).

Based on the allowed concentration of radioactive aerosols in the atmosphere, the relationship between the explosion yield and the allowable breakthrough time was determined. The relationship takes into account the time of formation of secondary aerosols, and the dilution

of the radioactive cloud during its movement within the national territory. The relationship between the initial breakthrough time of radioactive explosion by-products into atmosphere, and yield, is shown below:

Explosion yield	Allowed time, min
1	7 - 10
10	10 – 15
100	17 – 25
250	25 – 30
500	30 – 35
1000	35 – 40

To determine the minimum allowed depth of burial for the STS and NZTS we assume that the beginning of radioactive gas release into the atmosphere started at the minimum allowed time, and use rock properties characteristic for these regions (rock strength, elastic parameters, gas content, and filtering properties – porosity and permeability). In order to do so we use relationships 9.26 – 9.35 which show the dependence of gas venting time on the yield and DOB, under the specific conditions of the test.

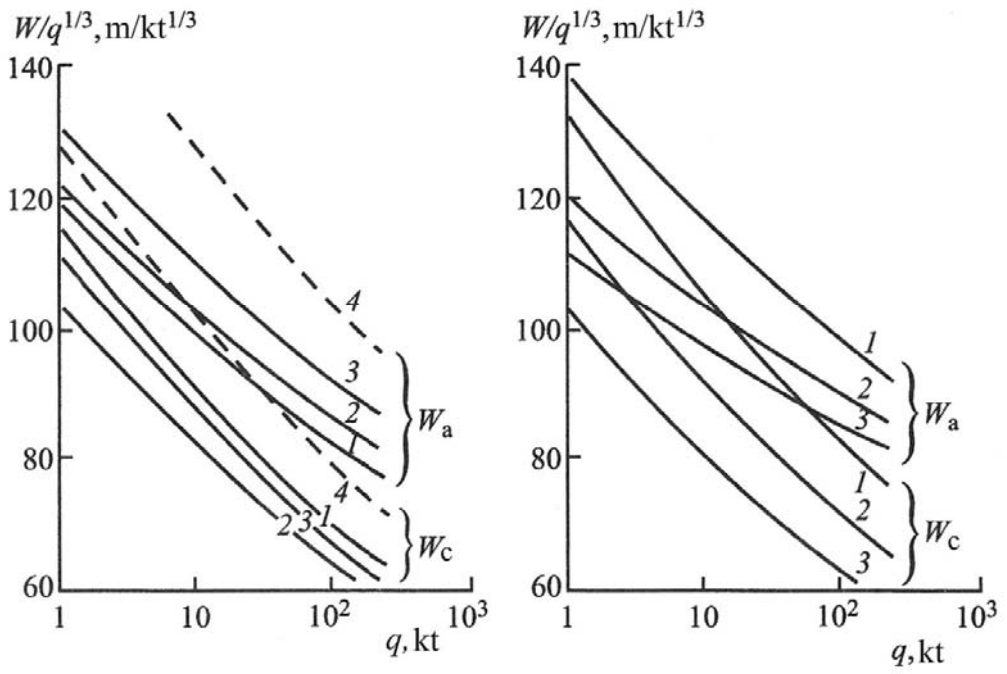

Figure 9.18: Minimum allowed W_a and minimal W_c depths, for fully contained explosions as a function of yield: a) for the NZTS for the following rock types: *1* – quartzite, *2* – sandstone, *3* – shale, *4* – limestone; and b) for the STS, for the following rock types: *1* – tuff-sandstone, *2* – alevrolite (shale), *3* – conglomerate.

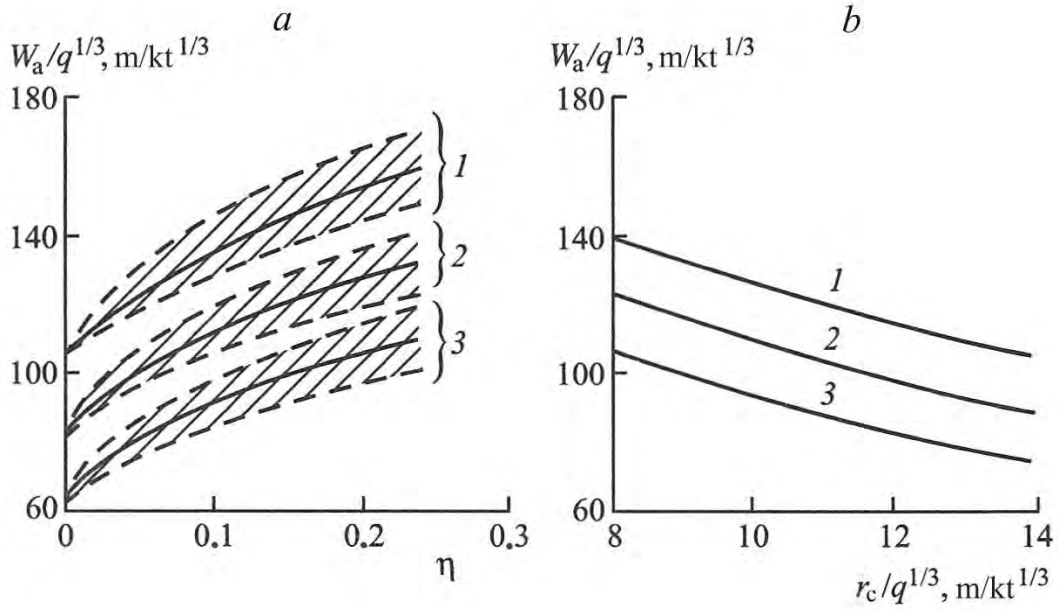

Figure 9.19: a) Effect of gas content and its main components, on minimum allowed W_a depth for fully contained explosions conducted in shales at the NZTS. b) Effect of the cavity radius on minimum allowed depth W_a, for fully contained explosions conducted in alevrolites (shales) at the STS. The lines correspond to explosions with different yields q in kt: *1* – 1, *2* – 10, *3* –100.

The determination of the minimally allowed depth of burial W_a for NZTS, using material properties from Table 9.11, are shown in Figure 9.18 a,b. Also shown is the minimum depth for a fully contained explosion W_c. According to the plots, scaled characteristic depths (normalized by $q^{1/3}$), required to achieve full containment, depend significantly on the explosion yield ($W_a \sim q^{0.26}$). For $q \sim$ 1kt the minimum and minimum allowed depths are similar. As the yield increases, so do the differences between these depths.

The relationships between minimally allowed depth and rock gas content, and physical properties, were investigated using formulas 9.26 – 9.35. Figure 9.19 shows the effect of gas content and the ratio between gas components, on the minimum allowed depth for shales of NZTS ($\bar{r}_c = 11.1$ m/kt$^{1/3}$). The lines in the middle correspond to equal amounts of the main gas components $\eta_\omega = \eta_{CO2}$, the upper dashed lines correspond to $\eta = \eta_\omega$, and the lower dashed line to $\eta = \eta_{CO2}$. The effect of the scaled cavity radius on minimum allowed depth is illustrated in Figure 9.19b for shales with $\eta = 0.12$, which typify STS. Calculating minimally allowed depth, as a function of explosion yield and rock properties, produced the following approximate formula:

$$\frac{W_c}{q^{1/3}} = \frac{B}{q^{0.07}}\left(\frac{1+5.8{\eta_e}^{0.7}}{\gamma}\left(\frac{r_c}{q^{1/3}}\right)^{-1.6}\right)^{1/3}, \qquad (9.39)$$

where B = 530 for typical conditions at the NZTS, and B = 480 for the STS. If accurate calculations are necessary then Equations 9.26 – 9.35 should be used in combination with specific data on yield and energy density, rock properties, and minimum allowed time for gas release into the atmosphere.

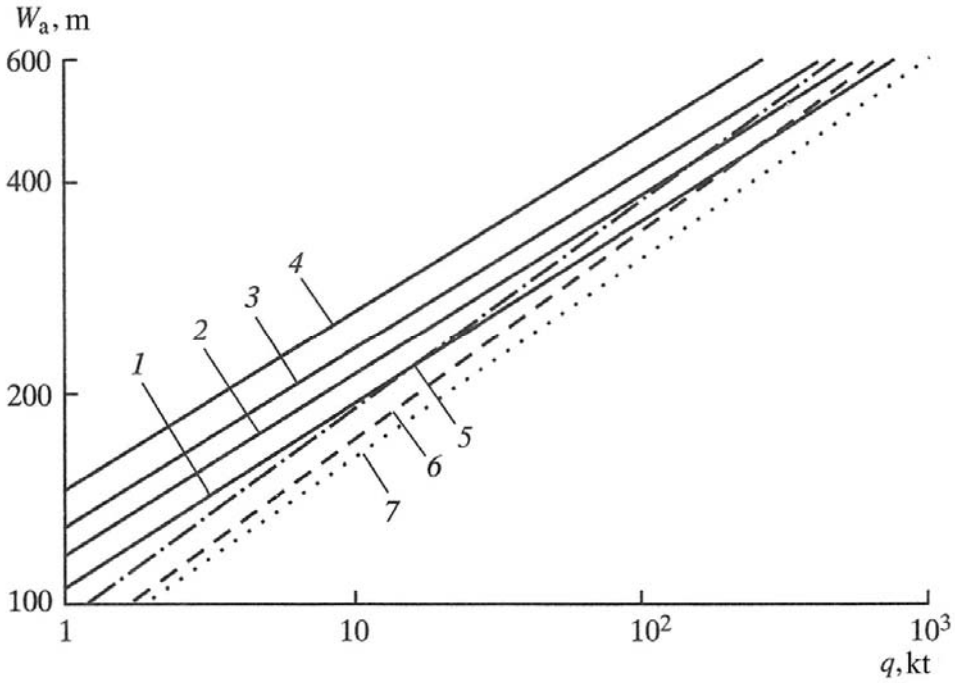

Figure 9.20: Minimum allowed depth W_a for fully contained explosions, as a function of yield for the NZTS for the following rock types: *1* – quartzite, *2* – sandstone, *3* – shale, *4* – limestone; *5* – $W_a = 95q^{1/3.4}$ (m); *6* – $W_a = A(\eta)q^{1/3.6}$ (m); and *7* – $W_a = 85q^{1/3.6}$ (m).

Let us compare the values of minimally-allowed depths of burial, for nuclear explosions with corresponding relationships used at NZTS and STS. Figure 9.20 shows such comparison for tunnel explosions of NZTS for rock properties shown in Tale 9.10. Typically the minimally allowed DOB is determined using a formula that ignores rock gas content:

$$W_a = 95q^{1/3.4} \text{ (m)}, \tag{9.40}$$

where q is in kt.

During the earlier stages of nuclear testing, the minimum allowed depth was determined using the formula

$$W_a = 85q^{1/3.6} \text{ (m)}, \tag{9.41}$$

where q is in kt.

Later, using the experience of earlier nuclear testing, a coefficient depending on rock gas content was inserted into the formula (9.41):

$$W_a = A(\eta)q^{1/3.6} \text{ (m)}, \tag{9.42}$$

where q is in kt.

Formula 9.42 was used for explosions conducted in limestones or carboniferous shales. Comparison between the calculations using Equations 9.40 – 9.42 and Equation 9.39 show that these calculations are in a good agreement for explosions in quartzites and sandstones.

The minimally-allowed depth of burial of explosions conducted in boreholes at the STS was determined using relationships that account for rock gas content:

$$W_a = 110q^{1/3.4} \text{ (m) for } 0 \le \eta \le 6\%,$$

$$W_a = 110q^{1/3.4}\left(\frac{1+0.36}{3.16}\right)^{1/3.4} \text{ (m) for } 6\% \le \eta \le 15\%, \tag{9.43}$$

where q is in kt.

Comparison between formula 9.43 for gas content of 6% and 12%, with the minimally allowed DOB using the equation developed in this work using the rock properties from Table 9.11, is shown in Figure 9.21. Overall, the results show good agreement, and therefore can be viewed as a validation. We conclude that relationships for calculation of the minimally-allowed DOB of nuclear charges, based on studies of radioactive gas migration according to the explosion, can be used to account for gas content, strength, and elastic properties of the emplacement rocks.

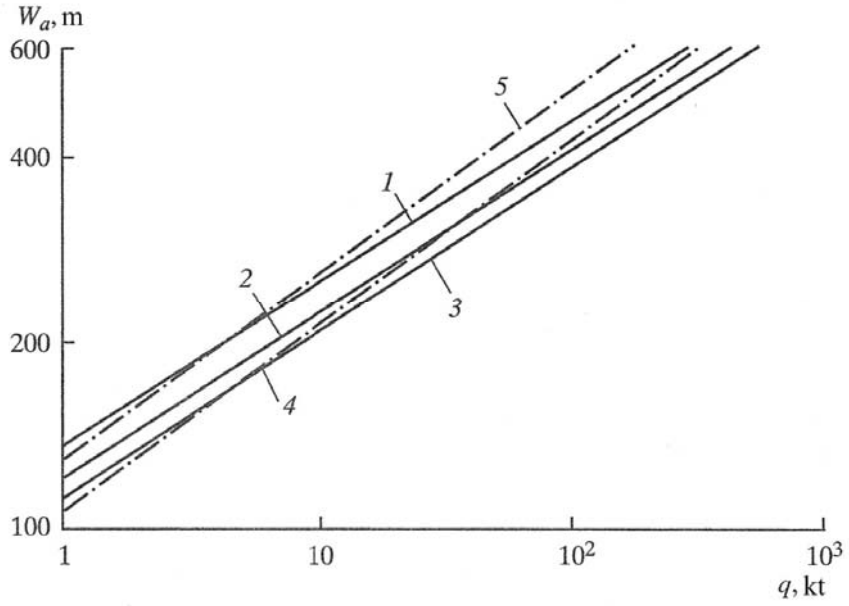

Figure 9.21. Minimum allowed depth W_a for fully contained explosions as a function of yield for the STS (Balapan and Murzhik testing areas), for the following rock types: *1* – tuff-sandstone, *2* – alevrolite (shale), *3* – conglomerate; *4* – $W_a = 110q^{1/3.4}$ (m); and *5* – $W_a = 110q^{1/3.4}\left(\frac{1+0.36}{3.16}\right)^{1/3.4}$ (m).

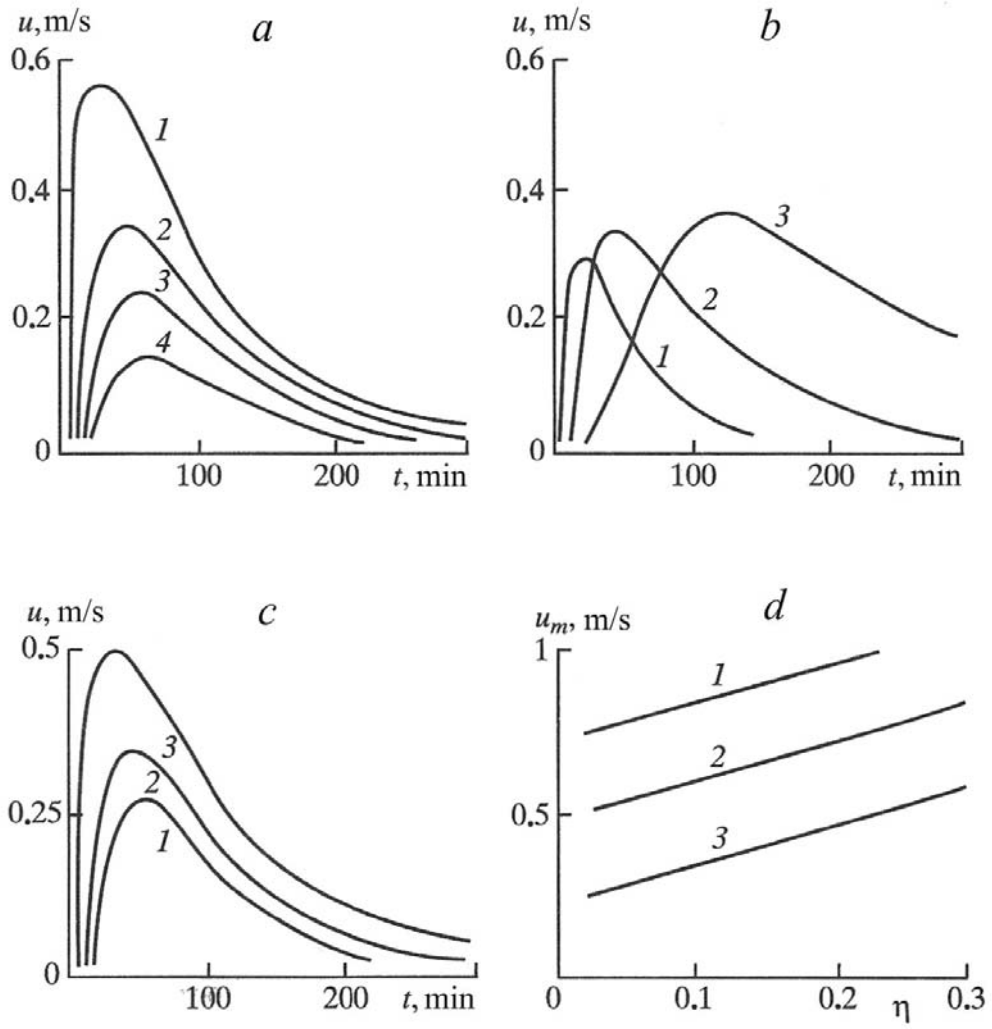

Figure 9.22: Gas flow dynamics for nuclear explosions conducted at the NZTS: a) q = 100 kt for $W/q^{1/3}$ = 80 m/kt$^{1/3}$ for the rock types: *1* – limestone, *2* – shale, *3* – sandstone, *4* – quartzite; b) effect of the explosion yield: *1* – q =10 kt with $W/q^{1/3}$ = 100 m/kt$^{1/3}$, *2* – q =10^3 kt with $W/q^{1/3}$ = 80 m/kt$^{1/3}$, *3* – q =10^3 kt with $W/q^{1/3}$ = 70 m/kt$^{1/3}$; d) effect of gas content (q =100 kt with $W/q^{1/3}$ = 80 m/kt$^{1/3}$) for η: *1* – 0.04, *2* – 0.08, *3* – 0.12; c) effect of gas content on maximum flow velocity for different yield: *1* – 1kt, *2* – 10 kt, *3* –100 kt ($W/q^{1/3}$ = 80 m/kt$^{1/3}$).

9.6. Dynamics of cavity gas flow into atmosphere

Using the transport model we have developed, we can investigate the spatial and temporal characteristics of gas flow into the atmosphere, and the effect of the explosion yield and rock properties on these processes. Below we show quantitative results for common conditions observed at NZTS and STS. The DOB of the nuclear charges was no less than what was

minimally allowed. The value of the transport parameter used in calculation was $k_1/m\mu = 3 \cdot 10^4$ D/cp for NZTS, and $k_1/m\mu = 7 \cdot 10^3$ D/cp for the STS. The rock porosity for damaged rocks was assumed to be 4%. Other parameters, including rock gas content, and initial pressure of non-condensable gas, were determined based on the rock type used as an emplacement medium.

The major rock parameters, characteristic for the NZTS, are shown in Table 9.10; and the gas front velocities are shown in Figure 9.22 a-d. For shales, sandstones, and quartzites, the equal amount of major gas component is used with a moisture content of 0.1%. According to Figure 9.22, the flow velocity for explosions in limestones is twice as high as for explosions in shales, and four times higher than for explosions in quartzites (if other parameters are kept equal). The duration of gas release also increases. Raising the explosion yield by two orders of magnitude, while keeping the minimally allowed DOB, did not change the maximum flow velocity significantly (Figure 9.22 b).

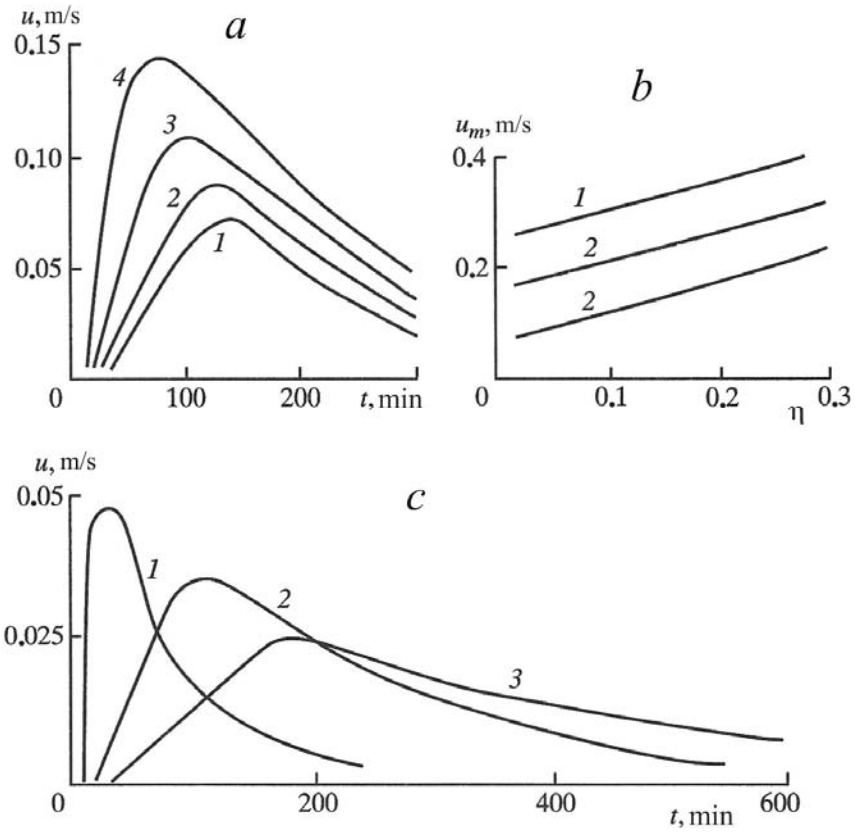

Figure 9.23: Gas flow dynamics for nuclear explosions conducted at the STS (Balapan and Murzhik testing areas): a) effect of gas content (q =100 kt with $W/q^{1/3}$ = 100 m/kt$^{1/3}$) for η: *1* – 0.03, *2* – 0.05, *3* – 0.1, *4* – 0.15; b) effect of gas content on maximum flow velocity for different yield: *1* – 1kt, *2* – 10 kt, *3* – 100 kt ($W/q^{1/3}$ = 80 m/kt$^{1/3}$); c) effect of the explosion yield: *1* – q = 1 kt, *2* – q = 10 kt, *3* – q = 100 kt ($W/q^{1/3}$ = 80 m/kt$^{1/3}$, η = 0.05).

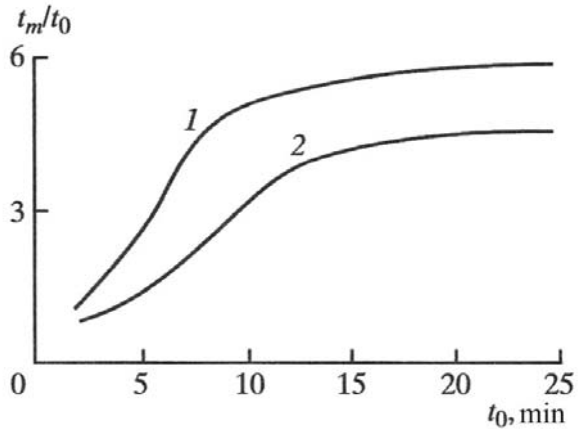

Figure 9.24: Time when the maximum flow velocity is reached as a function of breakthrough time, for: *1* – STS, *2* – NZTS.

This evidence suggests that our approach to choosing the minimally-allowed DOB (as a function of the explosion yield) is correct. However, the duration of gas release increases by a factor of 3 for an order-of-magnitude yield increase. Increase in rock gas content, causes increases in the maximum velocity and duration of the release.

The characteristic time for pressurized gas flow for a 100 kt explosion is 5 – 15 hours. If the rock properties and the explosion sDOB stay the same, the flow velocity increases linearly with gas content, and also depends on the explosion yield (Figure 9.22d).

The characteristic major rock parameters for the STS are shown in Table 9.11, and the gas-front velocities are shown in Figure 9.23 a-c. These flow velocities are lower than for NZTS, due to the greater sDOB of the STS explosions, and the reduction in rock gas content. An increase in rock gas content leads to an increase in maximum flow velocity and in the duration of gas release (Figure 9.23 a,b). Increased explosion yield, with other parameters kept the same, increased the duration of gas release and decreased the maximum flow velocity (Figure 9.23 b,c).

It is interesting to calculate the relationship between the gas venting time t_0 and the time when the maximum velocity of release is reached t_m. For short venting times, ($t_0 = 5$ to 10 min) the time when the maximum velocity is reached can be estimated as $t_m = (2 \text{ to } 3)\ t_0$. When the venting time increases ($t_0 \geq 15$ to 20 min), it becomes $t_m = (4 \text{ to } 6)\ t_0$. The fact that the ratio t_m/t_0 is higher for the STS than for the NZTS, is due to lower permeabilities at the Balapan and Murzhik testing areas, compared to conditions at the NZTS.

Another important characteristic for predicting the radiation effects of underground nuclear explosions is the mass of cavity gas, or the portion of it released into the atmosphere through the epicentral zone. The volume of gas released from the cavity into the atmosphere, at a distance of $r \geq W$ by the time *t*, is given by

$$V(t) = 4\pi\varphi m W^2 \int_0^t U(W,t)dt\ , \tag{9.44}$$

where φ is the segment of the spherical surface of radius *W*, $U(W,t)$ is the flow velocity of gas through the free surface. Calculations using $U(W,t)$ obtained as a result of the transport problem show that the major fraction of gas escapes into atmosphere through a surface within a solid

angle of approximately ~1 steradian (90°), or expressed as a fraction of a spherical surface as $\varphi \approx 0.16$. Using Equation 9.44 we obtain the expression for a relative mass of released gas:

$$\frac{M(t)}{M_0} = \frac{3\varphi m P_a W^2}{r_c^2 P_*} \int_0^t U(W,t)dt\,, \tag{9.45}$$

where M_0 is the total mass, P_* is the initial pressure of non-condensable gas in the cavity, and P_a is the atmospheric pressure. The results of these calculations using data from specific explosions are shown in Figure 9.25. For the NZTS, contained explosions conducted in shales with yields ranging between 1 and 10^2 kt were used, buried at the minimally allowed sDOB at W/q $^{1/3}$ = 120 m/kt$^{1/3}$ using scaled cavity radis $\bar{r}_c = 11.1$ m/kt$^{1/3}$ and gas content $\eta = 0.04$. For the STS, the calculations were for a 100 kt explosion with sDOB of $W/q^{1/3}$ = 100 m/kt$^{1/3}$ for different cavity radii (values ranging between 8.8 and 12.5 m/kt$^{1/3}$), and gas content $\eta = 0.05$. The curves in Figure 9.25 have an asymptotic character and show that for fully-contained explosions, conducted at the minimally-allowed sDOB in conditions typical for the NZTS and STS, the amount of gas released into atmosphere represents a small fraction of the total amount of non-condensable gas formed during the explosions.

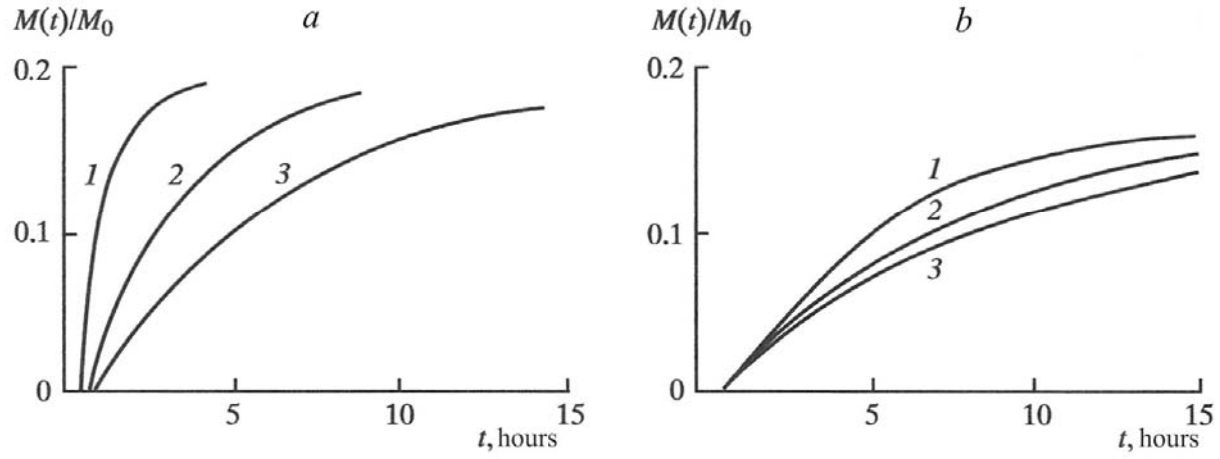

Figure 9.25: Change in the mass of gas released into the atmosphere as a function of time, for nuclear explosions conducted at: a) NZTS, the explosions conducted in shales at sDOB of $W/q^{1/3}$ = 100 m/kt$^{1/3}$; the lines are for different yield q in kt, namely: *1* – 1, *2* – 10, *3* – 100; b) STS, $r_c/q^{1/3}$, m/kt$^{1/3}$: *1* – 8.8, *2* – 11.1, *3* – 12.5.

9.7. Effect of the porosity of damaged rock on gas transport

The solution of the transport problem through porous media shows that the porosity of the damaged massif has a significant effect on movement of the gas front, the moving gas pressure distribution, and the pressure reduction in the cavity. An increase in porosity significantly

reduces the velocity and the duration of gas flow into the atmosphere. So the minimally allowed sDOB for explosions in more porous and more permeable rocks is lower than in rocks with lower porosity and permeability.

Increasing the porosity associated with an explosion is also an efficient mechanism for reducing the amount and duration of radioactive gas release into the atmosphere. This is supported by observations made for repeat shots, that is, explosions conducted in rock massifs affected by previously conducted explosions, and which therefore have higher porosity and permeability.

Using the values of the porosity of damaged rocks, the cavity radius r_c and the gas pressure P_*, one can estimate the maximum distance L_m reached by gas products due to expansion of a spherical front, until the pressure in the cavity becomes equal to atmospheric:

$$\frac{L_m}{r_c} = \left[\frac{1-\frac{1-m}{P_*}}{\frac{m}{P_*}}\right]^{1/3}, \tag{9.46}$$

where P_* is in kgf/cm^2 .

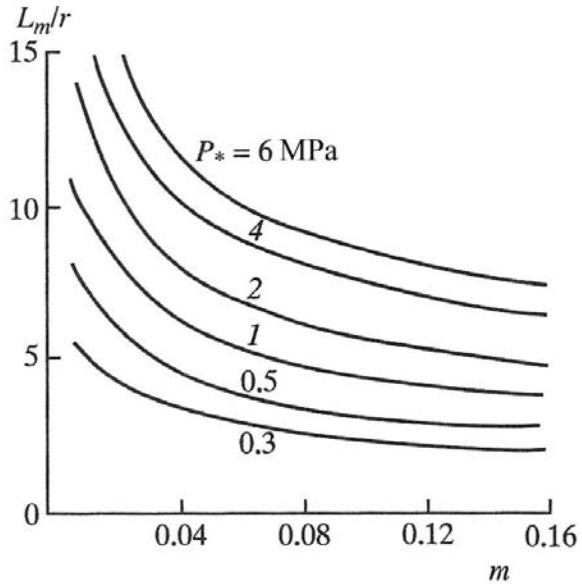

Figure 9.26: The effect of porosity and gas pressure in the cavity, on the size of the filtering zone (pressure values are shown next to the curves).

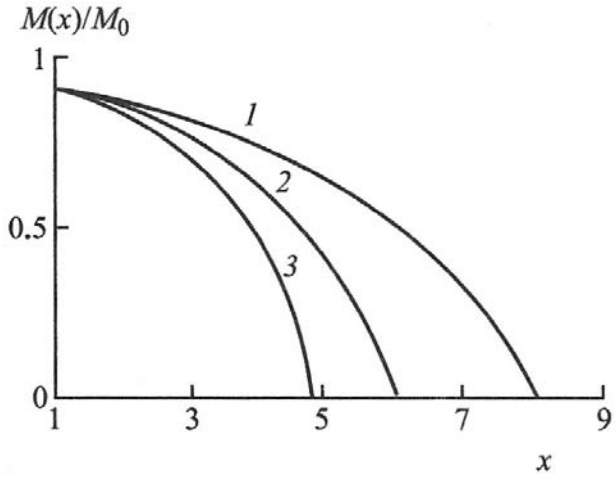

Figure 9.27: The effect of porosity on the amount of filtered gas, and the size of the filtering zone for the following values of porosity: *1* – 0.02, *2* – 0.04, *3* – 0.08.

Permeable space occupied by damaged rocks within distances $x \leq L_m/r_c$ represents a type of reservoir, which accumulates explosion gas products during their expansion. The limiting distance in 9.46 is plotted in Figure 9.26 as a function of the porosity of the damaged rock massif, for different values of the initial cavity pressure. Thus for an increase in final porosity from 2 to 8%, the volume that the explosion products can occupy increases by a factor of 2. This

volume will also increase by a factor of 2 due to a decrease in the initial cavity pressure, from 20 to 5 kgf/cm2, which corresponds to a reduction of rock gas content from 10 to 2%, for $\bar{r}_c = 11.1\ \mathrm{m/kt^{1/3}}$.

The mass of non-condensable gases moving from the cavity into the damaged rocks can be estimated as

$$M(t) = \int_{r_c}^{L_m} 4\pi\rho r^2 dr\ .$$

It also depends on rock porosity (m) and the mass of non-condensable explosion products (M_0.). Figure 9.27 shows the effect of porosity on the portion of gas which moved to distances larger than x = r/rc for the following parameters: $\bar{r}_c = 11.1\ \mathrm{m/kt^{1/3}}$, P_2 = 1.0 MPa, and η=0.05. In this case, assuming a porosity of 4%, the gas is localized in a volume with a radius of L_m = 6.2 r_c (~70 m/kt$^{1/3}$). If the rock porosity is 8% then gas can spread to L_m = 4.7 r_c (~50 m/kt$^{1/3}$).

Analysis and plots in Figures 9.26 and 9.27 indicate the values of porosity and rock gas content for which no pressurized venting will take place. However, the estimates used for the analysis assumed a spherically-symmetrical porosity change with radius, as well as gas motion in the damaged rocks. In reality, increased rock porosity occurs not only due to radial motion in the pressure wave, but also due to spallation and material movement toward the free surface. The input of each of these mechanisms into the final porosity depends on the explosion sDOB, and yield. Symmetrical porosity changes around the cavity are determined by the magnitude of the returning motion of the medium toward the explosion center. In hard rocks, the volume of induced pores is approximately equal to the final cavity size (Rodionov et al, 1971). The most efficient mechanism of porosity increase is the residual uplift of the free surface and formation of a retarc. From estimates of uplift sizes it is easy to estimate the average value of the damaged massif:

$$m = m_0 + \frac{\rho_0 - \rho_f}{\rho_0}, \tag{9.47}$$

where m_0 is the initial porosity ,and ρ_0 and ρ_f are the initial and final densities respectively. For example, Figure 9.28 shows the average porosity as defined in 9.47 as a function of sDOB and yield of explosions, for the following parameter values: m_0 = 0.02, ρ_0 = 2.7 g/cm^3, and $\bar{r}_c = 11.1\ \mathrm{m/kt^{1/3}}$. The major changes in porosity take place in the zone above the charge, within a solid angle of 90° (approximately 1/6 of the spherical volume of a radius equal to the DOB), as well as in the central damage zone, where the additional volume of pores is equal to the cavity volume. Dash-dot lines show the equivalent increase in porosity for a spherically-symmetric porosity change. Vertical dashed lines show minimal depths required for fully contained explosions (the boundary between partially and fully contained explosions is at $\eta = 0.04$). For partially contained explosions, the final porosity is sufficiently high. So pressurized gas escape (venting) is practically absent, even if the gas content of the emplacement medium is 5 – 10 %. For fully contained explosions, free surface uplift decreases and the final porosity approaches the sum of the initial porosity and the porosity in the central damage zone.

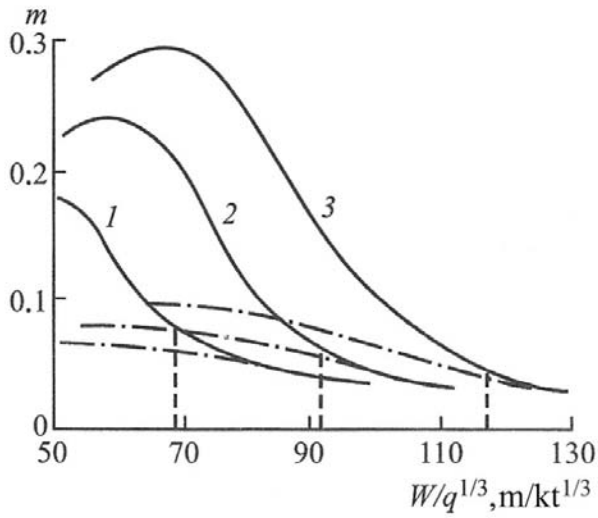

Figure 9.28: The porosity of damaged rock as a function of explosion depth and yield for different yields q in kt is: *1* – 100, *2* – 10, *3* – 1.

Knowing the final porosity of the damaged rocks, the cavity radius, and the pressure of non-condensable gas, it is therefore possible to estimate the depth of the nuclear charge which is needed to eliminate pressurized escape (venting) of radioactive products into the atmosphere. These estimates have been supported by experiments. For example, for nuclear explosions in the Degelen Testing Area at STS, the value of L_m = 7 to 8 r_c (50 – 70 m/kt$^{1/3}$) assuming the parameters $\eta = 0.01$ to 0.02, $\bar{r}_c = 11.1$ m/kt$^{1/3}$, $P_* = 0.5 \div 1.0\ MPa$, and m_0 = 0.02.

In reality, the depth of burial was 80 – 100 m/kt$^{1/3}$ and no pressurized gas escape (venting) took place. The estimates we have just obtained were confirmed by high-yield nuclear tests conducted at NZTS. For these explosions the sDOB is smaller[9], the intensity of damage is higher, and so the importance of the original porosity (in gas transport) increases, leading to an increase in gas breakthrough times. In these circumstances, an increase in residual deformations reduces the effect of tectonic faults and large fractures on gas flow (they represent the major pathways of gas escape for smaller explosions).

9.8. The effect of cavity collapse on gas transport

In previous chapters the problem of gas transport through porous medium was solved without taking cavity collapse into account. However, the collapse of the cavity soon after the explosion can lead to a decrease in the filtering layer by which gas travels to the surface, reducing the time for breakthrough of radioactive gas into the atmosphere. This possibility is determined by the time of formation and the height of the chimney formed above the detonation. For loose rocks (alluvium, tuff), the chimney height spans the entire interval between the charge and the surface, leading to the creation of subsidence craters. In hard rock the height of the chimney is approximately 3 – 5 r_c, which is approximately to the linear dimension of the intense damage

[9] Because the scaling for these computations is not proportional to $q^{1/3}$.

zone. An increase in DOB corresponds to an increase in rock strength and elastic moduli, so the height of the chimney is smaller (e.g. Houser, 1969). The time of the cavity (chimney) collapse is determined by many factors, including the rock type.

Several factors that may impede cavity collapse include a slow pressure decrease (in the cavity), high strength, low gas content, and a plastic character of deformations. For instance, cavities in salt are often stable (see e.g. Kedrovskii et al, 1972). Other factors, such as high porosity and moisture content, decrease the cavity stability, and promote collapse. For instance, during the later stages of explosions in wet rocks, a process of ejection develops, like rock throwing or expulsion, which reduces the stability of the cavity ceiling. The specific geological conditions, and tectonic structure, have a significant effect on the cavity collapse. Geophysical surveys have shown that chimneys have complex and asymmetrical shapes, depending on geological structure. Consequently, subsidence craters are often shifted along the [layer] strike.

The problem of cavity stability remains unsolved, due to a multiplicity of factors. Neither the conditions of stability nor the conditions of collapse were determined (which in many cases do not coincide). We therefore limit discussion to the analysis of known (historical) experimental data relating to cavity collapse, and compare these data with the characteristic time for gas transport (flow) through damaged rocks. The most abundant data related to cavity collapse were obtained for nuclear explosions conducted at the NTS (Springer, 1968)[10]. Other published results include data for explosions in Sahara granites (Delrich, 1970), which can be represented by the relationship:

$$r_c = 0.8t + 3, \tag{9.48}$$

where r_c is the cavity radius in meters, and t is the time before the collapse in minutes.

Seismic observations of cavity collapse for several explosions were obtained at the NZTS such as in Tunnel A-8 (5.5 min), B-1 (12.3 min), and in boreholes (Shafts) Yu-1 (44.3 min) and Yu-5 (4.5 min) —where the collapse occurred between 4.5 and 44 min after the explosion. However, data- interpretation is ambiguous: the reason for cavity collapse could be related to stress relaxation (associated with aftershocks). There are no cavity collapse data for STS explosions.

Relationships between the time of collapse and the cavity radius are plotted in Figure 9.2 using data from NTS. Despite significant scatter of the experimental data (σ=3 to 5), there is a noticeable trend with time, increasing as the cavity radius increases. This relationship can be approximated via empirical formulas:

$$\text{For alluvium: } t = 0.5 \cdot 10^{-2} r_c^{2.4} \text{ (min)} \tag{9.49}$$

$$\text{For tuff: } t = 2.5 \cdot 10^{-2} r_c^{2.1} \text{ (min)}$$

where r_c is the cavity radius in meters.

[10] A more recent reference, would be Donald L. Springer, Gayle A. Pawloski, Janet L. Ricca, Robert F. Rohrer, and David K. Smith, Seismic Source Summary for All U.S. Below-Surface Nuclear Explosions, Bulletin of the Seismological Society of America, Vol. 92, No. 5, pp. 1806–1840, June 2002. Note added by translators.

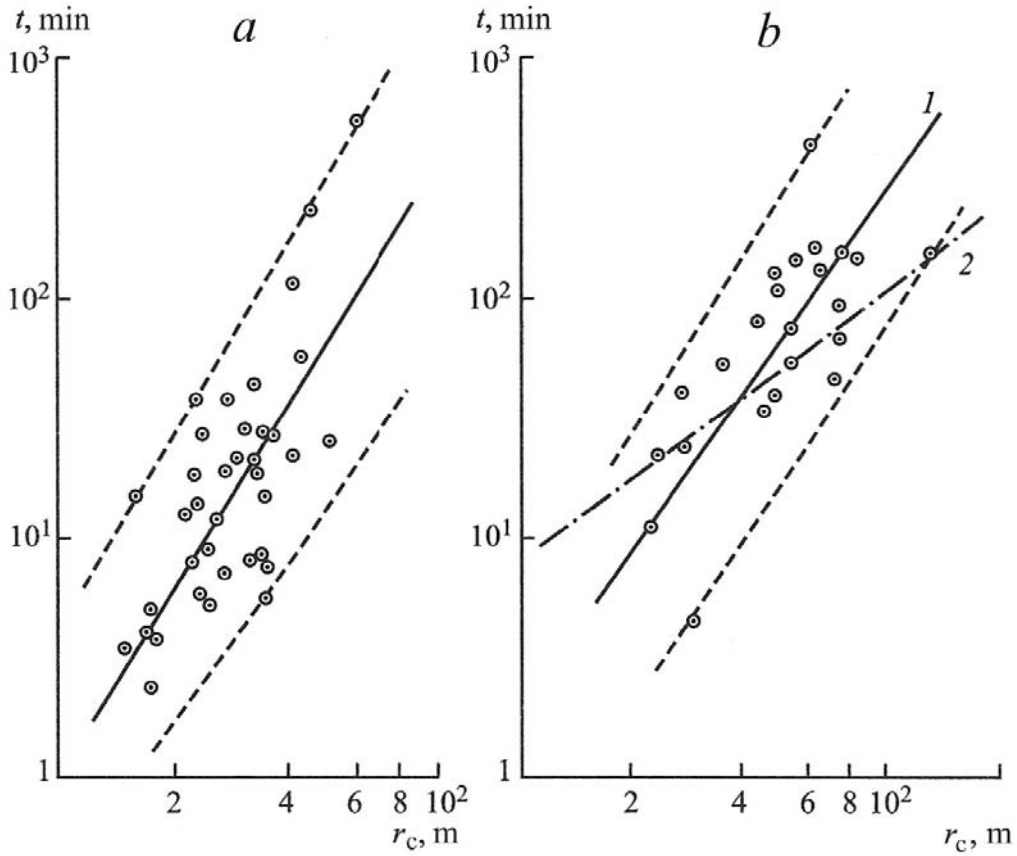

Figure 9.29: The effect of explosive cavity size on the time of cavity collapse, in a) alluvium, and b) tuff. Lines are for the following rock types: *1* – tuff, *2* – granite.

The relationship given in equation 9.48 is shown in Figure 9.29 b as a dash-dot line. While some individual points for explosions in tuff are close to the results of 9.48, overall the effect of cavity radius on collapse times is stronger for explosions in tuff.

Due to insufficient data the relationship between cavity size and collapse time was not determined. Explosions can be divided into three groups: a) long collapse time intervals on the order of 10 – 100 hours (e.g. HARDHAT – 11 h, MILROW – 37 h, BOURBON – 197 h); b) time intervals between several minutes to several hours (HALFBEAK – 3 h 18 min, BOXCAR – 1.7 min, NASH – 23.9 min, as well as the previously-mentioned NZTS explosions – A-8, B-1, Yu-1, and Yu-5); and c) short time intervals less than 1 min (RAINIER – 1 min, PILEDRIVER – 14 s).

To compare the collapse time intervals with gas front migration, we use the solution for non-stationary gas transport, (9.14). For small-yield nuclear explosions in alluvium, $\bar{r}_c = 15$ m/kt$^{1/3}$; and in tuff, $\bar{r}_c = 16.2$ m/kt$^{1/3}$. For large DOB, the value of cavity radius was reduced according to the (scaling) formula obtained by Murphy (1981), shown in Chapter 1. Moisture content is 10 – 15 % for alluvium, and 15 – 20 % for tuff. In these conditions, the partial pressure of water

vapor varies in the range 20 – 40 kgf/cm^2. For these values of cavity pressure, and a porosity of 5 – 10 %, the gas front movement with time is described using Equation 9.14:

$$\tau = 0.19(x-1)^{2.8}\ .$$

After replacing the non-dimensional parameters, we obtain an expression for gas front propagation:

$$\frac{t_0}{q^{2/3}} = 31.7\,\frac{m\mu}{k_1 P_*}\left(\frac{r_c}{q^{1/3}}\right)^2\left(\frac{W}{r_c}-1\right)^{2.8}\ , \tag{9.50}$$

where t_0 is time in minutes, q is yield in kt, r_c is in meters, k_1 is in Darcy, μ is in cP, and P_* is in kgf/cm^2.

There were no direct (in situ) measurements of permeability in alluvium and tuff after explosions. Therefore in (9.50) we take $k_1/m\mu = 3\cdot 10^4$ D/cp, which is the largest value of the permeability coefficient (Figure 9.12), with corresponding values for $r_c/q^{1/3}$ for alluvium and tuff. Comparison between cavity collapse times and gas front movement is shown in Figure 9.30, for alluvium and tuff. The solid lines show the front movement according to (9.50), while dotted circles show the observed time intervals of cavity collapse. Most of the data points are plotted above the travel time curve for the gas front, for both alluvium and tuff.

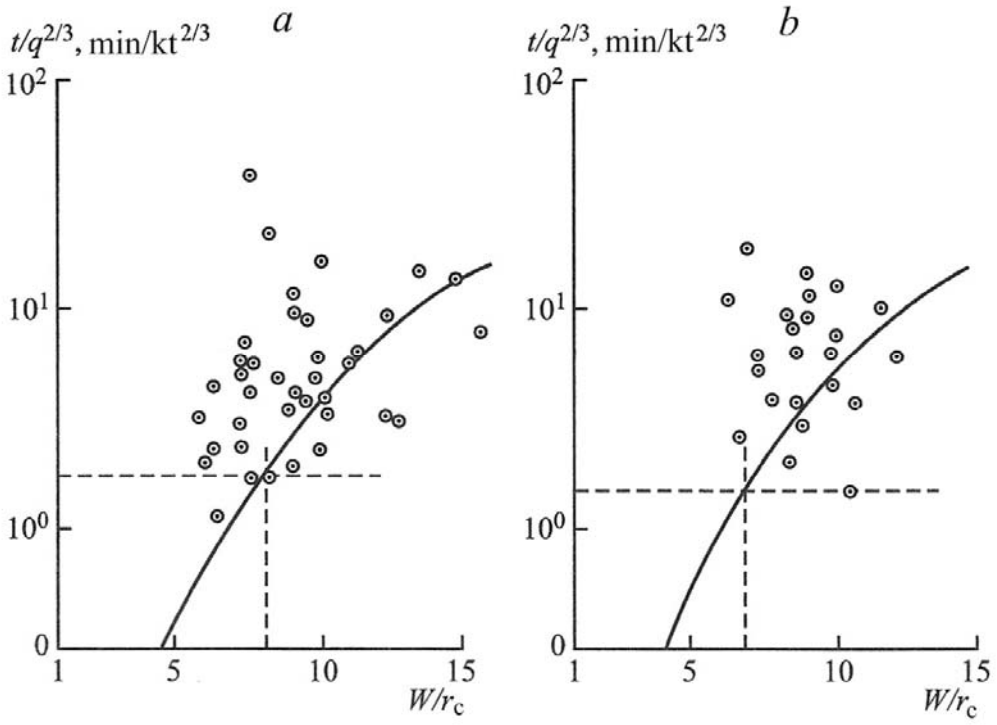

Figure 9.30: Comparison between cavity collapse times and propagation of the gas front, for a) alluvium, and b) tuff.

Therefore for these explosions the gas front passed before cavity collapse occurred. The points below the moving gas front are all plotted above the time $t/q^{2/3} = 1.5$ to $1.8\ min/kt^{2/3}$, marked with dashed lines based on the shortest time of collapse for all these data points. By that time, gas has spread to a distance of 7 – 8 r_c for depths of burial in the range 9 – 15 r_c. This means that even in cases when cavity collapse occurred before gas was released into the atmosphere, the period of gas transport was almost over.

The time to collapse and the duration of gas front migration for explosions in hard rock, were compared based on the relationships 9.28 – 9.35 for each explosion individually (due to a wide range of time differences and variations in the emplacement media).

For long collapse time intervals, on the order of 10 – 100 hours, no relationship between cavity collapse and front migration exist, because gas transport time scale is 1 – 3 orders of magnitude shorter than the collapse time scale.

For explosions with collapse time in the range between 10 min and 1 hour, for explosions with yields of 1 – 10 kt, cavity gas will already have been released into the atmosphere, and for explosions with yields 10 – 100 kt, the gas front will propagate through the entire fracture zone with radius of 5 – 10 r_c, therefore a chimney with height of 3 – 5 r_c will not significantly affect gas release into the atmosphere. In cases for which the cavity collapse occured within 1 – 10 min after the explosion, the gas front reached distances of only 3 – 5 r_c for explosions with yields of 1 – 10 kt, and 2 – 3 r_c for explosions with yields of 10 – 100 kt. Formation of a collapse chimney of comparable height does not change the position of the gas front, but it can change the velocity of gas front migration. It can also change the flow behind the gas front, due to non-condensable gas rapidly approaching the surface pressure.

However the temperature and pressure in the chimney will decay faster due to heat transfer, so we do not expect an increase in velocity and intensity of the flow. Only in the case of a very early cavity collapse, within 1 minute for explosions with yields of 1 – 10 kt and approximately 10 s explosions with yields of 10 – 100 kt, when the gas migration front is still at 1.5 – 2 r_c, can formation of a chimney with height of 3 – 5 r_c create a significant disturbance in the flow regime — which would reduce the gas breakthrough times, due to the reduction of the layer in which the gas needs to travel. If the free surface is located at distances on the order of 7 – 10 r_c, the breakthrough time can be reduced by a factor of 1.5 – 2.

Thus, gas breakthrough times scale with yield as $t_0 \sim q^{2/3}$, and the collapse time in alluvium also scales as $t \sim q^{2/3}$ as follows from (9.49). So for this type of rock the gas migration and the cavity collapse time have a similar dependence on yield; and it is reasonable to assume that in these rocks the processes of gas migration and cavity collapse are related. Moreover the process of gas migration determines cavity collapse, and regulates it.

For explosions in hard rock, gas breakthrough times relate to yield as $t_0 \sim q^{2/3}$ and grow faster than the growth of cavity collapse processes, which scale as $t \sim q^{1/3}$ according to (9.48). So for hard rock these processes are independent, and the time difference between the gas escape and the cavity collapse will increase, with an increase in the explosion yield.

9.9. The effect of the faults and fractures on gas transport

The physical model of gas transport from the cavity into the atmosphere is based on the assumption that the rock around the source is intensely damaged, and there are no channels (pathways) for predominant gas migration.

Analysis of data from NZTS and STS, performed in order to determine transport properties of damaged rocks, have shown that the filtration mechanism (through porous medium) for gas flow is the dominant process responsible for gas escape into the atmosphere. For example, 75% of explosions conducted at NZTS and 50% of explosions conducted in the boreholes at Balapan and Murzhik testing areas of the STS, satisfy this model to some degree (Adushkin, 2000).

Beside the filtering mechanism that enables gas transport, there is another mechanism responsible for early escape of radioactive gas into the atmosphere. As mentioned previously, early gas escape is related to the presence of natural or artificial discontinuities, and is more characteristic of smaller-yield explosions (on the order of 1 – 10 kt). Natural discontinuities are present in the medium in the form of large fracture systems, karst cavities, and/or other structural defects. Sometimes these discontinuities are formed as a result of a large explosion along tectonic faults, layer boundaries, and other contacts between rocks of different types.

Artificial discontinuities are related to the technologies of test preparation and are caused by defects in the stemming complex, the presence of structural boreholes, tubing casing annulus, and inter-cable space. The fraction of the natural and artificial discontinuities for NZTS explosions accompanied by gas release is approximately the same: in half of the cases gas was released along tectonic faults, and in the other half – along stemming complex and consequently through the tunnel mouth.

At the STS, in most cases, early gas release was through artificial defects (such as the stemming complex, tubing casing annulus, and borehole used for structural-analysis). For only a few explosions, was the early gas release related to natural discontinuities.

To predict radioactive gas breakthrough times, through artificial and natural pathways, one can use the results as shown in Figure 9.10 and 9.11. It was determined that in cases of early gas release (venting) into the atmosphere, the value of the transport parameter for NZTS was $k_1/m\mu = 5 \cdot 10^5$ D/cp; for explosions in boreholes at the STS it was $k_1/m\mu = 2.5 \cdot 10^5$ D/cp. Substituting these values into Equations 9.28 and 9.29 we obtain the relationships for estimation of the early gas release times through artificial and natural discontinuities for NZTS (using shale parameter values from Table 9.10):

$$t_0 = 0.4 \frac{q^{2/3}}{P_*} \left(\frac{W}{r_c} - 1\right)^{2.6}. \tag{9.51}$$

For explosions conducted in boreholes at the STS (using aleurolite from Table 9.11) we have:

$$t_0 = \frac{q^{2/3}}{P_*} \left(\frac{W}{r_c} - 1\right)^{2.6}, \tag{9.52}$$

where t_o is in seconds, q is the explosive yield in kt, and P_* is in kgf/cm^2.

The problem of early gas release can be divided into two main scenarios: the effect of man-made structures (channels) related to digging of the tunnel or drilling of the boreholes, and the effect of natural discontinuities within the rock massif. If stemming structures, in the charge and analysis (structural) boreholes, and other procedures are properly conducted, early release of gas through artificial channels can be avoided. The problem of gas venting through natural discontinuities should be solved separately for the STS and NZTS, as we next discuss.

As it was mentioned earlier, at the STS the hard rock, where the borehole tests were conducted, was covered with a thick layer of clay and clay-rich sand sediments. If the integrity of this layer was preserved, it prevented early gas release. Because of this there was no gas release into the atmosphere for approximately 25% of the nuclear tests in boreholes. Particular attention should be given to situations when this layer became thin and the crystalline hard rock was situated close to the free surface (i.e., close to the location of the shot borehole). This was especially true if steeply-dipping layers or tectonic faults were present. For example, one of the last nuclear tests in BH 1366 (February 12, 1989) was detonated in these conditions. The best solution to this problem is to avoid placing shot boreholes in these areas.

All rock massifs used for nuclear testing at the Northern Testing Area of NZTS are characterized by strongly-layered structure, and juxtaposition of different structural elements, often represented by rocks of different types. Overall rocks, are fractured (30 – 80 fractures per linear meter), with the predominant fracture direction along layer beds, and show significant anisotropy. In addition there is a significant amount of tectonic fracture discontinuities (on the order of 10 per 1 km of tunnel length), and several tectonic faults with thickness from 0.1 to 3 – 5 m per tunnel. Analysis of the experimental data, related to the gas breakthrough times during nuclear tests in these rocks, have shown:

- Processes of gas release into the atmosphere depend significantly upon the geological structure of the rock massif itself, and in particular on the presence of tectonic faults and discontinuities (fractures).
- In some cases, there is no correlation between the beginning of the gas release, sDOB, and the gas content of the emplacement medium.
- Early release of gas into atmosphere can be explained by the presence of tectonic faults and fractures, close to the charge location or to the stemming complex.

This analysis suggested that gas migration through the rock massif involved a combination of two mechanisms: a filtering movement of gas, through porous media via the crush zone (3 – 4 r_c); and via fractured zones (5 – 7 r_c), and then gas transport with almost no resistance along open pathways/channels adjacent to the damage zones. Based on these views we conclude that gas release in real conditions occurs as a combined model of transport through the zone of intense damage, with subsequent flow through open natural tectonic faults and fractures. Location of these faults and fractures, their aperture of opening and the connectivity with the free surface play significant role in gas transport.

In particular, observations suggest that large tectonic discontinuities, and contacts between rocks of different types, limit and localize the size (extent) of the zone of intense damage, and provide pathways for gas release.

Thus the problems of quantifying a possible effect of natural discontinuities on the gas release into the atmosphere, and estimating the location of a gas release, should be solved in each particular case by taking into account the explosion yield, the emplacement rock properties, and the geological and tectonic structure of the test bed or tunnel. Using information about the degree of heterogeneity and fracturing, the thickness of tectonic faults, the stress field, and the direction of stratification, allows creation of a model of the anisotropy in physical properties along different directions and a volumetric model of the rock massif as a whole with its multi-level block structure.

Using a model of the structure, the total picture of the mechanical effect of the explosion can then be created for each specific site, based on knowing the specific size and shape of the zones of damage, the location of elements of the stemming complex, and of the natural discontinuities between them, and the character of their juxtaposition to filtered zones. Based on this picture, the importance of damage zones and tectonic deformation zones for the gas migration can be evaluated. To estimate the time of gas release, Equation 9.28 – 9.30 should be used only for the central zones of damage, while the total time taken for gas migration to the surface should be calculated using Equation 9.51 to account for migration along natural and artificial pathways.

Observations show that thick (over 0.2 – 0.3 m) vertical faults zones, or steep (steeper than 50 – 60°) tectonic faults filled with broken rocks and quartz veins, are the most dangerous (for early gas release/venting). Also problematic, are large fracture systems, which can be open, and juxtaposition of rocks of different types located within 5 – 7 r_c (50 – 70 m/kt$^{1/3}$) from the charge, particularly for explosions with yields between 1 – 10 kt. In addition, smaller-yield explosions with lower energy density lead to a smaller filtering zone (with porous damage), which increases the role of faults in processes of gas release. With an increase in explosion yield, the extent of the fractured filtering zone increases, and the effect of natural discontinuities decreases.

(THIS PAGE INTENTIONALLY LEFT BLANK)

Chapter 10

Excavation using chemical explosions

Explosive excavation for purposes of constructing dams, channels, and trenches, and for removal of ore, and other applications requiring movement of large masses of rock, are an important application of chemical explosions. Typically in these cases, elongated or point (spherical) charges, made of up to thousands of tons of explosives, are placed within the rock mass. In some cases, groups of charges are used. Computation of the excavation action for these large-scale explosions of different shapes, often detonated with delays in different rock types and sometimes in the presence of topography, is a complex engineering task. Our years of experience show that the best estimates of the effect of large-scale excavation explosions are achieved by physical modeling (laboratory experimentation), using an analog apparatus (Chapter 2). Such analog modeling allows an evaluation of scale effects, charge shape, delay times, topography, and rock properties at the site (Adushkin et al, 1982).

In this chapter we present new expressions/formulas to estimate the effects of point charges and linear charges, based on laboratory experiments in a vacuum chamber. We provide comparison between the modeling results and the historical data for chemical excavation explosions. And we determine the depths of burial for charges below which self-similarity breaks down, due to increasing overburden, and for which the "gravitational similarity law" should be used.

10.1. Excavation explosions using point charges

The term "point charge" is typically used to describe a charge for which all three dimensions are approximately equal (there is no special direction), so that source processes obey spherical symmetry. The relationships between crater size and explosion yield and depth (equation 2.17) were obtained for sources with spherical symmetry, using laboratory experiments of the excavation processes in a vacuum chamber (Section 2.2), which, according to similarity criteria, can be applied to excavation explosions of any size. In order to use equation 2.17 for practical computations on the scale of an underground nuclear explosion, we express the energy of the cavity gas E using the total energy of the explosion, as $E = \zeta q$, and transform it as:

$$q = 0.28 \frac{(\rho g W + P_a) W^3}{\xi} 10^{n/0.9} . \qquad (10.1)$$

[is this a typo and ζ and ξ are the same parameter?]

The energy of the cavity gas can be expressed as

$$E = q - R, \qquad R = \int_{V_{ch}}^{V_c} P(V) dV , \quad \xi = 1 - \frac{R}{q}, \qquad (10.2)$$

where R is the work done by an explosion during its early stages, due to cavity expansion from the volume of the charge chamber V_{ch} to the final cavity size V_c. The work of the explosion during the early stage, R, spent on shock compression, plastic deformation, radial material movement (due to cavity expansion), and rock crushing, is not available for the intended purpose of excavation. Only a fraction of the work R is converted into kinetic energy of the medium during the pressure wave. Estimates show that the fraction of this energy is 5 – 10 % of all kinetic energy transferred into the medium by an explosion, and does not exceed 1 – 3 % of the total energy of the explosion. In each individual case, the work R is calculated by integration of the adiabatic processes using the products of decomposition of chemical explosives, taking into account the size of the (camouflet) cavity[1] determined by the specific properties of the explosive source (charge density, specific energy of the explosion, brisance etc).

Therefore the value of the coefficient ζ depends on specific explosion parameters (the "overshoot parameter", the density of explosives at the source, types of the explosives), and determines the part of the total energy of the explosion contained in the cavity, which is spent on the excavation. The size of the cavity (the camouflet size) formed by the chemical explosion is characterized by an "overshoot parameter"[2], equal to the ratio between the cavity volume to the weight of the explosives $\Pi = V_c/q$. Measurements of the "overshoot parameter" for the rocks of different types are compiled in various reference books (e.g. Reference …, 1962). Table 10.1 is based on the data provided in this reference.

Depending on the rock type, the value of the "overshoot parameter" varies by three orders of magnitude between 100 – 1000 m^3/t for clays, 70 – 200 m^3/t for sandy clays or loess, 1 – 10 m^3/t for hard rock. Such a broad range of the variation of this parameter can be explained by differences in cavity formation mechanisms between the loose sediments and hard rocks. In loose sediments, cavities are formed due to volumetric compaction of the medium in the region of plastic deformation and their formation significantly depends on the material porosity and moisture content. In hard rock, cavities are formed due to radial outward motion of the medium in the region of plastic deformations, therefore the values of the "overshoot parameter" are small and the range is narrow.

The rock properties in Table 10.1 are represented only by rock hardness (or strength category), while the overshoot parameter was estimated for explosions using ammonite #6ZhV with loose powder density. Using the data from Table 10.1 the overshoot parameter was plotted in Figure 10.1a as a function of the "hardness" coefficient f, (based on the M.M. Protodiakonov scale), and rock hardness according to the Construction Norms and Rules (CNAR) publication.[3]. The following empirical formula can be used for approximate estimates:

$$\Pi = 60\, f^{-1.3}, \quad f \approx \sigma_*/100, \quad 2 \le f \le 20. \tag{10.3}$$

[1] The camouflet cavity is defined as a cavity size produced by a fully contained explosion.

[2] Note that the use of the term "overshoot parameter" used in this book is different from the one used in the western literature

[3] Construction Norms and Rules (CNAR) – from Russian "Строительные Нормы и Правила" or СНИП

More detailed estimates taking into account physical properties of hard rocks can be obtained using V.N. Rodionov's formula (equation 1.5). For chemical explosions it is important to take into account the region of validity of equation 1.5 regarding the compressive strength and rock compressibility $10^{-3} < \frac{\sigma_*}{\rho C_p^2} < 10^{-2}$ and the initial pressure P_i in the cavity $1 < \frac{P_i}{\rho C_p^2} < 10$. For typical hard rocks [the characteristic values are] $\rho C_p^2 = 10^5 - 10^6 kg/cm^2$, $\sigma_* = 400 - 2500 kg/cm^2$, and the relationship $P_i > \rho C_p^2$ is satisfied only for the charge density $\rho_{ch} \geq 1.3 - 1.4 g/cm^3$ for fully tamped explosions. The range of change of the overshoot parameter according to Equation 1.5 is shown in Figure 10.1 as a lined region for rock density varying in the range $2 \leq \rho \leq 2.8 g/cm^3$ and the P-wave velocity varying in the range$2 \leq C_p \leq 6\ km/s$.

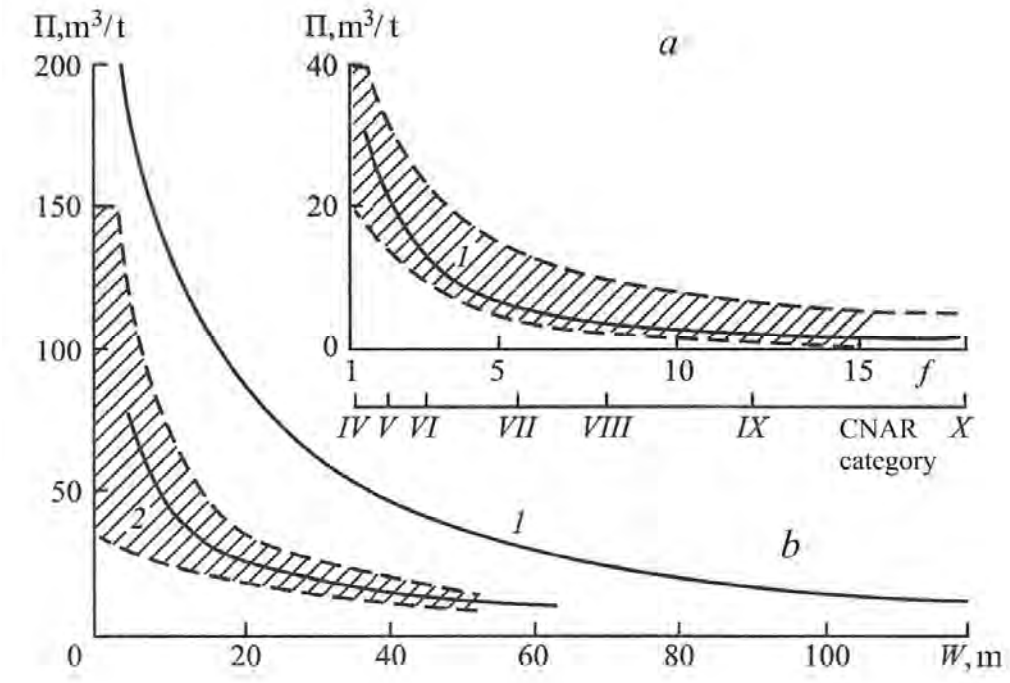

Figure 10.1: "Overshoot parameter" as a function of rock hardness (a) and depth of burial in loose sediments (b). The horizontal axis in (a) shows the CNAR category between IV and X. Lines *1* and *2* show zones described in the text.

In soft sediments the overshoot parameter depends mainly on sediment compressibility (Section 6.6). Therefore, with an increase in depth and a corresponding increase in density and seismic velocity, the size of the cavity will decrease in proportion to the parameter ρC_p^2. The relationship between the overshoot parameter and the shot depth for loess is plotted using these considerations (Figure 10.1b, line 1). For this sediment type, the overshoot parameter was determined experimentally for the shot depth of 1 – 2 m for $\rho = 1.6 g/cm^3$, and ω = 9.5 % for an explosion of ammonite-6 with density of 0.8 – 0.9 g/cm^3 (Belyaev, 1957). The velocity profile for loess was taken from Rulev (1968), according to which the velocity increases from 400 – 500 m/s at depths of 1 – 2 m to 1 km/s at the depth of 25 m and 1.5 km/s at 50 m. In dense sandy

clays ($\rho = 1.8 - 2.3 g/cm^3$) the overshoot parameter varies between 20 and 150 m^3/t (Reference …, 1962). With increasing depth, the range of change for the overshoot parameter becomes narrower and the following empirical formula can be used:

$$\Pi = \frac{250}{W^{0.8}}, \ (m^3/t) \tag{10.4}$$

where W is the depth in meters. The results of calculation, using formula 10.4, are shown in Figure 10.1b (line 2).

Table 10.1. Radius of the zones of increased permeability for some underground nuclear explosions

Rock type	Strength coefficient f	Strength category according to CNAR	"Overshoot parameter" Π, m^3/t
Plastic clay	-	II	500 – 1000
Hardened clay	1	III	200 – 400
Sandy clay, loess	1 – 2	III – IV	70 – 200
Chalk, gypsum, soft limestone, cemented gravel (conglomerate)	2	IV – V	30 – 70
Marl, shell limestone, fractured tuff, frozen [with permafrost] sandy clay	2 – 3	V – VI	10 – 30
Clay slate, hard marl, weathered granite, sandstone, limestone	3 – 4	VI – VII	7 – 10
Fractured granite and limestone, sandstone slate	4 – 8	VII – VIII	4 – 7
Granite, limestone and marble medium fractured	8 – 10	VIII – IX	3 – 5
Granite, strong sandstone, limestones and conglomerate, iron ore	10	IX	2 – 4
Strong granite, quartzite, amphibolites and scarnes	15	IX – X	1 – 2
Strong quartzite, basalts and porphyrites	20	X – XI	0.8 – 1

In some cases during preparations for excavation explosions it is useful to experimentally determine the overshoot parameter. The overshoot parameter can be used as an integral characteristic describing the physical properties of rocks.

In order to determine the energy of cavity gas using the overshoot parameter, one needs to know the expansion law for the gaseous explosion products (EP). Calculations of the isentropic expansion for hexogen EP with initial density varying between 0.5 and 1.8 g/cm^3 are presented in the article by Kuznetsov and Shvedov (1967). Figure 10.2 shows the relationship between the

EP pressure and the overshoot parameter ($\Pi = 1/\rho$, where ρ is the current density of the EP) for three different values of the initial density: 1.6 g/cm^3 (line 1), 1 g/cm^3 (line 2), 0.6 g/cm^3 (line *3*).

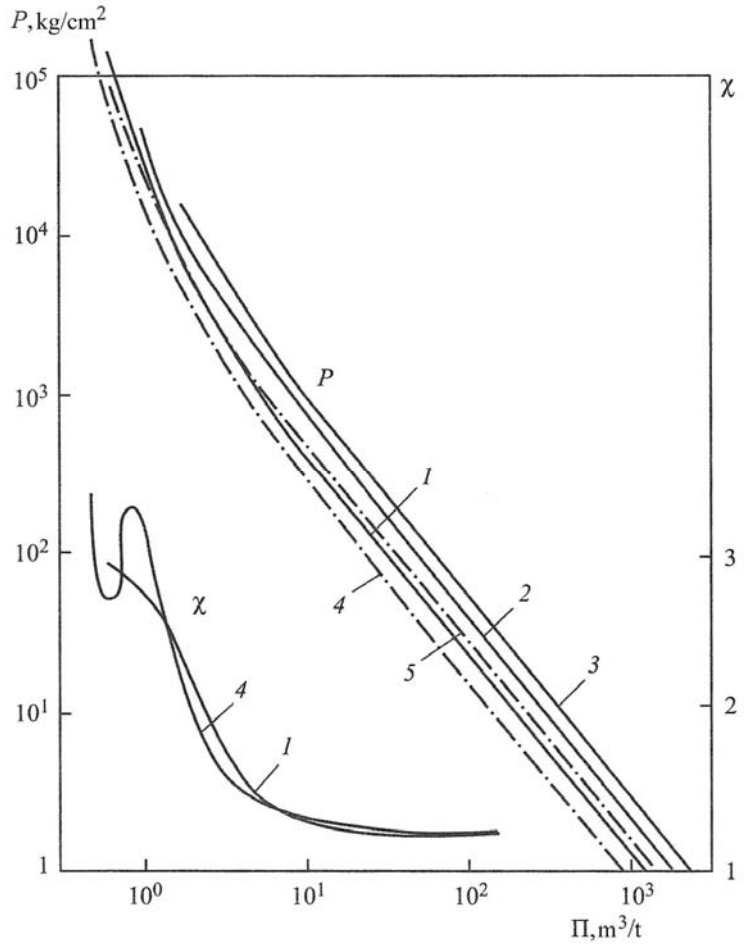

Figure 10.2: a) Pressure of the explosion products as a function of the "overshoot parameter" for TNT hand hexogen. b) Adiabatic exponent as a function of the "overshoot parameter" for TNT hand hexogen. Lines *1 – 3* show hexogen of different density: *1* – 1.6 g/cm^3, *2* – 1.0 g/cm^3, and *3* – 0.6 g/cm^3. Lines *4* and *5* show TNT of different density: *4* – 1.5 g/cm^3, *5* – 1.0 g/cm^3.

Jones and Miller (1948) provide the equations of state for the EP for TNT with two different values of initial density – 1.5 g/cm^3 (ε = 1271.3 kcal/kg), 1 g/cm^3 (ε = 937.4 kcal/kg). These results are also shown in Figure 10.2 with lines 4 and 5 respectively. It follows from Figure 10.2 that the gas pressure in the cavity depends on the overshoot parameter and the initial charge density. For example, for hard rock with $\Pi \leq 20$ m^3/t the pressure in the cavity $P \leq 10^2 - 10^3$ kg/cm^2. For an explosion in loose sediments with $\Pi \approx 10^2$ m^3/t, the pressure in the cavity is $P \approx$ 10 kg/cm^2, and for $\Pi \approx 10^3$ m^3/t the pressure is $P \approx 1.2 - 3$ kg/cm^2. Reduction of the initial density of the explosives from 1.6 to 0.6 g/cm^3 in a cavity of the same size, causes the pressure increase by a factor of 4.

Figure 10.2 also shows the change in value of the isentropic expansion parameter, as a function of the overshoot parameter, using results from Kuznetsov and Shvedov (1967) and Jones and Miller (1948). At the initial stages of expansion the adiabatic constant drops significantly from $\chi = 2.7 - 3.3$ to $\chi = 1.3$ for $\Pi \geq 10$ m^3/t, and subsequently stabilizes at $\chi = 1.25$. Under these conditions the EP can be considered an ideal gas with an effective value $\chi = 1.25$ and evaluate the energy of the cavity gas using the relationship:

$$E = \frac{pV}{\chi - 1}, \tag{10.5}$$

where $V = \Pi q$.

The following relationship between the cavity gas energy and the overshoot parameter was determined by integrating the adiabatic equations for hexogen EP namely:

$$E = \beta q \Pi^{\alpha} \qquad \text{for } \Pi \geq 3 \text{ m}^3/\text{t}, \tag{10.6}$$

where the values of the coefficients α and β, which depend only on the initial density of the explosives in the chamber, are shown in Table 10.2.

Table 10.2. Numerical values of the coefficients α and β

Parameter	Charge density ρ_c, g/cm^3					
	0.6	0.8	1.0	1.2	1.4	1.6
α	0.88	0.76	0.65	0.58	0.52	0.45
β	0.30	0.32	0.34	0.35	0.37	0.38

The results of integration of adiabatic expressions for the explosive products of TNT, for ρ_{ch} =1.5 g/cm^3 and ρ_{ch} =1 g/cm^3,are close to the relationships for hexogen with ρ_{ch} =1.5 g/cm^3 and ρ_{ch} =1 g/cm^3 in the range $2 \leq \Pi \leq 10^2$ m^3/t.

For other types of explosive the choice of the adiabatic curve for the EP is made based on density of the explosives in the explosive source $q_v = \rho_{ch}\varepsilon$, which characterizes the initial pressure of the EP in the cavity. The corresponding values of ρ_{ch} and ε for hexogen with different values of density are given below:

ρ_{ch}, g/cm^3	1.6	1.4	1.2	1.0	0.8	0.6
ε, kcal/kg	1455	1395	1335	1278	1220	1160

Table 10.3. Experimental data recorded in the field, for chemical excavation explosions

Explosion yield q, t	Parameter							
	W, m	Π, m^3/t	E/q	$\bar{E}$	R, m	n	H, m	H/W
1	2	3	4	5	6	7	8	9
Loess (Central Asia)								
0.08	2.0	250	0.11	33.6	3.25	1.62	1.8	0.9
	2.5	250	0.115	17.0	3.85	1.54	1.9	0.76
	2.75	240	0.116	12.2	3.7	1.35	1.7	0.62
	3.4	220	0.118	6.2	3.75	1.1	0.5	0.15
1.0	4.0	210	0.12	38.1	8.0	2.0	3.4	0.85
	5.0	190	0.123	21.3	7.0	1.4	2.85	0.56
	6.0	175	0.127	11.6	8.4	1.4	3.95	0.66
	7.0	160	0.13	6.9	8.5	1.2	3.1	0.44
Alluvium (Nevada, USA)								
0.116	1.0	250	0.065	276	3.1	3.1	1.65	1.65
					3.0	3.0	1.3	1.3
					2.5	2.5	1.25	1.25
	1.5	250	0.065	276	3.3	2.2	1.9	1.27
	1.9			35.6	3.9	2.1	2.2	1.16
					3.7	2.0	1.85	0.97
					3.5	1.9	1.85	0.97
					3.4	1.85	1.8	0.95
	2.9	230	0.068	9.6	4.6	1.6	2.4	0.83
					4.3	1.5	2.2	0.76
	3.8	210	0.07	3.9	4.3	1.15	2.05	0.54
					4.0	1.1	1.25	0.33
	4.0	210	0.07	3.29	4.4	1.1	1.65	0.41
	4.9	190	0.073	1.65	4.2	0.86	1.4	0.29
					4.1	0.84	0.8	0.16
					3.5	0.7	0.55	0.11
					2.1	0.45	1.15	0.23
	5.8	175	0.075	0.95	3.1	0.53	0.5	0.09
					2.8	0.5	0.7	0.12
					1.8	0.31	0.5	0.09
	6.0	175	0.075	0.85	2.5	0.4	0.3	0.05
1.16	2.1	250	0.11	427	6.2	2.95	3.3	1.57
1.36	4.4	200	0.12	45.5	8.0	1.83	4.24	0.96
8.2	5.2	190	0.12	347	15.2	2.9	7.2	1.38
	10.5	130	0.14	32.6	17.9	1.71	8.9	0.85
	24.5	70	0.17	1.66	17.4	0.71	2.4	0.1
454	38	50	0.19	8.4	47.0	1.25	22.7	0.6

1	2	3	4	5	6	7	8	9
Basalt (Nevada, USA)								
	1.46	20	0.23	992	4.57	3.1	2.28	1.56
	1.46							
	2.93			“	4.82	3.3	2.13	1.46
	.93			103	3.7	1.26	1.46	0.5
0.454	4.48			“	5.1	1.74	1.98	0.68
	4.48			24	4.77	1.06	1.58	0.35
	5.67			“	5.16	1.15	2.68	0.6
	7.37			9.9	3.25	0.57	1.16	0.2
				4	1.86	0.25	1.58	0.21
	7.73	10	0.3	162	13.61	1.76	7.59	0.98
18.2	13.02			26.1	17.37	1.33	10.58	0.81
	17.92			7.1	11.22	0.63	4.94	0.28
	12.7	10	0.3	15	14.1	1.1	7.8	0.61
18.2	15.3			14.3	15.0	0.97	7.95	0.52
	17.7			8.2	15.3	0.86	7.1	0.4
Slate								
17.8	13	30	0.2	17.7	24.5	1.9	9.9	0.76
17.6	14.1			12.6	23.9	1.69	9.0	0.64
18.5	16.1			8.1	23.2	1.44	9.8	061
18.5	17.3			6.1	19.8	1.15	7.7	0.44

In addition one needs to take in to account the effect of the initial charge density on the overshoot parameter, in cases when the overshoot parameter is known from experiments or calculated (using for instance Equation 10.4) for a different value of density. To do this one can assume that the cavity expansion continues until the pressure reaches a certain characteristic value, determined by the strength and elastic moduli of the medium (Rodionov et al, 1971). Thus in brittle hard rocks the damage occurs when the pressure in the cavity is

$$P = \sigma_* \left(\frac{\rho C_p^2}{4.5\sigma_*} \right)^{1/3} . \tag{10.7}$$

Therefore the effect of the initial charge density on the EP energy should be estimated using an estimate of the final pressure in the cavity assuming the explosion is fully contained. This pressure should be treated as a medium parameter.

Using parameters of the cavity for contained explosions as the initial conditions, we compare the experimental field data for sizes of craters formed by chemical explosions with the relationships established as a result of laboratory experiments (Section 2.2). The explosions used for the comparison were represented by point source detonations conducted in loess and sandy clays with flat topography (Belyaev, 1957; Dokuchaev et al, 1963), as well as in alluvium, basalt, and shales (Chabai, 1965; Murphy and Vortman, 1961; Nordyke, 1962; Vortman, 1968).

The parameters of the explosions and the linear dimensions of the resulting craters for the explosions in loess, alluvium, basalt, and shale—as well as the ratios between the cavity gas energy and the total energy E/q and the dimensionless energy $\bar{E}$ according to Equation 2.16 needed for this correlation—are shown in Table 10.3. The main properties of loess and alluvium are very similar. Both media are weakly-cohesive, are easily fragmented during the ejection, and have similar values of density and moisture content: $\rho = 1.6 g/cm^3$ and $\omega = 5 - 10\ \%$ in the near-surface layers, and $\rho = 1.8 - 1.9/cm^3$ and $\omega = 10 - 30\ \%$ at greater depth (Dokuchaev et al, 1963; Boardman et al, 1964).

The weights of the charges (used in these experiments) varied over four orders of magnitude, from 0.08 to 454 tons. Ammonite-6 with was used to conduct the explosions in loess with dry density of 0.8 – 0.9 g/cm^3. TNT charges were used in alluvium. These charges weighed 0.116 kg, had spherical shapes, and were made of cast TNT with density 1.6 g/cm^3. The depths of burial for these charges varied between 1 and 38 m. To calculate appropriate cavity dimensions, the relationships between the overshoot parameter and depth were taken into account (Figure 10.1b, line 1). As a result the energy of the cavity gas grew with depth, from 10% to 20 % of the total energy.

Existing data for chemical explosions in hard rock with a flat free surface is limited. The maximum yields for these explosions do not exceed 18 tons. Chemical explosions were conducted in the same rock massif as the nuclear explosion DANNY BOY (Chapter 2.1). The surface layer of basalt in that case was highly fractured with an average density of 2.25 g/cm^3 and porosity of 10 – 20 %. Below 6 – 7 m the basalt was more dense (ρ = 2.25 g/cm^3) and had greater strength $\sigma_* = 1000 - 1600$ kg/cm^2. The sources were represented by TNT charges with masses of 0.454 t and 18.2 t ($\rho_{ch} \approx 0.9$ g/cm^3, ε = 1000 kcal/kg) and nitrous methane with a mass of 18.1 t ($\rho_{ch} \approx 1.13$ g/cm^3, ε = 1083 kcal/kg). Under these conditions the overshoot parameter was $\Pi = 10 - 20$ m^3/t and the corresponding energy was $E = (0.23 - 0.3)q$.

Excavation explosions using nitrous methane charges with masses of 17.6 – 18.5 tons were conducted in shales with density of 2.1 – 2.2 g/cm^3, porosity of 10 – 20 % and compressive strength of 30 – 50 kg/cm^2. In these rocks the overshoot parameter was approximately 30 m^3/t and $E = 0.2\ q$.

The comparison between the crater sizes for chemical explosions in these rocks with empirical relationships determined using laboratory experiments, are shown in Figure 10.3. Good agreement is observed for the ejection index for loess, alluvium, and shale, between laboratory experiments (solid lines) and real (full scale) explosions. The observed ejection index for basalt is 30 – 40 % lower than the empirical relationships. Crater depths for the full-scale experiments agree with the model only for $n = 0.5 - 1.5$. If the ejection index increases, crater depths grow faster than the empirical model, with the exception of explosions in basalt, for which crater depths agree with the model. For these explosions the depth is related to the radius of the crater via

$$H = 0.27\ nW. \qquad (10.8)$$

For full scale explosions, crater depth is better described by the relationship

$$H = 0.27\ W\ (2n - 1), \tag{10.9}$$

shown in Figure 10.3b as a dashed line.

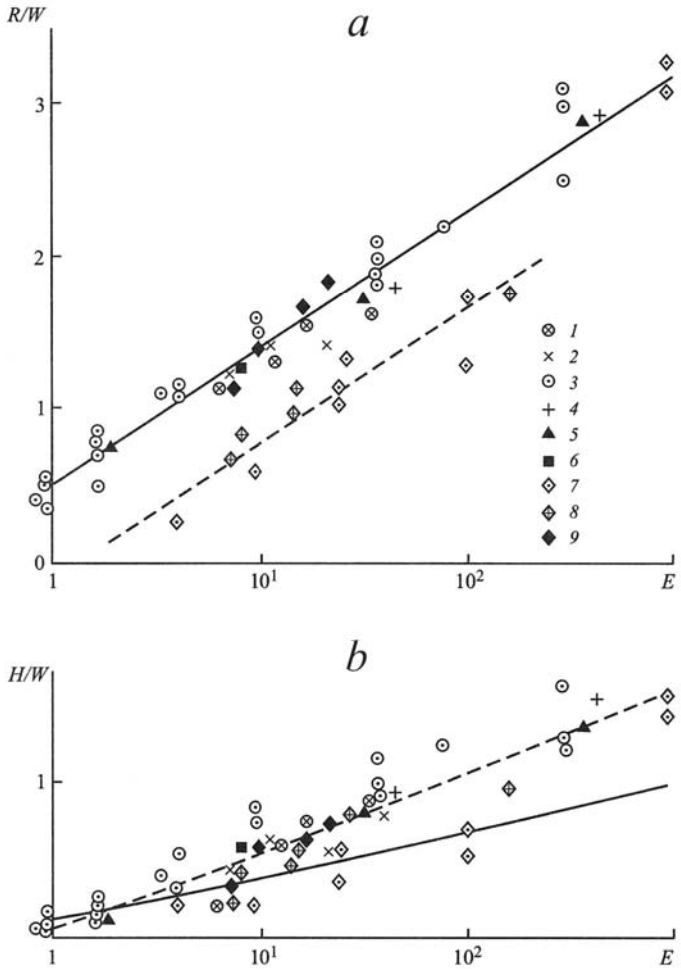

Figure 10.3: Ejection index (a) and the crater depths (b) as a function of energy of the explosive products from laboratory experiments (solid lines) and full-scale chemical explosions in the following rocks: *1, 2* – loess, *3–6* – alluvium, *7, 8* – basalt, and *9* – slate.

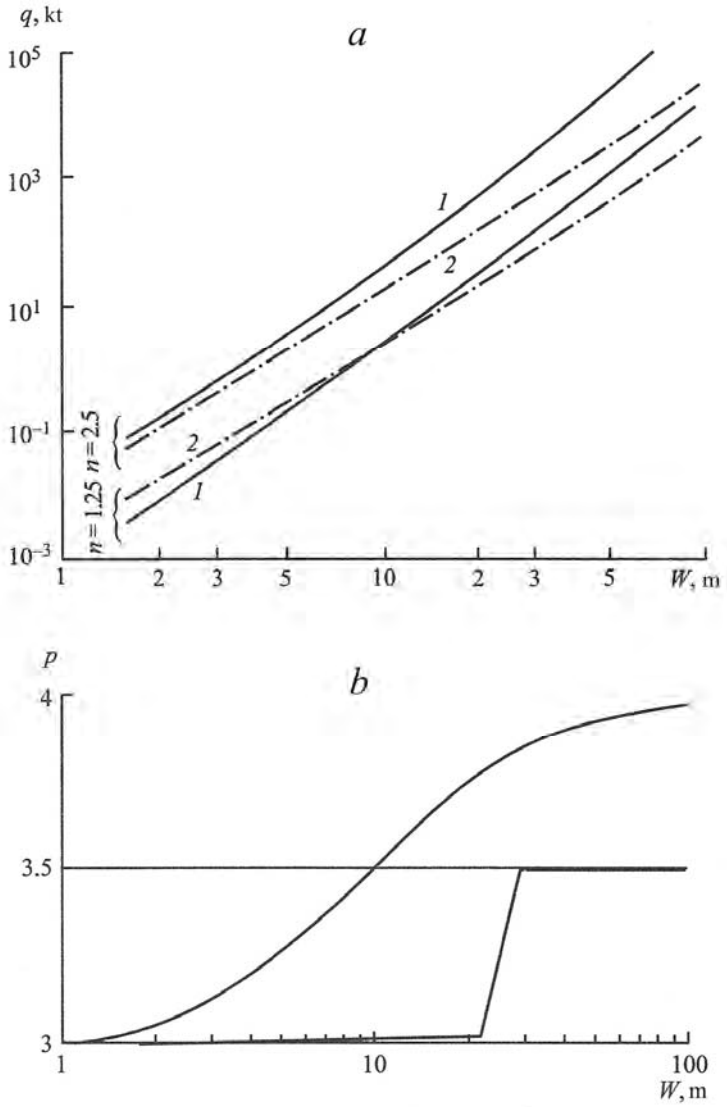

Figure 10.4: The value of the ejection charge (a) and the exponent *x* in the relationship $q \sim W^{x}$ (b) as a function of depth for n = 1.25 and n = 2.5. The numbered lines show the relationships: *1* – according to Equation 10.12, and *2* – according to the Boreskov formula.

Thus, full scale excavation chemical explosions in sediments or low-strength rocks agree with the results of laboratory experiments over a broad range of charge weights (yields or explosion energy), between 80 kg and 500 t. Only the crater sizes in high-strength basalt were lower than predicted. This correspondence supports use of the empirical relationships (10.1) for calculations related to full scale excavation explosions. Substituting the relationships for the overshoot parameter (Equation 10.6) into (10.1) we obtain:

$$q = \frac{0.28(\rho g W + P_a)W^3}{\beta \Pi^{-\alpha}} \cdot 10^{n/0.9}. \qquad (10.10)$$

Equation 10.10 allows calculation of the chemical charge as a function of needed ejection index n, and depth of burial W, for any rock type characterized by an overshoot parameter Π. The values of α and β depend on the charge density (Table 10.2). For a typical charge density of ρ_{ch} = 1 g/cm^3 the quantity ξ depends on the overshoot parameter as

$$\xi = 0.65\Pi^{-0.34}, \tag{10.11}$$

where Π is in m^3/t. Substitution of (10.11) into (10.10) yields a formula to calculate the chemical charge size (the yield), namely

$$q = 10^{-6}\, \Pi^{0.34}\, (\gamma W + 10)\, W^3 \cdot 10^{\,n/0.9}, \tag{10.12}$$

where $\gamma = \rho g$ is the average weight of the volume of rocks above the charge, in g/cm^3. \footnote{ Check the usage here, of symbols and units referring to weight or mass.}, q is in tons, W is in meters and Π is in m^3/t.

If the charge density deviates significantly from ρ_{ch} = 1 g/cm^3 (by more than 20 – 25 %), Equation 10.12 should be rewritten by substituting the corresponding relationship 10.6 into Equation 10.10. Effects of different properties of chemical explosives (explosive type, specific explosive energy) and the size of the emplacement chamber depend on the character of isentropic expansion of the explosive products. Expressions 10.10 and 10.12 account for the increase in overburden pressure needed for an increase of yield. Therefore the characteristic property of these equations is the monotonic increase of the exponent p in the relationship $q \sim W^p$ from p = 3 for small depths of burial ($W \sim 1$) m to p = 4 for larger depths ($W \sim 100$ m) (Figure 10.4b).

The relationship between the chemical explosion yield and the overshoot parameter accounts for the effects of specific physical properties of rocks surrounding the charge on the excavation efficiency, including the decrease of cavity size with depth. One condition of validity of Equation 10.12 is sufficient fragmentation of the ejected rock, to allow use of the dry friction law during the medium movement. This condition is satisfied for large-scale explosions in hard rock, and any explosions in soft rocks and sediments. This condition is not satisfied for explosions in clay, nor for small-scale explosions (q < 10 t) in hard rocks.

We compare Equation 10.12 with the well-known formula by M.M. Boreskov, which for a wide range of explosion depths can be written as

$$q = k\, W^3\, (0.4+0.6n^3) \quad \text{for } W < 25 \text{ m}, \tag{10.13}$$

$$q = k\, W^3\, \mathrm{sqrt}(W/25)\, (0.4+0.6n^3) \qquad \text{for } W > 25 \text{ m}.$$

We consider a medium represented by a hard rock with medium strength (VII, VIII strength category according to CNAR) and having the volume weight of γ = 2.5 g/cm^3 and the overshoot parameter Π = 10 m^3/t (which does not change with depth). For such rock the value of the specific weight of explosives according to (10.13) is k = 1.5 kg/m^3 (Reference …, 1962). Comparison between the results of calculations using) Equations 10.12 and 10.13, for the depth range 1 – 100 m, is shown in Figure 10.4a for two values of the ejection index n = 1.25 and n =

2.5. For shallow depths of burial $W < 10$ m the difference between the equations is insignificant. There is a tendency to underestimate the charge weight if the calculations are performed according to 10.12, if the ejection index and the depth of explosion decrease. For $W = 10 - 20$ m the situation changes and Equation 10.13 begins to underestimate the charge yield, especially when the ejection coefficient increases, despite the increase of the exponent (p) from 3 to 3.5 for depths $W > 25$ m.

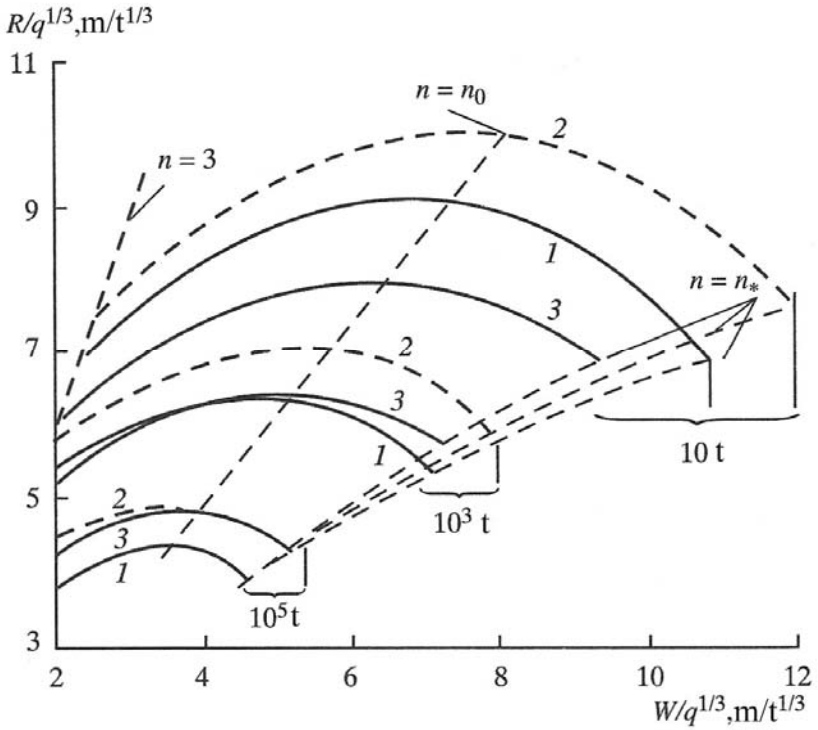

Figure 10.6: The effect of the explosion size in the range $10 \leq q \leq 10^5 t$ on the relationships between crater radius and the scaled charge depth for the following rocks: *1* – hard rock, *2* – alluvium with Π = 10 m^3/t, and 3 – alluvium with $\Pi = f(W)$.

Thus Equation 10.12 satisfies the self-similarity hypothesis for depth of burial for large-scale TNT charges, and continuously accounts for the increasing role of gravity for increasing explosion size.

Next we consider the effects of the explosion scale, and the rock properties, on crater size. Substituting Equation 10.6 into 10.10 we obtain the relationship between the crater radius and the yield and depth of the explosion:

$$\frac{R}{W} = 0.9lg\frac{3.6\,\beta\Pi^{-\alpha}}{(\rho g W + P_a)^{1/2}W^3}\,. \qquad (10.14)$$

Let us consider two rock types with constant density through the ejection column: hard rock with ρ = 2.5 g/cm^3 and Π = 10 m^3/t, and alluvium with ρ = 1.6 g/cm^3. We also consider two

different choices for the overshoot parameter: one depending on depth from Figure 10.1b (line 1), and a depth-independent value of Π = 10 m^3/t. For the first rock type the value of Π = 10 m^3/t is reached at a depth of approximately 100 m and does not change after that. Assuming that the charge density is ρ_{ch} = 1 g/cm^3 the coefficient ξ is related to the overshoot parameter through Equation 10.11. In this case if Π = 10 m^3/t the cavity radius is $\bar{r}_c = 1.34\, m/t^{1/3}$ and $E = 0.3q$. Figure 10.5 shows the relationships between crater radius and depth and yield of explosions in the range $10 \le q \le 10^5 t$ for these rock types. Optimum and maximum depth for excavation explosions are marked with dashed lines for $n = n_0$ and $n = n_*$ respectively.

The largest crater sizes are formed in alluvium if the overshoot parameter is Π = 10 m^3/t and does not change with depth. In reality the overshoot parameter in alluvium is depth-dependent, in which case the crater sizes are smaller for alluvium than for hard rock (if all other parameters are the same) due to the reduction of the energy of cavity gas.

However this situation is observed only for explosions with yields $q \le 100$ t. For $q \sim 1000$ t the crater sizes for hard rock and alluvium are approximately the same, while for $q \ge 10^4$ t the overshoot parameters become the same in alluvium and hard rock, and the crater sizes in hard rock become smaller than in alluvium (other parameters being equal). This reduction in the crater size is related only to the differences in the weight of the ejection column, and for the given values of density the reduction is 10 – 15 % for the radius and 25 – 35 % for the volume of the crater.

In addition to rock density, other rock properties affecting the overshoot parameter also have an influence on crater size. The effect of the overshoot parameter on the crater radius, we obtain by substituting Equation 10.11 into 10.14:

$$R = 0.9Wlg\frac{10^6 q}{\Pi^{0.34}(\gamma W + 10)W^3} \quad \text{for } \rho_{ch} = 1 \text{ g/cm}^3, \tag{10.15}$$

where q is in tons, W is in meters, γ is in g/cm^3, and Π is in m^3/t. It follows from Equation 10.15 that an increase in the overshoot parameter decreases the crater radius. In particular, an increase in the overshoot parameter by an order of magnitude from 2 to 20 m^3/t, a typical range of values for hard rock, decreases the crater radius by 20 – 25 % (in the range $n_0 \le n \le n_*$).

Next we evaluate the effect of the initial density of the explosive, on the overall efficiency of the explosion for purposes of excavation. In order to do this we use Equation 10.6 for explosives of low (ρ_{ch} = 0.6 g/cm^3) and high (ρ_{ch} = 1.6 g/cm^3) density. After substituting Equation 10.6 into 10.14 we obtain:

$$R = 0.9Wlg\frac{1.35\cdot 10^6 q}{\Pi^{0.3}(\gamma W + 10)W^3} \quad \text{for } \rho_{ch} = 0.6 \text{ g/cm}^3,$$

$$R = 0.9Wlg\frac{7\cdot 10^5 q}{\Pi^{0.38}(\gamma W + 10)W^3} \quad \text{for } \rho_{ch} = 1.6 \text{ g/cm}^3, \tag{10.16}$$

where q is in tons, W is in meters, γ is in g/cm^3, and Π is in m^3/t. It follows from Equation 10.16 that a reduction in the charge density increases the crater radius. In particular, for hard rock with

ρ = 2.5 g/cm^3 and Π = 10 m^3/t, the reduction in the charge density from 1.6 g/cm^3 to 0.6 g/cm^3 and other parameters kept equal, increases the crater radius by 25 – 30 % (in the range $n \approx n_0$).

The effect of the explosion size on the relationship between crater radius and explosion depth is shown in Figure 10.6, in "gravitational" scaling coordinates for hard rock (ρ = 2.5 g/cm^3 and Π = 10 m^3/t). The explosion yield varies in the range 10 t $\leq q \leq 10^5$ t. The plot shows that for an increase in yield the difference between the curves becomes smaller, and for $q \geq 10^5$ t the curves become almost indistinguishable. In these circumstances, $\rho g W \gg p_a$, and the relationship between the parameters of the explosion and the crater radius (Equation 10.15) becomes

$$\frac{R}{W} = 0.9 lg \frac{10^6 q}{\Pi^{0.34} \gamma W^4} \text{ for } \rho_{ch} = 1 \text{ g/cm}^3, \tag{10.17}$$

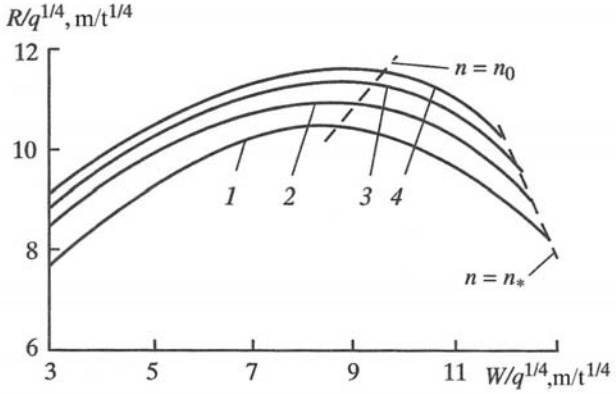

Figure 10.5: The effect of the chemical explosion size, in the range $10 \leq q \leq 10^5 t$, on the relationships between crater radius and the scaled charge depth, for hard rocks plotted in scaled coordinates, for the following yields: *1* – 10 tons, *2* – 100 tons, and *3* – 1000 tons.

Let us next determine the optimal and maximal depth for chemical excavation explosions. The optimal depth determines the crater with the largest volume (for a given yield). Laboratory studies have shown that the largest crater is formed when the value of the dimensionless parameter $\bar{E}_{opt} = 6.8 \pm 0.8$ and is characterized by the ejection index value of $n_{opt} = 1.2 - 1.3$. Using these values we obtain a relationship between the optimal depth and the explosion yield taking into account its relationship with the total gas energy $E = \xi q$ (also using Eq. 2.57):

$$(\rho g W_{opt} + P_a) W_{opt}^3 = 0.147 \xi q \, . \tag{10.18}$$

Denoting the average weight of the rocks above the charge as $\gamma = \rho g$, substituting Equation 10.11 for the coefficient ξ , and using Eq. 2.58, we obtain the relationship between the optimal depth of burial and the explosion yield:

$$(\gamma W_{opt} + 10) W_{opt}^3 = 4.1 \cdot 10^4 q / \Pi^{0.34}, \tag{10.19}$$

where W_{opt} is in meters, q is in t, γ is in g/cm^3, and Π is in m^3/t.

The maximum possible depth W_* for chemical explosions for which the crater still forms can be determined using Equation 2.61 by substituting the expression for $E = \xi q$:

$$(\rho g W_* + P_a) W_*^{2.4} = 0.23 \frac{\xi q}{(\bar{r}_c)^{0.6}}. \quad (10.20)$$

Using the average weight of the rocks above the charge as $\gamma = \rho g$ and expressing the cavity radius through the overshoot parameter $r_c = 0.62(\Pi q)^{1/3}$, we obtain the expression for the maximum possible depth for a TNT excavation explosion as a function of yield:

$$(\gamma W_* + 10) W_*^{2.4} = 6.8 \cdot 10^4 q^{0.8} / \Pi^{0.54}. \quad (10.21)$$

where W_{opt} is in meters, q is in t, γ is in g/cm^3, and Π is in m^3/t.

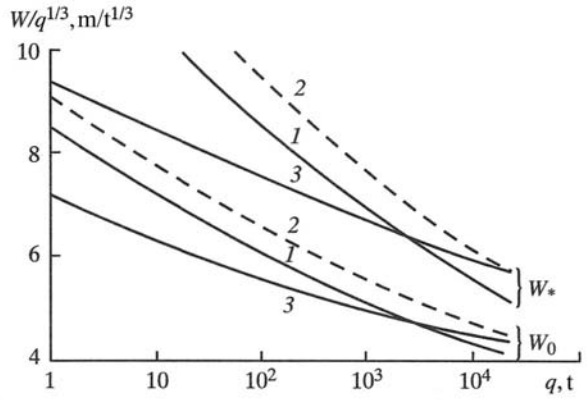

Figure 10.7: The effect of yield on the optimal and maximal depth of burial for hard rock (line *1*) and alluvium (lines *2* and *3*). The "overshoot parameter" for alluvium is defined as: *2* – alluvium with Π = 10 m^3/t, and *3* – alluvium with $\Pi = f(W)$.

According to Equations 10.18 – 10.21 the optimal and maximal depths for chemical excavation explosions depend on the explosion yield, the average volume weight of the rock above the charge, and the overshoot parameter. Figure 10.7 shows the relationships between these characteristic depths and the explosion energy in coordinates of geometrical similarity (universal coordinates). The plot shows the results for hard rock with γ = 2.5 g/cm^3 and Π = 10 m^3/t, and for alluvium with ρ = 1.6 g/cm^3 and the constant overshoot parameter Π = 10 m^3/t and with the depth dependent overshoot parameter (Figure 10.1, line *1*).

For any rock type, the scaled characteristic depth decreases with increasing yield. For instance, the increase in the charge yield from 1 to 10^5 tons leads to decreasing the optimal scaled depth by a factor of 1.8 – 2.5, while the maximum depth decreases by a factor of 2 – 2.8. Overall the highest values of the optimal and maximal depths are found for alluvium with a depth-independent overshoot parameter Π = 10 m^3/t. If the appropriate depth dependence was used, the characteristic depths decrease significantly. For yields $q < 10^3$ t these values are even smaller than for hard rock. Only for yields $q > 10^3$ t do the characteristic depths for excavation explosions for hard rock become smaller than those for alluvium, and this is because the overshoot parameters become approximately equal at these depths, while the weight of the ejected rocks is different (being greater for hard rock).

10.2. Excavation explosions using linear charges

Building dams and channels, or extracting mineral deposits, often calls for the more economical approach offered by linear charges, placed in elongated tunnels, rather than chambers. Depending on the rock type and topography, linear charges can be placed in either trenches or tunnels. To create elongated channels in soft sediments, charges placed in trenches are used. To make channels or build rock dams in hard rock in mountainous topography, the charges are placed in tunnels (Avdeev et al, 1977). The largest-scale explosions conducted in trenches were placed at depth of $W = 7 - 10$ m with linear charge density (weight of explosives per unit of length of the charge) of $q_1 = 1.5 - 2$ t/m. Many of the explosions used for building channels had significant scale, with $W = 10 - 40$ m and $q_1 = 3 - 11$ t/m.

The largest explosions using tunnel charges were conducted during the building of a protective dam in Medeo[4]: $W = 50 - 100$ m and $q_1 = 15 - 40$ t/m (Rodionov et al, 1971). Such large-scale excavation explosions require thorough calculations for the charge parameters, because possible miscalculations during the movement of large volumes of rocks can result in significant amounts of additional work. Using the laboratory techniques discussed in Chapter 2, a study of linear charges was conducted and new methods of calculations were developed (Adushkin, 1980). Due to the axial symmetry of linear sources, the relationships between the crater size and charge parameters (Section 2.2) after some simplifications can be written in the form

$$n = F\left(\bar{E}_l, \frac{W}{r_c}\right), \text{ where } \bar{E}_l = \frac{E_l}{(\rho g W + P_a)W^2}, \tag{10.22}$$

where $n = D/2W$, D is the width of the channel, W is the explosion depth, E_l is the energy of the cavity gas per unit length, $\rho g W$ is an overburden pressure, and P_a is the pressure above the ground surface. A series of laboratory experiments was conducted using parameters which can be scaled to the actual size for depths ranging over 1 – 100 m, assuming the following scaling relationships:

$$\frac{P}{\rho g W} \approx 10 - 100, \ \frac{P}{P_a} \sim 10 - 100, \frac{\rho g W}{P_a} \approx 10 - 100 \ \frac{P}{c} \approx 10 - 100,$$

where P is the gas pressure in the cavity after its expansion, c is the cohesion of the sediment or rock, assuming that the coefficients of internal friction are approximately the same for the model and the field conditions. The following empirical relationships for the ejection index and the depth of the channel were obtained, using least-square fitting of the results of the laboratory tests:

$$n = 1.35 \, lg \, \bar{E}_l + 0.2, \quad H/W = 0.5 \, lg \, \bar{E}_l + 0.12. \tag{10.23}$$

[4] Medeo is in mountainous terrain south of Almaty, the largest sity in Kazakhstan. Note added by translators.

Large-scale experiments with linear charges were used to compare with this empirical relationship. A series of such explosions was carried out during the building of canals at Irtysh-Karaganda (126 ton with length of 115 m, 236.6 t with the length of 285 m, 1500 t with the length of 1225 m), Karakum (149.6 ton with length of 400 m), Bol′shoi Namanganskii[5] (990 ton with length of 176 m), as well as the road between Alma-Ata[6] and Novoiliisk road (527 ton with length of 195 m) (Avdeev et al, 1977). The results of these explosions are summarized in Table 10.4, showing the rock types at the explosion sites, explosion types, linear charge density q_l converted to TNT equivalent, depth of burial *W*, and the channel dimensions in different sections. Also shown are the values of the dimensionless parameter $\bar{E}_l$ calculated using values of the overshoot parameter for each rock type: Π = 30 m^3/t, $\bar{E}_l = 0.24q_l$ for sandy clays; Π = 5 m^3/t, $\bar{E}_l = 0.43q_l$ for hard rock; and Π = 20 m^3/t, $\bar{E}_l = 0.27q_l$ for hardened clay-rich sand. In addition, data from small-scale explosions in soft rocks (sandy clay and loess) (Vovk, 1976) were used for comparison with the laboratory experiments. Sandy clays were taken to have density of ρ = 1.99 g/cm^3 and moisture content of ω = 14%, while the parameters for loess were ρ = 1.55 g/cm^3 and of ω = 7%. Due to a small depth of burial (0.5 – 2 m), the overshoot in sandy clays varied in the range $\Pi = 70 - 90$ m^3/t, with $\bar{E}_l = (0.15 - 0.2)q_l$; the overshoot in loess was $\Pi = 250 - 300$ m^3/t, with $\bar{E}_l = (0.15 - 0.2)q_l$.

Comparison of the field data with results from Equations 10.23 is shown in Figure 10.8. The plot shows that the field data for the half-width of the channel agree with the empirical formula over the entire range of change $1 \le R/W \le 4$ (line *1*). Field data also agree with the model in the optimal range of depth when the ejection index reaches its maximum (for *n* between 1 and 1.5). Increase in the ejection index the scaled [relative] depth of the channel grows faster for the field data than for the model, which can be explained by material compression below the charge during the pressure wave. The channel depth in the model (line 2 in Figure 10.8) is described by the relationship

$$H = 0.38nW. \tag{10.24}$$

Field experiments show significant scatter for the channel depths, and for small-scale explosions from Table 10.4 the channel depth is better described via

$$H = 0.32W(2n - 1), \tag{10.25}$$

shown as a dashed line 2′ in Figure 10.8. Increasing the explosion size decreases the scaled depth of the channel. Therefore, for explosions with $q_l = 1 - 10$ t/m from Table 10.4, the channel depth corresponds to the formula

$$H = 1.26W(2n - 1), \tag{10.26}$$

[5] Translated as “Large Namanganskii”

[6] The city now has a Kazakh name, Almaty. The meaning is Place of Apples, and indeed this is the region in which apple trees evolved.

shown as a dashed line 2″ in Figure 10.8, which almost coincides with the model relationship according to Equation 10.24. Equation 10.24 can be used as a limiting relationship for further increase of the explosion size, for the range $q_l > 10$ t/m.

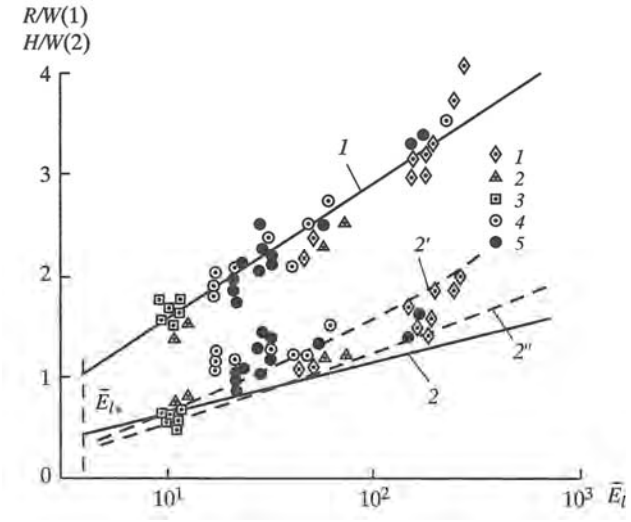

Figure 10.8: Half-width (a) and depth (b) of the channel as studied in the laboratory experiments (lines *1* and *2*) and full-scale chemical explosions from Table 10.4, in the following rocks: *1* – sandy clay (events #1 – 9), *2* – hard rock clay (events #10 – 13), *3* – clay-rich sand (events #14 – 19), *4* – sandy clay (events #20 – 28), and *5* – loess (events #29 – 40).

Comparison between the measurements for the laboratory model and field data shows that Equation 10.23 can be used for practical calculations of the ejection index and the depth of burial for linear charges. We transform Equation 10.23 by expressing the energy of the cavity gas per unit length via the linear charge density as

$$q_l = 0.71 \frac{(\rho g W + P_a) W^2}{\xi} 10^{n/1.35} \ . \tag{10.27}$$

Let us consider an explosion of a linear charge with length l_0 and ρ_{ch} = 1 g/cm^3, which forms a cylindrical cavity of length l_p. We denote the overshoot parameter for a linear charge as Π_l. For the specific explosive energy ε = 1 kcal/g, the energy of the cavity gas per unit length of the cavity is given by

$$E_l \ = \ 0.65 \, q_l \, \Pi_l^{-0.34} \, l_0 / l_p . \tag{10.28}$$

According to the results of Section 6.7, the overshoot parameter for the linear charge Π_l is smaller than the overshoot parameter for the spherical [or point] Π_s charge, and is and related to the latter through the expression

$$\Pi_l \ = \ 0.76 \Pi_s^{0.9} \ . \tag{10.29}$$

For long charges we assume that $l_{ch} \approx l_0$ and by substituting Equation 10.29 into 10.28 we obtain

$$\xi \ = \ 0.71 \Pi_s^{0.9} \ . \tag{10.30}$$

Table 10.4. Parameters of explosions conducted using different explosives in different rock media

Rock type	Explosive type	Parameter						
		q/l, t/m	*W*, m	$\bar{E}_l$	*D*, m	*n*	*H*, m	*H/W*
Sandy clay	6ZhV[?] [some sort of ammonite]	1.1 1.1	5.5 5.1	199 240	36 38	3.28 3.73	10.5 9.5	1.9 1.86
	Ammonite-6	1.0 1.0 0.8	5.7 5.6 5.0	165 170 182	36 32.6 31.8	3.15 2.93 3.18	9.8 8.2 7.8	1.7 1.49 1.56
	TG	1.7	6.0	245	50	4.1	12	2.0
	6ZhV[?]	0.31 0.45	6.0 6.5	43 52	26 32	2.17 2.46	6.7 7.7	1.1 1.18
	TG	0.27	3.2	179	19	2.98	4.6	1.44
Crystalline rock	Some fancy type of ammonite [hard rock ammonite?]	3.0 3.5 3.5 3.0	13 15 26 25	74 58 12.1 11.3	65 67 80 65	2.5 2.24 1.54 1.3	15 17 20 18	1.25 1.13 0.77 0.72
Clay-rich sand	6ZhV[?]	6.1 72 8.6 10.8 10.1 9.5	34.3 36.2 39.1 40.2 39.4 39.2	9.4 10.2 9.9 11.9 11.4 10.9	120 120 119 121 126 135	1.74 1.66 1.53 1.50 1.60 1.72	19 19 20 24 22.8 20.6	0.55 0.52 0.54 0.60 0.58 0.63
Sandy clay	Pressed TNT	$4 \cdot 10^{-3}$	1.0	18.2	4.0	2.0	1.22	1.22
		$4 \cdot 10^{-3}$	1.0	18.2	3.84	1.92	1.12	1.12
		$4 \cdot 10^{-3}$	1.0	18.2	3.6	1.8	1.15	1.15
	PETN	$4 \cdot 10^{-3}$	1.0	30.1	4.7	2.35	1.34	1.34
	6-ZhV	$4 \cdot 10^{-3}$	1.0	31.4	4.1	2.05	1.17	1.17
	Igdanit	$3.2 \cdot 10^{-3}$	1.85	61.7	10	2.73	2.7	1.5
	6ZhV	$4 \cdot 10^{-3}$	0.6	54.3	3.0	2.5	0.75	1.25
		$4 \cdot 10^{-3}$	0.3	228	2.1	3.5	0.5	1.65
		10^{-2}	1.0	45.7	4.1	2.05	1.25	1.25
Loess	Pressed TNT	$4 \cdot 10^{-3}$	0.8	21.1	3.0	1.88	0.8	2.0
		$4 \cdot 10^{-3}$	0.8	21.1	3.15	1.97	0.75	0.94
		$4 \cdot 10^{-3}$	0.8	21.1	2.85	1.78	0.7	0.88
		$2 \cdot 10^{-2}$	1.6	23.5	6.7	2.09	1.8	1.12
	Granulite[?]	$2 \cdot 10^{-2}$	1.6	29.5	6.6	2.09	1.6	1.0
		$2 \cdot 10^{-2}$	1.6	29.5	7.19	2.24	2.2	1.37
	6ZhV	$2 \cdot 10^{-2}$	1.6	29.5	8.0	2.5	2.08	1.3
	Igdanite	$2 \cdot 10^{-2}$	1.6	32	7.45	2.2	2.18	1.36
		$2 \cdot 10^{-2}$	1.6	32	7.95	2.1	2.05	1.28
		$4 \cdot 10^{-3}$	0.4	150	2.7	3.3	0.6	1.5
		$8 \cdot 10^{-3}$	0.52	176	3.5	3.37	0.83	1.6
	Granulite	$4 \cdot 10^{-3}$	0.6	57	3.0	2.5	0.8	1.3

After substitution of Equation 10.30 into 10.27 and using the average weight of the rocks above the charge $\gamma = \rho g$ we obtain the final formula for the excavation using linear charges:

$$q_l = 2.3 \cdot 10^{-6}\, \Pi_s^{-0.3}\, (\gamma W + 10)\, W^2 \cdot 10^{\,n/1.35}, \qquad (10.31)$$

where q_l is in t/m, W is in meters, γ is in g/cm^3, and Π is in m^3/t.

Equation 10.31 gives the linear charge density as a function of explosion depth, for a given average density of material above the charge and the overshoot parameter of the emplacement rock. Equation 10.31 satisfies the similarity principle with respect to changes in yield, and accounts for the increase in the overburden pressure if depth is increased. Thus for shallow depth of burial the charge density is proportional to $q_l \sim W^2$, for large depth $W \sim 100$ m and $\rho g W \gg p_a$ and the charge density is proportional to $q_l \sim W^3$.

The relationship between the overshoot parameter and the charge emplacement parameters in Equation 10.31 takes into account the effect of rock properties on the excavation efficiency of the explosion, including the decrease in cavity size with an increase in the depth of burial. Equation 10.31 is applicable for $n \leq 4$ and in the condition of sufficient fragmentation of the ejected rocks (for example compared with LLR) in order to satisfy the dry friction law during movement of the medium. This condition is satisfied for any explosions in soft rocks and sediments (loess, sandy clay etc), and for large-scale explosions in hard rock. This condition is neither satisfied for explosions in clay, nor for the small-scale explosions in hard rocks.

10.3. Comparison of the excavation efficiency between nuclear and chemical explosions

Detonation of chemical explosions differs from nuclear explosions in that the process of formation of the cavity gas is independent of the medium properties. This is due to the much lower temperatures and pressures associated with chemical detonations ($P \sim 10^5$ kg/cm^2, $T \sim$ 3000 – 5000º). At these values, no rock vaporization, melting or chemical decomposition occurs, and gas is represented solely by the products of chemical decomposition of the explosives.

Because of the different nature of formation of gaseous EP during nuclear and chemical explosions it is interesting to compare their excavation efficiency. In order to obtain a correct estimate this comparison should be conducted for rocks with similar properties and for the same scale of explosions (i.e. the yield and depth of burial should be the same). We consider two rock types: hard rock, and loose sediment similar to alluvium. In both cases the densities stay the same (ρ = 2.5 g/cm^3 and ρ = 1.6 g/cm^3 respectively). The explosion yields are taken to be in the range 10 t $\leq q \leq 10^5$ t.

We consider the case of a nuclear explosion in hard rock (ρ = 2.75 g/cm^3, C_p = 5000 m/s, $\sigma_* = 700\ kg/cm^2$) with mixed gas content (η = 0.12 and η = 0.24, $\eta_\omega = \eta_{CO2}$), described in Chapter 2 (Figure 2.28b). For a chemical explosion in rock with these properties, and for the charge density of ρ_{ch} = 1 g/cm^3 and the specific energy of ε = 1 kcal/g, the overshoot parameter is Π = 10 m^3/t. Figure 10.9a shows the relationships for the crater radii for nuclear and chemical explosions in this yield range 10 t $\leq q \leq 10^5$ t. According to the Figure the crater sizes for

chemical explosions in hard rocks are always greater than for nuclear explosions (other conditions being equal), even for considerable water content (η =0.24). We define a coefficient of efficiency with respect to crater radius, $K_R = R_n/R_{ch}$. The estimate shows that for explosions in hard rock with $\eta = 0.2$ ($\eta_\omega = \eta_{CO2}$) the value of the coefficient is $K_R = 0.74$, and for $\eta = 0.24$ ($\eta_\omega = \eta_{CO2}$) $K_R = 0.83$ (for the range of the ejection index $n_0 \le n \le n_*$).

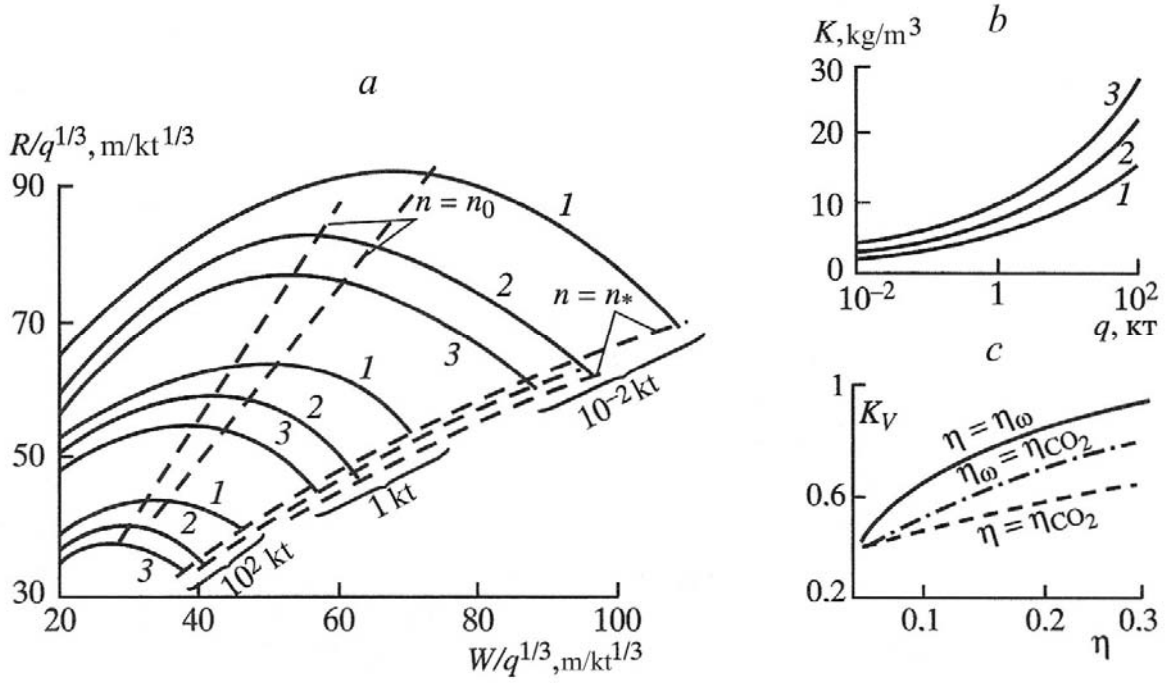

Figure 10.9: Comparison of the excavation efficiencies of nuclear and chemical explosions in hard rocks: a) the relationship between the crater radius and the explosion yield, b) relationship between specific energy consumption and yield, and c) "effective TNT equivalent" of nuclear explosions, as a function of gas content and its components. The numbered lines show: *1* – chemical explosions, *2* – nuclear explosions with $\eta = 0.24$ ($\eta_\omega = \eta_{CO2}$), and *3* nuclear explosions with $\eta = 0.12$ ($\eta_\omega = \eta_{CO2}$).

The comparison between crater radii for chemical and nuclear explosions in alluvium is shown in Figure 10.10a. To calculate the crater radii for nuclear explosions (Equation 2.46), the value of the average density for alluvium was taken as γ =1.6 g/cm^3, and the cavity radius was r_c = 5 m/kt$^{1/3}$. Two values of moisture content were used: $\eta_\omega = 0.12$ and $\eta_\omega = 0.3$.

In the case of a chemical explosion the charge density in the chamber was ρ_{ch} = 1 g/cm^3 and the relationship between the overshoot parameter and the depth of burial were accounted for according to Figure 10.1a (line *1*).It is clear that the situation in alluvium is more complex, and the explosion yield plays an important role in comparison between the nuclear and chemical explosions due to the effect of depth on the overshoot parameter. As it turns out, for small explosions $q \le 10^3$ t the crater sizes for TNT and nuclear explosions are approximately equal. For a high moisture content in alluvium and a decrease in the yield, the efficiency of a nuclear

explosion may exceed the efficiency of a chemical explosion ($K_R > 1$). For explosions with large yields, $q \geq 10^4$ t, craters in alluvium for chemical explosions are always greater than for nuclear explosions ($K_R = 0.7-0.9$).

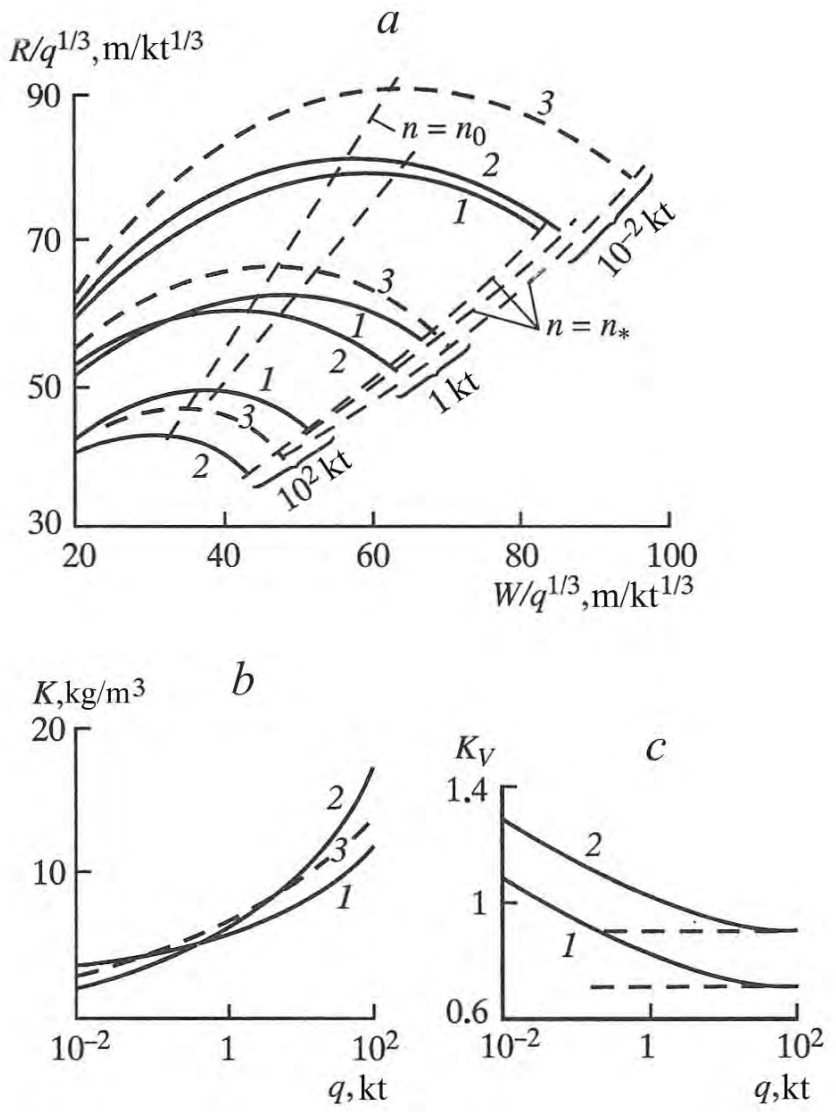

Figure 10.10: Comparison between the excavation efficiencies of nuclear and chemical explosions in alluvium: a) the relationship between the crater radius and the explosion yield, b) relationship between specific energy consumption and yield, and c) efficiencies of nuclear and chemical explosions as a function of yield. The numbered lines show: *1* – chemical explosions, *2* – nuclear explosions with $\eta = 0.12$, and *3* nuclear explosions with $\eta = 0.3$.

The reduction of the scaled crater radii with increasing yield is related to an increase of the [specific] energy consumption \footnote{Check terminology.}due to an increase in overburden pressure. The specific energy consumption for an excavation explosion is equal to the ratio

between the total energy released by the explosion, in TNT equivalent, and the volume of the crater. The volume of the crater is calculated from its radius and depth using Equation 2.48.

Figures 10.9b and 10.10b show the changes in energy used to create a crater for the optimal depth of burial, as a function of total energy, for both TNT and nuclear charges.

We note a significant increase in specific energy consumption with yield increase, for both explosion types. For example, the specific energy consumption increases from $k = 2 - 4$ kg/m^3 for q = 10^{-2} kt to $k = 12 - 28$ kg/m^3 for q = 10^2 kt. The specific energy consumption for a nuclear explosion in hard rock is always higher than for a chemical (TNT) explosion of the same size, and increases with decrease of water content. In alluvium this is true only for large yields, $q \geq 10$ kt. For lower yields the specific energy consumption decreases with the yield decrease at a higher rate than for chemical explosions, and may become smaller than for chemical explosions (Figure 10.10b).

An important parameter of relative excavation efficiency of chemical (TNT) and nuclear explosions is the ratio of their specific energy consumption values, which in essence represents the TNT equivalent for nuclear explosions $k_v = V_n/V_{TNT}$, where V_n and V_{TNT} are the volumes of the craters created by nuclear and TNT explosions for different energy and depth of the charges.

Analysis of the results shows that for explosions in hard rock with fixed properties, the TNT equivalent for purposes of making craters is independent of the explosion size, and is determined only by the gas content at the charge depth. The relationship between the nuclear-to-chemical equivalent and rock gas content (and its components) is shown in Figure 10.9b, for hard rock with the following properties: with respect to a TNT explosion the cavity radius is $\bar{r}_c = 13.4\, m/kt^{1/3}$ and Π = 10^3 m^3/t, [7] while for a nuclear explosion it is $\bar{r}_c = 11.1\, m/kt^{1/3}$ and Π = 5.73 m^3/t. It is clear that with the increase in gas content from 1 – 2 to 20 %, the nuclear-to-chemical equivalent changes in the range $0.4 \leq k_v \leq 0.8$. As the gas content increases, the role of the ratio between its components also increases. For instance, the nuclear-to-chemical equivalent with equal water and carbon dioxide content for η = 0.12 ($\eta_\omega = \eta_{CO2}$) is k_v = 0.6, while for η = 0.24 ($\eta_\omega = \eta_{CO2}$) the value of the nuclear-to-chemical equivalent is k_v = 0.72.

Thus the nuclear-to-chemical equivalent for hard rock increases with the increase in gas content around the charge, and its value depends on the ratio between the main components. In alluvium the relative efficiency of nuclear and chemical explosions significantly depends on the explosion yield (Figure 10.10b) until the overshoot parameter stabilizes for the chemical explosions. For a given relationship between the overshoot parameter and depth (Figure 10.1b, line *1*) this stabilization is achieved for the yields $q \leq 10^4$ t. Above this value the nuclear-to-chemical equivalent becomes yield-independent and is determined only by the alluvium moisture content according to Figure 10.10b for $\eta = \eta_\omega$. For $q \leq 1$ kt the efficiencies of TNT and nuclear explosions are approximately equal ($k_v = 0.8 - 1$), and for high moisture content the value of nuclear-to-chemical equivalent can become $k_v > 1$.

[7] To be checked --- this values is much higher than indicated in Table 10.3.

Concluding remarks

The 20th century was characterized by major scientific discoveries and technological breakthroughs in various fields. Computational technologies reached incredible levels in a short time. The basis for modern computing was established in the 20th century, and a high level of development was reached in a number of information and communication technologies, including the development of television and the internet. However we should not forget that the development of the information technology overshadows a series of technological advances in other fields, which not only significantly advanced the humankind toward the future technologies, but also initiated rapid development in other fields.

One of the most significant achievements of humankind in the 20th century was the discovery of nuclear reactions, and the creation of nuclear technology. The possibility of using atomic energy, led to the hope of becoming independent of energy derived from hydrocarbons. Atomic energetics created in the last century is still being successfully developed, and undoubtedly it has future prospects. Scientific and technological problems did not allow scientists to develop peaceful use of nuclear fusion technologies. However the first step in that direction has been made: humankind can extract this type of energy, but only as explosions, and not in a continuous regime,

The physics of nuclear explosions involves other fields, which allowed us to develop nuclear devices, to conduct nuclear explosive tests, and to modernize the technology using the results of these tests. Due to the extreme importance of developing nuclear weapons, significant numbers of scientists and engineers engaged in this field. This work conducted in the last half of the past century resulted in considerable advances in the fields of thermodynamics, statistical physics, gas dynamics and hydrodynamics, physics of the solid state, physical chemistry of the isotopes, as well as in other fields of natural science. In addition, significant progress was made in the study of the inner structure of the Earth and the atmosphere.

Geophysics became one of the most utilized scientific fields, whose advances significantly promoted the development of nuclear weapons. This was due to the fact that the majority of measurements of physical variables of nuclear explosions was performed by using geophysical methods. Without these measurements it would have been difficult (and in some cases impossible) to estimate the energy released during explosions, and qualitative and quantitative characteristics of explosion effects on different media. Underground nuclear explosions are the subject of greatest interest, because during the past 30 years nuclear explosions were conducted only under the ground. Unlike explosions in “transparent” media (atmosphere, space, water), determining the main features of underground nuclear explosions requires significant efforts, related not only to the development of more complex and expensive methods of data acquisition, and determining characteristics the medium and their changes as a result of explosions, but also in the creation of new models of the solid medium describing its behavior under strong deformations.

It is worthwhile to note in particular that geophysical studies of underground explosions were important not only because of their military applications. These studies resulted in a variety of technologies for civilian uses of nuclear energy. Peaceful uses of nuclear explosions were developed, and some of the projects were successfully implemented. This became possible only as a result of detailed study of the effects of underground nuclear explosions and development of the geophysical model of underground nuclear explosions.

The material presented in this monograph shows that to date all aspects of underground nuclear explosions are well studied to a large degree and that a sufficiently high level of understanding of nuclear explosions and their underlying processes have been achieved. It can be affirmed that the development and action of underground nuclear explosions can be described not only qualitatively, but also quantitatively. Moreover, we can state that overall studies of underground nuclear explosions are now complete. The main objective currently is to gather all available data and to finalize conclusions. We assume that developed countries will consider spending significant resources to enable such activities. [OK. this rewrite? I think this is what they indicate, even though we may disagree on the prospects.]

To this end the present monograph in some way finalizes the authors' study of the phenomenology and technical consequences of nuclear explosions at the Semipalatinsk and Novaya Zemlya Test Sites, and for the explosions conducted under the program of peaceful use of the nuclear energy. Laboratory modeling experiments were widely used in this work. In this concluding part of the monograph it would be useful to underscore the following major results we have presented:

1. The mechanical effects of nuclear explosions are determined by a number of factors, including the yield of the device, aspects of the charge placement (the most important of which are the depth of burial, geometry and size of the burial chamber, and characteristics of the auxiliary underground infrastructure such as tunnels, etc.), as well as the conditions of the emplacement medium: the rock type around the charge, the water content, mechanical properties, mineral content, texture and the tectonic structure of the rock mass, layers and fracture content, topography of the free surface etc. The following three main groups of underground explosions can be identified based on the character of their mechanical effects:

    - Excavation explosions resulting in the ejection of material located in a conical zone between the charge and the surface, and creation of a crater;
    - Loosening explosions (the material between the charge and the free surface is damaged, partially ejected outside of the epicentral zone, and partially collapsed into the crater). The explosions of this type create mounds (retarcs) with subsidence craters or ejection craters in the middle. The bottom of the crater can be either above or below the original ground surface;

- Fully contained [camouflet] explosions, which create only local surface damage due to spall effects without ejection of material. Formation of a subsidence crater is possible, as well as tensile fractures, elongated grooves and mounds.

These groups can be further divided into sub-groups depending on the specific features of explosions and their effects, however such details are secondary.

2. Mechanical effects of nuclear explosions determine their radiation effects. In this respect the proposed classification fully reflects the changes of the character and timing of the release of radioactive gases from the cavity into the atmosphere. During ejection explosions gases are ejected together with the rock material. For the loosening/partially confined explosions, the time of gas breakthrough is determined by the character of percolation or venting through damaged rocks in the chimney. For fully contained explosions, gas motion occurs only by filtration or convection. With sufficiently large depth of burial and favorable tectonic structure the radioactive isotopes can be fully contained (i.e. the radioactive gases are contained within the rock mass for long periods of time, with some insignificant release of inert radioactive gases into atmosphere).
   If in addition to these conditions (large depth of burial and small amount of fractures) the emplacement rock has low gas content, gas release into atmosphere can be completely eliminated.
3. The principal difference between nuclear and chemical explosions is based on the different dependences of their mechanical energy on the rock type, moisture content, and the presence of any mineral that can create gas by chemical decomposition. In other words, the TNT equivalent of an underground nuclear explosion is determined not only by the energy of the charge, but also by the capability of rock near the shot point to release gaseous products due to the heat released by nuclear detonations. These gaseous products add to the mechanical work exerted by explosions on surrounding material.
4. Explosion size and depth of burial are important factors in determining explosion effects on the rock mass. Energy similarity breaks down as the explosion scale increases, therefore we cannot transfer the laws determined in the laboratory experiments or during small scale explosions into large scale nuclear explosions in order to calculate their burial parameters. It is important to emphasize that there is no sharp transition between different regimes (which is sometimes suggested by some empirical relationships). Instead there can be a gradual increase in explosion effects that progressively lowering the relative efficiency of the mechanical (including excavation) and seismic effects of large scale explosions.

Bibliography[1]

1. Avdeev, V.V., V.L. Baron, I.L. Bleiman (1977). Proizvodstvo massovyx vzryvov (Industry of massive explosions), Moscow, Nedra, 312 pp.
2. Adushkin V.V. (1980). Issledovanie vzryvov na vybros lineinymi zaryadami (Study of excavation explosions with linear charges), Fiziko-Tekhnicheskiye Problemy Razrabotki Poleznykh Iskopayemykh (Physical-technical problems of mining of natural resources), 5, 54-69.
3. Adushkin V.V. (2000). Vliyanie geologicheskih faktorov na rasprostranenie radioaktivnyh produktov pri podzemnyx yadernyh vzryvah (The effect of geological factors on spread of radioactive products during underground nuclear explosions), Radioaktivnost' pri yadernyh izmereniyah, Gidrometoizdat, St Petersburg, 585-593.
4. Adushkin V.V. and V.A. An (1996). O registratsii ranee neob'yavlennyh podzemnyh yadernyh ispytanii SShA seismichaskimi stantsiayami byvshego Sovetskogo Soyuza (Registration of previously undeclared USA nuclear tests by the stations of the former Soviet Union), Doklady RAN, v. 349, 4, 525-529.
5. Adushkin V.V., V.A. An, P.B. Kaazik, and V.M. Ovchinnikov (1996). Podzemnyi yadernyi vzryv – instrument issledovaniya vnutrennego yadra Zemli (Underground nuclear explosions as an instrument for the study of the Earth Inner Core), Fizicheskie process v Geosferah, IDG RAN, 151-161. *Similar article is available in English*: Adushkin V.V., V.A. An, P.B. Kaazik, and V.M. Ovchinnikov (2001). Dynamic processes within the Earth's internal geospheres; evidence from the seismic wave traveltime data, Fizicheskie process v Geosferah, Doklady Earth Sciences, 381.9, 1119-1121.
6. Adushkin V.V., V.A. An, P.B. Kaazik, et al (1977). O skachke plotnosti na vnutrennei granitse zemnogo yadra po nablyudeniyam voln PKiKP na rasstoyah okolo 6° (Density jump at the inner boundary of the Earth Core based on the observations of PKiKP phases at distances of about 6°), Doklady AN SSSR, v. 354, 3, 382-385.
7. Adushkin V.V. and P.B. Kaazik (1976). Raschet vyhoda gazoobranyh porduktov podzemnogo vzryva v atmosferu (Calculations of discharge of gaseous products of underground explosions into the atmosphere), Zhurnal Prikladnoi Mehaniki I Tehnicheskoi Fiziki, 1, 111-120. *Available in English*: Adushkin V.V. and P.B. Kaazik (1976). Calculation of the discharge of underground explosion gases into the atmosphere, Journal of Applied Mechanics and Technical Physics, 17, 1, 89-96
8. Adushkin V.V., I.O. Kitov, O.P. Kuznetzov, and D.D. Sultanov (1991). Chastichnyi dekapling v soli (Partial decoupling in salt), Doklady AN SSSR, v. 320, 4, 839-843.

[1] The list of articles originally published in Russian is alphabetized separately in Russian alphabetical order. References to similar articles available in English are provided where possible. The list of articles in English is given separately in English alphabetical order.

Available in English: Adushkin V.V., I.O. Kitov, O.P. Kuznetzov, and D.D. Sultanov (1994). Partial decoupling in salt, Doklady. Earth Science Sections 327, 19-22.

9. Adushkin V.V. and A.I. Korotkov (1961). Parametry udarnoi volny vblizi zaryada VV pri vzryve v vozduhe (Parameters of the shock wave near the HE charge for the explosion in air), Zhurnal Prikladnoi Mehaniki i Tehnicheskoi Fiziki, 5, 119-123.
10. Adushkin V.V., V.N. Kostyuchenko, V.N. Nikolaevskii, and V.M. Tsvetkov (1973). Mehanika podzemnogo vzryva (Mechanics of an underground explosion), Mechanics of the Solid media, Moscow, VINITI, 87-197.
11. Adushkin V.V. and S.A. Koschii (1979). O zavisimosti razmerov kotlovoi polosti ot udlineniya tsilindricheskih zaryadov, Vzryvnoe delo (Explosive Engineering), Nedra, Moscow, 81/38, 61-78.
12. Adushkin, V.V., V.I. Kulikov, F.F., Safonov, and A.A. Solomonov (1990). Metodika opredeleniya energii podzemnogo vzryva po parametral seismicheskih voln v zone blizhnei seismiki (Method for yield estimate of underground explosion using seismic wave parameters [characteristics] in the near seismic zone), Izvestiya – Academy of Sciences, USSR. Physics of the [Solid] Earth, 12, 21-30. *Available in English*: Adushkin, V. V., V. I. Kulikov, F.F.,Safonov, and A.A. Solomonov (1990). Method for determining power of underground explosion from seismic wave parameters in near seismic zone, Izvestiya – Academy of Sciences, USSR. Physics of the Solid Earth, 26.12, 1002-1009.
13. Adushkin V.V. and V.A. Laushkin (1996). Opyt kontrolya za podzemnymi yadernymi vzryvami na seti seismicheskih stantsii byvshego SSSR, Information-Analytical Bulletin of the Federal System of Seismic Observations and Earthquake Forecast, Moscow, MChS RF, 3, 5-22.
14. Adushkin V.V., V.Ya. Libin and L. M. Pernik (1982). Analogovaya ustanovka dlya issledovaniya gruppovyh vzryvov na vybros (Analog apparatus for studies of group cratering explosions), Vzryvnoe delo (Explosive Engineering), Nedra, Moscow, 83/40, 36-44.
15. Adushkin V.V. and V. M. Ovchinnikov (1998). O skorosti otnositel'nogo vrascheniya vnutrennego yadra (Velocity of The Relative Rotational of the Earth's Inner Core), Doklady RAN, v. 362, 5, 683-686.
16. Adushkin V.V. and L. M. Pernik (1972). Osobenmnosty obrazovaniya proval'nyh voronok (Formation of the subsidence craters), Fizika Goreniya i Vzryva (Combustion, Explosion and Shock Waves), 8, 4, 541-552.
17. Adushkin V.V. and L. M. Pernik (1978). Proval'nye voronki pri podzemnyh vzryvah v slabosvyazannyh gruntah (Subsidence craters with underground explosions in weakly bound [weakly cohesive? Soft?] soils), Fizika Goreniya i Vzryva (Combustion, Explosion and Shock Waves), 14, 3, 349-356. *Available in English*: Adushkin V.V. andL. M. Pernik

(1978). Cave-in craters with underground explosions in weakly bound soils, Combustion, Explosion and Shock Waves, 14, 3, 349-356.

18. Adushkin V.V. and V.N. Rodionov (1982). Modelirovanie vzryvov na vybros pri pomoschi laboratornoi vakuumnoi ustanovki (Analog modeling of cratering explosions using laboratory vacuum [not sure if this is a correct term] apparatus), Vzryvnoe delo (Explosive Engineering), Nedra, Moscow, 64/21, 24-42.

19. Adushkin, V.V. and A.A. Spivak (1983). Utechka gazoobraznyh produktov pri geotekhnicheskoi podgotovke gornyh massivov krupnomasshabnym vzryvom (Motion of structural blocks under dynamic loading), Fiziko-Tekhnicheskiye Problemy Razrabotki Poleznykh Iskopayemykh, 6, 35-41.

20. Adushkin, V.V. and A.A. Spivak (1990). Dvizhenie strukturnyh blokov massiva pri dinamicheskom vozdeistvii (Motion of structural blocks under dynamic loading), Vzryvnoe delo (Explosive Engineering), Nedra, Moscow, 90/47, 25-30.

21. Adushkin, V.V. and A.A. Spivak (1993a). Geomekhanika krupnomasshtabnykh vzryvov (Geomechanics of large explosions), Nedra, Moscow, 319 pp. [This book in available in electronic format]

22. Adushkin, V.V. and A.A. Spivak (1993b). Izmenenie urovnya podzemnyh vod v rezul'tate provedeniya podzemnyh yadernyh vzryvov (Ground water level changes as a result of underground nuclear explosions), Bulletin of the Center of Public Information for Atomic Energy, Nedra, Moscow, 9, 38-43.

23. Adushkin, V.V. and A.A. Spivak (2000). Kharakteristiki vyhoda radioaktivnyh produktov podzemnogo vzryva v atmosferu (Characteristics of release of radioactive products of underground explosions to the Earth surface), Radioaktivnost' pri yadernyx vzryvah i avariyah, Gidrometeoizdat, St. Petersburg, 601-615.

24. Adushkin, V. V., A.A. Spivak (2004). Izmenenie svoistv gornyh porod I massivov pri podzemnyh yadernyh vzryvah (Changes in properties of rocks and rock massifs due to underground nuclear explosions), Fizika goreniya i vzryva (Combust. Explos. Shock Waves), 6, 15-26. *Available in English*: Adushkin, V. V., A.A. Spivak (2000). Changes in Properties of Rock Massifs Due to Underground Nuclear Explosions, Combustion, Explosion and Shock, 6, 624-634.

25. Adushkin, V.V., A.A. Spivak, E.M. Gorbunova, P.B. Kaazik, I.N. Nedbayev (1992). Osnovnye zakonomernosti dvizheniya podzemnyh vod (Main features of ground water movement accompanying large subsurface explosions), Izvestiya - Russian Academy of Sciences. Physics of the Solid Earth, 3, 80-9. *Available in English*: Adushkin, V. V., A.A. Spivak, E.M. Gorbunova, P.B. Kaazik, I.N. Nedbayev (1992). Principal regularities in ground water movement accompanying large subsurface explosions, Izvestiya - Russian

Academy of Sciences. Physics of the Solid Earth, 28.3, 249-258. [Love the expression "principal regularities". At least I made an effort to produce something readable☺]

26. Adushkin, V.V., A.A. Spivak, E.M. Gorbunova, E.N. Ferapontova (1993a). Gidrogeologicheskie effekty podzemnyh yadernyh vzryvov (Hydrogeological effects of underground nuclear explosions), Doklady of the Russian Academy of Sciences, 332. 80-93. *Available in English*: Adushkin, V. V., A.A. Spivak, E.M. Gorbunova, E.N. Ferapontova (1995). Hydrogeological [hydrological] effects of underground nuclear explosions, Transactions (Doklady) of the Russian Academy of Sciences. Earth Science Sections, 333. 13-16.

27. Adushkin, V. V., A.A. Spivak, and V.I. Kulikov (1993b).Vliyanie struktutno-tektonicheskogo stroeniya geofizicheskoi sredy na seismicheskie effekty na seismicheskie effekty podzemnogo yadernogo vzryva (Influence of structural-tectonic organization of geophysical medium on seismic effects of nuclear explosion), Izvestiya - Russian Academy of Sciences. Physics of the Solid Earth, 12, 54-64. *Available in English*: Adushkin, V. V., A.A. Spivak, and V.I. Kulikov (1994). Influence of structural-tectonic organization of geophysical medium on seismic effects of nuclear explosion, Izvestiya - Russian Academy of Sciences. Physics of the Solid Earth, 29.12, 1081-1091.

28. Adushkin, V. V., A.A. Spivak, V.I. Kulikov et al (1995b). On the Problem of Evasion of Control at Conducting of Underground Nuclear Explosions, Preprint of Inst. Geosphere Dynamics, Russ. Acad. Sci., Moscow, 41 pp.

29. Adushkin, V. V., A.A. Spivak, S.P. Solov'ev et al (2000). Geoekologicheskie posledstviya massovyh khimicheskih vzryvov na kar'erah ([Geo]Ecological consequences of large chemical explosions in quarries), Geoekologiya, 6, 571–580.

30. Adushkin, V.V. and A. P. Sukhotin (1961). O razrushenii tverdoi sredy vzryvom (Damage to solid medium from explosion), Zh. Prikl. Mekh. Tekh. Fiz., 4. 94-101.

31. Adushkin, V.V., S. V. Kondrat'ev, V. Ya. Libin, L. M. Pernik (1977). Instrumental'noe nablyudenie mekhanicheskogo I seismicheskogo deistviya vzryva na r. Burlykiya (Instrumental observations of the mechanical and seismic effects of an explosion along the Burlykiya River), Gidrotekhnicheskoe stroitel'stvo(Hydrotechnical Construction), 5, 32-35. *Related article available in English*: Adushkin, V.V., A. G. Fomichev, S. V. Kondrat'ev, V. Ya. Libin, V. L. Lavrinenko, L. M. Pernik, I. S. Svintsov (1977). Instrumental observations of the mechanical and seismic effects of an explosion along the Burlykiya River, Hydrotechnical Construction, 11, 5, 493-498.

32. Alekseenko, V.D. (1967). Eksperimental'noe issledovanie raspredeleniya energii pri kontaktnom vzryve (Experiemtnal study of energy partition for contact explosions), Fizika goreniya i vzryva (Combust. Explos. Shock Waves), 1, 152-155. *Available in English*: Alekseenko, V.D. (1967). Experimental investigation of the energy distribution in a contact explosion, Combust. Explos. Shock Waves, 3, 1, 97-98.

33. Al'tshuler, L.V., A. V. Balabanov, V. A. Batalov, V. A. Rodionov, D. M. Tarasov (1970). Rentgenograficheskoe issledovanie nachal'noi stadia razvitiya kamufletnoi plolosti v peschanom grunte (Radiographic study of the initial stage of development of an underground explosion in sandy soil), Fizika Goreniya I Vzryva (Combustion Explosion and Shock Waves), 6, 3, 363-373. *Available in English*: Al'tshuler, L.V., A. V. Balabanov, V. A. Batalov, V. A. Rodionov, D. M. Tarasov (1970). Radiographic study of the initial stage of development of an underground explosion in sandy soil, Combustion Explosion and Shock Waves, Combustion, Explosion and Shock, 6, 3, 320-326, DOI: 10.1007/BF00742507

34. Aptikaev, F.F. (1999). Problemy sozdaniya shkaly seismicheskoi intensivnosti novogo pokoleniya (Problems Arising in the Development of a New Generation Seismic Intensity Scale), Vulkanology and Seismology, 4/5, 23-28.

35. Belyaev, A.F. (1957). O raschete zaryadov pri vzryve na vybros (On calculation of charges for ejection [cratering] explosions), Gorn. Zhurn, 10, 61-62.

36. Bobrovskii, S. V., V. M. Gogolev and B. V. Zamyshlyaev et al (1976). Interpolyatsionnoe uravnenie sostoyaniya dlya slantsa i ego prilozheniya k issledovaniyu skorosti otkola pri sil'nyh udarnyh volnah (Interpolation equation of state for slate and its use for studying the spalling velocity caused by strong shock waves), Fizika goreniya i vzryva (Combust. Explos. Shock Waves), 2, 58-61.

37. Bocharov, V.S., L.P. Vladimirskii and A.M. Novikov (1988b). Evaluation of the accuracy of underground nuclear explosion yield estimation by a seismic method at known conditions, Atomnaya Ehnergiya, v. 65(2) p. 114-119.

38. Bocharov, V.S, M.N. Georgievskii, V.V. Kirichenko, and A.B. Peshkov (1988a). Metod otsenki moschnosti podzemnyh yadernh vzryvov s uchetom ih real'noi seismicheskoi effektivnosti (A method of yield estimate for underground nuclear explosions based on [taking into account] their [actual] seismic efficiency]), Atomnaya Energiya, 65, 2, 109-114.

39. Bocharov, V.S, S.A. Zelentsov, and V.N. Mikhailov (1989). Kharakteristiki 96 podzemnyh yadernyh vzryvov na Semipalatinskom ispytatel'nom poligone (Characteristics of 96 underground nuclear explosions at the Semipalatinsk Test Site), Atomnaya Energiya, 67, 3, 210-213.

40. Bronnikov, D. M. and A. A. Spivak (1981a). Vliyanie ekraniruyuschei scheli na vzryvnoe vozdeistvie v tverdoi srede (Influence of a screening slot on the action of blasting in a solid medium), Fiziko-Tekhnicheskiye Problemy Razrabotki Poleznykh Iskopayemykh, 3, 62-70. *Available in English*: Bronnikov, D. M. and A. A. Spivak (1981a). Influence of a screening slot on the action of blasting in a solid medium, Soviet Mining, 17, 3, 236-242.

41. Bronnikov, D. M. and A. A. Spivak (1981b). Nekotorye voprosy upravlyaemogo drobleniya gornyh porod vzryvom (Some problems of the controlled rock fragmentation by an explosion), Fiziko-Tekhnicheskiye Problemy Razrabotki Poleznykh Iskopayemykh, 8, 55-61.

Available in English: Bronnikov, D. M. and A. A. Spivak (1981a). Influence of a screening slot on the action of blasting in a solid medium, Soviet Mining, 17, 331-336.

42. Broud, H. (ed.) (1975[6?]). Calculation of Explosions by Computers. Gas Dynamics of Explosions. Mir Press, Moscow, 163 pp.

43. Butkovich, T. R. (1976). The Gas Equation of State of Natural Materials, in Broud, H. (ed.) Calculation of Explosions by Computers. Gas Dynamics of Explosions. Mir Press, Moscow, 135-162. *Available in English*: Butkovich, T. R. (197?). The Gas Equation of State of Natural Materials, UCRL-14729.

44. Viktorov, V. V. and R.D. Stepanov (1960). Modelirovanie deisviya vzryva sosredotochennyh zaryadov v odnorodnyh gruntah, Engineering Collection, Gosgortekhizd, Moscow, 28, 87-96.

45. Vovk, A. A. (1976) Principles of Applied Geodynamics of an Explosion. Naukova Dumka, Kiev, 272 pp.

46. Garnov, V.V. and A. A. Spivak (2004). Deformirovanie blochnoi sredy pri podzemnyh yadernyh vzryvah (Deformation of Block Environments in Underground Nuclear Explosions), Combustion, Explosion and Shock Waves, 6, 58-65. *Available in English*: Garnov, V.V. and A. A. Spivak (2004). Deformation of Block Environments in Underground Nuclear Explosions, Combustion, Explosion and Shock Waves, 40, 6, 663-669.

47. Gorbunova, E.M. and A.A. Spivak (1997).Izmenenie rezhima podzemnyh pri podzemnyh yadernyh vzryvah (Changes in the regime of underground waters due to an underground nuclear explosion), Geoékologiya, 6, 29-37.

48. Gubkin, K. E. (1978). O podobii vzryvov (The similarity of explosions), Izvestiya - Academy of Sciences, USSR. Physics of the Solid Earth, 14.10, 714-721. *Available in English*: Gubkin, K. E. (1979). The similarity of explosions, Izvestiya - Academy of Sciences, USSR. Physics of the Solid Earth, 14.10, 714-721.

49. Gushchin, V. V., Antonenko, V. A., Rosental, A. K., Godunov, A. S. (1975). Osobennosti vypuska rudy iz bloka, podgotovlennogo yadernym vzryvom (Specific features of ore exhaustion from a block prepared by a nuclear explosion), Tr. Inst. Gorno-Khim., 36, 48-57

50. Dokuchaev, M. M., Rodionov, V. N., Romashov, A. N. (1963). Cratering Explosions. Izd-vo AN SSSR, Moscow, 108 pp.

51. Zel'dovich, Ya. B., Raizer, Yu. P. (2002). Physics of Shock Waves and High-Temperature Hydrodynamic Phenomena, Dover Publications, Mineola, NY, 944 pp.

52. Ivanov, B.A. (1977). O mekhanicheskom deistvii vzryva vblizi poverhnosti grunta (Mechanical effect of explosion near the ground surface), Fizika Goreniya i Vzryva (Combustion Explosion and Shock Waves), 1, 110-114.

53. Izrael, Y. A. (1996) Radioactive fallout after nuclear explosions and accidents. Progress-Pogoda, Saint Petersburg , 355 pp. *Available in English*: Izrael', Yu.A. (2002). Radioactive Fallout after Nuclear Explosions and Accidents, Elsevier Science, Oxford, UK,? pp .

54. Isakov, A.L., V. P. Kokovkin and V. Kh. Rott (1976). Eksperimental'noe issledovanie treschinoobrazovaniya pri kamufletnom vzryve (Experimental study of fracture formation due to a fully contained [camouflet] explosion), Voprosy mekhaniki razrusheniya gornyh porod, Novosibirsk, Izd. IG Sib. Otd. Akad. Nauk SSSR.

55. Kedrovskii, O. L. (1970). Primenenie vzryvov naruzhnego deistviya v promyshlennosti I stroitel'stve (Using surface nuclear explosions in the industry and construction), Peaceful Nuclear Explosions, Vienna, Austria, IAEA, 377-404.

56. Kedrovskii, O. L., Ivanov, I. Y., Myasnikov, K. V. (1970). Osnovnye tekhnicheskie aspekty ispol'zovaniya podzemnyh yadernyh vzryvov v narodnom khozyaistve (Basic technical aspects of using underground nuclear explosions in the national economy), Atomic Explosion for Peaceful Purposes. Atomizdat, Moscow, pp. 5-51

57. Kedrovskiy, O. L., K.V. Myasnikov, V.A. Leonov, N.M. Romadin, V.F. Dorodnov et al (1972). Primeneniye kamufletnykh yadernykh vzryvov dlya sozdaniya podzemnykh yemkostey i opyt ikh ekspluatatsii pri khranenii gazovogo kondensata (The use of contained nuclear explosions to create underground reservoirs, and experience of operating these for gas condensate storage), Panel Proceedings Series - Peaceful Nuclear Explosions, Vienna, Austria (AUT), IAEA, 227-254. (Possibly in English)

58. Kireev, V. V.,N.N. Ershov and D.D. Protopopov (1971). Promyshlennye Yadernye vzryvy (Industrial Nuclear Explosions), Atomizdat, Moscow, 176 pp.

59. Kitov, I. O. (1992). Usloviya dlya polnogo seismicheskogo dekaplinga podzemnogo vzryva (Conditions for complete seismic decoupling of an underground explosion), Doklady RAN USSR, 327, 2, 70-73. *Available in English*: Kitov, I. O. (1993). Conditions for complete seismic decoupling of an underground explosion, Doklady – Russian Academy of Sciences, Earth Science Sections, 328, 12-16.

60. Kitov, I. O. (1995). Seismicheskie i akusticheskie effekty vzryva v geofizicheskoi srede (Seismic and acoustic effects of explosion in geophysical medium), Dissertation of Doctor of Physical and Technical Sciences, Moscow, 423 pp.

61. Komir, V.M, L.M. Leiman, and V.S. Kravtsov (1972). Modelirovanie razrushayuschego deistviya vzryva v gornyh porodah (Modeling of the damage by explosion in rocks), Nauka, Moscow, 250 pp.

62. Kompaneets A.S. (1950). Udarnye volny v plasticheskoi uplotnyayuscheisya srede (Shock Waves in a Plastic Compacting Medium), Doklady, Akademiya Nauk USSR, 1, 49-51. *Available in English*: Kompaneets A.S. (1963). Shock Waves in a Plastic Compacting Medium, Translated at CALIFORNIA UNIV LIVERMORE RADIATION LAB, (available

at http://oai.dtic.mil/oai/oai?verb=getRecord&metadataPrefix=html&identifier=ADA395898), 5 pp.

63. Korneev, G.N., V.P. Krivoshta and D.S. Podozerskii (1972). Vliyanie uslovii vzryvaniya na effectivnost' razrusheniya gornyh porod (Effect of the explosion conditions on the efficiency of rock fragmentation), Nauka, Moscow, 120 pp.

64. Korotkov, P. F. and V.S. Lobanov (1973). Raschet vzryva zaryada geksogena v alyuminii (Calculation of the explosion of hexogen in aluminum), Journal of Applied Mechanics and Technical Physics, 3, 156-162. *In English*: Korotkov, P. F. and V.S. Lobanov (1973). Calculation of the explosion of hexogen in aluminum, Journal of Applied Mechanics and Technical Physics, 14, 4, 569-574.

65. Korotkov, P. F. and Prosvirina, B. M. (1980). Similarity and the energy distribution in an explosion in an elastic-plastic medium, Zh. Prikl. Mekh. Tekh. Fiz., 2, 143-152.

66. Korchevskii, V.F. and G. N. Petrov (1977). Geotechnical investigations of the experimental blast-fill dam on the Burlykiya River, Hydrotechnical Construction, 11, 5, 477-487. (in English)

67. Kostyuchenko, V.N. (1985). Statistika povrezhdenii zdanii pri vzryvnyh rabotah I voprosy seismicheskoi bezopasnosti (), Fiziko-Tekhnicheskiye Problemy Razrabotki Poleznykh Iskopayemykh, 1, 67-73.

68. Kostyuchenko, V.N., S. V. Kondrat'ev and G. G. Kocharyan (1982). Experimental investigations of diffraction of seismic waves by planar screens, Soviet Mining, 18, 4, 284-288. (in English)

69. Kostyuchenko, V.N., S. V. Kondrat'ev and G. G. Kocharyan (1983). Issledovanie effektivnosti ekranov dlya zaschity ot seismicheskogo deistviya vzryvov (Study of the efficiency of hollow screens for protection from seismic effects of explosions), Vzryvnoe Delo, 85/42, 115-123.

70. Kostyuchenko, V N., V.N. Rodionov, D.D. Sultanov (1974). Seysmicheskiye volny pri podzemnykh yadernykh vzryvakh (Seismic waves generated by underground nuclear explosions), Panel Proceedings Series - Peaceful Nuclear Explosions, Vienna, Austria (AUT), IAEA, 447-451 (461). (Possibly in English)

71. Kocharyan, G. G. and A.A. Spivak (2001). Dvizheniye blokov gornoy porody pri krupnomasshtabnykh podzemnykh vzryvakh; Ch. 1, Eksperimental'nye dannye (Rock block movement during [as a result of] large-scale underground explosions; Part 2, Experimental data), Fiziko-Tekhnicheskiye Problemy Razrabotki Poleznykh Iskopayemykh, 1, 71-83.

72. Kocharyan, G.G. and A.A. Spivak (2002). Iyerarkhiya strukturnykh i geodinamicheskikh kharakteristik zemnoy kory (Hierarchy of crustal structural and geodynamic characteristics), Geoekologiya (Moskva), 6, 537-550.

73. Kocharyan, G.G. and A.A. Spivak (2004). Dinamika deformirovaniya blochnykh massivov gornykh porod (Dynamics of the deformation of rock massifs), Moscow, Russian Federation (RUS), IKTs "Akademkniga", 423 pp.

74. Kocharyan, G. G, A.A. Spivak, A.M. Budkov (2001). Dvizheniye blokov gornoy porody pri krupnomasshtabnykh podzemnykh vzryvakh; Ch. 2, Otsenki po analiticheskim modelyam, chislennyye raschety i sravnitel'nyy analiz teoreticheskikh i eksperimental'nykh dannykh (Rock block movement during [as a result of] large-scale underground explosions; Part 2, Assessments using analytical models, numerical calculations and comparative analysis of theoretical and experimental data), Fiziko-Tekhnicheskiye Problemy Razrabotki Poleznykh Iskopayemykh, 2, 37-57.

75. Koshelev E.A. (1975). Development of a camouflet cavity as a result of an explosion in soft ground, Journal of Applied Mechanics and Technical Physics, 16, 2, 223-228. (in English)

76. Kropotkin, P. N. (1996). Tektonicheskie napryazheniya v zemnoi kore (Tectonic stresses in the Earth's crust), Geotectonics, 30.2, 3-15. *May be available in English*: Kropotkin, P. N. (1996). Tectonic stresses in the Earth's crust, Geotectonics, 30.2 , 85-96.

77. Krukovskii, K.B. and L.M. Romanov (1990). Segment global’nogo obnaruzheniya yadernyh vzryvov sputnikovoi radionavigatsionnoi sistemoi Navstar (Global monitoring of nuclear explosions using satellite system NAVSTAR), Zarubezh. Radioelectr., 7, ??.

78. Kuznetsov, V. M. (1963) Efficiency of explosions in soil. Zhurnal Prikladnoi Mekhaniki Tekhicheskoi Fiziki, 4, 30-34.

79. Kuznetsov, V. M. (1977). Matematicheskie modeli vzryvnogo dela (Mathematical Models of Blasting), Nauka, Novosibirsk, 262 pp.

80. Kuznetsov, N. M. (1965). Thermodynamic Functions and Shock Adiabats of Air at High Temperatures. Mashinostroenie, Moscow, 190 pp.

81. Kuznetsov, N.M., K.K. Shvedov (1967). Izentropicheskoe rasshirenie produktov detonatsii geksogena (Isentropic Expansion of Detonation Products of Hexagen), Fiz. Goren. Vzryva, 3, 2, 203-210.

82. Kuliev G.G. (2000).(Opredelenie koeffitsienta Puassona v napryazhennyh sredah (Determination of Poisson coefficient in the stressed media), Reports of the Russian Academy of Sciences, Geophysics, 370, 4, 534–537.

83. Kulikov, V.I. (1987). Seismovzryvnye volny v napryazhennoi srede (Seismic waves from explosions in stressed media), Izestia Academy of Sciences, USSR, Physics of the Solid Earth, 5, 12-21.

84. Kulikov, V.I. (1990). Mekhanicheskoe deistvie vzryva v uprugo-plasticheskih sredah pri razlichnom zaglublenii zaryada (Mechanical effect of explosions in elasto-plastic media for

different charge depths of burial), in Deistvie vzryva v neodnorodnoi srede, Nedra, Moscow, 53-68.

85. Leibenszon, L.S. (1947). Dvizhenie prirodnyh zhidkostei I gazov v poristoi srede (Motion of Natural Liquids and Gases in a Porous Medium), Gostekhizdat, Moscow, 142 pp.
86. Leonov, Yu. G. (1996). Napryazheniya v litosfere i vnutriplitnaya tektonika (Stress in the lithosphere and intraplate tectonics), Geotektonika, 29, 3-21.
87. Loitsyanskii, L.G. (1966). Mechanics of Liquids and Gases, International Series of Monographs in Aeronautics and Astronautics (in English), Vol. 6, Pergamon, Oxford, 816 pp.
88. Lomize, G.M. (1951). Filtratsiya v treschinnovatyh porodah (Flow in Fractured Rock) (in Russian), Gosemergoizdat, Moscow, 164 pp.
89. Lunz, Ya.L. (1949). O rasprostranenii sfericheskih voln v uprugo-plasticheskoi srede (On the Propagation of Spherical Waves in an Elasto-Plastic Medium), Prikladnaya Matematika i Mekhanika (Applied Mathematics and Mechanics), 1, 55-78. (Available in English: http://oai.dtic.mil/oai/oai?verb=getRecord&metadataPrefix=html&identifier=ADA953164)
90. Lyakhov, G.M. and K. S. Sultanov (1983). Podobie volny v sredah, obladayuschih vyazkimi svoistvami (), Vzryvnoe Delo (Explosive Engineering), Nedra, Moscow, 85/42, 6-11.
91. Mangushev, K. I. and N. K. Prikhod'ko (1968). Primenenie yadernyh vzryvov v neftyanoi I gazovoi promyshlennosti (Application of Underground Nuclear Explosions in the Petroleum and Gas Industry). VNIIOÉNG, Moscow, 120 pp.
92. Medvedev, S. V.and N.V. Shebalin (1967). S zemletriaseniem mozhno sporit' (One can argue with an earthquake), Nauka, Moscow, 128 pp.
93. Arkhipov, V.N., V.A. Borisov , V. A., Budkov, A. M. et al (2002). Mekhanicheskoe deistvie yadernogo vzryva (Mechanical Effect of a Nuclear Explosion), Fizmatlit, Moscow, 383 pp. [I have this book in electronic format]
94. Morozov, N.F. (1984). Matematicheskie voprosy teorii treshchin (Mathematical issues [?] of fracture theory). Nauka, Moscow, 256 pp.
95. Mosinets, V. N. (1976). Drobyaschee I seismicheskoe deistvie vzryva v gornyh porodah (Crushing and Seismic Effect [action] of an Explosion in Rocks). Nedra, Moscow, 242 pp.
96. Mueller, R.A., and J.R. Murphy (1971a). Seismic characteristics of underground nuclear detonations: Part I, Seismic scaling law of underground detonations (English), Bull. Seism. Soc. Am., 61, 1675-1692. [I am not sure which part they are referring to]
97. Mueller, R.A., and J.R. Murphy (1971b). Seismic characteristics of underground nuclear detonations: Part II, Elastic energy and magnitude determination, Bull. Seism. Soc. Am., 61, 1693-1704.

98. Myasnikov, K V (1971). An investigation of completely contained nuclear explosions in rock salt with a view to developing techniques for the creation of underground storage cavities, Panel Proceedings Series – Peaceful Nuclear explosions, International Atomic Energy Agency, 201-208(209).

99. Nasonov, I. D. (1978). Modelirovanie gornyh processov (Modeling of Mining Processes), Nedra, Moscow, 256 pp.

100. Nikiforovsky, V.S. (1977). (The effect of a spherical vibration source near the surface in an elastic medium),), Fiz. Tekhn. Probl. Razrab. Poleznyh Iskopaemyh, 3, 48-59. *Available in English*: Nikiforovsky, V.S. (1977). Action of a spherical vibration source near the surface in an elastic medium, Soviet Mining, 13, 3, 254-262.

101. Nikiforovsky, V.S., Shemyakin, E.N. (1979). Dinamicheskoe razrushenie tverdykh tel (Dynamic damage of solid bodies [media]). Nauka, Novosibirsk, 271 pp.

102. Nikolis, G. and I. Prigozhin (1979). Samoorganizatsiya v neraavnovesnyh sistemah (Self-Organization in Nonequilibrium Systems), Mir, Moscow, 345 pp.

103. Nifontov, B. I., D. D. Protopopov, I. E. Sitnikov, and A. V. Kulikov (1965). Podzemnye yadernye vzryvy (Underground Nuclear Explosions) [in Russian], Atomizdat, 157 pp. (A similar book is available on Amazon, not sure what language though http://www.amazon.com/Underground-Explosions-Problems-Industrial-Explosions/dp/B00AGCLYUW)

104. Novaya Zemlya: ecological safety of underground nuclear explosions, Proc. Soviet-Finnish Symp, 1991 [?]

105. Austin, C.F. and G.W. Leonard (1973). Chemical explosive stimulation of geothermal wells, in Geothermal Energy (in English), P. Kruger and Cotte eds, Stanford University Press, Stanford, 276-298 [?check].

106. Pavlov, M. M. and D. A. Sudakov (1976). Izmereniya polya massovyh skorostei pri vzryve tsilindricheskogo zaryadav pressovannom NaCl (Measurement of the particle velocity field during explosion of a cylindrical in compacted NaCl), Vzryvnoe Delo (Explosive Engineering), Nedra, Moscow, 76/33, 65-74.

107. Panin, V. E., V. A. Likhachev and Yu.V. Grinyaev (1986). Strukturnye urovni deformatsii tverdyh tel (Structural Levels of Deformation in Solids) [in Russian]. Nauka, Novosibirsk, 230 pp.

108. Pasechnik, I. P. (1970). Kharakteristika seismicheskih voln pri yadernyh vzryvah I zemletryaseniyah (Characteristics of Seismic Waves from Nuclear Explosions and Earthquakes), Nauka, Moscow, 191 pp.

109. Petrov, V.N. and A.A. Ter-Saakov (1970). Output of inert radioactive gases into atmosphere and formation of secondary aerosols following ventilated underground nuclear

explosion, in Nuclear explosions for peaceful uses, Morokhov, I.D. (ed.), Atomizdat, Moscow, 94-97.

110. Underwater and Underground Explosions, Mir, Moscow– [It appears that this book is translated from English, but I am not sure about the source]

111. Underground Explosions, Moscow, 1962 – [It appears that this book is translated from English, but I am not sure about the source]

112. Pokrovskii, G. I. and I.S. Fedorov (1957). Deistvie udara I vzryva v deformiruemyh sredah (The Effect of Impact and Explosion in Deformable Media), Gosstroiizdat, Moscow, 276 pp.

113. Prediction of ground motion due to underground nuclear explosions (prognozirovanie kharakteristik dvizheniya grunta, vyzvannogo podzemnymi yadernymi vzryvami), (1976) Atomizdat, Moscow, 67 pp.

114. Pykhachev, G.B. and P.G. Isaev (1973) Podzemnaya gidravlika (underground hydraulics), Nedra, Moscow, 359 p.

115. Rodin, G (1974). Seismology of underground nuclear explosions. Mir, Moscow, 219 pp.

116. Rodionov, V.N. (1981). Excitation of low-frequency seismic body waves in an underground explosion, Journal of Applied Mechanics and Technical Physics, 22, 5, 723-724. (in English)

117. Rodionov, V.N., V.V. Adushkin, V.N. Kostyuchenko, V. Nikolaevskii and A. Romashov, A. (1971). Mehanicheskii effect podzemnogo vzryva (Mechanical Effect of an Underground Explosion), Moscow, Nedra, 224 pp. *Possibly available in English*: Rodionov, V.N., V.V. Adushkin, V.N. Kostyuchenko, V. Nikolaevskii and A. Romashov, A. (1971). Mechanical Effect of an Underground Explosion, Moscow, Nedra, 224 pp.

118. Rodionov, V. N., B. G. Lukishov, V. M. Tsvetkov, I. A. Sizov (1976b). O droblenii gornoi porody (Rock fragmentation due to a fully contained [camouflet] explosion), Fizika Goreniya I Vzryva, 2, 275-281. *Available in English*: Rodionov, V. N., V. M. Tsvetkov, I. A. Sizov, B. G. Lukishov (1976b). Crushing of rock in an internal explosion, Combustion, Explosion and Shock Waves, 12, 2, 243-248.

119. Rodionov, V. N. (1971) The Mechanical Effect of an Underground Explosion. Nedra, Moscow

120. Rodionov, V.N., A. N. Romashov, and A. P. Sukhotin (1958).Vzryv v uplotnyayuscheisya neogranichennoi srede (Explosions in infinite compacting medium), Dokl. Akad. Nauk SSSR, 123, 4, 627-630.

121. Rodionov, V.N., Sizov, I.A., Tsvetkov, V.M. (1986). Osnovy geomekhaniki (Elements of geomechanics). Nedra, Moscow, 301 pp.

122. Rodionov, V. N., A.A. Spivak, V.M. Tsvetkov (1976a). Method opredeleniya fil'tratsionnyh svoistv gornyh porod (Method of determining the filtration properties of rocks), Fiz. Tekhn. Probl. Razrab. Poleznyh Iskopaemyh, 5, 92-96.

123. Rodionov, V. N., A.A. Spivak, V.M. Tsvetkov (1981). Method opredeleniya fil'tratsionnyh svoistv gornyh porod (Method of determining of the filtration properties of rocks), Fiz. Tekhn. Probl. Razrab. Poleznyh Iskopaemyh, 1, 27-33. *Similar article is available in English*: Rodionov, V. N., A.A. Spivak, V.M. Tsvetkov (1979). Change in the permeability of a medium in the inelastic deformation zone during an underground explosion, Proceedings of the AIRAPT International High Pressure Conference 6, 397-406. Also here (https://inis.iaea.org/search/search.aspx?orig_q=RN:13647987)

124. Rodionov, V. N. and A. P. Sukhotin (1971). Parametry uprugih voln, izluchennyh pri sfericheskom vzryve v metallah s razlichnoi prochnost'yu (The parameters of elastic waves emitted by a spherical explosion in metals with various strengths), Fiz. Goreniya Vzryva, 1, 142-146.

125. Rodionov V. N., and V. M. Tsvetkov (1971). Nekotorye rezul'taty nablyudenii pri podzemnyh yadernyh vzryvah (Some results of observations of underground nuclear explosions), Atomic Energy, 30, 1, 31-36. *Available in English*: Rodionov, V. N., and V. M. Tsvetkov (1971). Some results of observations of underground nuclear explosions, Soviet Atomic Energy, 30, 1, 35-40

126. Romm, E.S. (1966). Fil'tratsionnye svoistva treshchinovatykh gornykh porod (Filtration properties of fractured rocks), Nedra, Moscow, 284 pp. *Available in English*: Romm, E.S. (1972). Fluid flow in fractured rocks, Phillips Petroleum Company, ?pp

127. Rulev, B.G. (1968). Dinamicheskie kharakteristiki seismicheskih voln pri podzemnyh vzryvah, Vzryvnoe delo (Explosive Engineering), Nedra, Moscow, 64/21, 109-158. *Available in English*: Rulev, B.G. (1974). Dynamic Characteristics of Seismic Waves During Underground Explosions, FOREIGN TECHNOLOGY DIV WRIGHT-PATTERSON AFB, OH, 66 pp. (http://www.dtic.mil/dtic/tr/fulltext/u2/779837.pdf)

128. Ruppeneit, K.V. (1975). Deformiruemost' massivov treshchinovatykh gornykh porod (Deformations [deformability] of fractured rock massifs), Nedra, Moscow, 223 pp.

129. Rybin, V.V. and A.A. Zisman (1986). Vnutrennie napryazheniya I povrezhdaemost' plasticheski deformiruemyh geterogennyh materialov (Internal stress and damage of plastically deformed heterogeneous materials), Fizika I mekhanika rarusheniya kompozitsionnyh materialov, Fiz. Tekhn. Institute A.F. Ioffe, 4-19.

130. Sadovskii (Sadovskiy) (1979). Estestvennaya kuskovatost' porod (Natural rock fragmentation), Izvestiya - Academy of Sciences, USSR, Physics of the Solid Earth, 247, 4, 929-931. *Similar article is available in English*: Sadovskii (Sadovskiy), M. A., L.G.

Bolkhovitinov and V.F. Pisarenko (1982). Discreteness of rocks, Izvestiya - Academy of Sciences, USSR, Physics of the Solid Earth, 18, 12, 919-929.

131. Sadovskii (Sadovskiy) M.A. (1983). O raspredelenii razmerov tverdyh otdel'nostei (On fragment size distribution), Izvestiya - Academy of Sciences, USSR, Physics of the Solid Earth, 269, 1, 69-72.

132. Sadovskii, M.A. (1987).Seismika vzryvov I seismologiya (Seismics of Explosions and Seismology), Izvesiya Akad. Nauk SSSR, Ser. Fiz. Zemli., 11, 34-42.

133. Sadovskii, M.A. and V.V. Adushkin (1988). Vliyanie nagretogo sloya na parametry udarnoi volny (Effect of a heated boundary layer on the parameters of a shock wave), Dokl. Akad. Nauk SSSR, 300, 1, 79-83.

134. Sadovskii, M. A., Adushkin, A. A., Spivak, A. A. (1989). O razmere zon neobratimogo deformirovaniya pri vzryve v blochnoi srede (on the dimension of zones of irreversible deformation due to an explosion in a block medium.), Doklady Academy of Sciences USSR, Fiz. Zemli , 9, 9-15

135. Sadovskiy, M. A., O. K. Kedrov, V. A. Laushkin and Pasechnik, I. L.(1985a). Seismic effect of underground blasts and problem of estimating total earthquake energy, Dokl. Akad. Nauk SSSR (Moscow), 281, 4, 825-829. (May have been translated to English http://adsabs.harvard.edu/abs/1985RpESc.....37S)

136. Sadovskii, M. A., O. K. Kedrov, I. P. Pasechnik (1985). O seismicheskoi energii I ob'eme ochagov pri korovyh zemletryaseniyah I podzemnyh vzryvah (On the seismic energy and volume of foci in crustal earthquakes and underground explosions), Dokl. Akad. Nauk SSSR, 283, 1153-1156

137. Sadovskii, M. A., Pisarenko, V. F., Shteinberg, V. V. (1983) On the dependence of earthquake energy on the volume of the seismic focus. Dokl. Akad. Nauk SSSR 271: pp. 598-602

138. Sadovskii, M. A. and V. N. Kostyuchenko (1974). O seismicheskom deistvii podzemnyh vzryvov (On Seismic Effect of Underground Explosions), Doklady - Academy of Sciences, USSR, 215, 5, 1097-1100. *Similar publication available in English*: Sadovskii, M. A., V. N. Kostyuchenko, G.A. Sobolev and L.B. Slavina, L B. (1974). Effect of Underground Explosions and Changes in Properties of a Medium in a Seismically Active Region, Performer: Joint Publications Research Service, Arlington, Va. 29 Jul 1974, 17pp.

139. Sedov, L.I. (1993) Similarity and Dimensional Methods in Mechanics. CRC Press, Boston.

140. Seismic treaty monitoring [?], Mir, Moscow, 216 pp.

141. Shkolnik V.S. (2002). The Semipalatinsk test site: creation, operation and convention, Sandia National Laboratories, SAND 2002, 3612 pp.

142. Sizov, I.A, A.A. Spivak and V.M. Tsvetkov (1974). Povedenie sredy v zone razrusheniya pri vzryve zaryada VV (Medium response in the crush [damage] zone due to a chemical explosion). Physics of burning and explosion, 3, 437-440. *Available in English*: Sizov, I.A, A.A. Spivak and V.M. Tsvetkov (1974). Behavior of the medium in the destruction zone during an explosion, *Combustion, Explosion and Shock Waves*, 10, 3, 380-382.

143. Spivak, A.A. (1973). Volny szhatiya v tverdoi srede pri vzryve malozaglublennogo zaryada (The compressional waves in the solid medium due to an underburied chemical explosion), Physics of burning and explosion, 2, 263-268. *Available in English*: Spivak, A.A. (1973). Compression waves in a solid medium associated with the explosion of an explosive material in an air cavity, Combustion, Explosion and Shock Waves, 9, 2, 225-228.

144. Spivak, A.A. (1974). Volny szhatiya v tverdoi srede pri vzryve VV zaryada v vozdushnoi polosti (The compressional waves in the solid medium due to a chemical explosion in an air-filled cavity), Physics of burning and explosion, 3, 440-444.

145. Spivak, A.A. (1978). Osobennosti vzryvnogo dvizheniya tverdoi sredy pri izmenenii parametrov istochnika (Characteristics of the explosive motion of a solid medium resulted from measurement of the parameters of the source), Physics of burning and explosion, 2, 126-130. *Available in English*: Spivak, A.A. (1978). Special characteristics of the explosive motion of a solid medium with measurement of the parameters of the source, Physics of burning and explosion, 14, 2, 239-243.

146. Spivak, A.A. (1980a). Otsenka narushennosti gornogo massiva po rezul'tatam fil'tratsionnyh ispytanii (Estimate of damage to the rock massif using the results of hydraulic testing), Gornyi Zhournal (Mining Journal), 5, 29-35.

147. Spivak, A. A. (1980b). Behavior of the medium affected by an underground explosion, Fiz. Tekh. Probl. Razrab. Polezn. Iskop., 4, 48-55.

148. Spivak, A.A. (1980c). Podobie dvizheniya tverdoi sredy pri izmenenii plotnosti zaryazhaniya vzryvnogo istochnika (The similarity of motion of the solid medium with variation of the loading [charge] density of the explosion source), Physics of burning and explosion, 1, 116-120.

149. Spivak, A.A. (1982). Povedenie sredy pri samoproizvol'nom razrushenii (Medium behavior during rock burst [spontaneous destruction]), Fiz. Tekhn. Probl. Razrab. Poleznyh Iskopaemyh, 4, 51-56.

150. Spivak, A.A. (1983).Vliyanie parametrov vzryvnogo istochnika na seismicheskoe deistvie podzemnogo vzryva (The effect of the parameters of the explosion source on seismic waves in the solid medium), Seismology of Industrial Explosions, Nedra, Moscow, 84-88 (Mining Engineering, 85/42).

151. Spivak, A.A. (1987). Fizicheskie osnovyprimeneniya krupnomasshtabnyh vzryvov v geotekhnologii (Physical basis of using large explosions in geotechnical engineering), Kompleks. Ispol. Miner. Syr., 5, 11-15.

152. Spivak, A.A. (1993). Aftershocks of a powerful underground explosion in an inhomogeneous medium. Dokl. Ross. Akad. Nauk 329: pp. 435-437.

153. Spivak, A.A. (1999a). Differential Motions of Block Structures under External Effects [external loading], Geoekologiya, 1999, no. 1, pp. 62–76 [Environmental Geosci. (Engl. Transl.), 1999, vol. 2, no. 1, pp. 78–91].

154. Spivak, A.A. (1999a). Osobennosti razrusheniya geologicheskoi sredy krupnomasshtabnym vzryvom pri nalichii tektonicheskih narushenii (Damage [fragmentation] of geological medium with tectonic faults [discontinuities/fractures] by a large explosion), *Fizicheskie problemy razrusheniya massivov gornyh porod*, RAN, Moscow, 80-84.

155. Spivak A.A. and Yu. V. Kondrat'ev (1979). Vliyanie plotnosti zaryazhaniya VV na parametry vzryvnogo vozdeistviya v tverdoi srede (The effect of the loading density of explosive charges on blast parameters in solid medium), Fiz.-Tekh. Probl. Razrab. Polezn. Iskop., 1, 36-42.

156. Spivak, A.A., Svintsov, I. S. (1982). A device for determining permeability of a rock massif. Explosive Engineering. Nedra, Moscow, pp. 71-88

157. Spivak, A.A. and V.G. Spungin (1990). Deformirovanie tverdoi sredy pri vzryve s protyazhennym ekranom (Deformation of the solid medium due to an explosion with extensive hollow screen [gap]), Deistvie Vzryva v Neodnorodnoi Srede, Nedra, Moscow, 42-53. (Mining engineering, 90/47).

158. Spivak, A. A., V.G. Spungin and I.L. Postnikov (1990). Deformirovanie strukturno-neodnorodnogo massiva gornyh porod pri podzemnom vzryve (Deformation of a structurally heterogeneous rock massif due to an underground explosion), Deistvie Vzryva v Neodnorodnoi Srede, Nedra, Moscow, 97-101. (Mining engineering, 90/47).

159. Spivak, A.A. and V. M. Tsvetkov (1973). O vzryve v tverdoi srede tipa gornoi porody (Blasting in solid rock [I don't like the expression "solid medium of rock type" or "such as rock"), Fiz. Tekhn. Probl. Razrab. Poleznyh Iskopaemyh, 5, 37-42. *Available in English*: Spivak, A.A. and V. M. Tsvetkov (1973). Blasting in a solid medium of the rock type, Soviet Mining, 9, 5, 496-499.

160. Spivak, A.A. and A.K. Chernyshev (1996). Concept of regional seismic monitoring to control compliance with the CTBT, in Federal Service of Seismological Observations and Earthquake Forecast, Moscow, 1/2. 118-121.

161. Handbook on Explosive Work in Construction [in Russian], Gostroiizdat, Moscow (1962), 392 pp. [In Russian]

162. Sultanov, D. D. (1996). Seismic Observations of UNTs on the NZTS, (in Russian),The Problems of Seismic Monitoring of Underground Nuclear Explosions. Federal System of Seismological Observations, 3, 23–26 (Moscow, 1996).

163. Taganov, G.I. (1968). Teoriya teplogo sloya Theory of dissipative ??? layer), Transactions, Vsesoyuznyi S'ezd po Teoreticheskoi I prikladnoi mekhanike, Nauka, Moscow.

164. Taylor, D.W. (2013). Fundamentals of soil mechanics, Literary Licensing, LLC, 714 pp, (Available from: http://www.amazon.com/Fundamentals-Soil-Mechanics-Donald-Taylor/dp/1258768925).

165. Trebin, G.F. (1953). Eksperimental'nye issledovaniya rezhimov techeniya zhidkosti I gaza v poristoi srede (Experimental studies of liquid and gas flow regimes in porous medium), GosTopTekhizdat, 3, 33-39.

166. Wilkins, M. L. (1967) Calculation of elastoplastic flows. Computational Methods in Fluid Dynamics. Mir, Moscow, 212-263. [It may have been a Russian translation]

167. Fedorenko, P.I. and I.N. Kovtun (1977). Issledovanie vliyaniya formy i razmerov kompensatsionnyh prostranstv na kachestvo drobleniya pri skvazhinnoi otboike rudy (Study of the effect of the size and shape of compensation al space on the quality of rock fragmentation in borehole [?] mining), Fiz. Tekhn. Probl. Razrab. Poleznyh Iskopaemyh, 1, 38-42.

168. Feller, W. (1968). An Introduction to Probability Theory and Its Applications (in English), Vol. 1, 3rd Edition, Wiley, 509 pp. *A different edition*: Feller, W. (1971). An Introduction to Probability Theory and Its Applications, Vol. 2, 2nd Edition, Wiley, 669 pp.

169. Loborev, V M, Zamyshlyaev, B V, Maslina, E P, Shilobreev, B A editors (1997). Fizika yadernogo vzryva (Physics of Nuclear Explosion), 2 Volumes. Fizmatgiz, Moscow, 528 pp. [There are newer editions and there might be up to 5 volumes now, but I suspect they are all in Russian].

170. Khakala, V.V. (1971). Osedanie poverhnosti vyzvannoe podzemnym vzryvom (Ground subsidence caused by an underground explosion), Mechanics, 4, 150-168.

171. Khanukaev, A. N. and V. P., Belyatskii (1974). Issledovanie blizhnei zony vzryva v gornyh porodah(Study of the near-source zone for underground explosions), Fiz-Tekh. Probl. Razrab. Polezn. Iskop., 2, 45-49.

172. Khanukaev, A. N., V. A. Borovikov, and V. P., Belyatskii (1979). Opredelenie ostatochnogo davleniya pri kamufletnom vzryve sfericheskogo zaryada v gornoi porode (Determining the residual pressure in the underground explosion of a spherical charge in a rock), Vzryvnoe delo (Explosive Engineering), Nedra, Moscow, 81/38, 95-98.

173. Khristianovich, S.A. (1998). Izbrannye raboty (Selected works [publications]), Nauka, Moscow, 2 volumes [?].

174. Khristoforov, B.D., L .D. Livshits and I.V. Belinskiy (1971). Vliyanie poristosti na parametry dinamicheskogo szhatiya NaCl (Influence of the porosity on the parameters of dynamic compression of NaCl), Izvestiya - Academy of Sciences, USSR. Physics of the Solid Earth, 8, 31-40. *Available in English*: Khristoforov, B.D., L .D. Livshits, I.V. Belinskiy and A.N. Averin (1972). Influence of the porosity on the parameters of dynamic compression of NaCl, Izvestiya - Academy of Sciences, USSR. Physics of the Solid Earth, 8, 549-554.

175. Khristoforov, B. D. and L.N. Romashov (1967). Opredelenie parametrov volny szhatiya v skal'nom grunte (Determination of compression wave parameters in rock), Fizika Goreniya i Vzryva (Combustion, Explosion and Shock Waves), 1, 137-142. *Available in English*: Khristoforov, B. D. and L.N. Romashov (1967). Determination of compression wave parameters in rock, Combustion, Explosion and Shock Waves, 3, 1, 87-90.

176. Chronology of nuclear tests conducted in the USSR in 1945 – 1990 at the Novaya Zemlya Test Site, History of the Nuclear Project, RNI "Kurchatovskii Institut", Moscow, 6/96, 131-140. [Couldn't find this publication to verify the authors etc]

177. Tsvetkov, V.M., B. G. Lukishov, and L. D. Livshits (1979). Formirovanie oskolkov pri droblenii khrupkoi sredy v usloviyah vsestoronnego szhatiya (Fragment formation in crushing a brittle medium under hydrostatic compression), Fiz.-Tekh. Probl. Razrab. Polez. Iskop. , 3, 46-51. *Possibly available in English*: Tsvetkov, V.M., B. G. Lukishov, and L. D. Livshits, Fragment formation in crushing a brittle medium under hydrostatic compression. Journal of mining science, 15, 3, 228-232.

178. Tsvetkov, V.M., I.A. Sizov, and A.D. Polikarpov (1977). O povedenii hrupko razrushaemoi sredy pri kamufletnom vzryve (Behavior of brittle medium damaged by a fully contained explosion [Brittle damage to the medium due to a fully contained explosion]), Fiz. Tekhn. Probl. Razrab. Poleznyh Iskopaemyh, 4, 36-42. *Somewhat similar publication available in English*: Tsvetkov, V.M., I.A. Sisov, and N.M. Syrnikov (1977). On fracture mechanism of rocks by explosion, New York, N.Y., United States (USA), Pergamon Press, 1977.

179. Chadwick, P., A. D. Cox and H. G. Hopkins (1964). Mechanics of Deep Underground Explosions, Royal Society of London. Philosophical transactions. Series A, Mathematical and physical sciences, Vol 256, 235-300.

180. Chernikov, A. G. (1976 or 1967) The effect of hydrostatic pressure on the rate and radius of fracturing in an organic glass explosion, The Mechanism of Rock Fracturing. Institute of Mining, Siberian Department, Academy of Sciences of the USSR, Novosibirsk.

181. Scheidegger, A.E. (1960). The Physics of Flow Through Porous Media , The Macmillan Company; 2nd edition, 330 pp.

182. Scheidegger, A.E. (2013). Principles of Geodynamics, Springer, Softcover reprint of the original 3rd ed. 1982, 398 pp.

183. Nuclear Tests in the USSR (1997 – 2000). Vol. 1 – 4 [in Russian], Inst. Exp. Phys., Sarov (1997-2000).

The references below are cited in English:

1. Adushkin V.V. (2001). Yield estimation for Semipalatinsk underground nuclear explosions using seismic surface-wave observations at near-regional distance, Pure and Appl. Geophys., 158, 2217-2226.
2. Adushkin V.V., I.O. Kitov, O.P. Kuznetsov et al (1993). Seismic efficiency of decoupled nuclear explosions, Geophys. Res. Lett., 20, 16, 1695-1698.
3. Adushkin, V.V. and A.A. Spivak (1996). Characterization of the aftershocks emission caused by underground nuclear explosions, J. Earthquake Predict. Res., 5, 4, 443-469.
4. Afrouz, A. and J. Harvey (1974). Rheology of Rocks Within the Soft to Medium Range. Int. J. Rock Mech. Min. Sci., 11, 281-290.
5. Allen, R. T. and R. E. Duff (1969). Effect of material properties on cavity size from an underground nuclear explosion, Nuclear Appl., 6, 6, 95—111.
6. Anderson B.D. (1970). A simple technique to determine the size distribution of nuclear crater fallback and efecta. - Proc. Symp. Eng. Nucl. Explos., Las Vegas, NE, 1726-1745.
7. Archer C.B. and N.J. Allen (1969). A cataloque of earthquakes in the lake Kariba area, 1959-1968. - Meteorological Services, Salisbary,.
8. Aussedat, G., M. Boulon and J. Gautier (1969). Craters crees par depetites charges d'explosifs chiniques dans le sable: Programme Dynasol, Centre d'etudes Nucl. De Grenoble Lab. D'applications Speciales de la Physique, Grenoble.
9. Ave, K. (1979). Site of great earthquakes of 1837 – 1974 inferred from tsunami date, J. Geophys. Res., 84, B4, 1561-1568.
10. Beers R.F. Project Shoal. Analysis of Shoal data on ground motion and containment. Iivermore: U.S. Atomic Energycomm., 1965. - 42 p.
11. Blake, F.G. (1952). Spherical wave propagation in solid media, J. Acoust. Soc. Amer., 2, 211-220.
12. Blume, J.A. (1969). Response of highrise buildings to ground motion from underground nuclear detonations, Bull. Seism. Soc. Amer., 6, 2343-2370.

13. Boardman, C. R. (1970). Engineering effects of underground nuclear explosions, in Proceedings - Symposium on Engineering with Nuclear Explosives: American Nuclear Society and U.S. Atomic Energy Commission Report CONF-700101, 1, 43-67.

14. Boardman, C. R., D.D. Rabb and R.D. McArthr (1964). Response of four rock media to contained nuclear explosions, J. Geophys. Res., 69, 16, 3457-3470, DOI: 10.1029/JZ069i016p03457.

15. Boardman, C. R. and J. Scrove (1966). Distribution of fracture permeability of granitic rock mass following a nuclear explosion, J. Petrol. Technol., 5, 619-623.

16. Brooks, D. and B.D. Anderson (1970). A simple technique to determine the size distribution of nuclear crater fallback and ejecta, Prop. Symp. Eng. Nucl. Explos., Las Vegas, NE, Springfield, Volume 2, 1726-1745.

17. Chabai, A.J. (1970). Scaling Dimensions of Craters Produced by Buried Explosions, J. Geophys. Res., 70, 20, 5075-5098, DOI: 10.1029/JZ070i020p05075.

18. Charlie, W.A., J. Shinn and S. Melzer (1979). Blast induced soil liquefaction, Proc. II US Nat Conf. Earthuake Eng., Stanford, CA, 1979, Berkeley, 997-1005.

19. Cheatham, J.B. (1968). Rock breakage by crushing, blasting and drilling, Eng. Geol., 5, 591-602.

20. Cherry, J.T. (1967). Computer calculation of explosion-produced craters, Intern. J. Rock Mech. And Mining Sci., 1, 1-22.

21. Closman, P.J. (1969). On prediction of cavity radius produced by an underground nuclear explosion, J. Geophys. Res., 74, 15, 3935-3939, DOI: 10.1029/JB074i015p03935.

22. Coffer, H.F., B.G. Bray and C.F. Knutson (1964). Application of nuclear explosives to increase effective well diameters, Proc. 3rd Plowshare Symp. Eng. Nuc. Explos., US Atom. Energy Comm., Las Vegas, NV, 269-288.

23. Crowley B.K. and L.S. Germain (1971). Energy released in the Benham aftershocks, Bull. Seism. Soc. Am., 61, 5, 1, 1293-1301.

24. Data Summary of US Underground Nuclear Explosions, 1961 – 1970, Ibid. 1972 [Not sure what this reference is]

25. Delort, F. (1970). Dimensional analysis for the mechanical effects of some underground explosions, Proc. Symp. Eng . Nucl. Explos., Volume 2, Las Vegas, NV, 1386-1405.

26. Derlich S. (1970). Underground nuclear explosion effects in granite rock fracturing, Proc. Symp. Eng . Nucl. Explos., Las Vegas, NV, 505-518.

27. Denny, M. D., and D. M. Goodman (1990). A case study of the seismic source function: Salmon and sterling reevaluated, J. Geophys. Res., 95(B12), 19705–19723, doi:10.1029/JB095iB12p19705.

28. Dickey D.D., F.A. McKeown and R.C. Bucknam (1972). Preliminary results of ground deformation measurements near the Cannikin explosion, Bull. Seism. Soc. Amer., 62, 6, 1505-1518.

29. Duncan, J. M., Witherspoon, P. A., Mitchell, J. K. (1972) Seepage and Groundwater Effects with Explosive Cratering. Depart. Civil. Eng. Inst. Univ. of California, Berkley, 126 pp.

30. Engineering with nuclear explosions, Proc. 3rd Plowshare Symp. Eng. Nucl. Explos., April 1964, US Atomic Energy Comm., Las Vegas, NV, 462 pp.

31. Favreau, R. F. (1969). Generation of strain waves in rock by an explosion in a spherical cavity, J. Geophys. Res., 74(17), 4267–4280, doi:10.1029/JB074i017p04267.

32. Glenn, L. A. (1993). Energy-density effects on seismic decoupling, J. Geophys. Res., 98(B2), 1933–1942, doi:10.1029/92JB02278.

33. Glenn, L. A., M. D. Denny and J. A. Rial (1987). Sterling revisited: The seismic source for a cavity-decoupled explosion, Geophys. Res. Lett., 14, 11, 1103-1106.

34. Glenn, L. A., and P. Goldstein (1994). Seismic decoupling with chemical and nuclear explosions in salt, J. Geophys. Res., 99(B6), 11723–11730, doi:10.1029/94JB00497.

35. Hansen SM., Lager A.R. How to make are from marginal deposites. - Eng. and Mining J., 1968, No 12, p. 75-81.

36. Helle, H. B. and E. Rygg (1984). Determination of tectonic release from surface waves generated by nuclear explosions in eastern Kazakhstan, Bull. Seism. Soc. of Am., 74(5), 1883-1898.

37. Hennet C.B. and G.E. Van der Vink (1996). Multi-use stations offer strong deterrent to clandestine nuclear weapons testing, EOS Trans. Amer. Geophys. Union, 77, 31, 289-301.

38. Herbst, R. F., G. C. Werth, and D. L. Springer (1961). Use of large cavities to reduce seismic waves from underground explosions, J. Geophys. Res., 66(3), 959–978, doi:10.1029/JZ066i003p00959.

39. Higgins, G. H. (1970). Nuclear explosions data for underground engineering application, Peaceful nuclear explosions, Vienna, IAEA, 111-122.

40. Higgins, G. H., and T. R. Butkovich (1967). Effect of water content, yield, medium, and depth of burst on cavity radii, Lawrence Radiat. Lab. Rep. UCRL-50203, Livermore, California.

41. Houser F.N. (1969). Subsidence related to underground nuclear explosions, Nevada Test Site, Bull. Seism. Soc. of Am., 59, 2231-2251.

42. Johnson, G. W., G. H. Higgins, and C. E. Violet (1959). Underground nuclear detonations, J. Geophys. Res., 64(10), 1457–1470, doi:10.1029/JZ064i010p01457.

43. Johnson, G. W. and G. H. Higgins (1965). Engineering applications of nuclear explosives, Project Plowshare, Rev. Geophysics, 3, 3, 365-385.

44. Jones, H. and A.R. Miller (1048). THe detonation of solid explosives, Proc. Roy. Soc. London, A-194, 480.

45. Kennedy EM., Miller C.E. Underground nuclear explosions. Washington: U.S. Congress, Office of Technology Assessment, 1989, p. 82.

46. Khan, S.A. and O. Gudmundson (2005). GPS analyses of the Sumatra-Andaman earthquake, EOS Trans. Amer. Geophys. Union, 86, 9, 92-94.

47. Knox, J. B., D. E. Rawson, and J. A. Korver (1965). Analysis of a groundwater anomaly created by an underground nuclear explosion, J. Geophys. Res., 70(4), 823–835, doi:10.1029/JZ070i004p00823.

48. Kocharyan, G.G. (1966). Experimental investigations on the dynamic deformation of underground excavations in rock, Proc. Of the 2nd North Amer. Rock Mech. Symp., NARMS'96, Rotterdam, Balkema, 1966, 1559-1566.

49. Krikorian, O.H. (1970). Thermodynamics of the silica-steam system, Proc. Symp. Eng . Nucl. Explos., Las Vegas, NV, 481-492.

50. Lackey, J.A. (1975). Solution mining (in situ leaching), Amdell Bull., 19, 40-61.

51. Latter, A. L., R. E. LeLevier, E. A. Martinelli, and W. G. McMillan (1961). A method of concealing underground nuclear explosions, J. Geophys. Res., 66(3), 943–946, doi:10.1029/JZ066i003p00943.

52. Lomboard D.B. (1961). Plowshare: a program for the peaceful uses of nuclear explosives, Phys. Today, 14, 10.

53. Murphy J.R. (1981). Seismic source function and magnitude determination for underground nuclear detonations, Bull. Seism. Soc. of Am., 71, 1, 223-248.

54. Murphy J.R. and J.A. Lahoud (1969). Analysis of seismic peak amplitudes from underground nuclear explosions, Bull. Seism. Soc. of Am., 59, 6, 2325-2341.

55. Murphey, B. F., and L. J. Vortman (1961). High-explosive craters in desert alluvium, tuff, and basalt, J. Geophys. Res., 66(10), 3389–3404, doi:10.1029/JZ066i010p03389.

56. Slichter, C.S. 1898. Theoretical investigations of the motion of ground waters. US Geological Survey, 19th Annual Report, Part 2, pp. 295–384.

57. Spivak, A.A. (1996). Methods of evading detection by a nuclear explosion monitoring network under special conditions, in Monitoring a Comprehensive Test Ban Treaty, edited by Husebye and Dainty, Kluwer, Dordrecht, The Netherlands.

58. Summary list of previously unannounced tests, US Dept. of Energy, Washington, DC, 1993. [?].

59. Sykes, L.L. and G. Ekstrom (1998). Comparison of seismic and hydrodynamic yield determination for the Soviet Joint Verification experiment of 1998, Proc. Nat. Acad. Sci. US, 86, 3456-3460.

60. Teller, E., W.K. Talley, G.H. Higgins and G.W. Johnson (1968). THe constructive uses of nuclear explosives, McGraw Hill, N.Y., 320 pp.

61. Terhune, R.W., T.F. Stubbs and J.T. Cherry (1970). Nuclear cratering from digital computer, Peaceful Nuclear explosions, Vienna, 415-440.

62. Tewes, H.A. (1970). Results of Schooner excavation experiment, Proc. Symp. Eng . Nucl. Explos., Vol 1, Las Vegas, NV, 306-333.

63. Toman, J. (1970). Results of cratering experiments, Proc. Panel Peaceful Nucl. Explos., Vienna, 345-376.

64. Viecelli, J. A. (1973). Spallation and the generation of surface waves by an underground explosion, J. Geophys. Res., 78(14), 2475–2487, doi:10.1029/JB078i014p02475.

65. Violet, C. E. (1961)., A generalized empirical analysis of cratering, J. Geophys. Res., 66(10), 3461–3470, doi:10.1029/JZ066i010p03461.

66. Vortman, L. J. (1968). Craters from surface explosions and scaling laws, J. Geophys. Res., 73(14), 4621–4636, doi:10.1029/JB073i014p04621.

67. Vortman, L. J. (1969). High explosive chemical cratering, Nucl. Appl. Technol., 7, 291-299.

68. Werth, G., and P. Randolph (1966). The Salmon Seismic Experiment, J. Geophys. Res., 71(14), 3405–3413, doi:10.1029/JZ071i014p03405.

69. White, J. W. (1971). Examination of cratering formulas and scaling methods, J. Geophys. Res., 76(35), 8599–8603, doi:10.1029/JB076i035p08599.